CELEBRATING THE WORK OF PROF. SOURAV PAL: COMPUTATIONAL APPROACHES IN CATALYSIS

EDITED BY: Soumyajit Roy, Sailaja Krishnamurty and Wolfgang Schöfberger

frontiers Research Topics

About Frontiers

Frontiers is more than just an open-access publisher of scholarly articles: it is a pioneering approach to the world of academia, radically improving the way scholarly research is managed. The grand vision of Frontiers is a world where all people have an equal opportunity to seek, share and generate knowledge. Frontiers provides immediate and permanent online open access to all its publications, but this alone is not enough to realize our grand goals.

Frontiers Journal Series

The Frontiers Journal Series is a multi-tier and interdisciplinary set of open-access, online journals, promising a paradigm shift from the current review, selection and dissemination processes in academic publishing. All Frontiers journals are driven by researchers for researchers; therefore, they constitute a service to the scholarly community. At the same time, the Frontiers Journal Series operates on a revolutionary invention, the tiered publishing system, initially addressing specific communities of scholars, and gradually climbing up to broader public understanding, thus serving the interests of the lay society, too.

Dedication to Quality

Each Frontiers article is a landmark of the highest quality, thanks to genuinely collaborative interactions between authors and review editors, who include some of the world's best academicians. Research must be certified by peers before entering a stream of knowledge that may eventually reach the public - and shape society; therefore, Frontiers only applies the most rigorous and unbiased reviews.
Frontiers revolutionizes research publishing by freely delivering the most outstanding research, evaluated with no bias from both the academic and social point of view. By applying the most advanced information technologies, Frontiers is catapulting scholarly publishing into a new generation.

What are Frontiers Research Topics?

Frontiers Research Topics are very popular trademarks of the Frontiers Journals Series: they are collections of at least ten articles, all centered on a particular subject. With their unique mix of varied contributions from Original Research to Review Articles, Frontiers Research Topics unify the most influential researchers, the latest key findings and historical advances in a hot research area! Find out more on how to host your own Frontiers Research Topic or contribute to one as an author by contacting the Frontiers Editorial Office: frontiersin.org/about/contact

CELEBRATING THE WORK OF PROF. SOURAV PAL: COMPUTATIONAL APPROACHES IN CATALYSIS

Topic Editors:
Soumyajit Roy, Indian Institute of Science Education and Research Kolkata, India
Sailaja Krishnamurty, National Chemical Laboratory (CSIR), India
Wolfgang Schöfberger, Johannes Kepler University of Linz, Austria

Table of Contents

Editorial: From "Cosmic Cooking" to Chemistry of the Future: A Collective Dialogue on Chemistry as a Tribute to Prof. Sourav Pal.

Soumyajit Roy[1]*, Sailaja Krishnamurty[2]* and Wolfgang Schoefberger[3]*

[1]Eco-Friendly Applied Materials Laboratory (EFAML), Materials Science Center, Department of Chemical Sciences, Indian Institute of Science Education and Research, Kolkata, India, [2]Physical Chemistry Division, CSIR-National Chemical Laboratory, Pune, India, [3]Institute of Organic Chemistry, Johannes Kepler University Linz, Linz, Austria

Editorial on the Research Topic

Celebrating the Work of Prof. Sourav Pal: Computational Approaches in Catalysis

The Research Topic that you hold in hand was an effort to synthesize a dialogue between Computation and Catalysis so that new insights can be created and new paths paved. It is our view that such dialogue would have been a befitting tribute to Prof. Pal, who has explored, encouraged, and enriched dialogues to create new chemical concepts. The response to this effort is what you are exploring now and what we had the pleasure to curate and edit.

The issue now spans a wide range of explorations: from the early Universe's "cosmic cooking" with insights into chemical reactions from HeH^+ to H_3^+ in a study led by the group of Dash et al., to a contribution investigating the source of background cosmic microwave radiation by the group led by Kumar et al. In doing so they compared their results with previous theoretical calculations and analyzed the sources for rotationally excited CN to be behind background cosmic microwave radiation of about 3 K from the interstellar media.

From the cosmic cauldron, we now move to chemical crucibles in the laboratory. The contributions therein can be broadly grouped into catalytic activation of small molecules like that of CO_2, N_2, and H_2O with an eye to harvesting energy. Agarwal et al. reports the data-driven discovery of 2D materials for solar water splitting. In doing so they employed a conditional variational autoencoder and sampled its latent space to generate several new 2D materials that could likely be effective in carrying out water splitting reactions. The Kumar et al. in their work computationally addresses the solvation of Sc ions with that of water splitting. In another effort, Rohj et al. explores the aspect of ferroelectrics in catalyst design. They demonstrate band gap reduction in $BaTiO_3$ through heterovalent doping for potential photocatalyst design. Moving from water to CO_2 activation, Parmar et al. show the effect of structural details like that of aromatic groups in Mn(I)NNN Pincer complexes on CO_2 activation using density functionals. They demonstrate that placing an aromatic group at C2-C3 carbons of the Mn(I) NNN Pincers leads to an enhanced effect on CO_2 hydrogenation. In another review Dedić et al. gives a very detailed account of the state of the art in the matter of Photo and electrochemical CO_2 activation with metal porphyrinoids. In the matter of N_2 activation the Choutipalli et al. demonstrated the synergy of doping with N_2 fixation at the edges of BN nanomaterials. In the context of NRR the Senthamaraikannan et al. used periodic density functionals and proposed a 2-D type catalytic system that has potential for dinitrogen activation. In another work, Das et al. explore cascade catalysis using SOMs as model catalyst systems to demonstrate first polymerization of aniline and then cascading the product catalyst conjugate as a catalyst for oxidation of nitrite to nitrate and aniline to nitrobenzene. The groups led by Raj et al. further take us to the study of gold catalyzed complementary internal redox process of nitroalkyne with a

DFT study. Das and Chattaraj comparative theoretical account of electrides take us further down to deeper theoretical explorations in the context of small molecule activation. In another work Yang and Cederbaum, 2022 explores the interesting electronic structural properties of an endocircular Li@C16 to indicates its potential as a catalyst candidate in the future. Tamukong and Hoffmann in his work explores the low lying electronic states of a Ni-dimer and shows certain states to be energetically high lying and 'van der Waals like in nature'.

Prof. Pal has contributed significantly to the studies of pristine and doped metal clusters in various oxidative catalytic processes, C-X activation, and small molecule activation, including N_2 activation chemistry. His works on the response properties to multi-reference coupled cluster (MRCC) theory have led to the development of books and book chapters. In this tribute, we have captured the essence of his contribution to chemistry that can nucleate a dialogue on topics ranging from chemistry in the early Universe to the future of our planet with CO_2, N_2 and water acting as feed-stocks for energy.

We hope you find joy as you go through the pages of this issue, and gain as much pleasure we did while curating it.

AUTHOR CONTRIBUTIONS

SR, SK, and WS ideated the issue and wrote the editorial together.

Self-Assembly and Cascade Catalysis by a Soft-Oxometalate (SOM) System

Kousik Das[1], Tingting Yan[2], Shounik Paul[1], Shilun Qiu[2], Teng Ben[2]* and Soumyajit Roy[1]*

[1] Eco-Friendly Applied Materials Laboratory, Department of Chemical Sciences, Indian Institute of Science Education and Research, Kolkata, India, [2] Department of Chemistry, Jilin University, Changchun, China

Cascade catalysis has gained importance due to its various applications. In this work, cascade catalysis was performed using a self-assembled soft-oxometalate (SOM) as a model system. At first, we synthesized an oxometalate (OM) hybrid with a polymerizable organic cation, namely tetrakis(4-aminophenyl)methane, and an OM, $K_8[SiW_{11}O_{39}]$. The hybrid in turn was converted into SOM in water, DMSO mixture, and characterized by different techniques, ranging from electron microscopy to DLS. The SOM state is endowed with the ability to polymerize the aniline based counter ions associated with it in the presence of UV-light. This polymerization is possible due to the presence of photocatalytic OMs (oxometalates) in the SOMs. The polymer-SOM hybrid in cascade oxidizes selectively aniline to nitrobenzene and nitrite to nitrate owing to the residual oxidizing property of the OM constituents in it. This is the first example of cascade catalysis in SOM chemistry.

Keywords: polyoxometalate, self-assembly, polymerization, cascade catalysis, oxidation

INTRODUCTION

Assembly of multicomponent, multifunctional architecture is a challenge. For instance successful assembly of organic-inorganic hybrid material (Hagrman et al., 1999) leads to the emergence of non-linear unusual properties (Kagan et al., 1999; Yin et al., 2012, 2014; Dualeh et al., 2014). The achievement of a successful working design is thus an immediate challenge for chemists. As part of this process, questions emerge, as to whether it is possible to synthesize an inorganic-organic hybrid architecture based on oxometallate. Can such an assembled supramolecular architecture be functional? Here we address these questions, asking more specifically whether is it possible to design an organic moiety and oxometalate (OM) based self-assembly of a soft-oxometalate (SOM). Can such SOM be catalytically polymerized to form a SOM hybrid? Can the resulting SOM hybrid in turn show cascade catalysis? Before we answer these questions we explore the literature and explain our design.

Polyoxometalates (POMs), (Pope et al., 2004) crystalline state of transition metal oxo-clusters (oxometalates) have gained immense research interest due to their tuneable size and morphology, unique electronic properties, and wide range of applications like catalysis, electronics, nano materials, medicine etc. (Wang et al., 2003; Cronin and Müller, 2012; Lv et al., 2012; Wang and Weinstock, 2012). Due to the high oxidation states and photoexcitation properties of transition

metals, polyoxometalates are very efficient and promising catalysts (Kikukawa et al., 2012; Suzuki et al., 2015; Wang and Yang, 2015). They have been used as catalysts for water splitting (Rausch et al., 2014), polymerization (Chen et al., 2013), and several other organic reactions over the past few decades. Our group has also published a series of catalytic reactions with oxometalates in recent years (Thomas et al., 2015; Das et al., 2016a,b,c). Oxometalates have a very unique solution behavior. Depending on their counter ions and volume fraction/concentration (Thomas et al., 2018), pH (Paul et al., 2018) oxometalates can show a heterogeneous/colloidal or soft-matter state, which has been called the soft-oxometalate (SOM) state (Roy, 2011, 2014). Owing to the intrinsic OM constituents in SOMs the latter holds promise to manifest the properties of OMs in higher length scales and bulk. SOMs thus provide a platform to manifest synergistic properties by the judicious assembly of large OMs (like PW_{12} Keggin, Mo_{132}, (Verhoeff et al., 2007) Mo_{154} (Liu et al., 2003), and their counter-ions. To date, self-assembled SOMs have used simple counter-ions like protons, ammonium and alkaline earth metal ions. Such ions leave the chemistry of SOMs dormant. Hence the challenge in SOM-engineering necessitates the judicious choice of OM and counter-ions that can open up the possibilities of new SOM chemistry. If the counter-ions are reactive, redox polymerizable organic ligands like amino-phenyl methane with multiple sites, can open up a host of possibilities for self-assembly. This approach of combining molecular oxometalates with suitable organic moieties to make crystalline POM-organic hybrids has already been explored in the context of crystalline POM chemistry (Zhang et al., 2010; Chen et al., 2013). In this study we adapt this approach to SOM chemistry and demonstrate cascade catalysis for the first time.

As mentioned earlier, the choice of the OM and the organic counter ion in SOMs needs to be judicious. For instance, these units have to be mutually compatible to form SOMs and if the organic counter-ion is polymerizable then the resulting organic polymers can have direct applications (Heeger, 1993; Macdiarmid, 2001). In this regard, it is important to mention some synthetically important networks such as metal organic frameworks (MOF), (Long and Yaghi, 2009), covalent organic frameworks (COF) (Wan et al., 2009), and porous aromatic frameworks (PAF) (Ben et al., 2009; Ren et al., 2010; Xu et al., 2015), etc., which have a well-defined structure and high surface area. The high surface area of such frameworks leads to better catalyst loading and their rigid structure makes them excellent support for heterogeneous catalysis (Dong et al., 2016). Recently, conductive polymers attracted a great deal of interest because of their high electrical conductivity (Shumaila et al., 2011). Among the family of conducting polymers, polyaniline is one of the most exciting polymers, due to its unique electrical conductivity, high environmental stability, and easy synthesis.

For the past few decades, scientists have been synthetically modifying their structure to use them in more commercial applications. There are several techniques of polymerization of such aniline based monomers of which redox polymerization (Kohut-Svelko et al., 2009) is worth mentioning in the present context, as it can utilize a redox-active OM center that can be built in the SOM. This redox polymerization is facile,

attractive, and has a short induction period attracting mild conditions that are conducive to SOM chemistry (Zengin et al., 2002; Fehse et al., 2007).

As mentioned earlier, various methods for the syntheses of oxometalate-organic hybrids have been reported in the literature (Bar-Nahum et al., 2003; Dolbecq et al., 2010). However simple organic ligands have been used in most of these methods and there are very few reports on the reactivity of their side chains (Rieger et al., 2012; Lachkar et al., 2016). There are still questions as to whether it is possible to synthesize an OM-organic hybrid that can catalyze a reaction on its side chain *in-situ*. After assembling the molecular hybrid, is it possible to superstructure the architecture as a SOM? Can the resulting SOM state have catalytic properties? This study addressed these questions by synthesizing a crystalline polyoxometalate-organic hybrid from a photo-redox active lacunary Keggin $K_8[SiW_{11}O_{39}]$ and tetrakis(4-aminophenyl)methane (Uribe-Romo et al., 2009; Liu et al., 2014) with a redox polymerizable aniline side chain which can grow to form a three dimensional polymeric network, and stabilize itself as a SOM and SOM-polymer hybrid. The SOM-polymer hybrid in turn, in the fashion of cascade catalysis, electrochemically oxidizes nitrite to nitrate and aniline to nitrobenzene. Thus, the assembly and cascade catalysis reported in this work has the following steps. First, the assembly of OMs with aniline based counter ions to SOMs; second, the catalytic formation of SOM-polymer hybrid; and third, a cascade catalytic conversion of aniline to nitrobenzene and nitrite to nitrate (**Figure 1**).

RESULTS AND DISCUSSION

This study initially focused on the synthetic aspects of the SOM, using the following steps to investigate the reaction. First, the crystalline molecular POM-organic hybrid is synthesized and self-assembled to SOMs. Then the hybrid is polymerized. Using this polymerized hybrid, cascade catalysis was then performed.

Synthesis and Characterization of OM-Organic Hybrid

The synthesized crystalline polyoxometalate hybrid has two components: tetrakis(4-aminophenyl)methane and $[SiW_{11}O_{39}]^{8-}$. To gain molecular structural insights on this hybrid we crystallized the hybrid (**Figure 2A**). The structure of the model compound shows that each of the oxometalate units is connected to 8 ammonium ions. It is also evident from the structure that in each organic moiety only two of the four $-NH_2$ groups are protonated. The crystal structure also shows two different cavities with a diameter of 6.3 and 7.4 nm (**Figures 2B,C**). This is due to the presence of asymmetric oxometalate units in $[SiW_{11}O_{39}]^{8-}$. These cavities are very important for the stabilization of organic oligomers and the oxometalates present around these cavities facilitate the polymerization reaction that leads to the formation of these oligomers.

This molecular oxometalate-organic hybrid further manifests in a dispersion soft-oxometalate structural state as vesicles.
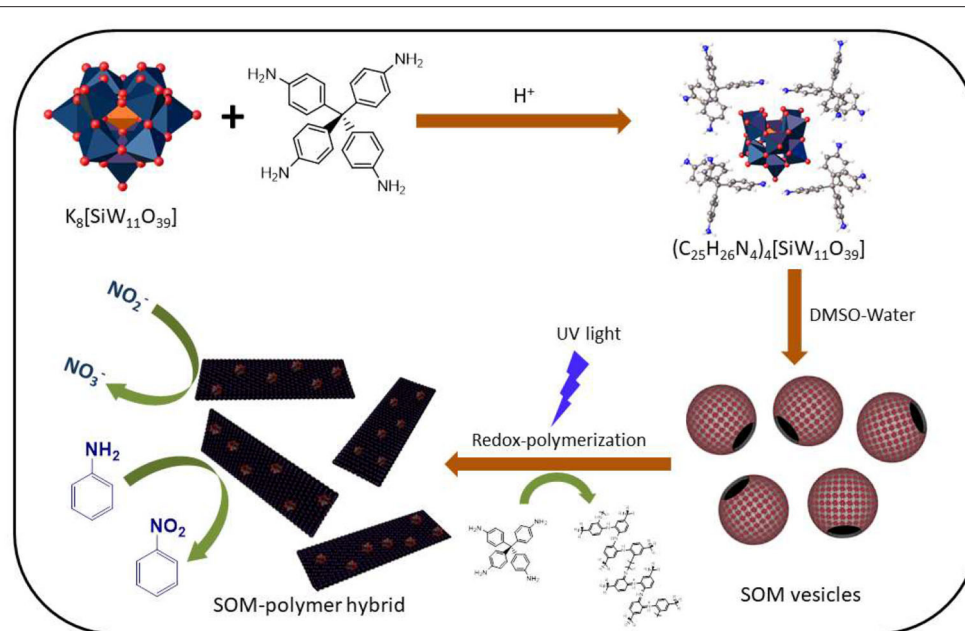
FIGURE 1 | Schematic image of the preparation of $(C_{25}H_{26}N_4)_4[SiW_{11}O_{39}]$ and the polymerization of the organic counter-ion thereafter by silicotungstate.
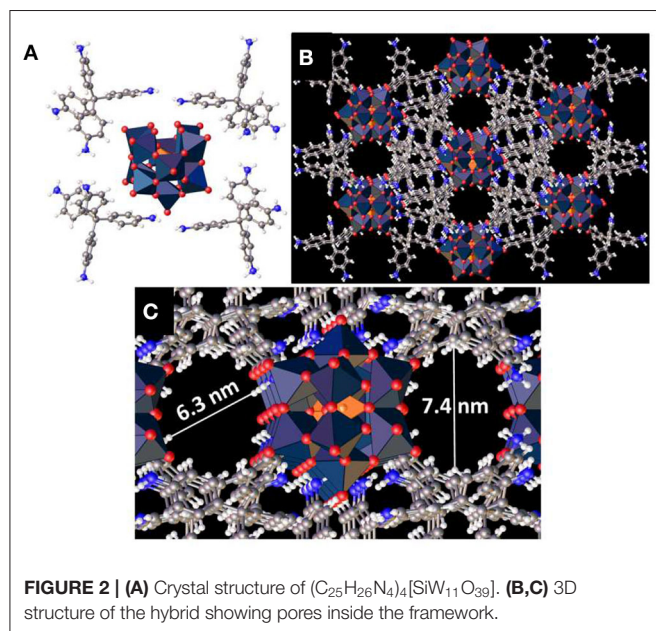
FIGURE 2 | (A) Crystal structure of $(C_{25}H_{26}N_4)_4[SiW_{11}O_{39}]$. **(B,C)** 3D structure of the hybrid showing pores inside the framework.

We assume that the hybrid retains its solid-state molecular architecture in the dispersion (soft-matter state) that facilitates the polymerization reaction in the cavity (Chen et al., 2013). To further analyze the structural integrity of oxometalate as well as the organic ion, we studied the FTIR spectrum of the hybrid. The following characteristic peaks of $[SiW_{11}O_{39}]^{8-}$, 952, 895, 844, and 800 cm^{-1} were found in hybrid oxometalate whereas the characteristic peaks of tetrakis(4-aminophenyl)methane were found at 1,508, 1,427 cm^{-1} (**Figure 3C**).

Preparation of Soft-Oxometalate From the Hybrid

We observed that the molecular hybrid shows an amphiphilic character. It can be easily dissolved in DMSO to make a stable dispersion. A relatively low scattering intensity in the dispersion confirms the absence of any large assemblies and the hybrid remains as a discrete molecular species in solution. Upon the addition of water into the DMSO solution, the solution becomes turbid, which suggests the formation of vesicle like SOM structures in the dispersion. We have characterized the vesicles by DLS and SEM analysis. The hydrodynamic radius (R_h) was measured by DLS (**Supplementary Figure 3**). At 1:9 DMSO water ratio, the vesicle size appears to be ca. 160 nm. In the hybrid structure, the $[SiW_{11}O_{39}]^{8-}$ unit acts as the hydrophilic part and the organic counter ion tetrakis(4-aminophenyl)methane acts as the hydrophobic part. Since the water content is more in dispersion, we believe that in the structure the oxometalate remains on the outer surface whereas the organic part remains on the inner surface.

The size of SOM vesicles was then varied by changing the solvent polarity (Verhoeff et al., 2007). The polarity of the solvent was varied by mixing different amounts of water and DMSO. We found that the vesicle size displayed a linear relationship with the inverse of the dielectric constant of the solvent (**Figure 3B**). This implies that the vesicle size can be varied by controlling the dielectric constant of the medium, implying counter ion condensation stabilizing the dispersion.

FIGURE 3 | (A) SEM image of the hollow vesicles of the hybrid prepared in water, DMSO mixture. **(B)** Plot of soft-oxometalate vesicle radius with respect to the inverse dielectric constant of the solvent mixture. **(C)** Comparison of IR spectra of oxometalate hybrid, tetrakis(4-aminophenyl)methane, and $[SiW_{11}O_{39}]^{8-}$.
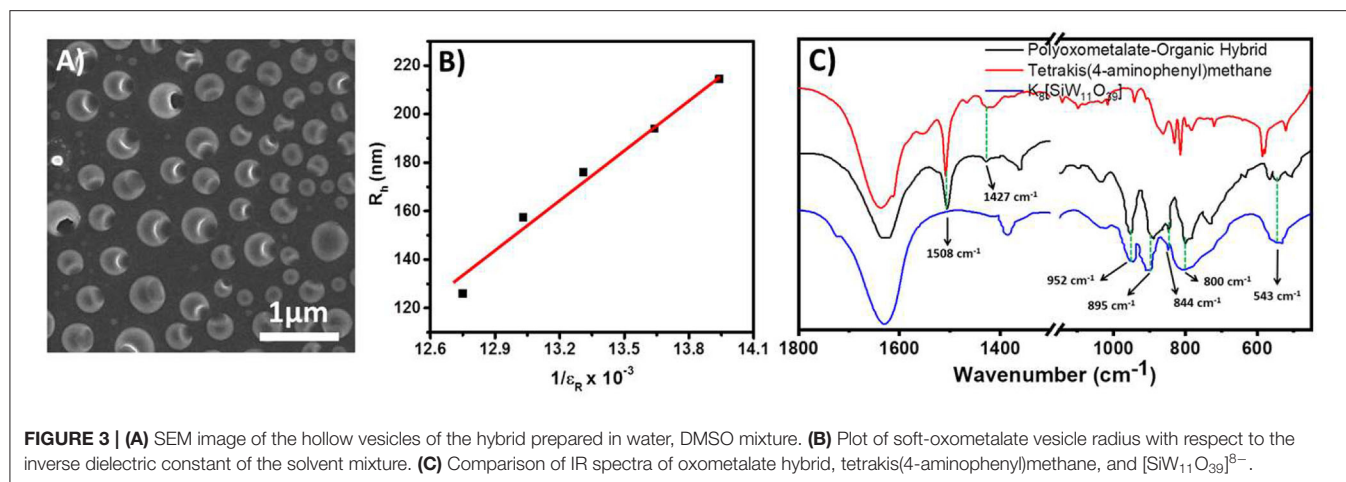
The spherical nature of the vesicle was characterized by SEM analysis. The sizes obtained from SEM images are also consistent with the LS analysis (Du and Chen, 2004; Verma et al., 2005; Leng et al., 2010). Each of the vesicles shows large pores on the surface (**Figure 3A**) at pH 4. We believe that this is due to disruption of the surface during the drying process. However, upon adding a base, the pore(s) on the vesicle surface did not appear (**Figure 4**) (Sandre et al., 1999). The pK_b of aniline moiety was 9.4. At low pH (4.6) the amine group remained at an equilibrium between $-NH_2$ and $-NH_3^+$. Hence the surface of the vesicle was much more labile. With the addition of a base, the pH of the solution increases, and thus the amine groups mainly remained in $-NH_2$ form and it was less prone to disrupt the hard skin of the surface during the drying process (Liu et al., 2005; Jeong et al., 2007).

From the TEM we observed that a SOM hybrid was formed with tetrakis(4-aminophenyl)methane and $[SiW_{11}O_{39}]^{8-}$ (**Figure 5**). The topology is spherical with a uniform molecular level distribution of elemental Si, W, O, N in the mesoscopic SOM structure (**Figure 6B**). We believe that the positively charged ammonium ions behave as an anchor for attaching the negatively charged oxometalates via electrostatic interaction.

In-situ Polymerization of the Hybrid

We then explored whether the hybrid possessed any catalytic properties. Oxometalates are well-known for their photocatalytic properties. Recently, we photo-polymerized monomers like styrene, and acrylic acid, etc., with PW_{12} based polyoxometalate in the presence of UV radiation. This approach polymerizes the monomers via cation-radical polymerization. In the present case, the $[SiW_{11}O_{39}]^{8-}$ also catalyzes the polymerization reaction of the tetrakis(4-aminophenyl)methane monomer in presence of UV-light (**Supplementary Figure 4**). The structure of the hybrid also plays an important role in polymerization. The solid state structure of the hybrid has cavities in it. We believe the hybrid retains its solid state structure in the dispersion (soft-matter state) through the formation of soft-oxometalate. We have previously shown that these cavities stabilize the monomer and facilitate the formation of the polymer (Chen et al., 2013). In this case, also, we believe that the monomers are stabilized in the structural cavity and the oxometalates present in the cavities polymerize

the monomers via photoredox polymerization. Tetrakis(4-aminophenyl)methane has four aniline units in its structure and can be polymerized by an oxidation reaction. The polymerization of the monomer happens in 2 weeks without any catalyst but in presence of oxometalate, the polymerization reaction happens in just 8 h (**Supplementary Figure 8**).

Characterization of the Polymer

The FTIR study showed several new peaks (985, 1,215, 1,322, and 2,576 cm^{-1}) after polymerization. The peaks ranging from 1,570 to 1,600 cm^{-1} occur because of the C=N stretching of the quinoid structure (**Figure 6A**) (Mostafaei and Zolriasatein, 2012).

^{1}H and ^{13}C NMR analysis of the polymer also showed several changes in the spectra, which confirms the polymerization of the monomer (**Supplementary Figures 10–16**). The peaks ranging from 6 to 8 ppm in the ^{1}H spectrum are due to the aromatic protons present in the polymeric structure (**Supplementary Figure 11**) (Yasuda and Shimidzu, 1993). The peaks at 148 and 150 ppm in ^{13}C NMR also confirm the presence of the quinoid structure of the polymer (**Supplementary Figure 16**). The H$^+$ ions present in the solution attach with the nitrogen atoms of the polymer to form ammonium or iminium ions. We believe that this is because the polymer is still charged (ammonium or imminium ion) and the oxometalate remains electrostatically attached to the polymer. This is also evident from the FTIR spectrum of the polymer, which shows both the peaks of the polymer as well as the silicotungstate ion in the resultant polymer hybrid (**Figure 6A**).

The EAS of the polymer shows a peak at 600 nm (**Figure 7B**). This peak corresponds to the blue color of the solution. These observations also suggest that the polymer has an emeraldine structure. The absorption band at 600 nm corresponds to the n-π* transitions of the quinine-imine groups (Yasuda and Shimidzu, 1993; Sapurina and Stejskal, 2008; Liu et al., 2010; Sapurina and Shishov, 2012). The band intensity increases with time, which suggests the formation of more polymeric structures. SOM-polymer hybrid has also been characterized by SEM and TEM (**Figure 7**). From the EDAX mapping of the hybrid (**Figure 8B**), we observed that the OMs are homogeneously
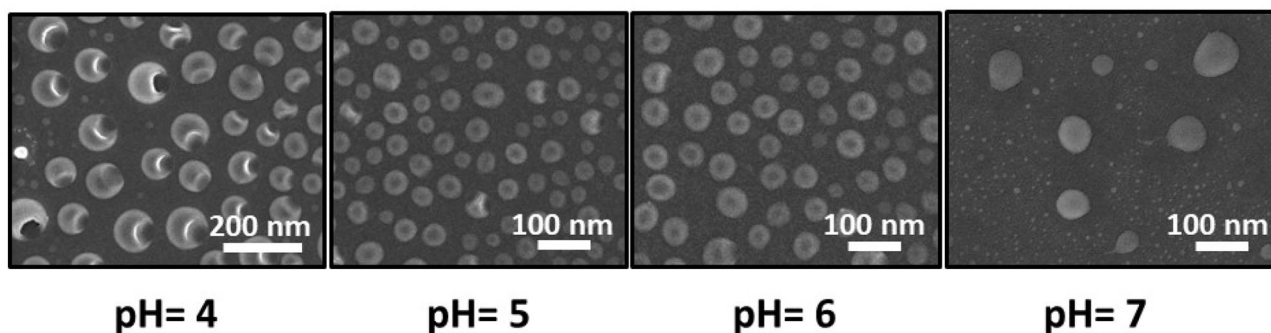
FIGURE 4 | Shape change of the vesicles in different pH. Porous vesicles were observed at ~pH = 4.
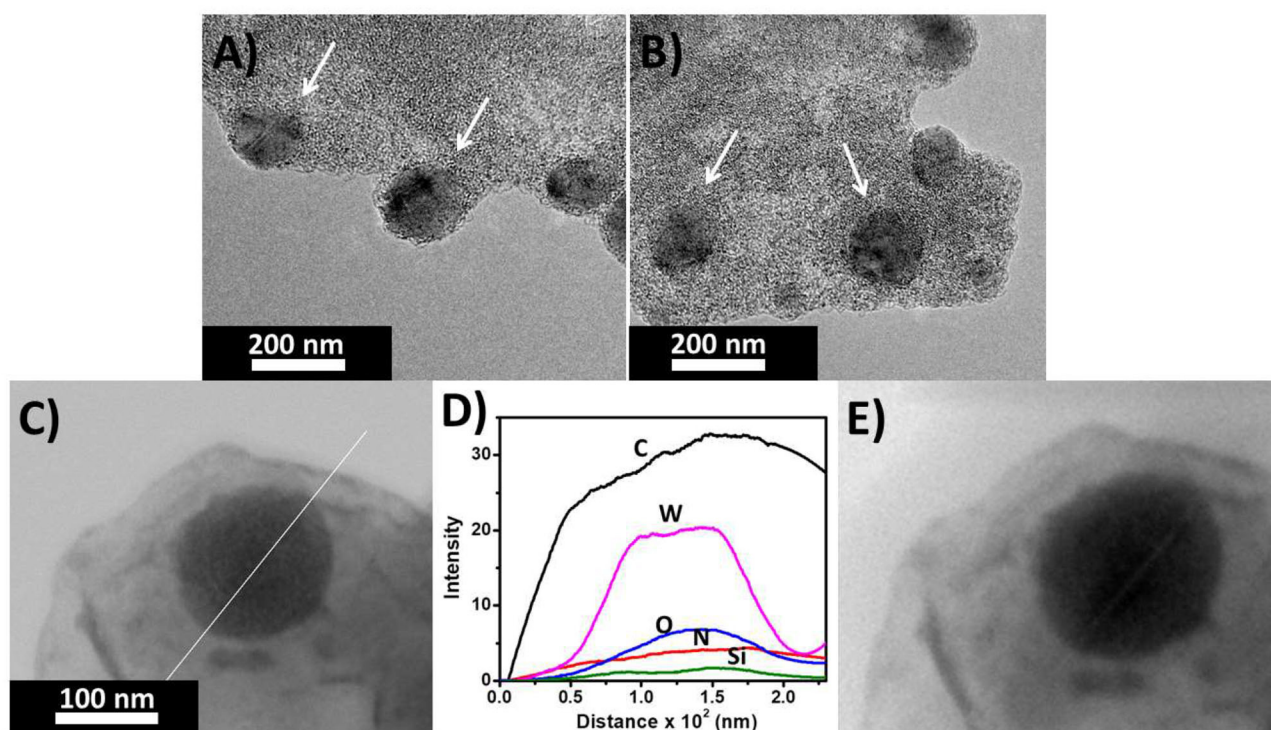
FIGURE 5 | (A,B) TEM image of the SOM vesicles of $(C_{25}H_{26}N_4)_4[SiW_{11}O_{39}]$ **(C)** Line scan image and **(D)** plot of intensity of different elements along the line. **(E)** Beam-damaged image of the hybrid after line scan.

distributed on the polymer surface. To locate the oxometalates in this hybrid polymer, we used porosity measurements. The BET surface areas of the chemically synthesized polymer and that of the SOM-Polymer hybrid are 19 and 14 m^2/g, respectively (**Figure 8A**). We believe that some of the pores present in the polymer are filled by the oxometalates and hence the measured surface area is less in the polymer-oxometalate hybrid.

This study then addressed whether it is possible to change the chain length of the polymer. The chain length variation was achieved by changing the loading of oxometalate in the dispersion. The same amount of monomer was dissolved in five reaction vessels and then a different amount of OM was added to it. The reaction vessels were kept for 1 day to polymerize. The polymers were then separated from the solution

and their chain length and molecular weight were measured by viscometry (**Supplementary Table 2**). The empirical rule of Mark-Houwink relation was used to measure the molecular weight of the polymers (Rana et al., 2011). We observed that the molecular weight, as well as the chain length of the polymer, decreases with the increased loading of oxometalate in the starting SOM (**Table 1**). The plot of the molecular weight of the polymer and loading of oxometalates shows a linear decrease (**Supplementary Figure 9**). This indicates that the polymerization happens via radical pathway. To ensure the operation of the radical pathway in the reaction, we added catechol to the reaction mixture as a radical quencher and the polymerization reaction did not take place in the presence of catechol.

FIGURE 6 | (A) Comparison of IR spectra of the polymer, OM-polymer hybrid, and $K_8[SiW_{11}O_{39}]$. (B) EDAX mapping and elemental percentage of the $(C_{25}H_{26}N_4)_4[SiW_{11}O_{39}]$ hybrid. C, N, O, Si, and W represent carbon, nitrogen, oxygen, silicon, and tungsten, respectively.

FIGURE 7 | (A) SEM image of the polymer prepared from the hybrid. (B) Time dependent EAS of the polymer in DMSO. (C,D) TEM images of the SOM-polymer hybrid.
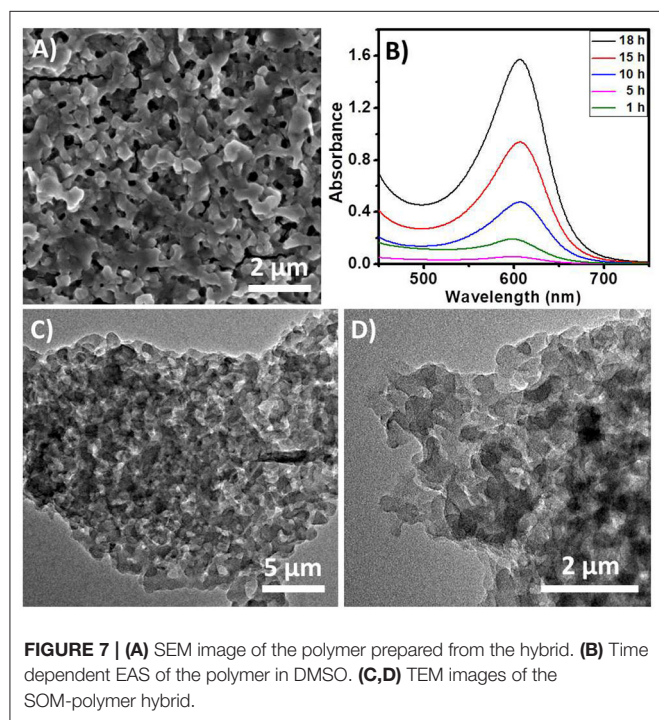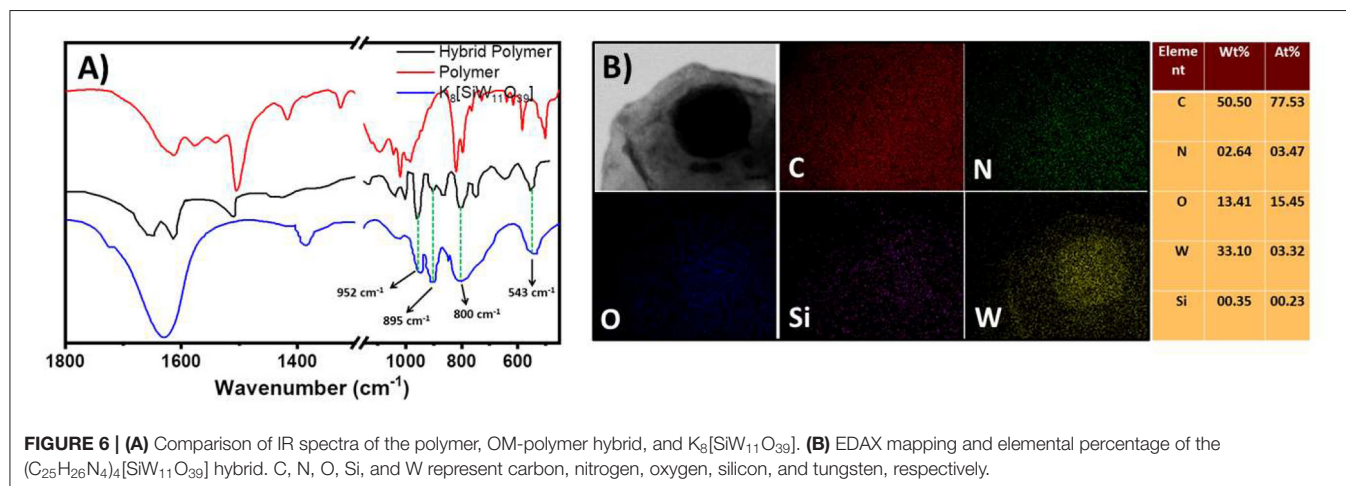
The chain length variation of the polymer is also evident from the different colors of the polymers dissolved in DMSO (**Supplementary Figure 7B**). This was because, as the chain length varies, the number of monomer units vary, and hence the degree of conjugation also varies. The different extent of conjugation in the different polymers leads to different colors of the solution. In electronic absorption spectra (EAS), the intensity of the 578 nm peak also decreases with the increase in polymer chain length (**Supplementary Figure 7A**). This is due to the presence of fewer polymer units in higher chain length polymers. The peak at 460 nm in EAS suggests the formation of the emeraldine of the polymer. We think that with the increase in OM concentration, the acidity of the solution increases, and hence more imine nitrogen gets protonated to give emeraldine salt of the polymer.

Oxidation of Aniline to Nitrobenzene

The selective oxidation of aniline to nitrobenzene is very important in industrial synthesis. The oxidation of aniline leads to several products namely nitrosobenzene, nitrobenzene, azoxybenzene, azobenzene, etc. (Zhu and Espenson, 1995; Priewisch and Rück-Braun, 2005; Tundo et al., 2008; Shiraishi et al., 2014). Although there are various reports in the literature involving aniline oxidation, very few have reported selective oxidation toward nitrobenzene (Meenakshi et al., 2018). Even some polyoxometalates as well as polyoxometalate-organic hybrids have been employed for the oxidation of aniline, although they require harsh reaction conditions and the catalyst has low selectivity and low recovery.

In this article, we have utilized the polymer-SOM hybrid as a catalyst for the oxidation of aniline (**Figure 9**). Due to the presence of redox active W centers and a robust support structure of the polymer network, the polymer-SOM hybrid acts as an excellent catalyst. The reaction was performed in the presence of H_2O_2 at 50°C. In this reaction condition, the polymer-SOM hybrid oxidizes aniline selectively to nitrobenzene. A negligible amount of nitrosobenzene was also detected. All the products were detected in gas chromatography (**Supplementary Figure 5**). To check the role of solvent, the reaction was carried out in different solvents (**Supplementary Table 1**). The catalyst was recovered after each catalytic cycle (**Supplementary Figure 6**). The highest yield was detected in acetonitrile and lowest in H_2O. It should also be noted that a very good yield was also detected in DMSO. However the recovery of the catalyst is low compared to other solvents. An increase in reaction temperature, increases the reaction rate, although a small amount of azoxybenzene was also detected at a higher temperature. At lower temperatures, the reaction rate was comparatively slow. Hence the optimum temperature was set to 50°C. In contrast, the polyoxometalate $(K_8[SiW_{11}O_{39}])$ has less conversion efficiency, and selectivity is also very low in the same reaction condition. It is also worth mentioning that the $(K_8[SiW_{11}O_{39}])$ is very unstable and thus has low recovery (**Table 2**).

By definition, a cascade reaction comprises two steps where the second reaction happens because the chemical change occurs in the first step. In our case, the first step is the polymerization

FIGURE 8 | (A) N$_2$ adsorption–desorption isotherms of polymer and SOM-polymer hybrid. **(B)** EDAX mapping and elemental percentage of the SOM-polymer hybrid. C, N, O, Si, and W represent carbon, nitrogen, oxygen, silicon, and tungsten, respectively.
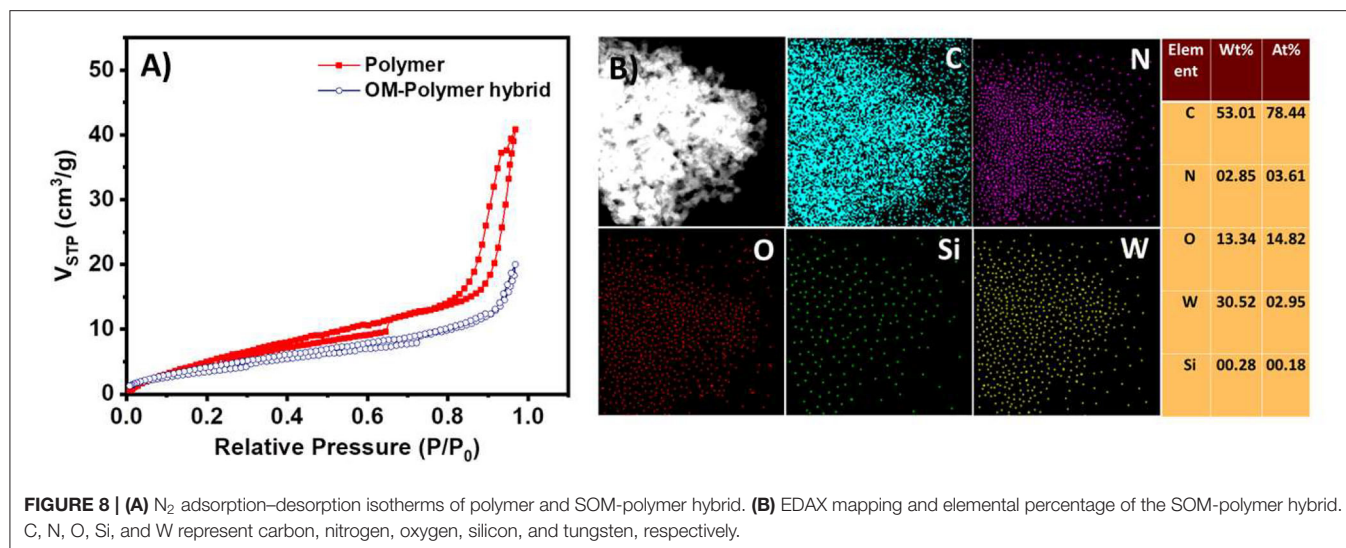
TABLE 1 | Chain length variation of the polymer by changing the amount of catalyst.

Sample no.	Amount of OM (mmol)	Amount of monomer (mg)	Molecular weight (kDa)
1	0.4	1	14
2	0.6	1	9.5
3	0.7	1	8.2
4	0.9	1	6.9
5	1.0	1	1.5

TABLE 2 | Comparison of aniline oxidation[a] to nitrobenzene by different catalysts.

Catalyst	Total conversion (%)	Products (%)		Recovery
		Nitrosobenzene	Nitrobenzene	
SOM-polymer	96	6	94	91
K$_8$[SiW$_{11}$O$_{39}$]	71	78	22	48

[a]Aniline (1 mmol), 30% H$_2$O$_2$ (3 mmol), acetonitrile (5 mL), catalyst (5 mg), 50°C, stirred for 4 h.

FIGURE 9 | Schematic of aniline oxidation by SOM-polymer hybrid in acetonitrile.
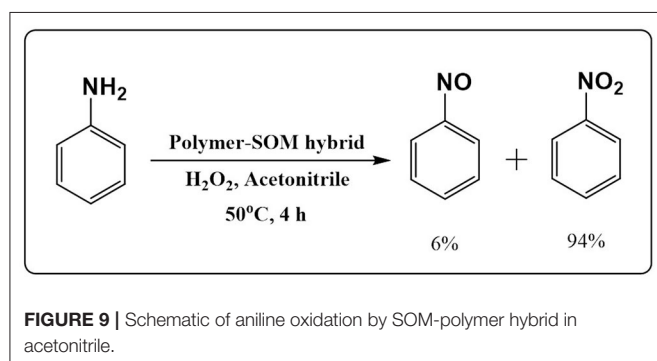
of tetrakis(4-aminophenyl)methane by [SiW$_{11}$O$_{39}$]$^{8-}$ in the presence of UV light. The SOM in-turn transforms into an SOM-polymer hybrid. The second step is the catalysis reaction performed by the SOM-polymer hybrid. The SOM-polymer can oxidize nitrite to nitrate electrochemically or selectively oxidize aniline to nitrobenzene thermally. In both cases, the catalysis does not occur with the SOM or the monomer and oxometalate alone. This is where cascade catalytic property emerges due to the presence of various interactions in the SOM-polymer hybrid. The polymeric network forms during the first photocatalytic experiment and endows the SOM-polymer with an emergent catalytic activity that manifests during the aniline

oxidation and carries out the concluding steps of cascade catalysis during nitrite oxidation. Without the polymeric network, the OM ([SiW$_{11}$O$_{39}$]$^{8-}$) has less stability, low conversion, and poor selectivity toward aniline oxidation.

To check the stability of the catalyst we have performed IR and EAS spectroscopy. After the reaction of aniline oxidation, the recovered catalyst was thoroughly washed with ethanol and water and dried over vacuuo. For IR spectroscopy the powdered catalyst was used, whereas the catalyst was dissolved in DMSO for EAS analysis. Both IR and EAS the spectra of the recovered catalyst did not show any significant changes (**Supplementary Figures 17**, **18**). This confirms that there was no leaching of OMs during the catalysis. The polymer network that is present in the hybrid prevents deterioration of OMs and provides the stability during oxidation of aniline.

Electrochemical Measurements

The electrochemical properties of the hybrid materials were measured in 0.5 M H$_2$SO$_4$ by cyclic voltammetry using the three electrode system. Cyclic voltammetry was carried out in a potential range between −0.2 and 1 V at different scan rates ranging from 10 to 100 mV. **Figure 10A** represents the comparative CVs of different hybrid materials. The CV of the SOM-polymer hybrid shows the characteristic peaks of pure polyoxometalate. The cyclic voltammogram of the pure polymer does not show any noticeable activity. **Figure 10B** represents
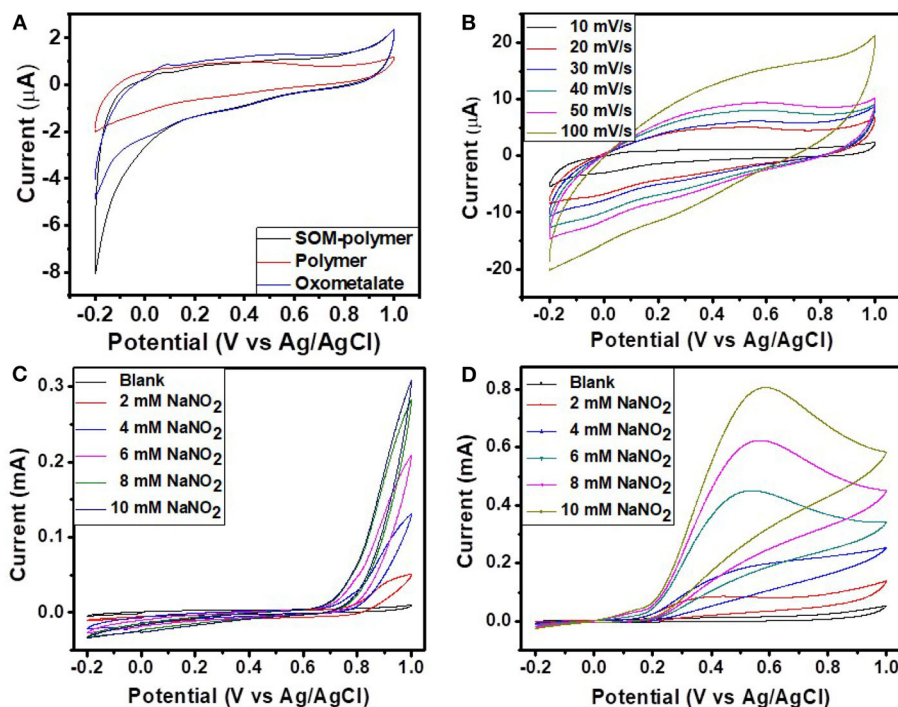
FIGURE 10 | (A) The comparison CVs of SOM-polymer, pure polymer, and pure oxometalate at a scan rate of 10 mV/s. **(B)** The CVs of the SOM-polymer hybrid at different scan rates ranging from 10 to 100 mV/s. CVs of **(C)** pure polymer and **(D)** SOM-polymer hybrid with different amounts of NaNO$_2$. All of the electrochemical measurements were done in 0.5 M H$_2$SO$_4$ using Ag/AgCl as a reference electrode.

the CVs of SOM-polymer hybrid at different scan rates (from 10 to 100 mVs^{-1}). The cathodic and anodic peak current as well as peak separation potential gradually increase with increasing scan rate. The electrochemical stability of the OM-polymer hybrid was also measured. The OM-polymer hybrid electrode was studied under a continuous cycle with a scan rate of 50 mVs^{-1} for 100 cycles. The cathodic and anodic peaks show very little change after the 100th cycle, which indicates very good stability of the hybrid. Compared to the hybrid, pure oxometalate is unstable and easily washed out during the electrochemical measurements.

We then explored whether it is possible to use this hybrid as a catalyst for an important oxidation reaction, the nitrite oxidation reaction. Nitrite is toxic to the human body. It forms nitrosamines and subsequently diazonium ions. The reactive diazonium ions disrupt normal cell function which leads to cell death. Nitrite can be detected by oxidation as well as reduction reaction. Though the reduction of nitrite is a little complicated, the oxidation reaction is pretty straight forward, which produces the only nitrate. Polyoxometalates are well-known for their catalytic activity. There are numerous reports of nitrite oxidation being performed by different catalytic materials but the question remains as to whether the SOM-polymer hybrid electrochemically catalyzes this reaction. In this article, we investigated nitrite oxidation using the SOM-polymer hybrid as a catalyst.

Nitrite oxidation of the SOM-polymer hybrid was performed in 0.5 M H$_2$SO$_4$, applying the potential range of -0.2 V to 1 V at a scan rate of 50 mVs^{-1}. **Figure 10D** is a cyclic

voltammogram of nitrite oxidation reaction with SOM-polymer hybrid at different concentrations of nitrite ranging from 2 to 10 mM. The oxidation peak for the SOM-polymer hybrid was found at around 0.57 V with respect to the Ag/AgCl reference electrode, though peak shift was observed for different concentrations of NaNO$_2$. The SOM-polymer hybrid showed an increase of 0.65 mA peak current for 10 mM NaNO$_2$ (**Figure 10D**). For a comparative study, we also performed the oxidation reaction with the pure polymer and pure polyoxometalate. There was no oxidation peak found in the same region for the polymer (**Figure 10C**) and negligible nitrite oxidation was observed for the pure polyoxometalate. The (C$_{25}$H$_{26}$N$_4$)$_4$[SiW$_{11}$O$_{39}$] also shows activity toward nitrite oxidation, though the current is not as high as in a polymer-SOM hybrid (**Supplementary Figures 1, 2**). This observation implies the emergence of catalytic activity of the SOM-Polymer hybrid that in a cascade catalyzes nitrite oxidation.

CONCLUSIONS

To conclude, this study successfully grafted a polymerizable organic ion onto an oxometalate. The structure of the molecular hybrid was confirmed by the SCXRD pattern and the hybrid forms SOM in water DMSO mixture. The composite SOM, by the virtue of having a redox active oxometalate, polymerizes the side chain of tetrakis(4-aminophenyl)methane into a polymer. We characterized the polymeric structure by IR as well as

NMR spectra, thus creating a system for a polymer-colloid (SOM) mixture. This can be used for nitrite oxidation and the selective oxidation of aniline in a cascade catalytic mode. Thus in short we show first a self-assembly of an organic-inorganic hybrid SOM. By then exploiting the intrinsic redox property and acidity of the contained oxometalate in SOM, we oxidized the aniline based side chain to polyaniline. This polymer-SOM composite, in turn, owing to its intrinsic residual redox property, oxidizes aniline to nitrobenzene selectively, and electrochemically oxidizes nitrite to nitrate. We have thus shown, for the first time, cascade catalysis in the context of SOM chemistry, which could further explorations in the context of sustainable chemistry.

DATA AVAILABILITY STATEMENT

The datasets generated for this study can be found in online repositories. The names of the repository/repositories and accession number(s) can be found at: CCDC, 1580136.

AUTHOR CONTRIBUTIONS

ACKNOWLEDGMENTS

SUPPLEMENTARY MATERIAL

REFERENCES

Bar-Nahum, I., Cohen, H., and Neumann, R. (2003). Organometallic-polyoxometalate hybrid compounds: metallosalen compounds modified by Keggin type polyoxometalates. *Inorg. Chem.* 42, 3677–3684. doi: 10.1021/ic034095s

Ben, T., Ren, H., Ma, S., Cao, D., Lan, J., Jing, X., et al. (2009). Targeted synthesis of a porous aromatic framework with high stability and exceptionally high surface area. *Angew. Chem.* 121, 9621–9624. doi: 10.1002/ange.200904637

Chen, D., Sahasrabudhe, A., Wang, P., Dasgupta, A., Yuan, R., and Roy, S. (2013). Synthesis and properties of a novel quarternerized imidazolium [α-PW$_{12}$O$_{40}$]$^{3-}$ salt as a recoverable photo-polymerization catalyst. *Dalton Trans.* 42, 10587–10596. doi: 10.1039/c3dt32916j

Cronin, L., and Müller, A. (2012). From serendipity to design of polyoxometalates at the nanoscale, aesthetic beauty and applications. *Chem. Soc. Rev.* 41, 7333–7334. doi: 10.1039/c2cs90087d

Das, S., Lai, D., Mallick, A., and Roy, S. (2016a). Photo redox mediated inexpensive one-pot synthesis of 1, 4-diphenyl substituted butane-1, 4-dione from styrene using polyoxometalate as a catalyst. *ChemistrySelect* 1, 691–695. doi: 10.1002/slct.201500052

Das, S., Misra, A., and Roy, S. (2016b). Enhancement of photochemical heterogeneous water oxidation by a manganese based soft oxometalate immobilized on a graphene oxide matrix. *New J. Chem.* 40, 994–1003. doi: 10.1039/C5NJ01099C

Das, S., Misra, A., and Roy, S. (2016c). Light driven decarboxylative cross coupling of acrylic acid and iodobenzene using [Mo$_{132}$] type keplerate as a catalyst. *Inorg. Chim. Acta.* 460, 77–82. doi: 10.1016/j.ica.2016.06.037

Dolbecq, A., Dumas, E., Mayer, C. R., and Mialane, P. (2010). Hybrid organic– inorganic polyoxometalate compounds: from structural diversity to applications. *Chem. Rev.* 110, 6009–6048. doi: 10.1021/cr1000578

Dong, Y., Das, S., Zhu, L., Ben, T., and Qiu, S. (2016). Standout electrochemical performance of SnO$_2$ and Sn/SnO$_2$ nanoparticles embedded in a KOH-activated carbonized porous aromatic framework (PAF-1) matrix as the anode for lithium-ion batteries. *J. Mater. Chem. A* 4, 18822–18831. doi: 10.1039/C6TA09384A

Du, J., and Chen, Y. (2004). Preparation of organic/inorganic hybrid hollow particles based on gelation of polymer vesicles. *Macromolecules* 37, 5710–5716. doi: 10.1021/ma0497097

Dualeh, A., Tétreault, N., Moehl, T., Gao, P., Nazeeruddin, M. K., and Grätzel, M. (2014). Effect of annealing temperature on film morphology of organic–inorganic hybrid pervoskite solid-state solar cells. *Adv. Funct. Mater.* 24, 3250–3258. doi: 10.1002/adfm.201304022

Fehse, K., Schwartz, G., Walzer, K., and Leo, K. (2007). Combination of a polyaniline anode and doped charge transport layers for high-efficiency organic light emitting diodes. *J. Appl. Phys.* 101:124509. doi: 10.1063/1.2748864

Hagrman, P. J., Hagrman, D., and Zubieta, J. (1999). Organic–inorganic hybrid materials: from "simple" coordination polymers to organodiamine-templated molybdenum oxides. *Angew. Chem. Int. Ed.* 38, 2638–2684. doi: 10.1002/(SICI)1521-3773(19990917)38:18<2638::AID-ANIE2638>3.0.CO;2-4

Heeger, A. J. (1993). Polyaniline with surfactant counterions: conducting polymer materials which are processible in the conducting form. *Synth. Met.* 57, 3471–3482. doi: 10.1016/0379-6779(93)90462-6

Jeong, U., Im, S. H., Camargo, P. H., Kim, J. H., and Xia, Y. (2007). Microscale fish bowls: a new class of latex particles with hollow interiors and engineered porous structures in their surfaces. *Langmuir* 23, 10968–10975. doi: 10.1021/la702324q

Kagan, C., Mitzi, D., and Dimitrakopoulos, C. (1999). Organic-inorganic hybrid materials as semiconducting channels in thin-film field-effect transistors. *Science* 286, 945–947. doi: 10.1126/science.286.5441.945

Kikukawa, Y., Suzuki, K., Sugawa, M., Hirano, T., Kamata, K., Yamaguchi, K., et al. (2012). Cyanosilylation of carbonyl compounds with trimethylsilyl cyanide catalyzed by an yttrium-pillared silicotungstate dimer. *Angew. Chem.* 124, 3746–3750. doi: 10.1002/ange.201200486

Kohut-Svelko, N., Pirri, R., Asua, J. M., and Leiza, J. R. (2009). Redox initiator systems for emulsion polymerization of acrylates. *J. Polym. Sci. A Polym. Chem.* 47, 2917–2927. doi: 10.1002/pola.23362

Lachkar, D., Vilona, D., Dumont, E., Lelli, M., and Lacôte, E. (2016). Grafting of secondary diolamides onto [P$_2$W$_{15}$V$_3$O$_{62}$]$^{9-}$ generates hybrid heteropoly acids. *Angew. Chem. Int. Ed.* 55, 5961–5965. doi: 10.1002/anie.201510954

Leng, W., Chen, M., Zhou, S., and Wu, L. (2010). Capillary force induced formation of monodisperse polystyrene/silica organic– inorganic hybrid hollow spheres. *Langmuir* 26, 14271–14275. doi: 10.1021/la102256t

Liu, B., Ben, T., Xu, J., Deng, F., and Qiu, S. (2014). Hydrogen bonding controlled catalysis of a porous organic framework containing benzimidazole moieties. *New J. Chem.* 38, 2292–2299. doi: 10.1039/c4nj00053f

Liu, S., Wang, J., Ou, J., Zhou, J., Chen, Y., and Yang, S. (2010). Fabrication of one dimensional polyaniline nanofibers by UV-assisted polymerization in the aqueous phase. *J. Nanosci. Nanotechnol.* 10, 933–940. doi: 10.1166/jnn.2010.1883

Liu, T., Diemann, E., Li, H., Dress, A. W., and Müller, A. (2003). Self-assembly in aqueous solution of wheel-shaped Mo154 oxide clusters into vesicles. *Nature* 426, 59–62. doi: 10.1038/nature02036

Liu, X., Kim, J.-S., Wu, J., and Eisenberg, A. (2005). Bowl-shaped aggregates from the self-assembly of an amphiphilic random copolymer of poly (styrene-co-methacrylic acid). *Macromolecules* 38, 6749–6751. doi: 10.1021/ma050665r

Long, J. R., and Yaghi, O. M. (2009). The pervasive chemistry of metal–organic frameworks. *Chem. Soc. Rev.* 38, 1213–1214. doi: 10.1039/b903811f

Lv, H., Geletii, Y. V., Zhao, C., Vickers, J. W., Zhu, G., Luo, Z., et al. (2012). Polyoxometalate water oxidation catalysts and the production of green fuel. *Chem. Soc. Rev.* 41, 7572–7589. doi: 10.1039/c2cs35292c

Macdiarmid, A. G. (2001). "Synthetic metals:" a novel role for organic polymers (Nobel lecture). *Angew. Chem. Int. Ed.* 40, 2581–2590. doi: 10.1002/1521-3773(20010716)40:14<2581::AID-ANIE2581>3.0.CO;2-2

Meenakshi, R., Shakeela, K., Kutti Rani, S., and Ranga Rao, G. J. C. L. (2018). Oxidation of aniline to nitrobenzene catalysed by 1-butyl-3-methyl imidazolium phosphotungstate hybrid material using m-chloroperbenzoic acid as an oxidant. *Catal. Lett.* 148, 246–257. doi: 10.1007/s10562-017-2214-2

Mostafaei, A., and Zolriasatein, A. (2012). Synthesis and characterization of conducting polyaniline nanocomposites containing ZnO nanorods. *Prog. Nat. Sci.: Mater. Int.* 22, 273–280. doi: 10.1016/j.pnsc.2012.07.002

Paul, S., Sreejith, S., and Roy, S. (2018). pH-induced phase transition and crystallization of soft-oxometalates (SOMs) into polyoxometalates (POMs): a study on crystallization from colloids. *Acta Crystallogr. Sect. C Struct. Chem.* 74:1274. doi: 10.1107/S2053229618007143

Pope, M., Mccleverty, J. A., and Meyer, T. J. (2004). Comprehensive coordination chemistry II. *Transition Metal Groups* 3, 635–678. doi: 10.1016/B0-08-043748-6/03035-8

Priewisch, B., and Rück-Braun, K. (2005). Efficient preparation of nitrosoarenes for the synthesis of azobenzenes. *J. Org. Chem.* 70, 2350–2352. doi: 10.1021/jo048544x

Rana, U., Chakrabarti, K., and Malik, S. (2011). *In situ* preparation of fluorescent polyaniline nanotubes doped with perylene tetracarboxylic acids. *J. Mater. Chem.* 21, 11098–11100. doi: 10.1039/c1jm12051d

Rausch, B., Symes, M. D., Chisholm, G., and Cronin, L. (2014). Decoupled catalytic hydrogen evolution from a molecular metal oxide redox mediator in water splitting. *Science* 345, 1326–1330. doi: 10.1126/science.1257443

Ren, H., Ben, T., Wang, E., Jing, X., Xue, M., Liu, B., et al. (2010). Targeted synthesis of a 3D porous aromatic framework for selective sorption of benzene. *Chem. Commun.* 46, 291–293. doi: 10.1039/B914761F

Rieger, J., Antoun, T., Lee, S. H., Chenal, M., Pembouong, G., Lesage De La Haye, J., et al. (2012). Synthesis and characterization of a thermoresponsive polyoxometalate–polymer hybrid. *Chem. Eur. J.* 18, 3355–3361. doi: 10.1002/chem.201101771

Roy, S. (2011). "Soft oxometalates" (SOMs): a very short introduction. *Comments Inorg. Chem.* 32, 113–126. doi: 10.1080/02603594.2011.608443

Roy, S. (2014). Soft-oxometalates beyond crystalline polyoxometalates: formation, structure and properties. *Crystengcomm* 16, 4667–4676. doi: 10.1039/C4CE00115J

Sandre, O., Moreaux, L., and Brochard-Wyart, F. (1999). Dynamics of transient pores in stretched vesicles. *Proc. Natl. Acad. Sci. U. S. A.* 96, 10591–10596. doi: 10.1073/pnas.96.19.10591

Sapurina, I., and Stejskal, J. (2008). The mechanism of the oxidative polymerization of aniline and the formation of supramolecular polyaniline structures. *Polym. Int.* 57, 1295–1325. doi: 10.1002/pi.2476

Sapurina, I. Y., and Shishov, M. (2012). "Oxidative polymerization of aniline: molecular synthesis of polyaniline and the formation of supramolecular structures," in *New Polymers for Special Applications*, ed A. D. S. Gomes (London, UK: IntechOpen), 272. doi: 10.5772/48758

Shiraishi, Y., Sakamoto, H., Fujiwara, K., Ichikawa, S., and Hirai, T. (2014). Selective photocatalytic oxidation of aniline to nitrosobenzene by Pt nanoparticles supported on TiO2 under visible light irradiation. *ACS Catal.* 4, 2418–2425. doi: 10.1021/cs500447n

Shumaila, S., Lakshmi, G., Alam, M., Siddiqui, A. M., Zulfequar, M., and Husain, M. (2011). Synthesis and characterization of Se doped polyaniline. *Curr. Appl. Phys.* 11, 217–222. doi: 10.1016/j.cap.2010.07.010

Suzuki, K., Jeong, J., Yamaguchi, K., and Mizuno, N. (2015). Visible-light-responsive multielectron redox catalysis of lacunary polyoxometalates induced by substrate coordination to their Lacuna. *Chem. Asian J.* 10, 144–148. doi: 10.1002/asia.201403072

Thomas, P., Chandel, S., Mallick, A., Sreejith, S., Ghosh, N., and Roy, S. (2018). Studying the crystallization of polyoxometalates from colloidal softoxometalates. *Cryst. Growth Des.* 18, 4068–4075. doi: 10.1021/acs.cgd.8b00443

Thomas, P., Pei, C., Roy, B., Ghosh, S., Das, S., Banerjee, A., et al. (2015). Site specific supramolecular heterogeneous catalysis by optically patterned soft oxometalate–porous organic framework (SOM–POF) hybrid on a chip. *J. Mater. Chem. A* 3, 1431–1441. doi: 10.1039/C4TA01304B

Tundo, P., Romanelli, G. P., Vázquez, P. G., Loris, A., and Aricò, F. (2008). Multiphase oxidation of aniline to nitrosobenzene with hydrogen peroxide catalyzed by heteropolyacids. *Synlett* 2008, 967–970. doi: 10.1055/s-2008-1072502

Uribe-Romo, F. J., Hunt, J. R., Furukawa, H., KlöCk, C., O'keeffe, M., and Yaghi, O. M. (2009). A crystalline imine-linked 3-D porous covalent organic framework. *J. Am. Chem. Soc.* 131, 4570–4571. doi: 10.1021/ja8096256

Verhoeff, A. A., Kistler, M. L., Bhatt, A., Pigga, J., Groenewold, J., Klokkenburg, M., et al. (2007). Charge regulation as a stabilization mechanism for shell-like assemblies of polyoxometalates. *Phys. Rev. Lett.* 99:066104. doi: 10.1103/PhysRevLett.99.066104

Verma, S., Hauck, T., El-Khouly, M. E., Padmawar, P. A., Canteenwala, T., Pritzker, K., et al. (2005). Self-assembled photoresponsive amphiphilic diphenylaminofluorene-C60 conjugate vesicles in aqueous solution. *Langmuir* 21, 3267–3272. doi: 10.1021/la047082f

Wan, S., Guo, J., Kim, J., Ihee, H., and Jiang, D. (2009). A photoconductive covalent organic framework: self-condensed arene cubes composed of eclipsed 2D polypyrene sheets for photocurrent generation. *Angew. Chem.* 121, 5547–5550. doi: 10.1002/ange.200900881

Wang, S.-S., and Yang, G.-Y. (2015). Recent advances in polyoxometalate-catalyzed reactions. *Chem. Rev.* 115, 4893–4962. doi: 10.1021/cr500390v

Wang, X., Liu, J., and Pope, M. (2003). New polyoxometalate/starch nanomaterial: synthesis, characterization and antitumoral activity. *Dalton Trans.* 5, 957–960. doi: 10.1039/b300920n

Wang, Y., and Weinstock, I. A. (2012). Polyoxometalate-decorated nanoparticles. *Chem. Soc. Rev.* 41, 7479–7496. doi: 10.1039/c2cs35126a

Xu, S., Roy, S., Ben, T., Pei, C., and Qiu, S. (2015). Enhanced recognition of a nitrogen containing organic compound by adjusting the acidity of the porous organic frameworks base (JUC-Z2). *J. Mater. Chem. A* 3, 2628–2633. doi: 10.1039/C4TA05640J

Yasuda, A., and Shimidzu, T. (1993). Chemical oxidative polymerization of aniline with ferric chloride. *Polym. J.* 25:329. doi: 10.1295/polymj.25.329

Yin, P., Bayaguud, A., Cheng, P., Haso, F., Hu, L., Wang, J., et al. (2014). Spontaneous stepwise self-assembly of a polyoxometalate–organic hybrid into catalytically active one-dimensional anisotropic structures. *Chem. Eur. J.* 20, 9589–9595. doi: 10.1002/chem.201402974

Yin, P., Wang, J., Xiao, Z., Wu, P., Wei, Y., and Liu, T. (2012). Polyoxometalate–organic hybrid molecules as amphiphilic emulsion catalysts for deep desulfurization. *Chem. Eur. J.* 18, 9174–9178. doi: 10.1002/chem.201201551

Zengin, H., Zhou, W., Jin, J., Czerw, R., Smith, D. W., Echegoyen, L., et al. (2002). Carbon nanotube doped polyaniline. *Adv. Mater.* 14, 1480–1483. doi: 10.1002/1521-4095(20021016)14:20<1480::AID-ADMA1480>3.0.CO;2-O

Zhang, J., Song, Y. F., Cronin, L., and Liu, T. (2010). Reverse-vesicle formation of organic–inorganic polyoxometalate-containing hybrid surfactants with tunable sizes. *Chem. Eur. J.* 16, 11320–11324. doi: 10.1002/chem.201000794

Zhu, Z., and Espenson, J. H. (1995). Kinetics and mechanism of oxidation of anilines by hydrogen peroxide as catalyzed by methylrhenium trioxide. *J. Org. Chem.* 60, 1326–1332. doi: 10.1021/jo00110a042

Comparison Between Electride Characteristics of Li$_3$@B$_{40}$ and Li$_3$@C$_{60}$

Prasenjit Das[1] and Pratim Kumar Chattaraj[1,2]*

[1]Department of Chemistry, Indian Institute of Technology Kharagpur, Kharagpur, India, [2]Department of Chemistry, Indian Institute of Technology Bombay, Mumbai, India

Density functional theory (DFT) based computation is performed on the endohedrally encapsulated Li$_3$ cluster inside the B$_{40}$ and C$_{60}$ cages namely, Li$_3$@B$_{40}$ and Li$_3$@C$_{60}$. For both these systems, the Li-Li bond lengths are shorter than that in the free Li$_3$ cluster. Due to confinement, the Li-Li vibrational frequencies increase in both the systems as compared to that in the free Li$_3$ cluster. Thermodynamically, the formation of these two systems is spontaneous in nature as predicted by the negative values of Gibbs' free energy changes (ΔG). For both the systems one non-nuclear attractor (NNA) is present on the middle of the Li$_3$ cluster which is predicted and confirmed by the electron density analysis. The NNA population and the percentage localization of electron density at the NNA of the Li$_3$@C$_{60}$ system are higher than that in the Li$_3$@B$_{40}$ system. At the NNA the values of the Laplacian of electron density are negative and an electron localization function basin is present at the center of the Li$_3$ cluster for localized electrons. Both systems show large values of nonlinear optical properties (NLO). Both the Li$_3$ encapsulated endohedral systems behave as electrides. Electrides have low work function and hence have a great potential in catalytic activity toward the activation of small molecules (such as CO$_2$, N$_2$). Even some electrides have greater catalytic activity than some well-studied metal-loaded catalysts. As the systems under study behave as electrides, they have the power to show catalytic activity and can be used in catalyzing the activation of small molecules.

Keywords: endohedral encapsulation, electride, non-nuclear attractor, electron localization function basin, nonlinear optical properties properties

INTRODUCTION

Electrons trapped inside the cavity of some interesting ionic systems behave as anions giving rise to electrides (Dye, 2003; Garcia-Borràs et al., 2012; Postils et al., 2015; Zhao et al., 2016; Saha et al., 2019). In recent year's electride properties of materials have generated great attention in experiments as well as in the theoretical studies. The inception of the concept of an electride took place during the study of the solvated electrons in the solution of alkali metal systems in ammonia (Greenlee and Henne, 1946; Zurek et al., 2009). Dye et al., 1970; Dye, 1990; Dye, 1991; Dye, 1997; Dye, 2003) provided valuable studies on electride materials. The trapped electrons are not attached to any particular atom but located at the cavities and the interstices of cryptands and solid crystals, respectively (Zhao et al., 2016; Dale and Johnson, 2018). The electron density analysis confirmed the presence of confined electrons in the cavities of solid alkali metals (Marqués et al., 2009; Mei et al., 1993). Ellaboudy et al. (1983) synthesized the first stable organic electride, Cs$^+$(18-crown-6)$_2$e$^-$in the crystalline form and Matsuishi et al. (2003) synthesized the first stable inorganic electride, [Ca$_{24}$Al$_{28}$O$_{64}$]$^{4+}$·(4e$^-$). In both cases, the excess electrons are confined in the empty area of those

crystals. This is followed by the synthesis and characterization of six temperature and air-stable electride systems (Ward et al., 1988, Ward et al.,1990a; Ward et al. 1990b; Wagner et al., 1994; Huang et al., 1997; Xie et al., 2000; Redko et al., 2005). In these systems, the cryptand ligands or crown ethers are complexed with alkali metals. Electride materials are very sensitive to temperature and air (Sun et al., 2016). So, it becomes a challenging task to generate and characterize electride materials which are stable related to air and temperature. The presence of cavity trapped loose electrons causes a lowering of the work function of electrides so that they can be used as an electron donor in chemical reactions. Moreover, the presence of loose electrons is responsible in making the electride systems very important because of their potential applications for example the emitting diodes for organic light (Yanagi et al., 2009), reversible hydrogen storage materials (Kitano et al., 2012), catalyst for the CO_2 activation (Toda et al., 2013), splitting of N_2 molecule (Kitano et al., 2012, 2015; Lu et al., 2016), powerful reducing agents (Buchammagari et al., 2007; Choi et al., 2014; Kim et al., 2014), and superconductivity (Miyakawa et al., 2007). The experimental identification of the position of localized trapped electrons is very difficult because of the low density of these localized electrons. So, experimentalist used indirect evidence for its experimental characterization (Singh et al., 1993; Dye, 1997). Therefore, computational studies can be helpful for the identification of electride materials. For that purpose, people used different computational tools to characterize electride materials. One can in silico characterize a material to behave as an electride and the necessary conditions for the same are, 1) presence of non-nuclear attractors (NNA) of the electron density (Dye, 2003; Lee et al., 2013; Dale et al., 2014); 2) the Laplacian of electron density ($\nabla^2\rho$) should be negative at the NNAs; 3) existence of electron localization function (ELF) basin at the NNA region; 4) high values of NLO properties. Some molecules which do not possesses confined electrons in electronic structure can show one or more of the above-mentioned properties. Thus, none of these conditions alone can be used to characterize electride systems, unambiguously. Some previous studies reported some molecules as electride material based on large NLOPs are not considered to be materials with electride properties on these days. When all of these four criteria are simultaneously satisfied, we can say that a cavity-trapped electron is present within the structure of a molecule and it constitutes a real electride material. We will analyze all of the above criteria in detail to check whether they present systems qualify to be termed as electrides. Most recently one theoretical work has shown that binuclear sandwich complexes of Be and Mg atoms bonded with isoelectronic $C_5H_5^-$, N_5^-, P_5^-, As_5^- ligands obeyed all these above-mentioned criteria to behave as electride materials (Das and Chattaraj, 2020).

After the discovery of buckminsterfullerene (C_{60}) in 1985, people became interested in using its cavity for the encapsulations of metals, and gas molecules (Kroto et al., 1985). Endohedral fullerenes are very useful in biology (Cagle et al., 1996), in molecular electronics (Jaroš et al., 2019), in

nuclear magnetic resonance (NMR) analysis, and in magnetic resonance imaging (Kato et al., 2003). The exterior surface of fullerenes has been used for various chemical reactions to take place (Levitt, 2013). The first experimentally synthesized endohedral fullerene is La@C_{60} (Heath et al., 1985). Experimentally, Hiroshi et al. reported the endohedral encapsulation of Li^+ ion inside the C_{60} cage (Ueno et al., 2015). Experimentally Li, Ca, Pr, Y, Ba, Ce, Nd, Gd metals (Ding and Yang, 1996; Kubozono et al., 1996; Wan et al., 1998; Okada et al., 2012) and He, Ne, Ar, Kr, Xe noble gases (Saunders et al., 1993; Saunders et al., 1994; Ohtsuki et al., 1998) were kept inside the C_{60} cage. Using the "molecular surgery" approach, it is experimentally reported for the endohedral encapsulation of H_2 (Komatsu et al., 2005; Murata et al., 2008), H_2O (Kurotobi and Murata, 2011), HF (Krachmalnicoff et al., 2016), CH_4 (Bloodworth et al., 2019) molecules inside fullerene. Several theoretical works have been reported for the encapsulation of different noble gases and metals inside the C_{60} cage (Andreoni and Curioni, 1996; Bühl et al., 1997; Strenalyuk and Haaland, 2008). Theoretically, Krapp and Frenking have studied the possibility of the encapsulation of noble gas dimers inside the C_{60} cage and showed the formation of noble gas-noble gas (Ng-Ng) 'genuine' chemical bond for Ar, Kr, and Xe, whereas weak interactions are present for He and Ne (Krapp and Frenking, 2007). Theoretically, Khatua et al. (2014a) studied the confinement of HF dimer inside the C_{60}, C_{70}, C_{80}, and C_{90} cages. Using the *ab-initio* molecular dynamics study the movement of Ng_2 dimer inside the C_{60} cage has been reported (Khatua et al., 2014b). Recently, endohedral encapsulation of Mg_2 molecule inside the C_{60} cage and the bonding interactions therein have also been studied (Das et al., 2020).

Borospherene, the boron analogue of fullerene has achieved great attention to the scientist. The first reported borospherene is B_{40} having a cage-like structure (Zhai et al., 2014). After that several borospherenes such as B_{28}, B_{38}, B_{44}, B_{46}, B_{29}^-, B_{37}^-, B_{38}^-, B_{39}^-, B_{44}^-, B_{39}^+, B_{40}^+, B_{41}^+, B_{42}^{2+} and their various metal doped homologues have been reported experimentally as well as theoretically (Lv et al., 2014; Chen et al., 2015; Zhao et al., 2015; Li et al., 2016a; Li et al., 2016b; Tai and Nguyen, 2016; Tian et al., 2016; Li et al., 2017; Tai and Nguyen, 2017). Pan et al. (2018) studied the endohedral encapsulation of noble gas monomer and dimer inside the B_{40} cage and the bonding interactions between Ng-B and Ng-Ng using density functional theory (DFT). Furthermore, the endohedral encapsulation of noble gas dimer inside the cavitand of cucurbit[6]uril and octa acid has been reported (Pan et al., 2015; Chakraborty et al., 2016). Theoretically, Das and Chattaraj (2014) studied the encapsulation of alkali and alkaline earth metals inside an aza crown analogue, $[(N_4C_2H_2)_4]^{2-}$ and the bonding interactions therein.

In this article we attempt to analyze molecules with electride property and for that purpose, we have encapsulated the Li_3 cluster in two different cages, B_{40} and C_{60} and they are denoted as Li_3@B_{40} and Li_3@C_{60}. We have used density functional theory (DFT) for the study of the structure, stability, and nature of bonding in these systems. We have computed the Gibbs' free
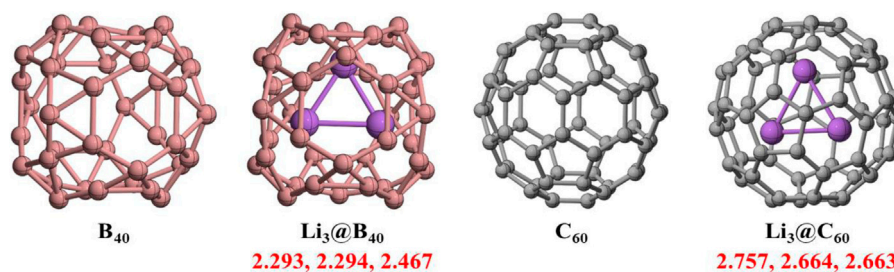
FIGURE 1 | The optimized geometries of B_{40}, C_{60} cages, and $Li_3@B_{40}$ and $Li_3@C_{60}$ systems at BP86-D3/def2-TZVPP method. The values in red color indicate Li-Li bond lengths (r_{Li-Li}). The bond lengths are in the Å unit.

energy change for the formation of both the electride systems in gas phase as well as in toluene and benzene solvent phases. The molecular orbital analysis and the electron density analysis of both these systems have been performed. Then we have calculated and compared the NLO properties of these systems. Finally, the electride characteristics of these two systems have been analyzed and the same between them have been compared.

COMPUTATIONAL DETAILS

We have used BP86-D3/def2-TZVPP method (Perdew, 1986; Becke, 1988; Weigend and Ahlrichs, 2005; Grimme et al., 2010) for geometry optimization and subsequent frequency calculations. The real harmonic frequency values indicate that these are the energy minimum structures on their respective potential energy surfaces. The Gaussian 16 program package has been used for all the computations (Frisch et al., 2016).

The atom centered density matrix propagation (ADMP) simulation has been carried out at BP86/6–31G method to know about the dynamical behavior of our systems at 300 K and 500 K temperatures and 1 atm pressure over 700 fs of time.

We have carried out the natural bond orbital (NBO) analysis to know the charge distribution on each atom. The computation for this analysis has been carried out at BP86-D3/def2-TZVPPD// BP86-D3/def2-TZVPP level of theory using NBO 3.1 version (Reed et al., 1988; Glendening et al., 1990) as implemented in Gaussian 16.

Multiwfn program package (Lu and Chen, 2012) has been used for atoms-in-molecule analysis (AIM) (Bader, 1990) of electron density. We have used BP86-D3/def2-TZVPPD// BP86-D3/def2-TZVPP method for this analysis and various bond critical points (BCP) have been generated. Both AIM and ELF basin population have been analyzed.

For the calculation of the average polarizability ($\overline{\alpha}$), first hyperpolarizability (β), and second hyperpolarizability ($\gamma_{\parallel}$), B3LYP/6-31+G(d)/6-31+G//BP86-D3/def2-TZVPP method has been used, where, 6-31+G(d) basis set is used for Li atoms and 6-31+G basis set is used for C and B atoms.

To compute the $\overline{\alpha}$, β and $\gamma_{\parallel}$ values the following equations have been used (Bishop and Norman, 2001),
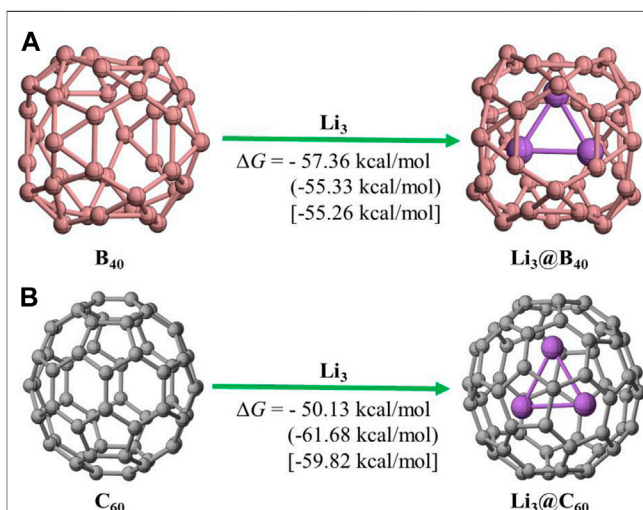
FIGURE 2 | The Schematic representation of the reaction path for **(A)** $Li_3@B_{40}$; **(B)** $Li_3@C_{60}$ systems considered in the study. The values without parentheses are calculated ΔG values at gas phase. The values within parentheses and within square brackets are calculated ΔG values at toluene and benzene solvent phases, respectively.

$$\overline{\alpha} = \frac{1}{3} \sum_{i=x,y,z} \alpha_{ii},$$

$$\beta = \left(\sum_{i=x,y,z} \beta_i^2 \right)^{1/2},$$

$$\text{where,} \beta_i = \frac{1}{3} \sum_{j=x,y,z} \left(\beta_{ijj} + \beta_{jij} + \beta_{jji} \right),$$

$$\gamma_{\parallel} = \frac{1}{15} \sum_{i,j=x,y,z} \left(\gamma_{iijj} + \gamma_{ijij} + \gamma_{ijji} \right).$$

RESULTS AND DISCUSSION

Geometries and Energetics

The optimized geometries of B_{40} and C_{60} cages and the $Li_3@B_{40}$ and $Li_3@C_{60}$ systems without any symmetry constraint are given in **Figure 1**. The B_{40} and C_{60} cages have D_{2d} and C_{2h} point groups of

FIGURE 3 | (A) and **(C)** Time evolution of total energy for $Li_3@B_{40}$ and $Li_3@C_{60}$ systems, respectively, **(B)** and **(D)** change in the Li-Li bond lengths with respect to the corresponding optimized value (at t = 0) against time for $Li_3@B_{40}$ and $Li_3@C_{60}$ systems, respectively.
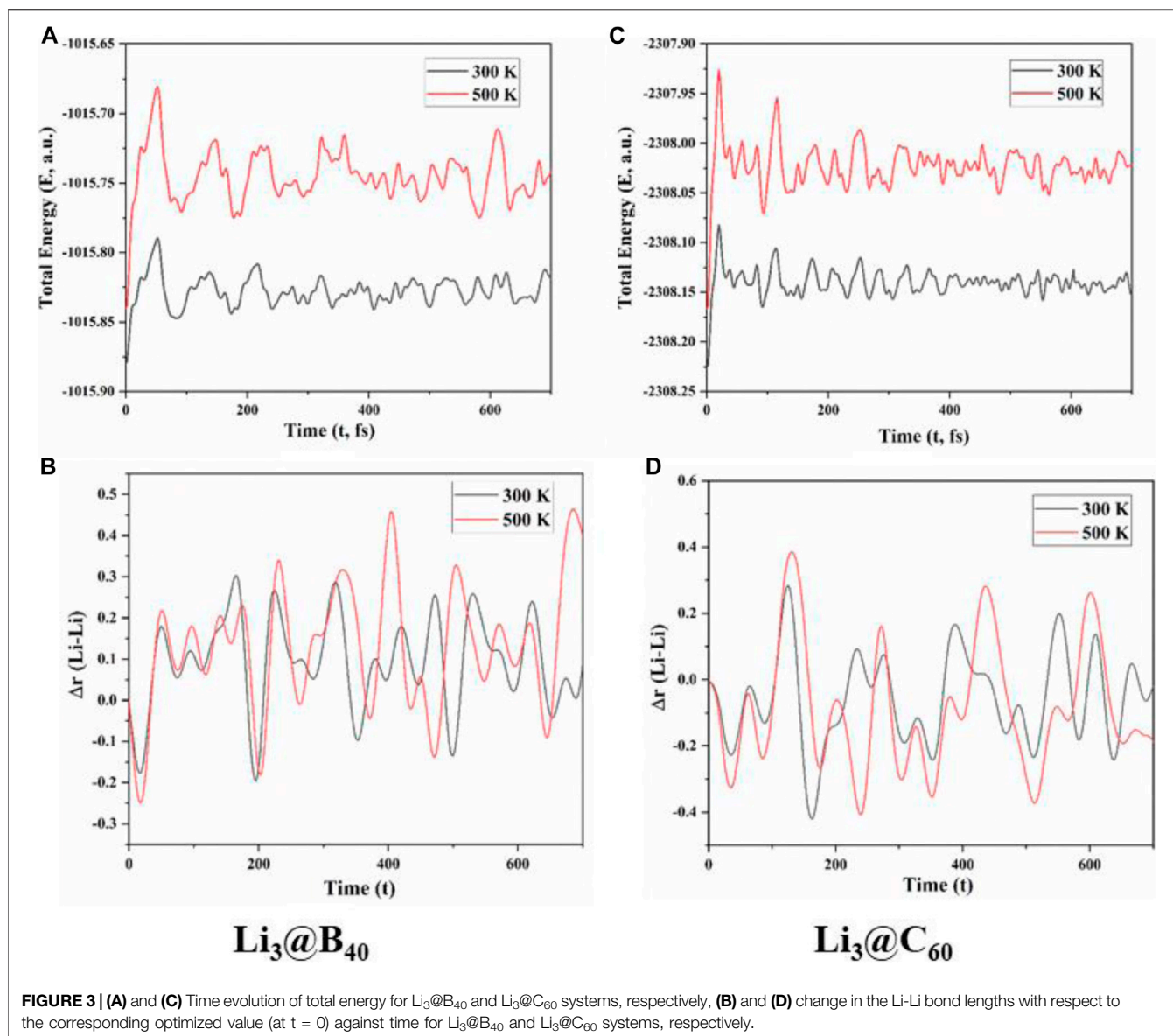
symmetry, respectively, and the $Li_3@B_{40}$ and $Li_3@C_{60}$ systems have C_1 point group of symmetry. The Li-Li bond lengths are 2.293 Å, 2.294 Å, and 2.467 Å for the $Li_3@B_{40}$ system, and for the $Li_3@C_{60}$ system, the Li-Li bond distances are 2.757 Å, 2.663 Å, and 2.664 Å. For both the systems the Li-Li bond lengths are shorter than that in the free Li_3 cluster. The confinement effect of B_{40} and C_{60} cages can account for this short Li-Li bond length for $Li_3@B_{40}$ and $Li_3@C_{60}$ systems, respectively. For the $Li_3@B_{40}$ system, the Li-Li bond lengths are shorter than that in the $Li_3@C_{60}$ systems. This is because of the comparatively smaller size of the B_{40} cage than that of the C_{60} cage. The numerical values of vibrational frequencies of Li-Li bonds for both $Li_3@B_{40}$ and $Li_3@C_{60}$ systems are presented in **Supplementary Table S1**. From the numerical values of Li-Li vibrational frequencies for both the systems, it has been found that there is an increase in the vibrational frequencies as compared to that in the free Li_3 cluster (139.6 cm^{-1}, 185 cm^{-1}, and 301.8 cm^{-1}). $Li_3@B_{40}$ system has higher

values of Li-Li vibrational frequency as compared to that of the $Li_3@C_{60}$ systems.

For these endohedral encapsulation processes the Gibbs' free energy changes (ΔG) in gas phase are −57.36 kcal/mol and −50.13 kcal/mol for $Li_3@B_{40}$ and $Li_3@C_{60}$ systems, respectively. For $Li_3@B_{40}$ system the ΔG values are −55.33 kcal/mol and −55.26 kcal/mol in toluene and in benzene solvents, respectively. However, for $Li_3@C_{60}$ system the ΔG values are −61.68 kcal/mol and −59.82 kcal/mol in toluene and in benzene solvents, respectively. The ΔG values are computed at BP86-D3/def2-TZVPP level of theory. The negative values of ΔG as shown in **Figure 2** indicate the spontaneous formation of these endohedral systems in gas phase as well as in the solvents. So, both the hosts, B_{40} and C_{60} cages can hold and stabilize the guest Li_3 cluster inside their cavity.

To know about the dynamical behavior of these systems we have carried out ADMP simulation at BP86/6-31G level of theory

FIGURE 4 | Snapshots at different time steps (time in fs) **(A)** at 300 K temperature, **(B)** at 500 K temperature of $Li_3@B_{40}$ system.

FIGURE 5 | Snapshots at different time steps (time in fs) **(A)** at 300 K temperature, **(B)** at 500 K temperature of $Li_3@C_{60}$ system.
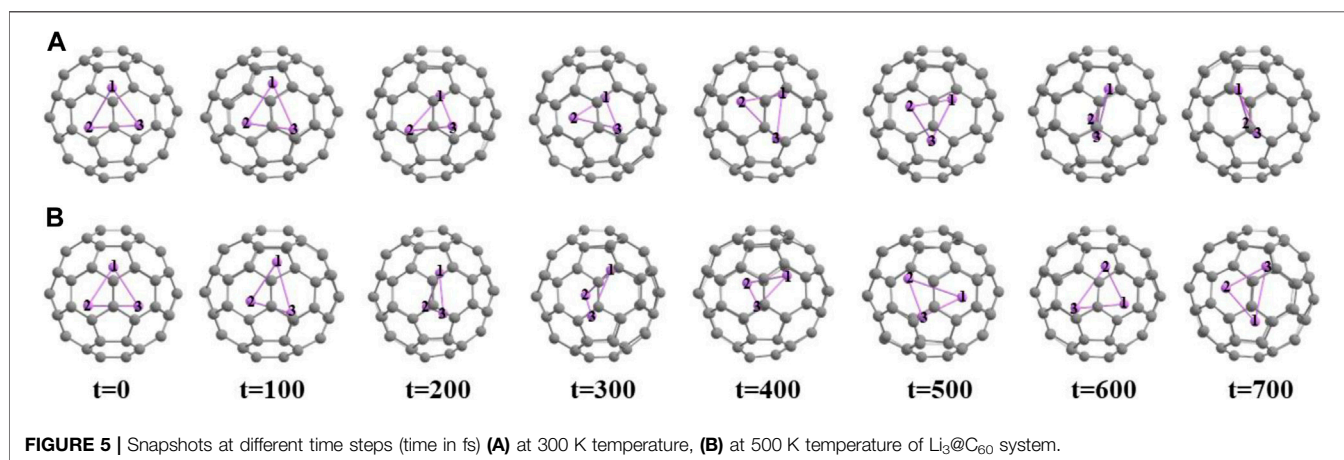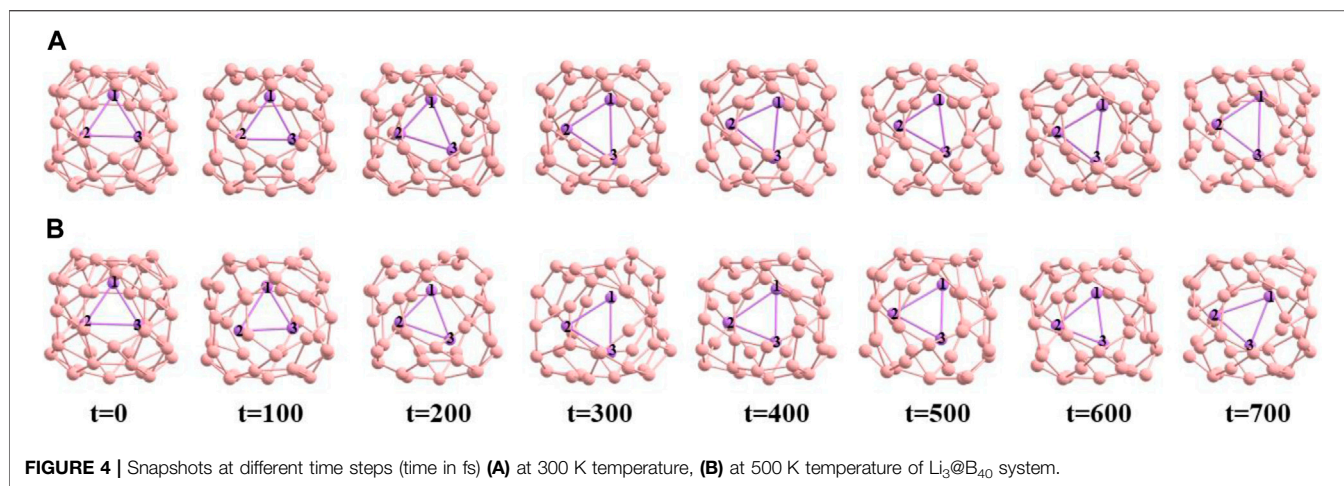
at both 300 K and 500 K temperature and at 1 atm pressure over 700 fs of time. We have presented the time evolution of the energy plots in **Figures 3A,C** for $Li_3@B_{40}$ and $Li_3@C_{60}$ systems, respectively. During structural deformation the nuclear kinetic energy of the systems increases which causes the oscillation in the time evolution of energy plots. From the time evolution plot of Li-Li bond length (**Figures 3B,D** for $Li_3@B_{40}$ and $Li_3@C_{60}$ systems, respectively) it is shown that the Li-Li bond lengths are fluctuating around the corresponding equilibrium values without disintegrating the systems. The different orientations of the Li_3 cluster inside the B_{40} and C_{60} cages at these temperatures at different time steps are shown in **Figures 4**, **5**, respectively. At both temperatures, the Li_3 cluster is only moving inside the cages without breaking the cages. So we can say that these two systems are stable at room temperature as well as at 500 K temperature. So, the guest Li_3 cluster can stay inside the B_{40} and C_{60} cages.

NATURE OF BONDING

Molecular Orbitals

We have used BP86-D3/def2-TZVPP method for molecular orbital analysis of both systems. The highest occupied

molecular orbital (HOMO), HOMO-1, and lowest unoccupied molecular orbital (LUMO) for the systems are presented in **Figure 6**. For the $Li_3@B_{40}$ system, the HOMO-1 and LUMO are distributed over the B_{40} cage but there is no contribution from the Li_3 moiety. For the $Li_3@C_{60}$ system, the HOMO and LUMO are π-type of orbitals and are distributed over the C_{60} cage but there is no contribution from the Li_3 moiety. The energy differences between HOMO and LUMO are 0.62 eV and 0.18 eV for $Li_3@B_{40}$ and $Li_3@C_{60}$ systems, respectively. The spin density plots are presented in **Figures 6C,D** for $Li_3@B_{40}$ and $Li_3@C_{60}$ system, respectively. The spin density plots show that the total spin density is distributed over the guest Li_3 cluster and the host B_{40} and C_{60} cages.

Natural Bond Orbital Analysis

The charge distribution over the atoms in both the systems has been analyzed by natural bond orbital analysis. For $Li_3@C_{60}$ system the natural charges on Li atoms are 0.60 $|e|$, 0.60 $|e|$, and 0.55 $|e|$. While the charges on Li atoms are 0.60 $|e|$, 0.73 $|e|$, and 0.74 $|e|$ for $Li_3@B_{40}$ system. The charges on the Li atoms are higher in case of $Li_3@B_{40}$ system as compared to that in the $Li_3@C_{60}$ system. In both the systems charge transfer takes place from the guest Li_3 cluster to the host B_{40} and C_{60} cages. In $Li_3@B_{40}$

FIGURE 6 | Plots of the HOMO-1, HOMO, and LUMO for **(A)** $Li_3@B_{40}$ system, **(B)** $Li_3@C_{60}$ system, **(C)** and **(D)** are spin density for $Li_3@B_{40}$ and $Li_3@C_{60}$ system, respectively. The values in the parenthesis are the energies of the corresponding orbitals in the eV unit.
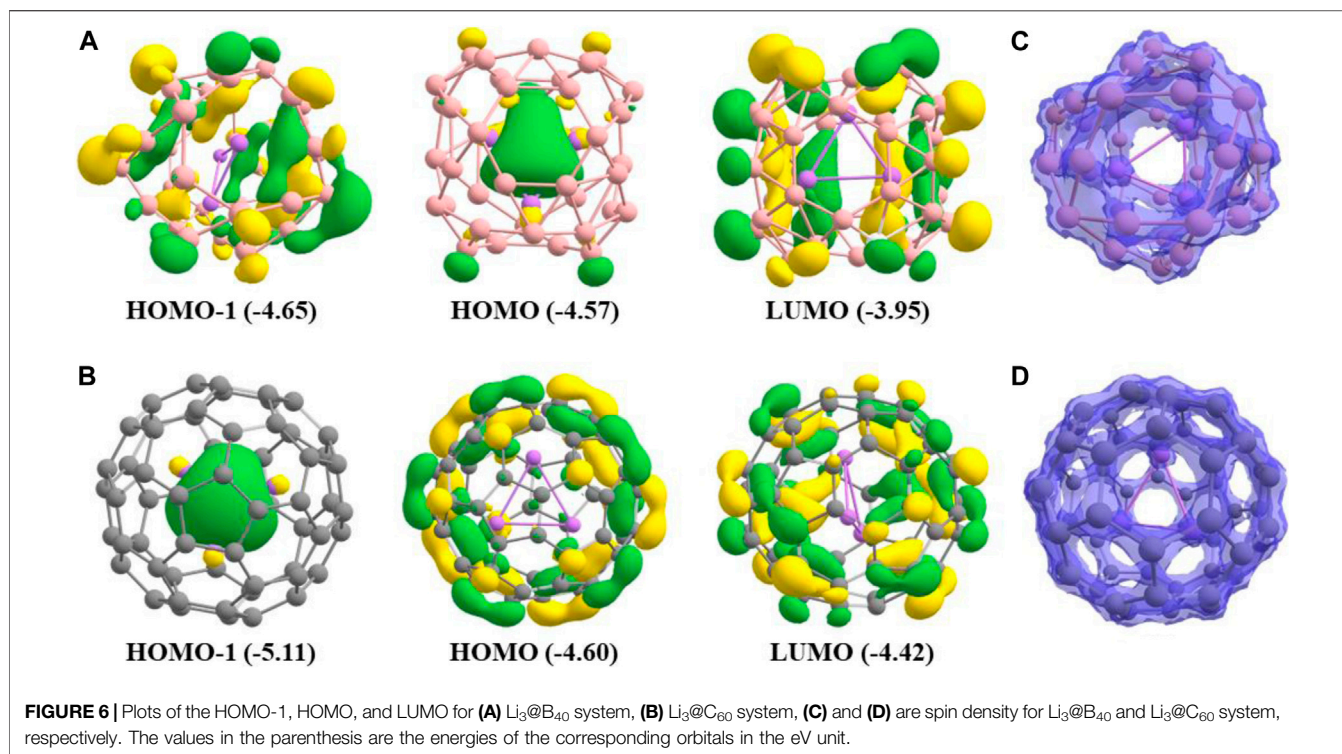
TABLE 1 | Electron Density [$\rho(r_c)$], Laplacian of Electron Density [$\nabla^2\rho(r_c)$], Kinetic Energy Density [$G(r_c)$], Potential Energy Density [$V(r_c)$], Total Energy Density [$H(r_c)$], Basin Population [N(pop)], Localization Index (LI), Percentage of Localization Index (% LI) at Different Critical Points (CP) of the $Li_3@B_{40}$ and $Li_3@C_{60}$ systems at BP86-D3/def2-TZVPPD//BP86-D3/def2-TZVPP level.

Systems	CP	Type	$\rho(r_c)$	$\nabla^2\rho(r_c)$	$G(r_c)$	$V(r_c)$	$H(r_c)$	N(pop)	LI	%LI
$Li_3@B_{40}$	NNA	(3,−3)	0.016	−0.015	0.001	−0.006	−0.005	0.17	0.02	12
	NNA–Li	(3,−1)	0.015	−0.004	0.003	−0.008	−0.005			
$Li_3@C_{60}$	NNA	(3,−3)	0.018	−0.018	0.000	−0.005	−0.005	0.59	0.27	46
	NNA–Li	(3,−1)	0.015	0.004	0.005	−0.008	−0.004			

system, a greater extent of charge transfer takes place from Li_3 to B_{40} cage as predicted by the greater positive charges on Li atoms for this system. It is reported that for $La@C_{82}$ system 3 $|e|$ transferred from the La atom to the C_{82} cage (Bethune et al., 1993). Again, in $Sc_3N@C_{80}$ system charge transfer occurs from Sc_3N fragment to C_{80} cage by 6 $|e|$ unit (Iiduka et al., 2005). But for $F_2@C_{60}$ system the charge transfer occurs in a reverse way i.e. from C_{60} cage to F_2 molecule (Foroutan-Nejad et al., 2018).

Atoms in Molecule Analysis

The electron density descriptors of both these systems have been computed at relevant bond critical points (BCPs) and the numerical values are given in **Table 1**. We have also generated the corresponding molecular graphs for these systems and are presented in **Figure 7**. From this analysis, it is confirmed that a non-nuclear attractor (NNA) [(3, −3) type of bond critical point] is present at the center of the Li_3 cluster for both these systems. The negative values of Laplacian of electron density [$\nabla^2\rho(r_c)$] at both the NNAs indicate the electron localization

therein. We have found that both $Li_3@B_{40}$ and $Li_3@C_{60}$ systems contained three NNA-Li bond paths which are (3,-1) type of bond critical points. The contour plots of $\nabla^2\rho(r)$ for both systems are presented in **Figure 8A**, which indicates a portion of the electron localization at the center of the Li_3 cluster. The NNA populations are 0.17 $|e|$ and 0.59 $|e|$ with 12% and 46% localization of electron density for $Li_3@B_{40}$ and $Li_3@C_{60}$ systems, respectively. The population of NNA and the percentage localization of electron density at the NNA for $Li_3@C_{60}$ system is higher than that of the $Li_3@B_{40}$ system. The electron-deficient nature of boron (B) atoms may cause the lowering of percentage of localization of electron density at the NNA for $Li_3@B_{40}$ system as compared to $Li_3@C_{60}$ system, where such an effect is absent. The B_{40} cage attracts the electron density from the Li_3 cluster more toward itself and hence decreases the electron density at the center of the Li_3 cluster.

We have generated the electron localization function basin (ELF) plots for both the studied systems and are presented in
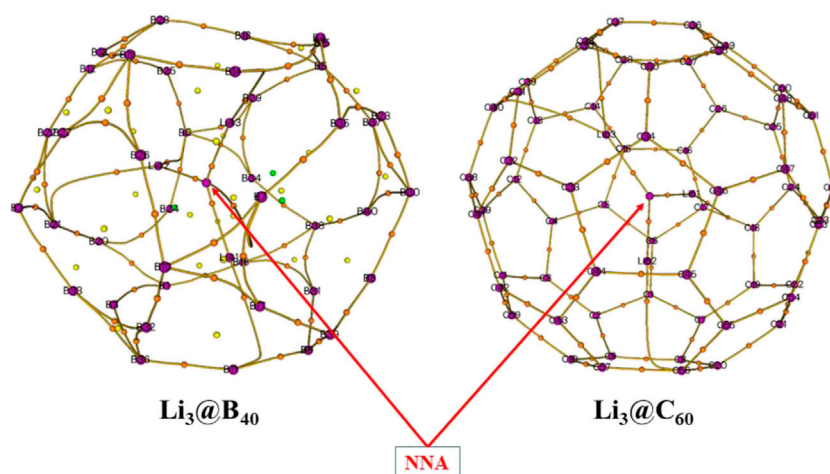
FIGURE 7 | The plots of molecular graphs of $Li_3@B_{40}$ and $Li_3@C_{60}$ systems generated at BP86-D3/def2-TZVPPD//BP86-D3/def2-TZVPP level.
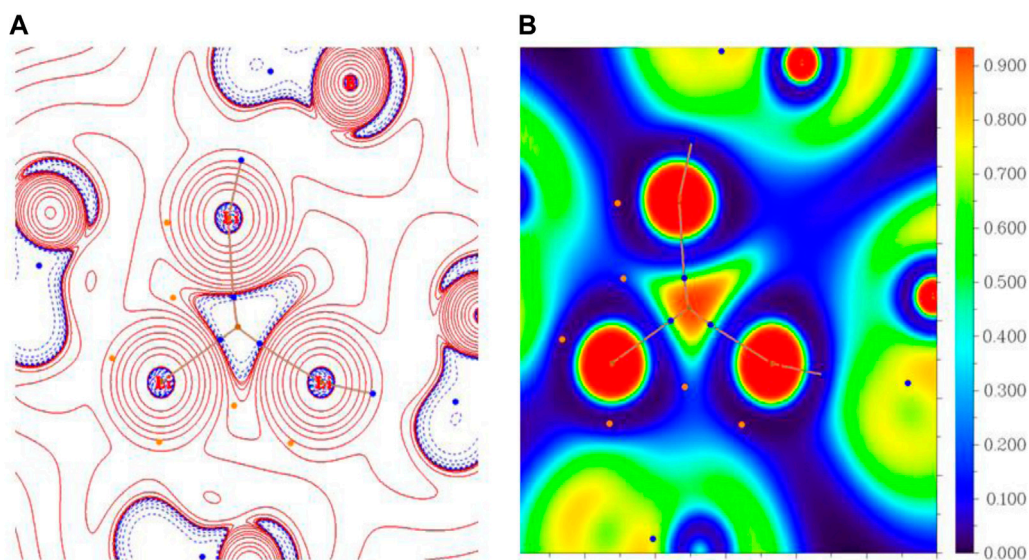
FIGURE 8 | The plots of **(A)** the Laplacian of electron density $[\nabla^2\rho(r)]$, blue dashed and red solid lines indicate $\nabla^2\rho(r) < 0$ and $\nabla^2\rho(r) > 0$ regions, respectively; **(B)** the electron localization function (ELF) basin of $Li_3@B_{40}$ and $Li_3@C_{60}$ systems.

Figure 8B. From the plot, it is shown that a basin is present at the center of the Li_3 cluster for both systems. The basin population is 0.58 $|e|$ with 22% localization of electron density for the $Li_3@B_{40}$ system. However, for the $Li_3@C_{60}$ system, the population of the basin is 1.01 $|e|$ with 56% localization of electron density. The ELF basin population of the $Li_3@C_{60}$ system is higher than that of the $Li_3@B_{40}$ system. The lowering of the basin population for the $Li_3@B_{40}$ system is due to the electron-deficient nature of boron (B) atoms. From these results, it can be said that a portion of electron density is localized at the center of the Li_3 cluster in both the systems. The higher values of NNA and ELF populations at the center of the

TABLE 2 | Average linear polarizability ($\bar{\alpha}$), first hyperpolarizability (β), and second hyperpolarizability ($\gamma_{\parallel}$) of $Li_3@B_{40}$ and $Li_3@C_{60}$ systems.

NLO property	$Li_3@B_{40}$	$Li_3@C_{60}$
$\bar{\alpha}$	554.2	584.7
β	129.4	79.9
$\gamma_{\parallel}$	3.6×10^5	2.1×10^5

Li_3 cluster of $Li_3@C_{60}$ system as compared to the $Li_3@B_{40}$ system indicates a greater extent of localization of electron density in the $Li_3@C_{60}$ system.

Nonlinear Optical Property

As electride materials contain loosely bound excess electrons, they showed high values of NLO properties. For this purpose, we have computed average polarizability ($\overline{\alpha}$), first hyperpolarizability (β), and second hyperpolarizability ($\gamma_\parallel$) for both the systems, and the numerical values are given in **Table 2**. Among both these systems $Li_3@C_{60}$ system shows higher values of $\overline{\alpha}$ and the $Li_3@B_{40}$ system shows higher values of β and $\gamma_\parallel$. We have compared the NLO values of our systems with some previously reported known electride materials, for example, M@calix (M = Li, Na; calix = calix [4]pyrrole), $Li@B_{10}H_{14}$ (Muhammad et al., 2011), and M_2 (TCNQ) (Li et al., 2008) (M = Li, Na; TCNQ = Tetracyanoquinodimethane) and are presented in **Supplementary Table S2**. Our systems show comparatively higher values of $\overline{\alpha}$ but lower values of β than the systems under comparison. The numerical values of $\gamma_\parallel$ of our systems are comparable with that of the systems being compared.

Electride Properties

It has been observed that in both the systems an NNA is present in the middle of the Li_3 cluster. An ELF basin has appeared in the position where the NNA is present and the values of $\nabla^2\rho$ are negative therein. Both the systems under study exhibit high values of NLO properties. All the criteria for an electride material have been satisfied by these systems. So, $Li_3@B_{40}$ and $Li_3@C_{60}$ systems can be classified as electrides. $Li_3@C_{60}$ system will show better electride characteristics than the $Li_3@B_{40}$ system.

SUMMARY AND CONCLUSION

The stability of $Li_3@B_{40}$ and $Li_3@C_{60}$ systems has been studied using density functional theory (DFT) based computations. The thermochemical results show the spontaneous formation of both the systems as predicted by the negative values of Gibbs' free energy change (ΔG). Due to the confinement, the Li-Li bonds in both the systems are shorter than that in the free Li_3 cluster and the Li-Li vibrational frequencies are increased on confinement. The Li-Li bonds are shorter in the $Li_3@B_{40}$ system as compared to that in the $Li_3@C_{60}$ system. The numerical values of Li-Li bond vibrational frequencies in the $Li_3@B_{40}$ system are higher than that in the $Li_3@C_{60}$ system. The results from the ADMP simulation showed that the systems are stable both at room temperature (300 K) and at 500 K temperature and 1 atm pressure. So, the host

B_{40} and C_{60} cages can take the Li_3 cluster inside their cavity and stabilize the cluster. The topological analysis of electron density shows the presence of an NNA at the center of the Li_3 cluster of both these systems and a portion of electron density gets localized therein. The Laplacian of electron density is negative at the NNAs. $Li_3@C_{60}$ system has higher values of NNA and ELF population than that of $Li_3@B_{40}$ system. Our designed endohedral $Li_3@B_{40}$ and $Li_3@C_{60}$ systems behave as electride. $Li_3@C_{60}$ system shows better electride characteristics than $Li_3@B_{40}$ system. As the systems under study behave as electrides, they have the potential to show catalytic activity.

DATA AVAILABILITY STATEMENT

The original contributions presented in the study are included in the article/**Supplementary Material**, further inquiries can be directed to the corresponding author.

AUTHOR CONTRIBUTIONS

PD designed the complex systems under study and executed the computational work. He prepared the first draft of the manuscript. PKC supervised the complete work and critically scrutinized the manuscript.

ACKNOWLEDGMENTS

SUPPLEMENTARY MATERIAL

The Supplementary Material for this article can be found online at: https://www.frontiersin.org/articles/10.3389/fchem.2021.638581/full#supplementary-material.

REFERENCES

Andreoni, W., and Curioni, A. (1996). Freedom and constraints of a metal atom encapsulated in fullerene cages. *Phys. Rev. Lett.* 77, 834. doi:10.1103/PhysRevLett.77.834

Bader, R. F. W. (1990). *Atoms in molecules. A quantum theory*. Oxford, United Kingdom: Oxford University Press

Becke, A. D. (1988). Density-functional exchange-energy approximation with correct asymptotic behavior. *Phys. Rev. A.* 38, 3098. doi:10.1103/PhysRevA.38.3098

Bethune, D. S., Johnson, R. D., Salem, J. R., de Vries, M. S., and Yannoni, C. S. (1993). Atoms in carbon cages: the structure and properties of endohedral fullerenes. *Nature* 366, 123–128. doi:10.1038/366123a0

Bishop, D. M., and Norman, P. (2001). *Handbook of advanced electronic and photonic materials*; Editor H. S. Nalwas, San Diego, CA: Academic, Vol. 9, 1–240.(.)

Bloodworth, S., Sitinova, G., Alom, S., Vidal, S., Bacanu, G. R., Elliott, S. J., et al. (2019). First synthesis and characterization of $CH_4@C_{60}$. *Angew. Chem. Int. Ed.* 58, 5038–5043. doi:10.1002/anie.201900983

Buchammagari, H., Toda, Y., Hirano, M., Hosono, H., Takeuchi, D., and Osakada, K. (2007). Room temperature-stable electride as a synthetic organic reagent: application to pinacol coupling reaction in aqueous media. *Org. Lett.* 9, 4287–4289. doi:10.1021/ol701885p

Bühl, M., Patchkovskii, S., and Thiel, W. (1997). Interaction energies and NMR chemical shifts of noble gases in C_{60}. *Chem. Phys. Lett.* 275, 14–18. doi:10.1016/s0009-2614(97)00733-1

Cagle, D. W., Thrash, T. P., Alford, M., Chibante, L. P. F., Ehrhardt, G. J., and Wilson, L. J. (1996). Synthesis, characterization, and neutron activation of holmium. *Metallofullerenes. J. Am. Chem. Soc.* 118, 8043–8047. doi:10.1021/ja960841z

Chakraborty, D., Pan, S., and Chattaraj, P. K. (2016). Encapsulation of small gas molecules and rare gas atoms inside the octa acid cavitand. *Theor. Chem. Acc.* 135, 119. doi:10.1007/s00214-016-1876-y

Chen, Q., Li, W-L., Zhao, Y-F., Zhang, S-Y., Hu, H-S., Bai, H., et al. (2015). Experimental and theoretical evidence of an axially chiral borosphere. *ACS Nano* 9, 754–760. doi:10.1021/nn506262c

Choi, S., Kim, Y. J., Kim, S. M., Yang, J. W., Kim, S. W., and Cho, E. J. (2014). Hydrotrifluoromethylation and iodotrifluoromethylation of alkenes and alkynes using an inorganic electride as a radical generator. *Nat. Commun.* 5, 1038–1046. doi:10.1038/ncomms5881

Dale, S. G., and Johnson, E. R. (2018). Theoretical descriptors of electrides. *J. Phys. Chem. A.* 122, 9371–9391. doi:10.1021/acs.jpca.8b08548

Dale, S. G., Otero-de-la-Roza, A., and Johnson, E. R. (2014). Density-functional description of electrides. *Phys. Chem. Chem. Phys.* 16, 14584–14593. doi:10.1039/C3CP55533J

Das, P., and Chattaraj, P. K. (2020). Electride characteristics of some binuclear sandwich complexes of alkaline earth metals, $M_2(\eta^5$-$L)_2$ (M = Be, Mg; L = $C_5H_5^-$, N_5^-, P_5^-, As_5^-). *J. Phys. Chem. A.* 124, 9801–9810. doi:10.1021/acs.jpca.0c08306

Das, P., Saha, R., and Chattaraj, P. K. (2020). Encapsulation of Mg_2 inside a C_{60} cage forms an electride. *J. Comput.Chem.* 31, 1645–1653. doi:10.1002/jcc.26207

Das, R., and Chattaraj, P. K. (2014). Guest–host interaction in an aza crown analog. *Int. J. Quan. Chem.* 114, 708–719. doi:10.1002/qua.24648

Ding, J., and Yang, S. (1996). Isolation and characterization of $Pr@C_{82}$ and $Pr_2@C_{80}$. *J. Am. Chem. Soc.* 118, 11254–11257. doi:10.1021/ja961601m

Dye, J. L., DeBacker, M. G., and Dorfman, L. M. (1970). Pulse radiolysis studies. XVIII. Spectrum of the solvated electron in the systems ethylenediamine–water and ammonia–water. *J. Chem. Phys.* 52, 6251–6258. doi:10.1063/1.1672935

Dye, J. L. (1991). Electrides and alkalides-comparison with metal solutions. *J. Phys. IV.* 1, 259–282. doi:10.1051/jp4:1991531

Dye, J. L. (1997). Electrides: from 1D heisenberg chains to 2D pseudo-metals. *Inorg. Chem.* 36, 3816–3826. doi:10.1021/ic970551z

Dye, J. L. (1990). Electrides: ionic salts with electrons as the anions. *Science* 247, 663–668. doi:10.1126/science.247.4943.663

Dye, J. L. (2003). Electrons as anions. *Science* 301, 607–608. doi:10.1126/science.1088103

Ellaboudy, A., Dye, J. L., and Smith, P. B. (1983). Cesium 18-crown-6 compounds. A crystalline ceside and a crystalline electride. *J. Am.Chem. Soc.* 105, 6490–6491. doi:10.1021/ja00359a022

Foroutan-Nejad, C., Straka, M., Fernàndez, I., and Frenking, G. (2018). Buckyball difluoride $F_2^-@C_{60}^+$—a single-molecule crystal. *Angew. Chem. Int. Ed.* 57, 13931–13934. doi:10.1002/anie.201809699

Frisch, M. J., Trucks, G. W., Schlegel, H. B., Scuseria, G. E., Robb, M. A., Cheeseman, J. R., et al. (2016). *Gaussian 16, Revision B.01.* Wallingford, CT: Gaussian, Inc.

Garcia-Borràs, M., Solà, M., Luis, J. M., and Kirtman, B. (2012). Electronic and vibrational nonlinear optical properties of five representative electrides. *J. Chem. Theor. Comput.* 8, 2688–2697. doi:10.1021/ct300433q

Glendening, E. D., Reed, A. E., Carpenter, J. E., and Weinhold, F. (1990). *NBO 3.1 QCPE bulletin*, 10, 58

Greenlee, K. W., and Henne, A. L. (1946). Sodium amide. *Inorg. Synth.* 2, 128–135. doi:10.1002/9780470132333.ch38

Grimme, S., Antony, J., Ehrlich, S., and Krieg, H. (2010). A consistent and accurate ab initio parametrization of density functional dispersion correction (DFT-D) for the 94 elements H-Pu. *J. Chem. Phys.* 132, 154104. doi:10.1063/1.3382344

Heath, J. R., O'Brien, S. C., Zhang, Q., Liu, Y., Curl, R. F., Tittel, F. K., et al. (1985). Lanthanum complexes of spheroidal carbon shells. *J. Am. Chem. Soc.* 107, 7779–7780. doi:10.1021/ja00311a102

Huang, R. H., Wagner, M. J., Gilbert, D. J., Reidy-Cedergren, K. A., Ward, D. L., Faber, M. K., et al. (1997). Structure and properties of Li^+(cryptand [2.1.1])e^-, an electride with a 1D "spin-ladder-like" cavity-channel geometry. *J. Am. Chem. Soc.* 119, 3765–3772. doi:10.1021/ja9640760

Iiduka, Y., Ikenaga, O., Sakuraba, A., Wakahara, T., Tsuchiya, T., Maeda, Y., et al. (2005). Chemical reactivity of $Sc_3N@C_{80}$ and $La_2@C_{80}$. *J. Am. Chem. Soc.* 127, 9956–9957. doi:10.1021/ja052534b

Jaroš, A., Bonab, E. F., Straka, M., and Foroutan-Nejad, C. (2019). Fullerene-based switching molecular diodes controlled by oriented external electric fields. *J. Am. Chem. Soc.* 141, 19644–19654. doi:10.1021/jacs.9b07215

Kato, H., Asakura, K., and Kudo, A. (2003). Highly efficient water splitting into H_2 and O_2 over lanthanum-doped $NaTaO_3$ photocatalysts with high crystallinity and surface nanostructure. *J. Am. Chem. Soc.* 125, 3082–3089. doi:10.1021/ja027751g

Khatua, M., Pan, S., and Chattaraj, P. K. (2014a). Confinement of $(HF)_2$ in C_n(n = 60, 70, 80, 90) cages. *Chem. Phys. Lett.* 616–617, 49–54. doi:10.1016/j.cplett.2014.10.025

Khatua, M., Pan, S., and Chattaraj, P. K. (2014b). Movement of Ng_2 molecules confined in a C_{60} cage: an ab initio molecular dynamics study. *Chem. Phys. Lett.* 610–611, 351–356. doi:10.1016/j.cplett.2014.06.052

Kim, Y. J., Kim, S. M., Hosono, H., Yang, J. W., and Kim, S. W. (2014). The scalable pinacol coupling reaction utilizing the inorganic electride $[Ca_2N]^+\cdot e^-$ as an electron donor. *Chem. Comm.* 50, 4791–4794. doi:10.1039/C4CC00802B

Kitano, M., Inoue, Y., Yamazaki, Y., Hayashi, F., Kanbara, S., Matsuishi, S., et al. (2012). Ammonia synthesis using a stable electride as an electron donor and reversible hydrogen store. *Nat. Chem.* 4, 934–940. doi:10.1038/nchem.1476

Kitano, M., Kanbara, S., Inoue, Y., Kuganathan, N., Sushko, P. V., Yokoyama, T., et al. (2015). Electride support boosts nitrogen dissociation over ruthenium catalyst and shifts the bottleneck in ammonia synthesis. *Nat. Commum.* 6, 6731–6739. doi:10.1038/ncomms7731

Komatsu, K., Murata, M., and Murata, Y. (2005). Encapsulation of molecular hydrogen in fullerene C_{60} by organic synthesis. *Science* 307, 238–240. doi:10.1126/science.1106185

Krachmalnicoff, A., Bounds, R., Mamone, S., Alom, S., Concistrè, M., Meier, B., et al. (2016). The dipolar endofullerene $HF@C_{60}$. *Nat. Chem* 8, 953–957. doi:10.1038/nchem.2563

Krapp, A., and Frenking, G. (2007). Is this a chemical bond? A theoretical study of $Ng_2@C_{60}$ (Ng=He, Ne, Ar, Kr, Xe). *Chem. Eur. J.* 13, 8256–8270. doi:10.1002/chem.200700467

Kroto, H. W., Heath, J. R., Obrien, S. C., Curl, R. F., and Smalley, R. E. (1985). C60: buckminsterfullerene. *Nature* 318, 162–163. doi:10.1038/318162a0

Kubozono, Y., Maeda, H., Takabayashi, Y., Hiraoka, K., Nakai, T., Kashino, S., et al. (1996). Extractions of $Y@C_{60}$, $Ba@C_{60}$, $La@C_{60}$, $Ce@C_{60}$, $Pr@C_{60}$, $Nd@C_{60}$, and $Gd@C_{60}$ with aniline. *J. Am. Chem. Soc.* 118, 6998–6999. doi:10.1021/ja9612460

Kurotobi, K., and Murata, Y. (2011). A single molecule of water encapsulated in fullerene C_{60}. *Science* 333, 613–616. doi:10.1126/science.1206376

Lee, K., Kim, S. W., Toda, Y., Matsuishi, S., and Hosono, H. (2013). Dicalcium nitride as a two-dimensional electride with an anionic electron layer. *Nature* 494, 336–340. doi:10.1038/nature11812

Levitt, M. H. (2013). Spectroscopy of light-molecule endofullerenes. *Phil Trans. R. Soc. A.* 371, 20120429. doi:10.1098/rsta.2012.0429

Li, H-R., Chen, Q., Tian, X-X., Lu, H-G., Zhai, H-J., and Li, S-D. (2016a). Cage-like B_{40}^+: a perfect borosphere monocation. *J. Mol. Model.* 22, 124. doi:10.1007/s00894-016-2980-6

Li, H. R., Jian, T., Li, W. L., Miao, C. Q., Wang, Y. J., Chen, Q., et al. (2016). Competition between quasi-planar and cage-like structures in the B_{29}^- cluster: photoelectron spectroscopy and ab initio calculations. *Phys. Chem. Chem. Phys.* 18, 29147–29155. doi:10.1039/C6CP05420J

Li, S., Zhang, Z., Long, Z., and Qin, S. (2017). Structures, stabilities and spectral properties of borosphere B_{44}^- and metalloborospheres $MB_{44}^{0/-}$ (M = Li, Na, and K). *Sci. Rep.* 7, 40081. doi:10.1038/srep40081

Li, Z.-J., Wang, F.-F., Li, Z.-R., Xu, H.-L., Huang, X.-R., Wu, D., et al. (2008). Large static first and second hyperpolarizabilities dominated by excess electron transition for radical ion pair salts $M_2^+TCNQ^-$ (M = Li, Na, K). *Phys. Chem. Chem. Phys.* 11, 402. doi:10.1039/b809161g

Lu, T., and Chen, F. (2012). Multiwfn: a multifunctional wavefunction analyzer. *J. Comput. Chem.* 33, 580–592. doi:10.1002/jcc.22885

Lu, Y., Li, J., Tada, T., Toda, Y., Ueda, S., Yokoyama, T., et al. (2016). Water durable electride Y_5Si_3: electronic structure and catalytic activity for ammonia synthesis. *J. Am. Chem. Soc.* 138, 3970–3973. doi:10.1021/jacs.6b00124

Lv, J., Wang, Y., Zhu, L., and Ma, Y. (2014). B38: an all-boron fullerene analogue. *Nanoscale* 6, 11692–11696. doi:10.1039/C4NR01846J

Marqués, M., Ackland, G. J., Lundegaard, L. F., Stinton, G., Nelmes, R. J., McMahon, M. I., et al. (2009). Potassium under pressure: a pseudobinary

ionic compound. *J. Phys. Rev. Lett.* 103, 115501. doi:10.1103/PhysRevLett.103.115501

Matsuishi, S., Toda, Y., Miyakawa, M., Hayashi, K., Kamiya, T., Hirano, M., et al. (2003). High-density electron anions in a nanoporous single crystal: $[Ca_{24}Al_{28}O_{64}]^{4+}(4e^-)$. *Science* 301, 626–629. doi:10.1126/science.1083842

Mei, C., Edgecombe, K. E., Smith, V. H., and Heilingbrunner, A. (1993). Topological analysis of the charge density of solids: bcc sodium and lithium. *International Journal Quantum Chemistry* 48, 287–293. doi:10.1002/qua.560480503

Miyakawa, M., Kim, S. W., Hirano, M., Kohama, Y., Kawaji, H., Atake, T., et al. (2007). Superconductivity in an inorganic electride $12CaO \cdot 7Al_2O_3 : e^-$. *J. Am. Chem. Soc.* 129, 7270–7271. doi:10.1021/ja0724644

Muhammad, S., Xu, H., and Su, Z. (2011). Capturing a synergistic effect of a conical push and an inward pull in fluoro derivatives of $Li@B_{10}H_{14}$ basket: toward a higher vertical ionization potential and nonlinear optical response. *J. Phys. Chem. A.* 115, 923–931. doi:10.1021/jp110401f

Murata, M., Maeda, S., Morinaka, Y., Murata, Y., and Komatsu, K. (2008). Synthesis and reaction of fullerene C70 encapsulating two molecules of H2. *J. Am. Chem. Soc.* 130, 15800–15801. doi:10.1021/ja8076846.Ohtsuki

Ohtsuki, T., Ohno, K., Shiga, K., Kawazoe, Y., Maruyama, Y., and Masumoto, K. (1998). Insertion of Xe and Kr atoms into C_{60} and C_{70} fullerenes and the formation of dimers. *Phys. Rev. Lett.* 81, 967. doi:10.1103/PhysRevLett.81.967

Okada, H., Komuro, T., Sakai, T., Matsuo, Y., Ono, Y., Omote, K., et al. (2012). Preparation of endohedral fullerene containing lithium ($Li@C_{60}$) and isolation as pure hexafluorophosphate salt ($[Li^+@C_{60}][PF_6^-]$). *RSC Adv.* 2, 10624–10631. doi:10.1039/C2RA21244G

Pan, S., Ghara, M., Kar, S., Zarate, X., Merino, G., and Chattaraj, P. K. (2018). Noble gas encapsulated B_{40} cage. *Phys. Chem. Chem. Phys.* 20, 1953–1963. doi:10.1039/C7CP07890K

Pan, S., Mandal, S., and Chattaraj, P. K. (2015). Cucurbit[6]uril: a possible host for noble gas atoms. *J. Phys. Chem. B.* 119, 10962–10974. doi:10.1021/acs.jpcb.5b01396

Perdew, J. P. (1986). Density-functional approximation for the correlation energy of the inhomogeneous electron gas. *Phys. Rev. B.* 33, 8822. doi:10.1103/PhysRevB.33.8822

Postils, V., Garcia-Borràs, M., Solà, M., Luis, J. M., and Matito, E. (2015). On the existence and characterization of molecular electrides. *Chem. Commun.* 51, 4865–4868. doi:10.1039/C5CC00215J

Redko, M. Y., Jackson, J. E., Huang, R. H., and Dye, J. L. (2005). Design and synthesis of a thermally stable organic electride. *J. Am. Chem. Soc.* 127, 12416–12422. doi:10.1021/ja053216f

Reed, A. E., Curtiss, L. A., and Weinhold, F. (1988). Intermolecular interactions from a natural bond orbital, donor-acceptor viewpoint. *Chem. Rev.* 88, 899–926. doi:10.1021/cr00088a005

Saha, R., Das, P., and Chattaraj, P. K. (2019). A complex containing four magnesium atoms and two Mg–Mg bonds behaving as an electride. *Eur. J. Inorg. Chem.* 2019 (38), 4105–4111. doi:10.1002/ejic.201900813

Saunders, M., Jimenez-Vazquez, H. A., Cross, R. J., Mroczkowski, S., Gross, M. L., Giblin, D. E., et al. (1994). Incorporation of helium, neon, argon, krypton, and xenon into fullerenes using high pressure. *J. Am. Chem. Soc.* 116, 2193–2194. doi:10.1021/ja00084a089

Saunders, M., Jiménez-Vázquez, H. A., Cross, R. J., and Poreda, R. J. (1993). Stable compounds of helium and neon: $He@C_{60}$ and $Ne@C_{60}$. *Science* 259, 1428–1430. doi:10.1126/science.259.5100.1428

Singh, D. J., Krakauer, H., Haas, C., and Pickett, W. E. (1993). Theoretical determination that electrons act as anions in the electride $Cs^+ (15\text{-}crown\text{-}5)_2 \cdot e^-$. *Nature* 365, 39–42. doi:10.1038/365039a0

Strenalyuk, T., and Haaland, A. (2008). Chemical bonding in the inclusion complex of He in adamantane (He@Adam): the origin of the barrier to dissociation. *Chem. Eur. J.* 14, 10223–10226. doi:10.1002/chem.200800715

Sun, W. -M., Li, X. -H., Li, Y., Ni, B. -L., Chen, J. -H., Li, C. -Y., et al. (2016). Theoretical study of the substituent effects on the nonlinear optical properties of a room-temperature- stable organic electride. *Chem. Phys. Chem.* 17, 3907–3915. doi:10.1002/cphc.201600970

Tai, T. B., and Nguyen, M. T. (2016). A new chiral boron cluster B44 containing nonagonal holes. *Chem. Commun.* 52, 1653–1656. doi:10.1039/C5CC09111J

Tai, T. B., and Nguyen, M. T. (2017). Aromatic cage-like B_{46}: existence of the largest decagonal holes in stable atomic clusters. *RSC Adv.* 7, 22243–22247. doi:10.1039/C7RA02870A

Tian, W. J., Chen, Q., Li, H. R., Yan, M., Mu, Y. W., Lu, H. G., et al. (2016). Saturn-like charge- transfer complexes $Li_4\&B_{36}$, $Li_5\&B_{36}^+$, and $Li_6\&B_{36}^{2+}$: exohedral metalloborospherenes with a perfect cage-like B_{36}^{4-} core. *Phys. Chem. Chem. Phys.* 18, 9922–9926. doi:10.1039/C6CP01279E

Toda, Y., Hirayama, H., Kuganathan, N., Torrisi, A., Sushko, P. V., and Hosono, H. (2013). Activation and splitting of carbon dioxide on the surface of an inorganic electride material. *Nat. Commun.* 4, 2378–2385. doi:10.1038/ncomms3378

Ueno, H., Nishihara, T., Segawa, Y., and Itami, K. (2015). Cycloparaphenylene-based ionic donor–acceptor supramolecule: isolation and characterization of $Li^+@C_{60} \subset [10]CPP$. *Angew. Chem. Int. Ed.* 54, 3707. doi:10.1002/anie.201500544

Wagner, M. J., Huang, R. H., Eglin, J. L., and Dye, J. L. (1994). An electride with a large six-electron ring. *Nature.* 368, 726–729. doi:10.1038/368726a0

Wan, S. M., Zhang, H. –W., Nakane, T., Xu, Z., Inakuma, M., Shinohara, H., et al. (1998). Production, isolation, and electronic properties of missing Fullerenes: $Ca@C_{72}$ and $Ca@C_{74}$. *J. Am. Chem. Soc.* 120, 6806–6807. doi:10.1021/ja972478h

Ward, D. L., Huang, R. H., and Dye, J. L. (1988). Structures of alkalides and electrides. I. Structure of potassium cryptand[2.2.2] electride. *Acta Crystallogr. Sect. C: Cryst. Struct. Commun.* 44, 1374–1376. doi:10.1107/S0108270188002847

Ward, D. L., Huang, R. H., and Dye, J. L. (1990a). The structures of alkalides and electrides. III. Structure of potassium cryptand[2.2.2] natride. *Acta Crystallogr. Sect. C: Cryst. Struct. Commun.* 46, 1833–1835. doi:10.1107/S0108270190001007

Ward, D. L., Huang, R. H., and Dye, J. L. (1990b). The structures of alkalides and electrides. V. Structures of caesium bis (15-crown-5) kalide and rubidium bis (15-crown-5) rubidide. *Acta Crystallogr. Sect. C: Cryst. Struct. Commun.* 46, 1838–1841. doi:10.1107/S0108270190002293

Weigend, F., and Ahlrichs, R. (2005). Balanced basis sets of split valence, triple zeta valence and quadruple zeta valence quality for H to Rn: design and assessment of accuracy. *Phys. Chem. Chem. Phys.* 7, 3297–3305. doi:10.1039/B508541A

Xie, Q., Huang, R. H., Ichimura, A. S., Phillips, R. C., Pratt, W. P., and Dye, J. L. (2000). Structure and properties of a new electride, $Rb^+(cryptand\text{-} [2.2.2])e^-$. *J. Am. Chem. Soc.* 122, 6971–6978. doi:10.1021/ja9943445

Yanagi, H., Kim, K.-B., Koizumi, I., Kikuchi, M., Hiramatsu, H., Miyakawa, M., et al. (2009). Low Threshold Voltage and Carrier Injection Properties of Inverted Organic Light-Emitting Diodes with $[Ca_{24}Al_{28}O_{64}]^{4+}(4e^-)$ Cathode and $Cu_{2-x}Se$ Anode. *J. Phys. Chem. C.* 113, 18379–18384. doi:10.1021/jp906386q

Zhai, H-J., Zhao, Y-F., Li, W-L., Chen, Q., Bai, H., Hu, H-S., et al. (2014). Observation of an all- boron fullerene. *Nat. Chem.* 6, 727–731. doi:10.1038/nchem.1999

Zhao, J., Huang, X., Shi, R., Liu, H., Sua, Y., and King, R. B. (2015). B$_{28}$: the smallest all- boron cage from an ab initio global search. *Nanoscale* 7, 15086–15090. doi:10.1039/C5NR04034E

Zhao, S., Kan, E., and Li, Z. (2016). Electride: from computational characterization to theoretical design. *Wires Comput. Mol. Sci.* 6, 430–440. doi:10.1002/wcms.1258

Zurek, E., Edwards, P. P., and Hoffmann, R. (2009). A molecular perspective on lithium- ammonia solutions. *Angew. Chem. Int. Ed.* 48, 8198–8232. doi:10.1002/anie.200900373

Low-Lying Electronic States of the Nickel Dimer

Patrick K. Tamukong and Mark R. Hoffmann *

Chemistry Department, University of North Dakota, Grand Forks, ND, United States

The generalized Van Vleck second order multireference perturbation theory (GVVPT2) method was used to investigate the low-lying electronic states of Ni_2. Because the nickel atom has an excitation energy of only 0.025 eV to its first excited state (the least in the first row of transition elements), Ni_2 has a particularly large number of low-lying states. Full potential energy curves (PECs) of more than a dozen low-lying electronic states of Ni_2, resulting from the atomic combinations $^3F_4 + ^3F_4$ and $^3D_3 + ^3D_3$, were computed. In agreement with previous theoretical studies, we found the lowest lying states of Ni_2 to correlate with the $^3D_3 + ^3D_3$ dissociation limit, and the holes in the d-subshells were in the subspace of delta orbitals (i.e., the so-dubbed $\delta\delta$-states). In particular, the ground state was determined as X $^1\Gamma_g$ and had spectroscopic constants: bond length (R_e) = 2.26 Å, harmonic frequency (ω_e) = 276.0 cm^{-1}, and binding energy (D_e) = 1.75 eV; whereas the $1\ ^1\Sigma_g^+$ excited state (with spectroscopic constants: R_e = 2.26 Å, ω_e = 276.8 cm^{-1}, and D_e = 1.75) of the $^3D_3 + ^3D_3$ dissociation channel lay at only 16.4 cm^{-1} (0.002 eV) above the ground state at the equilibrium geometry. Inclusion of scalar relativistic effects through the spin-free exact two component (sf-X2C) method reduced the bond lengths of both of these two states to 2.20 Å, and increased their binding energies to 1.95 eV and harmonic frequencies to 296.0 cm^{-1} for X $^1\Gamma_g$ and 297.0 cm^{-1} for $1\ ^1\Sigma_g^+$. These values are in good agreement with experimental values of R_e = 2.1545 ± 0.0004 Å, ω_e = 280 ± 20 cm^{-1}, and D_0 = 2.042 ± 0.002 eV for the ground state. All states considered within the $^3F_4 + ^3F_4$ dissociation channel proved to be energetically high-lying and van der Waals-like in nature. In contrast to most previous theoretical studies of Ni_2, full PECs of all considered electronic states of the molecule were produced.

Keywords: nickel dimer, metal dimers, multireference perturbation theory, generalized Van Vleck perturbation theory, electronic structure calculations

INTRODUCTION

Since Ni_2 has few holes in otherwise complete subshells, one might expect theoretical studies of Ni_2 to be less complicated than for other first row transition metal dimers, like Cr_2 where one has many more possibilities of distributing 12 electrons in 12 valence orbitals. Reported information on Ni_2, however, proves the contrary. For example, the exact symmetry of the *ground* electronic state of Ni_2 is still debated: Different studies have reported different space and spin symmetries for the molecule's ground term.

Experimental data on Ni_2 is sparse and the true ground state of the molecule is not unequivocally accepted. From the analysis of electronic absorption bands of Ni_2 in the visible spectral region in argon matrices, De Vore et al. (De Vore et al., 1975) determined ω_e = 192 cm^{-1}, whereas a frequency

of 380.9 cm^{-1} was found in solid argon matrix (Ahmed and Nixon, 1979). The latter result was later criticized by Rasanen et al. (Rasanen et al., 1987) In photoelectron spectroscopic studies of Ni$_2^-$, ω_e = 280 ± 20 cm^{-1} was determined for the lowest electronic state of Ni$_2$ (Ho et al., 1993). Second and third law analyses of information derived from a combination of Knudsen effusion and mass-spectrometric techniques led to a binding energy of D_0 = 2.03 ± 0.30 eV (second law result) and D_0 = 2.36 ± 0.22 eV (third law result) for ground state Ni$_2$ (Kant, 1964). By using time-delayed resonant two-photon ionization, Morse et al. (Morse et al., 1984) determined D_0 = 2.068 ± 0.010 eV and R_e = 2.200 ± 0.007 Å for the lowest state of Ni$_2$, but assigned as either $^3\Gamma_u$ or $^1\Gamma_g$. Also from two-photon ionization studies on supersonic jet-cooled Ni$_2$ in argon carrier gas, Pinegar et al. (Pinegar et al., 1995) determined D_0 = 2.042 ± 0.002 eV and R_e = 2.1545 ± 0.0004 Å for the lowest state of Ni$_2$ but were unable to ascertain the symmetry of this state.

Theoretical studies of the electronic states of Ni$_2$ are complicated by the fact that the first excited state of the Ni atom, $^3D_3$ (3d^{9}4s^1), is only 0.025 eV above the $^3F_4$ (3d^{8}4s^2) ground atomic state, which is the least excitation energy of any of the first row of transition elements (Harrison, 2000; Kramida et al., 2013). This low promotion energy supports the existence of several low-lying molecular states of the Ni$_2$ molecule resulting from the $^3F_4 + ^3F_4$ and $^3D_3 + ^3D_3$ atomic combinations. For example, limited configuration interaction (CI) calculations (Shim et al., 1979) found 84 states of Ni$_2$, corresponding to the $^3F_4 + ^3F_4$ dissociation limit, to lie within an energy range of only 300 K (0.026 eV), and 45 states, also within a narrow energy range, to correlate with the $^3D_3 + ^3D_3$ dissociation asymptote. Melius et al. (Melius et al., 1976) also noted that the manifold of electronic states within 0.50 eV of the ground state of Ni$_2$ was dense and complex.

Since the fully filled 4s-subshell of the $^3F_4$ (3d^{8}4s^2) ground state of Ni discourages significant bonding interaction, bonding in low-lying states of Ni$_2$ results largely from the coupling of excited state Ni atoms. In particular, the lowest states of the Ni$_2$ molecule can be expected to correlate with the $^3D_3$ (3d^{9}4s^1) + $^3D_3$ (3d^{9}4s^1) dissociation channel. At the generalized valence bond (GVB) and polarization CI (POL-CI) level of theory, (Upton and Goddard III, 1978) 30 of 45 low-lying states of Ni$_2$, within the $^3D_3 + ^3D_3$ dissociation channel, were found (Shim et al., 1979) to be singlets and triplets ordered energetically as

δδ (6 states) < πδ (8 states) < δσ (4 states) < ππ (6 states) < πσ (4 states) < σσ (2 states), with the six lowest (of symmetries $^1\Gamma_g$, $^1\Sigma_g^+$, $^3\Sigma_g^-$, $^1\Sigma_u^-$, $^3\Gamma_u$, and $^3\Sigma_u^+$) being virtually degenerate and having an average equilibrium bond length, R_e, of 2.04 Å, and binding energy, D_e, of 2.29 eV. The designations δδ, πδ, et cetera, specify the positions of the holes in the dominant configurations of the 3d-orbitals at each atomic center which has a 3d^{9}4s^1 configuration (Shim et al., 1979). In brief, the correct energy spacing of the low-lying states of the Ni dimer is problematic for both theory and experiment.

The determination of energy ordering and spacing is no less complicated for the Ni atom, and provides insight into necessary levels of experimental and theoretical approaches. The $^3F_4$ (3d^{8}4s^2) → $^3D_3$ (3d^{9}4s^1) excitation energy has been determined by at least one experimental study (Moore, 1952) to be negative (-0.029 eV). This negative value was supported by *ab initio* wave function and density functional theory (DFT) calculations (Bauschlicher et al., 1982; Raghavachari and Trucks, 1989; Russo et al., 1994). A more recent study, (Schultz et al., 2005) that employed several functionals at all five rungs of Jacob's ladder of DFT functionals, predicted the ground state configuration of the Ni atom as 3d^{9}4s^1 ($^3D_3$) with most of the functionals when using a triple-ζ quality basis set. On the other hand, multireference studies (Andersson and Roos, 1992; Murphy and Messmer, 1992) predicted a 3d^{8}4s^2 ($^3F_4$) ground state configuration for the Ni atom. Illustrating additional complexity, Upton and Goddard (Upton and Goddard III, 1978) found that averaging over J components (where J is the sum of spin and orbital angular momenta of the atom) of each state places the $^3D_3$ (3d^{9}4s^1) state lower energetically than the $^3F_4$ (3d^{8}4s^2) state.

One of the earliest theoretical studies (Cooper et al., 1972) on Ni$_2$ employed the extended Hückel molecular orbital method and found a $^3\Sigma_g^-$ ground state with R_e = 2.21 Å, ω_e = 370 cm^{-1}, and D_e = 2.45 eV, with dominant configuration 3dδ$_g^4$ 3dδ$_u^4$ 3dπ$_u^4$ 3dπ$_g^2$ 3dσ$_g^2$ 3dσ$_u^2$ 4sσ$_g^2$. On the other hand, the self-consistent field (SCF) scattered-wave (X_α-sw) method (Rösch and Rhodin, 1974) found a $^1\Sigma_g^+$ ground state with configuration 3dδ$_g^4$ 3dδ$_u^4$ 3dπ$_u^4$ 3dπ$_g^4$ 3dσ$_g^2$ 4sσ$_g^2$; whereas the generalized valence bond (GVB) method (Melius et al., 1976) also predicted a $^1\Sigma_g^+$ ground state for Ni$_2$, but with configuration 3dδ$_g^4$ 3dδ$_u^2$ 3dπ$_u^4$ 3dπ$_g^4$ 3dσ$_g^2$ 3dσ$_u^2$ 4sσ$_g^2$. A Hartree-Fock followed by limited CI study, (Shim et al., 1979) which explored a variety of states of Ni$_2$ resulting from the $^3F_4 + ^3F_4$ and $^3D_3 + ^3D_3$ atomic combinations, found the ground state to be $^1\Sigma_g^+$ with the same configuration as was reported by the GVB study(Melius et al., 1976). The states $^1\Gamma_g$ and $^1\Sigma_u^-$ were reported to be in close proximity to the $^1\Sigma_g^+$ state in the CI study. Other theoretical studies found the six δδ–hole states (i.e., $^1\Gamma_g$, $^1\Sigma_g^+$, $^3\Sigma_g^-$, $^1\Sigma_u^-$, $^3\Gamma_u$, $^3\Sigma_u^+$), resulting from the $^3D_3 + ^3D_3$ atomic coupling, to be quasidegenerate(Basch et al., 1980; Noell et al., 1980; Wood et al., 1980).

Using an effective core potential basis set specifically optimized for the Ni atom in the $^3D_3$ state within the generalized valence bond CI (GVBCI) method, Noell et al. (Noell et al., 1980) found the splitting of the six δδ–hole states of Ni$_2$ to be quite small (≤0.1 eV), with the lowest states being $^1\Gamma_g$ and $^1\Sigma_g^+$. Inclusion of polarization configurations involving single and double excitations to the virtual space (POLSDCI) placed the triplet states ($^3\Sigma_g^-$, $^3\Gamma_u$, $^3\Sigma_u^+$) approximately 0.07 eV below the singlets. At the singles and doubles CI (SDCI) level of theory, these authors found the energy splitting of the six lowest δδ–hole states of Ni$_2$ to be less than 0.009 eV, with an average bond length of 2.26 Å and binding energy of 1.88 eV.

With a basis set similar to that used by Noell et al., (Noell et al., 1980) a contemporaneous restricted Hartree-Fock (RHF) and CI with single and double excitations (CISD) study predicted a $^3\Sigma_u^+$ ground state for Ni$_2$, with spectroscopic data: R_e = 2.33 Å, ω_e = 211 cm^{-1}, and D_e = 1.43 eV(Basch et al., 1980). Calculations by these authors at the same levels of theory using an all electron basis set corroborated the prediction of the ground state symmetry as $^3\Sigma_u^+$. On the other hand, a local spin density

method (Harris and Jones, 1979) predicted a $^3\Sigma_g^-$ ground state with R_e = 2.18 Å, ω_e = 320 cm^{-1}, and D_e = 2.70 eV. A slightly earlier CASSCF/CASPT2 study (Pou-Amérigo et al., 1994) that used an atomic natural orbital (ANO) type contraction of the (21s15p10d6f4g) primitive basis to [6s5p4d3f2g] for calculations without correlation of the semi-core 3s3p electrons, and a [10s9p8d3f2g] contracted basis for calculations involving the correlation of 3s3p electrons, likewise found the six lowest $\delta\delta$–hole states of Ni_2 to lie within a particularly narrow energy gap (0.04 eV) with the triplet states higher in energy than the singlets. However, after inclusion of scalar relativistic effects, the ground term was predicted as $^1\Gamma_g$, with the $^1\Sigma_g^+$ term lying only 0.01 eV higher at the equilibrium geometry. Correlating the 3s3p electrons in these calculations predicted the $^1\Gamma_g$ and $^1\Sigma_g^+$ states to be degenerate to the reported accuracy, with slightly improved spectroscopic constants relative to reference experimental values [i.e., R_e = 2.23 Å, D_e = 2.06 eV; and ω_e = 293 cm^{-1} for $^1\Gamma_g$ versus ω_e = 294 cm^{-1} for $^1\Sigma_g^+$ compared with experimental values of R_e = 2.1545 ± 0.0004 Å, (Pinegar et al., 1995) D_0 = 2.042 ± 0.002 eV, (Pinegar et al., 1995) and ω_e = 280 ± 20 cm^{-1} (Ho et al., 1993)].

DFT studies of Ni_2 have also been inconclusive. Yanagisawa et al. (Yanagisawa et al., 2000) used various DFT functionals to study the $^3\Sigma_g^-$ and $^3\Sigma_u^+$ states of Ni_2 and found B3LYP (Becke, 1993) to predict the $^3\Sigma_u^+$ state to lie lower than $^3\Sigma_g^-$ whereas the rest of the functionals predicted the latter state to lie lower at the equilibrium geometry. However, the $^3\Sigma_g^-$ state that they found had a configuration that corresponded to the $\pi\pi$–hole manifold rather than the $\delta\delta$. Gutsev et al. (Gutsev and Bauschlicher, 2003) also found a $^3\Sigma_g^-$ ground state, with the same configuration as did Yanagisawa et al., (Yanagisawa et al., 2000) when using a variety of hybrid functionals. Contrarily, Diaconu et al. (Diaconu et al., 2004) found a singlet $\delta\delta$–hole ground state (with a mixture of $^1\Gamma_g$ and $^1\Sigma_g^+$) for Ni_2 when using B3LYP with the (14s11p6d3f)/[8s6p4d1f] basis set, whereas use of the Stuttgart RSC ECP basis set (Dolg et al., 1987) with the same functional gave a triplet $\delta\delta$–hole (with a mixture of $^3\Sigma_g^-$ and $^3\Gamma_u$ symmetries) that lay 0.001 eV lower than the singlet $\delta\delta$–hole state at the equilibrium geometry. Using functionals at all levels of Jacob's ladder of DFT functionals, Schultz et al. (Schultz et al., 2005) also found different functionals to predict different ground state symmetries for Ni_2, with all local spin density approximation (LSDA) functionals predicting a $^3\Sigma_g^-$ ground state and all generalized gradient approximation (GGA) and meta GGA functionals predicting a $^3\Pi_u$ ground state; whereas hybrid GGA and hybrid meta GGA functionals found either $^3\Sigma_u^+$ or $^3\Sigma_g^-$ to lie lowest energetically. Du et al. (Du et al., 2008) used various functionals to study the low-lying states of Ni_2. Their results that agreed best with experiment were obtained when using BLYP, which predicted a triplet $\sigma\delta$–hole ($3d_{z2}$ σ_u^{*1} $3d_{x2-y2}$ δ_u^{*1}) ground state. The space symmetry of this state was not reported. With the B3P86 functional, (Perdew, 1986; Becke, 1993) a quintet ground state was predicted for Ni_2, (Shi-Ying and Zheng-He, 2008) although the space symmetry was not reported. The Perdew-Burke-Ernzerhof (PBE) exchange correlation functional (Perdew et al., 1996) predicted a $^3\Sigma_g^-$ ground state for Ni_2, (Kamal et al., 2012) with spectroscopic

constants R_e = 2.93 Å, D_e = 3.09 eV, and ω_e = 334.08 cm^{-1}, which showed significant deviations from experimental values.

Some of the most recent wave function based calculations on Ni_2 include those due to Dong et al. (Dong et al., 2013) using the symmetry-adapted-cluster configuration interaction (SAC-CI) method (Nakatsuji, 1979) and Cheskidov et al. (Cheskidov et al., 2012) using the average coupled pair functional (ACPF), (Gdanitz and Ahlrichs, 1988) average quadratic coupled cluster (AQCC), (Szalay and Bartlett, 1993) internally contracted single and double multireference configuration interaction (MRCI or MRCI with Davidson corrections, i.e., MRCI + Q), (Werner and Knowles, 1990) and N-electron valence state second-order perturbation theory (NEVPT2) (Angeli et al., 2001) methods. The study by Dong et al. (Dong et al., 2013) predicted a $^3B_{1u}$ ground state (with R_e = 2.56 Å) for Ni_2 in D_{2h} symmetry which corresponds to $^3\Sigma_u^+$, $^3\Delta_u$ or $^3\Gamma_u$ in $D_{\infty h}$. The study by Cheskidov et al. (Cheskidov et al., 2012) used the Dunning-type quadruple-ζ quality basis set, cc-pVQZ-DK (22s18p11d3f2g1h/ [8s7p6d3f2g1h]), (Balabanov and Peterson, 2005) and found the $^1\Gamma_g$ and $^1\Sigma_g^+$ $\delta\delta$–hole states to be quasidegenerate for all five methods with the $^1\Sigma_g^+$ state lying lower when using AQCC, MRCI + Q, and MRCI methods and the two states fully degenerate (to the reported accuracy level) at the ACPF and NEVPT2 levels. At the ACPF level, the predicted ground state was instead $^1\Sigma_u^-$; inclusion of spin-orbit relativistic corrections within ACPF calculations led to an 0_g^+ ground state ($^1\Sigma_g^+$ + $^3\Sigma_g^-$ $\delta\delta$–hole states), whereas the 0_u^- term ($^1\Sigma_u^-$ + $^3\Sigma_u^+$ $\delta\delta$–hole states) lay at only 0.009 ± 0.004 eV above the predicted ground state.

The above synopsis of previous work on Ni_2 shows the difficulties involved in studying not only the spectroscopic constants, but even the ordering of the low-lying electronic states of Ni_2. Although wave function methods generally support $\delta\delta$–hole states ($^1\Gamma_g$, $^1\Sigma_g^+$, $^3\Sigma_g^-$, $^1\Sigma_u^-$, $^3\Gamma_u$, $^3\Sigma_u^+$) as lying lowest energetically, the methods predict different ground state symmetries with some finding all six states to be degenerate. Similarly, experimental spectroscopic data have been obtained but most of the studies could not ascertain the ground state symmetry of the molecule. Our current study exploits the ability of the GVVPT2 method (Khait et al., 2002; Jiang et al., 2009) to describe well full PECs of ground- and excited-electronic states of complicated transition element dimers, such as has already been demonstrated on other problematic transition metal molecules [e.g., Cr_2 and Y_2 (Tamukong et al., 2012; Tamukong et al., 2014)]. It should be noted that of all previous theoretical work described above on electronic states of Ni_2, only six of the articles reported full PECs of the states they investigated. Consequently, where other data is available, this study also provides further assessment of the capabilities of the GVVPT2 method for difficult transition metal dimers, including the bond breaking regions. We have constructed full PECs of 21 states of Ni_2. All (nonrelativistic) calculations used the Dunning-type cc-pVTZ basis set (Balabanov and Peterson, 2005), and calculations were performed using D_{2h} symmetry. Furthermore, low-lying $^1\Gamma_g$ and $^1\Sigma_g^+$ states were further studied with scalar relativistic effects included in GVVPT2 (Tamukong et al., 2014) through the spin-free exact two component (sf-X2C) method (Liu, 2010; Cheng and Gauss, 2011; Li et al., 2012; Li et al., 2013). Relativistic

calculations used the cc-pVTZ-DK basis set (Balabanov and Peterson, 2005). The rest of the paper is organized as follows: *Methods* section briefly reviews key features of GVVPT2 and the spin-free exact two component (sf-X2C) methods, and describes computational details; the results are presented and discussed in *Results and Discussion* section; while conclusions are drawn in *Conclusion* section.

METHODS

GVVPT2

The GVVPT2 method for electron correlation in molecules has been thoroughly described elsewhere, (Khait et al., 2002; Jiang et al., 2009) as has its application to some challenging systems (Mbote et al., 2010; Khait et al., 2012; Tamukong et al., 2012; Mokambe et al., 2013; Tamukong et al., 2014). Here, salient features of the GVVPT2 method relevant to the present study are reviewed. In GVVPT, the total Hilbert space of many-electron functions [e.g., configuration state functions (CSFs)] with appropriate molecular space and spin symmetry (L) is partitioned into a model space (L_M), and an external space (L_Q) whose electronic configurations are derived from configurations generated from the model space by single and double electron excitations into virtual orbitals, $L = L_M \oplus L_Q$. The model space is further partitioned into a primary subspace, spanned by a set of reference functions that are linear combinations of CSFs (typically the lowest MCSCF or CASSCF states), and a secondary subspace. States within the primary subspace are then perturbatively corrected through primary-external (P–Q) interactions whereas the secondary subspace serves as a buffer energetically separating the primary and external subspaces. This energy buffer circumvents most intruder state problems that plague many multireference perturbation theory techniques. An effective Hamiltonian matrix ($\mathbf{H}_{MM}^{eff}$) is constructed with the same dimension as the model space, and its diagonalization includes both perturbatively corrected primary and unperturbed secondary subspace states. To guarantee continuity and smoothness of CSF responses (and ultimately PECs) even in situations of quasidegeneracies between primary and external states, GVVPT2 uses a continuously varying nonlinear denominator shift that arises from a resolvent that is both degeneracy-corrected and contains a hyperbolic tangent function as a switching function from nondegenerate to degenerate regimes (Khait et al., 2002). This resolvent can be written

$$X_{qi} = \frac{\tanh(\Delta_i)}{\Delta_i} H_{qi} = \frac{\tanh(\Delta_i)}{\Delta_i} \sum_{m \in L_M} H_{qm} C_{mi} \quad (1a)$$

$$\Delta_i = \frac{1}{2}\left(\varepsilon_q^i - \varepsilon_i^{(0)}\right) + \frac{1}{2}\sqrt{\left(\varepsilon_q^i - \varepsilon_i^{(0)}\right)^2 + 4\sum_{q \in e} H_{qi}^2} \quad (1b)$$

where the C_{mi} denote components of eigenvectors of the unperturbed model Hamiltonian; $\varepsilon_i^{(0)}$ is the reference Møller-Plesset-type energy while $\varepsilon_q^{(0)}$ is the state-specific zeroth-order energy of external CSF q. As with all studies of specific molecules

with GVVPT2 since ca. 2005, semicanonical orbitals from the MCSCF are used. The mathematical robustness of GVVPT2 allows it to support both complete and incomplete model spaces. By construction, GVVPT2 is subspace-specific (N.B. excited states of the same symmetry as lower-lying states can be calculated) and is spin-adapted.

Spin-Free Exact Two Component Method

Matrix formulations of two-component relativistic methods have had significant successes in molecular electronic structure calculations, following Dyall's seminal Normalized Elimination of Small Component (NESC) paper (Dyall, 1997) in 1997. For a summary of development of matrix two-component methods, we refer the reader to Ref. (Liu, 2014). In this work, we adopt the spin-free version of exact two component (sf-X2C) (Liu, 2010; Cheng and Gauss, 2011; Li et al., 2012; Li et al., 2013) that was previously used with GVVPT2 (Tamukong et al., 2014). The following Hamiltonian, written in second quantization form, incorporates scalar relativistic effects through the sf-X2C approach

$$H = \sum_{pq}\left[\mathbf{h}_{+,sf}^{X2C}\right]_{pq} a_p^+ a_q + \frac{1}{2}\sum_{pqrs}(pr|qs)a_p^+ a_q^+ a_s a_r \quad (2)$$

where the first term is the one-electron spin-free part of the exact two-component (X2C) Hamiltonian, while the second is the unmodified Coulombic two-electron term. The sf-X2C Hamiltonian for positive energy states derives from a modified Dirac Hamiltonian, $\mathbf{h}^D$ which is decomposed into spin-free (sf) and spin-dependent (sd) parts.

$$\mathbf{h}^D = \mathbf{h}_{sf}^D + \mathbf{h}_{sd}^D = \begin{pmatrix} \mathbf{V} & \mathbf{T} \\ \mathbf{T} & \frac{\alpha^2}{4}\mathbf{W}_{sf} - \mathbf{T} \end{pmatrix} + \begin{pmatrix} \mathbf{0} & \mathbf{0} \\ \mathbf{0} & \frac{\alpha^2}{4}\mathbf{W}_{sd} \end{pmatrix} \quad (3)$$

where $\mathbf{V}$ is the matrix representation of the external nuclear attraction potential operator; $\mathbf{T}$ is the matrix representation of the kinetic energy operator; α is the fine-structure constant; while $\mathbf{W}$ is the matrix representation of the operator

$$\mathbf{W} = \left(\vec{\sigma} \cdot \vec{p}\right) \mathbf{V} \left(\vec{\sigma} \cdot \vec{p}\right) = \vec{p} \cdot \mathbf{V}\vec{p} + i\vec{\sigma} \cdot \left(\vec{p}\,\mathbf{V} \times \vec{p}\right)$$
$$= \mathbf{W}_{sf} + \mathbf{W}_{sd} \quad (4)$$

The spin-free (sf) part of W, that is $\mathbf{W}_{sf}$, describes scalar relativistic effects whereas the spin-dependent (sd) part, $\mathbf{W}_{sd}$, incorporates spin-orbit coupling effects.

Computational Details

Unperturbed wavefunctions for GVVPT2 calculations were obtained from multiconfigurational self-consistent field (MCSCF) reference functions, using the local code "undmol." The macroconfiguration approach (Khait et al., 2004) was used in all MCSCF and GVVPT2 calculations. In the macroconfiguration scheme, active orbitals are partitioned into orbital groups based on physical and mathematical intuition, such as orbital type or energy, and electrons are assigned to active orbital groups. Each

FIGURE 1 | Example of MCSCF 3d- and 4s-derived molecular orbitals of the Ni$_2$ molecule.
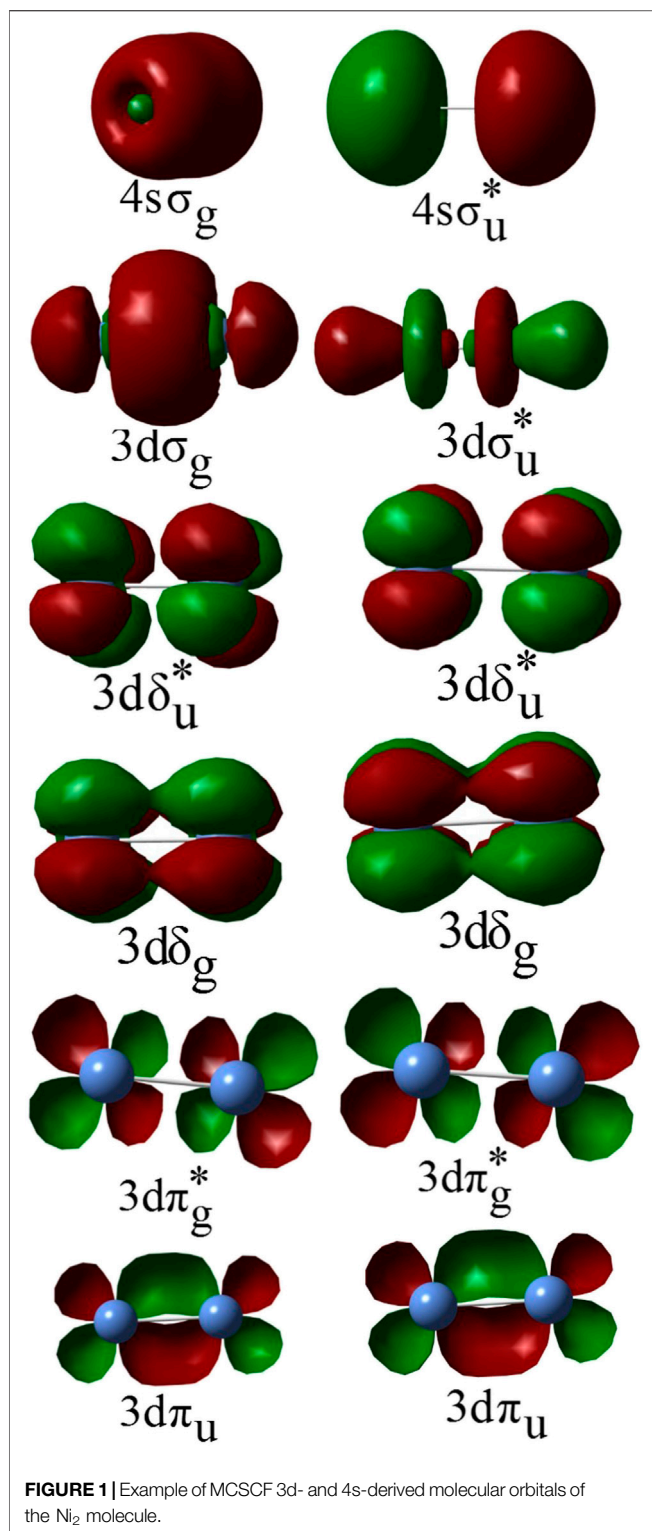
unique assignment of electrons to active orbital groups defines a macroconfiguration, $\kappa(\mathbf{n})$. Orbital rotations within each active orbital group are redundant (in MCSCF calculations), as all possible distributions of electrons within each group leading to the desired total spin and space symmetry are allowed. Each $\kappa(\mathbf{n})$

generates a unique set of configurations, and hence configuration state functions (CSFs) that are orthogonal to those of all other $\kappa(\mathbf{n})$. Additionally, the macroconfiguration approach permits a large number of noninteracting electronic configuration pairs to be efficiently screened by recognizing that all matrix elements resulting from configurations that differ by more than two electrons must be identically zero. The macroconfiguration formalism also provides an efficient way of generating excited configurations.

In all calculations, the active space consisted of 3d and 4s-derived molecular orbitals (MOs) of Ni$_2$ (**Figure 1** shows representative 3d and 4s-derived MOs that were used to constitute the active spaces in this study). Depending on the specific state being investigated, some of the 3d-derived MOs and/or 4s-derived MOs were restricted to be doubly occupied in the MCSCF calculations, but were included with the 3s- and 3p-derived MOs in the active core and correlated at the GVVPT2 level of theory. For example, in all MCSCF calculations of $\delta\delta$–hole states the $3d\sigma$ and $3d\pi$ MOs were placed in the active core and only correlated at the GVVPT2 level. Similarly, the $3d\sigma$ and $3d\pi$ electrons were kept doubly occupied in MCSCF calculations of $\pi\pi$–hole states while only the $3d\sigma$ electrons were kept doubly occupied in MCSCF calculations of $\delta\pi$–hole states, whereas the $4s\sigma$, or $4s\sigma + 3d\pi$, or $4s\sigma + 3d\sigma$ orbitals were kept doubly occupied in MCSCF calculations of states within the $^3F_4$ $(3d^84s^2)$ + $^3F_4$ $(3d^84s^2)$ dissociation channel. The remaining orbitals in the active space were partitioned into sets (or so-called orbital groups), leading to configurations that describe $\delta\delta$–, $\delta\pi$–, $\delta\sigma$–, $\pi\pi$–, $\pi\sigma$–, or $\sigma\sigma$–hole states from the $^3D_3$ $(3d^94s^1)$ + $^3D_3$ $(3d^94s^1)$ atomic combination or configurations that describe $^3D_3(3d^94s^1)$ +$^3F_4(3d^84s^2)$ and $^3F_4(3d^84s^2)$ + $^3F_4(3d^84s^2)$ atomic couplings. In the present study, we indicate the positions of holes within the subspace of active 3d–derived MOs by specifying the active orbital types that qualitatively describe where holes exist (e.g., $\delta\delta$–, $\delta\pi$–, $\pi\pi$–) as did Shim et al. (Shim et al., 1979) and Noel et al. (Noell et al., 1980)

All $\delta\delta$–states were computed using a single reference macroconfiguration,

$$\kappa_1\,(\mathbf{n}) = \left(3d\delta_g 3d\delta_u^* 3d\delta_g 3d\delta_u^*\right)^6 \left(4s\sigma_g 4s\sigma_u^*\right)^2 \qquad (5)$$

where the superscripts denote the number of electrons in each orbital group. The semi-core 3s3p electrons were correlated together with those derived from $3d_{z2}$, $3d_{xz}$ and $3d_{yz}$ at the GVVPT2 level. For four of the computed $\delta\delta$–states, additional calculations were also performed in which the 3s3p were kept doubly occupied throughout (i.e., at both the MCSCF and GVVPT2 levels). When using the cc-pVTZ basis set, (Balabanov and Peterson, 2005) reference $\kappa_1(\mathbf{n})$ generated 8 model and 27,891,120 total CSFs (in D$_{2h}$ symmetry) for the 1 $^3\Sigma_u^+$ and 1 $^3\Gamma_u$ states; 8 model and 15,290,666 total space CSFs for the 1$^1\Sigma_u^-$, 1$^1\Sigma_g^-$, and 1$^1\Gamma_u$ states; 10 model and 27,982,592 all space CSFs for the 1$^3\Sigma_g^-$ and 1$^3\Sigma_u^-$ states; and 12 model versus 15,270,687 all space CSFs for the X $^1\Gamma_g$ and 1 $^1\Sigma_g^+$ states. Without correlating the 3s3p electrons at the GVVPT2 level, the dimensions were: 12 model space CSFs versus 3,593,707 total CSFs for the X $^1\Gamma_g$ and 1 $^1\Sigma_g^+$ states; and 8 model versus 6,434,550

all space CSFs for the $1^3\Sigma_u^+$ and $1^3\Gamma_u$ states. Relativistic calculations on the X $^1\Gamma_g$ and 1 $^1\Sigma_g^+$ states utilized the same reference macroconfiguration, $\kappa_1(\mathbf{n})$. A $\delta\delta$ $^3\Gamma_u$ state was computed with 4 active electrons in 4 orbitals using reference

$$\kappa_2(\mathbf{n}) = \left(3d_{x^2-y^2}\delta_g 3d_{x^2-y^2}\delta_u^*\right)^6\left(4s\sigma_g 4s\sigma_u^*\right)^2 \quad (6)$$

which gave rise to 4 model space and 7,518,688 all space CSFs, using the cc-pVTZ basis set. The $\pi\pi$–states were computed using reference

$$\kappa_3(\mathbf{n}) = \left(3d\pi_u 3d\pi_g^* 3d\pi_u 3d\pi_g^*\right)^6\left(4s\sigma_g\ 4s\sigma_u^*\right)^2 \quad (7)$$

which is similar to $\kappa_1(\mathbf{n})$ but with delta replaced with pi orbitals. This macroconfiguration gave rise to 12 model space and 15,267,629 all space CSFs for the $1^1\Delta_g$ and $2^1\Sigma_g^+$ states when using the cc-pVTZ basis set and D_{2h} molecular space symmetry. The $\delta\pi$–states were computed from

$$\kappa_4(\mathbf{n}) = \left(3d\delta_g 3d\delta_u^* 3d\delta_g 3d\delta_u^*\right)^7\left(3d\pi_u 3d\pi_g^* 3d\pi_u 3d\pi_g^*\right)^7\left(4s\sigma_g 4s\sigma_u^*\right)^2 \quad (8)$$

$\kappa_4(\mathbf{n})$ generated 16 model space and 27,178,852 total space CSFs for the $1^1\Phi_g$ and $1^1\Pi_g$ states versus 20 model and 50,736,846 all space CSFs for the $1^3\Phi_g$ and $1^3\Pi_g$ states, when using the cc-pVTZ basis set.

Within the $^3F_4 + {}^3F_4$ manifold, the $3^1\Sigma_g^+$, $1^3\Sigma_g^+$, $2\ ^3\Sigma_g^+$, $1^3\Delta_u$, and $2\ ^3\Sigma_u^+$ $\delta\pi$–states were computed using

$$\kappa_5(\mathbf{n}) = \left(3d\delta_g 3d\delta_u^* 3d\delta_g 3d\delta_u^*\right)^6\left(3d\pi_u 3d\pi_g^* 3d\pi_u 3d\pi_g^*\right)^6 \quad (9)$$

In these calculations, the 3s, 3p, $3d_{z^2}$, and 4s electrons were kept doubly occupied at the MCSCF level but correlated at the GVVPT2 level of theory. Reference $\kappa_5(\mathbf{n})$ resulted in 40 model versus 55,053,638 total CSFs for the $3^1\Sigma_g^+$ state; 36 model and 103,306,512 all space CSFs for the $1^3\Sigma_g^+$ and $2\ ^3\Sigma_g^+$ states; and 40 model versus 103,312,902 all space CSFs for the $1^3\Delta_u$ and $2\ ^3\Sigma_u^+$ states when using the cc-pVTZ basis set.

Two $\delta\pi$–states, $2\ ^1\Gamma_g$ and $2\ ^1\Delta_g$, were computed within the $^3F_4 + {}^3F_4$ manifold using

$$\kappa_6(\mathbf{n}) = \left(3d\delta_g 3d\delta_u^* 3d\delta_g 3d\delta_u^*\right)^6\left(3d\sigma_g 3d\sigma_u^*\right)^2 \quad (10)$$

Reference $\kappa_6(\mathbf{n})$ generated 12 model space and 15,270,687 all space CSFs for the computed states using the cc-pVTZ basis set. Two quintet $\delta\pi\sigma$–states (i.e., $1^5\Phi_u$ and $1^5\Pi_u$) were also computed within the $^3F_4 + {}^3F_4$ manifold, using

$$\kappa_7(\mathbf{n}) = \left(3d\delta_g 3d\delta_u^* 3d\delta_g 3d\delta_u^*\right)^6\left(3d\pi_u 3d\pi_g^* 3d\pi_u 3d\pi_g^*\right)^7\left(3d\sigma_g 3d\sigma_u^*\right)^3 \quad (11)$$

This reference, $\kappa_7(\mathbf{n})$, led to 12 model versus 69,738,914 total CSFs for the computed quintet states. Lastly, a limited study was done on two quintet states within the $^3D_3(3d^94s^1) + {}^3F_4(3d^84s^2)$ manifold at short bond lengths. While reference

$$\kappa_8(\mathbf{n}) = \left(3d\delta_g 3d\delta_u^* 3d\delta_g 3d\delta_u^*\right)^7\left(3d\pi_u 3d\pi_g^* 3d\pi_u 3d\pi_g^*\right)^6\left(4s\sigma_g 4s\sigma_u^*\right)^3 \quad (12)$$

can describe the $1^5\Delta_g$ and $2\ ^5\Delta_g$ $\delta\pi\sigma$–states resulting from the $^3D_3(3d^94s^1) + {}^3F_4(3d^84s^2)$ manifold of molecular states adequately at short internuclear distances, it cannot be expected to do so at long internuclear distances and our studies were restricted to the shorter bond lengths for these two states. Reference $\kappa_8(\mathbf{n})$ generated 12 model CSFs versus 69,740,135 total space CSFs.

The reference macroconfigurations described above were used to define the active space, while all lower energy MOs were doubly occupied in MCSCF calculations. Initial MOs for MCSCF calculations were obtained from approximate natural orbitals of second-order restricted Møller–Plesset perturbation (RMP2) calculations from a closed-shell Hartree–Fock (HF) reference. At the GVVPT2 level, 3s, 3p, and all 3d and/or 4s electrons were correlated whether they were or were not at the MCSCF level. For comparison purposes, a few of the GVVPT2 calculations were performed without correlating the 3s and 3p electrons. Calculations that accounted for scalar relativistic effects employed the sf-X2C method described above. Finally, to aid in interpretation, the effective bond order (EBO) was computed, and used the following expression

$$\eta = \frac{\sum\limits_i \chi_i c_i^2}{\sum\limits_i c_i^2} \quad (13)$$

where η is the EBO, χ_i is the EBO for the ith CSF, while c_i^2 is its corresponding weight. For each CSF used to estimate EBO, χ_i was determined as

$$\chi_i = \frac{1}{2}\left(n_b - n_{ab}\right) \quad (14)$$

where n_b and n_{ab} are the numbers of bonding and antibonding electrons, respectively. Vibrational frequencies were obtained by 3-point finite differencing near the minima of the curves.

RESULTS AND DISCUSSION

Where indicated, the letter "R" in parentheses following a molecular term denotes that scalar relativistic effects were included in the calculations, while the expression "no 3s3p" in parentheses after a molecular term symbol denotes that 3s and 3p electrons were not correlated in GVVPT2 calculations.

The $\delta\delta$–Hole States

PECs of the $\delta\delta$–hole states are shown in **Figure 2** and the data describing them are in **Table 1**. In agreement with results from other high level *ab initio* methods, the lowest states of Ni$_2$ were found to be $\delta\delta$–hole states of the $^3D_3$ $(3d^94s^1) + {}^3D_3$ $(3d^94s^1)$ manifold. In particular, the ground state was found to be X $^1\Gamma_g$, with the $1^1\Sigma_g^+$ state lying only 16.40 cm^{-1} (0.002 eV) higher at the equilibrium geometry. After including scalar relativistic effects, the energy gap between these states slightly increased to 23.39 cm^{-1} at equilibrium, with the X $^1\Gamma_g$ term having spectroscopic constants: $R_e = 2.20$ Å, $D_e = 1.95$ eV, and $\omega_e = 296$ cm^{-1}. These results are in good agreement with experimental
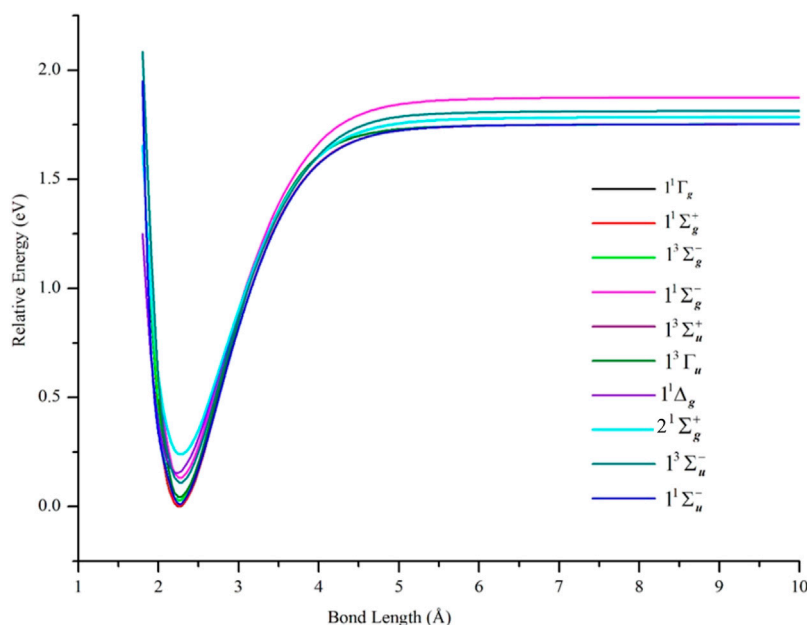
FIGURE 2 | PECs of low-lying electronic states of Ni$_2$ computed at the GVVPT2 level of theory using the cc-pVTZ basis set. All energies are plotted relative to the lowest energy value of the ground X $^1\Gamma_g$ term. For all states, the holes are in the 3d delta orbitals ($\delta\delta$–holes) except for $1^1\Delta_g$ and $2\ ^1\Sigma_g^+$ states which are $\pi\pi$–hole states.

TABLE 1 | Equilibrium bond lengths, R_e (Å), binding energies, D_e (eV), harmonic frequencies, ω_e (cm^{-1}), and adiabatic transition energies, T_e (cm^{-1}), of electronic states of Ni$_2$ calculated at the GVVPT2 level of theory using the cc-pVTZ basis set (or cc-pVTZ-DK for scalar relativistic calculations).

Molecular term	R_e (Å)	D_e (eV)	ω_e (cm^{-1})	T_e (cm^{-1})
		$\delta\delta$–hole states		
		Computed using $\kappa_1(\mathbf{n})$		
X $^1\Gamma_g$	2.26	1.75	276.0	
X $^1\Gamma_g$ (no 3s3p)	2.27	1.66	268.5	
X $^1\Gamma_g$ (R)	2.20	1.95	296.0	
Experiment	2.1545 ± 0.0004^a	2.042 ± 0.002^a	280 ± 20^b	
$1^1\Sigma_g^+$	2.26	1.75	276.8	16.40
$1^1\Sigma_g^+$ (R)	2.20	1.95	297.0	23.39
$1^1\Sigma_g^+$ (no 3s3p)	2.28	1.65	263.3	16.56
$1^1\Sigma_u^-$	2.27	1.74	274.2	91.09
$1^3\Sigma_u^+$	2.27	1.71	274.9	349.60
$1^3\Sigma_u^+$ (no 3s3p)	2.28	1.62	267.4	309.58
$1^3\Gamma_u$	2.27	1.71	274.9	351.11
$1^3\Gamma_u$ (no 3s3p)	2.28	1.62	267.4	310.31
$1^3\Sigma_g^-$	2.26	1.72	275.0	221.98
$1^3\Sigma_u^-$	2.27	1.70	273.9	882.59
$1^1\Sigma_g^-$	2.27	1.74	270.2	1058.87
$2\ ^1\Sigma_u^-$	2.75	0.11	73.5	18575.76
		Computed using $\kappa_2(\mathbf{n})$		
$2\ ^3\Gamma_u$	2.27	1.71	275.0	2442.21

^{a}Ref. (Cooper et al., 1972) (the reported binding energy is for D_0).
^{b}Ref. (Rösch and Rhodin, 1974).

data (R_e = 2.1545 ± 0.0004 Å, (Cooper et al., 1972) D_0^o = 2.042 ± 0.002 eV, (Cooper et al., 1972) and ω_e = 280 ± 20 cm^{-1}) (Rösch and Rhodin 1974) and with the relativistic CASSCF/CASPT2 results of Pou-Amérigo et al. (Pou-Amérigo et al., 1994) who also found the lowest $^1\Gamma_g$ and $^1\Sigma_g^+$ terms to be quasidegenerate (with R_e = 2.23 Å, D_e = 2.06 eV, and ω_e = 293 cm^{-1} for the $^1\Gamma_g$ term). These

results are also in good agreement with the time-delayed resonant two-photon ionization study of Morse and co-workers (Pinegar et al., 1995) that predicted either a $^3\Gamma_u$ or $^1\Gamma_g$ state as the ground state of Ni$_2$ and the scalar relativistic calculations of Cheskidov et al. (Cheskidov et al., 2012) who found the lowest $^1\Gamma_g$ and $^1\Sigma_g^+$ terms to be degenerate at the ACPF and NEVPT2 levels of theory and the
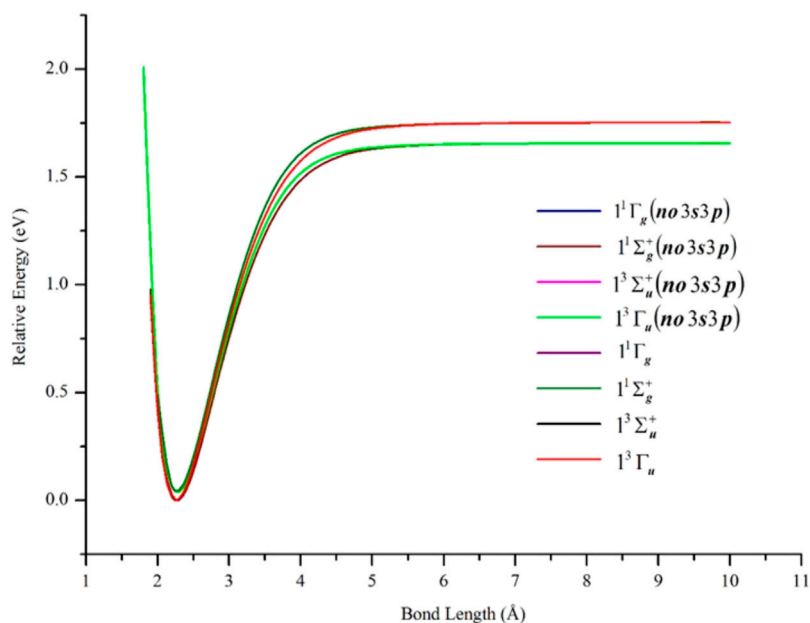
FIGURE 3 | PECs of low-lying δδ–hole electronic states of Ni$_2$ computed at the GVVPT2 level of theory, with and without the correlation of 3s3p semi-core electrons, using the cc-pVTZ basis set. All energies are plotted relative to the lowest energy value of the ground X $^1\Gamma_g$ term.
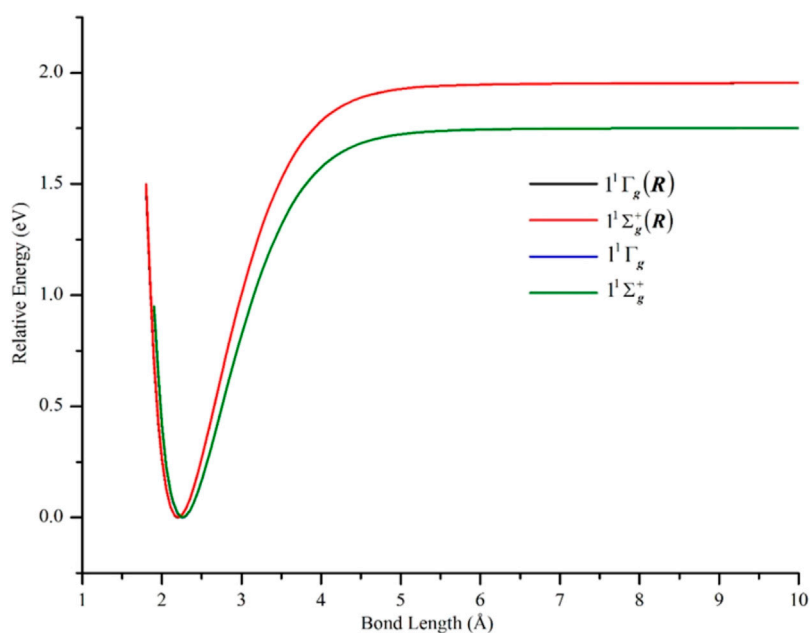
FIGURE 4 | PECs of the lowest-lying δδ–hole X $^1\Gamma_g$ and $1^1\Sigma_g^+$ states of Ni$_2$ computed at the GVVPT2 level of theory, with and without scalar relativity included, using the cc-pVTZ (or cc-pVTZ-DK) basis set. Non-relativistic energies are plotted relative to the lowest energy value of the ground X $^1\Gamma_g$ term while relativistic energies are plotted relative to the lowest energy of the X $^1\Gamma_g$ (R) term.

$^1\Sigma_g^+$ term to lie very slightly lower than the $^1\Gamma_g$ at the AQCC, MRCI, and MRCI + Q levels of theory. At 2.25 Å, we found the EBO to be 0.963 and 0.960 for the $^1\Gamma_g$ and $^1\Sigma_g^+$ states, respectively (using the largest dozen CSFs). In relativistic GVVPT2 calculations, these EBOs

increased slightly to 0.975 for $^1\Gamma_g$ and 0.972 for $^1\Sigma_g^+$ at this geometry. The major configurations describing the X $^1\Gamma_g$ and $1^1\Sigma_g^+$ states involved two holes in the same δ–type; i.e., $0.445 \times (3d_{xy}\delta_g^2$ $3d_{xy}\delta_u^{*2} \ 3d_{x2-y2}\delta_g^2 \ 4s\sigma_g^2 \ + \ 3d_{xy}\delta_g^2 \ 3d_{x2-y2}\delta_g^2 \ 3d_{x2-y2}\delta_u^{*2}$

$4s\sigma_g{}^2$) and $0.077 \times$ ($3d_{xy}\delta_g{}^2$ $3d_{xy}\delta_u{}^{*2}$ $3d_{x2-y2}\delta_u{}^{*2}$ $4s\sigma_u{}^{*2}$ - $3d_{xy}\delta_u{}^{*2}$ $3d_{x2-y2}\delta_g{}^2$ $3d_{x2-y2}\delta_u{}^{*2}$ $4s\sigma_u{}^{*2}$), where coefficients are amplitudes and each term within parentheses denotes active orbitals of each leading CSF of the GVVPT2 wavefunction.

The semi-core 3s3p electrons were found to be important in the description of low-lying states of Ni_2. The inclusion of 3s3p electron correlation at the GVVPT2 level increased the binding energies by 0.09 eV for X $^1\Gamma_g$, 0.10 eV for $1^1\Sigma_g{}^+$, and 0.09 eV for $1^3\Sigma_u{}^+$ and $1^3\Gamma_u$ states in non-relativistic calculations. As can be seen in **Figure 3** and **Table 1**, the effects of the 3s3p electrons on the equilibrium bond lengths and harmonic frequencies for these states are minimal whereas inclusion of such core-valence correlation raises, for example, the binding energy of X $^1\Gamma_g$ from 1.66 to 1.75 eV compared to a reference D_0 value of 2.042 ± 0.002 eV (Cooper et al., 1972). Scalar relativistic effects shortened the bond length of X $^1\Gamma_g$ by 0.06 Å and further increased the bond energy by 0.20 to 1.95 eV which agreed even better with the reference experimental values (see **Figure 4** and **Table 1**). The 3s3p electrons did not have any effect on the EBOs of X $^1\Gamma_g$ and $1^1\Sigma_g{}^+$; the EBOs were determined as 0.962 and 0.959 at 2.27 Å for X $^1\Gamma_g$ and $1^1\Sigma_g{}^+$, respectively, when the 3s3p electrons were not correlated compared to 0.963 vs. 0.960 when the semi-core electrons (3s3p) were correlated. Note the quasidegeneracy in the X $^1\Gamma_g$ and $1^1\Sigma_g{}^+$ states. For example, in **Figure 4**, the blue and green curves for the X $^1\Gamma_g$ and $1^1\Sigma_g{}^+$ states, respectively, lie on top of each other (only the green is visible). Also, the black and red curves for the X $^1\Gamma_g$ (R) and $1^1\Sigma_g{}^+$ (R) states lie on each other (only the red curve is visible).

The $1^1\Sigma_u{}^-$ state, which was predicted as the ground state of Ni_2 at the ACPF level of theory (Cheskidov et al., 2012) and found to lie quite close to a $^1\Sigma_g{}^+$ ground state in a limited CI study (Ahmed and Nixon, 1979), was found at the GVVPT2 level to lie 91.09 cm^{-1} above the X $^1\Gamma_g$ state at equilibrium. The $2^1\Sigma_u{}^-$ state, however, lay much higher energetically (18,575.76 cm^{-1} above the ground state at equilibrium).

As can be seen in **Table 1**, GVVPT2 predicted the triplet $\delta\delta$–hole states, $1^3\Sigma_g{}^-$, $1^3\Sigma_u{}^+$, and $1^3\Gamma_u$, to lie energetically in the order $1^3\Sigma_g{}^- < 1^3\Sigma_u{}^+ < 1^3\Gamma_u$. Cheskidov et al. (Cheskidov et al., 2012) found this same ordering at the ACPF, AQCC, MRCI and MRCI + Q levels of theory, whereas their NEVPT2 calculations predicted the ordering $1^3\Sigma_u{}^+ < 1^3\Gamma_u < 1^3\Sigma_g{}^-$, with the $1^3\Sigma_g{}^-$ state lying at least 139 cm^{-1} higher than the other two states. It should be noted that the vertical excitation energies in Ref. (Cheskidov et al., 2012) were not determined at the equilibrium geometries of the computed states. The $1^3\Sigma_u{}^+$ state, which was predicted as the ground state of Ni_2 in some previous wavefunction (Wood et al., 1980; Schultz et al., 2005) and DFT (Diaconu et al., 2004; Kramida et al., 2013) studies, was found in our current study to lie 349.60 cm^{-1} above the X $^1\Gamma_g$ state at the equilibrium geometry. Likewise, the $1^3\Sigma_g{}^-$ state reported in other studies (Murphy and Messmer, 1992; Diaconu et al., 2004; Kramida et al., 2013) as the ground state of Ni_2 lay 221.98 cm^{-1} higher at equilibrium. The $1^3\Sigma_u{}^-$ state was found to have a bond length and bond energy comparable to those of $1^3\Sigma_g{}^-$, $1^3\Sigma_u{}^+$, and $1^3\Gamma_u$ but

lying at least 531.48 cm^{-1} higher in energy. The EBOs for these triplet states were 0.971 for $1^3\Sigma_g{}^-$, 0.933 for $1^3\Sigma_u{}^+$ and $1^3\Gamma_u$, and 0.923 for $1^3\Sigma_u{}^-$ in the vicinity of their equilibrium geometries (again computed with 10 leading CSFs). The major configurations for the $\delta\delta$–hole triplet states involved a doubly occupied $4s\sigma_g$ bonding orbital.

The $1^3\Gamma_u$ state, in which both δ–holes were in the $3d_{x2-y2}$ δ_g and $\delta_u{}^*$ orbitals, was computed using reference $\kappa_2(\mathbf{n})$. As can be seen in **Table 1**, this state was found to have spectroscopic constants comparable to other $\delta\delta$–hole triplet states but lay much higher energetically (2442.21 cm^{-1} above the ground state at equilibrium). The present results suggest that the $3d\delta$ orbitals are indeed split in the bonding interaction. Since they are nondegenerate, the Aufbau principle suggests that energetically low-lying orbitals (the bonding $3d\delta$ orbitals) be occupied before higher ones. Moreover, Hund's rule suggests that orbitals with similar energies (in this case, $3d\delta_u{}^*$ orbitals) be singly occupied before electron pairing occurs. This seems to bring qualitative understanding into why the $1^3\Sigma_g{}^-$, $1^3\Sigma_u{}^+$, and $1^3\Gamma_u$ states in which the $3d_{x2-y2}\delta_u{}^*$ and $3d_{xy}\delta_u{}^*$ are singly occupied lie energetically lower than the $2^3\Gamma_u$ state for which the $3d_{x2-y2}\delta_g$ and $3d_{x2-y2}\delta_u{}^*$ are singly occupied.

The $\delta\pi$–Hole and $\pi\pi$–Hole States

The PECs of the computed $\pi\pi$–hole states ($1^1\Delta_g$ and $2^1\Sigma_g{}^+$) are shown in **Figure 2**, while those for the $\delta\pi$–hole states ($1^1\Phi_g$, $1^1\Pi_g$, $1^3\Pi_g$, and $1^3\Phi_g$) are shown in **Figure 5** and compared with the ground state PEC. The data describing these curves are in **Table 2**. GVVPT2 predicted the $\pi\pi$–hole states to lie higher in energy than the $\delta\pi$–hole states, in agreement with previous studies (Ahmed and Nixon, 1979; Rasanen et al., 1987; Russo et al., 1994). For all four $\delta\pi$–hole states studied, the major CSFs involved a doubly occupied $4s\sigma_g$ bonding orbital. Thus, the main configurations of the $1^1\Phi_g$ and $1^1\Pi_g$ states involved an unpaired spin-increasing electron in the $3d\delta$ subspace and an unpaired spin-decreasing electron in the $3d\pi$ subspace, e.g., $3d\delta_g{}^2$ $3d\delta_u{}^{*2}$ $3d\delta_g{}^2$ $3d\delta_u{}^{*(\uparrow)}$ $3d\pi_u{}^2$ $3d\pi_g{}^{*2}$ $3d\pi_u{}^2$ $3d\pi_g{}^{*(\downarrow)}$ $4s\sigma_g{}^2$, whereas the major configurations of the $1^3\Phi_g$ and $1^3\Pi_g$ states were similar to those of the corresponding singlet states but with two unpaired spin-increasing electrons: one in each of the $3d\delta$ and $3d\pi$ subspaces, e.g., $3d\delta_g{}^2$ $3d\delta_u{}^{*2}$ $3d\delta_g{}^2$ $3d\delta_u{}^{*(\uparrow)}$ $3d\pi_u{}^2$ $3d\pi_g{}^{*2}$ $3d\pi_u{}^2$ $3d\pi_g{}^{*(\uparrow)}$ $4s\sigma_g{}^2$.

At the equilibrium geometries, the EBOs were 0.930 for the singlet $1^1\Phi_g$ and $1^1\Pi_g$ states and 0.933 for the $1^3\Pi_g$ and $1^3\Phi_g$ states. GVVPT2 predicted the four $\delta\pi$–hole states to lie energetically in the order $1^1\Phi_g < 1^1\Pi_g < 1^3\Pi_g < 1^3\Phi_g$, in agreement with the Ref. (Cheskidov et al., 2012) study at the scalar relativistic ACPF, AQCC, MRCI, and MRCI + Q levels of theory. However, our calculations found all three states considered in Ref. (Cheskidov et al., 2012) (i.e., $1^1\Pi_g$, $1^3\Pi_g$, and $1^3\Phi_g$) to lie some 500 cm^{-1} closer to the ground state; e.g., at the scalar relativistic MRCI + Q level, the $1^3\Phi_g$ state was reported (Cheskidov et al., 2012) as lying 1238 cm^{-1} above the ground state at 2.5 Å while non-relativistic GVVPT2 calculations predicted this state to lie 546.76 cm^{-1} above the ground state at equilibrium. Based on our observation that including scalar relativistic effects increased the energy gap between the $1^1\Sigma_g{}^+$ and X $^1\Gamma_g$ states, it is likely that including

FIGURE 5 | PECs of low-lying $\delta\pi$–hole electronic states of Ni$_2$ computed at the GVVPT2 level of theory using the cc-pVTZ basis set compared with the PEC of the X $^1\Gamma_g$ ground term. All energies are plotted relative to the lowest energy value of the X $^1\Gamma_g$ ground term.
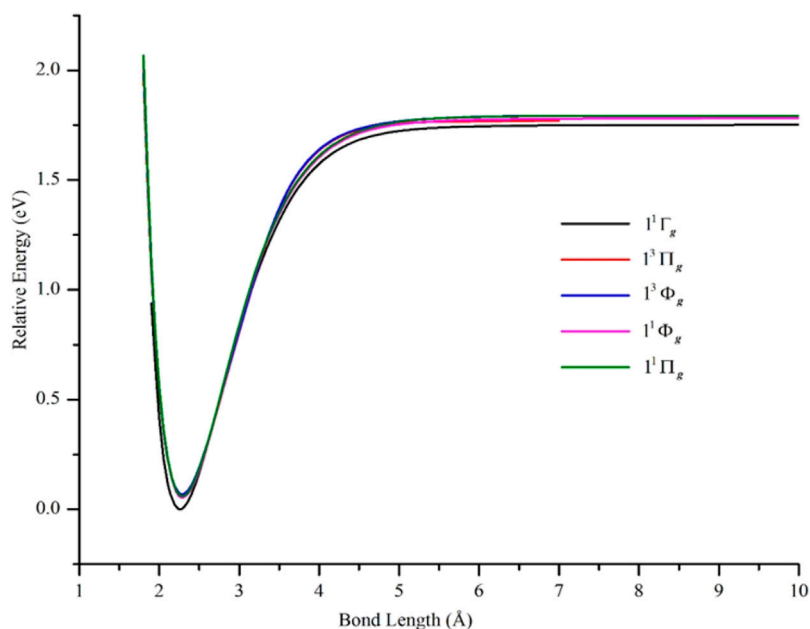
TABLE 2 | Equilibrium bond lengths, R_e (Å), binding energies, D_e (eV), harmonic frequencies, ω_e (cm^{-1}), and adiabatic transition energies, T_e (cm^{-1}), of electronic states of Ni$_2$ calculated at the GVVPT2 level of theory using the cc-pVTZ basis set and reference macroconfigurations $\kappa_3(\mathbf{n})$ to $\kappa_8(\mathbf{n})$.

Molecular term	R_e (Å)	D_e (eV)	ω_e (cm^{-1})	T_e (cm^{-1})
$\delta\pi$ States computed with $\kappa_4(\mathbf{n})$
$1^1\Phi_g$	2.29	1.73	263.7	427.86
$1^1\Pi_g$	2.29	1.73	269.7	485.09
$1^3\Pi_g$	2.29	1.72	261.9	518.14
$1^3\Phi_g$	2.29	1.72	261.3	546.76
$\pi\pi$ States computed with $\kappa_3(\mathbf{n})$
$1^1\Delta_g$	2.23	1.63	242.5	1241.68
$2\ ^1\Sigma_g^+$	2.28	1.55	240.5	1925.85
States computed with $\kappa_5(\mathbf{n})$
$1^3\Delta_u$	3.96	0.02	26.2	33555.78
$2\ ^3\Sigma_u^+$	3.96	0.02	26.2	33555.91
$2\ ^1\Delta_g$	3.93	0.03	26.6	34531.63
$1\ ^3\Sigma_g^+$	3.95	0.03	26.2	39160.31
$2\ ^3\Sigma_g^+$	3.96	0.03	26.0	39162.41
States computed with $\kappa_6(\mathbf{n})$
$2\ ^1\Gamma_g$	3.73	0.04	26.9	35412.38
$3\ ^1\Sigma_g^+$	3.73	0.04	26.9	35412.41
States computed with $\kappa_7(\mathbf{n})$
$1^5\Phi_u$	3.83	0.03	26.7	33144.35
$1^5\Pi_u$	3.84	0.03	26.9	33147.67
States computed with $\kappa_8(\mathbf{n})$
$1^5\Delta_g$	2.22		249.1	5123.66
$2^5\Delta_g$	2.54		150.1	9018.57

such effects in GVVPT2 calculations on the $\delta\pi$–hole states might lead to increases in corresponding adiabatic transition energies. It is not anticipated, however, that such effects would lead to any change in the energy ordering of the states.

Although lying higher in energy than the $\delta\pi$–hole states, the $\pi\pi$–hole states were found to have slightly shorter bond lengths and larger bond strengths than the $\delta\pi$–hole states. The $1\ ^1\Delta_g$ state was 0.06 Å shorter while the $2\ ^1\Sigma_g^+$ state was 0.01 Å shorter in bond length than the $\delta\pi$–hole states. At 2.24 Å, the EBOs of $1\ ^1\Delta_g$ and $2\ ^1\Sigma_g^+$ were 1.108 and 1.084 respectively (computed with a dozen CSFs); these were slightly higher than the EBOs of all computed $\delta\delta$–hole and $\delta\pi$–hole Ni$_2$ states. Near equilibrium, the major configurations of these $\pi\pi$–hole states involved a doubly occupied $4s\sigma_g$ bonding orbital and a configuration of the $3d\pi$ subspace that had the two π–holes in the same π–orbital; e.g., $3d\pi_u^2\ 3d\pi_g^{*2}\ 3d\pi_u^2\ 3d\pi_g^{*0}\ 4s\sigma_g^2$.

States of the $^3F_4 + {}^3F_4$ and $^3F_4 + {}^3D_3$ Manifolds

Figure 6 contains PECs of states belonging to the $^3F_4 + {}^3F_4$ manifold. The data describing these curves are in **Table 2**. Irrespective of how the model space was partitioned into macroconfigurations [i.e., $\kappa_i(\mathbf{n})$], all such states were found to be van der Waals-like with interaction energies ≤ 0.04 eV. For example, near the equilibrium geometry (i.e., 3.77 Å), the $2\ ^1\Gamma_g$ and $3\ ^1\Sigma_g^+$ states had EBO of only 0.005, while the $1^5\Phi_u$ and $1^5\Pi_u$ states had EBOs of 0.003 and 0.00, respectively, at 3.84 Å. These latter quintet states were computed using reference $\kappa_7(\mathbf{n})$ and found to have the lowest total energies among the computed states of the $^3F_4 + {}^3F_4$ manifold; the $1^5\Pi_u$ state is 3.312 cm^{-1} less stable than the $1^5\Phi_u$ state at equilibrium. The rest of the PECs in **Figure 6** were plotted relative to the $1^5\Phi_u$ PEC.

Lastly, the $1^5\Delta_g$ and $2\ ^5\Delta_g$ states of the $^3F_4 + {}^3D_3$ manifold were investigated, at short bond lengths only, using reference
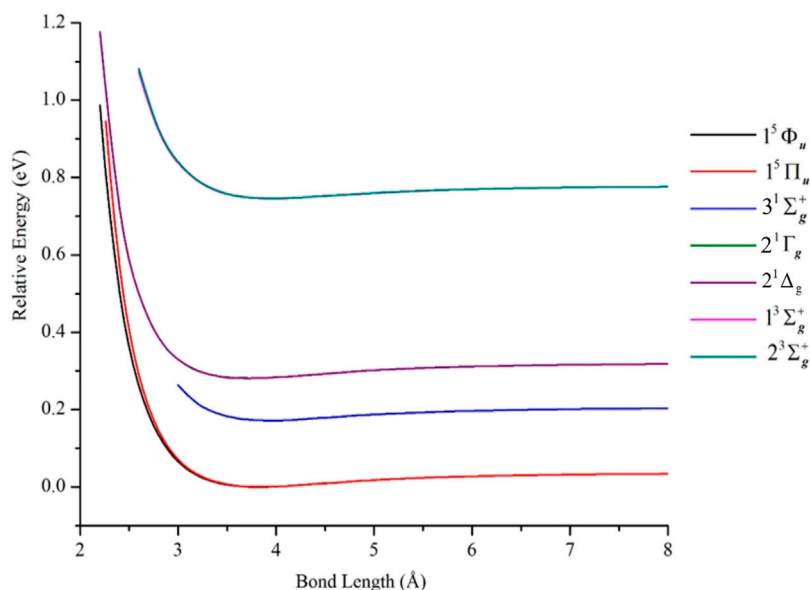
FIGURE 6 | PECs of electronic states of Ni_2 from the $^3F_4$ ($3d^84s^2$) + $^3F_4$ ($3d^84s^2$) manifold, computed at the GVVPT2 level of theory using the cc-pVTZ basis set and reference macroconfigurations $\kappa_5(\mathbf{n})$ to $\kappa_7(\mathbf{n})$. All energies are plotted relative to the lowest energy value of the $1^5\Phi_u$ term.

macroconfiguration $\kappa_8(\mathbf{n})$. The data for these states are included in **Table 2**. Whereas the $^3F_4$ ($3d^84s^2$) + $^3F_4$ ($3d^84s^2$) states are van der Waals-like, the short bond length (2.22 Å) and high frequency (249.1 cm^{-1}) of the $1^5\Delta_g$ state is suggestive of significant bonding interaction. At 2.22 Å, the major configuration for this state was $3d_{x2-y2}\delta_g^2\ 3d_{x2-y2}\delta_u^{*2}\ 3d_{xy}\delta_g^2\ 3d_{xy}\delta_u^{*1}\ 3d\pi_u^2\ 3d\pi_g^{*1}\ 3d\pi_u^2\ 3d\pi_g^{*1}\ 4s\sigma_g^2\ 4s\sigma_u^{*1}$, contributing 50% by weight to the total wave function. At this geometry, the EBO was found to be 1.186. However, one should approach these results for $^3F_4$ + $^3D_3$ derived states with some caution, as the macroconfiguration used cannot describe their dissociation limits.

CONCLUSION

The GVVPT2 method was used to study low-lying electronic states of Ni_2. The results indicate, in general, that bonding in these states involves predominantly the doubly occupied $4s\sigma_g$ bonding orbital with the 3d–3d electrons pairwise spin coupled (e.g., consistent with antiferromagnetism). This statement is corroborated by EBOs that were found to be approximately 1.0 for most states studied and, moreover, states that did not allow this type of interaction [e.g., belonging to the $^3F_4$ ($3d^84s^2$) + $^3F_4$ ($3d^84s^2$) manifold] were found to be bound only by weak polarization forces with bond orders close to zero. For computed states of the $^3D_3$ ($3d^94s^1$) + $^3D_3$ ($3d^94s^1$) dissociation limit, all major configurations involved a doubly occupied $4s\sigma_g$ bonding orbital and a vacant $4s\sigma_u^*$ antibonding orbital. The energy ordering of the computed states of the $^3D_3$ ($3d^94s^1$) + $^3D_3$ ($3d^94s^1$) manifold is in agreement with previous studies that found the $\delta\delta$–hole states to lie lowest in energy followed by the $\delta\pi$–hole and then the $\pi\pi$–hole states (Rasanen et al., 1987). For

the investigated $\delta\delta$–hole states, the singlets were more stable than the triplet states at the GVVPT2 level of theory. As expected, based on previous GVVPT2 studies of transition metal dimers, all computed PECs are smooth and without unphysical artifacts (e.g., wiggles).

The ground state of Ni_2 was predicted as X $^1\Gamma_g$ in agreement with previous results from other high level *ab initio* methods (Cheskidov et al., 2012; Pou-Amérigo et al., 1994). The determined equilibrium spectroscopic constants of the X $^1\Gamma_g$ state, using a cc-pVTZ (or cc-pVTZ-DK) basis, were within the uncertainties of experimental results. The lowest $^1\Sigma_g^+$ state was found to be only 0.002 eV (16.40 cm^{-1}) higher than the ground state at the equilibrium geometry. Core-valence correlation was found to be important in the description of low-lying states of Ni_2 where the inclusion of 3s3p electron correlation at the GVVPT2 level was shown to improve harmonic frequencies and bond energies (e.g., by an increase of 7.5 cm^{-1} in frequency and 0.09 eV in bond energy when 3s3p electron correlation was included in GVVPT2 calculations of the X $^1\Gamma_g$ state). Scalar relativistic effects were also shown to be important, especially for dissociation energy, where spectroscopic constants from relativistic calculations were predicted to agree better with reference data (e.g., a decrease of 0.06 Å in bond length, increase of 0.20 eV in bond energy, and an increase of 20.0 cm^{-1} in harmonic frequency when including scalar relativistic effects in calculations of the X $^1\Gamma_g$ state). In our previous study (Tamukong et al., 2014) on electronic states of Y_2, Mn_2, and Tc_2, we did not find scalar relativistic effects to be as important for the Mn_2 molecule as they have proven to be in the present study. The inclusion of spin-orbit coupling effects was previously found (Cheskidov et al., 2012; Rasanen et al., 1987; Pou-Amérigo et al., 1994) to mix the low-lying states of Ni_2,

leading to a $0_g^+[^1\Sigma_g^+(\delta\delta) + {}^3\Sigma_g^-(\delta\delta)]$ ground state. Since the two curves are close and nearly parallel for all internuclear separations in our study, we expect that including such effects after our scalar relativistic GVVPT2 treatment should lead to a similar mixing of states (i.e., and without change in spectroscopic constants).

The states investigated within the ${}^3F_4$ ($3d^84s^2$) + ${}^3D_3$ ($3d^94s^1$) manifold suggested significant bonding interaction, giving large harmonic frequencies and short bond lengths in comparison with states correlating with the ${}^3F_4$ ($3d^84s^2$) + ${}^3F_4$ ($3d^84s^2$) dissociation limit. Further work on Ni_2 should explore the ${}^3F_4$ ($3d^84s^2$) + ${}^3D_3$ ($3d^94s^1$) manifold more thoroughly, including possible expansion of the active space. It should be noted, however, that in the present study, we did not observe any significant electron excitations from the valence orbitals to 4p-dominated virtual orbitals. Also, while spin-free relativistic effects are noticeable (especially for bond dissociation energies), the parallelity and small energy separations for states in these manifolds are very similar to those in the ${}^3D_3$ ($3d^94s^1$) + ${}^3D_3$ ($3d^94s^1$) dissociation channel and, again, we do not expect that spin-dependent relativistic effects would change PECs appreciably, although current capabilities of our GVVPT2 code did not let us explore this.

In summary, the present study showed that Ni_2 does not form strong bonds with atomic configurations in which the 4s subshell is fully filled. This observation is consistent with other studies, by us and by others, of transition elements of the first row. Bonding in these systems is generally favored by atomic configurations that involve at least one of the participating atoms in an excited state ($3d^{n+1}4s^1$). For example, in our previous study (Tamukong et al., 2012) of the low-lying electronic states of Sc_2, Cr_2, and Mn_2, the lowest states of Sc_2 were shown to correlate with the ${}^2D$ ($3d^14s^2$) + ${}^4F$ ($3d^24s^1$) dissociation asymptote, while those of Cr_2 correlated with the ${}^7S$ ($3d^54s^1$) + ${}^7S$ ($3d^54s^1$) dissociation limit. However, bonding in transition metal dimers is subtle and the

most stable states of Mn_2 were obtained from weakly coupled ${}^5D$ ($3d^54s^2$) + ${}^5D$ ($3d^54s^2$) ground state Mn atoms, similar to the ${}^3F_4$ ($3d^84s^2$) + ${}^3F_4$ ($3d^84s^2$) coupling of ground state Ni atoms. Our results provide further evidence that GVVPT2, with sf-X2C treatment of relativistic effects, predict electronic excitation and bond energy trends in the first row transition metals consistent with experiment and the highest level *ab initio* calculations. In the present case, the quasidegeneracy of the ${}^3F$ and ${}^3D$ states of the Ni atom demonstrates that GVVPT2 can successfully be used for a system with an extraordinarily dense manifold of states, which generally requires computationally intensive variational treatments.

DATA AVAILABILITY STATEMENT

The raw data supporting the conclusions of this article will be made available by the authors, without undue reservation.

AUTHOR CONTRIBUTIONS

MH and PT contributed to conception and design of the study. PT performed numerical calculations. MH and PT interpreted data and organized presentation. PT wrote the first draft of the manuscript. All authors contributed to manuscript revision, read, and approved the submitted version.

FUNDING

REFERENCES

Ahmed, F., and Nixon, E. R. (1979). The A→X System of Ni2 in Argon Matrices. *J. Chem. Phys.* 71 (8), 3547–3549. doi:10.1063/1.438750

Andersson, K., and Roos, B. O. (1992). Excitation Energies in the Nickel Atom Studied with the Complete Active Space Scf Method and Second-Order Perturbation Theory. *Chem. Phys. Lett.* 191 (6), 507–514. doi:10.1016/0009-2614(92)85581-t

Angeli, C., Cimiraglia, R., Evangelisti, S., Leininger, T., and Malrieu, J.-P. (2001). Introduction Ofn-Electron Valence States for Multireference Perturbation Theory. *J. Chem. Phys.* 114 (23), 10252–10264. doi:10.1063/1.1361246

Balabanov, N. B., and Peterson, K. A. (2005). Systematically Convergent Basis Sets for Transition Metals. I. All-Electron Correlation Consistent Basis Sets for the 3d Elements Sc–Zn. *J. Chem. Phys.* 123 (6), 064107. doi:10.1063/1.1998907

Basch, H., Newton, M. D., and Moskowitz, J. W. (1980). The Electronic Structure of Small Nickel Atom Clusters. *J. Chem. Phys.* 73 (9), 4492–4510. doi:10.1063/1.440687

Bauschlicher, C. W., Jr, Walch, S. P., and Partridge, H. (1982). On Correlation in the First Row Transition Metal Atoms. *J. Chem. Phys.* 76 (2), 1033–1039. doi:10.1063/1.443095

Becke, A. D. (1993). Density-functional Thermochemistry. III. The Role of Exact Exchange. *J. Chem. Phys.* 98 (7), 5648–5652. doi:10.1063/1.464913

Cheng, L., and Gauss, J. (2011). Analytic Energy Gradients for the Spin-free Exact Two-Component Theory Using an Exact Block Diagonalization for the

One-Electron Dirac Hamiltonian. *J. Chem. Phys.* 135 (8), 084114. doi:10.1063/1.3624397

Cheskidov, A. V., Buchachenko, A. A., and Bezrukov, D. S. (2012). Ab Initio Spin-Orbit Calculations on the Lowest States of the Nickel Dimer. *J. Chem. Phys.* 136 (21), 214304. doi:10.1063/1.4721624

Cooper, W. F., Clarke, G. A., and Hare, C. R. (1972). Molecular Orbital Theory of the Diatomic Molecules of the First Row Transition Metals. *J. Phys. Chem.* 76 (16), 2268–2273. doi:10.1021/j100660a016

De Vore, T. C., Ewing, A., Franzen, H. F., and Calder, V. (1975). The Visible Absorption Spectra of Mn2, Fe2, and Ni2 in Argon Matrices. *Chem. Phys. Lett.* 35 (1), 78–81. doi:10.1016/0009-2614(75)85592-8

Diaconu, C. V., Cho, A. E., Doll, J. D., and Freeman, D. L. (2004). Broken-Symmetry Unrestricted Hybrid Density Functional Calculations on Nickel Dimer and Nickel Hydride. *J. Chem. Phys.* 121 (20), 10026–10040. doi:10.1063/1.1798992

Dolg, M., Wedig, U., Stoll, H., and Preuss, H. (1987). Energy-adjustedabinitiopseudopotentials for the First Row Transition Elements. *J. Chem. Phys.* 86 (2), 866–872. doi:10.1063/1.452288

Dong, C. D., Lefkidis, G., and Hübner, W. (2013). Quantum Isobaric Process in Ni2. *J. Supercond. Nov. Magn.* 26 (5), 1589–1594. doi:10.1007/s10948-012-1948-8

Du, J., Sun, X., and Wang, H. (2008). The Confirmation of Accurate Combination of Functional and Basis Set for Transition-Metal Dimers: Fe2, Co2, Ni2, Ru2, Rh2, Pd2, Os2, Ir2, and Pt2. *Int. J. Quan. Chem.* 108 (9), 1505–1517. doi:10.1002/qua.21684

Dyall, K. G. (1997). Interfacing Relativistic and Nonrelativistic Methods. I. Normalized Elimination of the Small Component in the Modified Dirac Equation. *J. Chem. Phys.* 106 (23), 9618–9626. doi:10.1063/1.473860

Gdanitz, R. J., and Ahlrichs, R. (1988). The Averaged Coupled-Pair Functional (ACPF): A Size-Extensive Modification of MR CI(SD). *Chem. Phys. Lett.* 143 (5), 413–420. doi:10.1016/0009-2614(88)87388-3

Gutsev, G. L., and Bauschlicher, C. W. (2003). Chemical Bonding, Electron Affinity, and Ionization Energies of the Homonuclear 3d Metal Dimers. *J. Phys. Chem. A.* 107 (23), 4755–4767. doi:10.1021/jp030146v

Harris, J., and Jones, R. O. (1979). Density Functional Theory and Molecular Bonding. III. Iron-Series Dimers. *J. Chem. Phys.* 70 (2), 830–841. doi:10.1063/1.437516

Harrison, J. F. (2000). Electronic Structure of Diatomic Molecules Composed of a First-Row Transition Metal and Main-Group Element (H–F). *Chem. Rev.* 100 (2), 679–716. doi:10.1021/cr980411m

Ho, J., Polak, M. L., Ervin, K. M., and Lineberger, W. C. (1993). Photoelectron Spectroscopy of Nickel Group Dimers: Ni_2^-, Pd_2^-, and Pt_2^-. *J. Chem. Phys.* 99 (11), 8542–8551. doi:10.1063/1.465577

Jiang, W., Khait, Y. G., and Hoffmann, M. R. (2009). Configuration-Driven Unitary Group Approach for Generalized Van Vleck Variant Multireference Perturbation Theory. *J. Phys. Chem. A.* 113 (16), 4374–4380. doi:10.1021/jp811082p

Kamal, C., Banerjee, A., Ghanty, T. K., and Chakrabarti, A. (2012). Interesting Periodic Variations in Physical and Chemical Properties of Homonuclear Diatomic Molecules. *Int. J. Quan. Chem.* 112 (4), 1097–1106. doi:10.1002/qua.23088

Kant, A. (1964). Dissociation Energies of Diatomic Molecules of the Transition Elements. I. Nickel. *J. Chem. Phys.* 41 (6), 1872–1876. doi:10.1063/1.1726169

Khait, Y. G., Song, J., and Hoffmann, M. R. (2002). Explication and Revision of Generalized Van Vleck Perturbation Theory for Molecular Electronic Structure. *J. Chem. Phys.* 117 (9), 4133–4145. doi:10.1063/1.1497642

Khait, Y. G., Song, J., and Hoffmann, M. R. (2004). Macroconfigurations in Molecular Electronic Structure Theory. *Int. J. Quan. Chem.* 99 (4), 210–220. doi:10.1002/qua.10852

Khait, Y. G., Theis, D., and Hoffmann, M. R. (2012). Nonadiabatic Coupling Terms for the GVVPT2 Variant of Multireference Perturbation Theory. *Chem. Phys.* 401, 88–94. doi:10.1016/j.chemphys.2011.09.014

Kramida, A., Ralchenko, Y., and Reader, J. (2013). *NIST Atomic Spectra Database (Ver. 5.1) [Online]*. Gaithersburg, MD: National Institute of Standards and Technology. Available at: http://physics.nist.gov/asd (Accessed Feb 7, 2014).

Li, Z., Suo, B., Zhang, Y., Xiao, Y., and Liu, W. (2013). Combining Spin-Adapted Open-Shell TD-DFT with Spin-Orbit Coupling. *Mol. Phys.* 111 (24), 3741–3755. doi:10.1080/00268976.2013.785611

Li, Z., Xiao, Y., and Liu, W. (2012). On the Spin Separation of Algebraic Two-Component Relativistic Hamiltonians. *J. Chem. Phys.* 137 (15), 154114. doi:10.1063/1.4758987

Liu, W. (2010). Ideas of Relativistic Quantum Chemistry. *Mol. Phys.* 108 (13), 1679–1706. doi:10.1080/00268971003781571

Liu, W. (2014). Advances in Relativistic Molecular Quantum Mechanics. *Phys. Rep.* 537 (2), 58–89. doi:10.1016/j.physrep.2013.11.006

Mbote, Y. E. B., Khait, Y. G., Hardel, C., and Hoffmann, M. R. (2010). Multireference Generalized Van Vleck Perturbation Theory (GVVPT2) Study of the NCO + HCNO Reaction: Insight into Intermediates†. *J. Phys. Chem. A.* 114 (33), 8831–8836. doi:10.1021/jp102051p

Melius, C. F., Moskowitz, J. W., Mortola, A. P., Baillie, M. B., and Ratner, M. A. (1976). A Molecular Complex Model for the Chemisorption of Hydrogen on a Nickel Surface. *Surf. Sci.* 59 (1), 279–292. doi:10.1016/0039-6028(76)90305-8

Mokambe, R. M., Hicks, J. M., Kerker, D., Jiang, W., Theis, D., Chen, Z., et al. (2013). GVVPT2 Multireference Perturbation Theory Study of Selenium Oxides. *Mol. Phys.* 111 (9-11), 1078–1091. doi:10.1080/00268976.2013.809163

Moore, C. E. (1952). Atomic Energy Levels. *Natl. Bur. Stand. U.S. Circ.* 467.

Morse, M. D., Hansen, G. P., Langridge-Smith, P. R. R., Zheng, L. S., Geusic, M. E., Michalopoulos, D. L., et al. (1984). Spectroscopic Studies of the Jet-cooled Nickel Dimer. *J. Chem. Phys.* 80 (11), 5400–5405. doi:10.1063/1.446646

Murphy, R. B., and Messmer, R. P. (1992). Correlation in First-Row Transition Metal Atoms Using Generalized Mo/ller-Plesset Perturbation Theory. *J. Chem. Phys.* 97 (7), 4974–4985. doi:10.1063/1.463850

Nakatsuji, H. (1979). Cluster Expansion of the Wavefunction. Electron Correlations in Ground and Excited States by Sac (Symmetry-Adapted-Cluster) and Sac Ci Theories. *Chem. Phys. Lett.* 67 (2), 329–333. doi:10.1016/0009-2614(79)85172-6

Noell, J. O., Newton, M. D., Hay, P. J., Martin, R. L., and Bobrowicz, F. W. (1980). An Ab Initio Study of the Bonding in Diatomic Nickel. *J. Chem. Phys.* 73 (5), 2360–2371. doi:10.1063/1.440386

Perdew, J. P. (1986). Density-Functional Approximation for the Correlation Energy of the Inhomogeneous Electron Gas. *Phys. Rev. B* 33 (12), 8822–8824. doi:10.1103/physrevb.33.8822

Perdew, J. P., Burke, K., and Ernzerhof, M. (1996). Generalized Gradient Approximation Made Simple. *Phys. Rev. Lett.* 77 (18), 3865–3868. doi:10.1103/physrevlett.77.3865

Pinegar, J. C., Langenberg, J. D., Arrington, C. A., Spain, E. M., and Morse, M. D. (1995). Ni2 Revisited: Reassignment of the Ground Electronic State. *J. Chem. Phys.* 102 (2), 666–674. doi:10.1063/1.469562

Pou-Amérigo, R., Merchan, M., Nebot-Gil, I., Malmqvist, P. Å., and Roos, B. O. (1994). The Chemical Bonds in CuH, Cu_2, NiH, and Ni_2 Studied with Multiconfigurational Second Order Perturbation Theory. *J. Chem. Phys.* 101 (6), 4893–4902.

Raghavachari, K., and Trucks, G. W. (1989). Highly Correlated Systems. Excitation Energies of First Row Transition Metals Sc-Cu. *J. Chem. Phys.* 91 (2), 1062–1065. doi:10.1063/1.457230

Rasanen, M., Heimbrook, L. A., and Bondybey, V. E. (1987). Rare Gas Matrix Studies of the Products of Vaporization of Nickel. *J. Mol. Struct.* 157 (1), 129–140. doi:10.1016/0022-2860(87)87088-6

Rösch, N., and Rhodin, T. N. (1974). Bonding of Ethylene to Diatomic Nickel According to a Self-Consistent-Field,Xα, Scattered-Wave Model. *Phys. Rev. Lett.* 32 (21), 1189–1192. doi:10.1103/physrevlett.32.1189

Russo, T. V., Martin, R. L., and Hay, P. J. (1994). Density Functional Calculations on First-row Transition Metals. *J. Chem. Phys.* 101 (9), 7729–7737. doi:10.1063/1.468265

Schultz, N. E., Zhao, Y., and Truhlar, D. G. (2005). Databases for Transition Element Bonding: Metal–Metal Bond Energies and Bond Lengths and Their Use to Test Hybrid, Hybrid Meta, and Meta Density Functionals and Generalized Gradient Approximations. *J. Phys. Chem. A.* 109 (19), 4388–4403. doi:10.1021/jp0504048

Shi-Ying, Y., and Zheng-He, Z. (2008). Spin Polarization Effect of Ni 2 Molecule. *Chin. Phys. B* 17 (12), 4498–4503. doi:10.1088/1674-1056/17/12/028

Shim, I., Dahl, J. P., and Johansen, H. (1979). Ab Initio Hartree-Fock and Configuration-Interaction Treatment of the Interaction between Two Nickel Atoms. *Int. J. Quan. Chem.* 15 (3), 311–331. doi:10.1002/qua.560150306

Szalay, P. G., and Bartlett, R. J. (1993). Multi-Reference Averaged Quadratic Coupled-Cluster Method: A Size-Extensive Modification of Multi-Reference CI. *Chem. Phys. Lett.* 214 (5), 481–488. doi:10.1016/0009-2614(93)85670-j

Tamukong, P. K., Hoffmann, M. R., Li, Z., and Liu, W. (2014). Relativistic GVVPT2 Multireference Perturbation Theory Description of the Electronic States of Y2and Tc2. *J. Phys. Chem. A.* 118 (8), 1489–1501. doi:10.1021/jp409426n

Tamukong, P. K., Theis, D., Khait, Y. G., and Hoffmann, M. R. (2012). GVVPT2 Multireference Perturbation Theory Description of Diatomic Scandium, Chromium, and Manganese. *J. Phys. Chem. A.* 116 (18), 4590–4601. doi:10.1021/jp300401u

Upton, T. H., and Goddard, W. A., III (1978). The Electronic States of Ni2 and Ni2+. *J. Am. Chem. Soc.* 100 (18), 5659–5668. doi:10.1021/ja00486a014

Werner, H.-J., and Knowles, P. J. (1990). A Comparison of Variational and Non-variational Internally Contracted Multiconfiguration-Reference Configuration Interaction Calculations. *Theor. Chim. Acta* 78 (3), 175–187.

Wood, C., Doran, M., Hillier, I. H., and Guest, M. F. (1980). Theoretical Study of the Electronic Structure of the Transition Metal Dimers, Sc₂, Cr₂, Mo₂ and Ni₂. *Faraday Symp. Chem. Soc.* 14, 159–169. doi:10.1039/fs9801400159

Yanagisawa, S., Tsuneda, T., and Hirao, K. (2000). An Investigation of Density Functionals: The First-Row Transition Metal Dimer Calculations. *J. Chem. Phys.* 112 (2), 545–553. doi:10.1063/1.480546

Band Gap Reduction in Ferroelectric BaTiO$_3$ Through Heterovalent Cu-Te Co-Doping for Visible-Light Photocatalysis

Rohit Kumar Rohj[1], Akmal Hossain[1], Priya Mahadevan[2] and D. D. Sarma[1]*

[1]Solid State and Structural Chemistry Unit, Indian Institute of Science, Bengaluru, India, [2]S. N. Bose National Centre for Basic Sciences, Kolkata, India

It is believed that ferroelectrics may serve as efficient photocatalysts as well as photovoltaic materials but for their large bandgaps which does not allow them to absorb a large part of the solar spectrum. We have explored theoretically within ab-initio density functional theory-based calculations, the efficacy of Cu and Te to co-dope BaTiO$_3$ in reducing its bandgap while retaining its ferroelectric properties. Examining a dopant concentration of 11%, we find an insulating ground state being realized with a band gap reduction of 0.42 eV from the value for undoped BaTiO$_3$ for some doping configurations. Ferroelectric distortions are found to survive even in the presence of doping suggesting possible applications in photocatalysis as well as photovoltaics.

Keywords: photocatalysis, co-doping, ferroelectrics, DFT, Jahn-Teller distortions, work function

INTRODUCTION

An increasing demand for energy has resulted in an over utilization of available natural resources, with most of them being non-renewable fossil fuels. This has led to a rapid increase in carbon emissions, causing global warming and environmental pollution, requiring an urgent need to find ways for sustainable energy production. Among the various ways and techniques to cope with the problem, photocatalysis and photovoltaics utilizing sunlight as a clean, inexpensive, and inexhaustible source are being extensively explored to face these challenges. Photocatalysis, in particular, has been applied in CO$_2$ reduction (Zhao et al., 2017), H$_2$ evolution via water splitting (Walter et al., 2010), dye degradation (Ajmal et al., 2014) and ammonia synthesis (Chen et al., 2018; Zhao et al., 2019). Since the seminal work of Fujishima and Honda (Fujishima and Honda, 1972) of using TiO$_2$ as a photocatalyst in 1972, various semiconducting materials including WO$_3$ (Dong et al., 2017), ZnO (Ong et al., 2018), Bi$_2$O$_3$ (Zhou et al., 2009), Bi$_5$O$_7$I (Cao et al., 2020), oxide tandem structures (Enesca, 2020) and CdS (Cheng et al., 2018) have been extensively investigated for photocatalytic applications. The operation of a photocatalyst has primarily three parts. The first involves using sunlight to generate electron-hole pairs in the material. The second part involves separating the electron and hole pairs before they recombine. Finally, the free electrons and holes need to be transported to the surface for surface redox reactions. Hence, in a material that is optimal for this purpose, the band gap should lie in a range that maximizes absorption of the solar spectrum. This corresponds to a band gap in the range of 1–1.5 eV where the solar spectrum peaks. Additionally, a material with a high absorption coefficient would also help in maximising the photo-generated carriers. The next step involves separating the electron and hole before they recombine. An indirect band gap material or a heterostructure of materials with Type II band
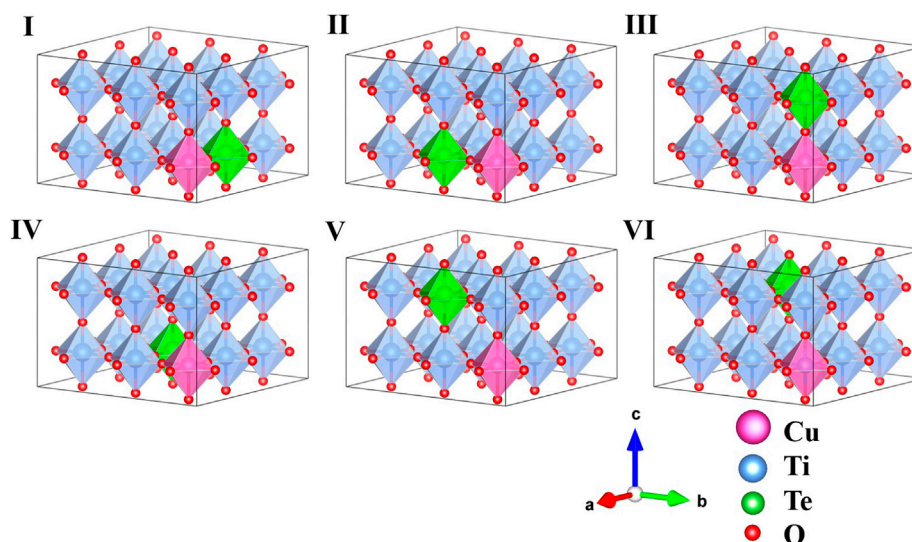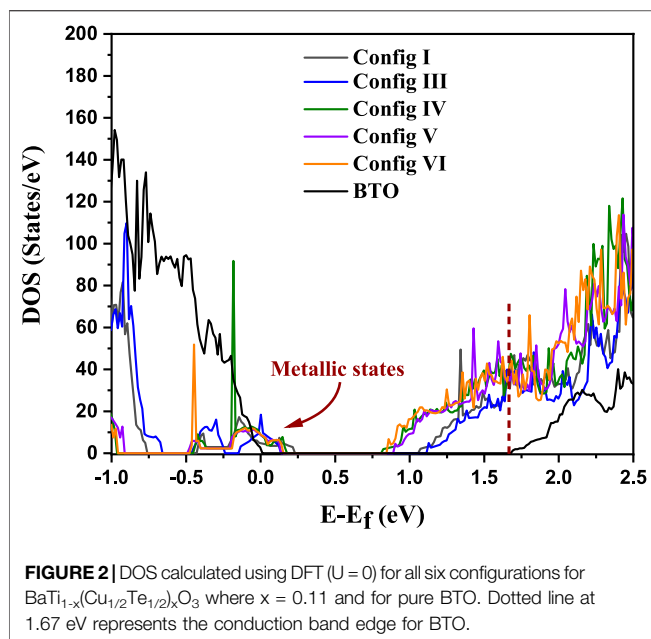
FIGURE 1 | Schematic representation of the six possible symmetry distinct configurations of 3 × 3 × 2 perovskite supercell of Cu-Te co-doped BaTiO$_3$. Barium (Ba) atoms are not shown for clarity.

TABLE 1 | Energies and metal oxygen bond lengths in the MO$_6$ octahedra for geometry optimized DFT calculations for all six configurations of BaTi$_{1-x}$(Cu$_{1/2}$Te$_{1/2}$)$_x$O$_3$ with x = 0.11. The axes having the largest off centering distortion in Ti-O bond lengths have been highlighted in bold.

Configuration	Relative stability (meV/f.u.)		Bond length (in Å)							
		Axis	[1]Ti-O		[2]Ti-O		Cu-O		Te-O	
I (–690.379 eV)	12	a	**2.042**	**1.942**	**2.067**	**1.932**	**2.106**	**2.147**	**1.891**	**1.904**
		b	1.997	1.997	1.997	1.997	2.072	2.072	1.958	1.958
		c	**1.942**	**2.076**	**1.902**	**2.130**	**2.091**	**2.098**	**1.978**	**1.991**
II (–690.379 eV)	12	a	1.997	1.997	1.997	1.997	2.072	2.072	1.958	1.957
		b	**2.042**	**1.942**	**2.067**	**1.932**	**2.106**	**2.147**	**1.891**	**1.904**
		c	**1.942**	**2.076**	**1.902**	**2.130**	**2.091**	**2.098**	**1.978**	**1.991**
III (–690.596 eV)	0	a	1.994	1.994	1.997	1.997	2.064	2.064	1.977	1.977
		b	1.994	1.994	1.997	1.997	2.064	2.064	1.977	1.977
		c	**1.906**	**2.128**	**1.892**	**2.141**	**2.148**	**2.142**	**1.888**	**1.888**
IV (–690.024 eV)	31	a	1.993	1.993	2.008	1.988	2.115	2.128	1.923	1.925
		b	1.993	1.993	2.008	1.988	2.115	2.128	1.923	1.925
		c	**1.936**	**2.089**	**1.897**	**2.130**	**2.100**	**2.113**	**1.958**	**1.973**
V (–690.072 eV)	29	a	1.998	1.998	1.996	1.996	2.107	2.107	1.933	1.933
		b	1.998	1.980	2.054	1.944	2.120	2.132	1.922	1.922
		c	**1.937**	**2.080**	**1.900**	**2.136**	**2.116**	**2.124**	**1.950**	**1.961**
VI (–689.994 eV)	33	a	2.002	1.987	2.044	1.953	2.099	2.122	1.927	1.930
		b	2.002	1.987	2.044	1.953	2.099	2.122	1.927	1.930
		c	**1.930**	**2.091**	**1.902**	**2.133**	**2.105**	**2.117**	**1.955**	**1.969**

alignment would be appropriate for this purpose. And finally, the surface potentials should have values that would be optimal for the envisaged reaction on the surface. To summarize, the important processes involved in the operation of a photocatalyst are charge generation via photo-absorption, charge separation, and charge collection. Out of these, charge collection is an interfacial phenomenon which depends on the energetics of electrons and holes and the medium involved in the particular reaction that one is considering. Since these interfacial effects would be reaction specific, we focus our attention on the present work to the issues of photo-absorption and charge separation.

Ferroelectric materials have a built-in potential due to their intrinsic electric polarization within each domain. This has been found to be useful in separating the electron-hole pairs as they migrate towards the surface before recombination (Stock and Dunn, 2012; Cui et al., 2013; Li et al., 2014; Wang et al., 2017). Most ferroelectrics have large band gaps and are hence unsuitable for this purpose. Optimising the band gap is usually achieved by co-doping with a combination of atoms which helps to retain the insulating, ferroelectric character, while at the same time reducing the band gap. Unfortunately, attempts to reduce the bandgap by doping other elements into a ferroelectric material most often lead to a rapid loss of ferroelectric properties, making the design

FIGURE 2 | DOS calculated using DFT (U = 0) for all six configurations for BaTi$_{1-x}$(Cu$_{1/2}$Te$_{1/2}$)$_x$O$_3$ where x = 0.11 and for pure BTO. Dotted line at 1.67 eV represents the conduction band edge for BTO.

of a small bandgap ferroelectric remain mostly elusive (Hill, 2000; Benedek and Fennie, 2013). Das et al. (2018), however, showed that a heterovalent, charge-compensated co-doping of Jahn-Teller Mn^{3+} ions and d^0 Nb^{5+} ions into BaTiO$_3$, led to one of the smallest bandgap materials largely retaining ferroelectric properties of BaTiO$_3$. This work also showed that the reduced band gap is determined by the Jahn-Teller splitting of the Mn^{3+} states. The dominantly Nb states were empty and did not contribute to the states in the band gap. A final requirement of any material chosen to be a photocatalytic material is that it should be chemically and thermally stable and should be resistant to photodegradation. It is interesting to note that most of the desirable attributes of a good photocatalyst, such as the right bandgap for the absorption of the large part of the solar spectrum, retention of ferroelectric properties for facile charge separation and a high degree of absorption, also make such materials suitable to explore efficient solar photovoltaic applications.

In this work, we theoretically explore the possibility of expanding the strategy introduced by Das et al. (2018) of charge-compensated heterovalent doping of a ferroelectric material with a Jahn-Teller active ion and a closed shell metal ion to achieve a lower bandgap compound that retains ferroelectric properties. We have considered the well-known ferroelectric BaTiO$_3$. This has been co-doped with Cu and Te at the Ti^{4+} site. The choice has been dictated by the similar ionic radii of the Jahn-Teller active d^9 Cu^{2+} (0.73 Å) which is the most stable valency of a Cu atom, and Ti^{4+} (0.60 Å) ion. This would lead to a valency of 6+ on the Te sites with an ionic size of 0.56 Å and a closed shell electronic configuration. Our results establish that Cu 3d derived states appear within the bandgap of the host BaTiO$_3$. The band gap calculated within generalised gradient approximation for the exchange correlation functional employed here gives us a band gap of the co-doped system to be 1.25 eV while retaining its ferroelectric polarisation to a substantial

extent, making this system an exciting one for possible photocatalytic and photovoltaic applications.
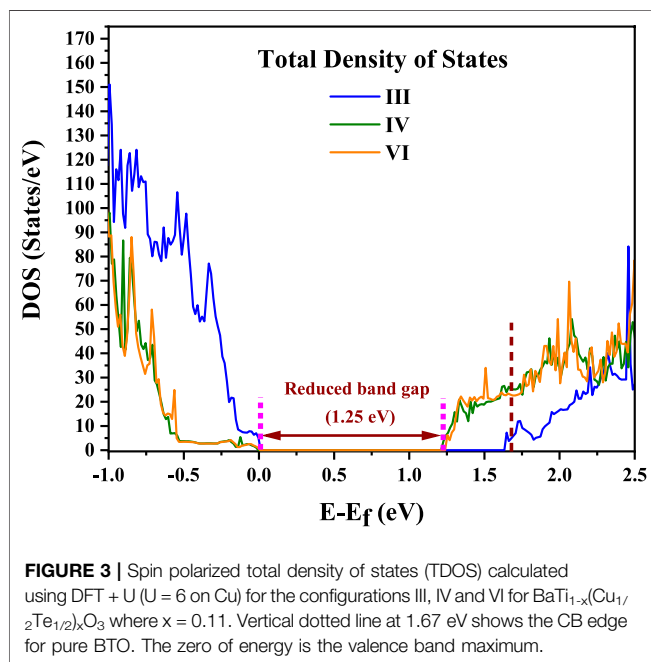
COMPUTATIONAL METHODOLOGY

We have performed density functional theory (DFT) calculations within a plane wave basis set using projector augmented wave (PAW) potentials as implemented in the Vienna *ab initio* Simulation Package (VASP). The experimental lattice constants of BaTiO$_3$ (BTO), **a** = **b** = 3.992 and **c** = 4.033 Å for the room temperature tetragonal phase, were taken and a unit cell was constructed allowing for the internal coordinates to be relaxed. After optimization, the Ti-O bond lengths in the **c**-direction were found to be 1.885 and 2.148 Å. A supercell was constructed out of the optimized unit cell with 3 × 3 × 2 repeat units along the three cartesian directions, and pairs of Ti atoms at various separations were replaced by a Cu and a Te atom to realize different configurations at a fixed level of doping (~11%). We have optimized the internal positions for each of these co-doped configurations till the forces on each atom were less than 10^{-2} eV/Å. Generalized Gradient Approximation (GGA) has been used for the exchange-correlation functional. An energy of 550 eV was chosen for the maximum kinetic energy of the plane waves included in the basis. A mesh of 6 × 6 × 6 k-points was used for the k-points integrations involved for the supercell and an appropriately scaled mesh for the primitive unit cell. In addition, beyond GGA calculations were also performed for the doped unit cells by including on-site Coulomb interactions of 6 eV at the Cu site using the Dudarev implementation (Dudarev et al., 1998). Spheres of radii of 1.31 were constructed about the Cu atoms for calculating the atom projected partial density of states as well as the magnetic moment at each atomic site. In order to calculate the work function (Φ), we consider two symmetric slabs containing 13 monolayers of tetragonal ferroelectric BaTiO$_3$, one terminating with BaO on both ends and the other one with TiO$_2$. 12 Å of vacuum has been introduced in the z-direction in both the slabs and in the xy plane, we have taken a 2 × 2 unit cell and two Ti atoms are replaced by a Cu atom and a Te atom at a distance as in configuration IV. The layer averaged potential is calculated after the self-consistent spin polarised density functional theory calculation for the slabs considered. The difference of the potential in the vacuum region where it is constant, and the fermi energy is used to define the work function (Kumar and Niranjan, 2014).

RESULTS AND DISCUSSION

The prescription of co-doping with Cu and Te to replace two Ti ions in the BTO supercell leads to six distinct configurations, labelled I-VI in order of their increased Cu-Te separation, and are shown in **Figure 1**. The tetragonal symmetry of the lattice makes configurations I and II, in which the dopant atoms sit at nearest neighbor Ti positions along the **a** and **b** lattice vector directions, identical. Configuration III has the dopant atoms lie on top of each other along the **c** axis. The rest of the configurations IV, V

TABLE 2 | Energies and metal oxygen bond lengths in the MO_6 octahedra for geometry optimized DFT + U (U = 6) calculations for the three configurations III, IV and VI of $BaTi_{1-x}(Cu_{1/2}Te_{1/2})_xO_3$ with x = 0.11. The axes having the largest off centering distortion in Ti-O bond lengths have been highlighted in bold.

Configuration	Relative stability (meV/f.u.)	Bond length (in Å)								
		Axis	^{1}Ti-O		^{2}Ti-O		Cu-O		Te-O	
III (−689.299 eV)	0	a	1.996	1.996	1.998	1.998	2.057	2.057	1.967	1.967
		b	1.996	1.996	1.998	1.998	2.057	2.057	1.967	1.967
		c	**1.900**	**2.134**	**1.891**	**2.142**	**2.146**	**2.148**	**1.884**	**1.888**
IV (−688.522 eV)	43	a	1.999	2.001	2.004	1.989	2.079	2.084	1.925	1.926
		b	1.999	2.001	2.004	1.989	2.079	2.084	1.925	1.926
		c	**1.924**	**2.077**	**1.897**	**2.138**	**2.139**	**2.152**	**1.957**	**1.972**
VI (−688.514 eV)	44	a	1.996	2.004	2.018	1.977	2.061	2.082	1.927	1.930
		b	1.996	2.004	2.018	1.977	2.061	2.082	1.927	1.930
		c	**1.920**	**2.086**	**1.897**	**2.008**	**2.142**	**2.155**	**1.956**	**1.970**

FIGURE 3 | Spin polarized total density of states (TDOS) calculated using DFT + U (U = 6 on Cu) for the configurations III, IV and VI for $BaTi_{1-x}(Cu_{1/2}Te_{1/2})_xO_3$ where x = 0.11. The vertical dotted line at 1.67 eV shows the CB edge for pure BTO. The zero of energy is the valence band maximum.

and VI correspond to next nearest neighboring geometry where the co-dopant distances are 5.65, 5.67, and 6.94 Å, respectively. The ground states obtained in each case are given in **Table 1**. All energies have been calculated per formula unit and have been given for each configuration relative to configuration III, since configuration III is found to have the lowest energy.

For configurations I and II with the dopant atoms at nearest neighbor positions along the **a** and **b** lattice vectors are substantially higher by 12 meV per formula unit. Energies for configurations with the dopant atoms at further distances are much higher appearing about 29–33 meV above that of configuration III. The metal-oxygen (M-O) bond lengths for Cu and Te in their respective octahedra have been tabulated for all configurations in **Table 1**. The observed bond lengths seem to be consistent with the assigned valencies of 2+ for Cu and 6+ for Te. Due to the larger ionic radius of Cu^{2+} than Te^{6+}, all Cu-O bond lengths are found to be longer than Te-O bond lengths (Longo and Raccah, 1973; Shannon, 1976; Flores et al., 2019).

In an octahedral symmetry environment arising from the ligands surrounding a transition metal site, one has a degeneracy lifting of the d orbitals into triply degenerate t_{2g} orbitals and doubly degenerate e_g orbitals. Examining the distortions in configuration III, we find that the two out-of plane Cu-O bond lengths are almost equal to each other, while these are considerably longer than the in-plane Cu-O bond lengths. This shows that the local symmetry is not octahedral but D_{4h}, establishing that Jahn-Teller effects are operational, as expected for the $3d^9$ electronic configuration of Cu^{2+}. This distortion lifts the degeneracy of the e_g orbitals with the $d_{x-y}^{2\ 2}$ orbitals lying at higher energies than the $d_{3z-r}^{2\ 2}$ orbitals. It is to be noted that the local distortion around the Cu^{2+} and Te^{6+} in configuration III are essentially non-polar in contrast to the polar distortions seen at the Ti^{4+} sites in **Table 1** for all configurations, responsible for the ferroelectricity. Thus, it appears that the Cu and Te co-doping sustains the ferroelectric distortions at the Ti site while not directly contributing via any ferroelectric distortions of the dopant ions. It is interesting to note that the presence of the dopant pairs in configurations I and II introduces an off-centering in the nearest neighbor Ti sites in the **a** or the **b** direction. This arises from inversion symmetry breaking in the structure, leading to the particular Ti atom having different neighbors on either side. This also induces an off-centering at the Cu sites. It is possibly from these additional lattice distortions than what one finds in configuration III that make configurations I and II have higher energy. Analysing the local geometry around the dopant sites, we have classified two kinds of Ti atoms in these supercell configurations. The ones which are immediate neighbors of dopant atoms are labelled as ^{1}Ti and others which are not immediate neighbors are labelled as ^{2}Ti as shown in **Table 1**. The local geometry around the dopant atoms in these relaxed supercells show that both the type of Ti atoms (^{1}Ti and ^{2}Ti) exhibit significant off-centering distortion as reflected in the dissimilar Ti-O bond lengths (marked in bold) and are averaged over the neighboring TiO_6 octahedra. This indicates that the off-centering of Ti^{4+} ions survive the doping. This is the most important criterion to make use of the ferroelectric polarization-generated electric field to efficiently separate photo-generated electrons and holes using the internal electric field.
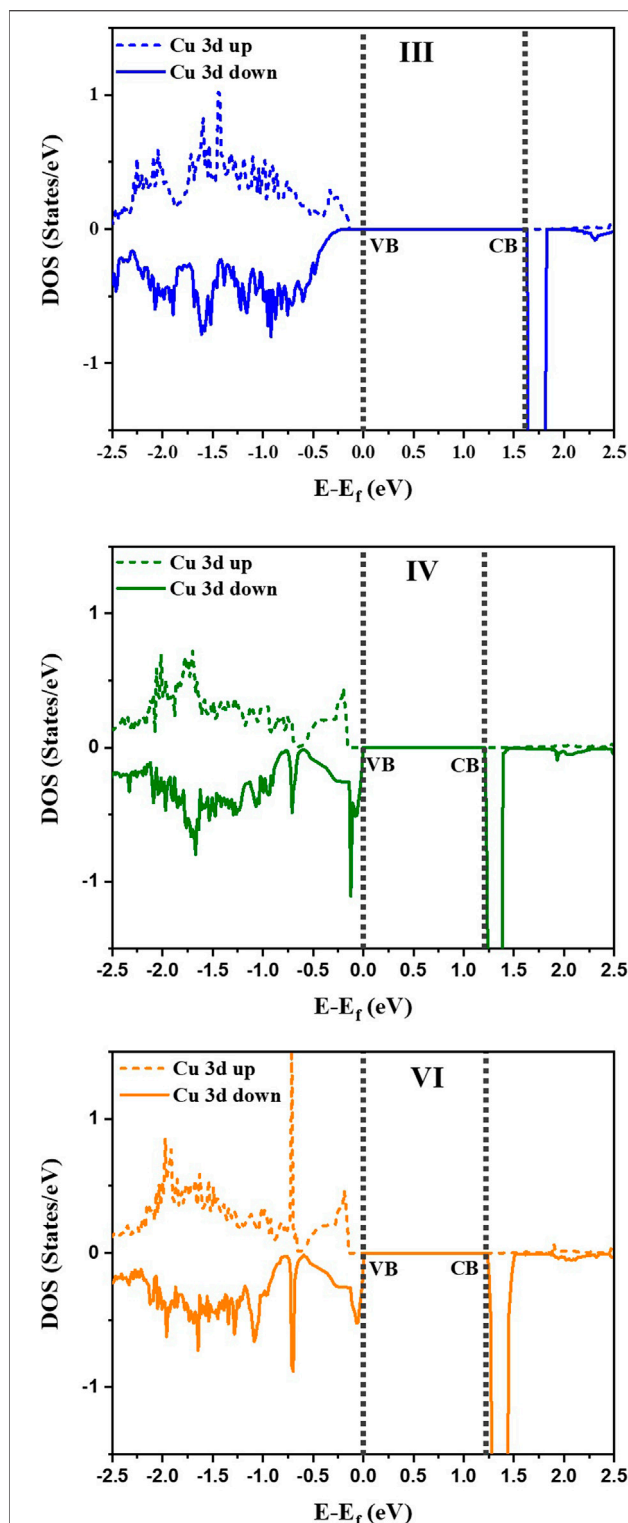
FIGURE 4 | Partial Density of States (PDOS) for Cu 3d spin up and spin down states for the configurations III, IV and VI. Vertical dotted lines represent VB and CB of the three doped configurations. The zero of energy is the valence band maximum.

It is obvious that any photocatalytic or photovoltaic material must be an insulator with a finite energy gap. In absence of any

such gap, the photoexcited electrons and holes will rapidly de-excite to the chemical potential to recombine without giving rise to any free electron and hole for any useful purpose. We examine if the dopant pairs that we have chosen lead to an insulating state. This is examined by calculating the density of states for configurations I to VI. The configurations I and II are essentially the same by tetragonal symmetry, thus we consider only one of them. For comparison, we also show the density of states for undoped BTO. The results are shown in **Figure 2**. The undoped BTO system is found to have a band gap of 1.67 eV in our calculations in contrast to the experimental value of 3.2 eV(Das et al., 2018). This underestimation of the band gap within GGA calculations is well-known. The insulating state of BTO is demonstrated by the absence of any density of electron states between the chemical potential at the top of the valence band (VB), marked by zero of the energy scale, and the bottom of the conduction band (CB) at 1.67 eV. Upon doping, all the supercell configurations (I–VI) are found to be metallic as shown by the finite density of electron states at the chemical potential. This is to be expected as Cu^{2+} has a partially filled d^9 configuration. The Jahn-Teller distortions discussed earlier in the context of configuration III will lead to the levels with dominantly $d_{x^2-y^2}$ character with spin degeneracy but being occupied by one electron, thereby, making the system metallic. Similar arguments can be extended to all other configurations. Since spin-polarization in the Cu 3d states can lift the spin-degeneracy of the $d_{x^2-y^2}$ orbitals at the Cu site, potentially turning the system into an insulator via spin-splitting of the d-band, it is important to explore spin polarisation in such calculations. It is well-known that the intra-site Coulomb interaction strength, U, within the Cu 3d states is large and it can drive the system to an insulating state even in absence of any spin-polarization.

We explore the consequence of Coulomb interactions and spin polarization by carrying out spin-polarized calculations within the GGA + U approach, discussed in the *Computational Methodology* section. This led to a magnetic moment of 0.71 μ_B developing on the Cu site. Following the literature (Isseroff and Carter, 2012), we set U to a typical value of 6 eV within Cu 3d states. Among the six analysed configurations, we have selected configuration III, with its lowest energy, serving the purpose of nearest neighbor geometry where dopant atoms separation is equal to the unit cell length in the **c** direction and configuration IV and VI serving as non-nearest neighbor geometries where the dopant atoms separation is 5.65 and 6.94 Å, respectively. Structural optimizations of three configurations were carried out allowing for spin polarizations of the states as well as including $U = 6$ eV within the Cu 3d states. Analysis of the ground state energies and bond lengths for these three chosen configurations are shown in **Table 2**.

It is observed that the configuration III has the lowest energy as in the earlier calculations without U or spin polarization. Examining the distortions of the Cu-O, Te-O and Ti-O octahedra, we see that the bond lengths turn out to be similar to the earlier result given in **Table 1**. The off-centering is sustained in the **c**-direction for the Ti atoms, while Cu^{2+} exhibits a strong tetragonal distortion leading to longer Cu-O bonds in the **c**-direction arising from first order Jahn Teller
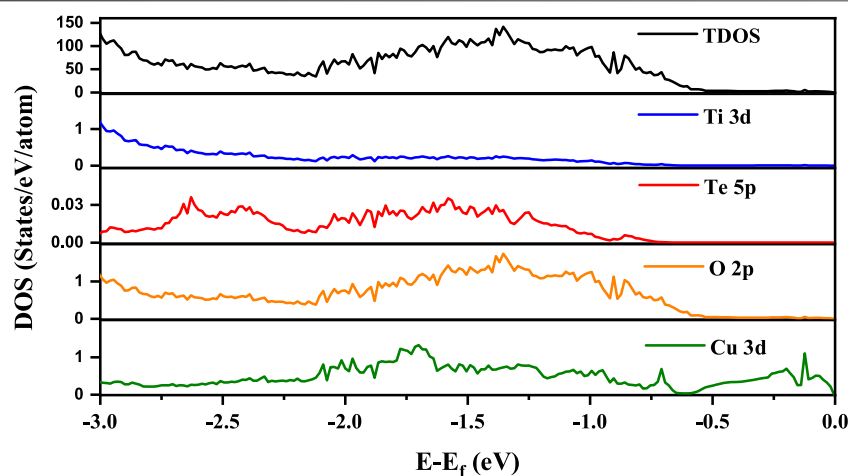
FIGURE 5 | PDOS for Ti 3d, Te 5p, O 2p and Cu 3d for the studied configuration IV in addition to the total density of states. The zero of energy is the valence band maximum in our calculations.
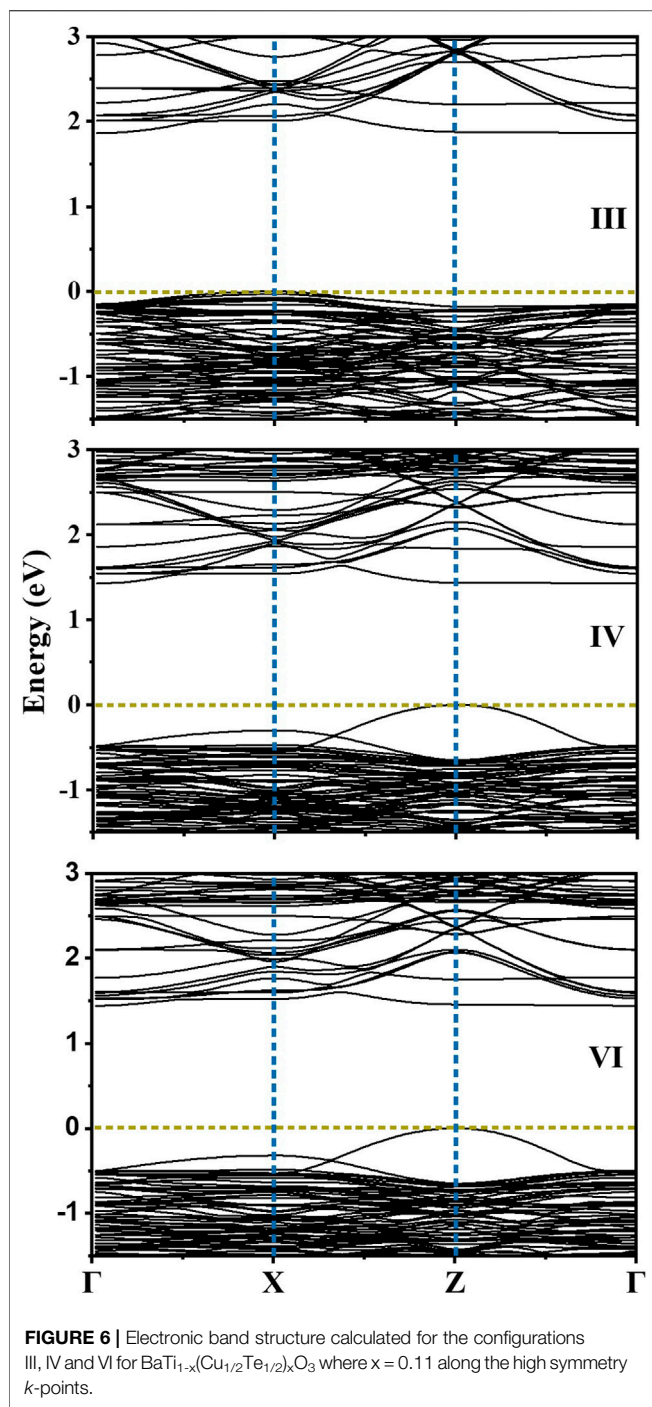
effects. Te^{6+} responds to the changes in the Cu-O bond lengths and has shorter Te-O bond lengths in the **c**-direction but has no second order Jahn-Teller effects operational and consequently has no off-centering of the Te atoms. Other features of the distortions for configurations IV and VI remain similar to what was found in **Table 1** with a marginal increase in the stability of configuration III with respect to configurations IV and VI. The most significant change in the electronic structure brought about by the inclusion of the spin polarization together with finite U is that all co-doped systems are driven into insulating states with a clear bandgap, as shown in **Figure 3**. As mentioned already, this is critical for possible applications of any compound as a photocatalyst or a photovoltaic material. Comparison of densities of states for different configurations with that of pure BTO, shown in **Figure 3**, establishes a significant reduction in the band gap to 1.25 eV for configurations IV and VI as compared to pure BTO which is 1.67 eV shown by the vertical dotted line. The lowest energy configuration III, however, does not exhibit a significant reduction in the band gap. In order to examine the origin of the reduction in the band gap, we examine the Cu 3d projected up and down spin partial density of states. This is plotted in **Figure 4** for each configuration. The vertical dashed lines indicate the positions of the valence and conduction band edges in each case. We find that the occupied Cu 3d states lie deep inside the valence band in configuration III with the host BTO states contributing to the valence band top.

The conduction band bottom, however, has the Cu d minority spin states almost merging with the host states indicating that in this case, one has a very small reduction in the band gap by co-doping. Both configurations IV and VI exhibit a significant reduction in the band gap of 0.42 eV. This seems surprising at first sight as the distortions of the Cu-O bond lengths are not significantly different in the three cases. This should therefore lead to similar band gap reductions. A possible origin for this could be the choice of the host supercell which has just two repeat units in the **c** direction. This leads to a chain formation of
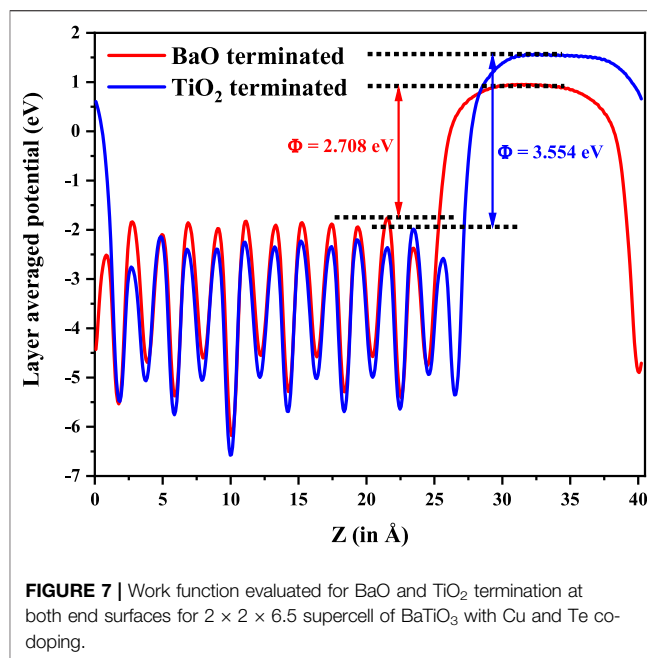
alternating Cu-Te atoms in the **c** direction for configuration III leading to the positioning of the unoccupied minority spin Cu d states just at the bottom of the conduction band. As this is a special consequence of the choice of unit cell, dictated by the increased computational demands for considering three repeat units in the **c** direction, we can safely conclude that the band gap reduction in the three cases should be similar.

Having established that by co-doping Cu and Te in BTO we are able to realize an insulating ground state with a reduced gap in which ferroelectric distortions of the Ti atoms still survive, we show the partial density of states (PDOS) in **Figure 5** for Ti 3d, Te 5p, O 2p and Cu 3d along with the total density of states (TDOS) in the energy interval from the top of the valence band to 3 eV below for one of the three configurations (config IV here) that we have studied.

From the position of the Cu d states in the valence band, it is evident that the Cu d states occur in the band gap of $BaTiO_3$. Their position can be experimentally probed by measuring the ultraviolet photoemission spectrum (UPS). The given partial density of states weighted by the cross-section at the particular photon energy used, may be used to compute the UPS. It is clearly seen that valence band spectrum in TDOS is mainly contributed by O 2p states. We then go on to examine the nature of the band gap. This is plotted along various symmetry directions in **Figure 6** for each configuration. In every case, the valence band top is contributed by a strongly dispersing band with Cu d character. This was evident from our analysis of the density of states also. The conduction band bottom is contributed by Cu $d_{x^2-y^2}$ states which are weakly dispersive in the ΓZ direction, with the minimum lying at Γ point. As the band extrema corresponding to the valence band maximum and the conduction band minimum are at different k-points, leading to an indirect bandgap, one expects the recombination rates to be low, which again is another requirement for a material to work as an efficient photocatalyst. Since the work function (Φ) of a material dictates the ease to remove an electron out of the surface, we compute the work function for one of the configuration (IV

FIGURE 6 | Electronic band structure calculated for the configurations III, IV and VI for $BaTi_{1-x}(Cu_{1/2}Te_{1/2})_xO_3$ where $x = 0.11$ along the high symmetry *k*-points.

FIGURE 7 | Work function evaluated for BaO and TiO_2 termination at both end surfaces for $2 \times 2 \times 6.5$ supercell of $BaTiO_3$ with Cu and Te co-doping.

CONCLUSION

Co-doping Cu and Te atoms into tetragonal $BaTiO_3$ has been explored as a route to reducing the band gap found in $BaTiO_3$ while retaining its ferroelectric order. Considering a dopant concentration of 11%, we find a band gap reduction of 0.42 eV in a few dopant distribution configurations, while partially retaining the ferroelectric distortions of the host compound. In each of these cases, the nature of the band gap is also found to be an indirect one. Slab calculations with $2 \times 2 \times 6.5$ supercell establish that the BaO terminated surface has a lower work function compared to the TiO_2 terminated one.

DATA AVAILABILITY STATEMENT

The original contributions presented in the study are included in the article, further inquiries can be directed to the corresponding author.

AUTHOR CONTRIBUTIONS

RR performed most of the calculations under the supervision of PM. AH helped RR in the calculations. DS conceived this project. All authors jointly wrote the manuscript.

FUNDING

here) by considering the slab of $2 \times 2 \times 6.5$ supercell of Cu-Te doped BTO as described in the *Computational Methodology* section. As shown in **Figure 7**, we have calculated the work function (defined as the potential difference between vacuum and fermi level) for both BaO and TiO_2 terminated surfaces. We find that BaO terminated surface ($\Phi = 2.708$ eV) has a smaller work function than the TiO_2 terminated one ($\Phi = 3.554$ eV) making the BaO surface easier to be oxidized by the removal of an electron from the surface.

REFERENCES

Ajmal, A., Majeed, I., Malik, R. N., Idriss, H., and Nadeem, M. A. (2014). Principles and Mechanisms of Photocatalytic Dye Degradation on TiO_2 based Photocatalysts: A Comparative Overview. *RSC Adv.* 4 (70), 37003–37026. doi:10.1039/c4ra06658h

Benedek, N. A., and Fennie, C. J. (2013). Why Are There So Few Perovskite Ferroelectrics? *J. Phys. Chem. C.* 117 (26), 13339–13349. doi:10.1021/jp402046t

Cao, B., Gong, S., Zubairu, S., Liu, L., Xu, Y., Guo, L., et al. (2020). Fabrication of Er^{3+}/Yb^{3+} Co-doped Bi_5O_7I Microsphere with Upconversion Luminescence and Enhanced Photocatalytic Activity for Bisphenol A Degradation. *Front. Chem.* 8, 773. doi:10.3389/fchem.2020.00773

Chen, X., Li, N., Kong, Z., Ong, W.-J., and Zhao, X. (2018). Photocatalytic Fixation of Nitrogen to Ammonia: State-Of-The-Art Advancements and Future Prospects. *Mater. Horiz.* 5 (1), 9–27. doi:10.1039/c7mh00557a

Cheng, L., Xiang, Q., Liao, Y., and Zhang, H. (2018). CdS-Based Photocatalysts. *Energy Environ. Sci.* 11 (6), 1362–1391. doi:10.1039/c7ee03640j

Cui, Y., Briscoe, J., and Dunn, S. (2013). Effect of Ferroelectricity on Solar-Light-Driven Photocatalytic Activity of $BaTiO_3$ - Influence on the Carrier Separation and Stern Layer Formation. *Chem. Mater.* 25 (21), 4215–4223. doi:10.1021/cm402092f

Das, S., Ghara, S., Mahadevan, P., Sundaresan, A., Gopalakrishnan, J., and Sarma, D. D. (2018). Designing a Lower Band Gap Bulk Ferroelectric Material with a Sizable Polarization at Room Temperature. *ACS Energy Lett.* 3 (5), 1176–1182. doi:10.1021/acsenergylett.8b00492

Dong, P., Hou, G., Xi, X., Shao, R., and Dong, F. (2017). WO_3-based Photocatalysts: Morphology Control, Activity Enhancement and Multifunctional Applications. *Environ. Sci. Nano* 4 (3), 539–557. doi:10.1039/c6en00478d

Dudarev, S. L., Botton, G. A., Savrasov, S. Y., Humphreys, C. J., and Sutton, A. P. (1998). Electron-energy-loss Spectra and the Structural Stability of Nickel Oxide: An LSDA+U Study. *Phys. Rev. B.* 57 (3), 1505–1509. doi:10.1103/physrevb.57.1505

Enesca, A. (2020). Enhancing the Photocatalytic Activity of SnO_2-TiO_2 and ZnO-TiO_2 Tandem Structures Toward Indoor Air Decontamination. *Front. Chem.* 8, 583270. doi:10.3389/fchem.2020.583270

Flores, A. V., Krueger, A. E., Stiner, A. J., Albert, H. M., Mansur, T., Willis, V., et al. (2019). Comparison of the Crystal Chemistry of Tellurium (VI), Molybdenum (VI), and Tungsten (VI) in Double Perovskite Oxides and Related Materials. *Prog. Solid State. Chem.* 56, 100251. doi:10.1016/j.progsolidstchem.2019.100251

Fujishima, A., and Honda, K. (1972). Electrochemical Photolysis of Water at a Semiconductor Electrode. *Nature* 238 (5358), 37–38. doi:10.1038/238037a0

Hill, N. A. (2000). Why Are There So Few Magnetic Ferroelectrics? *J. Phys. Chem. B.* 104 (29), 6694–6709. doi:10.1021/jp000114x

Isseroff, L. Y., and Carter, E. A. (2012). Importance of Reference Hamiltonians Containing Exact Exchange for Accurate One-Shot GW Calculations of Cu_2O. *Phys. Rev. B.* 85 (23), 235142. doi:10.1103/physrevb.85.235142

Kumar, V. S., and Niranjan, M. K. (2014). Effect of Surface Structure on Workfunction and Schottky- Barrier Height in $SrRuO_3/SrTiO_3$ (001) Heterojunctions. *J. Appl. Phys.* 115, 173705. doi:10.1063/1.4872466

Li, L., Salvador, P. A., and Rohrer, G. S. (2014). Photocatalysts with Internal Electric Fields. *Nanoscale* 6 (1), 24–42. doi:10.1039/c3nr03998f

Longo, J. M., and Raccah, P. M. (1973). The Structure of La_2CuO_4 and $LaSrVO_4$. *J. Solid State. Chem.* 6 (4), 526–531. doi:10.1016/s0022-4596(73)80010-6

Ong, C. B., Ng, L. Y., and Mohammad, A. W. (2018). A Review of ZnO Nanoparticles as Solar Photocatalysts: Synthesis, Mechanisms and Applications. *Renew. Sustain. Energy Rev.* 81, 536–551. doi:10.1016/j.rser.2017.08.020

Shannon, R. D. (1976). Revised Effective Ionic Radii and Systematic Studies of Interatomic Distances in Halides and Chalcogenides. *Acta Cryst. Sect A.* 32, 751–767. doi:10.1107/s0567739476001551http://abulafia.mt.ic.ac.uk/shannon/

Stock, M., and Dunn, S. (2012). Influence of the Ferroelectric Nature of Lithium Niobate to Drive Photocatalytic Dye Decolorization under Artificial Solar Light. *J. Phys. Chem. C.* 116 (39), 20854–20859. doi:10.1021/jp305217z

Walter, M. G., Warren, E. L., McKone, J. R., Boettcher, S. W., Mi, Q., Santori, E. A., et al. (2010). Solar Water Splitting Cells. *Chem. Rev.* 110 (11), 6446–6473. doi:10.1021/cr1002326

Wang, Z., Song, J., Gao, F., Su, R., Zhang, D., Liu, Y., et al. (2017). Developing a Ferroelectric Nanohybrid for Enhanced Photocatalysis. *Chem. Commun.* 53 (54), 7596–7599. doi:10.1039/c7cc02548c

Zhao, G., Huang, X., Wang, X., and Wang, X. (2017). Progress in Catalyst Exploration for Heterogeneous CO_2 Reduction and Utilization: A Critical Review. *J. Mater. Chem. A.* 5 (41), 21625–21649. doi:10.1039/c7ta07290b

Zhao, R., Xie, H., Chang, L., Zhang, X., Zhu, X., Tong, X., et al. (2019). Recent Progress in the Electrochemical Ammonia Synthesis under Ambient Conditions. *Energy Chem.* 1 (2), 100011. doi:10.1016/j.enchem.2019.100011

Zhou, L., Wang, W., Xu, H., Sun, S., and Shang, M. (2009). Bi_2O_3 Hierarchical Nanostructures: Controllable Synthesis, Growth Mechanism, and Their Application in Photocatalysis. *Chem. Eur. J.* 15 (7), 1776–1782. doi:10.1002/chem.200801234

Insights Into Chemical Reactions at the Beginning of the Universe: From HeH$^+$ to H$_3^+$

Soumya Ranjan Dash[1†], Tamal Das[1,2†] and Kumar Vanka[1,2]*

[1]Physical and Materials Chemistry Division, CSIR-National Chemical Laboratory (CSIR-NCL), Pune, India, [2]Academy of Scientific and Innovative Research (AcSIR), Ghaziabad, India

At the dawn of the Universe, the ions of the light elements produced in the Big Bang nucleosynthesis recombined with each other. In our present study, we have tried to mimic the conditions in the early Universe to show how the recombination process would have led to the formation of the first ever formed diatomic species of the Universe: HeH$^+$, as well as the subsequent processes that would have led to the formation of the simplest triatomic species: H$_3^+$. We have also studied some special cases: higher positive charge with fewer number of hydrogen atoms in a dense atmosphere, and the formation of unusual and interesting linear, dicationic He chains beginning from light elements He and H in a positively charged atmosphere. For all the simulations, the *ab initio* nanoreactor (*AINR*) dynamics method has been employed.

Keywords: density functional theory, ab initio molecular dynamics, ab initio nanoreactor, origin of molecules in the universe, the earliest lewis acid

INTRODUCTION

The way the Universe, and all the elements, came into being is one of the fascinating questions of science. Attempts to answer this question has led to the Big Bang theory, and an understanding of the primeval Universe and the entities that it was made up of (Meyer, 2008). Further advancement of science and technology has led to greater understanding, which led NASA's Stratospheric Observatory for Infrared Astronomy (SOFIA) to the detection of HeH$^+$ in the planetary nebula NGC 7027, the first molecule formed after the Big Bang (Güsten et al., 2019), 94 years after its discovery in the laboratory in 1925 (Hogness and Lunn, 1925).

As the first molecule, the significance of the role of HeH$^+$ in the evolution of other species cannot be overstated. One of these species, and perhaps the most important, is the simplest polyatomic molecule H$_3^+$, which has always intrigued researchers ever since its discovery in 1911 by J. J. Thomson (Sir Thomson, 1911). However, the importance H$_3^+$ in astrochemistry was realized only after it was detected on Jupiter in the 1980s (Oka, 1980; Drossart et al., 1989). High abundance of H$_3^+$ in the Universe and its ability to donate a proton established this triatomic cation as the interstellar acid of utmost importance for many extra-terrestrial reactions (Watson, 1973; Oka, 2013; Olah et al., 2016; Pelley, 2019). While there are many reports of H$_3^+$ formation from doubly ionized organic molecules (Townsend et al., 2004; De et al., 2006; Okino et al., 2006; Kushawaha and Bapat, 2008; Mebel and Bandrauk, 2008; Nakai et al., 2013; Ando et al., 2018;

Abbreviations: AIMD, *Ab initio* molecular dynamics; AINR, *Ab initio* nano reactor; DFT, Density functional theory.

GRAPHICAL ABSTRACT |
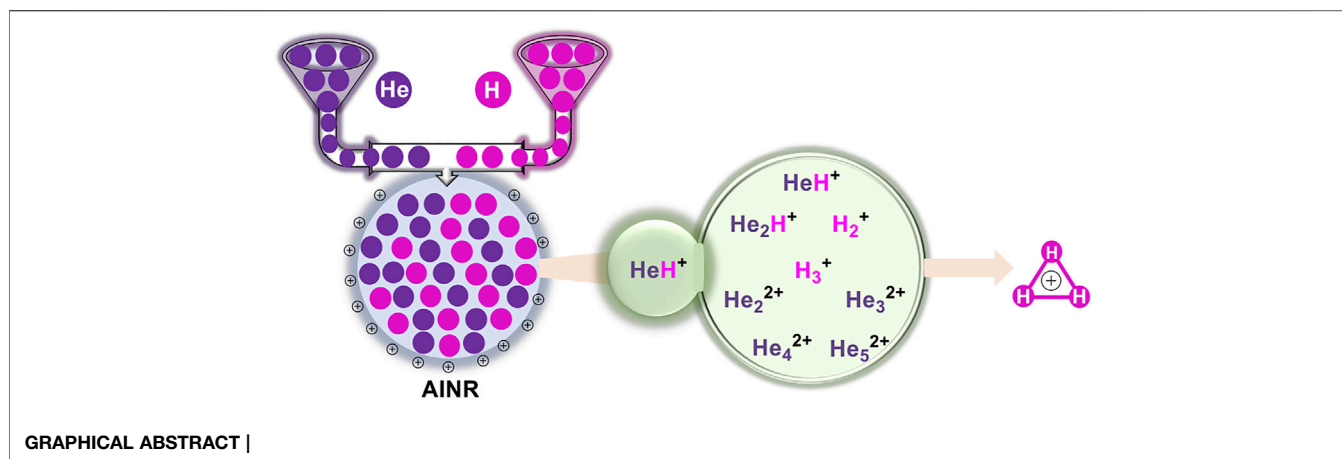
Ekanayake et al., 2018; Palaudoux and Hochlaf, 2019), our focus is on its origin and the role played by HeH^+ on its formation.

H_3^+ formation was first reported to occur primarily from the combination of H_2^+ and H_2, where H_2^+ would be formed from the ionization of H_2 (Sir Thomson, 1912; Oka, 2013). There are other reports which state that H_2^+ is more likely to be formed from the combination of HeH^+ and H (Bovino et al., 2011; Razio, 2014; Esposito et al., 2015; Fortenberry, 2019; González-Lezana et al., 2019). At the same time, the possibility of HeH^+ combining with H_2 to produce H_3^+ cannot be overlooked (McLaughlin and Thompson, 1973). Thus, many factors can influence the origin of H_3^+, but there have not been any conclusive studies yet.

In this work, we have employed the *ab initio* nanoreactor (AINR) method to carry out full quantum mechanical molecular dynamics (MD) simulations on systems containing atoms/ions of helium and hydrogen, and have obtained reaction profiles by varying their mixture ratio and the charge. The *AINR* method, developed by Martinez and co-workers, allows the determination of new reaction pathways and products, without the need of controlling the chemical system (Zimmerman, 2013; Rappoport et al., 2014; Wang et al., 2014). Our primary goal was to gain insight into the formation of different species from the combination of He and H in the presence of a positively charged atmosphere, as well as their further dissociation and recombination. As the Results and Discussion section will show, our studies provide interesting new insights into HeH^+ formation, and shed light on various short-lived intermediates that could have formed *en route* to obtaining H_3^+– the stable species that was known to exist in the early Universe (Oka, 2013).

COMPUTATIONAL METHODS

Ab Initio Molecular Dynamics Simulations

The AIMD simulations were performed with the TeraChem 1.9 (Ufimtsev and Martínez, 2008a; Ufimtsev and Martínez, 2008b; Ufimtsev and Martinez, 2009a; Ufimtsev and Martinez, 2009b; Ufimtsev et al., 2011; Isborn et al., 2011; Titov et al.,

2013) software package using the Hartree−Fock (HF) (Fischer, 1987) electronic wave function and the 6–311 g (Binkley et al., 1980) Gaussian basis set, to calculate the Born−Oppenheimer potential energy surface. This method has been implemented in TeraChem by Martinez and co-workers. This approach was deemed acceptable because the HF method is well-known for predicting chemically reasonable structures (Feller and Peterson, 1998). Also, it should be noted that HF was not employed to determine the thermodynamics of the reactions: its only role was in the discovery process. This was also the approach employed by Martinez and co-workers in their original *AINR* paper (employing HF/3–21 g), where they replicated the results obtained from the Urey−Miller experiment, as well as from the interaction of acetylene molecules. The same method (HF) was also employed by us in our previous report (Das et al., 2019) on reaction pathways leading to the formation of precursors of RNA and sugars. Electrostatic interactions were treated using two of the most common methods: the residue-based cutoff and particle mesh Ewald (PME). The PME method has been chosen because it takes care of long-range electrostatic interactions and is the most widely used approach.

The results were obtained from the *AINR* simulations by varying both the He to H ratio, as well as the positive charge of the system. Each simulation was repeated thrice. The system was constrained in a spherical boundary of 4.0 and 2.0 Å radii, so that the atoms resided in a space that alternated between the volumes created by these two radii, and collided with each other. Each *AINR* dynamics was evolved upto 15 ps, with a time step of 0.5 fs.

Newton's equations of motion were calculated using Langevin dynamics, with an equilibrium temperature of 1,000.0 K (also the starting temperature of the dynamics). We have used this high temperature in order to increase the average kinetic energy of the reactants and for faster dynamics (Novotný et al., 2019). We have employed the augmented direct inversion in the iterative subspace (ADIIS) algorithm (Hu and Yang, 2010) available in TeraChem as an alternative tool for self-consistent field calculations at each AIMD step in

which the default DIIS algorithm (Pulay, 1980) failed to converge. The nanoreactor simulations employ a virtual piston by fluctuating the radius of a spherical boundary, which allows the continuous expansion and compression of the system, thus artificially changing the pressure and the density for the collision cycles, which is necessary for the molecules to collide and also increases the rate of the reactions. Spherical boundary conditions (details in the ESI) were applied to prevent the molecules from flying away, a phenomenon known as the "evaporation" event. For more details, please check the original paper on the *AINR* by Martinez and co-workers (Wang et al., 2014).

The mechanistic pathways obtained from the *AINR* simulations were then analyzed with full quantum mechanical (QM) calculations. All the structures were optimized with coupled cluster singles doubles (CCSD) (Grotendorst et al., 2006) and with the 6–311++G (d,*p*) (McLean and Chandler, 1980) basis set. The Gaussian09 software (Frisch et al., 2009) was employed for the thermodynamic calculations. The complete solution of the H_3^+ problem requires the consideration of relativistic effects, nuclear motion, and breakdown of the Born-Oppenheimer (B-O) approximation (both adiabatic and non-adiabatic) (Miller et al., 2020). Recent studies have shown that relativistic effects for H_3^+ are quite negligible (Cencek et al., 1998; Bachorz et al., 2009). Issues of breakdown of the B-O approximation become relevant when considering transition frequencies of H_3^+, i.e., in spectroscopic studies. Since the current work is focused on understanding the possible chemical reactivity and thermochemistry of HeH^+ and H^+, leading eventually to H_3^+ formation, the current studies, done within the B-O approximation, are appropriate.

RESULTS AND DISCUSSIONS

In this section, we will briefly describe the formation of H_3^+ in the *AINR via* different short lived intermediates. We have taken a fixed composition of the He and H mixture and varied the overall positive charge density of the system (as shown in **Tables 1, 2**). During the simulations in each case, it was seen that HeH^+ was formed at the very beginning of the dynamics as the first molecular species. In our first set of simulations, we have taken a homogeneous mixture of 30 atoms each of H and He. The *AINR* makes them collide with each other at a temperature of 1,000.0 K. The simulation with no positive charge in the system does not produce any intermediates and H_3^+ at all throughout the dynamics. This led us to consider the possibility that a more appropriate set-up would include a positively charged system, which would mimic the collisions between the ionized state of the helium and hydrogen atoms present at the beginning of Universe (Oka, 2013). A positively charged environment for the formation of H_3^+ had also been considered by many previous reports, while investigating its origin from different organic molecules (Pilling et al., 2007). Therefore, we have varied the positive charge of the system by even numbers (**Table 1**) during the *AINR* dynamics. As the dynamics progressed, various short lived species such as He_2^{2+}, He_3^{2+} and He_2H^+ (snapshots shown in the **Supplementary Figures S1–S5** in the Supporting Information (ESI) file) were seen to have formed in almost every simulation, though their time of appearance was different in each case. It was also observed that with the increase of the positive charge of the system, the formation of H_3^+ ions also increased, up to a point. The number of H_3^+ ions generated was equal to the positive charge in the system, up to a charge of +6 (see **Table 1**).

TABLE 1 | *AINR* simulations with 30 He atoms and 30 H atoms: different entries represent the variation of the total positive charge of the system–by even numbers.

Total charge	First molecule	Intermediate species	Dominant end molecule	No. of H_3^+
0	-	-	-	-
2	HeH^+	He_2^{2+}, He_3^{2+}, He_2H^+, H^+, H_2	H_3^+	2
4	HeH^+	He_2^{2+}, He_2H^+, H^+, H_2	H_3^+	4
6	HeH^+	He_2^{2+}, He_3^{2+}, He_2H^+, H^+, H_2	H_3^+	6
8	HeH^+	He_2^{2+}, He_3^{2+}, He_2H^+, H^+, H_2	H_3^+	7
10	HeH^+	He_2^{2+}, He_3^{2+}, He_2H^+, H^+, H_2	H_3^+	7
20	HeH^+	He_2^{2+}, He_2H^+, H^+, H_2	H_3^+	5

TABLE 2 | *AINR* simulations with 30 He atoms and 29 H atoms: different entries represent the variation of the total positive charge of the system–by odd numbers.

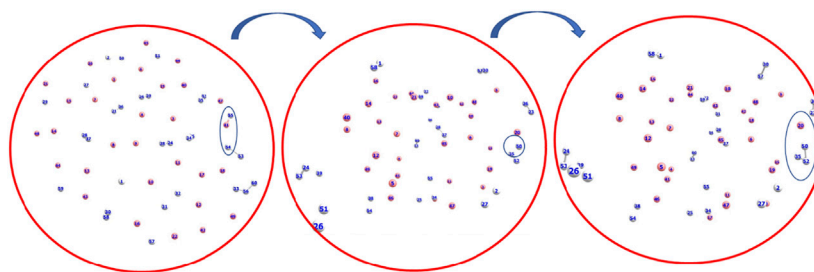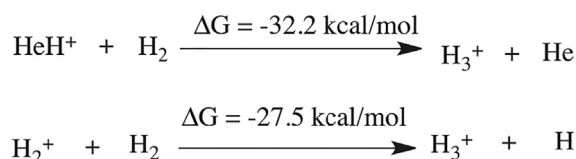| Total charge	First molecule	Intermediate species	Dominant end molecule	No. of H_3^+
0	-	-	-	-
1	HeH^+	He_2H^+, H^+, H_2	H_3^+	1
3	HeH^+	He_2^{2+}, He_2H^+, H^+, H_2	H_3^+	3
5	HeH^+	He_2^{2+}, He_2H^+, H^+, H_2	H_3^+	5
7	HeH^+	He_2^{2+}, He_3^{2+}, He_2H^+, H^+, H_2	H_3^+	6
9	HeH^+	He_2^{2+}, He_3^{2+}, He_2H^+, H^+, H_2	H_3^+	7
11	HeH^+	He_2^{2+}, He_2H^+, H^+, H_2	H_3^+	7
21	HeH^+	He_2^{2+}, He_2H^+, H^+, H_2	H_3^+, HeH^+	4

FIGURE 1 | Snapshots of *AINR* simulations showing the progress of the dynamics starting from atomic He and H, leading toward the formation of H_3^+ from HeH^+ and dihydrogen. HeH^+ was seen to be formed very early–near the beginning of the dynamics (Color: He - peach, H - white).

$$HeH^+ + H_2 \xrightarrow{\Delta G = -32.2 \text{ kcal/mol}} H_3^+ + He$$

$$H_2^+ + H_2 \xrightarrow{\Delta G = -27.5 \text{ kcal/mol}} H_3^+ + H$$

SCHEME 1 | Thermodynamics of H_3^+ formation.

However, upon further increase in the positive charge of the system beyond six–to eight or ten, the number of H_3^+ ions formed was not seen to be equal to the total positive charge of the system. Instead of H_3^+, the remaining positive charge of the system was balanced by H^+ or, in some cases, HeH^+. As shown in **Table 1**, in case of a positive charge of 10 and after 250 fs, we observed only seven H_3^+ ions remaining with three H^+, which balanced the total charge of the system. The natural population analysis (NPA), or the formal charge analyzed data for all the atoms in several snapshots, has been shown in **Supplementary Tables S1–S4** in the ESI.

Similarly, in another set of MD simulations, we have taken 29 H with 30 He atoms and varied the overall charge of the system by an odd number: one, three, five and so on. These observations have been shown in **Table 2**. We have observed a similar trend for the formation of H_3^+ as the only end product up to a certain limit (here, the value is 5) of positive charge and beyond that, the total charge of the system was seen to be balanced by the sum of H_3^+, H^+ and HeH^+, as seen in the previous section when the positive charge was varied by even numbers.

In short, we can say that in all the cases of AINR dynamics studied, the formation of HeH^+ as the first molecule was observed. However, upon varying the total positive charge of the whole system, several short-lived species (He_2H^+, He_3^{2+}, He_2^{2+}) were observed (**Tables 1, 2**) after HeH^+ formation. At the end of the simulation, H_3^+ and H_2 were found to be the only stable species left in the reaction mixture.

The Timescale of Formation of H_3^+ and Other Short Lived Molecules

The formation timescale of different short lived species, along with the stable H_3^+, has been observed from femtosecond *AINR* simulations. In each and every simulation, HeH^+, which has been proposed to be the first formed molecule, was seen to be formed soon after the beginning of the dynamics. The time of appearance

of HeH^+ was within 15 fs timesteps. Subsequently, other short lived species (He_2H^+, He_3^{2+}, He_2^{2+}) were formed within the timescale of 0.1 ps (shown in **Table 3**). The observed timescale for the existence of such transient species is around 5–10 fs. Once these molecules were formed, they quickly dissociated and this ultimately led to the formation of H_3^+, which was observed for every case. From the AINR dynamics, we have analyzed the data and found two pathways for the formation of H_3^+, starting from He and H in atomic states within the positively charge atmosphere. Both of the pathways involved the well-known roaming hydrogen mechanism (Townsend et al., 2004; Nakai et al., 2013; Palaudoux and Hochlaf, 2019). An mp4 file (**Supplementary Movie S1**) of a movie made of a part of an *AINR* simulation is included in the ESI. The most feasible pathway for H_3^+ formation is the abstraction of a proton from the first molecule HeH^+ by the roaming dihydrogen (shown in **Figure 1**).

The thermodynamics for this step has been calculated to be -32.2 kcal/mol (shown in **Scheme 1**). In another mechanistic pathway, there is no involvement of HeH^+. Instead of HeH^+, the proton abstraction occurs from a mono-cationic dihydrogen molecule by the roaming dihydrogen. This process is thermodynamically favourable by 27.5 kcal/mol.

The total number of H_3^+ molecules formed was also found to be directly correlated with the total charge of the system, as well as

TABLE 3 | Time (in fs) of the first appearance of different species.

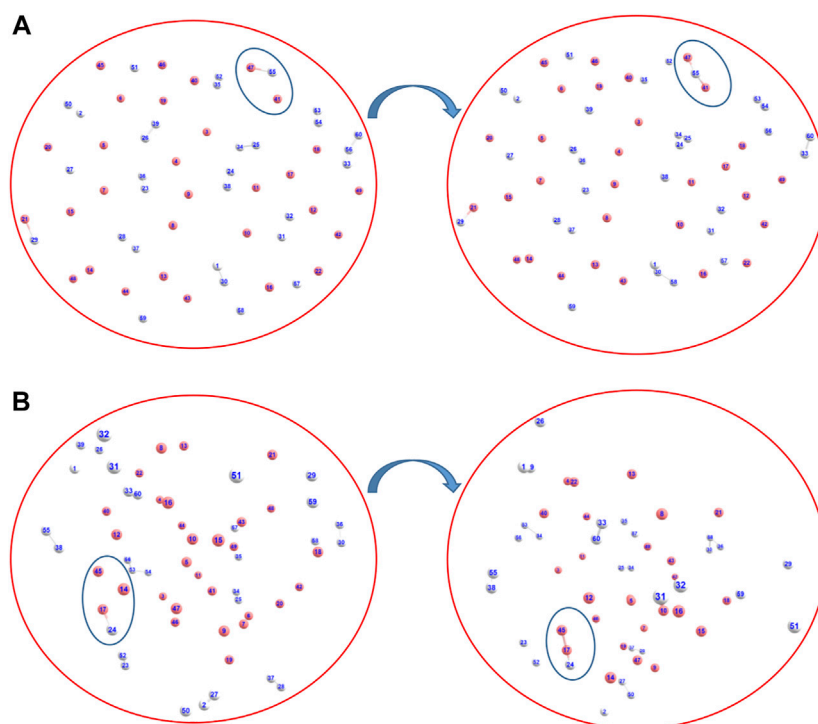| Total charge	HeH$^+$	He$_2$H$^+$	He$_2^{2+}$	He$_3^{2+}$	H$_3^+$
0	-	-	-	-	-
2	4.5	11.0	10.0	25.5	27.0
4	9.0	25.5	19.5	80.0	45.0
6	5.0	12.5	16.0	49.5	9.0
8	4.0	12.5	22.5	53.0	8.0
10	5.5	18.0	14.0	19.0	7.0
20	4.0	26.5	14.5	22.0	9.0

FIGURE 2 | Snapshots of *AINR* simulations revealing the pathway toward the making of He_2H^+, in the form of **(A)** $[He-H-He]^+$ and **(B)** $[He-He-H]^+$ (Color: He - peach, H - white).

the number of He and H atoms taken. Greater charge in the system yielded more short-lived species during the simulations. Most of the intermediate species were found to be formed within 100 fs (**Table 3**) and they were found to exist for only about 5–10 fs during the *AINR* simulations.

Since it has been postulated that different ratios of helium to hydrogen atoms could have existed in the early Universe (Meyer, 2008), we have further performed *AINR* dynamics with a 1:3 ratio of helium to hydrogen atoms and varied the total positive charge of the system (see **Table 4**). Furthermore, in order to investigate the effect of temperature on cosmic reionization (Novotný et al., 2019), we have also carried out *AINR* simulations while varying the temperature (**Table 5**), with a 1:3 ratio of He:H and a fixed positive charge (8^+). In all such simulations, we have observed trends similar to those discussed in the previous sections, like the formation of HeH^+ as the first molecule and the subsequent

formation of transient species (He_2H^+, He_3^{2+}, He_2^{2+}), leading eventually to H_3^+ formation.

We have also addressed the speculation on the exact nature of the formed ion He_2H^+: whether it was formed as $[He-H-He]^+$ or as $[He-He-H]^+$ (Kim and Lee, 1999), *via AINR* dynamics followed by static CCSD calculations. As shown in **Figures 2A,B**, two different routes leading to the formation of $[He-H-He]^+$ and $[He-He-H]^+$ were observed during the simulations, generated from the collision of HeH^+ and He. The thermodynamics was evaluated and it was found that the formation of the $[He-H-He]^+$ species was exergonic by 32.3 kcal/mol, whereas the formation of $[He-He-H]^+$ was only favourable by 4.5 kcal/mol. In other words, our calculations indicate that He_2H^+ would have formed predominantly as $[He-H-He]^+$ rather than $[He-He-H]^+$.

In another set of simulations, we have taken a different ratio of helium to dihydrogen and simultaneously varied the total charge

TABLE 4 | Time of occurrence (in fs) of different species from the *AINR* simulation of 1: 3 ratio of helium to hydrogen while varying total positive charge of the system.

Total charge	HeH$^+$	He$_2$H$^+$	He$_2^{2+}$	He$_3^{2+}$	H$_3^+$
0	-	-	-	-	-
4	5.0	74.5	14.0	24.0	12.5
6	9.5	15.5	12.0	27.0	17.0
8	6.0	54.0	15.0	19.5	21.5
10	10.0	16.0	14.5	30.0	19.0
12	6.5	70.5	16.0	23.0	23.0

TABLE 5 | Time of occurrence (in fs) of different species from the *AINR* simulation of a 1: 3 ratio of helium to hydrogen while varying the temperature, with a fixed total positive charge of system (8^+).

Temperature (K)	HeH$^+$	He$_2$H$^+$	He$_2^{2+}$	He$_3^{2+}$	H$_3^+$
3,300	3.0	24.5	10.0	26.0	5.5
2,500	8.5	27.0	14.0	18.0	63.0
2,000	7.0	22.0	16.0	19.0	25.0
1,500	7.0	14.0	11.5	17.0	60.0
1,000	6.0	54.0	15.0	19.5	21.5
500	8.0	16.0	15.0	20.5	47.0

of the system. In these cases, due to the high charge density, the dihydrogen quickly dissociated into a proton and atomic hydrogen. Here too, we have observed similar trends: 1) HeH^+ is the first molecule to be formed, followed by 2) the formation of other short lived species, leading to H_3^+, which remained at the end, along with one or two molecules of HeH^+ (shown in **Table 5**). For the case of 20 He and five H_2 having a total of eight positive charge in the system, for instance, we observed that after a few collisions, there was still one HeH^+ molecule present along with one H_3^+ and that they were in equilibrium with each other, due to the instantaneous proton transfer between HeH^+ and H_2. Similar trends were observed for other simulations where the total positive charge of the system was high (in our simulation conditions, the values were ≥ 16). It is worth mentioning that in this high positive charge atmosphere with comparatively low H atom density, the number of H_3^+ that survived after the collisions was either one or two, depending upon the ratio of He to H_2 (shown in **Table 6**). Also, due to the very high positive charge density and high temperature (1,000.0 K) the movement of the light H^+ ions was seen to be extremely fast and they

repelled each other, going far away. This reduced the propensity toward the formation of H_3^+ in such simulations.

Formation of Unique Dicationic He Chains

Previously, there have been some reports (Marinetti et al., 2008; Oleksy et al., 2010) with regard to the formation of mono-cationic He ion clusters. Our current *AINR* based dynamics study reveals that there is a possibility of the formation of a dicationic helium chain of up to five He atoms: He_3^{2+}, He_4^{2+} and He_5^{2+}. This interesting result was obtained when we took a homogeneous mixture of H and He (15 atoms each) in the AINR, with an overall positive charge of 20 for the system. After a certain amount of time had elapsed (1 ps), we observed that a chain like structure had formed comprising of up to five helium atoms (shown in **Figure 3**).

An mp4 file (**Supplementary Movie S2**) of a movie made of a part of such an *AINR* simulation is included in the ESI. We have taken snapshots during the dynamics and carried out natural population analysis (NPA), in order to calculate the charge on the

TABLE 6 | Different ratios of He to dihydrogen while varying the total positive charge of the system.

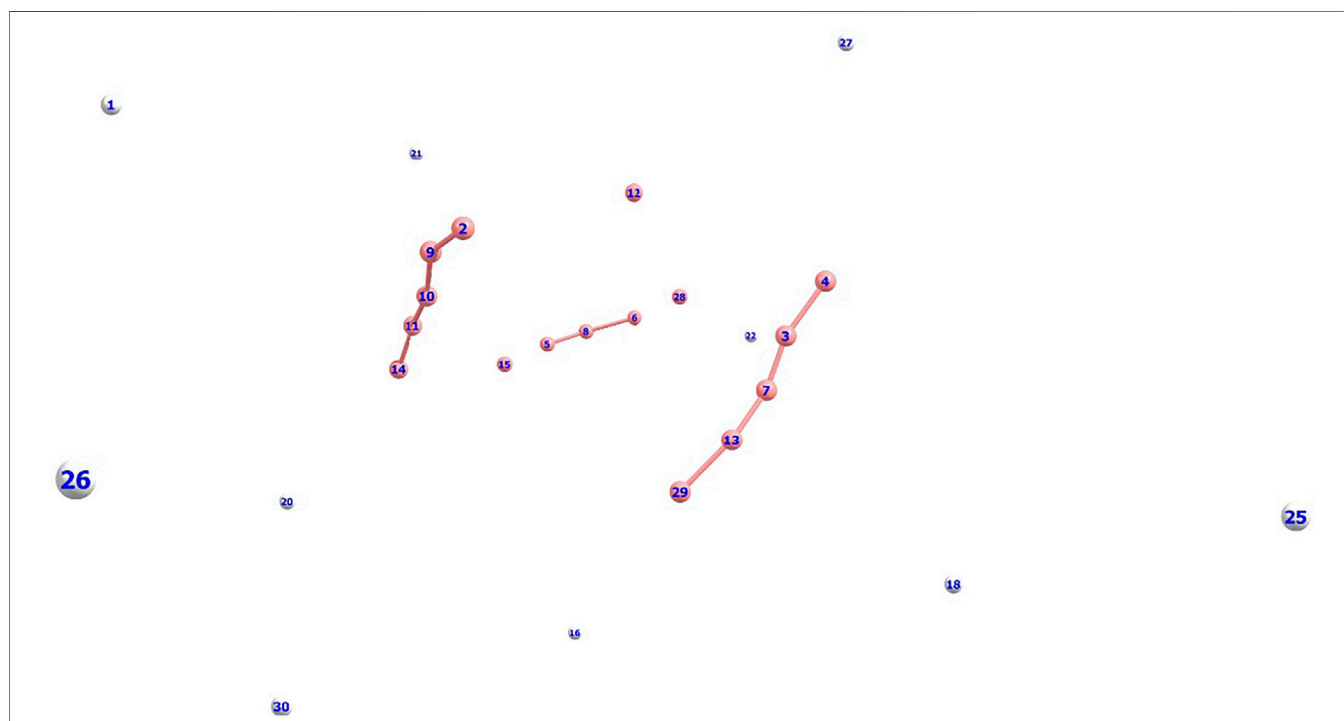| No. of He	No. of H_2	Total charge	First molecule	Intermediate species	Dominating end molecule	No. of H_3^+
20	5	8	HeH^+	He_2^{2+}, H^+	HeH^+, H_3^+	1
30	10	16	HeH^+	He_2^{2+}, He_3^{2+}, He_2H^+, H^+	HeH^+, H_3^+	1
30	15	24	HeH^+	He_2^{2+}, He_2H^+, H^+	HeH^+, H_3^+	1
30	15	26	HeH^+	He_2^{2+}, He_2H^+, H^+	HeH^+, H_3^+	1
15	10	8	HeH^+	He_2^{2+}, He_2H^+, H^+	H_3^+	4
30	15	20	HeH^+	He_2^{2+}, He_3^{2+}, He_2H^+, H^+	HeH^+, H_3^+	4

FIGURE 3 | Dicationic He chain formation during an *AINR* simulation of 15 H and 15 He atoms, with an overall positive charge of 20 (Color: He - peach, H - white).
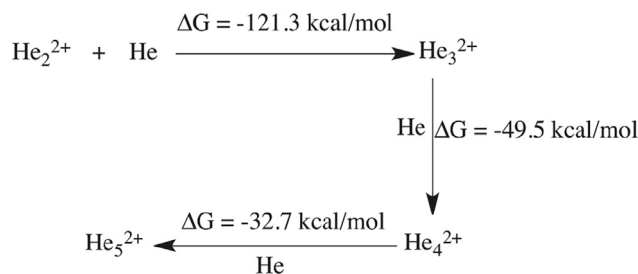
SCHEME 2 | Thermodynamics of helium chain formation (up to He_5^{2+}).

He atoms in the formed linear chain. From the NPA charge analysis (shown in **Supplementay Table S6** in the ESI), it has been confirmed that all the formed He chains (He_3^{2+}, He_4^{2+}, He_5^{2+}) were dicationic in nature. For further confirmation of the stability of these dicationic He chains, we have done thermodynamics calculations for the formation of the He chain starting from He_2^{2+} (shown in **Scheme 2**). The Gibbs free energy values suggest that the formation of the dicationic helium chain up to He_5^{2+} is favourable, but further formation of He_6^{2+} is thermodynamically not feasible. For this reason, we did not observe any He chain beyond five He atoms in our *AINR* simulations.

CONCLUSION

In our current work, we have tried to shed light on the chemical reactions that might have taken place at the beginning of the Universe. We have focused on how, at the very beginning, simple molecules came into being after the Big Bang. We have investigated how He and H atoms, which were the first atoms formed, collided with each other in a positively charged atmosphere. This has been done by using a fresh computational approach–by employing the *ab initio* nanoreactor (*AINR*). The simulations reveal the presence of unique dicationic helium chains of up to five atoms, which should act as a fillip for investigating the possibility of the presence of such species in helium clusters, which have received attention both from experimental and theoretical studies (Bieske and Dopfer, 2000; Marinetti et al., 2008; Oleksy et al., 2010). Our studies also confirm that HeH$^+$ was indeed the first molecule to be formed and that it played a vital role in the origin of H_3^+. The preservation of H_3^+, as a relatively stable species, in each of the simulations after every collision cycle, also explains the high abundance of H_3^+ in the early Universe. As such, our work provides interesting computational insights into the origin of unique and interesting molecules at the dawn of the Universe.

REFERENCES

Ando, T., Shimamoto, A., Miura, S., Iwasaki, A., Nakai, K., and Yamanouchi, K. (2018). Coherent Vibrations in Methanol Cation Probed by Periodic H_3^+ Ejection after Double Ionization. *Comm. Chem.* 1, 7. doi:10.1038/s42004-017-0006-7

DATA AVAILABILITY STATEMENT

The original contributions presented in the study are included in the article/**Supplementary Material**, further inquiries can be directed to the corresponding author.

AUTHOR CONTRIBUTIONS

SD and TD have carried out the research work and written the manuscript, with the guidance and supervision of KV.

FUNDING

ACKNOWLEDGMENTS

SUPPLEMENTARY MATERIAL

The Supplementary Material for this article can be found online at: https://www.frontiersin.org/articles/10.3389/fchem.2021.679750/full#supplementary-material

Bachorz, R. A., Cencek, W., Jaquet, R., and Komasa, J. (2009). Rovibrational Energy Levels of H 3+ with Energies above the Barrier to Linearity. *J. Chem. Phys.* 131, 024105. doi:10.1063/1.3167795

Bieske, E. J., and Dopfer, O. (2000). High-resolution Spectroscopy of Cluster Ions. *Chem. Rev.* 100, 3963–3998. doi:10.1021/cr990064w

Binkley, J. S., Pople, J. A., and Hehre, W. J. (1980). Self-consistent Molecular Orbital Methods. 21. Small Split-Valence Basis Sets for

First-Row Elements. *J. Am. Chem. Soc.* 102 (3), 939–947. doi:10.1021/ja00523a008

Bovino, S., Gianturco, F. A., and Tacconi, M. (2011). Chemical Destruction of Rotationally "Hot" HeH$^+$: Quantum Cross Sections and Mechanisms of its Reaction with H. *Chem. Phys. Lett.* 554, 47–52. doi:10.1016/j.cplett.2012.10.027

Cencek, W., Rychlewski, J., Jaquet, R., and Kutzelnigg, W. (1998). Sub-microhartree Accuracy Potential Energy Surface for H3+ Including Adiabatic and Relativistic Effects. I. Calculation of the Potential Points. *J. Chem. Phys.* 108, 2831–2836. doi:10.1063/1.4757027

Das, T., Ghule, S., and Vanka, K. (2019). Insights into the Origin of Life: Did it Begin from HCN and H2O? *ACS Cent. Sci.* 5 (9), 1532–1540. doi:10.1021/acscentsci.9b00520

De, S., Rajput, J., Roy, A., Ghosh, P. N., and Safvan, C. P. (2006). Formation of H$_3^+$ Due to Intramolecular Bond Rearrangement in Doubly Charged Methanol. *Phys. Rev. Lett.* 97, 1–4. doi:10.1103/physrevlett.97.213201

Drossart, P., Maillard, J.-P., Caldwell, J., Kim, S. J., Watson, J. K. G., Majewski, W. A., et al. (1989). Detection of H3+ on Jupiter. *Nature* 340, 539–541. doi:10.1038/340539a0

Ekanayake, N., Severt, T., Nairat, M., Weingartz, N. P., Farris, B. M., Kaderiya, B., et al. (2018). H$_2$ Roaming Chemistry and the Formation of H$_3$ $^+$ from Organic Molecules in Strong Laser Fields. *Nat. Comm* 9, 5186. doi:10.1038/s41467-018-07577-0

Esposito, F., Coppola, C. M., and De Fazio, D. (2015). Complementarity between Quantum and Classical Mechanics in Chemical Modeling. The H + HeH+ → H2+ + He Reaction: A Rigorous Test for Reaction Dynamics Methods. *J. Phys. Chem. A.* 119 (51), 12615–12626. doi:10.1021/acs.jpca.5b09660

Feller, D., and Peterson, K. A. (1998). An Examination of Intrinsic Errors in Electronic Structure Methods Using the Environmental Molecular Sciences Laboratory Computational Results Database and the Gaussian-2 Set. *J. Chem. Phys.* 108, 154–176. doi:10.1063/1.475370

Fischer, C. F. (1987). General Hartree-Fock Program. *Comput. Phys. Comm.* 4, 355–365. doi:10.1016/0010-4655(87)90053-1

Fortenberry, R. C. (2019). The Oldest Molecular Ancestor Finally Brought into the Light. *Chem* 5, 1012–1030. doi:10.1016/j.chempr.2019.04.016

Frisch, M. J., Trucks, G. W., Schlegel, H. B., Scuseria, G. E., Robb, M. A., Cheeseman, J. R., et al. (2009). *Gaussian 09, Revision A.01*. Wallingford CT: Gaussian, Inc.

González-Lezana, T., Bossion, D., Scribano, Y., Bhowmick, S., and Suleimanov, Y. V. (2019). Dynamics of H + HeH+(v = 0, J = 0) → H2+ + He: Insight on the Possible Complex-Forming Behavior of the Reaction. *J. Phys. Chem. A.* 123 (49), 10480–10489. doi:10.1021/acs.jpca.9b06122

Grotendorst, J., Blugel, S., and Marx, D. (2006). Beyond Hartree-Fock: MP2 and Coupled-Cluster Methods for Large Systems. *Comput. Nanoscience* 31, 245–278.

Güsten, R., Wiesemeyer, H., Neufeld, D., Menten, K. M., Graf, U. U., Jacobs, K., et al. (2019). Astrophysical Detection of the Helium Hydride Ion HeH+. *Nature* 568, 357–359. doi:10.1038/s41586-019-1090-x

Hogness, T. R., and Lunn, E. G. (1925). The Ionization of Hydrogen by Electron Impact as Interpreted by Positive Ray Analysis. *Phys. Rev.* 26, 44–55. doi:10.1103/physrev.26.44

Hu, X., and Yang, W. (2010). Accelerating Self-Consistent Field Convergence with the Augmented Roothaan−Hall Energy Function. *J. Chem. Phys.* 132, 054109. doi:10.1063/1.3304922

Isborn, C. M., Luehr, N., Ufimtsev, I. S., and Martínez, T. J. (2011). Excited-State Electronic Structure with Configuration Interaction Singles and Tamm-Dancoff Time-dependent Density Functional Theory on Graphical Processing Units. *J. Chem. Theor. Comput.* 7 (6), 1814–1823. doi:10.1021/ct200030k

Kim, S. T., and Lee, J. S. (1999). Ab Initio study of He2H+ and Ne2H+: Accurate Structure and Energetics. *J. Chem. Phys.* 110, 4413–4418. doi:10.1063/1.478324

Kushawaha, R. K., and Bapat, B. (2008). Fragmentation Dynamics of the Methanol Dication. *Chem. Phys. Lett.* 463, 42–46. doi:10.1016/j.cplett.2008.08.019

Marinetti, F., Bodo, E., Gianturco, F. A., and Yurtsever, E. (2008). Energetics and Structures of Charged Helium Clusters: Comparing Stabilities of Dimer and Trimer Cationic Cores. *ChemPhysChem* 9, 2618–2624. doi:10.1002/cphc.200800457

McLaughlin, D. R., and Thompson, D. L. (1973). Ab Initio dynamics: HeH+ + H2 → He + H3+ (C 2v) Classical Trajectories Using a Quantum Mechanical Potential-energy Surface. *J. Chem. Phys.* 59, 4393–4405. doi:10.1063/1.1680637

McLean, A. D., and Chandler, G. S. (1980). Contracted Gaussian Basis Sets for Molecular Calculations. I. Second Row Atoms, Z=11-18. *J. Chem. Phys.* 72, 5639–5648. doi:10.1063/1.438980

Mebel, A. M., and Bandrauk, A. D. (2008). Theoretical Study of Unimolecular Decomposition of Allene Cations. *J. Chem. Phys.* 129, 224311. doi:10.1063/1.3037204

Meyer, B. S. (2008). Origin of the Elements: Nucleosynthesis in Stars. *ACS Symp. Ser.* 981 (3), 39–60. doi:10.1021/bk-2008-0981.ch003

Miller, S., Tennyson, J., Geballe, T. R., and Stallard, T. (2020). Thirty Years of H$_3^+$ Astronomy. *Rev. Mod. Phys.* 92, 035003. doi:10.1103/revmodphys.92.035003

Nakai, K., Kato, T., Kono, H., and Yamanouchi, K. (2013). Communication: Long-Lived Neutral H$_2$ in Hydrogen Migration within Methanol Dication. *J. Chem. Phys.* 139, 1–5. doi:10.1063/1.4830397

Novotný, O., Wilhelm, P., Paul, D., Kálosi, Á., Saurabh, S., Becker, A., et al. (2019). Quantum-state-selective Electron Recombination Studies Suggest Enhanced Abundance of Primordial HeH+. *Science* 365, 676–679. doi:10.1126/science.aax5921

Oka, T. (2013). Interstellar H3+. *Chem. Rev.* 113, 8738–8761. doi:10.1021/cr400266w

Oka, T. (1980). Observation of the Infrared Spectrum of H3+. *Phys. Rev. Lett.* 45 (7), 531–534. doi:10.1103/physrevlett.45.531

Okino, T., Furukawa, Y., Liu, P., Ichikawa, T., Itakura, R., Hoshina, K., et al. (2006). Coincidence Momentum Imaging of Ejection of Hydrogen Molecular Ions from Methanol in Intense Laser Fields. *Chem. Phys. Lett.* 419, 223–227. doi:10.1016/j.cplett.2005.11.059

Olah, G. A., Mathew, T., and Prakash, G. K. S. (2016). Relevance and Significance of Extraterrestrial Abiological Hydrocarbon Chemistry. *J. Am. Chem. Soc.* 138 (22), 6905–6911. doi:10.1021/jacs.6b03136

Oleksy, K., Karlický, F., and Kalus, R. (2010). Structures and Energetics of Helium Cluster Cations: Equilibrium Geometries Revisited through the Genetic Algorithm Approach. *J. Chem. Phys.* 133, 164314. doi:10.1063/1.3489346

Palaudoux, J., and Hochlaf, M. (2019). Formation of H3+ through Chloromethane Dication Fragmentation. *ACS Earth Space Chem.* 3 (6), 980–985. doi:10.1021/acsearthspacechem.9b00045

Pelley, J. (2019). Probing the Universe with H$_3^+$. *ACS Cent. Sci.* 5 (5), 741–744. doi:10.1021/acscentsci.9b00555

Pilling, S., Andrade, D. P. P., Neves, R., Ferreira-Rodrigues, A. M., Santos, A. C. F., and Boechat-Roberty, H. M. (2007). Production of H+3 via Photodissociation of Organic Molecules in Interstellar Clouds. *Mon. Not. R. Astron. Soc.* 375 (4), 1488–1494. doi:10.1111/j.1365-2966.2006.11415.x

Pulay, P. (1980). Convergence Acceleration of Iterative Sequences. The Case of SCF Iteration. *Chem. Phys. Lett.* 73, 393–398. doi:10.1016/0009-2614(80)80396-4

Rappoport, D., Galvin, C. J., Zubarev, D. Y., and Aspuru-Guzik, A. (2014). Complex Chemical Reaction Networks from Heuristics-Aided Quantum Chemistry. *J. Chem. Theor. Comput.* 10, 897–907. doi:10.1021/ct401004r

Razio, D. D. (2014). The H + HeH$^+$ → He + H$_2$$^+$ Reaction from the Ultra-cold Regime to the Three-Body Breakup: Exact Quantum Mechanical Integral Cross Sections and Rate Constants. *Phys. Chem. Chem. Phys.* 16, 11662–11672. doi:10.1039/c4cp00502c

Sir Thomson, J. J. (1911). Rays of Positive Electricity. *Philos. Mag.* 6 (21), 225. doi:10.1080/14786440208637024

Sir Thomson, J. J. (1912). Rays of Positive Electricity. *Philos. Mag.* 6 (24), 209. doi:10.1080/14786440808637325

Titov, A. V., Ufimtsev, I. S., Luehr, N., and Martinez, T. J. (2013). Generating Efficient Quantum Chemistry Codes for Novel Architectures. *J. Chem. Theor. Comput.* 9 (1), 213–221. doi:10.1021/ct300321a

Townsend, D., Lahankar, S. A., Lee, S. K., Chambreau, S. D., Suits, A. G., Zang, X., et al. (2004). The Roaming Atom: Straying from the Reaction Path in Formaldehyde Decomposition. *Science* 306, 1158–1161. doi:10.1126/science.1104386

Ufimtsev, I. S., Luehr, N., and Martinez, T. J. (2011). Charge Transfer and Polarization in Solvated Proteins from *Ab Initio* Molecular Dynamics. *J. Phys. Chem. Lett.* 2 (14), 1789–1793. doi:10.1021/jz200697c

Ufimtsev, I. S., and Martínez, T. J. (2008a). Graphical Processing Units for Quantum Chemistry. *Comput. Sci. Eng.* 10, 26–34. doi:10.1109/mcse.2008.148

Ufimtsev, I. S., and Martínez, T. J. (2008b). Quantum Chemistry on Graphical Processing Units. 1. Strategies for Two-Electron Integral Evaluation. *J. Chem. Theor. Comput.* 4 (2). 222–231.doi:10.1021/ct700268q

Ufimtsev, I. S., and Martinez, T. J. (2009a). Quantum Chemistry on Graphical Processing Units. 2. Direct Self-Consistent-Field Implementation. *J. Chem. Theor. Comput.* 5 (4), 1004–1015. doi:10.1021/ct800526s

Ufimtsev, I. S., and Martinez, T. J. (2009b). Quantum Chemistry on Graphical Processing Units. 3. Analytical Energy Gradients, Geometry Optimization, and First Principles Molecular Dynamics. *J. Chem. Theor. Comput.* 5 (10), 2619–2628. doi:10.1021/ct9003004

Wang, L.-P., Titov, A., McGibbon, R., Liu, F., Pande, V. S., and Martínez, T. J. (2014). Discovering Chemistry with an *Ab Initio* Nanoreactor. *Nat. Chem* 6, 1044–1048. doi:10.1038/nchem.2099

Watson, W. D. (1973). The Rate of Formation of Interstellar Molecules by Ion-Molecule Reactions. *ApJ* 183, L17–L20. doi:10.1086/181242

Zimmerman, P. M. (2013). Automated Discovery of Chemically Reasonable Elementary Reaction Steps. *J. Comput. Chem.* 34, 1385–1392. doi:10.1002/jcc.23271

Gold-Catalyzed Complementary Nitroalkyne Internal Redox Process: A DFT Study

K. Vipin Raj[1,2], Pawan S. Dhote[2,3], Kumar Vanka[1,2]* and Chepuri V. Ramana[2,3]*

[1]Physical and Materials Chemistry Division, CSIR-National Chemical Laboratory, Pune, India, [2]Academy of Scientific and Innovative Research (AcSIR), Ghaziabad, India, [3]Organic Chemistry Division, CSIR-National Chemical Laboratory, Pune, India

Gold-catalysis, in this century, is one of the most emerging and promising new areas of research in organic synthesis. During the last two decades, a wide range of distinct synthetic methodologies have been unveiled employing homogeneous gold catalysis and aptly applied in the synthesis of numerous natural products and biologically active molecules. Among these, the reactions involving α-oxo gold carbene/α-imino gold carbene intermediates are of contemporary interest, in view of their synthetic potential and also due to the need to understand the bonding involved in these complexes. In this manuscript, we document the theoretical investigations on the regio-selectivity dependence of substitution on the gold-catalyzed cycloisomerization of *o*-nitroarylalkyne derivatives. We have also studied the relative stabilities of α-oxo gold carbene intermediates.

Keywords: gold-catalysis, internal redox, cycloisomerization, α-oxo gold carbene, DFT calculation

INTRODUCTION

Gold catalyzed reactions have been increasingly emerging in the literature over the past few decades (Hashmi, 2007; Pflästerera and Hashmi, 2015). The majority of these reactions are based on the propensity of gold complexes to act as carbophilic Lewis acids in the activation of carbon–carbon multiple bonds, thus allowing the formation of new C–C and C–hetero atom bonds by inter-/intramolecular addition of nucleophiles across the Au-complexed multiple bonds (Corma et al., 2011). An interesting class of gold-catalyzed reactions that needs a mention in this context are the catalytic internal redox cyclisation's (Xiao and Li, 2011; Zhang, 2014; Yeom and Shin, 2014). The oxygen atom transfer to alkynes catalyzed by gold complexes is a well-known addition–elimination process employing nucleophilic oxygen atom donors such as nitro (Asao et al., 2003; Li et al., 2005; Ramana et al., 2010), amine-/pyridine N-oxides (Cui et al., 2009; Nosel et al., 2013), nitrone (Heom et al., 2008; Pati and Liu, 2009; Chen et al., 2011), sulfoxides (Shapiro and Toste, 2007; Lu et al., 2013), and epoxides (Hashmi et al., 2008; Lin et al., 2008), reacting with the activated alkynes.

The Au-catalyzed cycloisomerizaton of nitrotolans documented by Yamamoto and co-workers in 2003 (**Scheme 1**, Eq. 1) (Asao et al., 2003), is an important advancement to synthesize 2-arylisatogens. Interestingly, when the pendant alkyne substituent is an alkyl group, the internal redox process proceeds in a complementary mode resulting in the formation of a benzo[*c*]isoxazole, trivially known as anthranil. A mechanism founded upon the addition of the oxygen of the nitro group in a 6-*endo*-dig fashion has been postulated as the key step involved for the intramolecular redox process. Initially, it has been proposed that the resulting gold-ate complex **A** undergoes protonolysis followed by ring opening with water to produce a nitrosobenzene. There exist two possibilities for the subsequent dehydrative cyclization leading to isatogens (*path a*) or anthranil
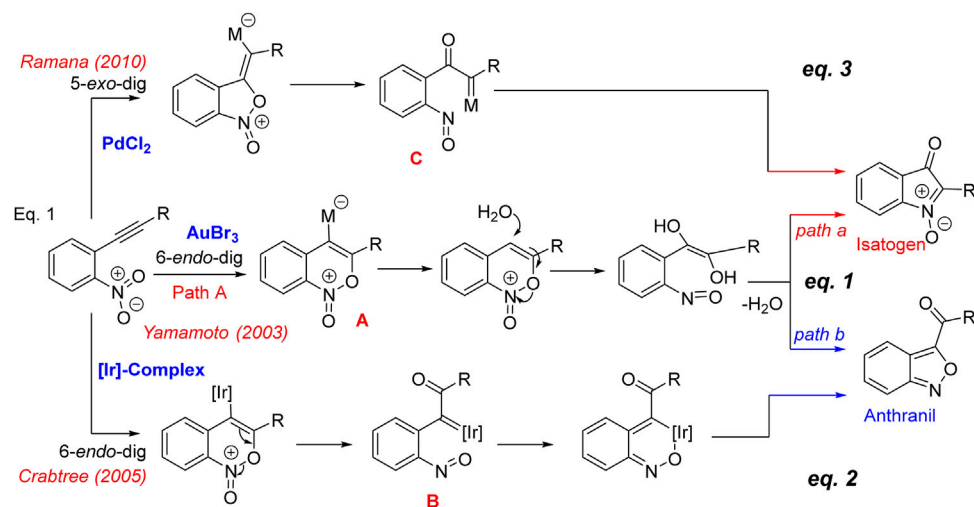
SCHEME 1 | Mechanism of nitroalkyne cycloisomerization.
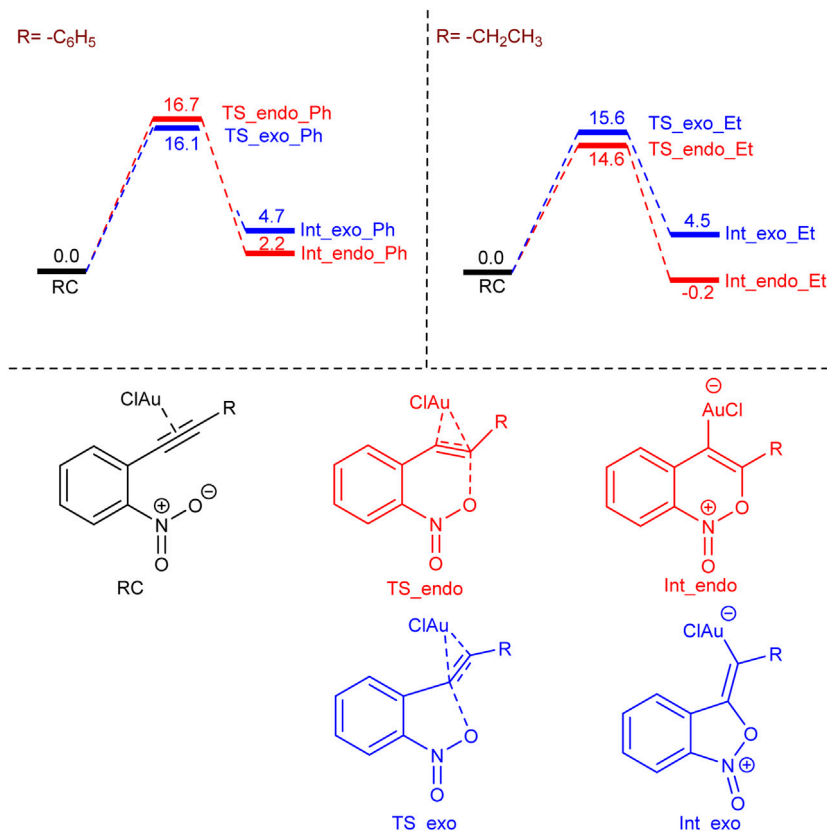
SCHEME 2 | The free energy profile for the formation of -endo and -exo intermediates for –phenyl and –ethyl substitutions. Values are in kcal/mol.

(*path b*). Though this explains the possible paths, it does not account for why these paths are substituent dependent. In a later report, Crabtree's group has documented (**Scheme 1**, Eq. 2) a

similar nitroalkynes cycloisomerization by iridium hydrides leading to anthranils (Li et al., 2005). With the help of single crystal structural analysis, it has been proved that there exists an

FIGURE 1 | The relative free energies of α-oxo gold carbenes with respect to the most stable one (E for the phenyl substitution and G for the ethyl substitution). Values are in kcal/mol.
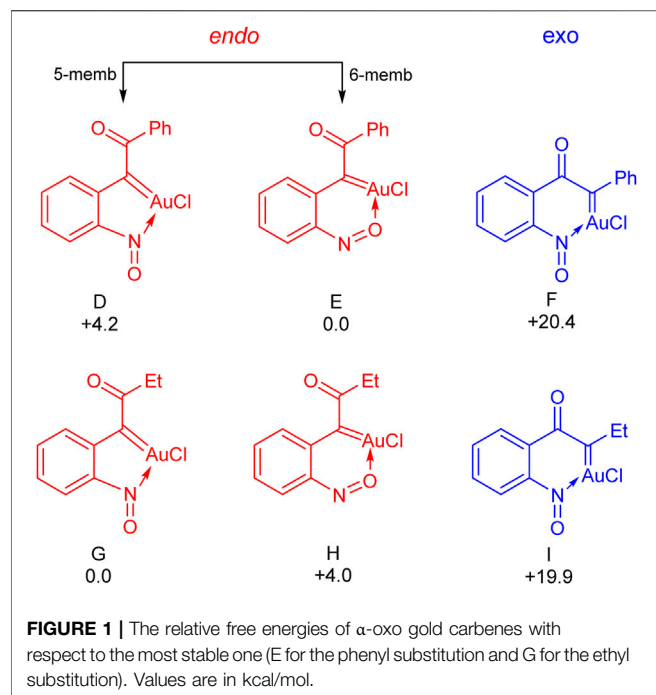
intermediate iridium(III) nitroso complex **B**, which results after the initial oxygen transfer from nitro to alkyne in a 6-*endo*-dig fashion. In this context, as a part of the total synthesis of the pseudoindoxyl class of natural products (Ramana et al., 2010; Patel et al., 2013), we have speculated on the possibility of complementing this process by employing Pd-complexes which was successfully realized to come up with a general method for the synthesis of 2-aryl and 2-alkyl isatogens *via* an internal nitro-alkyne redox process (**Scheme 1**, Eq. 3) (Ramana et al., 2010). We have also studied in detail the mechanistic aspects with density functional theory (DFT) and reasoned that the formation of an α-oxo metal carbenoid **C** occurs by the 5-*exo*-dig mode of cyclization of the nitro group on the alkyne, which subsequently undergoes a 6n-electro cyclization to isatogen. In this manuscript, we document the DFT calculations on the [Au]-catalysed complementary nitroalkyne redox process that leads to α-oxo gold carbenes **B** and **C**, especially focusing on the energies associated with oxygen transfer and carbene transfer. This has been undertaken considering the importance of gold catalyzed processes that proceed through the α-imino and/or α-oxo gold carbenes and their promising applications in the heterocyclic synthesis (Aguilar and Santamaría, 2019; Zhang, 2014). These processes in general proceed through the carbene and/or nitrene transfer from the [Au]-centre (Ye, 2020). However, in case of the Au-carbenes **B** and **C**, such a transfer is challenging, as the internal electrocyclization along with the nitroso group is highly favored with either of them. The possibility of trapping these reactive intermediates has been attempted with internal and external nucleophiles. However, on both instances, it has been realized that the intramolecular process leading to isatogens or anthranil has exclusively taken place and the products obtained are from the reaction of the nucleophile employed with the

isatogen. Thus, a qualitative understanding of the relative energies of **B** and **C** and the energies associated in their formation is expected to provide some clues on the possible trapping.

RESULTS AND DISCUSSION

In order to understand the selectivity (*endo* or *exo*) dependence on the substitution (alkyl or aromatic) on the nitro alkyne, we have performed density functional theory (DFT) calculations using the Turbomole 7.2 program package (TURBOMOLE V7.2, 2017). We have chosen the ethyl ($-CH_2CH_3$) and phenyl ($-C_6H_5$) groups as the representatives for alkyl and aromatic substitutions and considered AuCl as the catalyst instead of $AuCl_3$, in accordance with previously reported work (Straub, 2004). The *endo* or *exo* selectivity arises due to the two different possibilities of oxygen (of the nitro group) attack on the C–C triple bond (see **Scheme 2**), and our calculations indicate that the *exo* transition state (TS_exo_Ph) is favorable by 0.6 kcal/mol over the *endo* transition state (TS_endo_Ph) for phenyl substitution (see **Scheme 2**). In contrast, the *endo* transition state (TS_endo_Et) is favorable by 1.0 kcal/mol over the *exo* transition (TS_exo_Et) state for ethyl substitution, which corroborates with the experimental observations. Furthermore, in the case of ethyl substitution, the *endo* intermediate (Int_endo_Et) is more preferable than the *exo* intermediate (Int_exo_Et) by 4.7 kcal/mol, but in the case of phenyl substitution, the *exo* intermediate (Int_exo_Ph) is less favorable than the *endo* intermediate (Int_endo_Ph) by 2.5 kcal/mol. In other words, the *endo* pathway to form the first intermediate is favorable both kinetically and thermodynamically for the ethyl substitution, but the *exo* pathway is only kinetically favorable for the phenyl substitution.

Next, the energies of the six different possible oxo gold carbenes (D to I in **Figure 1**) have been calculated to see their relative stability. As shown in **Figure 1**, depending upon the heteroatom of the nitroso group involved in the coordination, there exists two possibilities for the oxo gold carbene resulting from the 6-*endo* dig path – with the nitrogen atom, a five–membered coordination (D and G for Ph and Et respectively) and six-membered coordination with the oxygen atom (E and H for Ph and Et respectively). Interestingly, with both phenyl and ethyl, the [Au]-carbenes derived from the 6-*endo* dig path are more stable. In case of the phenyl, E, the six-membered coordination is more stable than the D, five-membered coordination, by 4.2 kcal/mol. However, with the ethyl substituent, this was seen to be exactly reversed. G, the five-membered coordination was seen to be more stable than H, the six-membered coordination, by 4.0 kcal/mol. When it comes to the 5-*exo* dig path, in both the ethyl (19.9 kcal/mol unfavourable compared to G) and phenyl (20.4 kcal/mol unfavourable compared to E) cases, the energies associated with resulting carbenes reveal that they are unfavourable.

Overall, these preliminary calculations indicate that the α-oxo gold carbenes resulting from the 6-*endo*-dig mode of oxygen transfer are favored in general, though the energies associated

with this process vary with respect to the substituent. For example, as discussed already, the formation of the first intermediate *via* the 6-*endo*-dig mode is kinetically and thermodynamically favourable for ethyl substitution. However, the corresponding mode is only thermodynamically favourable for phenyl substitution. This indicates that energies associated with the internal oxygen transfer lead to the α-oxo gold carbene B and also, given its comparable stability, that the chances of the carbene transfer from this reactive intermediate are greater.

CONCLUSION

To conclude, DFT calculations on the internal oxygen transfer of the Au-catalyzed *o*-nitroalkyne cycloisomerization reactions have been carried out to understand the relative energies associated with the oxygen transfer and the energies of the resulting α-oxo gold carbenes. These calculations clearly reveal that the α-oxo gold carbenes resulting from the 6-*endo* dig addition of the oxygen to the alkyne is thermodynamically stable, when compared to the alternative α-oxo gold carbene that results from the 5-*exo* dig addition. Our calculations also suggest that the substitutions on the *o*-nitroalkynes have a significant role in altering the regio-selectivity of the reaction.

COMPUTATIONAL DETAILS

All the calculations in this study have been performed with density functional theory (DFT), with the aid of the Turbomole 7.2 suite of programs (TURBOMOLE V7.2, 2017), using the M06-2X functional (Zhao and Truhlar, 2008). The def-TZVP basis set has been employed (Schäfer et al., 1994; Eichkorn et al., 1997). The resolution of identity (RI) (Eichkorn et al., 1995), along with the multipole accelerated resolution of identity (marij) (Sierka et al., 2003) approximations have been employed for an accurate and efficient treatment of the electronic Coulomb term in the DFT calculations. Solvent correction were incorporated with optimization calculations using the COSMO model (Klamt and Schüürmann, 1993), with toluene ($\varepsilon = 2.374$) as the solvent. The values reported are ΔG values, with zero-point energy corrections, internal energy and entropic contributions were

included through frequency calculations on the optimized minima, with the temperature taken to be 298.15 K. Harmonic frequency calculations were performed for all stationary points to confirm them as a local minima or transition state structures. The XYZ coordinates of the optimized geometries of all the structures are provided in the **Supplementary Material**.

DATA AVAILABILITY STATEMENT

The original contributions presented in the study are included in the article/**Supplementary Material**, further inquiries can be directed to the corresponding author.

AUTHOR CONTRIBUTIONS

CR and KV: Problem Identification and Manuscript Writing. KVR: DFT Calculations and Assistance in Manuscript Writing and PD Support for DFT and Assistance in Manuscript Writing.

ACKNOWLEDGMENTS

SUPPLEMENTARY MATERIAL

The Supplementary Material for this article can be found online at: https://www.frontiersin.org/articles/10.3389/fchem.2021.689780/full#supplementary-material

REFERENCES

Aguilar, E., and Santamaría, J. (2019). Gold-catalyzed Heterocyclic Syntheses through α-imino Gold Carbene Complexes as Intermediates. *Org. Chem. Front.* 6, 1513–1540. doi:10.1039/C9QO00243J

Asao, N., Sato, K., and Yamamoto, Y. (2003). AuBr3-catalyzed Cyclization of O-(alkynyl)nitrobenzenes. Efficient Synthesis of Isatogens and Anthranils. *Tetrahedron Lett.* 44, 5675–5677. doi:10.1016/S0040-4039(03)01357-1

Chen, D., Song, G. Y., Jia, A. Q., and Li, X. W. (2011). Gold- and Iodine-Mediated Internal Oxygen Transfer of Nitrone- and Sulfoxide-Functionalized Alkynes. *J. Org. Chem.* 76, 8488–8494. doi:10.1021/jo201347r

Corma, A., Leyva-Pérez, A., and Sabater, M. J. (2011). Gold-Catalyzed Carbon–Heteroatom Bond-Forming Reactions. *Chem. Rev.* 111 (3), 1657–1712. doi:10.1021/cr100414u

Cui, L., Peng, Y., and Zhang, L. (2009). A Two-step, Formal [4 + 2] Approach toward Piperidin-4-Ones via Au Catalysis. *J. Am. Chem. Soc.* 131, 8394–8395. doi:10.1021/ja903531g

Eichkorn, K., Treutler, O., Öhm, H., Häser, M., Ahlrichs, R., Öhm, H., et al. (1995). Auxiliary Basis Sets to Approximate Coulomb Potentials. *Chem. Phys. Lett.* 240, 283–290. doi:10.1016/0009-2614(95)00621-A

Eichkorn, K., Weigend, F., Treutler, O., and Ahlrichs, R. (1997). Auxiliary Basis Sets for Main Row Atoms and Transition Metals and Their Use to Approximate Coulomb Potentials. *Theor. Chem. Acc. Theor. Comput. Model. (Theoretica Chim. Acta).* 97, 119–124. doi:10.1007/s002140050244

Hashmi, A. S. K., Bührle, M., Salathé, R., and Bats, J. W. (2008). Gold Catalysis: Synthesis of 3-Acylindenes from 2-Alkynylaryl Epoxides. *Adv. Synth. Adv. Synth. Catal.* 350, 2059–2064. doi:10.1002/adsc.200800385

Hashmi, A. S. K. (2007). Gold-Catalyzed Organic Reactions. *Chem. Rev.* 107, 3180–3211. doi:10.1021/cr000436x

Heom, H. S., Lee, J. E., and Shin, S. (2008). Gold-Catalyzed Waste-free Generation and Reaction of Azomethine Ylides: Internal Redox/Dipolar Cycloaddition Cascade. *Angew. Chem. Int. Ed.* 47, 7040–7043. doi:10.1002/anie.200802802

Klamt, A., and Schüürmann, G. (1993). COSMO: a New Approach to Dielectric Screening in Solvents with Explicit Expressions for the Screening Energy and its Gradient. *J. Chem. Soc. Perkin Trans.* 2, 799–805. doi:10.1039/P29930000799

Li, X., Incarvito, C. D., Vogel, T., and Crabtree, R. H. (2005). Intramolecular Oxygen Transfer from Nitro Groups to C:C Bonds Mediated by Iridium Hydrides. *Organometallics.* 24, 3066–3073. doi:10.1021/om050116+

Lin, G.-Y., Li, C.-W., Hung, S.-H., and Liu, R.-S. (2008). Diversity in Gold- and Silver-Catalyzed Cycloisomerization of Epoxide–Alkyne Functionalities. *Org. Lett.* 10, 5059–5062. doi:10.1021/ol802047g

Lu, B., Li, Y., Wang, Y., Aue, D. H., Luo, Y., and Zhang, L. (2013). [3,3]-Sigmatropic Rearrangement versus Carbene Formation in Gold-Catalyzed Transformations of Alkynyl Aryl Sulfoxides: Mechanistic Studies and Expanded Reaction Scope. *J. Am. Chem. Soc.* 135, 8512–8524. doi:10.1021/ja401343p

Nösel, P., dos Santos Comprido, L. N. T., Lauterbach, M., Rominger, F., and Hashmi, A. S. K. (2013). 1,6-Carbene Transfer: Gold-Catalyzed Oxidative Diyne Cyclizations. *J. Am. Chem. Soc.* 135, 15662–15666. doi:10.1021/ja4085385

Patel, P., Reddy, B. N. P., and Ramana, C. V. (2013). The Synthesis of the central Tricyclic Core of the Isatisine A: Harmonious Orchestration of [metal]-Catalyzed Reactions in a Sequence. *Tetrahedron.* 70, 510–516. doi:10.1016/j.tet.2013.11.026

Pati, K., and Liu, R. S. (2009). Efficient Syntheses of α-pyridones and 3(2H)-Isoquinolones through Ruthenium-Catalyzed Cycloisomerization of 3-En-5-Ynyl and O-Alkynylphenyl Nitrones Chem. *Commun.*14, 5233–5235. doi:10.1039/B910773H

Pflästerera, D., and Hashmi, S. (2015). Gold Catalysis in Total Synthesis – Recent Achievements. *Chem. Soc. Rev.* 45, 1331–1367. doi:10.1039/C5CS00721F

Ramana, C. V., Patel, P., Vanka, K., Miao, B. C., and Degterev, A. (2010). A Combined Experimental and Density Functional Theory Study on the Pd-Mediated Cycloisomerization of O-Alkynylnitrobenzenes—Synthesis of Isatogens and Their Evaluation as Modulators of ROS-Mediated Cell Death. *Eur. J. Org. Chem.* 2010 (31):5955–5966. doi:10.1002/ejoc.201000769

Schäfer, A., Huber, C., and Ahlrichs, R. (1994). Fully Optimized Contracted Gaussian Basis Sets of Triple Zeta Valence Quality for Atoms Li to Kr. *J. Chem. Phys.* 100, 5829–5835. doi:10.1063/1.467146

Shapiro, N. D., and Toste, F. D. (2007). Rearrangement of Alkynyl Sulfoxides Catalyzed by Gold(I) Complexes. *J. Am. Chem. Soc.* 129, 4160–4161. doi:10.1021/ja070789e

Sierka, M., Hogekamp, A., and Ahlrichs, R. (2003). Fast Evaluation of the Coulomb Potential for Electron Densities Using Multipole Accelerated Resolution of Identity Approximation. *J. Chem. Phys.* 118, 9136–9148. doi:10.1063/1.1567253

Straub, B. F. (2004). Gold(i) or Gold(iii) as Active Species in AuCl3-Catalyzed Cyclization/cycloaddition Reactions? *Chem. Commun.* 2004, 1726–1728. doi:10.1039/B404876H

TURBOMOLE V7.2 (2017). A development of University of Karlsruhe and Forschungszentrum Karlsruhe GmbH, 1989-2007, TURBOMOLE GmbH, since 2007. Available at: http://www.turbomole.com (Accessed May 18, 2018)

Xiao, J., and Li, X. (2011). Gold α-Oxo Carbenoids in Catalysis: Catalytic Oxygen-Atom Transfer to Alkynes, *Angew. Chem. Int. Ed.* 50, 7226–7236. doi:10.1002/anie.201100148

Ye, L. W., Zhu, X., Sahani, R., Xu, Y., Qian, P. C., and Liu, R. S. (2020). Nitrene Transfer and Carbene Transfer in Gold Catalysis. *Chem. Rev.* 2020, 121. doi:10.1021/acs.chemrev.0c00348

Yeom, H.-S., and Shin, S. (2014). Catalytic Access to α-Oxo Gold Carbenes by N-O Bond Oxidants. *Acc. Chem. Res.* 47, 966–977. doi:10.1021/ar4001839

Zhang, L. (2014). A Non-diazo Approach to α-Oxo Gold Carbenes via Gold-Catalyzed Alkyne Oxidation. *Acc. Chem. Res.* 47, 877–888. doi:10.1021/ar400181x

Zhao, Y., and Truhlar, D. G. (2008). The M06 Suite of Density Functionals for Main Group Thermochemistry, Thermochemical Kinetics, Noncovalent Interactions, Excited States, and Transition Elements: Two New Functionals and Systematic Testing of Four M06-Class Functionals and 12 Other Functionals. *Theor. Chem. Account.* 120, 215–241. doi:10.1007/s00214-007-0310-x

Recent Progress in (Photo-)-Electrochemical Conversion of CO$_2$ With Metal Porphyrinoid-Systems

Dženeta Dedić[1,2], Adrian Dorniak[1], Uwe Rinner[2] and Wolfgang Schöfberger[1]*

[1]Institute of Organic Chemistry, Johannes Kepler University Linz, Linz, Austria, [2]IMC Fachhochschule Krems, Krems an der Donau, Austria

Since decades, the global community has been facing an environmental crisis, resulting in the need to switch from outdated to new, more efficient energy sources and a more effective way of tackling the rising carbon dioxide emissions. The activation of small molecules such as O$_2$, H$^+$, and CO$_2$ in a cost—and energy-efficient way has become one of the key topics of catalysis research. The main issue concerning the activation of these molecules is the kinetic barrier that has to be overcome in order for the catalyzed reaction to take place. Nature has already provided many pathways in which small molecules are being activated and changed into compounds with higher energy levels. One of the most famous examples would be photosynthesis in which CO$_2$ is transformed into glucose and O$_2$ through sunlight, thus turning solar energy into chemical energy. For these transformations nature mostly uses enzymes that function as catalysts among which porphyrin and porphyrin-like structures can be found. Therefore, the research focus lies on the design of novel porphyrinoid systems (e.g. corroles, porphyrins and phthalocyanines) whose metal complexes can be used for the direct electrocatalytic reduction of CO$_2$ to valuable chemicals like carbon monoxide, formate, methanol, ethanol, methane, ethylene, or acetate. For example the cobalt(III)triphenylphosphine corrole complex has been used as a catalyst for the electroreduction of CO$_2$ to ethanol and methanol. The overall goal and emphasis of this research area is to develop a method for industrial use, raising the question of whether and how to incorporate the catalyst onto supportive materials. Graphene oxide, multi-walled carbon nanotubes, carbon black, and activated carbon, to name a few examples, have become researched options. These materials also have a beneficial effect on the catalysis through for instance preventing rival reactions such as the Hydrogen Evolution Reaction (HER) during CO$_2$ reduction. It is very apparent that the topic of small molecule activation offers many solutions for our current energy as well as environmental crises and is becoming a thoroughly investigated research objective. This review article aims to give an overview over recently gained knowledge and should provide a glimpse into upcoming challenges relating to this subject matter.

Keywords: catalysis, carbon dioxide reduction, metal complexes, corroles, porphyrins, phthalocyanines, electrocatalysis

INTRODUCTION

The aim of this review is to give an overview of different metal porphyrinoid electrocatalysts and to outline their ability to activate and reduce CO_2. In order to explain the difficulties of this electrocatalytic process, we discuss the mechanisms of CO_2 reduction and show current of such catalysts. The most recent findings in catalyst development, in respect to different metal ions as central atoms and ligand systems used are discussed in detail.

Porphyrins, Corroles, and Phthalocyanines

Porphyrins are naturally occurring cyclic macromolecules, which consist of four pyrrole rings connected *via* methine groups. Corroles differ from porphyrins as one of the methine groups is missing. In phthalocyanine macrocycles, four isoindole groups are linked together *via* nitrogen bridges. **Figure 1** presents the general structures of porphyrin, corrole, and phthalocyanine with IUPAC numeration. The positions 5, 10, and 15 (or 5, 10, 15, and 20 in case of porphyrin) are called meso-positions (Moss, 1988; Sorokin, 2013; Zhang et al., 2017a; Barata et al., 2017).

Porphyrin and corrin derivatives are responsible for many important biochemical processes and often play an important role in living organisms, mainly serving as biocatalysts. These macrocycles serve as ligands as they tend to form coordinative bonds between the nitrogen atoms of the pyrrole units and transition metal ions such as Fe, Ni or even alkaline earth metals such as Mg.

A well-known example of a naturally occurring tetrapyrrole system is hemoglobin. The central atom of the compound (iron) forms coordinative bonds with oxygen and enables the oxygen transport in blood. Another example is chlorophyll, the green pigment present in plants, algae, and some bacteria. This complex of chlorin (reduced structure of porphyrin) with magnesium ion is responsible for the conversion of solar energy into chemical energy during photosynthesis. Cofactor F_{430} and cobalamin (vitamin B_{12}) are other examples of naturally occurring tetrapyrroles. Despite similar properties, corroles, and phthalocyanines have not been isolated from natural sources so far (Shooling-Jordan and Cheung, 1999; Layer et al., 2010; Sorokin, 2013; Sawicki et al., 2015).

Coordinatively bonded tetrapyrrole systems strongly absorb electromagnetic radiation in the in the visible range. These compounds typically are highly stable in the solid and solution states, which simplifies characterization and structure elucidation and furthermore provides advantages for mechanistic investigations. Tetrapyrrol systems are easily modified and/or functionalized which paves the way for sophisticated applications in various ways. Changing substituents at meso- and β-positions as well as introducing additional functional groups at the second coordination sphere enables precise tuning of chemical and physical properties. Such modifications also include metalation, synthesis of macrocycles from previously functionalized educts or postfunctionalization of the inner core on peripheral positions. Examples of such modifications are halogenation, formylation, carboxylation, nitration, amination, sulfonation, oligomerization, chlorosulfonation, nucleophilic aromatic substitution or metal catalyzed cross-coupling reactions (Paolesse et al., 2001; Vicente and Smith, 2014; Barata et al., 2017; Hiroto et al., 2017; Orłowski et al., 2017; Nardis et al., 2019).

During the metalation process, tetrapyrrol systems are deprotonated at the inner core, leading to a four-coordinated square-planar configuration of the complex. Corroles differ from porphyrins or phthalocyanines by the number of hydrogen atoms in the inner core, which leads to different behavior during the metalation process. Deprotonated corrole binds metal ions with three bonds, while porphyrin or phthalocyanine chelates to metal ions with only two bonds. The trianionic ligand derived from corrole stabilizes metal ions more effectively in high oxidation states than their analogs with increased ring size. This has a positive effect on the formation and also the cleavage of coordinative bonds which will be discussed in subsequent sections of this chapter (Hiroto et al., 2017).

Porphyrins and corroles substituted at meso and β-positions are interesting for a variety of different applications. Fine-tuning of optical, electronic, and biochemical properties of these coordination compounds is generally achieved *via* the installation of different functional groups whereas the nature of the functionality and the position of the modifications defines the properties of the final product. (Pinto et al., 2016; Barata et al., 2017).

Different routes towards the preparation of corroles and porphyrines have been reported. Generally, the condensation of pyrroles with the requisite aldehydes are used to establish
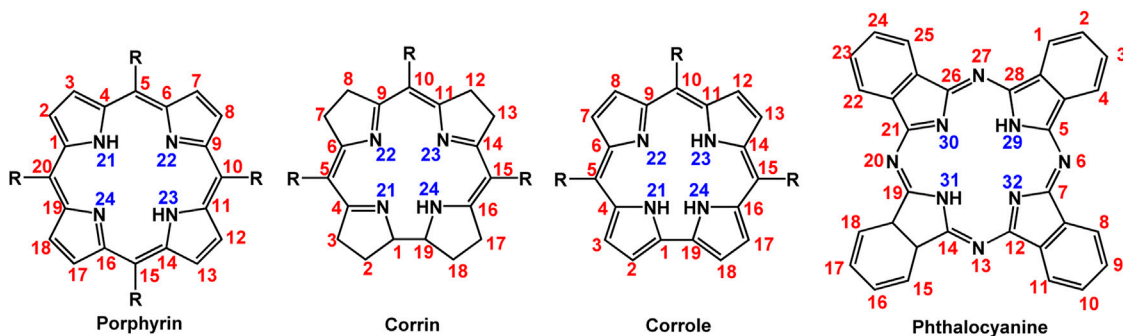

FIGURE 1 | General structures of tetrapyrrole molecules.

the macrocyle. This reaction, typically catalyzed by acids, is then followed by oxidation with *p*-chloranil or DDQ to complete the process (Lindsey et al., 1987; Vicente and Smith, 2014; König et al., 2016; Pinto et al., 2016). Quite often, yields are low as the reactivity of intermediates increases with growing chain length, resulting in the formation of undesired side products (Blumenfeld et al., 2015). Also, the purification is often tricky and difficult to perform on larger scale. Summarizing, very often, the complicated preparation of these compounds strongly limits their potential use in the industry.

A general approach based on the strategy outlined above was reported by Lindsey's group in 1986. Various meso-substituted porphyrins were obtained in high-overall yield when the condensation reaction of pyrrole and an aldehyde was carried out in high dilution (Lindsey et al., 1987). Initial attempts towards the preparation of corroles were quite limited in respect to the complexity of the desired final products (Paolesse et al., 1994).

A great improvement in the synthesis of meso-substituted corroles was reported by Koszarna and Gryko in 2006. By employing biphasic reaction mixtures, the authors were able to drastically improve on previously reported yields. Simultaneously bilanes, which exhibit lower solubility, precipitated from the reaction mixture, preventing the product from undergoing unwanted side reactions and oligomerization. The protocol furthermore enabled the synthesis of corroles, substituted with strongly electron-donating groups, in good overall yield. Previously reported methods did not allow the synthesis of this important class of modified corroles (Koszarna and Gryko, 2006; König et al., 2016).

Despite the progress in the preparation of tetrapyrrole systems, scale up is still economically challenging, as all protocols rely on the use of large amounts of solvents. The solution to this problem may be the use of mechanochemistry. It has been demonstrated, that solvent-free synthesis of porphyrine in ball mills is possible, giving hope for the potential industrial-scale production of this class of compounds (Shy et al., 2014).

Among other tetrapyrrolic systems, phthalocyanines seem to be the best-suited catalysts for small molecule activation (Boutin et al., 2020). These compounds provide several advantages over corroles and porphyrins. Precursors and starting materials required for the syntheses are often inexpensive, which allows for the large-scale preparation of these compounds and the preparation and the purification of the products is well-established. Similar to corroles and porphyrins, the synthesis of both symmetric as well as asymmetric phthalocyanines has been described. Fine-tuning of solubility properties in a variety of common organic solvents as well as water is possible *via* the addition and incorporation of appropriate substituents (Sakamoto and Ohno-Okumura, 2009; Sorokin, 2013; Nemykin et al., 2014; Denekamp et al., 2019; Araújo et al., 2020).

Electrocatalytic Reduction of CO₂

Global warming and the emissions of climate-relevant gases such as carbon dioxide have been a major area of discussion in recent years and decades. Comprehensive solutions are required with respect to CO₂ management in order to maintain the maximum

level of global warming below a threshold of +1.75°C. Since the reduction of CO₂ emissions alone will probably not be sufficient, other methods such as the storage and recycling of CO₂ must also be increasingly addressed. Such concepts of CO₂-recycling include thermochemical-, (bio)-electrochemical reduction or by plasma-driven catalytic reduction methods (Villano et al., 2010; Bajracharya et al., 2017; Yuan et al., 2019; Bogaerts and Centi, 2020; Liu et al., 2020) of carbon dioxide to fuels such as methane, methanol, and ethanol (**Figure 2**). If the electrical energy required for this conversion was solely generated from renewable sources, a completely sustainable and climate-friendly cycle would become possible (**Figure 3**). The electrical energy required for the reduction of CO₂ could be directly obtained *via* light harvesting using semiconductors. As the storage of electrical energy remains an unsolved problem to date, the direct conversion of CO₂ to value-added products also could serve as solution to this tricky challenge. In this respect, wind or solar energy surpassing the capacity of the power grid could be used for the production of methanol or ethanol. With the conversion of one ton of CO₂ equivalents, almost 1,400 kWh of energy could be stored under ideal conditions. If necessary, the methanol can then be used again, for example, as fuel in a direct methanol/ethanol fuel cell (DMFC).

To date, efforts to selectively convert CO₂ into methanol, ethanol or long-chain hydrocarbons continuously and at high rates have so far failed because the electrochemical reduction of CO₂ is associated with several problems: 1) The solubility of CO₂ in water is low and thus leads to low reaction rates. 2) The reduction of CO₂ is a reaction that takes place in several steps and leads to a number of possible organic compounds. The reaction mechanism is highly dependent on the experimental conditions and it is difficult to control the selectivity of the process (Zhang et al., 2017a). The reduction of CO₂ usually takes place at potentials at which the hydrogen evolution occurs. This side reaction greatly reduces the efficiency of the process (Sorokin, 2013). Additionally, the electrocatalytic activity of the respective metal catalysts might decrease significantly with time. Therefore, a thorough determination of the stability of the respective catalyst system is a necessity.

Despite the importance of the overall process, and the effort devoted to this field, answers to the questions outlined above have not yet found.

Although the reduction of CO₂ and light-induced water-splitting is possible, these processes require the application of novel catalysts. The reduction of CO₂ typically affords complex product mixtures. As nature has clearly demonstrated the feasibility of this approach, porphyrinoid-based catalysts seem highly suitable as catalysts as such protocols mimic photosynthesis (Mele et al., 2014; Zhang et al., 2017a; Nardis et al., 2019; Boutin et al., 2020; Min Park et al., 2020).

REDUCTION OF CARBON DIOXIDE—PROBLEMATIC ISSUE

The modern lifestyle of mankind with its continued combustion of fossil fuels has resulted in a dramatic increase of green-house
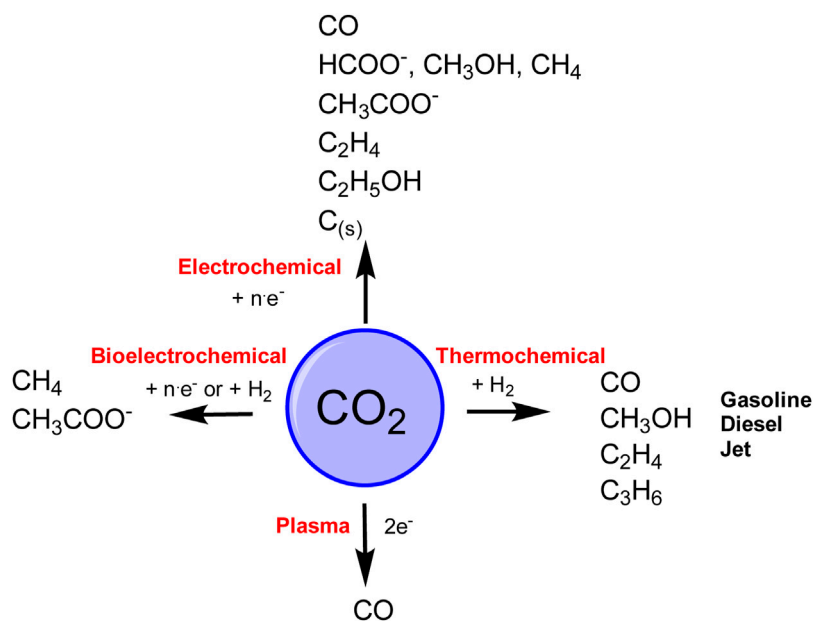
FIGURE 2 | Electrochemical-, bioelectrochemical-, thermochemical- and Plasma reduction of CO$_2$ (e$^-$—direct pathway, H$_2$—indirect pathway).
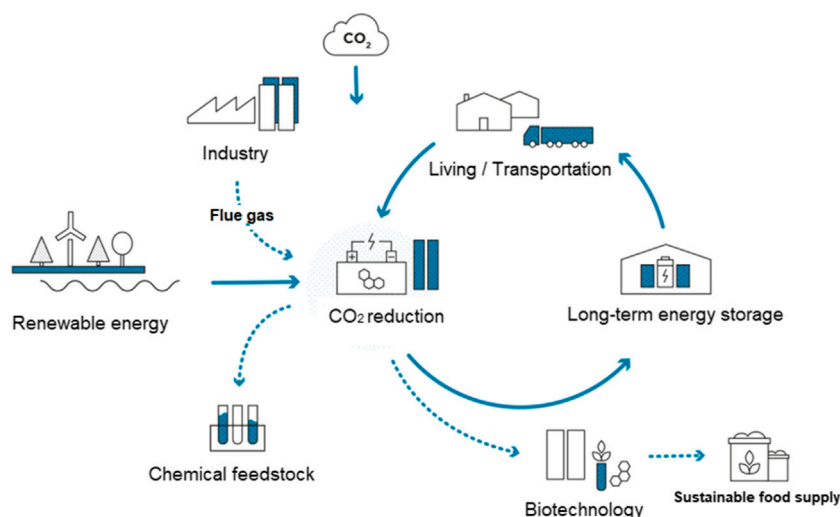

FIGURE 3 | CO$_2$ Utilization—a sustainable and climate-friendly cycle.

gases such as CO$_2$. The increase of CO$_2$ in our atmosphere results in global warming and climate change (Aresta et al., 2013; Qiao et al., 2014; Álvarez et al., 2017). In 2018, the combustion of fossil fules led to an increase of the CO$_2$-level in the atmosphere of 33.1 GT. In the same year, the emission was further increased by 1.7% (IEA, 2019). Ideally, the excess of CO$_2$ produced by mankind should be converted in re-usable chemicals to close the circle and provide environmental stability (Qiao et al., 2014).

With the growing importance of capturing and managing man-made CO$_2$, different technologies have been evaluated.

While one approach envisages the capture of CO$_2$ with subsequently sequester it geologically, another approach explores the conversion of CO$_2$ *via* chemical methods, such as photo—and electrocatalytical protocols, using homogeneous or heterogeneous catalysts (Aresta et al., 2013; Khezri et al., 2017). The latter approach would allow the production of low-carbon fuels and other important synthons for industrial processes, such as carbon monoxide (CO), formic acid (HCOOH), acetic acid (CH$_3$COOH), methane (CH$_4$), ethylene (C$_2$H$_2$), oxalate (C$_2$O$_4^{2-}$), formaldehyde (HCOH), and methanol (CH$_3$OH) or ethanol (CH$_3$CH$_2$OH).
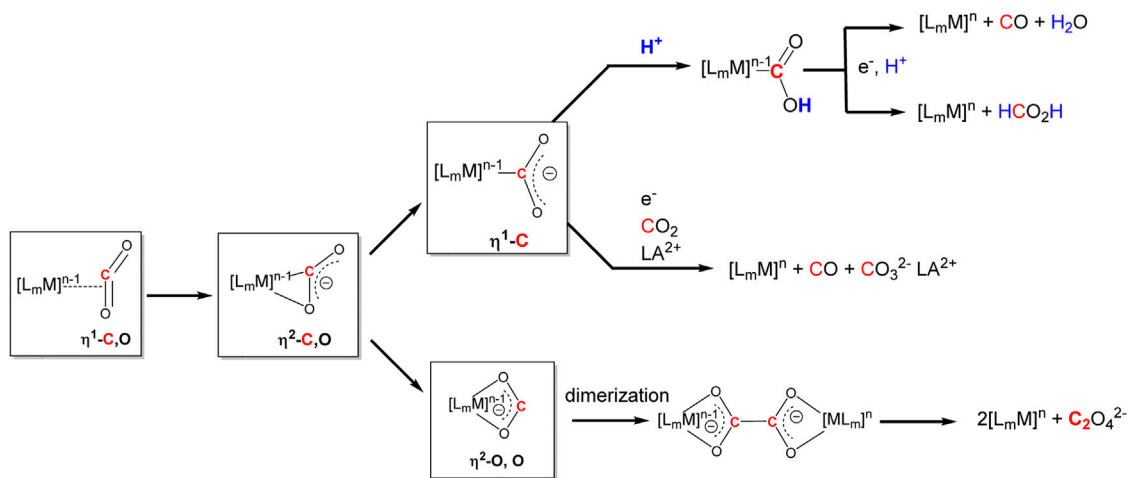
SCHEME 1 | Modification possibilities for CO_2 activation *via* transition metals. Redrawn from (Grice, 2017; Paparo and Okuda, 2017; Kinzel et al., 2021).

In the last years, the electrochemical CO_2 reduction has attracted great attention and many research groups entered the quest for a sustainable economic and ecological solution of this ever-growing problem. The process of CO_2 reduction is interesting as the process is easily controllable *via* temperature and electrode potentials. Supporting electrolytes can be fully recycled, electricity for the processes can be obtained from renewable sources, such as geothermal, solar or wind. Furthermore, the electrochemical units required for the conversion of CO_2 to value-added products are compact and do not require much space (Qiao et al., 2014; Khezri et al., 2017). Although, these points sound very positive, some challenges remain. Major points are high-overpotentials, due to slow reaction kinetics, stability of catalysts and low product selectivity. As a result, one of the biggest challenges is consequently the development of new stable and selective electrocatalysts (Enthaler et al., 2010; Kondratenko et al., 2013; Qiao et al., 2014; Khezri et al., 2017).

Reactivity and Activation of Carbon Dioxide

CO_2 shows a high thermodynamic stability ($\Delta G = -393.5$ kJ mol^{-1}) (Álvarez et al., 2017). Thus, the compounds must be activated *via* homogenous or heterogeneous catalysis before a transformation can take place at ambient temperature. In the case of electrocatalysis, this activation proceeds *via* surface-catalyzed electro-activation (Álvarez et al., 2017). Transformations of CO_2 can be initiated *via* electrophilic activation of the oxygen or nucleophilic activation of the carbon atom. Furthermore, direct coordination to the carbon atom to the metal is also possible (**Scheme 1**). Moreover, CO_2 can be simultaneously activated by two metal atoms, which allows for the design of highly sophisticated metal complexes as efficient and selective catalysts. (Grice, 2017; Paparo and Okuda, 2017; Kinzel et al., 2021).

The electrodes and more importantly, electrocatalysts, play an important role in the product formation and product distribution. Typically, the electrocatalyst is absorbed at the

TABLE 1 | Selected CO_2 reduction processes and the corresponding standard redox potentials E^0 for aqueous solutions (Francke et al., 2018).

Half-electrochemical thermodynamic reactions	E^0 vs RHE/V
$2H^+ + 2e^- \rightarrow H_2$ (g)	0.00
CO_2 (g) + e$^-$ → $CO_2^{\cdot-}$	−1,90
CO_2 (g) + 2H$^+$ + 2e$^-$ → HCOOH (l)	−0.25
CO_2 (g) + H$_2$O (l) + 2e$^-$ → HCOO$^-$ (aq) + OH$^-$	−1.08
CO_2 (g) + 2H$^+$ + 2e$^-$ → CO (g) + H$_2$O (l)	−0.11
CO_2 (g) + H$_2$O (l) + 2e$^-$ → CO (g) + 2OH$^-$	−0.93
CO_2 (g) + 4H$^+$ + 4e$^-$ → HCHO (l) + H$_2$O (l)	−0.07
CO_2 (g) + 3H$_2$O (l) + 4e$^-$ → HCHO (l) + 4OH$^-$	−0.90
CO_2 (g) + 6H$^+$ + 6e$^-$ → CH$_3$OH (l) + H$_2$O (l)	+0.02
CO_2 (g) + 5H$_2$O (l) + 6e$^-$ → CH$_3$OH (l) + 6OH$^-$	−0.81
CO_2 (g) + 8H$^+$ + 8e$^-$ → CH$_4$ (l) + 2H$_2$O (l)	+0.17
CO_2 (g) + 6H$_2$O (l) + 8e$^-$ → CH$_4$ (g) + 8OH$^-$	−0.66
$2CO_2$ (g) + 2H$^+$ + 2e$^-$ → H$_2$C$_2$O$_4$ (aq)	−0.50
$2CO_2$ (g) + 2e$^-$ → C$_2$O$_4^{2-}$ (aq)	−0.59
$2CO_2$ (g) + 12H$^+$ +12e$^-$ → C$_2$H$_4$ (g) + 4H$_2$O (l)	+0.06
$2CO_2$ (g) + 12H$^+$ +12e$^-$ → CH$_3$CH$_2$OH (l) + 3H$_2$O (l)	+0.08

cathode and interacts with CO_2 during the electrochemical reduction. Charge transfer proceeds through the interface of the electrode where the catalyst is absorbed, and CO_2, followed by desorption of the reduced products.

Typically, the reduction commences with the formation of a radical anion (CO_2^-). This initial step requires a substantial amount of energy ($E^0 = 1.90$ V vs NHE, pH 7), as the linear molecule is converted to a bent radical anion. While this initial step is kinetically problematic, subsequent steps are typically energetically favored, driving the reaction to completion. Thermodynamic potentials of common reactions and reaction products are listed in **Table 1**. Generally, the overall reaction consists of a series of individual steps, including electron and proton transfer reactions (Benson et al., 2009; Zhang et al., 2017a; Khezri et al., 2017; Álvarez et al., 2017).

Commonly, electrocatalysts are electron transfer agents, which are operating, in an ideal case, near the thermodynamic potential

of the desired reaction. However, in most cases the transformation of CO$_2$ proceeds at much higher negative potentials compared to the theoretical ones, and this results in the so-called overpotential. This additionally energy depends on the electrode, the electrolyte, the CO$_2$-concentration, the pH value as well as the temperature and the pressure (Benson et al., 2009; Álvarez et al., 2017). This overpotential can be affected by chemical fine-tuning of the ligands of the macrocycle. Moreover, in the presence of an aqueous electrolyte, CO$_2$ reduction becomes more challenging due to the competing hydrogen evolution reaction (HER), the low solubility and reactivity of CO$_2$ in water, which impedes the transformation. As a consequence, the development of catalysts for electrocatalytic CO$_2$ reduction in aqueous environment remains a big challenge. Further research is required to find methods to selectively suppress the formation of hydrogen while simultaneously favoring the reduction of CO$_2$ (Khezri et al., 2017; Gonglach et al., 2019).

Obstacles and Possible Solutions in the Electrochemical CO$_2$ Reduction Reaction

The high electrochemical potential required for the reduction of CO$_2$ ($E^0_{CO_2/CO_2} = -1.98$ V vs NHE in DMF), triggers a variety of other problems which potentially reduce the overall efficiency of the process. When oxygen is present during the electrochemical reaction, highly reactive intermediates, such as O$_2^-$ or H$_2$O$_2$ can be formed. These side products are capable of damaging the electrode material or the electrocatalyst by oxidizing or degrading ligands. Therefore, it is important to employ catalysts which are "immune" to oxygen reduction reaction (ORR). Three different approaches have been described in the recent years. One possibility is to introduce a co-catalyst, which quenches any partially reduced oxygen species before damage can occur. Alternatively, a catalyst should be used that reduces oxygen to water. The last method is to use a catalyst which is highly selective towards CO$_2$ so that the reduction can take place in presence of O$_2$ (Mondal et al., 2019).

METAL MACROCYCLES FOR CO$_2$ ELECTROREDUCTION

The most investigated electrocatalysts suitable to mediate the reductive transformation of CO$_2$ are without doubt transition metals and their corresponding metal complexes, respectively. The great potential of these metals can be attributed to their vacant orbitals and active d-electrons, where it is postulated that they favor the formation of an adduct between CO$_2$ and the metal and promote afterwards the desorption of reduced products. The metal-type and ligand-structure play an extensive role in their catalytic behavior (Qiao et al., 2014; Kinzel et al., 2021). Generally, molecular catalysts are often less durable compared to solid-materials, since the main reduction product is CO and examples for more than two-electron reduced compounds are rare. Enormous effort was devoted to the preparation of efficient catalysts utilizing earth

abundant elements, which address transition metal complexes with the most prominent metals, Fe, Cu, Co, Mn, and Ni (Takeda et al., 2017). Within the past decades, Co or Fe-macrocycles were of great interest for many research groups (**Figure 3**, compounds **1–11**). Already in the early 1970's Meshitsuka and co-worker found that Co- and Ni-phthalocyanines electrocatalyze CO$_2$ reduction (Meshitsuka et al., 1974; Wang, 2017). Furthermore, in the 1980's, the research groups of Eisenberg and Sauvage presented the electrochemical reduction of CO$_2$ to CO *via* Co– and Ni-tetraazacomplexes with high selectivity (Sauvage: FE 96%, −0.86 V vs SCE) (Fisher and Eisenberg, 1980; Collin et al., 1988; Collin and Sauvage, 1989; Benson et al., 2009; Wang, 2017). In 1998, Savéant investigated, the Fe(0)porphyrins mediated transformation of CO$_2$ to CO in the presence of weak Brønsted acids, such as 1-propanol, 2-pyrrolidine or trifluoromethanol to facilitate the cleavage of one of the C-O bonds in CO$_2$. Hydrogen formation could be suppressed, efficiency and lifetime enhanced. Problematic was the use of a mercury working electrode and the quite negative operating potential (−1.5 V vs SCE, DMF) (Bhugun et al., 1996a). Of course, catalytic abilities of diverse other complexes, for instance, with bipyridine or phosphine as ligands were studied which are omitted as this section emphasizes on the application of tetrapyrroles.

The publication of Grodkowski in 2002 has been the only report on CO$_2$ reduction with Co– and Fe-corroles for a long time. Stable metal corroles, PPh$_3$-Co(III)-TpFPC, Cl-Fe(IV)-TpFPC, Cl-Fe(IV)-TdCC [5,10,15-tris-(2,6-dichlorophenyl) corrole] were studied *via* chemical, electrochemical, and photochemical methods, whereas Co(I) as well as Fe(I) were identified as catalytically active species. As result, the latter Fe-macrocycle showed the highest CO$_2$ reduction ability in acetonitrile to form CO. Compared to porphyrins, which can only react with metals with an oxidation state of zero, corroles are able to mediate transformation of CO$_2$ with metals with an oxidation state of +I (Grodkowski et al., 2002).

More often, various examples of porphyrins are found as electrocatalysts in the literature. Robert et al. described Fe-porphyrins to be most efficient in aprotic solvents (DMF, ACN), in respect to their catalytic rate, their selectivity and robustness to yield CO. Additionally, Brønsted and Lewis acids improve catalysis as already found by Savéant. By introduction of positively charged trimethylanilinium moieties into tetraarylporphyrins, CO$_2$ to CO conversion is promoted via through-space substituent effects, resulted in a turnover frequency (TOF) of 10^6 s^{-1} with a low overpotential of 0.220 V and a selectivity of 100% (CO) and stability over 84 h long-term electrolysis (Azcarate et al., 2016a; Takeda et al., 2017).

CO$_2$ Reduction With Metal Porphyrin Complexes

Iron porphyrins, illustrated in **Figure 4**, were first described in photocatalytic systems for CO$_2$ reduction by Neta et al. in 1997
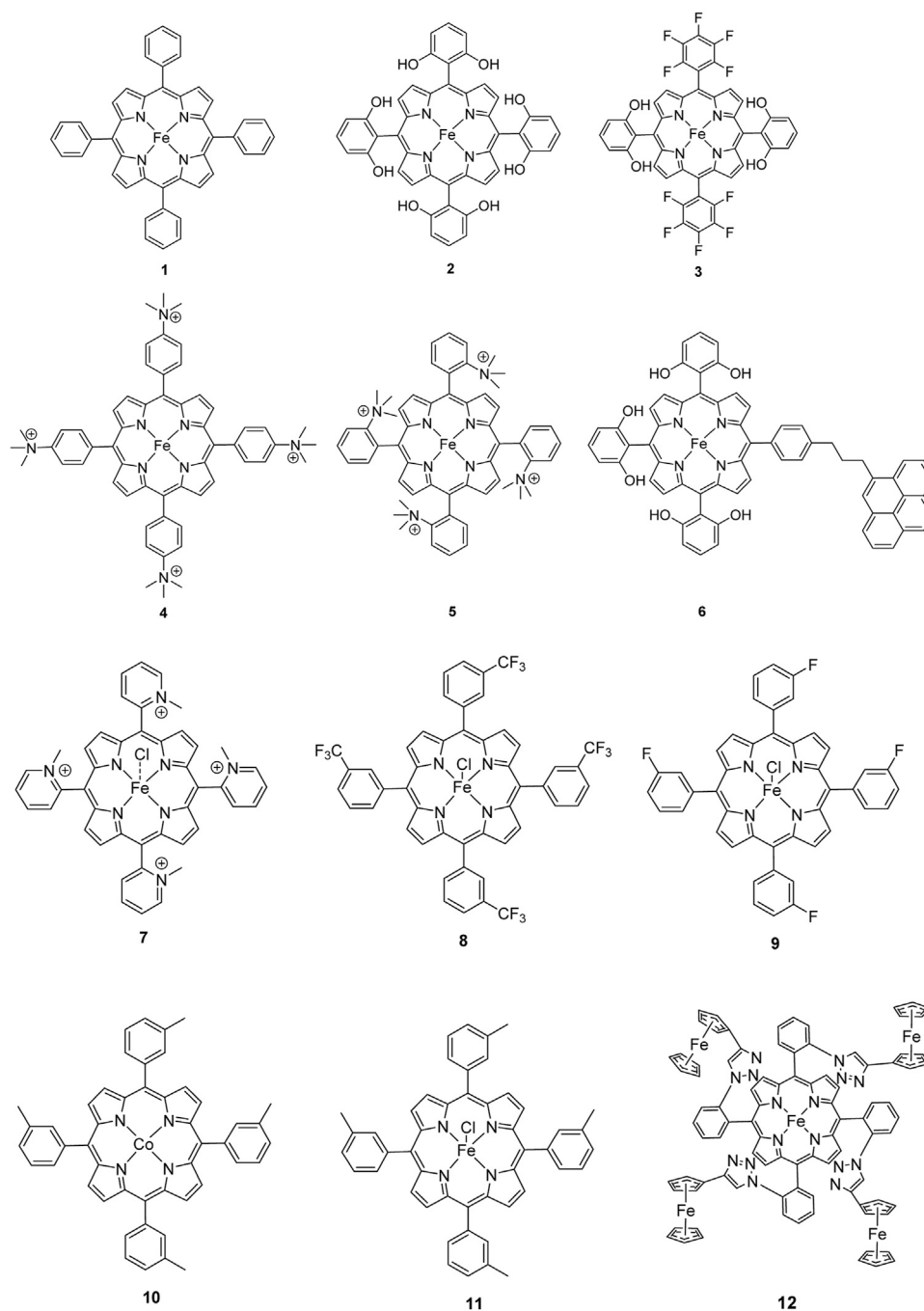
FIGURE 4 | Examples of Fe– and Co-Porphyrin complexes for CO_2 reduction to CO (Mondal et al., 2019).

(Grodkowski et al., 1997). Photoexcitation of the ligand-to-metal charge transfer (LMCT) absorption band at 360 nm of a DMF/TEA (5%) solution containing compound **1** with an axial chloride ligand caused a one-electron reduction of the central metal from Fe^{III} to Fe^{II}, simultaneously releasing the chloride ligand. The Fe^{II} species could be further reduced to Fe^{I} by triethylamine (TEA). Disproportionation of two Fe^{I} molecules produces the catalytically active Fe^0 species, which coordinates to CO_2. The product of the CO_2 reduction was CO with a turn-over-number of the reaction of $TON_{CO} \sim 70$, and H_2 was formed as a minor product. During the catalytic process, photo-Birch reduction of the porphyrin ring occured, converting it to the corresponding chlorin structure, followed by further photochemical decomposition.

The cationic Fe porphyrin **7** has also been reported to function as a photocatalyst, generating CO from CO$_2$ by photoexcitation in an aqueous solution (pH 8.8) containing TEA as sacrificial electron-donor (SD) and NaHCO$_3$. Because the efficiencies of the photochemical reduction of the Fe porphyrins were very low, the CO$_2$ photoreduction proceeds with extremely low efficiencies. Addition of *p*-terphenyl as a photosensitizer (PS) to photocatalytic systems using Fe porphyrins (FeP), was investigated in order to overcome the above mentioned problems (Dhanasekaran et al., 1999). The standard reduction potential of PS-OERS of the PS was negative enough (−2.45 V vs SCE in dimethylamine) to reduce the Fe^{II}P species −1.05 V vs SCE for **1**, −1.02 V vs SCE for **8**, and −1.00 V vs SCE for **9** and Fe^{I}P (−1.66 V vs SCE for **1**, −1.61 V vs SCE for **8**, and −1.55 V vs SCE for **9**) so as to form the corresponding Fe^{0}P species. This system exhibited 10 times higher photocatalytic efficiencies than those measured in the absence of the PS. The Co porphyrin **10** can also be used to produce CO, and its photocatalytic efficiency was about 1.5 times higher compared to that of the corresponding Fe porphyrin (**11**, **Table 2**; Dhanasekaran et al., 1999).

A promising candidate for this particular reduction is the FeFc$_4$-porphyrin complex **12**, which has four ferrocene moieties attached and a bromide as an axial ligand (**Figure 4**). This particular catalyst has the ability to catalyze the reduction of O$_2$ to H$_2$O when the oxidation state is Fe(II) (4H$^+$/4e$^-$) and reduce CO$_2$ to CO (2H$^+$/2e$^-$) in the presence of Fe (0). During ORR three of four ferrocenes are oxidized together with the Fe(II) center, therefore providing the four electrons to conduct the ORR (Mondal et al., 2019). In this experiment, phenol served as proton source. The two forms, Fe(II) in presence of Fe(0), are obtained by choosing two different onset-potentials to achieve the desired catalyzed reaction. Those onset-points are determined through cyclic voltammetry and the cyclic voltametric responses. In case of the FeFc$_4$-porphyrin complex the needed potentials are 0.0 V to −0.67 V for the ORR and −2.50 V for CO$_2$RR. Overall, the CO$_2$ reduction to CO happens with a Faradaic efficiency of >92%.

The selectivity of this porphyrin complex is confirmed by inducing the CO$_2$ reduction in the presence of O$_2$ and maintaining the catalytic current for the CO$_2$RR at −2.50 V even when the pressure of O$_2$ is increased. Bulk electrolysis with 20% O$_2$ shows that only 5–6% partially reduced oxygen species are found, produced by this porphyrin-complex when the oxidation state is Fe(II). However, the oxidation of the Fe(0) porphyrin-complex by O$_2$ happens rather unlikely, given that the Faradaic yield for the CO$_2$RR is 43% when a 1:3 mixture of CO$_2$:O$_2$ is induced. The selectivity of the Fe (0) porphyrin-complex for CO$_2$RR over ORR can be argued in different ways. Thermodynamically speaking, the formation of Fe(II)-O$_2^{2-}$ is favored over Fe(II)-CO$_2^{2-}$ with a difference in absolute free energy of around 22.68 kcal/mol, showing that thermodynamics are not the reason for the preference. On the other hand, reaction of the complex with both gases separately shows in absorption spectroscopy that the specific Soret-band for porphyrins shifts immediately after inducing

CO$_2$ while the reaction with O$_2$ shows little to no change. Hence, the kinetic barrier for the reaction with CO$_2$ is lower, making the CO$_2$RR 500 times faster when pseudo first-order kinetics is assumed. Involving the different solubilities of the gases in acetonitrile (CO$_2$ = 0.28 M and O$_2$ = 0.01 M), one can determine that the rate constants for the first- and second-order are one magnitude higher for CO$_2$ reduction (Mondal et al., 2019).

CO$_2$ Reduction Reaction With Metal Phthalocyanine Complexes

As mentioned in previous sections, a suitable catalyst for the CO$_2$RR should be selective to CO$_2$ or in other words be "immune" against the hydrogen evolution reaction HER, should have a high chemical and thermal stability and be inexpensive in production. Therefore, catalysts such as porphyrins or phthalocyanines using non-noble metals and having all the above-mentioned properties are the center of investigations. (Zhang et al., 2017a) In one described case, De Riccardis et al. investigated a phthalocyanine complex metalated with Co and with pyridine as a peripheral substituent (**Figure 5**). The second electrochemical reduction of this complex Co(II)Pc-Pyr happens at −0.4 V vs. Ag/AgCl, resulting in a catalytically active [Co(I)Pc-Pyr$^-$]$^{-2}$ species. The Faradaic efficiency for CO reaches a total of 95% at this specific onset-potential. Such a high FE is achieved through the inductive effect of the pyridine moieties, which supports the CO$_2$ adsorption and increases the electron affinities of the metal center. In comparison to the non-substituted CoPc complex that only has 80% FE at −0.6 V vs RHE for the conversion of CO$_2$ to CO and polycrystalline Ag requiring at least −0.7 V to conduct the same reduction, the CoPc-Pyr shows to be a promising candidate for CO$_2$RR. Additionally, at an onset-potential of—0.7 V vs RHE, the turnover frequency of this phthalocyanine complex is around 6.9 s^{-1} when 10^{-8} mol are present (Riccardis et al., 2020).

Other examples of Mn-based molecular catalysts capable of formate formation during electrochemical CO$_2$ reduction are the systems reported by Mahmood et al. The Mn–phthalocyanines synthesized by this research group exhibited an FE of 26% at −2.00 V vs. saturated calomel electrode (SCE) after attachment to a PTFE-bonded carbon gas diffusion electrode. Hydrogen generation (FE = 77%) exceeded the formation of formic acid, but no further mechanistic investigations were pursued (Mahmood et al., 1987).

CO$_2$ Reduction Reaction With Metal Corrole Complexes

Metal corroles are structural similar to metal porphyrins with both the metal centers and ligands participating in multielectron redox processes and are promising candidates for efficient proton-coupled electron transfer (Zhang et al., 2017b; Hu et al., 2017; Shen et al., 2015). These metal complexes stabilize radical intermediates thus providing an effective pathway to facilitate C–C step-up. (Behar et al., 1998; Kortlever et al., 2015) Cobalt and iron corroles have been previously found to

TABLE 2 | Comparison of catalyst systems, major products, maximum FEs, and mechanisms of macrocyclic complexes in electrochemical CO_2 reduction (n.a., not available; prop., proposal; comp., computational investigation; exp., experimental evidence).
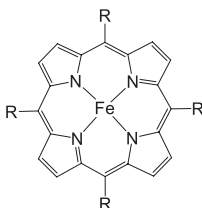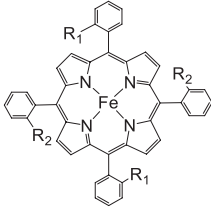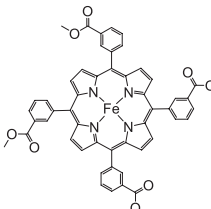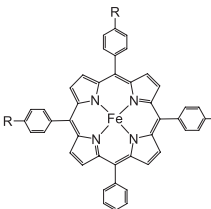
Entry	Catalyst systems	Substitution(s)	Major product	Max.FE (%)	Mechanism	Basis	Method	References
Porphyrins								
1		R = Ph, C_6F_5, pyren-1-yl, meso-thien-2-yl, meso-5-methylthien-2-yl	CO/H_2O HCO_2^-	100 72	ET_M	Comp.	DFT	Hammouche et al. (1988), Hammouche et al. (1991), Bhugun et al. (1994), Bhugun et al., (1996a), Bhugun et al. (1996b), Costentin et al. (2013), Costentin et al. (2015), Azcarate et al. (2016a), Ambre et al. (2016), Azcarate et al. (2016b), Choi et al. (2016), Okabe et al. (2017), and Margarit et al. (2020a)
2		$R_1 = R_2 = CO_2Me$, NHCOtBu, $NHCOC_6H_4CH_2MeIm^+$, NMe_3^+, trFc₂, trCO₂Me, tr-4-tBu $R_1\backslash R_1/R_2\backslash R_2 = NHCO$-$(CH_2)_{10}CONH$, NHCO-$(CH_2)_{10}ImCONH$	CO/H_2O	100	ET_M	Comp. Ambre et al. (2016), and Sen et al. (2019)	DFT	Hammouche et al. (1988); Hammouche et al. (1991), Azcarate et al. (2016a), Ambre et al. (2016), Khadhraoui et al. (2018), Mondal et al. (2019), and Sen et al. (2019)
3		-	CO/H_2O	65	ET_M	Comp.	DFT	Ambre et al. (2016)
4		R = Ph, pyren-1-yl, CO_2Me, NMe_3^+, SO_3^-	CO/H_2O H_2	100 (66) 84 (67)	ET_M	Comp.	DFT	Costentin et al. (2015), Azcarate et al. (2016a), Ambre et al. (2016), Tatin et al. (2016), Okabe et al. (2017), and Torbensen et al. (2020)
5		$R_1 = CH_2CONHC_6H_3$-$(CF_3)_2$, $NHCOCH_2C_6H_3$-$(CF_3)_2$, NHCONH-Fe-TPP, OMe R_2 = -H, -NH_2, -OMe Y= CH, N	CO/H_2O CH_4	90 (79) 41 (80)	ET_M	Comp.	DFT	Nichols et al., (2018), Abdinejad et al. (2019), Abdinejad et al., (2020a), and Abdinejad et al. (2020b)
6		R = -OH, -OMe	CO/H_2O	94 (83)	ET_M	Prop.	n.a.	

TABLE 2 | (*Continued*) Comparison of catalyst systems, major products, maximum FEs, and mechanisms of macrocyclic complexes in electrochemical CO₂ reduction (n.a., not available; prop., proposal; comp., computational investigation; exp., experimental evidence).
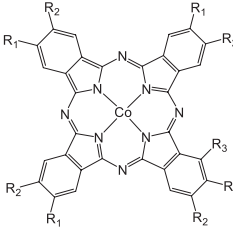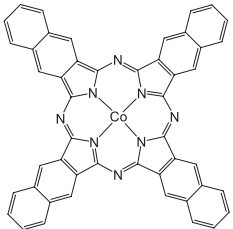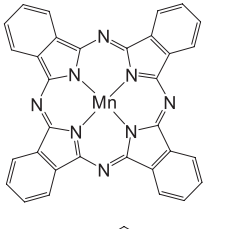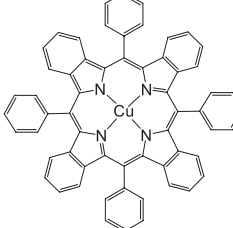
Entry	Catalyst systems	Substitution(s)	Major product	Max.FE (%)	Mechanism	Basis	Method	References
								Costentin et al. (2012), Costentin et al. (2015), and Azcarate et al. (2016b)
7		R = -propylpyrene	CO/H₂O	97	n.a.	n.a.	n.a.	Maurin and Robert (2016)
8		R = -CH₂CONHC₆H₃-(CF₃)₂, NHCOCH₂C₆H₃(CF₃)₂, -OH	CO/H₂O	96 (85)	ET$_M$	Comp.	DFT	Nichols et al. (2018) and Sinha and Warren (2018)
9		R₁ = 3,4,5-trimethoxyphenyl R₂ = CNHNH₂, -C₆H₄OH, -C₆H₄SO₃H	CO/H₂O	96	ET$_M$	Comp.	DFT	Margarit et al. (2019)
10		R₁ = 3,4,5-trimethoxyphenyl R₂ = 3,4,5-trimethoxyphenyl	CO/H₂O	100	ET$_M$	Prop.	n.a.	Margarit et al. (2020b)
11		R = Ph, Me₃C₆H₂, C₆F₅, 2,6-Cl₂C₆H₃, 2,6-F₂C₆H₃	CO/H₂O	92 (88)	ET$_M$	Prop. Zahran et al., (2016)	n.a.	Mohamed et al. (2015) and Zahran et al. (2016)
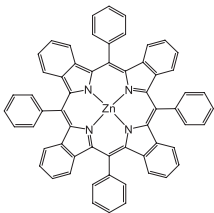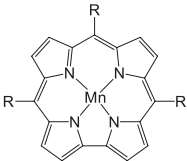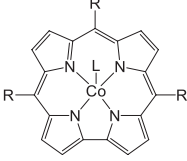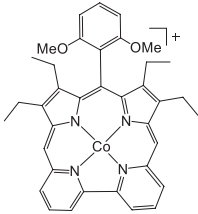
(Continued on following page)

TABLE 2 | (*Continued*) Comparison of catalyst systems, major products, maximum FEs, and mechanisms of macrocyclic complexes in electrochemical CO_2 reduction (n.a., not available; prop., proposal; comp., computational investigation; exp., experimental evidence).

Entry	Catalyst systems	Substitution(s)	Major product	Max.FE (%)	Mechanism	Basis	Method	References
12		Ar=Ph, $C_6H_4CF_3$, $C_6H_4NH_2$, $C_6H_4NMe_3^+$, $C_6H_3(OH)_2$, C_6H_4OMe, $C_6H_3(OMe)_2$, C_6H_4Cl, C_6H_4Br, C_6H_4F, C_6F_5 $n = 0, 1$ $X = $ -Cl	CO/H_2O	97 (90)	ET_M	Prop. Hu et al., (2017)	n.a.	Behar et al. (1998), Lin et al. (2015), Alenezi (2016), Hu et al. (2017), Zhu et al., (2019), Hu et al. (2020), and Jack et al. (2020)
13		-	CO/H_2O	89	ET_M	Prop.	n.a.	Aoi et al. (2015)

Phthalocyanines

14		R_1 = H, *t*Bu, OC_8H_{17}, O-py	CO/H_2O	100 (60)	ET_M	Exp.	PSCAS	Mahmood et al. (1987), Abe et al. (1996), Han et al. (2017), Zhang et al. (2018), Wang (2019b), Choi et al. (2019), Liu and McCrory (2019); Ren et al. (2019), Boutin et al. (2020), Hu et al. (2020), and Riccardis et al. (2020)
		R_2 = H, *t*Bu, OC_8H_{17}, O-py	H_2	72 (60)		Comp.	DFT	
		R_3 = H, NMe_3^+	MeOH	MeOH(20)				
15		-	CO	97	n.a.	n.a.	n.a.	Wang et al. (2019a)
16		-	$HCOO^-$ H_2	26 77	n.a.	na.	na.	Mahmood et al. (1987)
17		-	CO	48	n.a.	n.a.	n.a.	Apaydin et al. (2018)

TABLE 2 | (*Continued*) Comparison of catalyst systems, major products, maximum FEs, and mechanisms of macrocyclic complexes in electrochemical CO$_2$ reduction (n.a., not available; prop., proposal; comp., computational investigation; exp., experimental evidence).

Entry	Catalyst systems	Substitution(s)	Major product	Max.FE (%)	Mechanism	Basis	Method	References
18		-	CO	33	n.a.	n.a.	n.a.	Apaydin et al. (2018)
Corroles								
19		R = -C$_6$F$_4$-S-(PEG7)-OCH$_3$	CH$_3$OH	23	ETM	Exp.	EAS, [b] GCMS, IL, IR-, UV/Vis-SEC, NMR DFT	De et al. (2020)
			CH$_3$CO$_2^-$ $_-$	63		comp.		
20		L = -PPh$_3$ R = -C$_6$F$_5$-S-(PEG7)-OCH$_3$	HCO$_2^-$ CH$_3$OH	12 59				Gonglach et al. (2019)
			HCOH CH$_3$CH$_2$OH CH$_3$CO$_2^-$ H$_2$	10 48 13 36				
21		-	CO/H$_2$O	77	n.a.	n.a.	n.a.	Ogawa et al. (2019)
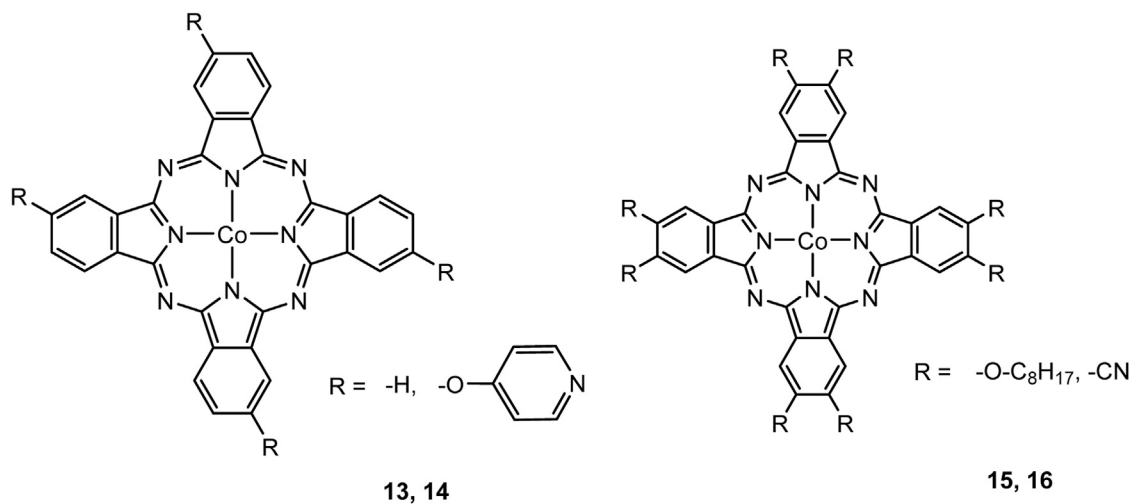
FIGURE 5 | Co– and Fe phthalocyanine complexes for CO$_2$RR (Zhang et al., 2017b).
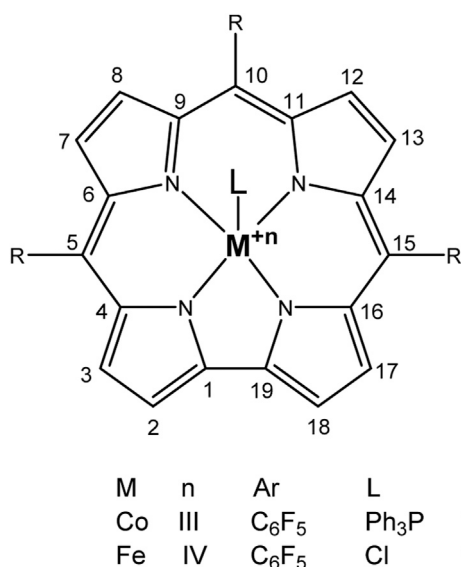
FIGURE 6 | Co and Fe corroles for the homogeneous CO_2 reduction to CO and H_2 in MeCN solutions.
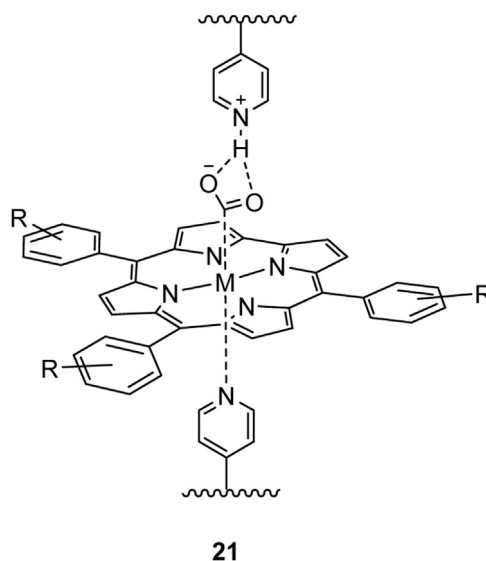
FIGURE 8 | Immobilization of CoPc catalysts on P4VP (Kramer and McCrory, 2016).
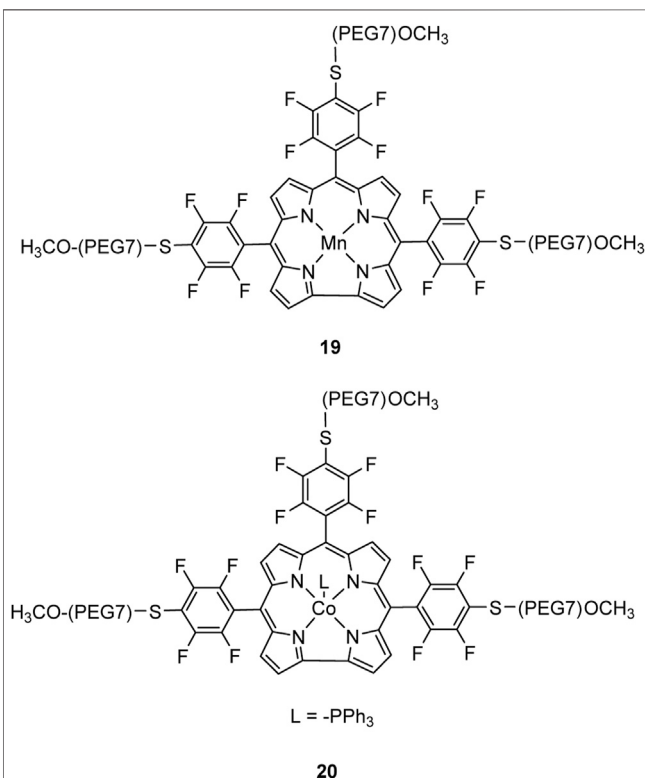
FIGURE 7 | Co– and Mn-corrole complexes reported by Roy and Schöfberger et al. (Gonglach et al., 2019).

electrode, as an example of a manganese catalyst capable of producing MeOH (FE = 23%) and acetate (FE = 63%). (De et al., 2020) Although a detailed mechanistic investigation has not yet been performed, the authors propose an ETM pathway with a possible Mn(III) carboxyhydroxyl intermediate towards methanol formation and an oxalate type key species for acetate production. As another example for immobilized Co macrocycles in electrochemical CO_2 reduction, the polyethylene glycol derivatized Co–corrole (**Figure 7**) reported by Gonglach et al. showed remarkable catalytic activity when used on carbon paper electrodes (Gonglach et al., 2019). More specifically, it produces ethanol and methanol in a Faradaic efficiency of 47 and 59%, respectively, at −0.73 V vs. reverse hydrogen electrode. Employment of GC-MS (in combination with [2]D- and ^{13}C-labeling), NMR, EPR, IR-SEC, and complementary control experiments resulted in the proposed mechanism(s).

ORGANIC INORGANIC/POLYMER HYBRID MATERIALS FOR CO_2 REDUCTION

Organic–inorganic hybrid materials, which are usually defined as multicomponent compounds containing organic (biological) and inorganic components in the sub-micrometric and nanometric scale can be used to integrate excellent properties, such as selectivity (Sanchez et al., 2005). In general, the organic and inorganic components can be linked by noncovalent bonds (such as van der Waals, hydrogen bonds, or electrostatic bonds) and/or covalent bonds in hybrid systems. This kind of materials not only effectively combine the advantages of organic materials (variety, flexibility, etc.) and inorganic materials (large surface area, conductivity, etc.) (Judeinstein and Sanchez,

be catalytically active for CO_2 reduction to CO (**Figure 6**; Grodkowski et al., 2002).

Our group recently reported a polyethylene glycol (PEG)-modified Mn–corrole complex immobilized on a carbon paper
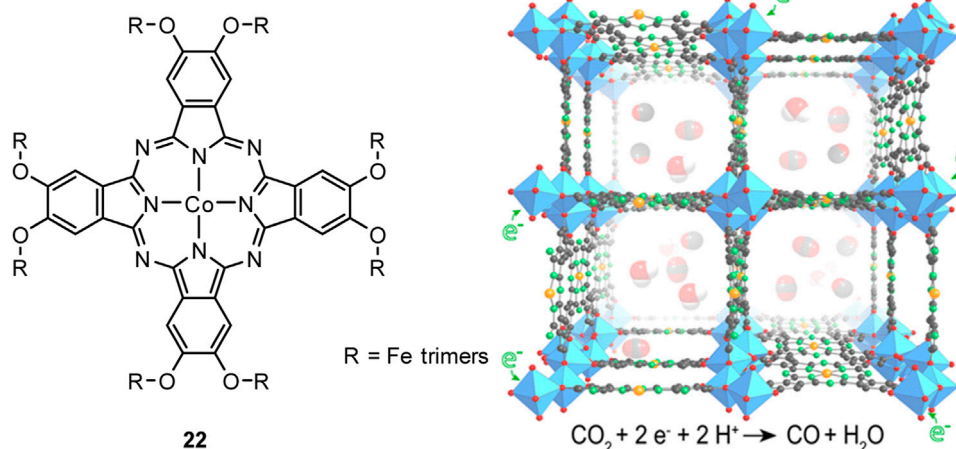
FIGURE 9 | CoPc with Fe$_3$ (-C$_2$O$_2$-)$_6$(OH$_2$)$_2$ trimers **22** forming a 3D metal-catecholate framework. [Reprinted with permission from Matheu et al. (2019)].

1996; Faustini et al., 2018; Zhang et al., 2019; Rebber et al., 2020; Yang et al., 2020), but also improve the physicochemical properties, such as the increased CO$_2$ adsorption and conductivity, enriched types of active sites, maximized exposure of active sites, and manipulated reaction pathways by tuning the stability of intermediates, thereby synergistically reducing the overpotential and promoting product selectivity (Nam et al., 2020; Sun et al., 2020). As an example, Kramer et al. grafted a cobalt metalated phthalocyanine complex onto a pyridine-substituted polymer that resulted in an increase of selectivity towards CO due to an axial coordination between carbon monoxide and the metal center (Kramer and McCrory, 2016). Immobilization of cobalt phthalocyanine in poly-4-vinylpyridine dramatically improves its activity as a catalyst for the reduction of CO$_2$ to CO (**Figure 8**). The polymer membrane slows the competing HER catalytic pathway while also increasing rate of CO$_2$RR compared to the polymer free catalyst.

Liang, Wang and co-workers showed that immobilizing the catalyst onto carbon nanotubes decreases the measured overpotential (Jiang et al., 2019). The group prepared a series of metal (Co, Fe, Mn) phthalocyanine/carbon nanotube hybrids and study their catalytic performance for CO$_2$ electroreduction. Both CoPc/CNT and FePc/CNT are active catalysts to reduce CO$_2$ to CO and are able to deliver a reduction current density of −1.0 mA/cm^2 above −0.47 V. FePc/CNT is just slightly less active than CoPc/CNT, but superior to CoPc/CNT with higher FEs for CO at low overpotentials. Manthiram and coworkers suggest that loading catalysts onto electrodes could have a positive impact on the TOF.

Another observation of Chio et al. showed that alkoxy substituents on a cobalt phthalocyanine suppress the aggregation of the complex on graphene sheets *via* π-π stacking and enhance the catalytic activity per single CoPc-A molecule, resulting in FE of 75% at an overpotential of 480 mV. (Choi et al., 2019) An attractive class of solids for the CO$_2$RR are metal-organic frameworks (MOFs), which can be used to build porous extended structures. Matheu et al. have shown that the active sites on Co are sterically accessible when applied on a 3D metal-catecholate framework/carbon black cathode materials. The 3D metal-catecholate framework was synthesized by linking tetratopic cobalt phthaloocyanin-2, 3, 9, 10, 16, 17, 23, 24-octanol linkers with Fe$_3$ (-C$_2$O$_2$-)$_6$(OH$_2$)$_2$ trimers. (Matheu et al., 2019) These cathodes based on MOF-1992 and carbon black (CB) display a high coverage of electroactive sites (270 nmol cm^{-2}) and a high current density (−16.5 mA cm^{-2}; overpotential, −0.52 V) for the CO$_2$ to CO reduction reaction in water (faradaic efficiency, 80%). Over the 6 h experiment, MOF-1992/CB cathodes reach turnover numbers of 5,800 with turnover frequencies of 0.20 s^{-1} per active site (**Figure 9**).

CONCLUSION

In this mini-review, we have discussed mechanistic details of various porphyrinoid based catalyst systems during the (photo-)-electroelectrochemical CO$_2$ reduction reaction. We have compared the electrocatalytic performance and product distribution of a variety of iron, manganese and cobalt porphyrin, corrole, and phthalocyanine complexes. The reduction efficiency of carbon dioxide by different metal porphyrinoid systems based materials can be extracted from **Table 1**. One of the future research directions will focus on how to regulate and modify the structure of porphyrinoids. In addition to the efficient reduction of carbon dioxide, it is necessary to consider whether the reduction products can be efficiently further employed. Next to this, one has to consider if the catalyst materials can be synthesized environmentaly friendly.

Advances in experimental techniques have revealed a wealth of mechanistic information in recent years, yet detailed operando-spectroscopic, thermodynamic and kinetic studies of proton and CO$_2$ binding to the reduced metal catalysts would help to understand the mechanisms for CO$_2$ reduction.

Groundbreaking research has to be continued to produce renewable fuels (CO, and ultimately further reduced species such as methanol, methane, ethanol acetic acid etc.) *via* low-energy pathways using durable and selective earth-abundant catalysts for creating carbon-neutral energy sources.

AUTHOR CONTRIBUTIONS

AD, DD, UR, and WS. contributed to conception and design of the review article. DD, AD, and WS wrote the first draft of the manuscript. All authors contributed to manuscript revision, read, and approved the submitted version.

FUNDING

ACKNOWLEDGMENTS

REFERENCES

Abdinejad, M., Dao, C., Deng, B., Dinic, F., Voznyy, O., Zhang, X.-a., et al. (2020). Electrocatalytic Reduction of CO₂ to CH₄ and CO in Aqueous Solution Using Pyridine-Porphyrins Immobilized onto Carbon Nanotubes. *ACS Sustain. Chem. Eng.* 8, 9549–9557. doi:10.1021/acssuschemeng.0c02791

Abdinejad, M., Dao, C., Deng, B., Sweeney, M. E., Dielmann, F., Zhang, X. a., et al. (2020). Enhanced Electrochemical Reduction of CO₂ to CO upon Immobilization onto Carbon Nanotubes Using an Iron-Porphyrin Dimer. *ChemistrySelect* 5, 979–984. doi:10.1002/slct.201904580

Abdinejad, M., Seifitokaldani, A., Dao, C., Sargent, E. H., Zhang, X.-a., and Kraatz, H. B. (2019). Enhanced Electrochemical Reduction of CO₂ Catalyzed by Cobalt and Iron Amino Porphyrin Complexes. *ACS Appl. Energ. Mater.* 2, 1330–1335. doi:10.1021/acsaem.8b01900

Abe, T., Taguchi, F., Yoshida, T., Tokita, S., Schnurpfeil, G., Wöhrle, D., et al. (1996). Electrocatalytic CO₂ Reduction by Cobalt Octabutoxyphthalocyanine Coated on Graphite Electrode. *J. Mol. Catal. A: Chem.* 112, 55–61. doi:10.1016/1381-1169(96)00242-7

Alenezi, K. (2016). Electrocatalytic Study of Carbon Dioxide Reduction by Co(TPP) Cl Complex. *J. Chem.* 2016 (1501728), 7. doi:10.1155/2016/150172

Álvarez, A., Borges, M., Corral-Pérez, J. J., Olcina, J. G., Hu, L., Cornu, D., et al. (2017). CO₂ Activation over Catalytic Surfaces. *ChemPhysChem* 18, 3135–3141. doi:10.1002/cphc.201701165

Ambre, R. B., Daniel, Q., Fan, T., Chen, H., Zhang, B., Wang, L., et al. (2016). Molecular Engineering for Efficient and Selective Iron Porphyrin Catalysts for Electrochemical Reduction of CO₂ to CO. *Chem. Commun.* 52, 14478–14481. doi:10.1039/c6cc08099e

Aoi, S., Mase, K., Ohkubo, K., and Fukuzumi, S. (2015). Selective Electrochemical Reduction of CO₂ to CO with a Cobalt Chlorin Complex Adsorbed on Multi-Walled Carbon Nanotubes in Water. *Chem. Commun.* 51, 10226–10228. doi:10.1039/c5cc03340c

Apaydin, D. H., Portenkirchner, E., Jintanalert, P., Strauss, M., Luangchaiyaporn, J., Sariciftci, N. S., et al. (2018). Synthesis and Investigation of Tetraphenyltetrabenzoporphyrins for Electrocatalytic Reduction of Carbon Dioxide. *Sustain. Energ. Fuels* 2, 2747–2753. doi:10.1039/c8se00422f

Araújo, A. R. L., Tomé, A. C., Santos, C. I. M., Faustino, M. A. F., Neves, M. G. P. M. S., Simões, M. M. Q., et al. (2020). Azides and Porphyrinoids: Synthetic Approaches and Applications. Part 2-Azides, Phthalocyanines, Subphthalocyanines and Porphyrazines. *Molecules* 25. doi:10.3390/molecules25071745

Aresta, M., Dibenedetto, A., and Angelini, A. (2013). Catalysis for the Valorization of Exhaust Carbon: from CO₂ to Chemicals, Materials, and Fuels. Technological Use of CO₂. *Chem. Rev.* 114, 1709–1742. doi:10.1021/cr4002758

Azcarate, I., Costentin, C., Robert, M., and Savéant, J.-M. (2016). Dissection of Electronic Substituent Effects in Multielectron-Multistep Molecular Catalysis. Electrochemical CO₂-to-CO Conversion Catalyzed by Iron Porphyrins. *J. Phys. Chem. C* 120, 28951–28960. doi:10.1021/acs.jpcc.6b09947

Azcarate, I., Costentin, C., Robert, M., and Savéant, J.-M. (2016). Through-Space Charge Interaction Substituent Effects in Molecular Catalysis Leading to the Design of the Most Efficient Catalyst of CO₂-to-CO Electrochemical Conversion. *J. Am. Chem. Soc.* 138, 16639–16644. doi:10.1021/jacs.6b07014

Bajracharya, S., Vanbroekhoven, K., Buisman, C. J. N., Strik, D. P. B. T. B., and Pant, D. (2017). Bioelectrochemical Conversion of CO₂ to Chemicals: CO₂ as a Next Generation Feedstock for Electricity-Driven Bioproduction in Batch and Continuous Modes. *Faraday Discuss.* 202, 433–449. doi:10.1039/c7fd00050b

Barata, J. F. B., Neves, M. G. P. M. S., Faustino, M. A. F., Tomé, A. C., Cavaleiro, J. A. S., and Cavaleiro, J. A. S. (2017). Strategies for Corrole Functionalization. *Chem. Rev.* 117, 3192–3253. doi:10.1021/acs.chemrev.6b00476

Behar, D., Dhanasekaran, T., Neta, P., Hosten, C. M., Ejeh, D., Hambright, P., et al. (1998). Cobalt Porphyrin Catalyzed Reduction of CO₂. Radiation Chemical, Photochemical, and Electrochemical Studies. *J. Phys. Chem. A.* 102, 2870–2877. doi:10.1021/jp9807017

Benson, E. E., Kubiak, C. P., Sathrum, A. J., and Smieja, J. M. (2009). Electrocatalytic and Homogeneous Approaches to Conversion of CO₂ to Liquid Fuels. *Chem. Soc. Rev.* 38, 89–99. doi:10.1039/b804323j

Bhugun, I., Lexa, D., and Savéant, J.-M. (1996). Catalysis of the Electrochemical Reduction of Carbon Dioxide by Iron(0) Porphyrins: Synergystic Effect of Weak Brönsted Acids. *J. Am. Chem. Soc.* 118, 1769–1776. doi:10.1021/ja9534462

Bhugun, I., Lexa, D., and Savéant, J.-M. (1996). Catalysis of the Electrochemical Reduction of Carbon Dioxide by Iron(0) Porphyrins. Synergistic Effect of Lewis Acid Cations. *J. Phys. Chem.* 100, 19981–19985. doi:10.1021/jp9618486

Bhugun, I., Lexa, D., and Saveant, J.-M. (1994). Ultraefficient Selective Homogeneous Catalysis of the Electrochemical Reduction of Carbon Dioxide by an Iron(0) Porphyrin Associated with a Weak Broensted Acid Cocatalyst. *J. Am. Chem. Soc.* 116, 5015–5016. doi:10.1021/ja00090a068

Blumenfeld, C., Fisher, K. J., Henling, L. M., Grubbs, R. H., Gray, H. B., and Virgil, S. C. (2015). Control of Oligomerization and Oxidation Steps in the Synthesis of Tris(pentafluorophenyl)corrole. *Eur. J. Org. Chem.* 2015, 3022–3025. doi:10.1002/ejoc.201500276

Bogaerts, A., and Centi, G. (2020). Plasma Technology for CO₂ Conversion: A Personal Perspective on Prospects and Gaps. *Front. Energ. Res.* 8, 111. doi:10.3389/fenrg.2020.00111

Boutin, E., Merakeb, L., Ma, B., Boudy, B., Wang, M., Bonin, J., et al. (2020). Molecular Catalysis of CO₂ Reduction: Recent Advances and Perspectives in Electrochemical and Light-Driven Processes with Selected Fe, Ni and Co Aza Macrocyclic and Polypyridine Complexes. *Chem. Soc. Rev.* 49, 5772–5809. doi:10.1039/d0cs00218f

Choi, J., Benedetti, T. M., Jalili, R., Walker, A., Wallace, G. G., and Officer, D. L. (2016). High Performance Fe Porphyrin/Ionic Liquid Co-catalyst for Electrochemical CO₂ Reduction. *Chem. Eur. J.* 22, 14158–14161. doi:10.1002/chem.201603359

Choi, J., Wagner, P., Gambhir, S., Jalili, R., MacFarlane, D. R., Wallace, G. G., et al. (2019). Steric Modification of a Cobalt Phthalocyanine/Graphene Catalyst to Give Enhanced and Stable Electrochemical CO₂ Reduction to CO. *ACS Energ. Lett.* 4, 666–672. doi:10.1021/acsenergylett.8b02355

Collin, J. P., Jouaiti, A., and Sauvage, J. P. (1988). Electrocatalytic Properties of (Tetraazacyclotetradecane)nickel$^{(2+)}$ and Ni₂(biscyclam)$^{4+}$ with Respect to Carbon Dioxide and Water Reduction. *Inorg. Chem.* 27, 1986–1990. doi:10.1021/ic00284a030

Collin, J., and Sauvage, J. P. (1989). Electrochemical Reduction of Carbon Dioxide Mediated by Molecular Catalysts. *Coord. Chem. Rev.* 93, 245–268. doi:10.1016/0010-8545(89)80018-9

Costentin, C., Drouet, S., Passard, G., Robert, M., and Savéant, J.-M. (2013). Proton-Coupled Electron Transfer Cleavage of Heavy-Atom Bonds in Electrocatalytic Processes. Cleavage of a C-O Bond in the Catalyzed Electrochemical Reduction of CO₂. *J. Am. Chem. Soc.* 135, 9023–9031. doi:10.1021/ja4030148

Costentin, C., Drouet, S., Robert, M., and Savéant, J.-M. (2012). A Local Proton Source Enhances CO₂ Electroreduction to CO by a Molecular Fe Catalyst. *Science* 338, 90–94. doi:10.1126/science.1224581

Costentin, C., Robert, M., Savéant, J.-M., and Tatin, A. (2015). Efficient and Selective Molecular Catalyst for the CO₂-to-CO Electrochemical Conversion in Water. *Proc. Natl. Acad. Sci. USA* 112, 6882–6886. doi:10.1073/pnas.1507063112

De, R., Gonglach, S., Paul, S., Haas, M., Sreejith, S. S., Gerschel, P., et al. (2020). Electrocatalytic Reduction of CO₂ to Acetic Acid by a Molecular Manganese Corrole Complex. *Angew. Chem. Int. Ed.* 59, 10527–10534. doi:10.1002/anie.202000601

Denekamp, I. M., Veenstra, F. L. P., Jungbacker, P., and Rothenberg, G. (2019). A Simple Synthesis of Symmetric Phthalocyanines and Their Respective Perfluoro and Transition-metal Complexes. *Appl. Organomet. Chem.* 33, e4872. doi:10.1002/aoc.4872

Dhanasekaran, T., Grodkowski, J., Neta, P., Hambright, P., and Fujita, E. (1999). p-Terphenyl-Sensitized Photoreduction of CO₂ with Cobalt and Iron Porphyrins. Interaction between CO and Reduced Metalloporphyrins. *J. Phys. Chem. A.* 103, 7742–7748. doi:10.1021/jp991423u

Enthaler, S., von Langermann, J., and Schmidt, T. (2010). Carbon Dioxide and Formic Acid-The Couple for Environmental-Friendly Hydrogen Storage? *Energy Environ. Sci.* 3, 1207–1217. doi:10.1039/b907569k

Faustini, M., Nicole, L., Ruiz-Hitzky, E., and Sanchez, C. (2018). History of Organic-Inorganic Hybrid Materials: Prehistory, Art, Science, and Advanced Applications. *Adv. Funct. Mater.* 28, 1704158. doi:10.1002/adfm.201704158

Fisher, B. J., and Eisenberg, R. (1980). Electrocatalytic Reduction of Carbon Dioxide by Using Macrocycles of Nickel and Cobalt. *J. Am. Chem. Soc.* 102, 7361–7363. doi:10.1021/ja00544a035

Francke, R., Schille, B., and Roemelt, M. (2018). Homogeneously Catalyzed Electroreduction of Carbon Dioxide-Methods, Mechanisms, and Catalysts. *Chem. Rev.* 118, 4631–4701. doi:10.1021/acs.chemrev.7b00459

Gonglach, S., Paul, S., Haas, M., Pillwein, F., Sreejith, S. S., Barman, S., et al. (2019). Molecular Cobalt Corrole Complex for the Heterogeneous Electrocatalytic Reduction of Carbon Dioxide. *Nat. Commun.* 10, 3864. doi:10.1038/s41467-019-11868-5

Grice, K. A. (2017). Carbon Dioxide Reduction with Homogenous Early Transition Metal Complexes: Opportunities and Challenges for Developing CO₂ Catalysis. *Coord. Chem. Rev.* 336, 78–95. doi:10.1016/j.ccr.2017.01.007

Grodkowski, J., Behar, D., Neta, P., and Hambright, P. (1997). Iron Porphyrin-Catalyzed Reduction of CO₂. Photochemical and Radiation Chemical Studies. *J. Phys. Chem. A.* 101, 248–254. doi:10.1021/jp9628139

Grodkowski, J., Neta, P., Fujita, E., Mahammed, A., Simkhovich, L., and Gross, Z. (2002). Reduction of Cobalt and Iron Corroles and Catalyzed Reduction of CO₂. *J. Phys. Chem. A.* 106, 4772–4778. doi:10.1021/jp013668o

Hammouche, M., Lexa, D., Momenteau, M., and Saveant, J. M. (1991). Chemical Catalysis of Electrochemical Reactions. Homogeneous Catalysis of the Electrochemical Reduction of Carbon Dioxide by Iron("0") Porphyrins. Role of the Addition of Magnesium Cations. *J. Am. Chem. Soc.* 113, 8455–8466. doi:10.1021/ja00022a038

Hammouche, M., Lexa, D., Savéant, J. M., and Momenteau, M. (1988). Catalysis of the Electrochemical Reduction of Carbon Dioxide by Iron("0") Porphyrins. *J. Electroanalytical Chem. Interfacial Electrochemistry* 249, 347–351. doi:10.1016/0022-0728(88)80372-3

Han, N., Wang, Y., Ma, L., Wen, J., Li, J., Zheng, H., et al. (2017). Supported Cobalt Polyphthalocyanine for High-Performance Electrocatalytic CO₂ Reduction. *Chem.* 3, 652–664. doi:10.1016/j.chempr.2017.08.002

Hiroto, S., Miyake, Y., and Shinokubo, H. (2017). Synthesis and Functionalization of Porphyrins through Organometallic Methodologies. *Chem. Rev.* 117, 2910–3043. doi:10.1021/acs.chemrev.6b00427

Hu, B., Xie, W., Li, R., Pan, Z., Song, S., and Wang, Y. (2020). How Does the Ligands Structure Surrounding Metal-N4 of Co-based Macrocyclic Compounds Affect Electrochemical Reduction of CO₂ Performance?. *Electrochimica Acta* 331, 135283. doi:10.1016/j.electacta.2019.135283

Hu, X.-M., Rønne, M. H., Pedersen, S. U., Skrydstrup, T., and Daasbjerg, K. (2017). Enhanced Catalytic Activity of Cobalt Porphyrin in CO₂ Electroreduction upon Immobilization on Carbon Materials. *Angew. Chem. Int. Ed.* 56, 6468–6472. doi:10.1002/anie.201701104

IEA (2019). Global Energy & CO₂ Status Report 2019. Available at: https://www.iea.org/reports/global-energy-co2-status-report-2019. Paris: IEA.

Jack, J., Park, E., Maness, P.-C., Huang, S., Zhang, W., and Ren, Z. J. (2020). Selective Ligand Modification of Cobalt Porphyrins for Carbon Dioxide Electrolysis: Generation of a Renewable H₂/CO Feedstock for Downstream Catalytic Hydrogenation. *Inorg. Chim. Acta* 507, 119594. doi:10.1016/j.ica.2020.119594

Jiang, Z., Wang, Y., Zhang, X., Zheng, H., Wang, X., and Liang, Y. (2019). Revealing the Hidden Performance of Metal Phthalocyanines for CO₂ Reduction Electrocatalysis by Hybridization with Carbon Nanotubes. *Nano Res.* 12, 2330–2334. doi:10.1007/s12274-019-2455-z

Judeinstein, P., and Sanchez, C. (1996). Hybrid Organic-Inorganic Materials: a Land of Multidisciplinarity. *J. Mater. Chem.* 6, 511–525. doi:10.1039/jm9960600511

Khadhraoui, A., Gotico, P., Boitrel, B., Leibl, W., Halime, Z., and Aukauloo, A. (2018). Local Ionic Liquid Environment at a Modified Iron Porphyrin Catalyst Enhances the Electrocatalytic Performance of CO₂ to CO Reduction in Water. *Chem. Commun.* 54, 11630–11633. doi:10.1039/c8cc06475j

Khezri, B., Fisher, A. C., and Pumera, M. (2017). CO₂ reduction: the Quest for Electrocatalytic Materials. *J. Mater. Chem. A.* 5, 8230–8246. doi:10.1039/c6ta09875d

Kinzel, N. W., Werlé, C., and Leitner, W. (2021). Transition Metal Complexes as Catalysts for the Electroconversion of CO₂: An Organometallic Perspective. *Angew. Chem. Int. Ed. N/a.* 60(21):11628-11686. doi:10.1002/anie.202006988

Kondratenko, E. V., Mul, G., Baltrusaitis, J., Larrazábal, G. O., and Pérez-Ramírez, J. (2013). Status and Perspectives of CO₂ Conversion into Fuels and Chemicals by Catalytic, Photocatalytic and Electrocatalytic Processes. *Energ. Environ. Sci.* 6, 3112–3135. doi:10.1039/c3ee41272e

König, M., Faschinger, F., Reith, L. M., and Schöfberger, W. (2016). The Evolution of Corrole Synthesis - from Simple One-Pot Strategies to Sophisticated ABC-Corroles. *J. Porphyrins Phthalocyanines* 20, 96–107. doi:10.1142/s1088424616300056

Kortlever, R., Shen, J., Schouten, K. J. P., Calle-Vallejo, F., and Koper, M. T. M. (2015). Catalysts and Reaction Pathways for the Electrochemical Reduction of Carbon Dioxide. *J. Phys. Chem. Lett.* 6, 4073–4082. doi:10.1021/acs.jpclett.5b01559

Koszarna, B., and Gryko, D. T. (2006). Efficient Synthesis of Meso-Substituted Corroles in a H₂O−MeOH Mixture. *J. Org. Chem.* 71, 3707–3717. doi:10.1021/jo060007k

Kramer, W. W., and McCrory, C. C. L. (2016). Polymer Coordination Promotes Selective CO₂ Reduction by Cobalt Phthalocyanine. *Chem. Sci.* 7, 2506–2515. doi:10.1039/c5sc04015a

Layer, G., Jahn, D., Deery, E., Lawrence, A. D., and Warren, M. J. (2010). Biosynthesis of Heme and Vitamin B12. *Compr. Nat. Prod.* 7, 445–499. doi:10.1016/b978-008045382-8.00144-1

Lin, S., Diercks, C. S., Zhang, Y.-B., Kornienko, N., Nichols, E. M., Zhao, Y., et al. (2015). Covalent Organic Frameworks Comprising Cobalt Porphyrins for Catalytic CO₂ reduction in Water. *Science* 349, 1208–1213. doi:10.1126/science.aac8343

Lindsey, J. S., Schreiman, I. C., Hsu, H. C., Kearney, P. C., and Marguerettaz, A. M. (1987). Rothemund and Adler-Longo Reactions Revisited: Synthesis of Tetraphenylporphyrins under Equilibrium Conditions. *J. Org. Chem.* 52, 827–836. doi:10.1021/jo00381a022

Liu, C., Yuan, X., Gu, Y., Chen, H., Sun, D., Li, P., et al. (2020). Enhancement of Bioelectrochemical CO₂ Reduction with a Carbon Brush Electrode *via* Direct Electron Transfer. *ACS Sustain. Chem. Eng.* 8, 11368–11375. doi:10.1021/acssuschemeng.0c03623

Liu, Y., and McCrory, C. C. L. (2019). Modulating the Mechanism of Electrocatalytic CO$_2$ Reduction by Cobalt Phthalocyanine through Polymer Coordination and Encapsulation. *Nat. Commun.* 10, 1683. doi:10.1038/s41467-019-09626-8

Mahmood, M. N., Masheder, D., and Harty, C. J. (1987). Use of Gas-Diffusion Electrodes for High-Rate Electrochemical Reduction of Carbon Dioxide. II. Reduction at Metal Phthalocyanine-Impregnated Electrodes. *J. Appl. Electrochem.* 17, 1223–1227. doi:10.1007/bf01023606

Margarit, C. G., Asimow, N. G., Costentin, C., and Nocera, D. G. (2020). Tertiary Amine-Assisted Electroreduction of Carbon Dioxide to Formate Catalyzed by Iron Tetraphenylporphyrin. *ACS Energ. Lett.* 5, 72–78. doi:10.1021/acsenergylett.9b02093

Margarit, C. G., Asimow, N. G., Gonzalez, M. I., and Nocera, D. G. (2020). Double Hangman Iron Porphyrin and the Effect of Electrostatic Nonbonding Interactions on Carbon Dioxide Reduction. *J. Phys. Chem. Lett.* 11, 1890–1895. doi:10.1021/acs.jpclett.9b03897

Margarit, C. G., Schnedermann, C., Asimow, N. G., and Nocera, D. G. (2019). Carbon Dioxide Reduction by Iron Hangman Porphyrins. *Organometallics* 38, 1219–1223. doi:10.1021/acs.organomet.8b00334

Matheu, R., Gutierrez-Puebla, E., Monge, M. Á., Diercks, C. S., Kang, J., Prévot, M. S., et al. (2019). Three-Dimensional Phthalocyanine Metal-Catecholates for High Electrochemical Carbon Dioxide Reduction. *J. Am. Chem. Soc.* 141, 17081–17085. doi:10.1021/jacs.9b09298

Maurin, A., and Robert, M. (2016). Noncovalent Immobilization of a Molecular Iron-Based Electrocatalyst on Carbon Electrodes for Selective, Efficient CO$_2$-to-CO Conversion in Water. *J. Am. Chem. Soc.* 138, 2492–2495. doi:10.1021/jacs.5b12652

Mele, G., Annese, C., D'Accolti, L., De Riccardis, A., Fusco, C., Palmisano, L., et al. (2014). Photoreduction of Carbon Dioxide to Formic Acid in Aqueous Suspension: a Comparison between phthalocyanine/TiO$_2$ and porphyrin/TiO$_2$ Catalysed Processes. *Molecules* 20, 396–415. doi:10.3390/molecules20010396

Meshitsuka, S., Ichikawa, M., and Tamaru, K. (1974). Electrocatalysis by Metal Phthalocyanines in the Reduction of Carbon Dioxide. *J. Chem. Soc. Chem. Commun.*, 158–159. doi:10.1039/c39740000158

Min Park, J., Lee, J. H., and Jang, W.-D. (2020). Applications of Porphyrins in Emerging Energy Conversion Technologies. *Coord. Chem. Rev.* 407, 213157. doi:10.1016/j.ccr.2019.213157

Mohamed, E. A., Zahran, Z. N., and Naruta, Y. (2015). Efficient Electrocatalytic CO$_2$ Reduction with a Molecular Cofacial Iron Porphyrin Dimer. *Chem. Commun.* 51, 16900–16903. doi:10.1039/c5cc04273a

Mondal, B., Sen, P., Rana, A., Saha, D., Das, P., and Dey, A. (2019). Reduction of CO$_2$ to CO by an Iron Porphyrin Catalyst in the Presence of Oxygen. *ACS Catal.* 9, 3895–3899. doi:10.1021/acscatal.9b00529

Moss, G. P. (1988). Nomenclature of Tetrapyrroles. Recommendations 1986 IUPAC-IUB Joint Commission on Biochemical Nomenclature (JCBN). *Eur. J. Biochem.* 178, 277–328. doi:10.1111/j.1432-1033.1988.tb14453.x

Nam, D.-H., De Luna, P., Rosas-Hernández, A., Thevenon, A., Li, F., Agapie, T., et al. (2020). Molecular Enhancement of Heterogeneous CO$_2$ Reduction. *Nat. Mater.* 19, 266–276. doi:10.1038/s41563-020-0610-2

Nardis, S., Mandoj, F., Stefanelli, M., and Paolesse, R. (2019). Metal Complexes of Corrole. *Coord. Chem. Rev.* 388, 360–405. doi:10.1016/j.ccr.2019.02.034

Nemykin, V. N., Dudkin, S. V., Dumoulin, F., Hirel, C., and Ahsen, A. G. V. (2014). Synthetic Approaches to Asymmetric Phthalocyanines and Their Analogues. *ARKIVOC* 2014, 142–204. doi:10.3998/ark.5550190.p008.412

Nichols, E. M., Derrick, J. S., Nistanaki, S. K., Smith, P. T., and Chang, C. J. (2018). Positional Effects of Second-Sphere Amide Pendants on Electrochemical CO$_2$ Reduction Catalyzed by Iron Porphyrins. *Chem. Sci.* 9, 2952–2960. doi:10.1039/c7sc04682k

Ogawa, A., Oohora, K., Gu, W., and Hayashi, T. (2019). Electrochemical CO$_2$ Reduction by a Cobalt Bipyricorrole Complex: Decrease of an Overpotential Value Derived from Monoanionic Ligand Character of the Porphyrinoid Species. *Chem. Commun.* 55, 493–496. doi:10.1039/c8cc08876d

Okabe, Y., Lee, S. K., Kondo, M., and Masaoka, S. (2017). Syntheses and CO$_2$ Reduction Activities of π-expanded/extended Iron Porphyrin Complexes. *J. Biol. Inorg. Chem.* 22, 713–725. doi:10.1007/s00775-017-1438-3

Orłowski, R., Gryko, D., and Gryko, D. T. (2017). Synthesis of Corroles and Their Heteroanalogs. *Chem. Rev.* 117, 3102–3137. doi:10.1021/acs.chemrev.6b00434

Paolesse, R., Licoccia, S., Bandoli, G., Dolmella, A., and Boschi, T. (1994). First Direct Synthesis of a Corrole Ring from a Monopyrrolic Precursor. Crystal and Molecular Structure of (Triphenylphosphine)(5,10,15-triphenyl-2,3,7,8,12,13,17,18-octamethylcorrolato)Cobalt(III)-Dichloromethane. *Inorg. Chem.* 33, 1171–1176. doi:10.1021/ic00084a033

Paolesse, R., Nardis, S., Sagone, F., and Khoury, R. G. (2001). Synthesis and Functionalization Ofmeso-Aryl-Substituted Corroles. *J. Org. Chem.* 66, 550–556. doi:10.1021/jo005661t

Paparo, A., and Okuda, J. (2017). Carbon Dioxide Complexes: Bonding Modes and Synthetic Methods. *Coord. Chem. Rev.* 334, 136–149. doi:10.1016/j.ccr.2016.06.005

Pinto, S. M. A., Henriques, C. A., Tomé, V. A., Vinagreiro, C. S., Calvete, M. J. F., Dąbrowski, J. M., et al. (2016). Synthesis of Meso-Substituted Porphyrins Using Sustainable Chemical Processes. *J. Porphyrins Phthalocyanines* 20, 45–60. doi:10.1142/s1088424616300020

Qiao, J., Liu, Y., Hong, F., and Zhang, J. (2014). A Review of Catalysts for the Electroreduction of Carbon Dioxide to Produce Low-Carbon Fuels. *Chem. Soc. Rev.* 43, 631–675. doi:10.1039/c3cs60323g

Rebber, M., Willa, C., and Koziej, D. (2020). Organic-inorganic Hybrids for CO$_2$ Sensing, Separation and Conversion. *Nanoscale Horiz.* 5, 431–453. doi:10.1039/c9nh00380k

Ren, S., Joulié, D., Salvatore, D., Torbensen, K., Wang, M., Robert, M., et al. (2019). Molecular Electrocatalysts Can Mediate Fast, Selective CO$_2$ Reduction in a Flow Cell. *Science* 365, 367–369. doi:10.1126/science.aax4608

Riccardis, A. de., Lee, M., Kazantsev, R. V., Garza, A. J., Zeng, G., Larson, D. M., et al. (2020). Heterogenized Pyridine-Substituted Cobalt(II) Phthalocyanine Yields Reduction of CO$_2$ by Tuning the Electron Affinity of the Co Center. *ACS Appl. Mater. Inter.* 12, 5251–5258. doi:10.1021/acsami.9b18924

Sakamoto, K., and Ohno-Okumura, E. (2009). Syntheses and Functional Properties of Phthalocyanines. *Materials* 2, 1127–1179. doi:10.3390/ma2031127

Sanchez, C., Julián, B., Belleville, P., and Popall, M. (2005). Applications of Hybrid Organic-Inorganic Nanocomposites. *J. Mater. Chem.* 15, 3559–3592. doi:10.1039/b509097k

Sawicki, K. T., Chang, H-C., and Ardehali, H. (2015). Role of Heme in Cardiovascular Physiology and Disease. *J. Am. Heart Assoc.* 4, 1–14. doi:10.1161/jaha.114.001138

Sen, P., Mondal, B., Saha, D., Rana, A., and Dey, A. (2019). Role of 2nd Sphere H-Bonding Residues in Tuning the Kinetics of CO$_2$ Reduction to CO by Iron Porphyrin Complexes. *Dalton Trans.* 48, 5965–5977. doi:10.1039/c8dt03850c

Shen, J., Kortlever, R., Kas, R., Birdja, Y. Y., Diaz-Morales, O., Kwon, Y., et al. (2015). Electrocatalytic Reduction of Carbon Dioxide to Carbon Monoxide and Methane at an Immobilized Cobalt Protoporphyrin. *Nat. Commun.* 6, 8177. doi:10.1038/ncomms9177

Shooling-Jordan, P. M., and Cheung, K.-M. (1999). Biosynthesis of Heme. *Compr. Nat. Prod. Chem.* 4, 61–107. doi:10.1016/b978-0-08-091283-7.00161-2

Shy, H., Mackin, P., Orvieto, A. S., Gharbharan, D., Peterson, G. R., Bampos, N., et al. (2014). The Two-step Mechanochemical Synthesis of Porphyrins. *Faraday Discuss.* 170, 59–69. doi:10.1039/c3fd00140g

Sinha, S., and Warren, J. J. (2018). Unexpected Solvent Effect in Electrocatalytic CO$_2$ to CO Conversion Revealed Using Asymmetric Metalloporphyrins. *Inorg. Chem.* 57, 12650–12656. doi:10.1021/acs.inorgchem.8b01814

Sorokin, A. B. (2013). Phthalocyanine Metal Complexes in Catalysis. *Chem. Rev.* 113, 8152–8191. doi:10.1021/cr4000072

Sun, L., Reddu, V., Fisher, A. C., and Wang, X. (2020). Electrocatalytic Reduction of Carbon Dioxide: Opportunities with Heterogeneous Molecular Catalysts. *Energ. Environ. Sci.* 13, 374–403. doi:10.1039/c9ee03660a

Takeda, H., Cometto, C., Ishitani, O., and Robert, M. (2017). Electrons, Photons, Protons and Earth-Abundant Metal Complexes for Molecular Catalysis of CO$_2$ Reduction. *ACS Catal.* 7, 70–88. doi:10.1021/acscatal.6b02181

Tatin, A., Comminges, C., Kokoh, B., Costentin, C., Robert, M., and Savéant, J.-M. (2016). Efficient Electrolyzer for CO$_2$ Splitting in Neutral Water Using Earth-Abundant Materials. *Proc. Natl. Acad. Sci. USA* 113, 5526–5529. doi:10.1073/pnas.1604628113

Torbensen, K., Han, C., Boudy, B., Wolff, N., Bertail, C., Braun, W., et al. (2020). Iron Porphyrin Allows Fast and Selective Electrocatalytic Conversion of CO$_2$ to CO in a Flow Cell. *Chem. Eur. J.* 26, 3034–3038. doi:10.1002/chem.202000160

Vicente, M., and Smith, K. (2014). Syntheses and Functionalizations of Porphyrin Macrocycles. *Cos* 11, 3–28. doi:10.2174/15701794113106660083

Villano, M., Aulenta, F., Ciucci, C., Ferri, T., Giuliano, A., and Majone, M. (2010). Bioelectrochemical Reduction of CO$_2$ to CH$_4$ *via* Direct and Indirect Extracellular Electron Transfer by a Hydrogenophilic Methanogenic Culture. *Bioresour. Tech.* 101, 3085–3090. doi:10.1016/j.biortech.2009.12.077

Wang, F. (2017). Artificial Photosynthetic Systems for CO$_2$ Reduction: Progress on Higher Efficiency with Cobalt Complexes as Catalysts. *ChemSusChem* 10, 4393–4402. doi:10.1002/cssc.201701385

Wang, J., Huang, X., Xi, S., Lee, J. M., Wang, C., Du, Y., et al. (2019a). Linkage Effect in the Heterogenization of Cobalt Complexes by Doped Graphene for Electrocatalytic CO$_2$ Reduction. *Angew. Chem. Int. Ed.* 58, 13532–13539. doi:10.1002/anie.201906475

Wang, M. (2019b). CO$_2$ Electrochemical Catalytic Reduction with a Highly Active Cobalt Phthalocyanine. *Nat. Commun.* 10, 3602. doi:10.1038/s41467-019-11542-w

Yang, C., Li, S., Zhang, Z., Wang, H., Liu, H., Jiao, F., et al. (2020). Organic-Inorganic Hybrid Nanomaterials for Electrocatalytic CO$_2$ Reduction. *Small* 16, 2001847. doi:10.1002/smll.202001847

Yuan, M., Kummer, M. J., and Minteer, S. D. (2019). Strategies for Bioelectrochemical CO$_2$ Reduction. *Chem. Eur. J.* 25, 14258–14266. doi:10.1002/chem.201902880

Zahran, Z. N., Mohamed, E. A., and Naruta, Y. (2016). Bio-inspired Cofacial Fe Porphyrin Dimers for Efficient Electrocatalytic CO$_2$ to CO Conversion: Overpotential Tuning by Substituents at the Porphyrin Rings. *Sci. Rep.* 6, 24533. doi:10.1038/srep24533

Zhang, W., Lai, W., and Cao, R. (2017). Energy-Related Small Molecule Activation Reactions: Oxygen Reduction and Hydrogen and Oxygen Evolution Reactions Catalyzed by Porphyrin- and Corrole-Based Systems. *Chem. Rev.* 117, 3717–3797. doi:10.1021/acs.chemrev.6b00299

Zhang, X., Wu, Z., Zhang, X., Li, L., Li, Y., Xu, H., et al. (2017). Highly Selective and Active CO$_2$ Reduction Electrocatalysts Based on Cobalt Phthalocyanine/carbon Nanotube Hybrid Structures. *Nat. Commun.* 8, 14675. doi:10.1038/ncomms14675

Zhang, X., Chen, Z., Mou, K., Jiao, M., Zhang, X., and Liu, L. (2019). Intentional Construction of High-Performance SnO$_2$ Catalysts with a 3D Porous Structure for Electrochemical Reduction of CO$_2$. *Nanoscale* 11, 18715–18722. doi:10.1039/c9nr06354d

Zhang, Z., Xiao, J., Chen, X.-J., Yu, S., Yu, L., Si, R., et al. (2018). Reaction Mechanisms of Well-Defined Metal-N4 Sites in Electrocatalytic CO$_2$ Reduction. *Angew. Chem. Int. Ed.* 57, 16339–16342. doi:10.1002/anie.201808593

Zhu, M., Yang, D.-T., Ye, R., Zeng, J., Corbin, N., and Manthiram, K. (2019). Inductive and Electrostatic Effects on Cobalt Porphyrins for Heterogeneous Electrocatalytic Carbon Dioxide Reduction. *Catal. Sci. Technol.* 9, 974–980. doi:10.1039/c9cy00102f

Role of Chemical Structure of Support in Enhancing the Catalytic Activity of a Single Atom Catalyst Toward NRR: A Computational Study

Thillai Govindaraja Senthamaraikannan[1,2]*, Selvaraj Kaliaperumal[2] and Sailaja Krishnamurty[3]*

[1]Department of Environmental Engineering, Chungbuk National University, Cheongju, Korea, [2]Nano and Computational Material Lab, Catalysis Division, CSIR-National Chemical Laboratory, Pune, India, [3]Physical Chemistry Division, CSIR-National Chemical Laboratory, Pune, India

Using the periodic density functional theory–based methodology, we propose a potential catalytic system for dinitrogen activation, viz., single metal atoms (Mo, Fe, and V) supported on graphene-based sheets. Graphene-based sheets show an excellent potential toward the anchoring of single atoms on them (Mo, Fe, and V) with adsorption energies ranging between 1.048 and 10.893 eV. Factors such as defects and BN doping are noted to enhance the adsorption energies of single metal atoms on the support. The adsorption of a dinitrogen molecule on metal atom–anchored graphene-based supports is seen to be highly favorable, ranging between 0.620 and 2.278 eV. The adsorption is driven through a direct hybridization between the d orbitals of the metal atom (Mo, Fe, and V) on the support and the p orbital of the molecular nitrogen. Noticeably, BN-doped graphene supporting a single metal atom (Mo, Fe, and V) activates the N_2 molecule with a red shift in the N–N stretching frequency (1,597 cm^{-1} as compared to 2,330 cm^{-1} in the free N_2 molecule). This red shift is corroborated by an increase in the N–N bond length (1.23 Å from 1.09 Å) and charge transfer to an N_2 molecule from the catalyst.

Keywords: N_2 activation, single metal atom, pristine graphene, defective graphene, BN-functionalized graphene

INTRODUCTION

Ammonia is an important chemical substance for the agriculture, pharmaceuticals, and chemical industries. Natural and synthetic N_2 fixation is necessary for the existence of all forms of life on Earth. Though the availability of dinitrogen (N_2) is abundant in air, it requires high energy for fixation and activation owing to its existence of inert triple bonds between nitrogen atoms. Currently, the well-known Haber–Bosch process invented more than a century ago is used for converting dinitrogen (N_2) in the atmosphere into NH_3 in the presence of the iron catalyst at an extreme temperature (500°C) and pressure (200 atm) (Fryzuk and Johnson, 2000). The energy- and carbon-intensive Haber–Bosch process consumes 1–2% global energy and, in addition, produces 3% of global CO_2 emission (Cherkasov et al., 2015). Nevertheless, N_2 fixation can occur readily under mild conditions by nitrogenase mechanism, the enzyme secreted from very few prokaryotic organisms (Kim and Rees, 1992; Sellmann and Sutter, 1997; Einsle et al., 2002). Researchers have demonstrated the occurrence of biological N_2 fixation under reasonable or mild conditions in the presence of nitrogenase enzymes, most preferably at the active sites that are rich in Fe and S and also

Graphical Abstract | XXX
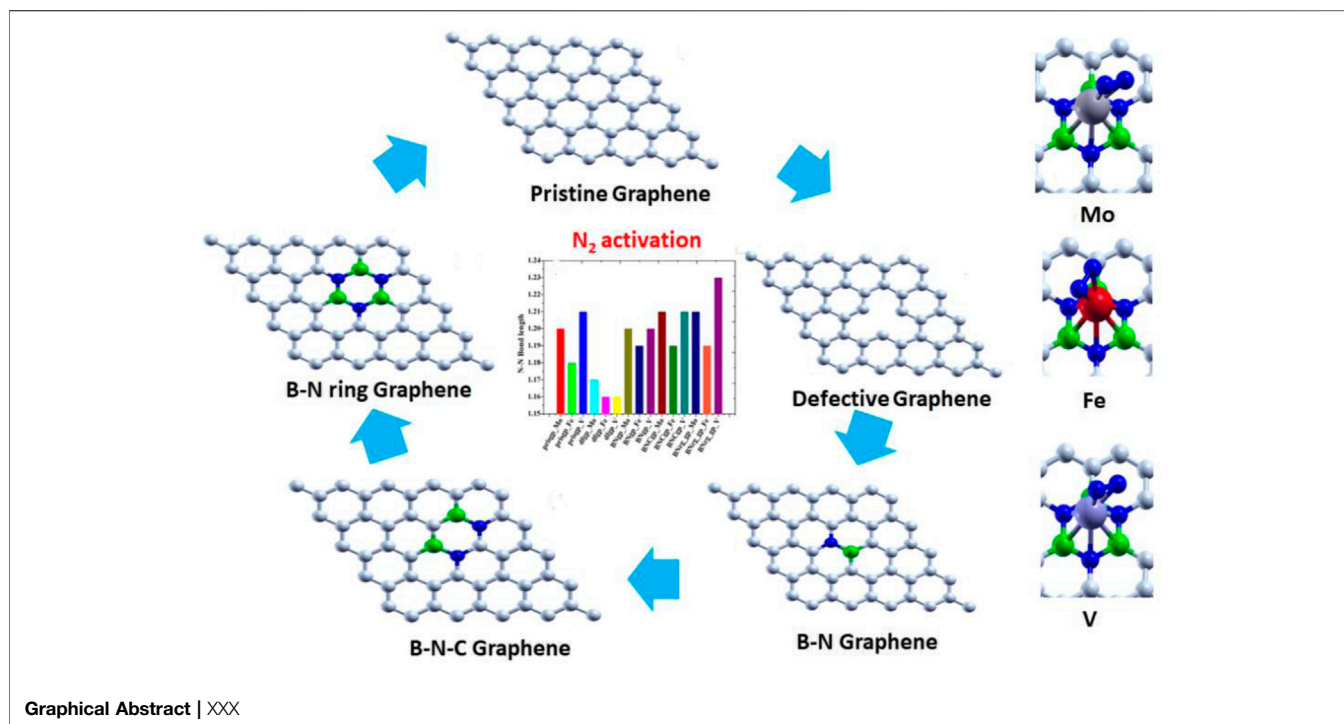
additionally contain Mo or V atoms (Dance, 2008; Stüeken et al., 2015; Tanabe and Nishibayashi, 2016), yet the through kinetics are still disputed. Consequently, exploring an efficient N_2 reduction catalyst in ammonia synthesis is the main challenge for the organo-metallic researchers. Naturally, N_2 fixation and activation require a potential catalytic active center to promote nitrogen reduction reaction, via electrons overlapping between the σ bond of N_2 and the d orbital of the metal center, and the occupied d orbital overlaps with the empty π^* bond of N_2, resulting in the activation of N_2 by a π bond back-donation mechanism.

On accounting for the quantum confinement of electrons, metal clusters are widely explored as catalysts. Using experimental and theoretical strategies, researchers have explored N_2 activation on potential inorganic metal clusters (Seh et al., 2017; Liu et al., 2018; Wang et al., 2018). Significantly, Kerpal et al. (2013) have evaluated dinitrogen (N_2) activation using infrared multiphoton dissociation (IR-MPD) on neutral Ru clusters. Similarly, Roy et al. (2009) have noticed the red-shifted N–N bond stretching frequency around 810 cm^{-1} on solid Li_n (2 < n < 8) clusters, particularly the Li_8 metal cluster showing an exothermic trend in splitting the N–N bond completely. In the midst of metal clusters for evaluating N_2 activation reaction, Al clusters play a remarkable role. Previously, Jarrold et al. observed low energy barriers for N_2 activation on Al_{44} and Al_{100} clusters at high temperatures using concerted experimental and theoretical techniques (Cao et al., 2010). Similarly, in another previous report by this group, N_2 activation potential was observed to be dependent on the phase and structure of the metal cluster (Cao et al., 2009).

During the course of N_2 activation mechanism, conformations with high energy display low energy potential toward the activation of the N_2 molecule (Kulkarni et al., 2011). Nevertheless, excited state conformations are meta-stable in nature and are notably present only at some characteristic finite temperatures. Hence, there is an obvious demand for more reliable and stable ground state conformations for N_2 activation. Consequently, heteroatoms such as silicon and phosphorus doped on aluminum clusters appear to be a possible alternative and have better activation than their pristine aluminum clusters (Das et al., 2014).

Moreover, an alternative and experimentally supported route is to enhance the activity of metal-based catalysts by anchoring metal centers on 2D material supports such as graphene and BN, which offers a substantial support to the metal centers to adsorb and activate the N_2 molecule. Moreover, specific activity per metal atom increases by downsizing the metals from nanoparticles to nanocrystals or hetero-nano framework (Yang et al., 2013; Chen et al., 2014). Single atom catalysts (SACs) have gained more attention in downsizing metals considerably and exhibit the potential of well-dispersed active single atom sites available for atomic utilization (Qiao et al., 2011). Based on these circumstances, SACs exhibiting unique activity with high density of active sites supported on 2D materials can make use of electron sharing for the activation of the inert dinitrogen molecule. A single transition-metal atom or atom clusters supported on N-doped graphene show good nitrogen reduction reaction (NRR) activity (Choi et al., 2015; Li et al., 2016; Fajardo and Peters, 2017; Fei et al., 2018; Yan et al., 2019). Systems such
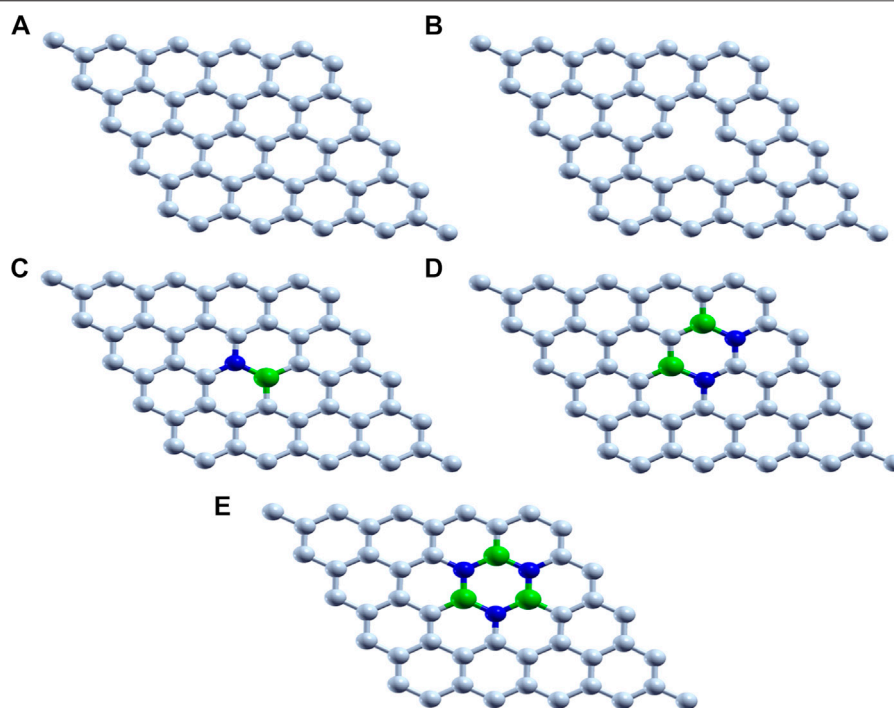
FIGURE 1 | Optimized structure of **(A)** pristine graphene, **(B)** defective graphene, **(C)** BN-doped graphene, **(D)** BNC-ring graphene, and **(E)** BN-ring graphene (C, white; B, green; and N, blue).

as BiOBr nanosheets, boron anti-sites on BN nanotubes, and Mo-doped boron nitride (BN) have also been reported to have high N_2 fixation potential (Li et al., 2015; Kumar and Subramanian, 2017; Zhao and Chen, 2017; Légaré et al., 2018).

In the midst of 2D materials, graphene-based supports attract enormous attention in numerous reactions such as water splitting, Guo et al. (2018), and hydrogen evolution reaction (HER) Ouyang et al. (2018). Few experimental groups reported N_2 fixation using a graphene-based catalytic support (Jeon et al., 2013; Lu et al., 2016; Yan et al., 2018). Several computational investigations have also been explored using graphene-based nanomaterials for N_2 fixation to compare with the experimental findings. Le et al. reported that the Mo/N-doped graphene-based support dissociates the N_2 molecule using the density functional theory (DFT) methodology (Le et al., 2014). In a similar approach, Li et al. observed an N_2 molecule activation to nearly 2.5 Å by fixing the FeN_3 molecule on a graphene support, in which nitrogen atoms are used as anchoring elements, while iron does the activation job in the FeN_3 molecule (Li et al., 2016). Kumar et al. (2016) reported N_2 activation using aluminum clusters doped on the BN-doped graphene support. The rare ability of certain transition complexes to bind to N_2, which is attributed to their advantageous combination of unoccupied and occupied d-orbitals that have appropriate energy and symmetry to synergistically accept/back-donate electron density from/to N_2, can thus be contrived by giving the appropriate

environment to a p-block element. In short, activation of N_2 is performed by exploiting the electron reservoir property of 2D graphene-based materials. Recently, in our previous investigations, we identified the most active and recyclable SAC/B-graphene composite as the catalyst for NRR activity (Maibam et al., 2019; Maibam and Krishnamurty, 2021). In the present work, using the density functional theory (DFT)-based methodology, we evaluate the possible dinitrogen activation by single metal atoms (Mo, Fe, and V) supported on graphene-based systems such as pristine graphene, defective graphene, BN-doped graphene, BNC-ring graphene, and BN-ring graphene as support materials.

Computational Details

We use the Vienna Ab Initio Simulation Package (VASP) (Kresse and Furthmller, 1996) with the PBE functional (Perdew et al., 1996) to perform all the first-principles calculations in the present work. The projected augmented wave (PAW) (Blöchl, 1994) method is employed using an energy cutoff of 520 eV to describe the plane wave basis set. The two-dimensional graphene sheets are simulated using periodic boundary conditions. To avoid the interactions between the different nearest neighboring layers, a vacuum space of 20 Å is created along the Z-direction. The 5×5 supercell with 50 atoms is used as the graphene surface model, and the optimized C–C bond length in the graphene sheet is 1.42 Å.

Pristine graphene, defective graphene, BN-doped graphene, BNC-ring graphene, and BN-ring graphene are designed surface
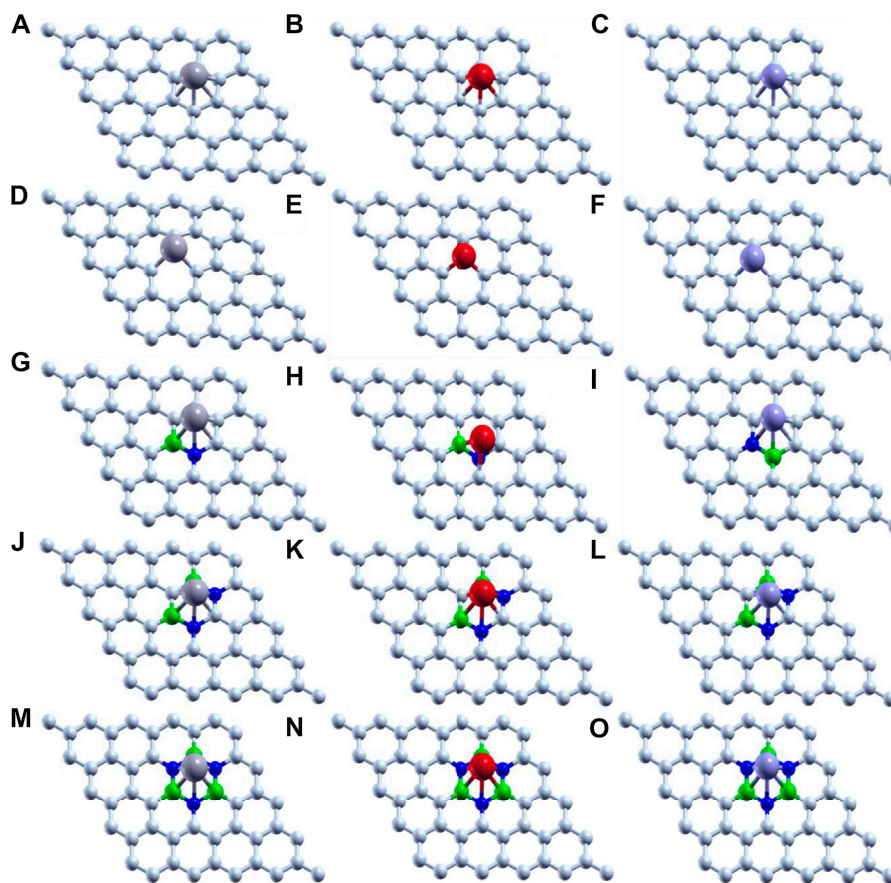
FIGURE 2 | Optimized structure of adsorption of Mo (gray), Fe (red), and V (purple) on **(A–C)** pristine graphene, **(D–F)** defective graphene, **(G–I)** BN-doped graphene, **(J–L)** BNC-ring graphene, and **(M–O)** BN-ring graphene.

supports, and the structures are further optimized. The structural optimization of all geometries is carried out using the conjugate gradient method (Payne et al., 1992). The Brillouin zone is sampled by a (2 × 2×1) K-point grid using the Monkhorst–Pack scheme (Monkhorst and Pack, 1976). For density of states (DOS) calculations, Monkhorst and Pack generated a (9 × 9×1) set of K points.

The ground state geometries of single transition-metal clusters (Mo, Fe, and V) are adsorbed on the above-mentioned supports and the complexes optimized. The adsorption energy of Mo, V, and Fe on these supports is calculated as follows:

$$E_{ad} = E_{(M--system)} - E_{(M)} - E_{(system)},$$

where $E_{(M--system)}$ represents the energy of the optimized single transition-metal cluster (Mo, Fe, and V) and the designed surface supports. $E_{(M)}$ and $E_{(system)}$ represent the energy of a single metal and surface support, respectively.

Finally, the N$_2$ molecule is adsorbed on these active metal clusters (Mo, Fe, and V) on graphene-based surface supports. A parallel mode of adsorption (both the nitrogen atoms are exposed to the metal) is used as this mode has been found to be more

TABLE 1 | Interatomic distances and adsorption energies of Mo, Fe, and V on various graphene-based supports (pristine graphene, defective graphene, BN-doped graphene, BNC-ring graphene, BN-ring graphene, and adsorption energy are abbreviated as prisgp, dfgp, BNgp, BNCgp, BNrg_gp, and E$_{ad}$).

System	C–metal (Å)	B–metal (Å)	N–metal (Å)	E$_{ad}$ (eV)
prisgp_Mo	2.200–2.213	—	—	−4.653
prisgp_Fe	2.069–2.080	—	—	−2.602
prisgp_V	2.147–2.170	—	—	−3.145
dfgp_Mo	1.932–1.956	—	—	−10.893
dfgp_Fe	1.766–1.768	—	—	−9.329
dfgp_V	1.863–1.873			−9.744
BNgp_Mo	2.145–2.261	2.258	2.211	−3.929
BNgp_Fe	2.012–2.473	2.303	1.861	−1.090
BNgp_V	2.079–2.192	2.215	2.172	−2.494
BNCgp_Mo	2.072–2.305	2.279–2.28	2.224–2.226	−3.864
BNCgp_Fe	1.947–2.148	2.106–2.218	2.01–2.225	−1.728
BNCgp_V	2.072–2.306	2.279–2.28	2.224–2.226	−2.498
BNrg_gp_Mo	—	2.216–2.219	2.267–2.273	−3.016
BNrg_gp_Fe	—	2.063–2.124	2.073–2.197	−1.048
BNrg_gp_V	—	2.17–2.227	2.204–2.226	−1.467

effective as compared to the vertical mode. In the vertical mode, only one N atom in the N$_2$ molecule interacts with the metal leading to weak activation (Song et al., 2021).
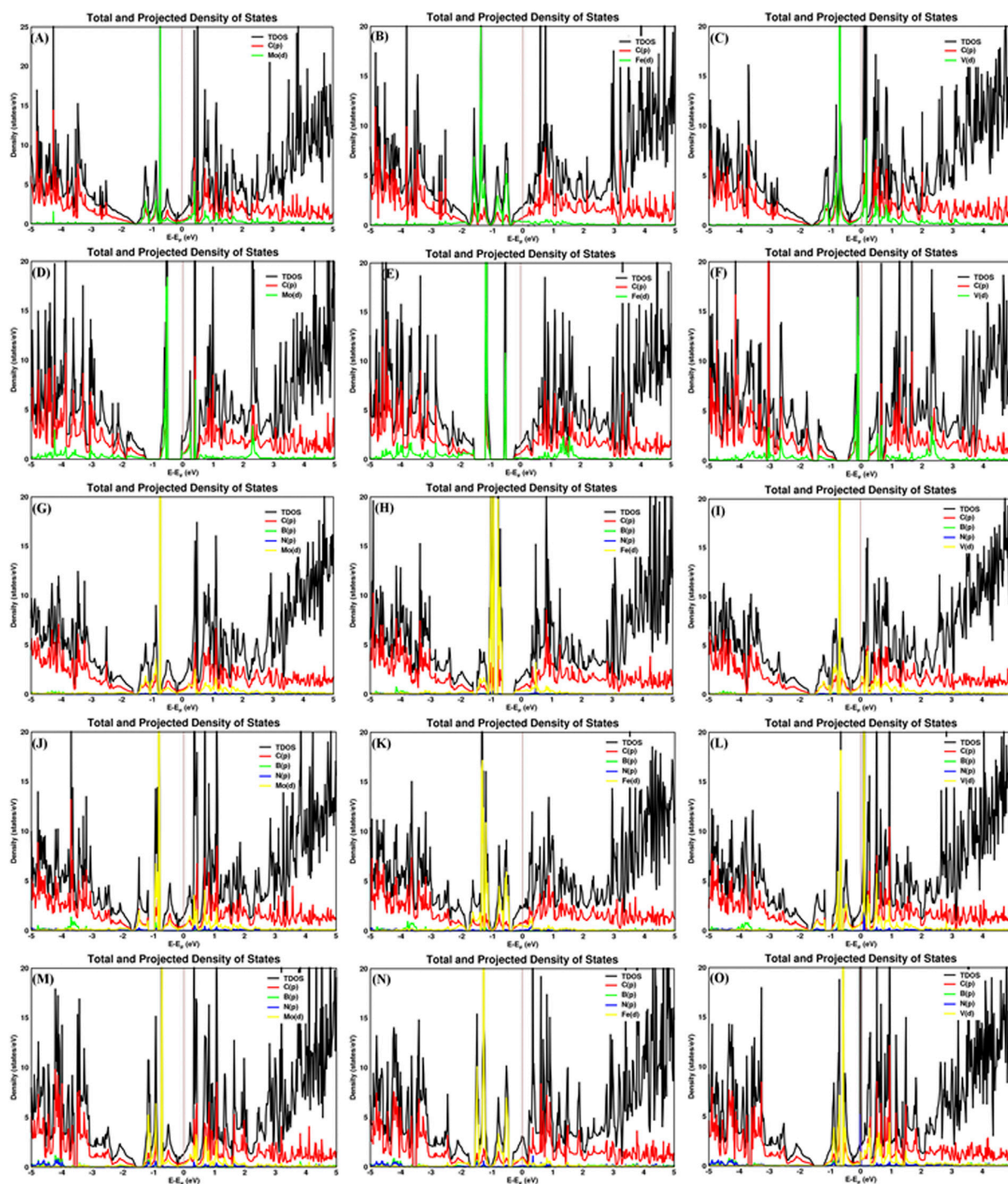
FIGURE 3 | Total and projected density of states of Mo, Fe, and V on **(A–C)** pristine graphene, **(D–F)** defective graphene, **(G–I)** BN-doped graphene, **(J–L)** BNC-ring graphene, and **(M–O)** BN-ring graphene.

The dissociated adsorption energy of the N_2 molecule on the catalytic systems is calculated as follows:

$$E_{ad} = E_{(N2----M--system)} - E_{(N2)} - E_{(M--system)},$$

where $E_{(N2----M--system)}$ represents the energy of the dissociated N_2 molecule on the catalytic systems. $E_{(N2)}$ and $E_{(M--system)}$ represent

the energy of the N_2 molecule and metal-adsorbed various surface supports, respectively. Nudged elastic band (NEB) calculations were performed toward prediction of energy barrier of N_2 activation on metal-adsorbed BN-doped graphene-based substrates.

FIGURE 4 | Optimized structure of the N$_2$ molecule adsorbed on Mo (gray), Fe (red), and V (purple) on various supports: **(A–C)** pristine graphene, **(D–F)** defective graphene, **(G–I)** BN-doped graphene, **(J–L)** BNC-ring graphene, and **(M–O)** BN-ring graphene.
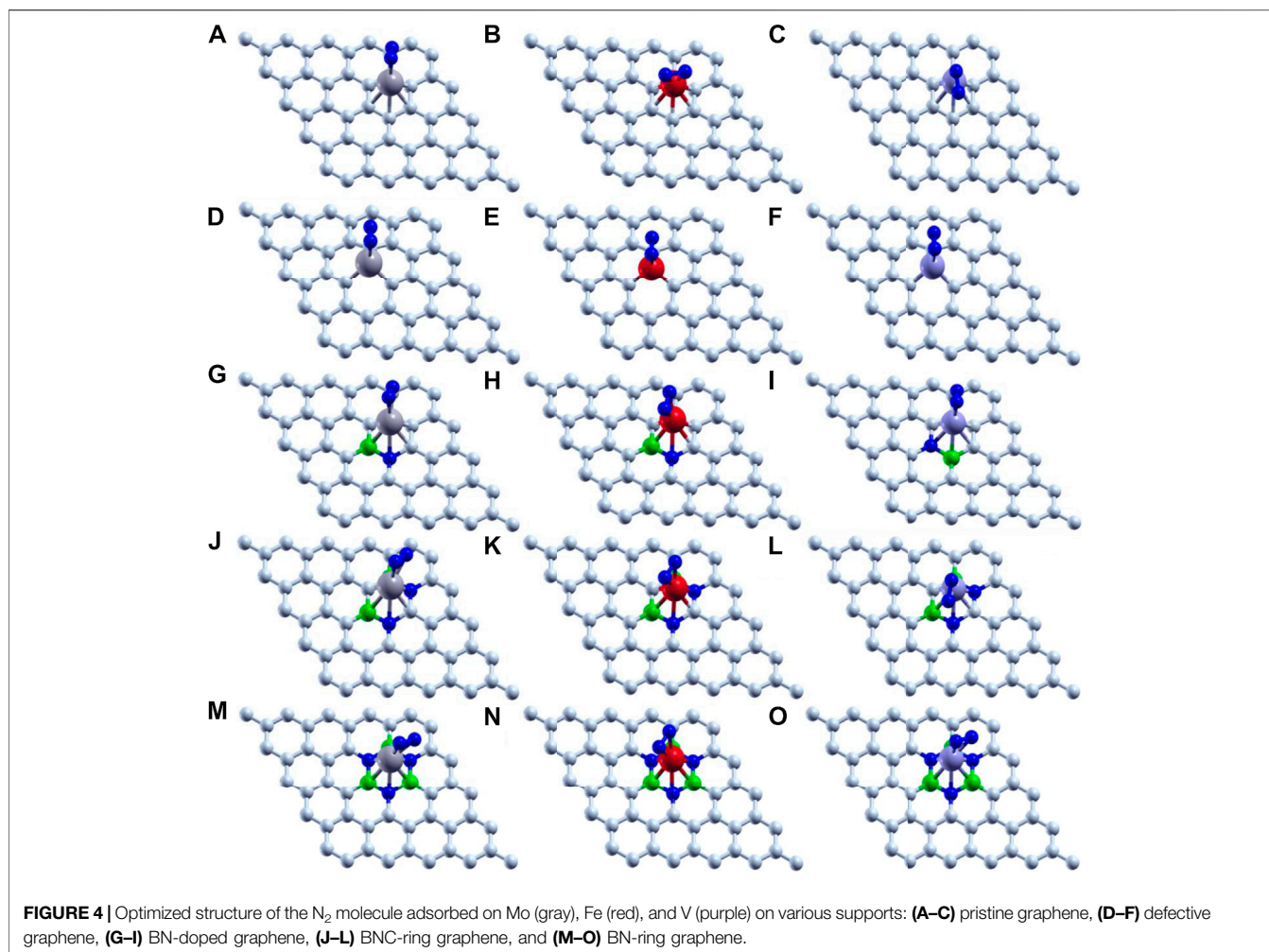
RESULTS AND DISCUSSION

Anchoring of Single Metal Atom (Mo, Fe, and V) on Various Graphene-Based Supports

Graphene-based 2D materials which act as an electron reservoir are used as the support for adsorbing the single atom cluster (Mo, Fe, and V) which increases the catalytic activity of the metal center. The five graphene-based supports are designed, viz., 1) pristine graphene (50 carbon atoms), 2) defective graphene (49 carbon atoms with a single vacancy at the center), 3) BN-doped graphene (4% heteroatom doping in which boron and nitrogen are substituted instead of carbon in the pristine graphene), 4) BNC-ring graphene (8% heteroatom doping), and 5) BN-ring graphene (12% heteroatom doping). All these graphene-based supports are designed and optimized to the local minima as shown in **Figure 1**.

Thus, we have tried to establish the relative reactivity of single atom clusters (Mo, Fe, and V) chemisorbed on the above-mentioned surfaces. The optimized structure of adsorption of

Mo (gray), Fe (red), and V (purple) on various surface supports is shown in **Figure 2**. The adsorption energy of a single metal atom (Mo, Fe, and V) on pristine graphene, defective graphene, BN-doped graphene, BNC-ring graphene, and BN-ring graphene is 4.653, 2.602, and 3.145 eV; 10.893, 9.329, and 9.744 eV; 3.929, 1.090, and 2.494 eV; 3.864, 1.728, and 2.498 eV; and 3.016, 1.048, and 1.467 eV, respectively. Comparatively, the adsorption energy of Mo on the designed supports is ~2 eV more due to its bulky nature with respect to other metals (Fe and V). Interestingly, the dangling carbon atoms at the center increase the adsorption energies for a defective graphene support better than the rest, and also the increase in the percentage of heteroatom (B and N) doping decreases the adsorption energies of the single metal atom on supports.

The carbon–metal (C–M) interatomic distance of Mo, Fe, and V on pristine graphene, defective graphene, BN-doped graphene, and BNC-ring graphene is 2.200–2.213, 2.069–2.080, and 2.147–2.170 Å;1.932–1.956, 1.766–1.768, and 1.863–1.873 Å; 2.145–2.261, 2.012–2.473, and 2.079–2.192 Å; and 2.072–2.305, 1.947–2.148, and 2.072–2.306 Å, respectively. The boron–metal (B–M) interatomic distance of Mo, Fe, and V on BN-doped

TABLE 2 | Interatomic distances and adsorption energies of N₂ on Mo, V, and Fe on various graphene-based supports (pristine graphene, defective graphene, BN-doped graphene, BNC-ring graphene, BN-ring graphene, and adsorption energy are abbreviated as prisgp, dfgp, BNgp, BNCgp, BNrg_gp, and E_ad).

System	C–metal (Å)	B–metal (Å)	N$_{doped}$–metal (Å)	N$_{ad}$–metal (Å)	E$_{ad}$ (eV)
prisgp_Mo	2.228–2.313	—	—	2.039–2.117	−1.739
prisgp_Fe	2.077–2.162	—	—	1.92–1.923	−1.334
prisgp_V	2.190–2.264	—	—	1.911–1.994	−1.996
dfgp_Mo	1.946–2.013	—	—	2.22–2.221	−0.887
dfgp_Fe	1.777–1.847	—	—	1.964–2.078	−0.620
dfgp_V	1.871–1.925	—	—	2.161–2.218	−0.628
BNgp_Mo	2.194–2.257	2.313	2.32	2.027–2.091	−1.844
BNgp_Fe	2.096–2.144	2.18	2.202	1.902–1.907	−2.278
BNgp_V	2.133–2.234	2.319	2.223	1.918–2	−1.988
BNCgp_Mo	2.111–2.319	2.316–2.407	2.239–2.328	2–2.057	−1.870
BNCgp_Fe	2.004–2.172	2.219–2.222	2.165–2.173	1.889–1.89	−1.544
BNCgp_V	2.048–2.241	2.303–2.342	2.23–2.242	1.908–1.979	−2.116
BNrg_gp_Mo	—	2.244–2.41	2.274–2.341	2–2.068	−1.868
BNrg_gp_Fe	—	2.141–2.216	2.083–2.234	1.9	−1.510
BNrg_gp_V	—	2.256–2.371	2.264–2.297	1.869–1.928	−2.258

graphene, BNC-ring graphene, and BN-ring graphene is 2.258, 2.303, and 2.215 Å; 2.279–2.28, 2.106–2.218, and 2.279–2.28 Å; and 2.216–2.219, 2.063–2.124, and 2.17–2.227 Å, respectively. The nitrogen–metal (N–M) interatomic distance of Mo, Fe, and V on BN-doped graphene, BNC-ring graphene, and BN-ring graphene is 2.211, 1.861, and 2.172 Å; 2.224–2.226, 2.01–2.225, and 2.224–2.226 Å; and 2.267–2.273, 2.073–2.197, and 2.204–2.226 Å, respectively. The interatomic distances and adsorption energies of Mo, Fe, and V on various graphene-based supports are shown in **Table 1**. Thus, the significance of the result shows that the adsorption energies of a single metal atom on the surface support provide a stable and potential catalyst for N₂ activation. The total density of states and projected density of states of a single metal atom (Mo, Fe, and V) on graphene-based supports are shown in **Figure 3**. The total density of states (TDOS) and partial density of states (PDOS) reveal that the d-states of a single metal atom (Mo, Fe, and V) strongly hybridize with the p-state of unsaturated carbon atoms and heteroatoms (B and N). The d-state of a single metal atom shows its maximum density of states between −2 and 2 eV. On comparing, the p-state of unsaturated carbon atoms is maximum in pristine and defective supports which reveals that, in the other three supports, the p-state of both boron and nitrogen is hybridized with the d-state of metal.

N₂ Activation on Single Metal Atom (Mo, Fe, and V) Anchored on Various Graphene-Based Supports

The adsorption energies of N₂ on a single metal atom (Mo, Fe, and V) on pristine graphene, defective graphene, BN-doped graphene, BNC-ring graphene, and BN-ring graphene are 1.739, 1.334, and 1.996 eV; 0.887, 0.620, and 0.628 eV; 1.844, 2.278, and 1.988 eV; 1.870, 1.544, and 2.116 eV; and 1.868, 1.510, and 2.258 eV, respectively. Comparatively, the adsorption energies of N₂ on a single metal atom (Mo, Fe, and V) on the defective graphene support are less compared to those on the rest of the support. Moreover, there is an eventual increase in adsorption energies of N₂ on V on supports (BN-doped

graphene, BNC-ring graphene, and BN-ring graphene) due to more vacant d orbitals (less than half-filled), which is vice versa in Fe (more than half-filled d orbitals) on the same supports. The optimized structure of adsorption of N₂ on a single metal atom (Mo, Fe, and V) on various surface supports is shown in **Figure 4**.

The carbon–metal (C–M) interatomic distance of N₂ on a single metal atom (Mo, Fe, and V) on pristine graphene, defective graphene, BN-doped graphene, and BNC-ring graphene is 2.228–2.313, 2.077–2.162, and 2.190–2.264 Å; 1.946–2.013, 1.777–1.847, and 1.871–1.925 Å; 2.194–2.257, 2.096–2.144, and 2.133–2.234 Å; and 2.111–2.319, 2.004–2.172, and 2.048–2.241 Å, respectively. The boron–metal (B–M) interatomic distance of N₂ on a single metal atom (Mo, Fe, and V) on BN-doped graphene, BNC-ring graphene, and BN-ring graphene is 2.313, 2.18, and 2.319 Å; 2.316–2.407, 2.219–2.222, and 2.303–2.342 Å; and 2.244–2.41, 2.141–2.216, and 2.256–2.371 Å, respectively. The nitrogen–metal (N$_{doped}$–M) interatomic distance of N₂ on a single metal atom (Mo, Fe, and V) on BN-doped graphene, BNC-ring graphene, and BN-ring graphene is 2.32, 2.202, and 2.223 Å; 2.239–2.328, 2.165–2.173, and 2.23–2.242 Å; and 2.274–2.341, 2.083–2.234, and 2.264–2.297 Å, respectively.

The nitrogen–metal (N$_{ad}$–M) interatomic distance of N₂ on a single metal atom (Mo, Fe, and V) on pristine graphene, defective graphene, BN-doped graphene, BNC-ring graphene, and BN-ring graphene is 2.039–2.117, 1.92–1.923, and 1.911–1.994 Å; 2.22–2.221, 1.964–2.078, and 2.161–2.218 Å; 2.027–2.091, 1.902–1.907, and 1.918–2 Å; 2–2.057, 1.889–1.89, and 1.908–1.979 Å; and 2–2.068, 1.9, and 1.869–1.928 Å, respectively. The interatomic distances and adsorption energy of N₂ on a single metal atom (Mo, Fe, and V) on various substrate systems are shown in **Table 2**. The total density of states and projected density of states of N₂ on a single metal atom (Mo, Fe, and V) on the graphene-based support are shown in **Figure 5**. The total density of states (TDOS) and partial density of states (PDOS) reveal that the d-states of a single metal atom (Mo, Fe, and V) hybridize with the p-state of adsorbed nitrogen as well as carbon, boron, and nitrogen atoms doped on the support. Thus, the d-state of a single metal atom shares its vacant orbital with the p-state of hybridizing atoms.

FIGURE 5 | Total and projected density of states of the N_2 molecule adsorbed on Mo, Fe, and V on various supports: **(A–C)** pristine graphene, **(D–F)** defective graphene, **(G–I)** BN-doped graphene, **(J–L)** BNC-ring graphene, and **(M–O)** BN-ring graphene.
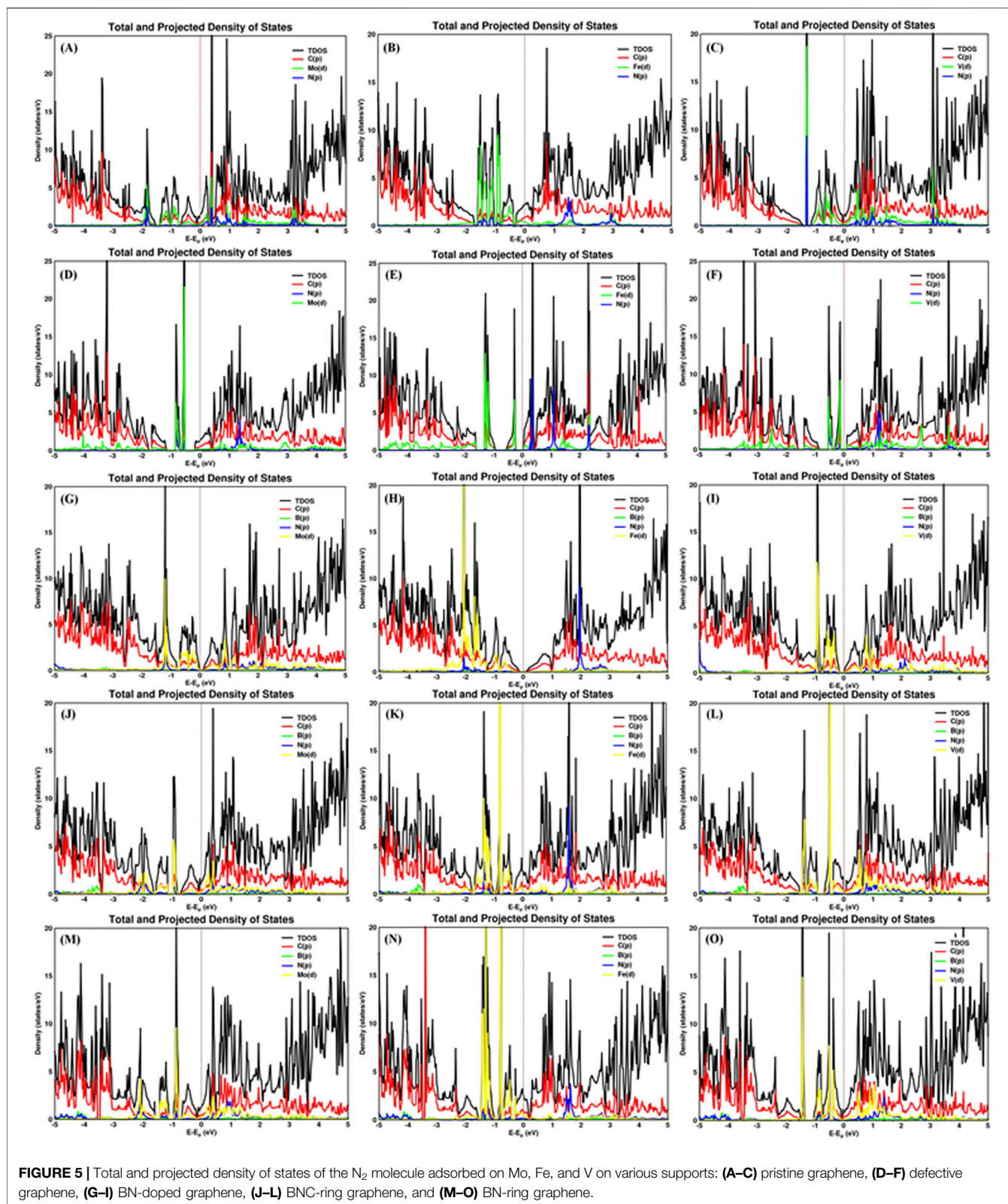
TABLE 3 | Structural, electronic, and vibrational properties of various catalytic systems for N$_2$ activation (pristine graphene, defective graphene, BN-doped graphene, BNC-ring graphene, and BN-ring graphene are abbreviated as prisgp, dfgp, BNgp, BNCgp, and BNrg_gp).

System	N–N bond length	IR stretching	Charge on N$_2$ (e)	
	(Å)	(cm^{-1})		
prisgp_Mo	1.2	1735	−0.3239	−0.2274
prisgp_Fe	1.18	1823	−0.1556	−0.3095
prisgp_V	1.21	1,692	−0.4328	−0.1847
dfgp_Mo	1.17	1907	−0.3055	−0.1237
dfgp_Fe	1.16	2009	−0.1954	−0.1228
dfgp_V	1.16	1997	−0.1359	−0.1935
BNgp_Mo	1.2	1701	−0.2088	−0.363
BNgp_Fe	1.19	1802	−0.2152	−0.252
BNgp_V	1.2	1711	−0.2733	−0.3433
BNCgp_Mo	1.21	1,636	−0.2783	−0.3213
BNCgp_Fe	1.19	1777	−0.2714	−0.2093
BNCgp_V	1.21	1,688	−0.2711	−0.352
BNrg_gp_Mo	1.21	1,666	−0.2584	−0.3194
BNrg_gp_Fe	1.19	1796	−0.314	−0.1728
BNrg_gp_V	1.23	1,597	−0.2666	−0.4262

N–N Bond Stretching Frequency Analysis on Designed Catalytic Systems

To probe the stretching frequency of the adsorbed N$_2$ molecule on a single metal atom (Mo, Fe, and V) on the graphene-based support, we investigated the spectral range of 1,300–2,300 cm^{-1}, which covers the typical frequencies of the different N$_2$ species known to exist on transition-metal surfaces. The stretching frequency of the unbound N$_2$ molecule is attributed to 2,330 cm^{-1}, and the N–N bond length is 1.09 Å (Shi and Jacobi, 1992). The N–N bond length and IR stretching frequency ν(N–N) of N$_2$ on a single metal atom (Mo, Fe, and V) on pristine graphene, defective graphene, BN-doped graphene, BNC-ring graphene, and BN-ring graphene are 1.20 Å (1735 cm^{-1}), 1.18 Å (1823 cm^{-1}), and 1.21 Å (1,692 cm^{-1}); 1.17 Å (1907 cm^{-1}), 1.16 Å (2009 cm^{-1}), and 1.16 Å (1997 cm^{-1}); 1.20 Å (1701 cm^{-1}), 1.19 Å (1802 cm^{-1}), and 1.20 Å (1711 cm^{-1}); 1.21 Å (1,636 cm^{-1}), 1.19 Å (1777 cm^{-1}), and 1.21 Å (1,688 cm^{-1}); and 1.21 Å (1,666 cm^{-1}), 1.19 Å (1796 cm^{-1}), and 1.23 Å (1,597 cm^{-1}), respectively.

The Bader charge analysis (Bader, 1991; Tang et al., 2009) clearly demonstrates the charge redistribution between the activated nitrogen atoms and the active metal centered on support-based catalysts. The structural, electronic, and vibrational properties of various catalytic systems for N$_2$ activation are listed in **Table 3**. The N–N stretching frequency, N–N bond length, and charge on nitrogen of the N$_2$ molecule adsorbed on Mo, Fe, and V on various graphene supports are shown in **Supplementary Figure S1**.

As a case study, the potential of the Mo-adsorbed BN-doped graphene catalyst for the activation of N$_2$ is discussed in **Supplementary Figure S2**. NEB calculation is performed in between these reactants and products to confirm the N$_2$ activation energy barrier. Mo-adsorbed BN-doped graphene and gaseous nitrogen are considered reactants. Thus, the Mo-adsorbed BN-doped graphene catalyst shows more feasible N$_2$ activation with an effective energy barrier of 3.21 eV. The activation barrier plot of the N$_2$ molecule adsorbed on Mo on the BN-doped graphene support is shown in **Supplementary Figure S2** (Liu et al., 2021).

CONCLUSION

In this work, we explore the potential of various graphene-based 2D materials, viz., pristine, defective, BN-doped graphene, etc., as a support for a single atom cluster (Mo, Fe, and V). These graphene-based supports show excellent potential toward the anchoring of a single atom cluster (Mo, Fe, and V) with adsorption energies ranging between 1.048 and 10.893 eV. Thus, the adsorption energies vary substantially with respect to the graphene-based supports, viz., pristine, defective, BN doped, etc. This is attributed to the size and nature of hybridization between the d orbitals of the interacting single metal atom (Mo, Fe, and V) and the sp^2 orbitals of unsaturated carbon atoms of various designed graphene-based supports. The catalytic performance of a single metal atom (Mo, Fe, and V) on graphene-supported catalysts is explored for the activation of molecular nitrogen. The adsorption energies of the nitrogen molecule on a graphene-supported single atom cluster (Mo, Fe, and V) range between 0.620 and 2.278 eV, which is attributed to the interacting environment of the active metal centered on the support and the p orbital of adsorbed molecular nitrogen. Bader charge and density of states analyses corroborate an enhanced hybridization between the d states of the single metal atoms (Mo, Fe, and V) and adsorbed molecular nitrogen for activation. The N–N stretching frequencies are found which are considerably red-shifted ranging from 2009 cm^{-1} (1.16 Å) to 1,597 cm^{-1} (1.23 Å) compared to that of the unbound N$_2$ molecule (2,330 cm^{-1} (1.09 Å)). Thus, from the results, we understood that even a single metal atom (Mo, Fe, and V) with functionalized (BN-doped) graphene supports can highlight the excellent potential for nitrogen activation.

DATA AVAILABILITY STATEMENT

AUTHOR CONTRIBUTIONS

SaK conceptualized the research idea. TS investigated the data and wrote the original draft. TS, SeK, and SaK were involved in formal analysis. TS and SaK validated the results and reviewed and edited the paper. SeK and SaK supervised the work. SeK was involved in funding acquisition and project administration.

FUNDING

ACKNOWLEDGMENTS

SUPPLEMENTARY MATERIAL

REFERENCES

Bader, R. F. W. (1991). A Quantum Theory of Molecular Structure and its Applications. *Chem. Rev.* 91, 893–928. doi:10.1021/cr00005a013

Blöchl, P. E. (1994). Projector Augmented-Wave Method. *Phys. Rev. B* 50, 17953–17979. doi:10.1103/physrevb.50.17953

Cao, B., Starace, A. K., Judd, O. H., Bhattacharyya, I., Jarrold, M. F., López, J. M., et al. (2010). Activation of Dinitrogen by Solid and Liquid Aluminum Nanoclusters: a Combined Experimental and Theoretical Study. *J. Am. Chem. Soc.* 132, 12906–12918. doi:10.1021/ja103356r

Cao, B., Starace, A. K., Judd, O. H., Bhattacharyya, I., and Jarrold, M. F. (2009). Metal Clusters with Hidden Ground States: Melting and Structural Transitions in Al115+, Al116+, and Al117+. *J. Chem. Phys.* 131, 124305. doi:10.1063/1.3224124

Chen, C., Kang, Y., Huo, Z., Zhu, Z., Huang, W., Xin, H. L., et al. (2014). Highly Crystalline Multimetallic Nanoframes with Three-Dimensional Electrocatalytic Surfaces. *Science* 343, 1339–1343. doi:10.1126/science.1249061

Cherkasov, N., Ibhadon, A. O., and Fitzpatrick, P. (2015). A Review of the Existing and Alternative Methods for Greener Nitrogen Fixation. *Chem. Eng. Process. Process Intensification* 90, 24–33. doi:10.1016/j.cep.2015.02.004

Choi, W. I., Wood, B. C., Schwegler, E., and Ogitsu, T. (2015). Combinatorial Search for High-Activity Hydrogen Catalysts Based on Transition-Metal-Embedded Graphitic Carbons. *Adv. Energ. Mater.* 5, 1501423. doi:10.1002/aenm.201501423

Dance, I. (2008). The Chemical Mechanism of Nitrogenase: Calculated Details of the Intramolecular Mechanism for Hydrogenation of η2-N2 on FeMo-Co to NH3. *Dalton Trans.* 43, 5977–5991. doi:10.1039/b806100a

Das, S., Pal, S., and Krishnamurty, S. (2014). Dinitrogen Activation by Silicon and Phosphorus Doped Aluminum Clusters. *J. Phys. Chem. C* 118, 19869–19878. doi:10.1021/jp505700a

Einsle, O., Tezcan, F. A., Andrade, S. L., Schmid, B., Yoshida, M., Howard, J. B., et al. (2002). Nitrogenase MoFe-Protein at 1.16 A Resolution: A Central Ligand in the FeMo-Cofactor. *Science* 297, 1696–1700. doi:10.1126/science.1073877

Fajardo, J., Jr, and Peters, J. C. (2017). Catalytic Nitrogen-To-Ammonia Conversion by Osmium and Ruthenium Complexes. *J. Am. Chem. Soc.* 139, 16105–16108. doi:10.1021/jacs.7b10204

Fei, H., Dong, J., Feng, Y., Allen, C. S., Wan, C., Volosskiy, B., et al. (2018). General Synthesis and Definitive Structural Identification of MN4C4 Single-Atom Catalysts with Tunable Electrocatalytic Activities. *Nat. Catal.* 1, 63–72. doi:10.1038/s41929-017-0008-y

Fryzuk, M. D., and Johnson, S. A. (2000). The Continuing story of Dinitrogen Activation. *Coord. Chem. Rev.* 200-202, 379–409. doi:10.1016/s0010-8545(00)00264-2

Guo, X., Liu, S., and Huang, S. (2018). Single Ru Atom Supported on Defective Graphene for Water Splitting: DFT and Microkinetic Investigation. *Int. J. Hydrogen Energ.* 43, 4880–4892. doi:10.1016/j.ijhydene.2018.01.122

Jeon, I. Y., Choi, H. J., Ju, M. J., Choi, I. T., Lim, K., Ko, J., et al. (2013). Direct Nitrogen Fixation at the Edges of Graphene Nanoplatelets as Efficient Electrocatalysts for Energy Conversion. *Sci. Rep.* 3, 2260–2267. doi:10.1038/srep02260

Kerpal, C., Harding, D. J., Lyon, J. T., Meijer, G., and Fielicke, A. (2013). N2 Activation by Neutral Ruthenium Clusters. *J. Phys. Chem. C* 117, 12153–12158. doi:10.1021/jp401876b

Kim, J., and Rees, D. (1992). Structural Models for the Metal Centers in the Nitrogenase Molybdenum-Iron Protein. *Science* 257, 1677–1682. doi:10.1126/science.1529354

Kresse, G., and Furthmüller, J. (1996). Efficiency of Ab-Initio Total Energy Calculations for Metals and Semiconductors Using a Plane-Wave Basis Set. *Comput. Mater. Sci.* 6, 15–50. doi:10.1016/0927-0256(96)00008-0

Kulkarni, B. S., Krishnamurty, S., and Pal, S. (2011). Size- and Shape-Sensitive Reactivity Behavior of Aln (N = 2-5, 13, 30, and 100) Clusters toward the N2 Molecule: A First-Principles Investigation. *J. Phys. Chem. C* 115, 14615–14623. doi:10.1021/jp203452a

Kumar, C. V. S., and Subramanian, V. (2017). Can boron Antisites of BNNTs Be an Efficient Metal-free Catalyst for Nitrogen Fixation? - A DFT Investigation. *Phys. Chem. Chem. Phys.* 19, 15377–15387. doi:10.1039/c7cp02220d

Kumar, D., Pal, S., and Krishnamurty, S. (2016). N2 Activation on Al Metal Clusters: Catalyzing Role of BN-Doped Graphene Support. *Phys. Chem. Chem. Phys.* 18, 27721–27727. doi:10.1039/c6cp03342c

Le, Y.-Q., Gu, J., and Tian, W. Q. (2014). Nitrogen-fixation Catalyst Based on Graphene: Every Part Counts. *Chem. Commun.* 50, 13319–13322. doi:10.1039/c4cc01950d

Légaré, M.-A., Bélanger-Chabot, G., Dewhurst, R. D., Welz, E., Krummenacher, I., Engels, B., et al. (2018). Nitrogen Fixation and Reduction at boron. *Science* 359, 896–900. doi:10.1126/science.aaq1684

Li, H., Shang, J., Ai, Z., and Zhang, L. (2015). Efficient Visible Light Nitrogen Fixation with BiOBr Nanosheets of Oxygen Vacancies on the Exposed {001} Facets. *J. Am. Chem. Soc.* 137, 6393–6399. doi:10.1021/jacs.5b03105

Li, X.-F., Li, Q.-K., Cheng, J., Liu, L., Yan, Q., Wu, Y., et al. (2016). Conversion of Dinitrogen to Ammonia by FeN3-Embedded Graphene. *J. Am. Chem. Soc.* 138, 8706–8709. doi:10.1021/jacs.6b04778

Liu, B., Manavi, N., Deng, H., Huang, C., Shan, N., Chikan, V., et al. (2021). Activation of N2 on Manganese Nitride-Supported Ni3 and Fe3 Clusters and Relevance to Ammonia Formation. *J. Phys. Chem. Lett.* 12, 6535–6542. doi:10.1021/acs.jpclett.1c01752

Liu, J.-C., Tang, Y., Wang, Y.-G., Zhang, T., and Li, J. (2018). Theoretical Understanding of the Stability of Single-Atom Catalysts. *Natl. Sci. Rev.* 5, 638–641. doi:10.1093/nsr/nwy094

Lu, Y., Yang, Y., Zhang, T., Ge, Z., Chang, H., Xiao, P., et al. (2016). Photoprompted Hot Electrons from Bulk Cross-Linked Graphene Materials and Their Efficient Catalysis for Atmospheric Ammonia Synthesis. *ACS nano* 10, 10507–10515. doi:10.1021/acsnano.6b06472

Maibam, A., Govindaraja, T., Selvaraj, K., and Krishnamurty, S. (2019). Dinitrogen Activation on Graphene Anchored Single Atom Catalysts: Local Site Activity or Surface Phenomena. *J. Phys. Chem. C* 123, 27492–27500. doi:10.1021/acs.jpcc.9b06757

Maibam, A., and Krishnamurty, S. (2021). Nitrogen Activation to Reduction on a Recyclable V-SAC/BN-graphene Heterocatalyst Sifted through Dual and Multiphilic Descriptors. *J. Colloid Interf. Sci.* 600, 480–491. doi:10.1016/j.jcis.2021.05.027

Monkhorst, H. J., and Pack, J. D. (1976). Special Points for Brillouin-Zone Integrations. *Phys. Rev. B* 13, 5188–5192. doi:10.1103/physrevb.13.5188

Ouyang, Y., Li, Q., Shi, L., Ling, C., and Wang, J. (2018). Molybdenum Sulfide Clusters Immobilized on Defective Graphene: a Stable Catalyst for the Hydrogen Evolution Reaction. *J. Mater. Chem. A.* 6, 2289–2294. doi:10.1039/c7ta09828f

Payne, M. C., Teter, M. P., Allan, D. C., Arias, T. A., and Joannopoulos, J. D. (1992). Iterative Minimization Techniques Forab Initiotal-Energy Calculations: Molecular Dynamics and Conjugate Gradients. *Rev. Mod. Phys.* 64, 1045–1097. doi:10.1103/revmodphys.64.1045

Perdew, J. P., Burke, K., and Ernzerhof, M. (1996). Generalized Gradient Approximation Made Simple. *Phys. Rev. Lett.* 77, 3865–3868. doi:10.1103/physrevlett.77.3865

Qiao, B., Wang, A., Yang, X., Allard, L. F., Jiang, Z., Cui, Y., et al. (2011). Single-atom Catalysis of CO Oxidation Using Pt1/FeOx. *Nat. Chem* 3, 634–641. doi:10.1038/nchem.1095

Roy, D., Navarro-Vazquez, A., and Schleyer, P. v. R. (2009). Modeling Dinitrogen Activation by Lithium: A Mechanistic Investigation of the Cleavage of N2 by Stepwise Insertion into Small Lithium Clusters. *J. Am. Chem. Soc.* 131, 13045–13053. doi:10.1021/ja902980j

Seh, Z. W., Kibsgaard, J., Dickens, C. F., Chorkendorff, I., Nørskov, J. K., and Jaramillo, T. F. (2017). Combining Theory and experiment in Electrocatalysis: Insights into Materials Design. *Science* 355, eaad4998. doi:10.1126/science.aad4998

Sellmann, D., and Sutter, J. (1997). In Quest of Competitive Catalysts for Nitrogenases and Other Metal Sulfur Enzymes. *Acc. Chem. Res.* 30, 460–469. doi:10.1021/ar960158h

Shi, H., and Jacobi, K. (1992). Evidence for Physisorbed N2 in the Monolayer on Ru(001) at 40 K. *Surf. Sci.* 278, 281–285. doi:10.1016/0039-6028(92)90664-r

Song, R., Yang, J., Wang, M., Shi, Z., Zhu, X., Zhang, X., et al. (2021). Theoretical Study on P-Coordinated Metal Atoms Embedded in Arsenene for the Conversion of Nitrogen to Ammonia. *ACS omega* 6, 8662–8671. doi:10.1021/acsomega.1c00581

Stüeken, E. E., Buick, R., Guy, B. M., and Koehler, M. C. (2015). Isotopic Evidence for Biological Nitrogen Fixation by Molybdenum-Nitrogenase from 3.2 Gyr. *Nature* 520, 666–669. doi:10.1038/nature14180

Tanabe, Y., and Nishibayashi, Y. (2016). Catalytic Dinitrogen Fixation to Form Ammonia at Ambient Reaction Conditions Using Transition Metal-Dinitrogen Complexes. *Chem. Rec.* 16, 1549–1577. doi:10.1002/tcr.201600025

Tang, W., Sanville, E., and Henkelman, G. (2009). A Grid-Based Bader Analysis Algorithm without Lattice Bias. *J. Phys. Condens. Matter* 21, 084204. doi:10.1088/0953-8984/21/8/084204

Wang, A., Li, J., and Zhang, T. (2018). Heterogeneous Single-Atom Catalysis. *Nat. Rev. Chem.* 2, 65–81. doi:10.1038/s41570-018-0010-1

Yan, H., Zhao, X., Guo, N., Lyu, Z., Du, Y., Xi, S., et al. (2018). Atomic Engineering of High-Density Isolated Co Atoms on Graphene with Proximal-Atom Controlled Reaction Selectivity. *Nat. Commun.* 9, 3197–3199. doi:10.1038/s41467-018-05754-9

Yan, X., Liu, D., Cao, H., Hou, F., Liang, J., and Dou, S. X. (2019). Nitrogen Reduction to Ammonia on Atomic-Scale Active Sites under Mild Conditions. *Small Methods* 3, 1800501. doi:10.1002/smtd.201800501

Yang, X.-F., Wang, A., Qiao, B., Li, J., Liu, J., and Zhang, T. (2013). Single-Atom Catalysts: A New Frontier in Heterogeneous Catalysis. *Acc. Chem. Res.* 46, 1740–1748. doi:10.1021/ar300361m

Zhao, J., and Chen, Z. (2017). Single Mo Atom Supported on Defective boron Nitride Monolayer as an Efficient Electrocatalyst for Nitrogen Fixation: a Computational Study. *J. Am. Chem. Soc.* 139, 12480–12487. doi:10.1021/jacs.7b05213

frontiers
in Materials

Check for updates

Data-Driven Discovery of 2D Materials for Solar Water Splitting

Abhishek Agarwal, Sriram Goverapet Srinivasan* and Beena Rai

TCS Research, Tata Consulatncy Services Ltd., Pune, India

Hydrogen economy, wherein hydrogen is used as the fuel in the transport and energy sectors, holds significant promise in mitigating the deleterious effects of global warming. Photocatalytic water splitting using sunlight is perhaps the cleanest way of producing the hydrogen fuel. Among various other factors, widespread adoption of this technology has mainly been stymied by the lack of a catalyst material with high efficiency. 2D materials have shown significant promise as efficient photocatalysts for water splitting. The availability of open databases containing the "computed" properties of 2D materials and advancements in deep learning now enable us to do "inverse" design of these 2D photocatalysts for water splitting. We use one such database (Jain et al., ACS Energ. Lett. 2019, 4, 6, 1410–1411) to build a generative model for the discovery of novel 2D photocatalysts. The structures of the materials were converted into a 3D image–based representation that was used to train a cell, a basis autoencoder and a segmentation network to ascertain the lattice parameters as well as position of atoms from the images. Subsequently, the cell and basis encodings were used to train a conditional variational autoencoder (CVAE) to learn a continuous representation of the materials in a latent space. The latent space of the CVAE was then sampled to generate several new 2D materials that were likely to be efficient photocatalysts for water splitting. The bandgap of the generated materials was predicted using a graph neural network model while the band edge positions were obtained *via* empirical correlations. Although our generative modeling framework was used to discover novel 2D photocatalysts for water splitting reaction, it is generic in nature and can be used directly to discover novel materials for other applications as well.

Keywords: generative modeling, variational autoencoder, inverse design, photocatalysts, water splitting reaction

INTRODUCTION

Hydrogen as an alternate fuel and energy carrier has the potential to substantially mitigate carbon emissions for a green and sustainable future (Turner, 2004). Since it is not naturally available in free form for large scale applications, hydrogen is produced synthetically through a variety of processes (Sigfusson, 2007). Photocatalytic/photoelectrochemical splitting of water using sunlight, a suitable photocatalyst, water, and renewable electricity is perhaps the environmentally most benign method to produce hydrogen at scale (Edwards et al., 2007). Ever since the demonstration of solar water splitting by Fujishima and Honda (1972) using TiO_2 electrodes, enormous amount of efforts has been put in identifying new photocatalysts. Various materials, such as metal oxides, nitrides, sulfides, oxysulfides, oxynitrides, and Z-scheme materials, have been developed with enhanced efficiencies for solar water splitting. A detailed overview of these developments and the progress made in the field has been documented in several excellent review articles (Osterloh, 2008; Kudo and Miseki, 2009;

Maeda and Domen, 2010; Osterloh and Parkinson, 2011; Tachibana et al., 2012; Hisatomi et al., 2014; Ahmad et al., 2015; Zou and Zhang, 2015; Moniruddin et al., 2018; Prasad, 2020). The emergence of 2D materials, heralded by the discovery of graphene (Novoselov et al., 2004), has added a new dimension in the search of efficient photocatalysts. In addition to stability and suitable electronic structure, these materials provide a large surface to volume ratio, higher charge carrier mobility, and reduced recombination rates, all of which aid in enhancing the reaction rates at the photocatalyst surface (Li et al., 2017). Various 2D materials, mostly chalcogenides such as SnS and SnSe (Sun et al., 2014), CdS (Xu et al., 2013), WS_2 (Voiry et al., 2013), SnS_2 (Sun et al., 2012), and MoS_2 (Maitra et al., 2013) have been synthesized and shown to have enhanced photocatalytic performance.

With rapid advancements in first principles methods and computational power, in-silico design/screening of materials has emerged as a promising alternative method to narrow the search space of novel functional materials (Agrawal and Choudhary, 2016). For instance, high-throughput density functional theory (DFT) calculations have been used to identify oxynitrides (Wu et al., 2013), perovskites (Castelli et al., 2012a; Castelli et al., 2012b), and chalcogenides (Zhuang and Hennig, 2013a; Zhuang and Hennig, 2013b; Singh et al., 2015) as potential photocatalysts for water splitting. Properties of a vast number of materials computed in such high-throughput fashion using accurate first principles methods have been made openly available in repositories such as the Materials Project (MP) (Jain et al., 2013), the Open Quantum Materials Database (OQMD) (Saal et al., 2013), Automatic FLOW for materials discovery (AFLOW) (Curtarolo et al., 2012), and Novel Materials Discovery (NOMAD) (The NOMAD (Novel Materials Discovery) Center of Excellence (CoE), (2021)). While these repositories primarily contain data on bulk materials, two different datasets containing DFT-computed properties for 2D materials were also published recently (Haastrup et al., 2018; Zhou et al., 2019). Knowledge stored in these repositories has then been mined to screen materials for diverse applications (Zhang et al., 2018; Singh et al., 2019; Zhang et al., 2019). In addition, machine learning models have also been trained using data from these repositories to predict properties of novel materials (Ahmad et al., 2018; Xie and Grossman, 2018; Ye et al., 2018; Joshi et al., 2019; Liu et al., 2020). In a recent article, Sorkun et al. (2020) identified several potential 2D materials for photocatalytic water splitting, CO_2 reduction, and N_2 reduction by training AI models on the computational 2D materials database and using the predictions from these models to screen a vast chemical space obtained by systematic elemental substitution in 2D material prototypes.

An alternate approach to the high-throughput screening is to build unsupervised deep learning (DL) models that can learn the encodings of materials in a continuous latent space. This latent space could then be sampled to generate novel materials. When linked with one or more material property, such techniques can enable discovery of novel materials conditioned on certain properties (i.e., inverse design of functional materials). Variational autoencoder (VAE) (Kingma and Welling, 2019)

and generative adversarial network (GAN) (Goodfellow et al., 2014) are two of the most widely used generative models. VAEs use concepts of variational inference to learn the representation of input data by minimizing the reconstruction loss (formally called maximizing the log likelihood of observations) as well as divergence of the learned distribution from an assumed prior distribution (formally called Kullback-Leibler divergence) (Kingma and Welling, 2019). On the other hand, GANs use concepts from game theory to adversarially train a generative and a discriminative network. While the objective of the generative network is to fool the discriminator by generating realistic samples, the discriminator aims to correctly distinguish fake samples created by the generator from true samples (Goodfellow et al., 2014). Recently, both VAEs and GANs have been used for the generation of novel inorganic materials. In their iMatGen framework, Noh et al. (2019) used an image-based representation of crystal structures and trained a VAE to generate novel phases of vanadium oxides. While their model was restricted to only two element types (V and O), Hoffmann et al. (2019) introduced a generalization of this concept via inclusion of a segmentation network, to generate novel materials containing multiple types of elements. Court et al. (2020) used these concepts to build a conditional VAE for the generation of novel binary alloys, ternary perovskites, and Heusler compounds, all in cubic symmetry. Ren et al. (2020) used an invertible representation of crystal structures by a combination of descriptors in both real and reciprocal spaces and trained a VAE to generate novel thermoelectric materials. Long et al. (2020) and Kim et al. (2020) used GANs to discover a new crystal structure of the Bi-Se and Mg-Mn-O systems, respectively.

In this study, we have developed a generative modeling framework for the discovery of novel 2D materials as photocatalysts for water splitting. In comparison to prior works, our framework does not place any restriction on the structure or the stoichiometry of the materials. The bandgap of the generated materials was predicted using the CGCNN model (Xie and Grossman, 2018) while their band edge positions were computed using empirical correlations. Using this framework, we have discovered several novel 2D materials as potentially good photocatalyst for water splitting. While we have demonstrated the discovery of 2D photocatalysts as an application, our framework is generic enough to be applied for any kind of functional material discovery.

METHODS

Data Preparation and Representation

The dataset of 2D materials, to train our hierarchical generative model was obtained from the earlier published study of Jain et al. (2019). This dataset included data for all the materials that were included in earlier 2D materials' databases such as C2DB (Haastrup et al., 2018) and 2DMatPedia (Zhou et al., 2019) as well as the materials cloud (Mounet et al., 2018). Furthermore, properties such as the bandgap and energy above hull for all the materials were reported using a uniform level of theory, thereby
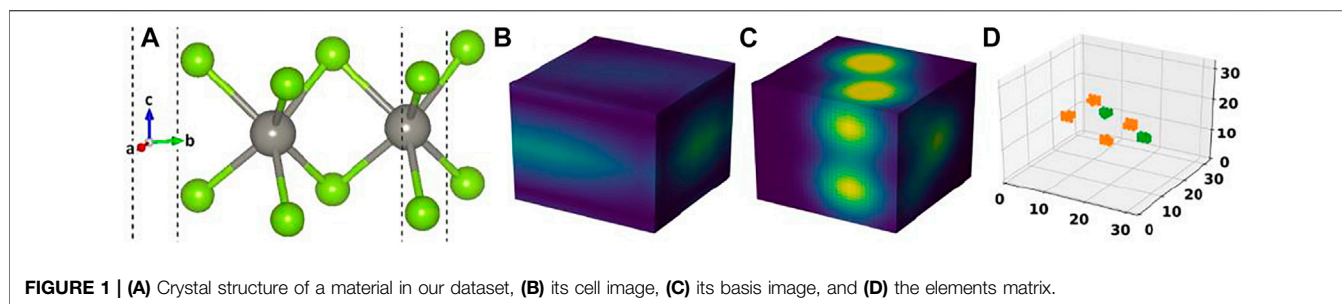
FIGURE 1 | (A) Crystal structure of a material in our dataset, **(B)** its cell image, **(C)** its basis image, and **(D)** the elements matrix.

providing us a consistent set of data to learn from. Around 7,500 unique 2D materials were present in the dataset whose structures were provided as *cif* files. These structures were converted to image-based representations which were subsequently used to train all our models.

In order to represent the crystal structures as images, we followed the same concept as proposed by Noh et al. (2019) in their iMatGen framework. Just as a crystal structure is construed as a "basis" of atoms in an underlying "lattice", each structure in our dataset was represented using a "cell" and a "basis" 3D image. Both the images had a dimension of $(32 \times 32 \times 32)$. The voxel values of the cell image were obtained using a Gaussian function as:

$$F_{ijk} = exp\left(\frac{-r_{ijk}^2}{2\sigma^2}\right), \qquad (1)$$

where r_{ijk} is the Euclidean distance between the center of the lattice and $(i, j, k)^{th}$ voxel. The basis image was generated using an atomic number weighted Gaussian transformation as described by Hoffmann et al. (2019). Concretely, the voxel values of the basis image were obtained as follows:

$$G_{ijk} = \frac{1}{\sigma^3 (2\pi)^{1.5}} \sum_l Z_l exp\left(\frac{-d\left(Z_l, (i,j,k)\right)^2}{2\sigma^2}\right), \qquad (2)$$

where Z_l is the atomic number at site "l" of the material, $d[Z_l, (i,j,k)]$ is the Euclidean distance between the site "l" and the $(i, j, k)^{th}$ voxel, and "σ" is the width of the Gaussian. We used a value of $\sigma = 1.0$, consistent with earlier works by Noh et al. (2019) and Hoffmann et al. (2019), since testing with lower values of σ resulted in larger errors. In contrast, Court et al. (2020) used the ionic radius of various elements for σ instead of a constant value. Prior to generating the basis image, the atoms in a material were translated such that their center of geometry lay at the center of a cube of length 10 Å. Together with the basis image, an elements matrix was also constructed to ascertain the positions and types of atoms from the basis image. The elements matrix had the same dimensionality as the basis image (i.e., $32 \times 32 \times 32$). The voxel values of the "elements matrix" were assigned as:

$$S_{ijk} = \begin{cases} Z_l \ if \ d\left(Z_l, (i,j,k)\right) \leq 0.5\text{Å} \\ 0 \ otherwise \end{cases}. \qquad (3)$$

Use of a larger value for the cutoff (larger than 0.5Å) would result in an overlap of nearby atoms, thereby rendering unique assignment of

atomic numbers to voxels difficult. On the other hand, the use of a smaller value of the cutoff would result in too few voxels (or data) having non-zero values among the $32 \times 32 \times 32$ voxels, making it difficult for the segmentation network to correctly identify atoms. **Figure 1** shows a representative crystal structure from our dataset, its cell and basis images and the corresponding elements matrix. In order to ensure that the generated images had adequate resolution to faithfully represent a crystal structure as well as limit the memory requirement, we only considered those materials from our dataset whose lattice dimensions along the basal plane directions as well the slab thickness were not more than 10 Å each. The resulting dataset had a total of about 6,300 structures. This dataset was augmented by creating supercells as well as applying random translations and rotations to the crystal structures to ensure that each element was represented in at least 3,000 structures. Overall, this augmentation resulted in a dataset containing about 0.2 million structures which was split in a 90:10 ratio for train and test.

Deep Learning Model and Network Architecture

We constructed a two-step hierarchical deep learning model like the iMatGen framework (Noh et al., 2019) to learn the representations of the 2D materials in our dataset and to generate novel materials by sampling from learned continuous representations. The first step of the model consisted of training a cell and basis autoencoder as well as a segmentation network for identification of atomic positions and corresponding element types from the basis image and the elements matrix. Both the autoencoders were constructed as 3D convolutional neural networks (3D CNNs). The encoder of the cell autoencoder consisted of four 3D convolutional layers while the decoder used four 3D convolution transpose layers (i.e., a mirror image of the encoder). Similarly, the encoder of the basis autoencoder consisted of four 3D convolutional layers followed by a fully connected layer. However, the decoder used upsampling instead of 3D convolution transpose. The dimensions of cell and basis encoding vectors (i.e., the autoencoder bottleneck dimension) were 128 and 256, respectively. While training, mean squared error (MSE) was used as the loss function. The detailed architecture of cell and basis autoencoders is shown in **Figures 2**, **3**, respectively.

After training of the basis autoencoder, the segmentation network [a 3D attention U-net model (Oktay et al., 2018)] was trained independently using the reconstructed basis images (i.e., images obtained as the output from the decoder of the basis autoencoder) to identify location and types of elements at that location as atomic
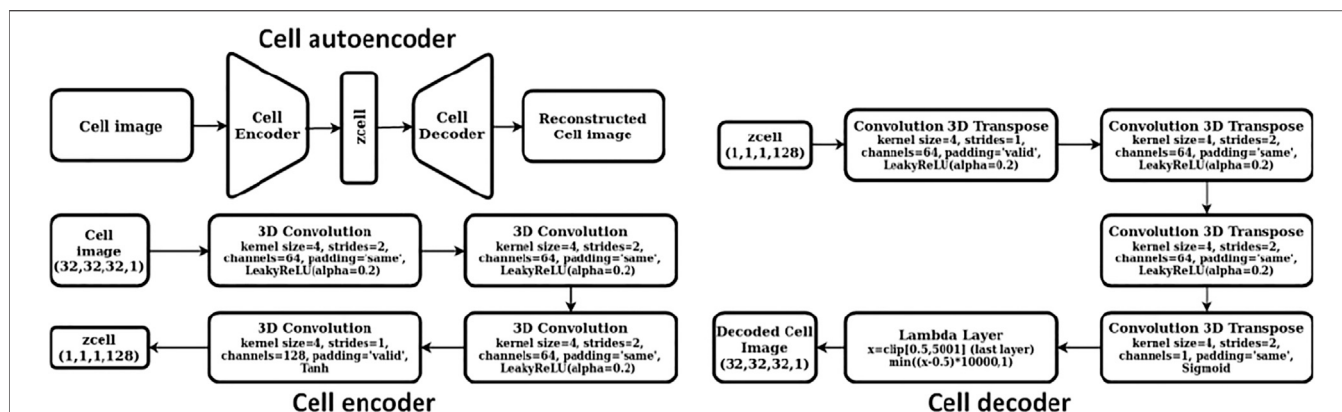
FIGURE 2 | Architecture of the cell autoencoder.
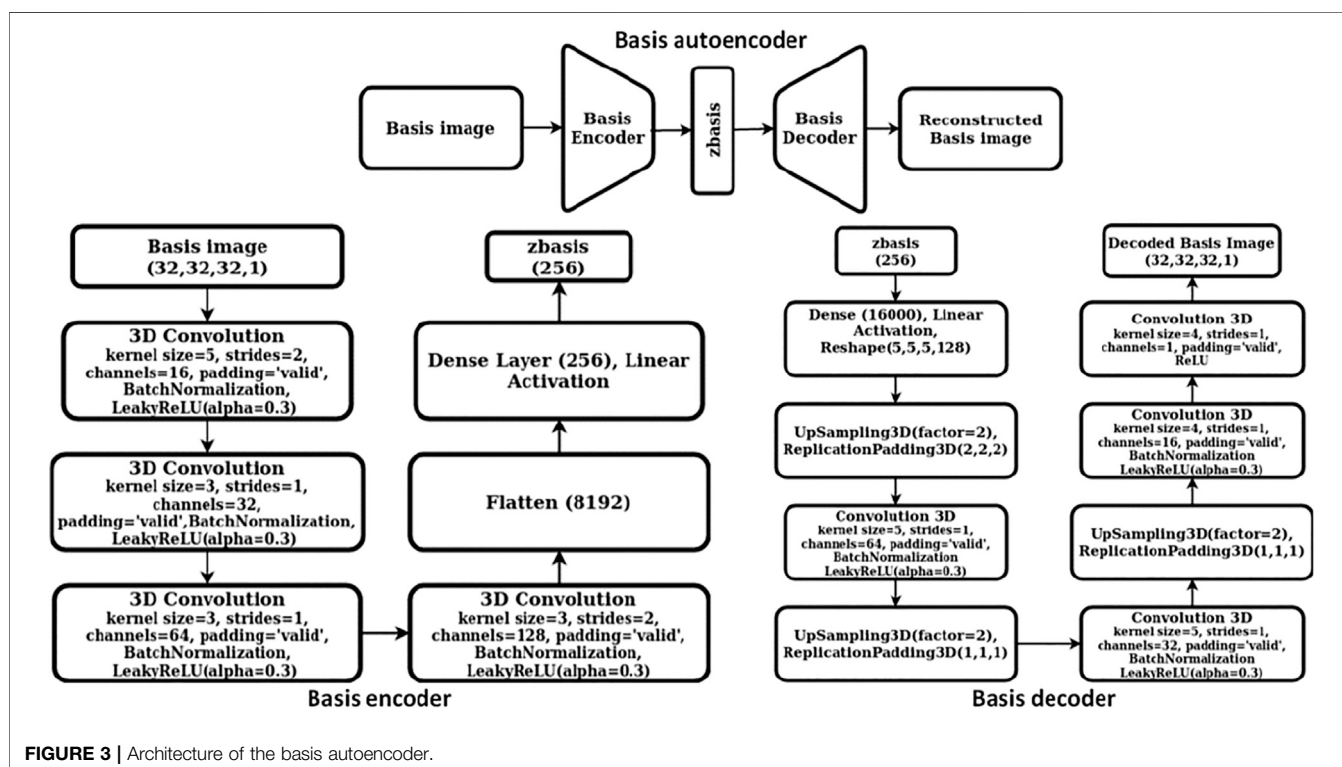
FIGURE 3 | Architecture of the basis autoencoder.

clusters. This contrasts with the study of Hoffmann et al. (2019) who trained their segmentation network together with the basis autoencoder in an end-to-end fashion to identify the locations of atoms in a material. The elements matrix prepared earlier for each structure was converted into a species matrix via one hot encoding into 95 classes at each grid point. Of these 95 classes, one class represented the background (or vacuum) while the other 94 classes corresponded to different elements. If a particular element type was present at a grid point of the elements matrix, its corresponding class was set to 1 while the rest of the values of the one hot vector remained as zeros. Thus, for each material, the ground truth to train the segmentation network was a species matrix of dimension ($32 \times 32 \times$

32×95). The binary cross entropy (BCE) loss was used while training the segmentation network.

In the second step of our hierarchical model, we trained a generative model to obtain a continuous representation of the 2D materials that can be sampled to discover novel materials. Thermodynamic stability and the presence of a bandgap are two necessary conditions that any 2D material must satisfy to qualify as a potential photocatalyst for water splitting reaction. As a thumb rule, we considered a material in our database to be stable if its energy above the hull (e_hull) value was less than 150 meV per atom. Thus, the materials in our training dataset were classified into four categories as shown in **Table 1**.

TABLE 1 | Classification of the 2D materials in our dataset into four different classes based on their bandgap and energy above the hull values.

Condition	One hot encoding	Category
1) Gap > 0 eV, e-hull <= 0.15 eV/atom	(1,0,0,0)	Nonmetal, stable
2) Gap = 0 eV, e-hull <= 0.15 eV/atom	(0,1,0,0)	Metal, stable
3) Gap > 0 eV, e-hull > 0.15 eV/atom	(0,0,1,0)	Non-metal, unstable
4) Gap = 0 eV, e-hull > 0.15 eV/atom	(0,0,0,1)	Metal, unstable

FIGURE 4 | CVAE network architecture.
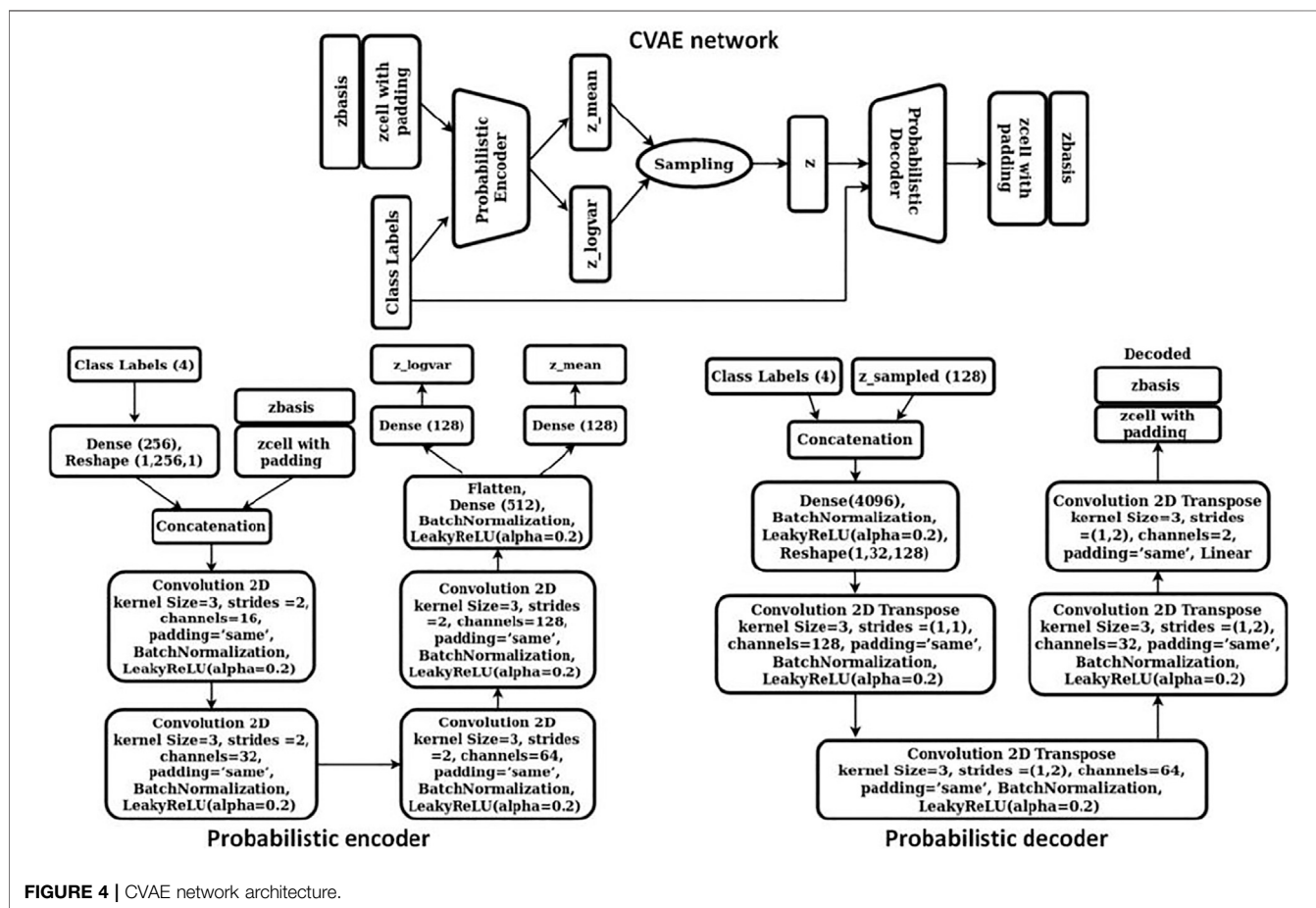
The objective of our study was to discover novel 2D materials belonging to class 1) (i.e., thermodynamically stable with a finite electronic bandgap) so that potential photocatalysts for water splitting reaction could be identified. Accordingly, a conditional variational autoencoder (CVAE) was chosen as our generative model so that, while sampling the latent space for new materials, control could be exerted over the class of material to be generated (i.e., material belonging to class 1) described above). Our CVAE model was trained using the cell and basis encodings from the previous step (step 1) together with the one hot encoded class vectors. Cell encodings were padded with zeros such that both the cell and basis encodings were 256-dimension vectors. Subsequently, these were scaled using the normal quantile transformer with 1000

quantiles. The four dimensional one-hot encoded vector was connected to a 256 dimension hidden layer so that the cell, basis, and the class encodings were all 256 dimensional vectors. These vectors were then concatenated as "channels" so that each training data was now represented by a (256 × 3) dimension image. The CVAE network comprised of a probabilistic encoder and a probabilistic decoder. We represented both the encoder and the decoder *via* 2D CNNs. The detailed architecture of our CVAE model is shown in **Figure 4**.

The probabilistic encoder encoded the input into a distribution with mean μ and standard deviation σ. A latent vector was then sampled from this distribution using the reparameterization trick, $z = \mu + \varepsilon * \sigma$, where ε is a random variable from a normal distribution. This

vector was passed through the probabilistic decoder to obtain the cell and basis encodings as the output. To train CVAE, we implemented optimal σ-VAE variant, a simple and effective methodology suggested by Rybkin et al. (2020), that did not require tuning the weight on the KL divergence term of the objective function as hyperparameter. The implementation automatically balances the two terms of CVAE objective function, namely, reconstruction loss (or MSE) and KL-divergence. The objective function for our CVAE network was defined as:

$$L_{CVAE} = Dln\sigma + \frac{D}{2\sigma^2} MSE(\hat{x}, x) + D_{KL}(q(z|x)\|(p(z)), \quad (4)$$

where D is dimensionality of the input (x), D_{KL} is the KL divergence, q (z|x) is the encoding distribution, p(z) is the prior distribution (chosen as a normal distribution with zero mean and unit standard deviation), and σ is the weighting parameter to balance the KL-divergence and MSE terms.

Bandgap and Band Edge Positions of 2D materials

The bandgap of a material and its band edge positions must be of appropriate values for a material to be a potentially good photocatalyst for water splitting. While DFT has been the method of choice to compute these properties of a material, several DL models with good accuracy have been reported recently that are well suited for rapid screening of novel materials. We used the CGCNN model (Xie and Grossman, 2018) to predict the bandgaps of the materials obtained from our model. The weights of the CGCNN model were retrained using our 2D materials dataset. Since data augmentation of the aforementioned kind is irrelevant for graph-based models, we considered only those materials from the original dataset that had a non-zero bandgap. The bandgap predicted from the trained CGCNN model was used to compute the band edge positions using the empirical equations given below:

$$E_{CB}^0 = \omega(X) - E_{SHE} - \frac{1}{2}E_g, \quad (5)$$

$$E_{VB}^0 = \omega(X) - E_{SHE} + \frac{1}{2}E_g, \quad (6)$$

$$\omega(X) = \sqrt[N]{X_1^a X_2^b X_3^c \dots X_n^q}, \quad (7)$$

where E_{CB}^0 and E_{VB}^0 are the conduction and valence band edge energies, E_g is the bandgap predicted by the CGCNN model, E_{SHE} is the absolute electrode potential of the standard hydrogen electrode (= 4.4 V), and X_i is the electronegativity of the constituent elements in a material while $a,b,c..q$ are there number of each of these elements in the materials' unit cell. "ω" is the geometric mean of the electronegativities of the constituent elements in a material.

RESULTS

Deep Learning Model Training

A two-step hierarchical DL model using an image-based representation of materials was developed to discover novel 2D materials as potential photocatalysts for water splitting reaction. The first step of the model consisted of autoencoders and a segmentation network to encode the cell and basis images and ascertain the location and types of atoms from the basis images. The subsequent step used the cell and basis encodings together with a conditional property vector to obtain a continuous latent space encoding of the 2D materials using a CVAE. This latent space could be sampled to generate novel 2D materials whose bandgaps and band edge positions were predicted using a reparametrized CGCNN model and empirical correlations, respectively. While the usual practice of training these DL models initializes the weights of the networks to random values, we used a more "informed" initial guess by pretraining these networks on the data from the Materials Project (MP) database (Jain et al., 2013). Details of the dataset used for this pretraining as well as all the model hyperparameters are provided in **Supplementary Tables S1, S2** of the supplementary material. We first present the training results for individual models and then present the error metrics upon execution of the entire pipeline.

Table 2 provides a summary of the test set error after training our individual DL models from the first step on the 2D materials dataset. For the cell and basis autoencoders, the MSE and MAE correspond to the error incurred in reconstructing the input images while for the segmentation network, the MAE corresponds to the error in reproducing the species matrix. Clearly, we see that the networks were able to accurately reconstruct the cell and basis images. **Figure 5** compares a 2D-slice from the input 3D cell image for a material in our test set as well as the corresponding reconstructed image produced by the cell autoencoder.

While the autoencoders learned to reconstruct the images well, the cell parameters of the materials (i.e., the cell lengths and angles) themselves were obtained from the output of the cell autoencoder (i.e., the decoded cell image) by feeding the voxel values to the inverse of the Gaussian function that was used to construct the cell images originally. **Table 3** lists the reconstruction errors in the cell parameters. Firstly, we observed that the intrinsic error (i.e., the error in transforming the lattice parameters to the cell image and back calculating the lattice parameters from the constructed image) in the cell image representation was zero, suggesting that the lattice to image transformation was perfect. Secondly, we observed that the error in cell lengths and angles obtained upon inverting the output image from the cell autoencoder was also very small, suggesting that the learned cell encodings represented the cell images well.

In comparison to cell parameters, obtaining the atomic positions from the output of basis autoencoder and segmentation network required a multi-step post processing. Firstly, the output of segmentation network was converted to elements matrix using the argmax function on one-hot encoded species matrix. This assigned atomic numbers to each site in the elements matrix. Then clusters of atoms were found from the elements matrix using the skimage package (Van der Walt et al., 2014). Finally, positions of the atoms were assigned as the centroids of clusters while the type of atom at that location (i.e. the atomic number) was assigned based on majority voting among sites belonging to that cluster. The error in the atomic position was obtained by computing the distance between the predicted atom "i" in the output element matrix and the nearest

TABLE 2 | Test set errors in the cell and basis autoencoder and the segmentation network after training these models on the 2D materials dataset.

	Mean squared error (MSE)	Mean absolute error (MAE)
Cell autoencoder	3.17×10^{-8}	8.32×10^{-6}
Basis autoencoder	1.99×10^{-4}	6.59×10^{-3}
—	Binary cross entropy loss (BCE)	Mean Absolute Error (MAE)
Segmentation network	3.60×10^{-5}	2.17×10^{-5}
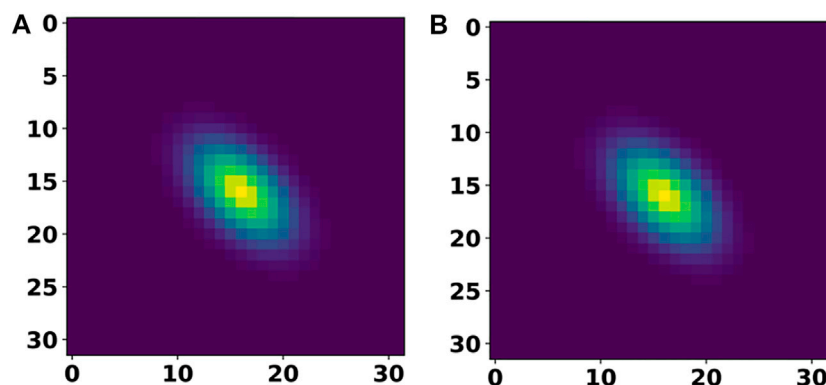
FIGURE 5 | A 2D slice of the input cell image **(A)** and its comparison with the corresponding 2D slice from the reconstructed (output of cell autoencoder) cell image **(B)**.

TABLE 3 | Reconstruction error in the cell parameters for 2D materials.

	Δa (Å)	Δb(Å)	$\Delta \alpha$(°)	$\Delta \beta$(°)	$\Delta \gamma$(°)
Intrinsic	0.00	0.00	0.00	0.00	0.00
Test set	0.04	0.04	0.70	0.61	0.87

true atom "j" in the original element matrix (i.e., ground truth) of that material. **Figure 6A** shows the test set predictions from the segmentation network as a parity plot between the predicted vs. true number of atoms while **Figure 6B** shows a parity plot between the predicted vs. true atom types for those materials predicted to have correct number of atoms. Clearly, from **Figure 6** and the loss values mentioned in **Table 2**, it can be inferred that the networks were able to closely reconstruct the materials in the test set.

Further analysis of these predictions revealed that for 87.7% of materials in the test set, the basis autoencoder and segmentation network was able to predict the correct number of atoms as well as material composition with a very small RMSE of 0.06 Å in the atomic positions. Such good accuracy of the basis autoencoder and segmentation network can also be gleaned from **Figure 7** which shows a 2D slice of an input and reconstructed basis images of a material from the test set as well as the corresponding elements matrices.

Having trained the cell, basis autoencoders and the segmentation network, we next trained the generative model

(CVAE) with the cell and basis encodings, one hot property vector as the inputs. Once again, pretrained weights from the MP dataset were taken as the initial guess for the CVAE model. The main objective of this study being the discovery of novel 2D materials for photocatalytic water splitting, it was essential that the learned latent space be smooth and continuous for generating realistic materials. The kernel density estimate (KDE) plot in **Figure 8** shows that the 128-dimensional latent space was mostly smooth and continuous and approximately followed a unit Gaussian profile. This is further elucidated by the tSNE plot (Van der Maaten and Hinton, 2008) shown in **Supplementary Figure S1** of the supplementary material, which shows a uniform distribution of the latent space encodings. Note that unlike conventional autoencoders, the CVAE latent space is not expected to be segregated into different regions based on the class of material since every sampling produces an instance of a material of a particular class (Atienza, 2018). The average mean and variance of the latent vectors were found to be 10^{-3} and 0.99, respectively. The test set KL loss was 1.97, while the reconstruction loss was 0.014.

After training the individual models, we ran the entire two-step generative model pipeline to obtain the errors in our test set prediction upon end-to-end execution. The cell and basis encodings of the test set materials obtained from the respective autoencoders together with their appropriate one hot encoded property values were passed through the CVAE
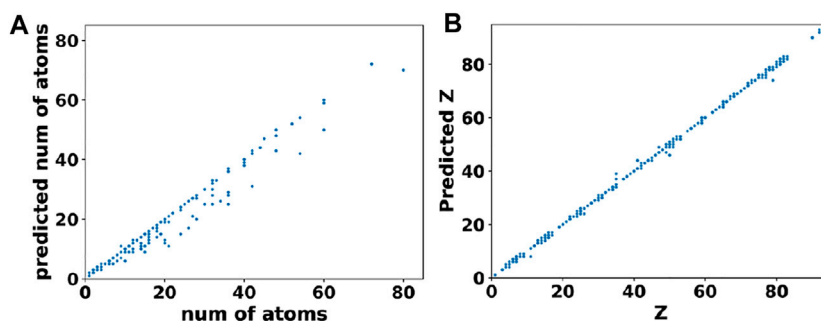
FIGURE 6 | Performance of the segmentation network. **(A)** Predicted vs. true number of atoms in materials from the test set. **(B)** Predicted vs. true atomic numbers of atoms in those materials that were predicted to have the correct number of atoms.
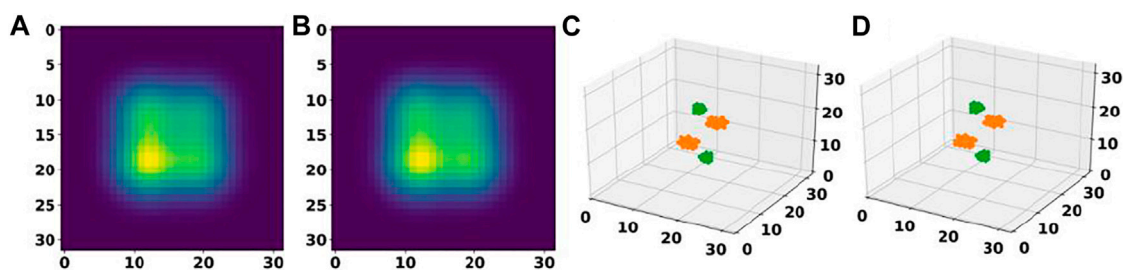
FIGURE 7 | Performance of a basis autoencoder and a segmentation network. **(A)** and **(B)** panels show a 2D slice of the input and reconstructed basis images for a material from the test set, respectively. **(C)** and **(D)** panels show the corresponding input and output elements matrices, respectively.
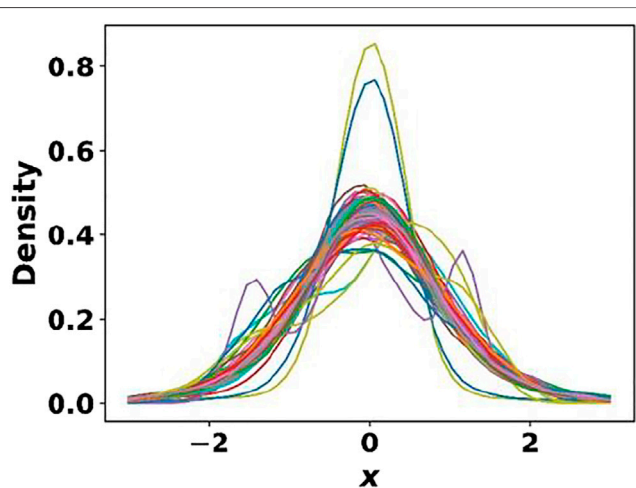
FIGURE 8 | Kernel density estimate plot for the 128-dimensional CVAE latent space. The learned latent space was mostly smooth and continuous and approximately followed a unit Gaussian.

network. The output cell and basis encodings from the CVAE network were passed through the decoders of the respective autoencoders. The output cell images were then inverted to obtain the cell parameters, while the output basis images were

segmented to obtain the positions of atoms in each material. Analysis of the results revealed that for 93.8% of the materials, the pipeline was able to predict the correct number of atoms. Among those materials predicted to have the correct number of atoms, 51% of materials were predicted to have the correct stoichiometry. For 22.4% of materials, the largest deviation in the atomic number of any atom constituting the material was within ±2. 26.6% of materials and had larger than ±2 deviation in the predicted atomic numbers. When all the test set materials were included, the errors in the lattice parameters were 0.07 Å in "a" and "b" cell lengths, 0.85°, 0.86°, and 1.13° in the α, β, and γ cell angles, respectively. These values reduced to 0.05Å and 0.06Å for "a", "b" cell lengths and 0.73°, 0.72°, and 0.93° for α, β, and γ cell angles, respectively, when only those materials in the test set with correctly reconstructed stoichiometry were considered. While the accuracy in reconstructing the lattice and basis of the materials slightly reduced upon end-to-end execution of the pipeline, they are comparable to those reported by Hoffmann et al. (2019).

Finally, to predict the bandgap of the generated materials, we reparameterized the CGCNN model with our 2D dataset. Use of the network weights directly from the original CGCNN model resulted in a large MAE in the bandgap of 0.727 eV. To reduce the prediction error, we retrained the network beginning with the original CGCNN model weights as the initial guess. A dropout of 0.5 was introduced after the pooling layer of the model to prevent

overfitting. The trained model gave a test set MAE of 0.567 eV. While this error is smaller than the original model error of 0.727 eV on our dataset, it is still larger than the CGCNN model error of 0.388 eV reported for bulk materials (Xie and Grossman, 2018). Nevertheless, owing to the generalizability of the model as well as rapid prediction of bandgaps, we used this model to predict the bandgaps of the generated materials.

Generation of Novel 2D Materials

The trained DL models were used to generate novel 2D materials by sampling from the CVAE latent space. While the latent space can be sampled in several different ways, we chose to explore the space around the encodings of the materials belonging to class 1 in our training set (i.e., thermodynamically stable and non-metal) so that the generated materials are likely to share the characteristics of the pivot material. Specifically, for each of the 1000 randomly chosen materials belonging to class 1 in our model training set, we drew 100 samples from a normal distribution of the form $N(\mu_{pivot}, 0.1)$, where μ_{pivot} was the mean of the distribution learned by the CVAE for the pivot material (i.e., the material in the training set). The sample drawn from the normal distribution was then passed through the probabilistic decoder of the CVAE and subsequently through the cell and basis autoencoders to get the respective images. The lattice and atomic basis of the materials were obtained from these images as described earlier. After constructing the crystal structure, the materials were subjected to a set of post-processing steps to filter improbable structures as well as narrow our search space for photocatalysts. These steps were as follows:

1) Hydrogen atom position curation: Hydrogen atoms that were more than 1.8 Å away from atoms in the generated crystal structure were deemed "free" hydrogen atoms in vacuum, which were generated due to segmentation network errors. Such hydrogen atoms were deleted from the structure.
2) Bond distance–based filtering: Those materials in which the interatomic distance between any pair of atoms without hydrogen was less than 1.2 Å, were discarded. If an atom pair contained hydrogen atom, this distance threshold was set to 0.8 Å.
3) Number of elements–based filtering: We discarded those materials that contained more than four element types.

In all, ~45% of the sampled materials were discarded after the above screening procedure. The crystal structure of the remaining materials was passed through the CGCNN model to obtain an estimate of their bandgap. Finally, the obtained bandgap was used in empirical **equations 5–7** to obtain the position of the valence and conduction band edges. Analysis of the filtered materials firstly revealed that the sampling generated 411 materials with 73 unique compositions that were present in the test set, but not in the training set. Of these, the crystal structures of 42 materials closely matched with that in the test set. **Supplementary Table S3** in the supplementary material lists these compositions as well as the absolute deviations in the predicted lattice parameters and bond lengths from their true values. The crystal structures of the predicted materials ranged from simple metal halide structures (such as MoI$_2$, containing alternate layers of metal and halide

ions) to more complicated structures containing molecular species such as carbonates (e.g., MnC$_2$O$_6$) and phosphates (e.g., Mo$_2$P$_2$O$_{10}$). These results show that our model was able to generate not only realistic material compositions unseen by it during training but also closely predict their crystal structure, further emphasizing on the accuracy of model training and reliability of its predictions. In addition, the model was also able to suggest different phases (i.e., crystal structure) for a given material composition.

Having established the reliability of the trained model, we analyzed the filtered materials to search for novel 2D materials as potential water splitting catalysts. Attention was paid to those materials that were present neither in our training nor test set, so that the generated materials were truly novel. In addition to the material composition, the bandgap and the band edges of the material had to be in suitable ranges to qualify as a potential photocatalyst. Specifically, the bandgap of the material had to be between 1.6 and 3 eV, while the conduction and valence band edge had to lie below and above 0 eV and 1.23 eV, respectively. Such alignment of band edges ensures that the holes generated in the valence band upon photoexcitation are able to oxidize water [since they lie at a more positive potential than the water oxidation potential (= 1.23 V vs. SHE)] while the electrons populating the conduction band are able to reduce protons [since they lie at a more negative potential than the hydrogen evolution potential (= 0 V vs. SHE)]. Furthermore, we imposed a constraint of charge neutrality on the generated materials by assigning formal atomic charges corresponding to all the well-known oxidation states of each atom in a material. Then the charges on all the sites were summed up to ensure that at least one combination of oxidation states led to a net zero charge. Considering these aspects, our model generated about 150 new materials as potential photocatalysts for water splitting. A list of these materials, together with their bandgap, band edge positions, and lattice parameters are given in **Supplementary Table S4** of the supplementary material.

To further narrow this set down to a few tens of materials, we used a CGCNN-based model to classify the materials as stable vs. unstable using a more stringent criteria for e_above_hull ≤ 50 meV/atom. As before, the CGCNN model was pretrained on the MP dataset followed by training on the 2D materials data. Details of the model training and hyperparameters are provided in **Supplementary Table S5** of the supporting information. The test accuracy of the model was 0.87 while the area under the receiver operating characteristic curve (AUC curve) was 0.924. Subsequently, the ~150 materials identified above were passed through the classification network resulting in 19 materials that had a probability of >0.99 to belong to the stable class (i.e., e_above_hull ≤ 50 meV/atom). These 19 materials are listed at the beginning of **Supplementary Table S4** in bold while their structures are provided as *cif* files. From **Supplementary Table S4** we see that all the materials generated were either halides or oxides/chalcogenides apart from Ag$_2$PdN$_2$, LiRhN$_2$, and InRhN$_2$. This stems from the fact that halides were the dominant materials in the 2D materials dataset followed by oxides and chalcogenides. Furthermore, analysis of the e_above_hull values of the materials in class 1 of the dataset revealed that the mean value was 47 meV/atom for halides while

it was 69 meV/atom for oxides. Consistently, all 19 shortlisted materials were seen to be halides.

Visualization of the structure of these 19 materials revealed that they belonged to a few different structural prototypes. $Ce_2N_2I_2$, $Dy_2S_2Cl_2$, $Lu_2S_2Cl_2$, $Tm_2S_2Br_2$, and $W_2P_2Cl_2$ had a BiOCl oxyhalide-like orthorhombic structure with each metal ion coordinated to 4 S/P/N atoms which were in turn coordinated to four metal ions. The halide ion occupied the hollow site above the metal ions. Other halides such as LuClI, LuSeCl, LuSCl, and RePBr adopted the $2H$-MoS_2-like hexagonal structure while InSCl adopted the $1T$-MoS_2-like structure. In both cases, each metal ion was coordinated to six anions, and each anion was coordinated to three metal ions. It must be noted that both BiOCl (Faraji et al., 2019) and MoS_2 (Li et al., 2013) depicted excellent photocatalytic activity for water splitting reaction themselves. Given that these newly generated materials display favorable bandgap and band edge positions, high confidence of being thermodynamically stable and adopting a structure similar to known photocatalysts, they could perhaps be considered as new targets for synthesis and evaluation.

$Ce_2Se_2Br_4$, $Nb_2S_4Cl_2$, $ScTiCl_6$, $CeNdBr_6$, $NdTbBr_6$, and $PrNdCl_6$ had a metal trihalide-like structure, with the former three adopting a BiI_3-like trigonal structure and the latter three adopting an $NdBr_3$-like orthorhombic structure. Earlier reports have shown that metal trihalides depicted interesting magnetic behavior and could potentially be used in magnetic and spintronic applications (McGuire, 2017; Tomar et al., 2019). Thus, in addition to photocatalysts, these newly generated materials could be studied for other interesting applications as well. Finally, GaSCl adopted an HgI_2-like structure with four coordinated metal ions and two coordinated anions while W_2CCl_2 adopted an MXene-like structure with chloride termination.

DISCUSSION

With rapid increase in computational power and advancements in AI algorithms, applications of generative models in synthesizing realistic data has widespread appeal in various fields. Application of these techniques in materials science holds significant promise for realizing in-silico design/discovery/screening of functional materials. In this study, we have demonstrated one such generative modeling approach for the discovery of novel 2D materials as photocatalysts for water splitting. Using an image-based representation of crystal structures, our two-step model first built cell and basis autoencoders to obtain a representation of these images in a lower dimensional space. The reconstructed images from the basis autoencoder were used to train a segmentation network so that the positions and types of atoms in a material could be ascertained. Next, a CVAE model was trained using the cell and basis encodings together with a conditional one hot property vector to obtain a continuous latent space that can be sampled to generate new materials. The bandgap of the generated materials was predicted using a reparameterized CGCNN model, which was then used to obtain their band edge positions via empirical relations. Evaluation of the model showed good accuracy in reconstructing materials from the test set. The latent space was then sampled to generate novel 2D materials by exploring the region around materials from the training set. An important metric of reliability for any generative model is its ability to produce realistic samples, which in our case is the crystal structure of known materials that were previously unseen by the model. To that end, our model was able to predict 73 different compositions that were present in the test set but not in the training set. Of these, the structures of 42 compounds matched closely with their true structures. Further analysis of the sampled materials gave several novel materials as potential photocatalysts for water splitting.

Our generative modeling framework is an advancement over other related models reported in the literature. While our model is conceptually similar to the iMatGen framework (Noh et al., 2019), the latter was restricted to predicting novel phases of vanadium oxides only. The use of atomic number weighted gaussians to construct the basis image together with segmentation allowed us to generalize the model to all crystal and atom types. While Court et al. (2020) used a somewhat similar approach in their model, lack of an explicit representation of the lattice precluded the application of their model to non-orthogonal systems. Furthermore, all these generative models hold an advantage over high-throughput virtual screening approaches such as those reported by Sorkun et al. (2020), since they possess the capability to not only identify new material compositions but also new phases for known material compositions. However, this in no way undermines the importance of high-throughput screening approaches. A large amount of data is usually required to build accurate generative models. In cases where such data is absent (which often happens in materials science), building shallow models with available data and using these models in high-throughput screening is perhaps the only viable approach to identifying novel materials.

Although our generative modeling framework showed good accuracy, admittedly, there is scope for improvement. For instance, the cell and basis accuracies deteriorated upon end-to-end execution of the full model owing to the reconstruction error of the CVAE network. Better performance of the VAE network could perhaps be achieved by using deep feature consistent (DFC) VAEs (Hou et al., 2017), as was demonstrated by Court et al. (2020). Instead of minimizing the pixel-to-pixel difference between the input and reconstructed images (via MSE loss), DFC-VAEs attempt to minimize the difference in the hidden representations between the two images (called feature perceptual loss), which eventually leads to a truer (less noisy) reconstruction of the input image. Accurate reconstruction of the cell and basis encodings would then reflect in better accuracies in cell parameters, atomic positions, and element types. Furthermore, while we suggested several novel 2D photocatalysts for water splitting reaction by sampling from thermodynamically stable class of non-metals, this screening has been entirely based on bandgap and band edge positions. In addition to these necessary conditions, low aqueous solubility, small exciton binding energies and recombination rates, and favorable surface reaction kinetics are some of the other necessary conditions for a viable 2D water splitting photocatalyst (Singh et al., 2015). Our study, as also other reports based on high-throughput screening, do not currently

incorporate these properties, primarily owing to the exorbitant cost associated with computing some of these quantities. Finally, any material designed in-silico gains relevance only when it is realized experimentally and displays anticipated properties. In the current era of big data, this calls for automated laboratories that could rapidly synthesize (or show otherwise) and characterize new materials. Such high-throughput experimentation when combined with data-based predictive models can significantly accelerate the discovery of novel functional materials. For instance, one could imagine a scenario in which our own generative modeling framework is trained in an active learning fashion by integrating with automated experimentation (*via* orchestration software such as ChemOS (Roch et al., 2018)). The generated materials could be rapidly evaluated in experiments and the outcome could be fed back to the training set so that the model can be improved iteratively. In our view, implementation of such frameworks could significantly help us move closer to realizing the vision of truly inverse design of materials.

DATA AVAILABILITY STATEMENT

The original contributions presented in the study are included in the article/**Supplementary Material**; further inquiries can be directed to the corresponding author.

REFERENCES

AUTHOR CONTRIBUTIONS

SGS and AA conceptualized the idea. AA implemented the generative modeling framework. SGS and AA jointly wrote the manuscript. All authors discussed the results, their implications, and reviewed the manuscript.

SUPPLEMENTARY MATERIAL

The Supplementary Material for this article can be found online at: https://www.frontiersin.org/articles/10.3389/fmats.2021.679269/full#supplementary-material

Agrawal, A., and Choudhary, A. (2016). Perspective: Materials Informatics and Big Data: Realization of the "Fourth Paradigm" of Science in Materials Science. *Apl Mater.* 4 (5), 053208. doi:10.1063/1.4946894

Ahmad, H., Kamarudin, S. K., Minggu, L. J., and Kassim, M. (2015). Hydrogen from Photo-Catalytic Water Splitting Process: A Review. *Renew. Sust. Energ. Rev.* 43, 599–610. doi:10.1016/j.rser.2014.10.101

Ahmad, Z., Xie, T., Maheshwari, C., Grossman, J. C., and Viswanathan, V. (2018). Machine Learning Enabled Computational Screening of Inorganic Solid Electrolytes for Suppression of Dendrite Formation in Lithium Metal Anodes. *ACS Cent. Sci.* 4 (8), 996–1006. doi:10.1021/acscentsci.8b00229

Atienza, R. (2018). *Advanced Deep Learning with Keras: Apply Deep Learning Techniques, Autoencoders, GANs, Variational Autoencoders, Deep Reinforcement Learning, Policy Gradients, and More.* Birmingham, United kingdom: Packt Publishing Ltd.

Castelli, I. E., Landis, D. D., Thygesen, K. S., Dahl, S., Chorkendorff, I., Jaramillo, T. F., et al. (2012). New Cubic Perovskites for One- and Two-Photon Water Splitting Using the Computational Materials Repository. *Energy Environ. Sci.* 5 (10), 9034–9043. doi:10.1039/c2ee22341d

Castelli, I. E., Olsen, T., Datta, S., Landis, D. D., Dahl, S., Thygesen, K. S., et al. (2012). Computational Screening of Perovskite Metal Oxides for Optimal Solar Light Capture. *Energ. Environ. Sci.* 5 (2), 5814–5819. doi:10.1039/c1ee02717d

Court, C. J., Yildirim, B., Jain, A., and Cole, J. M. (2020). 3-D Inorganic Crystal Structure Generation and Property Prediction via Representation Learning. *J. Chem. Inf. Model.* 60 (10), 4518–4535. doi:10.1021/acs.jcim.0c00464

Curtarolo, S., Setyawan, W., Wang, S., Xue, J., Yang, K., Taylor, R. H., et al. (2012). AFLOWLIB.ORG: A Distributed Materials Properties Repository from High-Throughput Ab Initio Calculations. *Comput. Mater. Sci.* 58, 227–235. doi:10.1016/j.commatsci.2012.02.002

Edwards, P. P., Kuznetsov, V. L., and David, W. I. F. (2007). Hydrogen Energy. *Phil. Trans. R. Soc. A* 365 (1853), 1043–1056. doi:10.1098/rsta.2006.1965

Faraji, M., Yousefi, M., Yousefzadeh, S., Zirak, M., Naseri, N., Jeon, T. H., et al. (2019). Two-dimensional Materials in Semiconductor Photoelectrocatalytic Systems for Water Splitting. *Energ. Environ. Sci.* 12 (1), 59–95. doi:10.1039/c8ee00886h

Fujishima, A., and Honda, K. (1972). Electrochemical Photolysis of Water at a Semiconductor Electrode. *nature* 238 (5358), 37–38. doi:10.1038/238037a0

Goodfellow, I. J., Pouget-Abadie, J., Mirza, M., Xu, B., Warde-Farley, D., Ozair, S., et al. (2014). *Generative Adversarial Networks.* arXiv preprint arXiv:1406.2661.

Haastrup, S., Strange, M., Pandey, M., Deilmann, T., Schmidt, P. S., Hinsche, N. F., and Thygesen, K. S. (2018). The Computational 2D Materials Database: High-Throughput Modeling and Discovery of Atomically Thin Crystals. *2D Mater.* 5 (4), 042002. doi:10.1088/2053-1583/aacfc1

Hisatomi, T., Kubota, J., and Domen, K. (2014). Recent Advances in Semiconductors for Photocatalytic and Photoelectrochemical Water Splitting. *Chem. Soc. Rev.* 43 (22), 7520–7535. doi:10.1039/c3cs60378d

Hoffmann, J., Maestrati, L., Sawada, Y., Tang, J., Sellier, J. M., and Bengio, Y. (2019). *Data-driven Approach to Encoding and Decoding 3-D crystal Structures.* arXiv preprint arXiv:1909.00949.

Hou, X., Shen, L., Sun, K., and Qiu, G. (2017).Deep Feature Consistent Variational Autoencoder. in 2017 IEEE Winter Conference on Applications of Computer Vision (WACV). IEEE, Santa Rosa, CA, March 24,2017 – March 31, 2017, 1133–1141.

Jain, A., Ong, S. P., Hautier, G., Chen, W., Richards, W. D., Dacek, S., et al. (2013). Commentary: The Materials Project: A Materials Genome Approach to Accelerating Materials Innovation. *APL Mater.* 1 (1), 011002. doi:10.1063/1.4812323

Jain, A., Wang, Z., and Nørskov, J. K. (2019). Stable Two-Dimensional Materials for Oxygen Reduction and Oxygen Evolution Reactions. *ACS Energ. Lett.* 4 (6), 1410–1411. doi:10.1021/acsenergylett.9b00876

Joshi, R. P., Eickholt, J., Li, L., Fornari, M., Barone, V., and Peralta, J. E. (2019). Machine Learning the Voltage of Electrode Materials in Metal-Ion Batteries. *ACS Appl. Mater. Inter.* 11 (20), 18494–18503. doi:10.1021/acsami.9b04933

Kim, S., Noh, J., Gu, G. H., Aspuru-Guzik, A., and Jung, Y. (2020). Generative Adversarial Networks for crystal Structure Prediction. *ACS Cent. Sci.* 6 (8), 1412–1420. doi:10.1021/acscentsci.0c00426

Kingma, D. P., and Welling, M. (2019). *An Introduction to Variational Autoencoders.* arXiv preprint arXiv:1906.02691. doi:10.1561/9781680836233

Kudo, A., and Miseki, Y. (2009). Heterogeneous Photocatalyst Materials for Water Splitting. *Chem. Soc. Rev.* 38 (1), 253–278. doi:10.1039/b800489g

Li, Y., Li, Y.-L., Araujo, C. M., Luo, W., and Ahuja, R. (2013). Single-layer MoS2 as an Efficient Photocatalyst. *Catal. Sci. Technol.* 3 (9), 2214–2220. doi:10.1039/c3cy00207a

Li, Y., Li, Y.-L., Sa, B., and Ahuja, R. (2017). Review of Two-Dimensional Materials for Photocatalytic Water Splitting from a Theoretical Perspective. *Catal. Sci. Technol.* 7 (3), 545–559. doi:10.1039/c6cy02178f

Liu, H., Cheng, J., Dong, H., Feng, J., Pang, B., Tian, Z., et al. (2020). Screening Stable and Metastable ABO3 Perovskites Using Machine Learning and the Materials Project. *Comput. Mater. Sci.* 177, 109614. doi:10.1016/j.commatsci.2020.109614

Long, T., Fortunato, N. M., Opahle, I., Zhang, Y., Samathrakis, I., Shen, C., et al. (2020). *CCDCGAN: Inverse Design of crystal Structures.* arXiv preprint arXiv:2007.11228.

Maeda, K., and Domen, K. (2010). Photocatalytic Water Splitting: Recent Progress and Future Challenges. *J. Phys. Chem. Lett.* 1 (18), 2655–2661. doi:10.1021/jz1007966

Maitra, U., Gupta, U., De, M., Datta, R., Govindaraj, A., and Rao, C. N. R. (2013). Highly Effective Visible-Light-Induced H2Generation by Single-Layer 1T-MoS2and a Nanocomposite of Few-Layer 2H-MoS2with Heavily Nitrogenated Graphene. *Angew. Chem. Int. Ed.* 52 (49), 13057–13061. doi:10.1002/anie.201306918

McGuire, M. (2017). Crystal and Magnetic Structures in Layered, Transition Metal Dihalides and Trihalides. *Crystals* 7 (5), 121. doi:10.3390/cryst7050121

Moniruddin, M., Ilyassov, B., Zhao, X., Smith, E., Serikov, T., Ibrayev, N., et al. (2018). Recent Progress on Perovskite Materials in Photovoltaic and Water Splitting Applications. *Mater. Today Energ.* 7, 246–259. doi:10.1016/j.mtener.2017.10.005

Mounet, N., Gibertini, M., Schwaller, P., Campi, D., Merkys, A., Marrazzo, A., et al. (2018). Two-dimensional Materials from High-Throughput Computational Exfoliation of Experimentally Known Compounds. *Nat. Nanotech* 13 (3), 246–252. doi:10.1038/s41565-017-0035-5

Noh, J., Kim, J., Stein, H. S., Sanchez-Lengeling, B., Gregoire, J. M., Aspuru-Guzik, A., et al. (2019). Inverse Design of Solid-State Materials via a Continuous Representation. *Matter* 1 (5), 1370–1384. doi:10.1016/j.matt.2019.08.017

Novoselov, K. S., Geim, A. K., Morozov, S. V., Jiang, D., Zhang, Y., Dubonos, S. V., et al. (2004). Electric Field Effect in Atomically Thin Carbon Films. *science* 306 (5696), 666–669. doi:10.1126/science.1102896

Oktay, O., Schlemper, J., Folgoc, L. L., Lee, M., Heinrich, M., Misawa, K., and Rueckert, D. (2018). *Attention U-Net: Learning where to Look for the Pancreas.* arXiv preprint arXiv:1804.03999.

Osterloh, F. E. (2008). Inorganic Materials as Catalysts for Photochemical Splitting of Water. *Chem. Mater.* 20 (1), 35–54. doi:10.1021/cm7024203

Osterloh, F. E., and Parkinson, B. A. (2011). Recent Developments in Solar Water-Splitting Photocatalysis. *MRS Bull.* 36 (1), 17–22. doi:10.1557/mrs.2010.5

Prasad, U. (2020). BiVO4-Based Photoanodes for Photoelectrochemical Water Splitting. *Clean. Energ. Mater.* 1364, 137–167. doi:10.1021/bk-2020-1364.ch005

Ren, Z., Noh, J., Tian, S., Oviedo, F., Xing, G., Liang, Q., and Buonassisi, T. (2020). *Inverse Design of Crystals Using Generalized Invertible Crystallographic Representation.* arXiv preprint arXiv:2005.07609.

Roch, L. M., Häse, F., Kreisbeck, C., Tamayo-Mendoza, T., Yunker, L. P., Hein, J. E., et al. (2018). ChemOS: Orchestrating Autonomous Experimentation. *Sci. Robotics* 3 (19). doi:10.1126/scirobotics.aat5559

Rybkin, O., Daniilidis, K., and Levine, S. (2020). *Simple and Effective VAE Training with Calibrated Decoders.* arXiv preprint arXiv:2006.13202.

Saal, J. E., Kirklin, S., Aykol, M., Meredig, B., and Wolverton, C. (2013). Materials Design and Discovery with High-Throughput Density Functional Theory: the Open Quantum Materials Database (OQMD). *Jom* 65 (11), 1501–1509. doi:10.1007/s11837-013-0755-4

Sigfusson, T. I. (2007). Pathways to Hydrogen as an Energy Carrier. *Phil. Trans. R. Soc. A.* 365 (1853), 1025–1042. doi:10.1098/rsta.2006.1960

Singh, A. K., Mathew, K., Zhuang, H. L., and Hennig, R. G. (2015). Computational Screening of 2D Materials for Photocatalysis. *J. Phys. Chem. Lett.* 6 (6), 1087–1098. doi:10.1021/jz502646d

Singh, A. K., Montoya, J. H., Gregoire, J. M., and Persson, K. A. (2019). Robust and Synthesizable Photocatalysts for CO 2 Reduction: a Data-Driven Materials Discovery. *Nat. Commun.* 10 (1), 1–9. doi:10.1038/s41467-019-08356-1

Sorkun, M. C., Astruc, S., Koelman, J. V. A., and Er, S. (2020). An Artificial Intelligence-Aided Virtual Screening Recipe for Two-Dimensional Materials Discovery. *npj Comput. Mater.* 6 (1), 1–10. doi:10.1038/s41524-020-00375-7

Sun, Y., Cheng, H., Gao, S., Sun, Z., Liu, Q., Liu, Q., et al. (2012). Freestanding Tin Disulfide Single-Layers Realizing Efficient Visible-Light Water Splitting. *Angew. Chem. Int. Ed.* 51 (35), 8727–8731. doi:10.1002/anie.201204675

Sun, Y., Sun, Z., Gao, S., Cheng, H., Liu, Q., Lei, F., et al. (2014). All-Surface-Atomic-Metal Chalcogenide Sheets for High-Efficiency Visible-Light Photoelectrochemical Water Splitting. *Adv. Energ. Mater.* 4 (1), 1300611. doi:10.1002/aenm.201300611

Tachibana, Y., Vayssieres, L., and Durrant, J. R. (2012). Artificial Photosynthesis for Solar Water-Splitting. *Nat. Photon* 6 (8), 511–518. doi:10.1038/nphoton.2012.175

The NOMAD (Novel Materials Discovery) Center of Excellence (CoE)(2021). Available at: https://nomad-coe.eu (last Accessed March 9, 2021).

Turner, J. A. (2004). Sustainable Hydrogen Production. *Science* 305 (5686), 972–974. doi:10.1126/science.1103197

Van der Maaten, L., and Hinton, G. (2008). Visualizing Data Using T-SNE. *J. machine Learn. Res.* 9 (11). 2579–2605.

Van der Walt, S., Schönberger, J. L., Nunez-Iglesias, J., Boulogne, F., Warner, J. D., Yager, N., and Gouillart, E. (2014). Scikit-Image: Image Processing in Python. *PeerJ* 2, e453. doi:10.7717/peerj.453

Voiry, D., Yamaguchi, H., Li, J., Silva, R., Alves, D. C. B., Fujita, T., et al. (2013). Enhanced Catalytic Activity in Strained Chemically Exfoliated WS2 Nanosheets for Hydrogen Evolution. *Nat. Mater* 12 (9), 850–855. doi:10.1038/nmat3700

Wu, Y., Lazic, P., Hautier, G., Persson, K., and Ceder, G. (2013). First Principles High Throughput Screening of Oxynitrides for Water-Splitting Photocatalysts. *Energ. Environ. Sci.* 6 (1), 157–168. doi:10.1039/c2ee23482c

Xie, T., and Grossman, J. C. (2018). Crystal Graph Convolutional Neural Networks for an Accurate and Interpretable Prediction of Material Properties. *Phys. Rev. Lett.* 120 (14), 145301. doi:10.1103/physrevlett.120.145301

Xu, Y., Zhao, W., Xu, R., Shi, Y., and Zhang, B. (2013). Synthesis of Ultrathin CdS Nanosheets as Efficient Visible-Light-Driven Water Splitting Photocatalysts for Hydrogen Evolution. *Chem. Commun.* 49 (84), 9803–9805. doi:10.1039/c3cc46342g

Ye, W., Chen, C., Dwaraknath, S., Jain, A., Ong, S. P., and Persson, K. A. (2018). Harnessing the Materials Project for Machine-Learning and Accelerated Discovery. *MRS Bull.* 43 (9), 664–669. doi:10.1557/mrs.2018.202

Zhang, X., Zhang, Z., Wu, D., Zhang, X., Zhao, X., and Zhou, Z. (2018). Computational Screening of 2D Materials and Rational Design of Heterojunctions for Water Splitting Photocatalysts. *Small Methods* 2 (5), 1700359. doi:10.1002/smtd.201700359

Zhang, Z., Zhang, X., Zhao, X., Yao, S., Chen, A., and Zhou, Z. (2019). Computational Screening of Layered Materials for Multivalent Ion Batteries. *ACS omega* 4 (4), 7822–7828. doi:10.1021/acsomega.9b00482

Zhou, J., Shen, L., Costa, M. D., Persson, K. A., Ong, S. P., Huck, P., et al. (2019). 2DMatPedia, an Open Computational Database of Two-Dimensional Materials from Top-Down and Bottom-Up Approaches. *Scientific data* 6 (1), 1–10. doi:10.1038/s41597-019-0097-3

Zhuang, H. L., and Hennig, R. G. (2013). Single-layer Group-III Monochalcogenide Photocatalysts for Water Splitting. *Chem. Mater.* 25 (15), 3232–3238. doi:10.1021/cm401661x

Zhuang, H. L., and Hennig, R. G. (2013). Computational Search for Single-Layer Transition-Metal Dichalcogenide Photocatalysts. *J. Phys. Chem. C* 117 (40), 20440–20445. doi:10.1021/jp405808a

Zou, X., and Zhang, Y. (2015). Noble Metal-free Hydrogen Evolution Catalysts for Water Splitting. *Chem. Soc. Rev.* 44 (15), 5148–5180. doi:10.1039/c4cs00448e

Tomar, S., Ghosh, B., Mardanya, S., Rastogi, P., Bhadoria, B. S., Chauhan, Y. S., et al. (2019). Intrinsic magnetism in monolayer transition metal trihalides: A comparative study. *Journal of Magnetism and Magnetic Materials*, 489, 165384. doi:10.1016/j.jmmm.2019.165384

Fate of Sc-Ion Interaction With Water: A Computational Study to Address Splitting Water Versus Solvating Sc Ion

Nandan Kumar[1,2], Y. Bhargav Kumar[2,3], Himakshi Sarma[3] and G. Narahari Sastry[1,2,3]*

[1]Centre for Molecular Modelling, CSIR-Indian Institute of Chemical Technology, Hyderabad, India, [2]Academy of Scientific and Innovative Research (AcSIR), Ghaziabad, India, [3]Advanced Computation and Data Sciences Division, CSIR-North East Institute of Science and Technology, Jorhat, India

An exhaustive study of Sc-ion interaction with water molecules in all its possible oxidation and spin states has been carried out to delineate the relative propensity of Sc ions toward solvation and water splitting. Potential energy surface analysis of the Sc-ion reaction with water molecules, topological analysis of bonds, and the effect of sequential solvation up to 6 water molecules have been examined. Calculated values showed good agreement with the available experimental results. Close-shell systems such as singlet mono- and tricationic Sc ions prefer to split the water molecules. In contrast, the open-shell systems such as triplet mono- and doublet dicationic Sc ions prefer to get solvated than split the water molecule. Topological analysis of electron density predicted the $Sc^{+/2+}$–water bond as a noncovalent bond while Sc^{3+}–OH_2, Sc^{2+}–OH, and Sc^+–H bonds as partially covalent in nature. Energy decomposition analysis revealed that Sc ion–water interactions are driven by electrostatic energy followed by polarization energy. The current study reveals that transition metal catalysis can be one of the most effective tools to employ in water splitting, by properly tuning the electrons, spin, and ligands around the catalytic center.

Keywords: metal cation–water interaction, binding energy, electron density, laplacian of electron density, energy decomposition analysis

INTRODUCTION

The reaction of bare transition metal ions is of utmost importance, given the role they play in a variety of biological and chemical processes (Williams, 1968; Sundberg et al., 1974; Armentrout et al., 1989; Armentrout, 1991; Hippeli et al., 1999; Mahadevi et al., 2013; Swart et al., 2016; Goodman et al., 2019). However, understanding the chemistry of these ions is a challenging endeavor due to variable oxidation states and multiple spin states (Poli, 1996; Harvey et al., 2003). The reaction of transition metal ions, main-group atomic ions, and lanthanide ions with water molecules is studied using experimental methods (Kauffman et al., 1985; Rosi et al., 1989; Dalleska et al., 1994; Trachtman et al., 1998; Cheng et al., 2007; Mo et al., 2007; Saha and Sastry, 2015a). These studies have been followed by several detailed computational analyses on the nature of metal ions interacting with one, two, or more water molecules (Rao et al., 2008; Neela et al., 2013a; Neela et al., 2013b; Mahadevi and Sastry, 2014; Magnera et al., 1989; Marinelli et al., 1989; Tilson et al., 1991; Irigoras et al., 1998, Irigoras et al., 1999a; Irigoras et al., 2000; Chiodo et al., 2004; Meng et al., 2012; Sharma et al., 2016). These studies have provided valuable insights into the coordination preferences of the corresponding metal ions. Solvation of transition and nontransition metal ions has been investigated by employing high levels

of theory for the calculation of the accurate structure and strength of the small cation–water clusters (Russo and Sicilia, 2001; Neela et al., 2010; Sharma et al., 2011; Umadevi et al., 2011; Mahadevi et al., 2014; Umadevi et al., 2014; Sharma et al., 2015; Saha and Sastry, 2015b; Sharma et al., 2016). Clemmer et al., 1993 reported that early first-row transition metal ions are more reactive than their oxides, while the oxides are more reactive than the metal ions for late first-row transition metal ions. Sharma et al., 2015 and Kumar et al., 2021 have reported that the interaction of alkali and alkaline earth metal ions (except Li^+) with water molecules are primarily electrostatic driven. These studies have provided valuable insights into the behavior and chemistry of these ions in the solvent and gas phase. Metal ion–mediated reactions are studied exhaustively for the examination of properties of metal ions, and in a number of cases, the products occurring at intermediate steps along the reaction path are by themselves very interesting species with unique chemical properties. In this work, a rigorous theoretical investigation of Sc ion interaction with water molecules in all the possible oxidation and spin states has been carried out. A metal ion interacts with water, essentially leading to these possibilities, 1) hydrate: $M^{z+}(OH_2)_n$, 2) hydrolyse: $H–M^{z+}–OH$ $(H_2O)_{n-1}$ or $H_2–M^{z+}–(OH)_2$ $(H_2O)_{n-2}$, and 3) dehydrogenate: $M^{z+}O + H_2$. Additionally, the metal ion may lead to the formation of 4) metal hydroxide: $M^{(z-1)+}OH$ or 5) metal hydride: $M^{(z-1)+}H$. Special emphasis is given on understanding the preference of the Sc ion in its variable oxidation states and its corresponding spin states either to split the water molecule by breaking the covalently bonded O–H electron pair or to get solvated by interacting with the lone pair on the oxygen atom. The goal of studying the hydrated ions is to relate the intrinsic physical properties of bare ions to those in an aqueous solution. Understanding the chemistry of a bare metal ion interacting with water molecule is interesting in its own right. The fundamental question in this regard is which of the following mechanisms are predominant: 1) solvation of the metal ion or 2) splitting of the water molecule, with the production of species such as metal hydroxide, metal-hydride, and metal oxide. Thus, the question to be addressed in the current study is that when a bare metal ion interacts with a water molecule in the gas phase, does the process involve a noncovalent interaction limiting to a solvation process or involve the rupturing of bonds in the water molecule leading to covalent bonds. Obviously, the chemistry of water splitting is extremely important with wide-ranging application potential in the energy sector, oxygen generation, and other processes involving O–H bond activation. The current study aims to address the question of Sc-ion interaction with water molecules in the gas phase, followed by the study of microsolvation processes involving the first and second solvation shells. From such measurements, the role of the solvent in the metal-ion structure and reactivity can be comprehended. Potential energy surface analysis of Sc-ion reaction with water molecules and the sequential solvation effects are inspected in detail. However, the quantum theory of atoms in molecules (QTAIM) is used to explore the nature of the interaction, and localized molecular orbital energy decomposition analysis (LMOEDA) is used to examine the

contribution of energy components into the metal ion–water interaction.

COMPUTATIONAL DETAILS

Geometry optimization and frequency calculations were carried out at MP2/6-31G* and B3LYP/6-31G* levels of theory. The energy status of the bare Sc^+ ion interacting with water was comprehensively examined at 48 levels of theory by making combinations of six methods, that is, HF, PBEPBE, B3LYP, M06, MP2, and CCSD(T), with eight different basis sets, that is, LanL2DZ, DGDZVP, Def2TZVP, 6-31G*, 6-311+G*, 6-311G**, cc-pVTZ, and aug-cc-pVTZ. Subsequently, the best combinations were selected to delineate the interaction of the Sc ion with water molecules. Interaction energy (IE) and sequential binding energy (ΔE_{seq}) were calculated using **Eqs. 1** and **2**, respectively. The schematic depiction of the representative structure of $Sc(OH_2)_n$, where n = 1–6, ion complexes and their nomenclature are shown in **Figure 1**.

$$IE = E_{M(H_2O)_n} - \left(E_M + E_{(H_2O)_n} \right) \quad (1)$$

$$\Delta E_{seq} = E_{M(H_2O)_n} - \left(E_{M(H_2O)_{n-1}} + E_{H_2O} \right) \quad (2)$$

where $E_{M(H_2O)_n}$ is the total energy of the metal ion–water complex, E_M is the energy of the metal ion, $E_{(H_2O)_n}$ is the energy of water molecules, $E_{M(H_2O)_{n-1}}$ is the energy of the metal ion–water complex after taking away a water molecule, and E_{H_2O} is the energy of a water molecule that has been taken away. The energies of the monomers, that is, $E_M, E_{(H_2O)_n}, E_{M(H_2O)_{n-1}}$, and E_{H_2O}, are computed on the frozen geometries as they occur in the complex with the metal ion. Natural population analysis (NPA) was performed to examine the charge transfer between the Sc ion and surrounding water molecules. All these calculations were performed using Gaussian16 software (Frisch et al., 2009).To obtain deeper insights into the intermolecular interactions, energy decomposition analysis was carried out using the LMOEDA scheme, implemented in the GAMESS program (Su et al., 2009). In the LMOEDA scheme, interaction energy (ΔE_{int}) decomposes into electrostatic (ΔE_{ele}), exchange (ΔE_{ex}), repulsion (ΔE_{rep}), polarization (ΔE_{pol}), and dispersion (ΔE_{disp}) components, as shown in **Eq. 3**:

$$\Delta E_{int} = \Delta E_{ele} + \Delta E_{ex} + \Delta E_{rep} + \Delta E_{pol} + \Delta E_{disp} \quad (3)$$

In LMOEDA, ΔE_{ele} describes the classical Coulomb interaction energy between the occupied orbitals of interacting moieties. The ΔE_{pol} component describes the orbital relaxation energy that comprises both polarization and charge-transfer interactions. The ΔE_{ex} and ΔE_{rep} components are associated with Pauli's exclusion principle where ΔE_{ex} occurs in like-spin only, whereas ΔE_{rep} is expressed by the orthonormal orbitals of monomers. The ΔE_{disp} component alludes to the MP2 correction to the Hartree-Fock interaction energy. Bader's theory of atoms in molecules (AIM) was used to analyze the topological parameters at critical points (CPs) for the considered systems using the AIM2000 package (Bader, 1985), and the relation of kinetic energy density, that is, G(**r**), and potential energy density, that
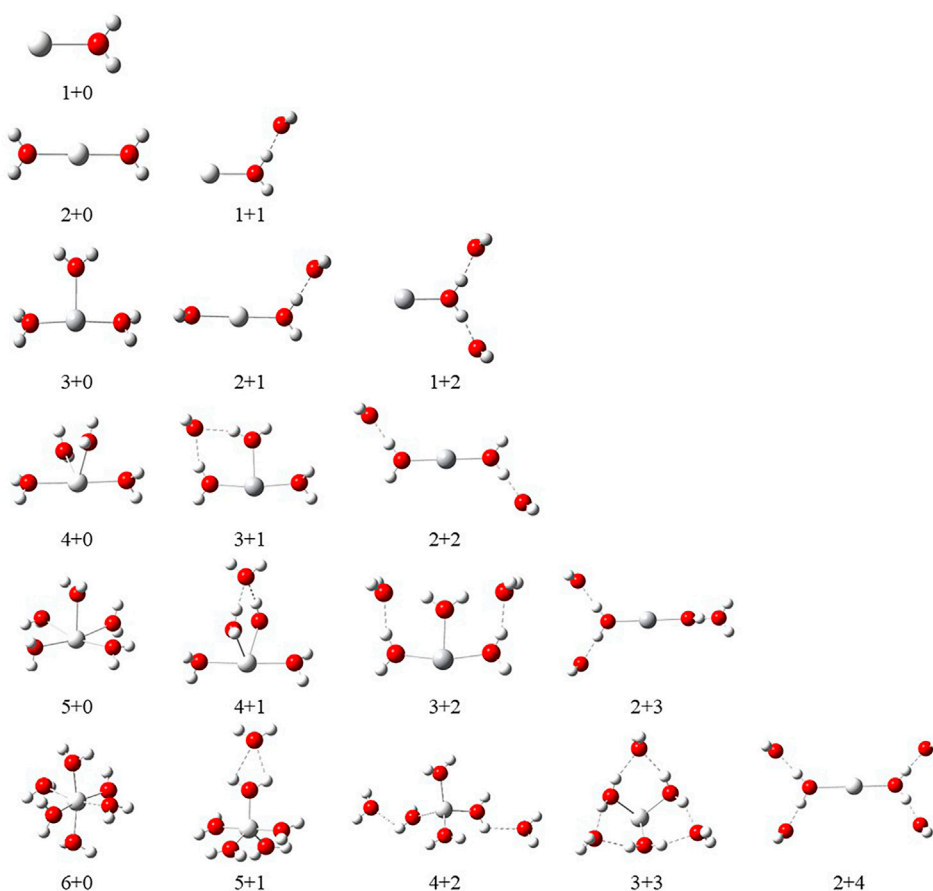
FIGURE 1 | Schematic representation of $Sc^{z+}(OH_2)_n$, where z = 1–3 and n = 1–6, complexes and their nomenclature by a label of X + Y (X = number of water molecules in the first solvation shell and Y = number of water molecules in the second solvation shell).

is, V(**r**), was elucidated using **Eqs. 4** and **5** to obtain the Laplacian of electron density ($\nabla^2\rho$) and total energy density, that is, H(**r**)

$$\frac{1}{4}\nabla^2\rho = 2G(\mathbf{r}) + V(\mathbf{r}) \tag{4}$$

$$H(\mathbf{r}) = G(\mathbf{r}) + V(\mathbf{r}) \tag{5}$$

RESULTS AND DISCUSSION

Geometrical Parameters and Ground-State Multiplicity Prediction

In this study, we have tried to adequately approximate the singlet–triplet energy gap ($\Delta S–\Delta T$), and therefore, open-shell singlet (OSS) and close-shell singlet (CSS) geometries of $Sc^+(OH_2)_n$, where n = 1–2, complexes have also been considered. Geometrical parameters showed that OSS geometries of $Sc^+(OH_2)_n$, where n = 1–2, complexes are closer to the triplet-state (TS) geometry. The geometrical parameters at B3LYP/6-31G* and MP2/6-31G* are shown in **Figures 2**, **3** and showed good agreement with results reported by Trachtman et al., 1998, Irigoras et al., 1999b, and Russo et al., 2001. The

OSS geometry is obtained to be very similar to that of TS than the CSS because of its similarity in the orbital occupancy to the TS. Additionally, analysis of the geometrical parameters showed that the $Sc^+–O$ bond distance increases, and the H–O–H bond angle decreases as we move from low-spin complexes to high-spin complexes. The geometrical parameters of the water molecules slightly change while forming $Sc^+(OH_2)_n$, where n = 1–2, complexes. For instance, the H–O–H bond angle of the water molecule changes around 3–4° during complexation, whereas an appreciable difference is not observed in the O–H bond distance of the water molecule. The $O–Sc^+–O$ bond angle of $Sc^+(OH_2)_2$ complexes in both the singlet state (SS) and triplet state (TS) is observed to be 180.0° (linear molecular geometry); however, a nonlinear molecular geometry (O–Sc$^+$–O bond angle of 117.3°) is observed for the tricationic complex at both B3LYP/6-31G* and MP2/6-31G* levels of theory. It can be noticed from **Figure 2** that the MP2 method predicts a linear molecular geometry (180.0°) for the $Sc^{2+}(OH_2)_2$ complex, whereas B3LYP predicts a nonlinear molecular geometry (150.4°). As a result, the $O–Sc^{2+}–O$ bond angle indicates structural relaxation upon the use of the MP2 method. In the case of insertion complexes, large differences are observed in the $Sc^+–H$ bond distance of SS and TS complexes, as shown in **Figure 3**. The $Sc^+–H$ bond distance for HSc^+OH

FIGURE 2 | Geometrical parameters of the close-shell singlet (CSS), open-shell singlet (OSS), and triplet-state (TS) geometry of $Sc^+(OH_2)_n$, doublet-state (DS) geometry of $Sc^{2+}(OH_2)_n$, and singlet-state (SS) geometry of $Sc^{3+}(OH_2)_n$, where n = 1-2, complexes obtained at B3LYP (normal) and MP2 (bold) using the 6-31G* basis set. Bond distances and angles are given in angstrom and degree, respectively.
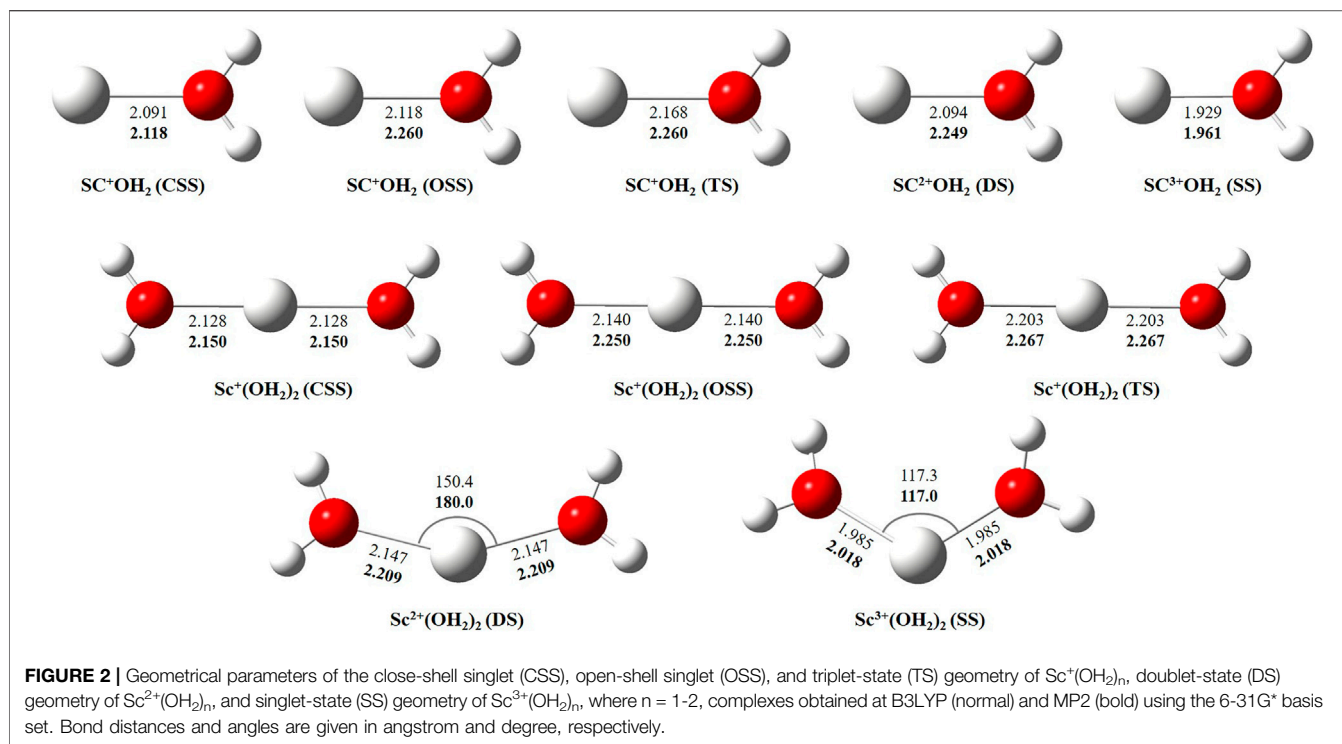
complexes obtained in the SS and TS is 1.755 Å and 2.563 Å at B3LYP and 1.791 Å and 4.370 Å at MP2, respectively. However, it is 1.780 Å and 2.626 Å at B3LYP and 1.819 Å and 2.712 Å at MP2, respectively, in the case of $HSc^+OH(OH_2)$ complexes. In the case of the $H_2Sc^+(OH)_2$ complex, long Sc^+-H bonds, that is, 2.379 Å and 2.588 Å at B3LYP and 2.447 Å and 2.716 Å at MP2, are obtained for SS and TS complexes, respectively. Thus, the computed Sc^+-H bond of the low-spin insertion complex was found to be substantially shorter compared to that of the high-spin complex. Hereby, long Sc^+-H bond-containing insertion complexes may essentially correspond to H + Sc^+OH, H + $Sc^+OH(OH_2)$, H_2 + $Sc^+(OH)_2$, H + $Sc^{2+}OH$, H + $Sc^{2+}OH(OH_2)$, H_2 + $Sc^+(OH)_2$, and H + $Sc^{2+}OH$ rather than HSc^+OH and $HSc^{2+}OH$ complexes. Therefore, the bond between the Sc ion and H of these insertion complexes is largely due to the electrostatic interaction, and also, the interaction is not entirely covalent in nature (**Figure 3**). A careful observation of the figure reveals that the trends of the structural parameters and their absolute values are very comparable, and thus, the qualitative results obtained in the study appear to be independent of the method employed. Therefore, to make a consistent choice of geometry, for further analysis, the structures optimized at the MP2/6-31G* level of theory have been undertaken.

The accurate estimation of the relative energy of spin states of transition metal ions is very important to describe the reactivity and other properties of these ions (Shaik et al., 2011; Costas et al., 2013). Since the energetics of transition metal ions are extremely difficult to predict accurately using any one computational method (Ashley et al., 2017), we have predicted the relative energy of SS and TS bare Sc^+ ions, Sc^+-OH_2, and HSc^+OH complexes at 48 different levels of theory. These methods are HF, PBEPBE, B3LYP, M06, MP2, and CCSD(T) using LanL2DZ, DGDZVP, Def2TZVP, 6-31G*, 6-311+G*, 6-311G**, cc-pVTZ, and aug-cc-pVTZ basis sets, as shown in **Supplementary Table S1A**. To calculate an adequate approximation of ΔS−ΔT for the bare Sc^+ ion and complexes, the procedure proposed by Yamaguchi et al., 1988 is used to correct the spin contamination problem of the OSS bare Sc^+ ion. The calculated ΔS−ΔT values of the bare Sc^+ ion, Sc^+OH_2, and HSc^+OH complexes are shown in **Supplementary Tables S1, S2**. A total of 14 different methods predicted a reasonably good value of ΔS−ΔT, that is, relative energy of contamination-corrected open-shell singlet (CC_OSS) and TS of the bare Sc^+ ion, and showed an excellent agreement with the experimental value (7.38 kcal/mol) reported by Chen et al., 1994, as shown in **Table 1**. As expected, TS ($3d^1$ $4s^1$) is predicted as a ground-state multiplicity for the bare Sc^+ ion. These 14 methods, except M06, have also predicted TS ($3d^1$ $4s^1$) as a ground-state multiplicity for the Sc^+OH_2 complex. In contrast, M06 predicted SS ($4s^2$ $3d^0$) as a ground-state multiplicity for the Sc^+OH_2 complex, as shown in **Supplementary Table S1B**. The values obtained at PBEPBE (with few exceptions), B3LYP, MP2, and CCSD(T) showed a reasonable agreement with the reported theoretical values (8.63 kcal/mol to 20.30 kcal/mol) by Irigoras et al., 1999a. However, all the considered methods predicted SS ($4s^2$ $3d^0$) as the ground-state multiplicity for insertion complexes.

Topological Analysis of Bonds

Quantum theory of atoms in molecules (QTAIM) is useful to examine the interaction between atoms based on the topology of the electron density at CPs (Bader, 1998). We have examined ρ, $\nabla^2\rho$, H(**r**), [-(G(**r**)/V(**r**)], and percentage contribution of G(**r**) at
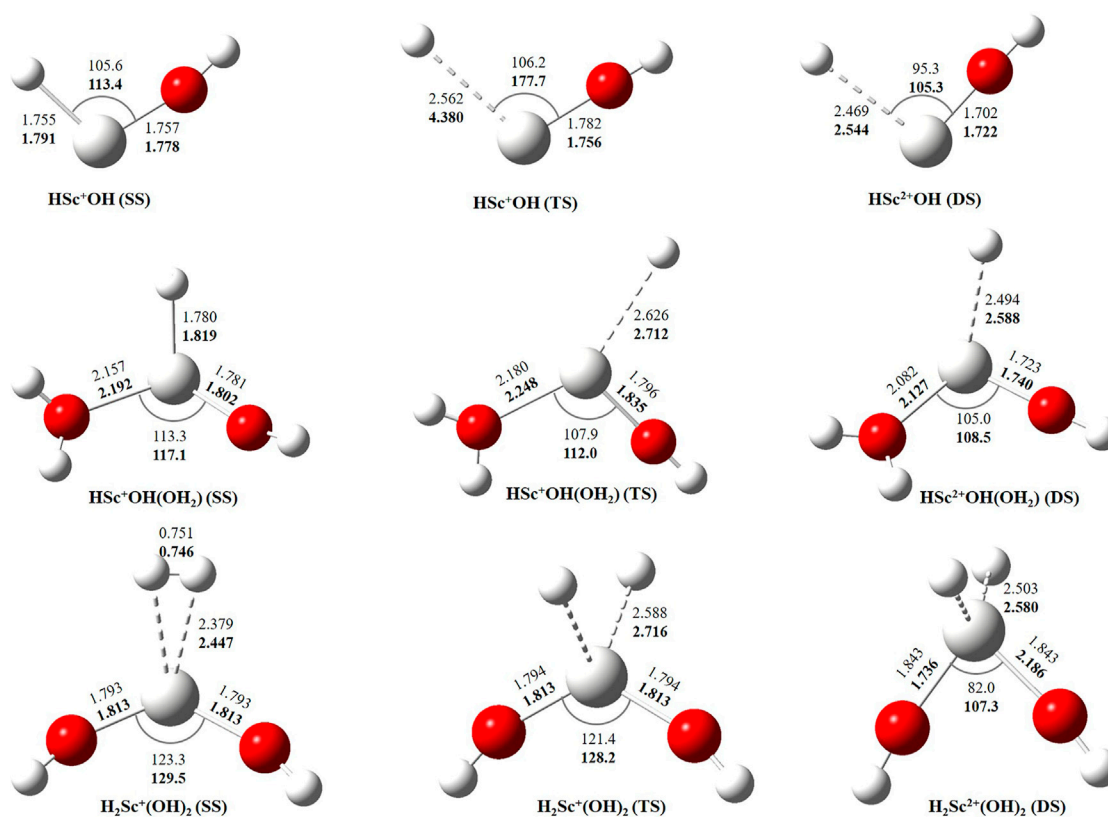
FIGURE 3 | Geometrical parameters of singlet-state (SS), doublet-state (DS), and triplet-state (TS) geometries of HSc$^{+/2+}$OH, HSc$^{+/2+}$OH(OH$_2$), and H$_2$Sc$^{+/2+}$(OH)$_2$ complexes obtained at B3LYP (normal) and MP2 (bold) using the 6-31G* basis set. Bond distances and angles are given in angstrom and degree, respectively.

TABLE 1 | Reaction energy (ΔE_R) for the reaction Sc$^+$ + OH$_2$ → Sc$^+$O + H$_2$ + ΔE, sequential binding energy (ΔE_{seq}) of ground-state Sc$^+$OH$_2$ complex, and ΔS–ΔT for the bare Sc$^+$ ion. All values are reported in kcal/mol.

Methods	ΔS–ΔT	ΔE_{seq}	ΔE_R
HF/LanL2DZ	9.31	−41.08	−13.93
B3LYP/DGDZVP	7.80	−37.19	38.66
B3LYP/6-31G*	6.30	−41.49	53.79
B3LYP/aug-cc-pVTZ	8.00	−33.73	37.78
M06/Def2TZVP	8.62	−36.61	51.43
M06/6-31G*	5.25	−42.21	64.69
M06/6-311+G*	7.32	−40.08	58.36
M06/cc-pVTZ	8.54	−37.86	52.44
M06/aug-cc-pVTZ	8.88	−35.30	50.05
MP2/LanL2DZ	8.59	−42.37	66.30
MP2/6-311+G*	9.48	−34.98	53.61
MP2/cc-pVTZ	8.80	−31.94	46.16
MP2/aug-cc-pVTZ	8.75	−28.76	43.44
CCSD(T)/6-311G**	6.46	−31.12	35.88
Exp	7.38	−31.40 ± 3	46.81 ± 1.38

the bond critical point (BCP) of the MP2/6-31G* optimized geometries of Sc ion–water and their insertion complexes to elucidate the nature of the Sc-ion bond with H$_2$O, OH, and H, as shown in **Figure 4** and **Supplementary Table S3**. A high value

of ρ and a negative value of ∇^2ρ indicate covalent interaction, while in general, a low value of ρ and a positive value of ∇^2ρ suggest a noncovalent or close-shell type bonding (Kumar et al., 2021). However, the sign of H(**r**) and the value of [-G(**r**)/V(**r**)] explain the covalent nature of the bond. It may be noticed that the value of ρ increases and that of ∇^2ρ and H(**r**) decreases for the Sc–O bond of Sc$^{+/2+/3+}$–OH$_2$ and Sc$^{+/2+}$–OH complexes when moving from low-spin to high-spin complexes, corresponding to a covalent interaction. (**Figure 4**). However, in the case of Sc$^+$(OH$_2$)$_n$, where n = 1–2, and HSc$^{+/2+}$OH(OH$_2$) complexes, a positive value of both ∇^2ρ and H(**r**) with a small value of ρ (0.03–0.06 a.u.) and [−G(**r**)/V(**r**) > 1] has been observed at the BCP of the Sc$^{+/2+}$–OH$_2$ bond, suggesting a noncovalent bond. A positive value of ∇^2ρ and a negative value of H(**r**) with a significant value of ρ (~0.10 a.u.) and 1 <[−G(**r**)/V(**r**)]> 0.5 suggest that the Sc^{3+}–water bond possesses a partial covalent character. In the case of insertion complexes, a positive value of ∇^2ρ and a negative H(**r**) with a ρ value of 0.08–0.17 a.u. have been observed for Sc$^+$–OH, Sc^{2+}–OH, and Sc$^+$–H bonds, as shown in **Figure 4** and **Supplementary Table S3A**. The value of [−G(**r**)/V(**r**)] is observed to be less than 1 (**Figure 4**), and the percentage contribution of G(**r**) into H(**r**) (**Supplementary Table S3B**) was less than 50% at the BCP of Sc$^{+/2+}$–OH and Sc$^+$–H bonds of HSc$^{+/2+}$OH and HSc$^{+/2+}$OH(OH$_2$) complexes, that is, the lowering of the kinetic energy may be traced to the
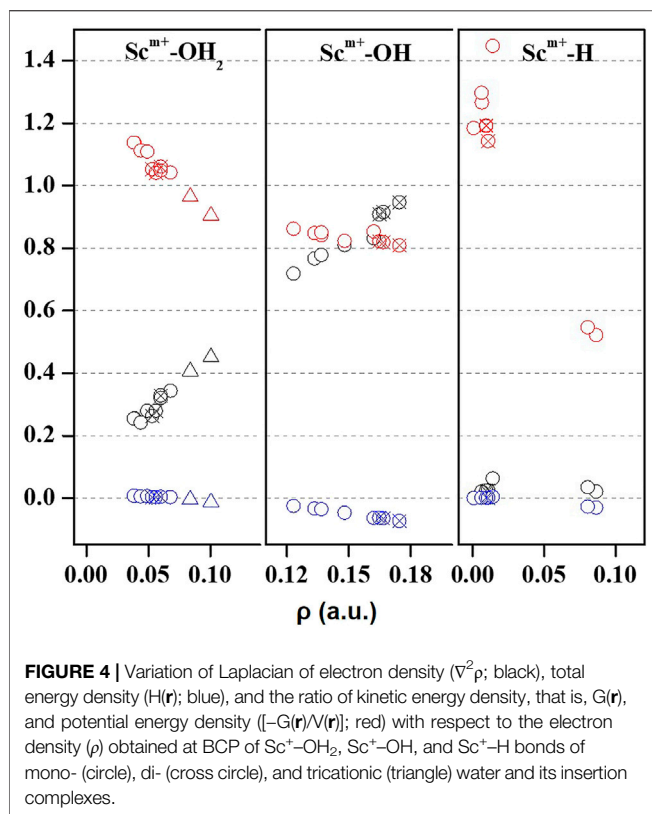
FIGURE 4 | Variation of Laplacian of electron density ($\nabla^2\rho$; black), total energy density (H($\mathbf{r}$); blue), and the ratio of kinetic energy density, that is, G($\mathbf{r}$), and potential energy density ($[-G(\mathbf{r})/V(\mathbf{r})]$; red) with respect to the electron density (ρ) obtained at BCP of Sc$^+$–OH$_2$, Sc$^+$–OH, and Sc$^+$–H bonds of mono- (circle), di- (cross circle), and tricationic (triangle) water and its insertion complexes.

enhancement of the covalent nature in these bonds (Zhao et al., 2019). Besides, it may also be noted that the contribution of G($\mathbf{r}$) decreases with the increase in ρ at the BCP of the bond in most of the cases except for Sc$^{+/2+}$–H bonds, which are clearly indicated as loose bonds. Furthermore, the bond length of Sc$^{+/2+}$–H is long, clearly indicating that the Sc$^{+/2+}$–H bond is not formed in the insertion complexes on the TS and doublet-state (DS) potential energy surfaces (see **Supplementary Table S3A**). Thus, topological analysis of Sc ion–water and its insertion complexes indicated that Sc$^{+/2+}$–OH$_2$ bonds are noncovalent in nature. A closer look at the structural and topological parameters reveals that Sc^{3+}–OH$_2$, Sc^{2+}–OH, and Sc$^+$–H bonds have a strong admixture of covalent nature.
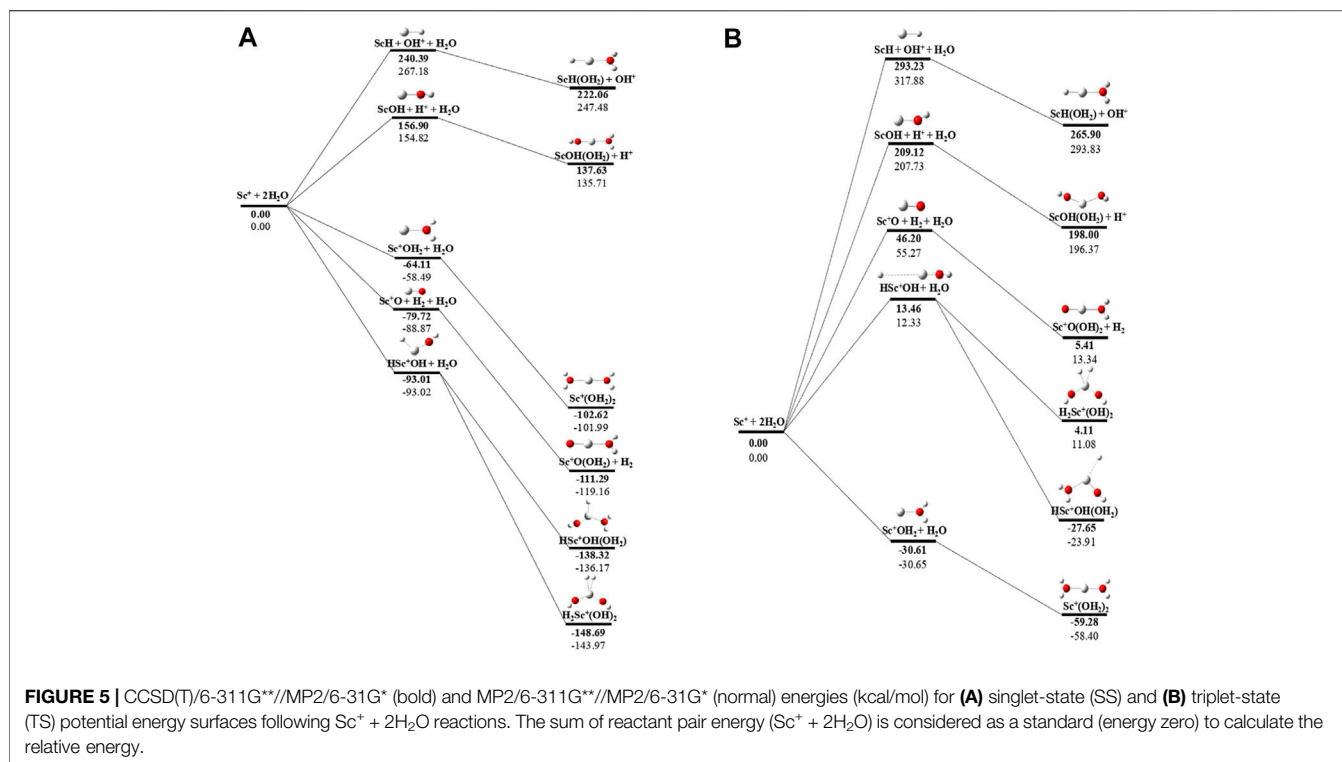
Analysis of Binding and Reaction Energies

The binding and reaction energies are calculated using the aforementioned 14 methods such as HF in conjugation with the LanL2DZ basis set, B3LYP in conjugation with DGDZVP, 6-31G*, and aug-cc-pVTZ basis sets, M06 in conjugation with 6-31G*, 6-311+G*, cc-pVTZ, and aug-cc-pVTZ basis sets, MP2 in conjugation with LanL2DZ, 6-311+G*, cc-pVTZ, and aug-cc-pVTZ basis sets, and CCSD(T) in conjugation with the 6-311G** basis set, as shown in **Table 1** and **Supplementary Table S4**. The computed Sc$^+$–OH$_2$ binding energy is in fair agreement with the experimental observations and earlier computational results for the ground state of the Sc$^+$OH$_2$ complexes (Magnera et al., 1989) (**Table 1**). In comparison to the other theoretical values, our values calculated at B3LYP/aug-cc-pVTZ, MP2/cc-pVTZ, and

CCSD(T)/6-311G** levels of theory showed a very good agreement with the value reported by Irigoras et al., 1999a and Sharma et al., 2016, that is, −32.52 kcal/mol and −31.18 kcal/mol at CCSD(T)/TZVP + G(3df2p) and CCSD(T)/def2-TZVP levels of theory, respectively. Moreover, our calculated values suggested that binding energy increases by moving from high spin to low spin and from lower to higher oxidation states, that is, from monocationic to tricationic, as shown in **Supplementary Table S4**. **Figures 2** and **3** depict the optimized geometric parameters with two water molecules and provide interesting insights into the onset of microsolvation of the metal ion and the change in the propensity of competing pathways, in the presence of two water molecules. Rosi et al., 1989 have reported a similar study which is in good qualitative agreement with the results obtained here. Calculated values suggested that ΔE_{seq} decreases with the addition of the second water molecule to the Sc ion in all the considered methods (**Supplementary Table S4**). Reaction energy (ΔE_R) has been calculated using the equation Sc$^+$ + OH$_2 \rightarrow$ Sc$^+$O+ H$_2$ + ΔE, as shown in **Table 1**. A large inconsistency is observed among the calculated ΔE values using 14 different methods. The results clearly reveal the grossly poor performance of the bulk of methods employed in estimating the reaction energies. The calculated values at B3LYP in conjugation with DGDZVP and aug-cc-pVTZ basis sets, MP2 in conjugation with cc-pVTZ and aug-cc-pVTZ basis sets, and CCSD(T) in conjugation with the 6-311G** basis set have shown good agreement with the experimental value (Chen et al., 1994). Thus, an exothermic reaction and the formation of the low-spin Sc$^+$O+ H$_2$ product are observed. In addition, our calculated values at MP2 in conjugation with cc-pVTZ and aug-cc-pVTZ, B3LYP in conjugation with DGDZVP and aug-cc-pVTZ, and CCSD(T) in conjugation with 6-311G** basis sets showed good agreement and seem to be better than other reported theoretical values (Tilson et al., 1991; Ye et al., 1997; Irigoras et al., 1999b). The binding and reaction energy values have also been computed at BP86, B97D, and B3LYP-D3 using 6-311G** and aug-cc-pVTZ basis sets, and the obtained values are observed to be similar to those observed using other DFT methods, as shown in **Table 1** and **Supplementary Table S10**.

Thus, the calculated values $\Delta S - \Delta T$, ΔE_{seq}, and ΔE_R suggested that B3LYP in conjugation with DGDZVP and aug-cc-pVTZ, MP2 in conjugation with 6–311+G*, cc-pVTZ, and aug-cc-pVTZ, and CCSD(T) in conjugation with the 6-311G** basis set predict the energetics of Sc ions accurately, and therefore, these methods can be used to delineate the interaction of the Sc ion with water molecules. We have opted the CCSD(T)/6-311G**//MP2/6-31G* method for further analysis.

Potential Energy Surface Analysis

The potential energy surface analysis has been carried out for interaction of the Sc^{z+} ion with water molecules leading to 1) hydrate: Sc^{z+}(H$_2$O)$_n$, 2) hydrolyse: H–Sc^{z+}–OH (H$_2$O)$_{n-1}$ or H$_2$–Sc^{z+}–(OH)$_2$(H$_2$O)$_{n-2}$, 3) dehydrogenate: Sc^{z+}O+ H$_2$, 4) metal hydroxide: Sc$^{(z-1)+}$OH, and 5) metal hydride: Sc$^{(z-1)+}$H at CCSD(T)/6-311G**//MP2/6-31G* level of theory, as shown in **Figures 5–7**. No stationary point on the potential energy surface has been obtained corresponding to the OSS complex of Sc$^+$OH$_2$,

FIGURE 5 | CCSD(T)/6-311G**//MP2/6-31G* (bold) and MP2/6-311G**//MP2/6-31G* (normal) energies (kcal/mol) for **(A)** singlet-state (SS) and **(B)** triplet-state (TS) potential energy surfaces following $Sc^+ + 2H_2O$ reactions. The sum of reactant pair energy ($Sc^+ + 2H_2O$) is considered as a standard (energy zero) to calculate the relative energy.

as the putative structure collapses to CSS in a barrierless fashion upon the formation of the insertion complex (HSc^+OH), which corroborates well with the earlier observations (Irigoras et al., 1999a). The reaction starts from bare Sc^+ ions separated from water molecules at an infinite distance and leads to the formation of the hydrated complex, insertion complex, metal oxide, metal hydroxide, and metal hydride, as shown in **Supplementary Figure S1**. Considering the well-known limitations of the MP2 methods, when dynamic electron correlation is substantial, in properly reproducing the geometry of small systems, we would like to benchmark the method more systematically. Thus, geometry optimization of the considered metal oxide, hydroxide, and hydride complexes has been performed at five different levels of theory. The insertion complex formed by Sc^+ insertion into the O–H bond of water molecules, as the valance electrons of Sc^+ ions are shared by -OH and -H atoms, making the complex a singlet, **Figures 5–7**, which depicts the energetics of the competing pathways, from which it can be seen that the insertion complex, that is, HSc^+OH, is substantially stable in the singlet compared to that of the triplet, while the energetics of the spin states of the bare metal ion exhibit completely contrasting trends. The observed spin-crossover following the insertion reveals that there is a possibility for multiple electronic states crossing along the reaction paths on the potential energy surfaces. Thus, modeling of these molecules warrants careful consideration of various electronic states as there is a great potential for crossover of the spin and electronic states due to the vast variation in the energetics of these species even with small geometric changes along with the reaction coordinate. The insertion complex, on the triplet potential energy surface, is essentially a hydrogen

elimination process with the formation of a low-spin Sc^+O+ H_2 as the product, which is in agreement with the earlier study by Irigoras et al., 1999b. Thus, the metal ions under the right condition have a definitive potential to generate hydrogen, which is of course of great industrial significance. In the case of metal oxide, a relatively stable Sc^+O complex has been observed on the SS potential energy surface than the corresponding Sc^+OH_2 complex. However, HSc^+OH is relatively more stable than the Sc^+O complex on the SS potential energy surface. The energetics of the formation of a metal hydroxide ScOH and metal hydride ScH suggest that both the reactions are energetically unfavorable on both SS and TS potential energy surfaces. We have further expanded the scope of this study by examining the interaction of monohydrated, insertion, oxide, hydroxide, and hydride complexes with the second water molecule. The hydrated products of monohydrated, insertion, oxide, hydroxide, and hydride complexes are observed to be more stable than their predecessors on both SS and TS potential energy surfaces, as shown in **Figure 5**. Interestingly, the hydrated TS insertion complex $H^{...}Sc^+OH(OH_2)$ is lower than both TS insertion complexes, $H^{...}Sc^+OH$ and the reactant pair $Sc^+ + 2H_2O$ by 41.11 kcal/mol and 27.65 kcal/mol, respectively, and nearly degenerates (~2.96 kcal/mol) to the TS monohydrated complex Sc^+OH_2. It can be inferred that splitting the second water molecule slightly destabilizes the TS monohydrated complex, and thus, two water molecules appeared to be required to reach a stable complex on the potential energy surface. Thus, when performing the computations with two water molecules, Sc^+ insertion into the O–H bond of the second water molecule eventually forms metal dihydroxide, that is, $Sc^+(OH)_2 + 2H$ on

FIGURE 6 | CCSD(T)/6-311G**//MP2/6-31G* (bold) and MP2/6-311G**//MP2/6-31G* (normal) energies (kcal/mol) for doublet-state (DS) potential energy surfaces following $Sc^{2+} + 2H_2O$ reaction. The sum of reactant pair energy ($Sc^{2+} + 2H_2O$) is considered as a standard (energy zero) to calculate the relative energy.
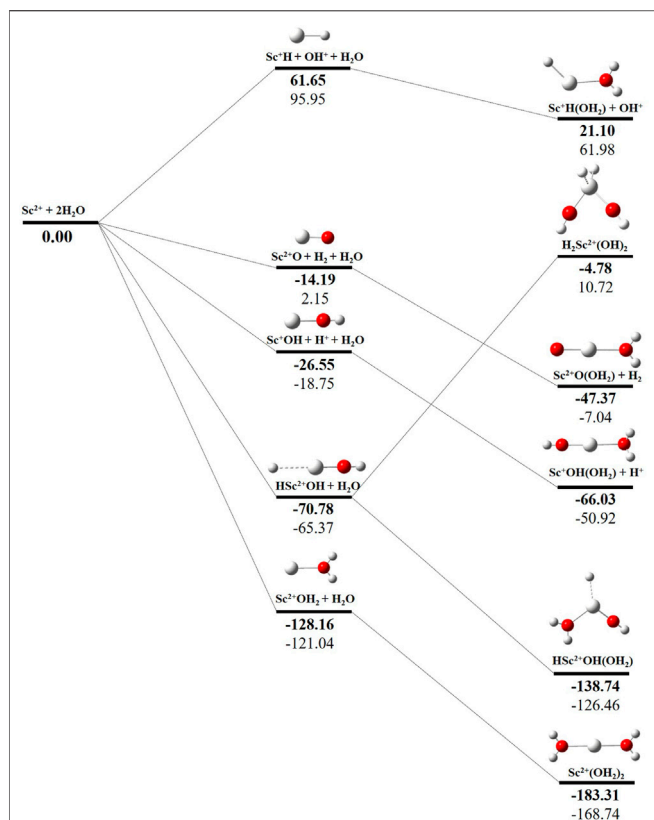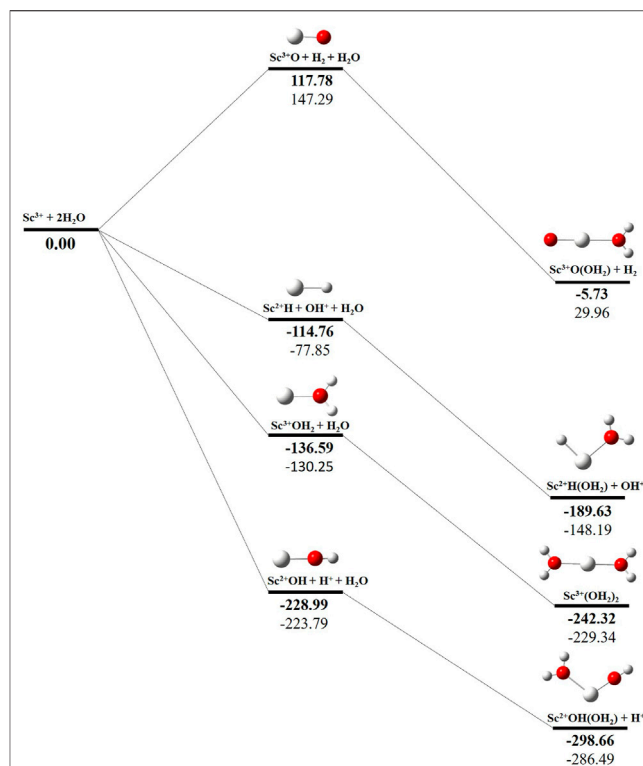

FIGURE 7 | CCSD(T)/6-311G**//MP2/6-31G* (bold) and MP2/6-311G**//MP2/6-31G* (normal) energies (kcal/mol) for singlet-state (SS) potential energy surfaces following $Sc^{3+} + 2H_2O$ reaction. The sum of reactant pair energy ($Sc^{3+} + 2H_2O$) is considered as a standard (energy zero) to calculate the relative energy.

the TS potential energy surface and $Sc^{+}(OH)_2 + H_2O$ on the SS potential energy surface. It is interesting to observe that there is a great propensity exhibited for water splitting compared to solvation, with the $Sc^{+}(OH)_2 + H_2$ product on the SS being observed well below the ground-state reactant pair $Sc^{+} + 2H_2O$ and $Sc^{+}(OH_2)_2$ complexes. The examination of di- and tricationic Sc-ion reactions with a water molecule indicates that the hydrated complex of Sc^{2+} and hydroxide of Sc^{3+} lie below the reactant and the corresponding complexes on the DS and SS potential energy surfaces, respectively (**Figures 6, 7**). Therefore, it may be inferred that the Sc^{2+} ion is likely to adopt a more feasible solvation pathway compared to the corresponding insertion alternative (**Figure 6**). However, the affinity of the Sc^{3+} ion to form a metal hydroxide, $Sc^{2+}OH$, is observed to be higher than getting solvated to form $Sc^{3+}(OH_2)$ as hydroxide complexes lie above the corresponding hydrated complex (**Figure 7**).

Analysis of Sequential Solvation

In order to investigate the sequential solvation effect on the nature of Sc ion–water complexes, we have examined the microsolvation process of up to 6 water molecules and probed the relative propensity of water molecules to occupy the first and second solvation shells. The schematic depiction of the representative structure of $Sc(OH_2)_n$, where n = 1–6, ion complexes and their nomenclature are shown in **Figure 1**. We have used the nomenclature X + Y (X = number of water molecules in the first solvation shell and Y = number of water molecules in the second solvation shell) to present the number of water molecules in the solvation shells. Starting from one water molecule, various conformers of $Sc(OH_2)_n$, where n = 1–6, ion complexes in all possible oxidation and spin states have been explored and the lowest energy conformers are selected for further discussion, as shown in **Figure 8** and **Supplementary Figure S3**. A cursory look of interaction energy (IE) of these complexes, obtained at the CCSD(T)/6-311G**//MP2/6-31G** level of theory, suggests that IE increases as the number of water molecules increase either in the first or both in the first and second solvation shells, as shown in **Figure 9** and **Supplementary Figure S2**. IE has also been obtained using different methods to ensure that the obtained values are not biased (**Supplementary Table S5**). We have considered IE of each structure as a criterion to describe the stability of $Sc(OH_2)_n$, where n = 1–6, ion complexes. The sequential binding ΔE_{seq} energy of these stable complexes, obtained at the CCSD(T)/6-311G**//MP2/6-31G** level of theory, suggests that ΔE_{seq} energy decreases with the addition of every subsequent water molecule to the complexes except for the 4 + 0 structure of the triplet $Sc^{+}(OH_2)_4$ complex, as shown in **Figure 8**. Our calculated values showed a good
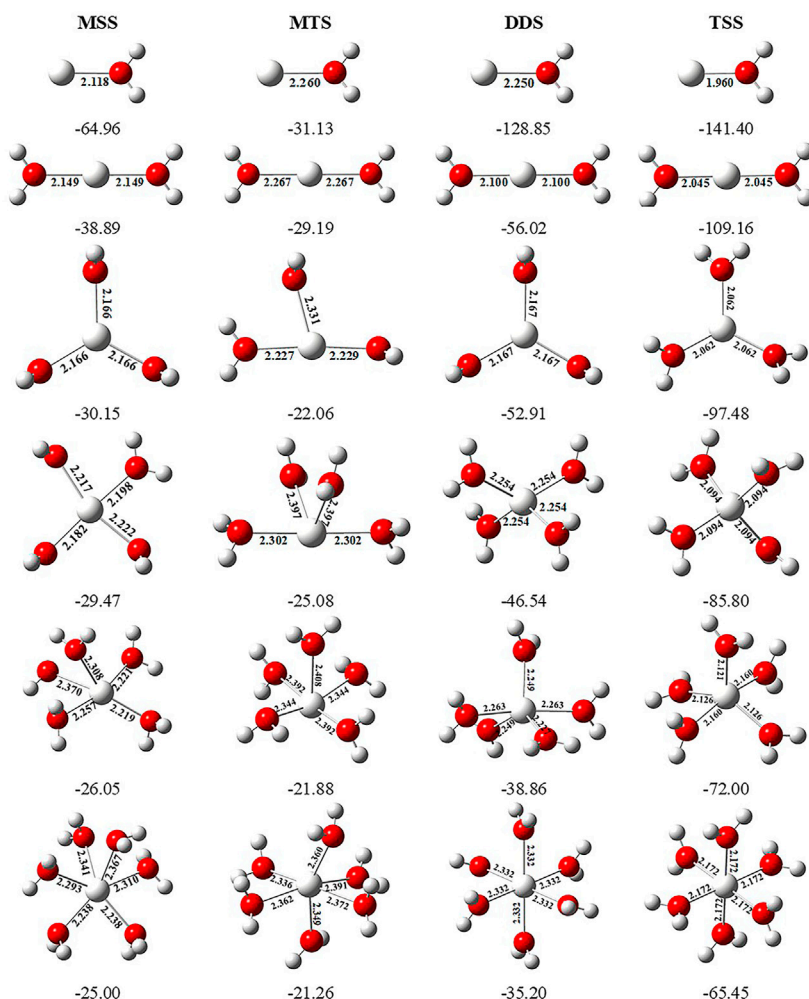
FIGURE 8 | Geometrical parameters (bond distances in angstrom) of the monocationic singlet state (MSS) and triplet state (MTS), dicationic doublet state (DDS), and tricationic singlet state (TSS) of $Sc^{z+}(OH_2)_n$, where z = 1–3 and n = 1–6, ion complexes, obtained at the MP2/6-31G* level of theory. Sequential binding energy (ΔE_{seq}; kcal/mol) of these complexes obtained at the CCSD(T)/6-311G**//MP2/6-31G* level of theory.

agreement with the available experimental and theoretical results reported by Rosi et al., 1989, Magnera et al., 1989, and Dalleska et al., 1994.

IE increases as the number of water molecules increases in the second solvation shell for each CN of Sc ions irrespective of oxidation and spin states, that is, it increases from 1 + 0 to 1 + 2 (CN = 1), 2 + 0 to 2 + 4 (CN = 2), 3 + 0 to 3 + 3 (CN = 3), 4 + 0 to 4 + 2 (CN = 4), and 5 + 0 to 5 + 1 (CN = 5), shown in **Figure 9** and **Supplementary Figure S2**. Thus, this result suggests that $Sc(OH_2)_n$, where n = 1–6, ion complexes in each CN are more stable with the maximum number of water molecules in the second solvation shell. Furthermore, the analysis of the bond distance between the Sc ion and first solvation shell water molecules suggested that the average M–O distance of $Sc(OH_2)_n$, where n = 1–6, ion complexes increases with increasing number of water molecules around the Sc ion. Among the complexes with the same number of water molecules in the second solvation shell, the average M–O distance increases with the increase in the CN of the Sc ion and vice versa. In addition, it has also been observed that the average M–O distance increased by moving from low- to high-spin $Sc^+(OH_2)_n$, where n = 1–6, ion complexes and decreased by moving from mono- to tricationic ground-state complexes, as shown in **Supplementary Table S6**. The topological analysis predicted $Sc^{+/2+}–OH_2$ bonds to be a noncovalent bond as the calculated values of $\nabla^2\rho$ and H(**r**) are positive, and $[−(G(\mathbf{r})/V(\mathbf{r})]$ is less than 1 irrespective of the spin states. However, the $Sc^{3+}–OH_2$ bond is predicted as partially covalent in nature, as shown in **Supplementary Table S7**.

Charge and Energy Decomposition Analysis

Natural population analysis has been carried out on all the considered structures of $Sc(OH_2)_n$, where n = 1–6, ion complexes to examine the charge transfer between the Sc ion and the water molecules. The variation in charge on the Sc ion with the increase in the CN of $Sc^+(OH_2)_n$, where n = 1–6,
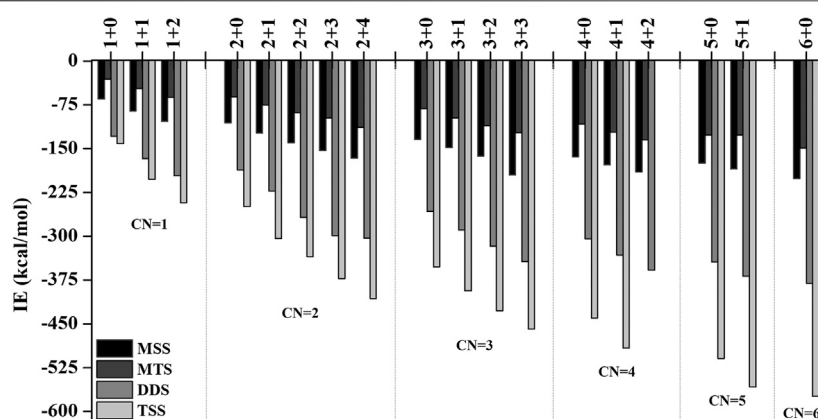
FIGURE 9 | Variation of interaction energy (IE in kcal/mol) with the increase in coordination number (CN) of the monocationic singlet state (MSS) and triplet state (MTS), dicationic doublet state (DDS), and tricationic singlet state (TSS) of the Sc ion in $Sc^{z+}(OH_2)_n$; $z = 1$–3 and $n = 1$–6 complexes calculated at the CCSD(T)/6-311G**// MP2/6-31G* level of theory.

complexes is shown in **Supplementary Figure S4**. The figure shows that the charge on the Sc ion decreases monotonically as the number of water molecules is increased in the complexes. Besides, the charge on the Sc ion seemed to be decreasing as the number of water molecules increases in the second solvation shell for each coordination number (i.e., CN = 1–6) and vice versa. Such differences can be explained based on the differences in the

organization of water molecules around the Sc ion. The most stable structure of every CN complex showed a minimum charge on the Sc ion. A cursory view of **Supplementary Table S8** shows that IE is inversely proportional to the charge on the Sc ion, which signifies that charge transfer plays an important role in the stabilization of $Sc(OH_2)_n$, where n = 1–6, ion complexes. Localized molecular orbital energy decomposition analysis is
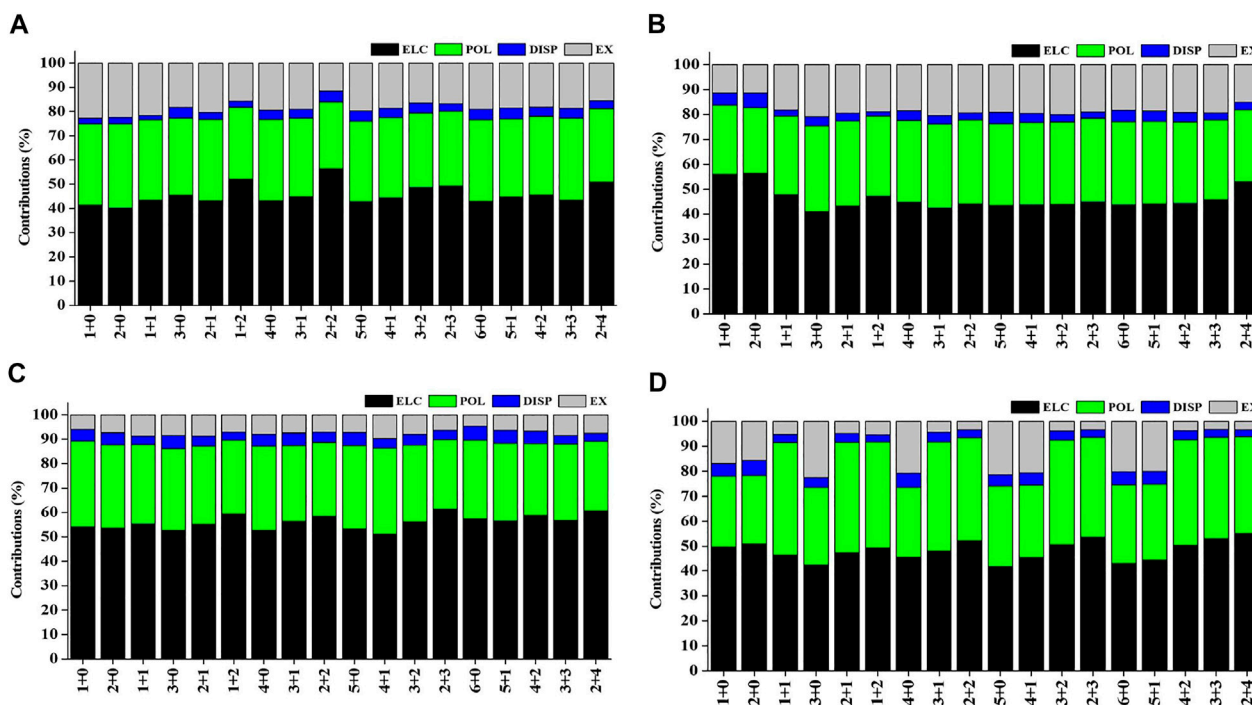
FIGURE 10 | Percentage contribution of energy components such as electrostatic (ELC), polarization (POL), dispersion (DISP), and exchange (EX) into the interaction energy of the **(A)** monocationic singlet state (MSS), **(B)** monocationic triplet state (MTS), **(C)** dicationic doublet state (DDS), and **(D)** tricationic singlet state (TSS) of $Sc^{z+}(OH_2)_n$; $z = 1$–3 and $n = 1$–6 complexes obtained using the LMO-EDA scheme at B3LYP/6-311G**//MP2/6-31G* for hydrogen (H) and oxygen (O) and B3LYP/cc-pVTZ//MP2/6-31G* for the Sc^{z+} ion.

carried out to examine the contribution of energy components into the Sc ion–water interaction, as shown in **Figure 10** and **Supplementary Table S9**. The figure shows that the contribution of the ΔE_{ele} component dominates the Sc and water interaction followed by the contribution of the ΔE_{pol} component, irrespective of oxidation and spin states. However, the contribution of the ΔE_{disp} component is found to be negligible with around a contribution of 2–6%, as shown in **Figure 10**.

CONCLUSION

The present study reveals that a bare metal ion, in general, and Sc ion, in particular, have a great propensity in participating in multiple mechanistic pathways, and the relative propensity and feasibility of these pathways are dependent on a number of factors. As expected, water molecules in the first solvation shell bestow higher levels of stability for the complexes compared to the situation where they are occupying the second solvation shell. Following similar trends, within the case for each coordination number (CN = 1–5), the complexes with the proportionately higher number of water molecules in the closer solvation shell are found to be more stable. The sequential solvation analysis suggested that $Sc(OH_2)_n$, where n = 1–6, ion complexes are stable when all water molecules are in the first solvation shell, that is, 1 + 0, 2 + 0, 3 + 0, 4 + 0, 5 + 0, and 6 + 0 structures. ΔE_{seq} decreases with the addition of every subsequent water molecule to the complexes irrespective of oxidation and spin states, without any exception. The oxidation and spin states and the microenvironment around the ion–water interaction will have a profound influence on the relative feasibility of these competing pathways, giving rise to the power of fine-tuning the

electrons and microenvironment around the metal to achieve the preference for a given pathway. Thus, transition metal catalysis to split water and produce important gases such as H_2 and O_2 is a very promising and viable approach, and the key is to electronically fine-tune the metal ion center.

DATA AVAILABILITY STATEMENT

The raw data supporting the conclusion of this article will be made available by the authors, without undue reservation.

AUTHOR CONTRIBUTIONS

GNS has provided the idea and supervised the study. NK and YBK performed calculations. GNS, HS, and NK have undertaken the data analysis, interpreted results, and wrote the article.

ACKNOWLEDGMENTS

SUPPLEMENTARY MATERIAL

The Supplementary Material for this article can be found online at: https://www.frontiersin.org/articles/10.3389/fchem.2021.738852/full#supplementary-material

REFERENCES

Armentrout, P. B., and Beauchamp, J. L. (1989). The Chemistry of Atomic Transition-Metal Ions: Insight into Fundamental Aspects of Organometallic Chemistry. *Acc. Chem. Res.* 22 (9), 315–321. doi:10.1021/ar00165a004

Armentrout, P. B. (1991). Chemistry of Excited Electronic States. *Science* 251, 175–179. doi:10.1126/science.251.4990.175

Ashley, D. C., and Jakubikova, E. (2017). Ironing Out the Photochemical and Spin-Crossover Behavior of Fe(II) Coordination Compounds with Computational Chemistry. *Coord. Chem. Rev.* 337, 97–111. doi:10.1016/j.ccr.2017.02.005

Bader, R. F. W. (1998). A Bond Path: a Universal Indicator of Bonded Interactions. *J. Phys. Chem. A.* 102, 7314–7323. doi:10.1021/jp981794v

Bader, R. F. W. (1985). Atoms in Molecules. *Acc. Chem. Res.* 18, 9–15. doi:10.1021/ar00109a003

Chen, Y.-M., Clemmer, D. E., and Armentrout, P. B. (1994). Kinetic and Electronic Energy Dependence of the Reactions of Sc+ and Ti+ with D2O. *J. Phys. Chem.* 98, 11490–11498. doi:10.1021/j100095a034

Cheng, P., Koyanagi, G. K., and Bohme, D. K. (2007). Heavy Water Reactions with Atomic Transition-Metal and Main-Group Cations: Gas Phase Room-Temperature Kinetics and Periodicities in Reactivity. *J. Phys. Chem. A.* 111, 8561–8573. doi:10.1021/jp072661p

Chiodo, S., Kondakova, O., Michelini, M. d. C., Russo, N., Sicilia, E., Irigoras, A., et al. (2004). Theoretical Study of Two-State Reactivity of Transition Metal Cations: The "Difficult" Case of Iron Ion Interacting with Water, Ammonia, and Methane. *J. Phys. Chem. A.* 108, 1069–1081. doi:10.1021/jp036558l

Clemmer, D. E., Aristov, N., and Armentrout, P. B. (1993). Reactions of Scandium Oxide (ScO+), Titanium Oxide (TiO+) and Vanadyl (VO+) with Deuterium:

M+-OH Bond Energies and Effects of Spin Conservation. *J. Phys. Chem.* 97, 544–552. doi:10.1021/j100105a005

Costas, M., and Harvey, J. N. (2013). Discussion of an Open Problem. *Nat. Chem* 5, 7–9. doi:10.1038/nchem.1533

Dalleska, N. F., Honma, K., Sunderlin, L. S., and Armentrout, P. B. (1994). Solvation of Transition Metal Ions by Water. Sequential Binding Energies of M+(H2O)x (X = 1-4) for M = Ti to Cu Determined by Collision-Induced Dissociation. *J. Am. Chem. Soc.* 116, 3519–3528. doi:10.1021/ja00087a044

Frisch, M. J., Trucks, G. W., Schlegel, H. B., Scuseria, G. E., Robb, M. A., Cheeseman, J. R., et al. (2009). *Gaussian.* Wallingford. CT: Gaussian Inc.

Goodman, H., Mei, L., and Gianetti, T. L. (2019). Molecular Orbital Insights of Transition Metal-Stabilized Carbocations. *Front. Chem.* 7, 365. doi:10.3389/fchem.2019.00365

Harvey, J., Poli, R., and Smith, K. M. (2003). Understanding the Reactivity of Transition Metal Complexes Involving Multiple Spin States. *Coord. Chem. Rev.* 238-239, 347–361. doi:10.1016/S0010-8545(02)00283-7

Hippeli, S., and Elstner, E. F. (1999). Transition Metal Ion-Catalyzed Oxygen Activation during Pathogenic Processes. *FEBS Lett.* 443, 1–7. doi:10.1016/S0014-5793(98)01665-2

Irigoras, A., Elizalde, O., Silanes, I., Fowler, J. E., and Ugalde, J. M. (2000). Reactivity of Co+(3F,5F), Ni+(2D,4F), and Cu+(1S,3D): Reaction of Co+, Ni+, and Cu+with Water. *J. Am. Chem. Soc.* 122, 114–122. doi:10.1021/ja991657r

Irigoras, A., Fowler, J. E., and Ugalde, J. M. (1998). On the Reactivity of Ti+($^4F,^2F$). Reaction of Ti+ with OH^2. *J. Phys. Chem. A.* 102, 293–300. doi:10.1021/jp973143p

Irigoras, A., Fowler, J. E., and Ugalde, J. M. (1999a). Reactivity of Cr+($^6S,^4D$), Mn+($^7S,^5S$), and Fe+($^6D,^4F$): Reaction of Cr+, Mn+, and Fe+ with Water. *J. Am. Chem. Soc.* 121, 8549–8558. doi:10.1021/ja984469u

Irigoras, A., Fowler, J. E., and Ugalde, J. M. (1999b). Reactivity of Sc$^+$(^{3}D,^{1}D) and V$^+$(^{5}D,^{3}F): Reaction of Sc$^+$ and V$^+$ with Water. *J. Am. Chem. Soc.* 121, 574–580. doi:10.1021/ja9805829

Kauffman, J. W., Hauge, R. H., and Margrave, J. L. (1985). Studies of Reactions of Atomic and Diatomic Chromium, Manganese, Iron, Cobalt, Nickel, Copper, and Zinc with Molecular Water at 15 K. *J. Phys. Chem.* 89, 3541–3547. doi:10.1021/j100262a023

Kumar, N., Saha, S., and Sastry, G. N. (2021). Towards Developing a Criterion to Characterize Non-covalent Bonds: A Quantum Mechanical Study. *Phys. Chem. Chem. Phys.* 23, 8478–8488. doi:10.1039/D0CP05689H

Magnera, T. F., David, D. E., and Michl, J. (1989). Gas-phase Water and Hydroxyl Binding Energies for Monopositive First-Row Transition Metal Ions. *J. Am. Chem. Soc.* 111, 4100–4101. doi:10.1021/ja00193a051

Mahadevi, A. S., and Sastry, G. N. (2013). Cation−π Interaction: Its Role and Relevance in Chemistry, Biology, and Material Science. *Chem. Rev.* 113, 2100–2138. doi:10.1021/cr300222d

Mahadevi, A. S., and Sastry, G. N. (2016). Cooperativity in Noncovalent Interactions. *Chem. Rev.* 116 (5), 2775–2825. doi:10.1021/cr500344e

Mahadevi, A. S., and Sastry, G. N. (2014). Modulation of Hydrogen Bonding upon Ion Binding: Insights into Cooperativity. *Int. J. Quan. Chem.* 114, 145–153. doi:10.1002/qua.24529

Marinelli, P. J., and Squires, R. R. (1989). Sequential Solvation of Atomic Transition-Metal Ions. The Second Solvent Molecule Can Bind More Strongly Than the First. *J. Am. Chem. Soc.* 111, 4101–4103. doi:10.1021/ja00193a052

Meng, L., Hu, A., Pang, R., and Lin, Z. (2012). Extensive Computational Study on Coordination of Transition Metal Cations and Water Molecules to Glutamic Acid. *J. Phys. Chem. A.* 116, 7177–7188. doi:10.1021/jp303289p

Mó, O., Yáñez, M., Salpin, J. Y., and Tortajada, J. (2007). Thermochemistry, Bonding, and Reactivity of Ni + and Ni 2+ in the Gas Phase. *Mass. Spectrom. Rev.* 26, 474–516. doi:10.1002/mas.20134

Neela, Y. I., Mahadevi, A. S., and Sastry, G. N. (2013a). Analyzing Coordination Preferences of Mg2+ Complexes: Insights from Computational and Database Study. *Struct. Chem.* 24, 637–650. doi:10.1007/s11224-012-0113-0

Neela, Y. I., Mahadevi, A. S., and Sastry, G. N. (2013b). First Principles Study and Database Analyses of Structural Preferences for Sodium Ion (Na+) Solvation and Coordination. *Struct. Chem.* 24, 67–79. doi:10.1007/s11224-012-0032-0

Neela, Y. I., Mahadevi, A. S., and Sastry, G. N. (2010). Hydrogen Bonding in Water Clusters and Their Ionized Counterparts. *J. Phys. Chem. B* 114, 17162–17171. doi:10.1021/jp108634z

Poli, R. (1996). Open-shell Organometallics as a Bridge between Werner-type and Low-Valent Organometallic Complexes. The Effect of the Spin State on the Stability, Reactivity, and Structure. *Chem. Rev.* 96, 2135–2204. doi:10.1021/cr9500343

Rao, J. S., Dinadayalane, T. C., Leszczynski, J., and Sastry, G. N. (2008). Comprehensive Study on the Solvation of Mono- and Divalent Metal Cations: Li$^+$, Na$^+$, K$^+$, Be^{2+}, Mg^{2+} and Ca^{2+}. *J. Phys. Chem. A.* 112, 12944–12953. doi:10.1021/jp8032325

Rosi, M., and Bauschlicher, C. W., Jr (1989). The Binding Energies of One and Two Water Molecules to the First Transition-row Metal Positive Ions. *J. Chem. Phys.* 90, 7264–7272. doi:10.1063/1.456204

Russo, N., and Sicilia, E. (2001). Reaction of Sc$^+$(^{1}D,^{3}D) with H$_2$O, NH$_3$, and CH$_4$: A Density Functional Study. *J. Am. Chem. Soc.* 123, 2588–2596. doi:10.1021/ja000658c

Saha, S., and Sastry, G. N. (2015a). Cooperative or Anticooperative: How Noncovalent Interactions Influence Each Other. *J. Phys. Chem. B* 119, 11121–11135. doi:10.1021/acs.jpcb.5b03005

Saha, S., and Sastry, G. N. (2015b). Quantifying Cooperativity in Water Clusters: an Attempt towards Obtaining a Generalised Equation. *Mol. Phys.* 113, 3031–3041. doi:10.1080/00268976.2015.1072648

Shaik, S., Chen, H., and Janardanan, D. (2011). Exchange-Enhanced Reactivity in Bond Activation by Metal-Oxo Enzymes and Synthetic Reagents. *Nat. Chem* 3, 19–27. doi:10.1038/nchem.943

Sharma, B., Neela, Y. I., and Narahari Sastry, G. (2016). Structures and Energetics of Complexation of Metal Ions with Ammonia, Water, and Benzene: A Computational Study. *J. Comput. Chem.* 37, 992–1004. doi:10.1002/jcc.24288

Sharma, B., Rao, J. S., and Sastry, G. N. (2011). Effect of Solvation on Ion Binding to Imidazole and Methylimidazole. *J. Phys. Chem. A.* 115, 1971–1984. doi:10.1021/jp1120492

Sharma, B., Srivastava, H. K., Gayatri, G., and Sastry, G. N. (2015). Energy Decomposition Analysis of Cation-π, Metal Ion-Lone Pair, Hydrogen Bonded, Charge-Assisted Hydrogen Bonded, and π-π Interactions. *J. Comput. Chem.* 36, 529–538. doi:10.1002/jcc.23827

Su, P., and Li, H. (2009). Energy Decomposition Analysis of Covalent Bonds and Intermolecular Interactions. *J. Chem. Phys.* 131, 014102. doi:10.1063/1.3159673

Sundberg, R. J., and Martin, R. B. (1974). Interactions of Histidine and Other Imidazole Derivatives with Transition Metal Ions in Chemical and Biological Systems. *Chem. Rev.* 74 (4), 471–517. doi:10.1021/cr60290a003

Swart, M., and Gruden, M. (2016). Spinning Around in Transition-Metal Chemistry. *Acc. Chem. Res.* 49 (12), 2690–2697. doi:10.1021/acs.accounts.6b00271

Tilson, J. L., and Harrison, J. F. (1991). Electronic and Geometric Structures of Various Products of the Scandium+ + Water Reaction. *J. Phys. Chem.* 95, 5097–5103. doi:10.1021/j100166a036

Trachtman, M., Markham, G. D., Glusker, J. P., George, P., and Bock, C. W. (1998). Interactions of Metal Ions with Water: Ab Initio Molecular Orbital Studies of Structure, Bonding Enthalpies, Vibrational Frequencies and Charge Distributions. 1. Monohydrates. *Inorg. Chem.* 37, 4421–4431. doi:10.1021/ic971613o

Umadevi, D., Panigrahi, S., and Sastry, G. N. (2014). Noncovalent Interaction of Carbon Nanostructures. *Acc. Chem. Res.* 47 (8), 2574–2581. doi:10.1021/ar500168b

Umadevi, D., and Sastry, G. N. (2011). Molecular and Ionic Interaction with Graphene Nanoflakes: A Computational Investigation of CO2, H2O, Li, Mg, Li+, and Mg2+ Interaction with Polycyclic Aromatic Hydrocarbons. *J. Phys. Chem. C* 115, 9656–9667. doi:10.1021/jp201578p

Williams, R. J. P. (1968). Role of Transition Metal Ions in Biological Processes. *R. Inst. Chem. Rev.* 1, 13–38. doi:10.1039/RR9680100013

Yamaguchi, K., Jensen, F., Dorigo, A., and Houk, K. N. (1988). A Spin Correction Procedure for Unrestricted Hartree-Fock and Møller-Plesset Wavefunctions for Singlet Diradicals and Polyradicals. *Chem. Phys. Lett.* 149, 537–542. doi:10.1016/0009-2614(88)80378-6

Ye, S. (1997). Theoretical Study of the Dehydrogenation Reaction of Water by Sc+. *J. Mol. Struct. THEOCHEM* 417, 157–162. doi:10.1016/S0166-1280(97)00055-9

Zhao, L., Schwarz, W. H. E., and Frenking, G. (2019). The Lewis Electron-Pair Bonding Model: the Physical Background, One century Later. *Nat. Rev. Chem.* 3, 35–47. doi:10.1038/s41570-018-0052-4

Unraveling the Effect of Aromatic Groups in Mn(I)NNN Pincer Complexes on Carbon Dioxide Activation Using Density Functional Study

Saurabh Vinod Parmar[1], Vidya Avasare[1,2]* and Sourav Pal[2,3]*

[1]Department of Chemistry, Sir Parashurambhau College, Pune, India, [2]Department of Chemistry, Ashoka University, Sonipat, India, [3]Indian Institute of Science Education and Research, Kolkata, India

Carbon dioxide utilization is necessary to reduce carbon footprint and also to synthesize value-added chemicals. The transition metal pincer complexes are attractive catalysts for the hydrogenation of carbon dioxide to formic acid. There is a need to understand the factors affecting the catalytic performance of these pincer complexes through a structure–activity relationship study using computational methods. It is a well-established fact that aromatic functionalities offer stability and selectivity to transition metal catalysts. However, their impact on the performance of the catalysts is lesser known in the case of metal pincer complexes. Hence, it is necessary to investigate the catalytic performance of Mn(I)NNN pincer complexes with variably activated aromatic functionalities. In this context, 15 catalysts are designed by placing different types of aromatic rings at the pincer carbons and two terminal nitrogen of Mn(I)NNN pincer complexes. A benzene moiety, placed at C2–C3 carbons of Mn(I)NNN pincer complex with identical aromatic groups at the terminal nitrogen, is found to be most efficient toward CO_2 hydrogenation than the rest of the catalysts. On the other hand, when N,N-dimethyl aniline is placed at C2–C3 carbons of Mn(I)NNN pincer complexes, then the catalytic performance is significantly decreased. Thus, the present study unravels the impact of aromatic groups in Mn(I) NNN pincer complexes toward the catalytic hydrogenation of carbon dioxide.

Keywords: Mn pincer complexes, carbon dioxide, hydrogenation, NNN pincer ligands, density functional theory

INTRODUCTION

The burning of fossil fuels continuously increases CO_2 concentration in the atmosphere, leading to a substantial and negative impact on the world climate. About 33,890.8 million tons of CO_2 was released into the atmosphere in 2018, and the global CO_2 concentration in the atmosphere reached 407.65 (BP Statistical Review of World Energy, 2019; Global Monitoring Division, 2019) Nearly ~35 GT of CO_2 is being added to the atmosphere per year, and there is a considerable gap between the amount of CO_2 produced and utilized. Therefore, carbon dioxide utilization becomes a necessity to save the world from global warming. CO_2 utilization would not only help to remove CO_2 from the atmosphere but also helps to get alternate fuels and to reduce dependence on petrochemicals and, thus, restricts CO_2 expulsion in the atmosphere (Centi and Perathoner, 2009; Balaraman et al., 2011). Apart from forming fuels from carbon dioxide, many synthetically useful chemicals are being synthesized from carbon dioxide (Aresta, 2010). The conversion of formic acid from carbon dioxide has manifold benefits to the environment and economy. Formic acid is considered to be potential chemical hydrogen storage material because of its stability, nontoxicity, and easy accessibility

GRAPHICAL ABSTRACT | TOC for paper.
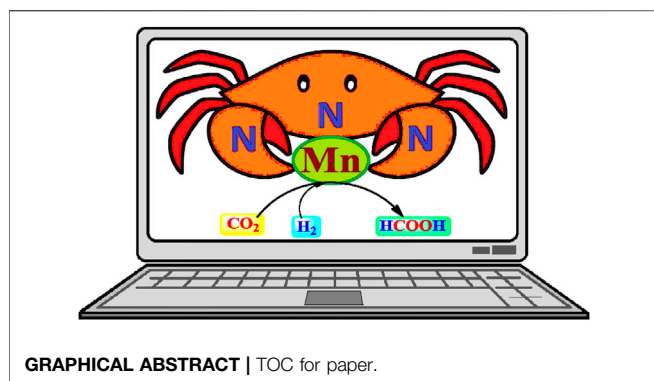
(Dörthe et al., 2016; Jörg et al., 2017; Miriam et al., 2019; Ganesh, 2014; Kassem et al., 2020). The global formic acid market is growing at a CAGR of 1.3%, and it is expected to reach US$828.1 million by 2025 due to its wide applications in agriculture, leather, textile, rubber, chemical and pharmaceuticals, and industries (https://dataintelo.com/report/formic-acid-market). Therefore, developing an energy-efficient and environmentally benign protocol to get formic acid from CO$_2$ becomes significant.

In carbon dioxide activation and formation of formic acid or formate derivatives, the use of rhodium, ruthenium, and iridium pincer complexes have made remarkable progress in recent years (Wen, et al., 2021; Wang et al., 2013; Huff and Sanford, 2011; Wesselbaum et al., 2012; Kothandaraman et al., 2016; Wesselbaum et al., 2015; Campos et al., 2014). However, the high price and limited availability of these metals restrict their wide applications to an industrial scale. Therefore, the development of new catalytic technologies based on earth-abundant metals such as Fe, Mn, Ni, and Co is of considerable interest (**Figure 1**) (Zell and Milstein, 2015; Furstner, 2016; Langer et al., 2011; Zhang et al., 2015; Ge et al., 2016; Choi and Lee, 2020; Curley et al., 2018). The transition metal pincer complexes of these earth-abundant metals are of particular

importance due to their thermal stability, cost efficiency, and flexibility for modification. The flexibility in the modification could be useful to fine-tune structural and electronic properties of the metal pincer complexes to make them more reactive as well as more selective (Peris and Crabtree, 2018). In this context, Mn pincer complexes in catalytic carbon dioxide hydrogenation have seen much progress over a much shorter time (Bertini et al., 2017; Garbe et al., 2017; Kar et al., 2017). The PNP, PCP PNN pincer complexes have been commonly used to develop transition metal pincer complexes (Kumar et al., 2019; Bernskoetter and Hazari, 2017; Irina et al., 2016; Bertini et al., 2016; Jan et al., 2020). It is necessary to understand the donor–acceptor strength of the ligand during the rational ligand designing for new catalyst development. In all the cases, the metal–ligand interaction will depend highly on the choice of the transition metal, oxidation state, coordinating sites of the ligands, and the substituents on ligands. Steric bulk is also an extremely important aspect not only for enhancing the stability of the complexes but also for providing stereoselectivity (Garbe et al., 2019; Wen et al., 2021; Jessica et al., 2017). The NNN pincer ligands are of particular importance due to their accessibility, scalability, stability, and affordability. In the recent review, Crabtree mentioned that there is a necessity to explore transition metal NNN pincer complexes and to understand their catalytic performance (Peris and Crabtree, 2018). Herein, 15 Mn(I)NNN pincer complexes are designed to understand steric and electronic factor ligands on the catalytic efficacy toward carbon dioxide hydrogenation (**Figure 2**). However, it would be difficult to understand the efficacy of these 15 Mn(I)NNN complexes and also to throw light on the impact of aromatic and heterocyclic rings present in the NNN pincer ligands by using experimental methods. Therefore, the use of computational methods to assess a large number of complexes by evaluating the mechanistic pathway and energetics of the reaction is highly desirable.

FIGURE 1 | Recently developed NNN pincer ligands with varying electron withdrawing and donating moieties.
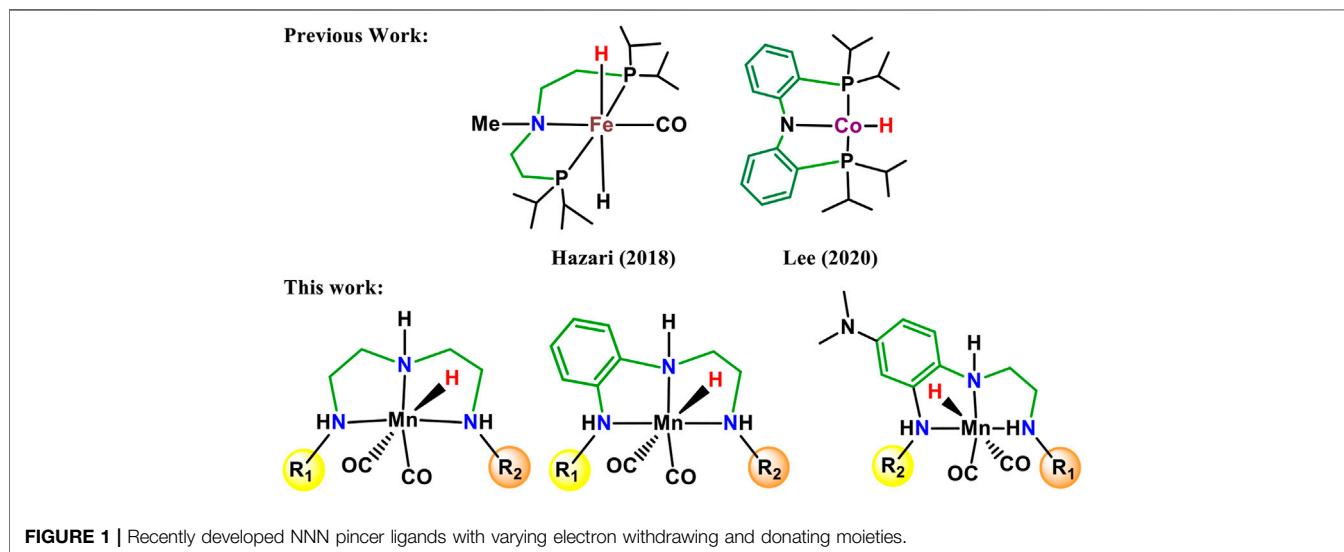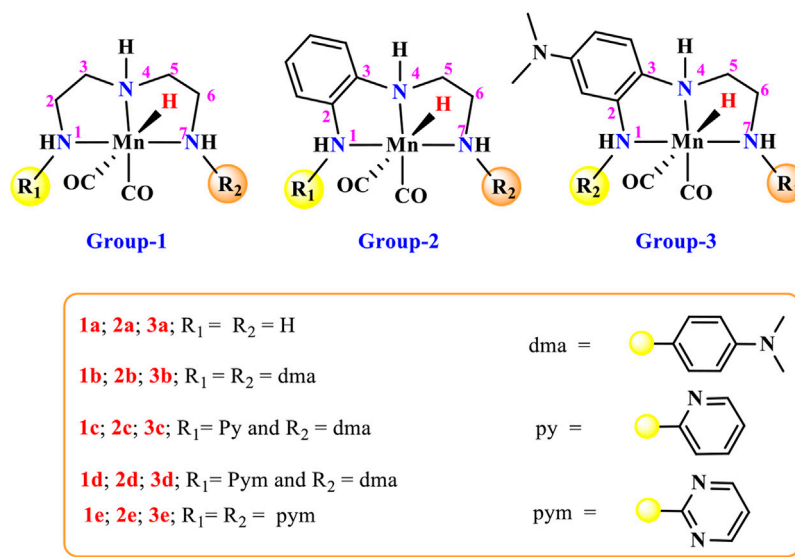
FIGURE 2 | Mn(I)NNN complexes designed for the computational study of the impact of aromatic substituents on carbon dioxide hydrogenation.

COMPUTATIONAL DETAILS

The Gaussian-16 program package was used to perform the computational calculations (Frisch et al., 2016). The meta-GGA hybrid M06 functional with dispersion corrections without the imposition of any symmetry constraints were used to optimize reactants and intermediates (Zhao and Truhlar, 2008a). M06 is the accurate, economical functional for transition metals than B3LYP functional (Hehre et al., 1972). The SDD basis set was used for manganese, and Pople's 6-31G(d,p) basis set was used for all the main group elements (Hariharan and Pople, 1973; Hay and Wadt, 1985). All complexes were treated as neutral species to compute optimized energies. The ground states of intermediates and transition states were confirmed as singlets through the comparison with optimized high-spin analogs. All transition states exhibited a single imaginary frequency, corresponding to the eigenvector along the reaction path. Frequency analysis of all the stationary points was performed at the same level of theory to confirm stationary points as minima or first-order saddle points along with the reaction coordinate (Liu et al., 2012; Jain et al., 2018; Zhao and Truhlar, 2008b). Intrinsic reaction coordinates (IRCs) were carried out on the transition states to endorse that such structures were indeed connecting the two minima, reactant, and product (Fukui, 1970; Fukui, 1981). All the calculations presented in this work were performed in the presence of water (dielectric constant = 78.39) using the integral equation formalism variant-like solvation model based on density (SMD) (Aleksandr et al., 2009; Aleksandr et al., 2009).

NBO analysis was carried out using the NBO 3.1 suite as implemented in Gaussian-16 (Foster and Weinhold, 1980; Reed et al., 1985; Reed and Weinhold, 1985; Glendening et al., 1987; Carpenter et al., 1988; Reed et al., 1988). The second-order perturbative estimation of donor–acceptor stabilization energy (E$_s$) was calculated using the following equation,

$$E_s = \Delta E_{ij} = q_i \frac{F_{ij}^2}{\Delta \varepsilon_{ji}} \qquad (1)$$

where q_i is the donor orbital occupancy number, and F_{ij} is the off-diagonal element of the Fock matrix in the NBO basis. $\Delta \varepsilon_{ji} = \varepsilon_j - \varepsilon_i$ is the orbital energy difference between the acceptor (j) and donor (i) NBO.

The solvent-corrected relative Gibbs free energies (ΔG) for the transition states and intermediate as well as overall activation Gibbs free energies ($\Delta G^\square$) for the catalytic cycle was calculated at 1 atm pressure and 298.15 K temperature. Visualization of all optimized structures was performed using the CYLview software (CYLview, 2020), and imaging of all NBO structures and orbitals was performed using the Chemcraft Visualization software (Chemcraft, 2021).

CATALYST DESIGNING

A large number of pincer catalysts have been developed for various catalytic applications. (Bernskoetter and Hazari, 2017; Irina et al., 2016; Garbe et al., 2019; Kumar et al., 2019; Kar et al., 2020; Wen et al., 2021). However, PNP and PCP pincer complexes have been studied mostly than NNN pincer complexes (Bernskoetter and Hazari, 2017; Bertini et al., 2016; Kar et al., 2019; Tang et al., 2019). Therefore, it is necessary to explore the efficacy of Mn(I)NNN pincer complexes toward the activation of carbon dioxide. In many instances, aromatic systems
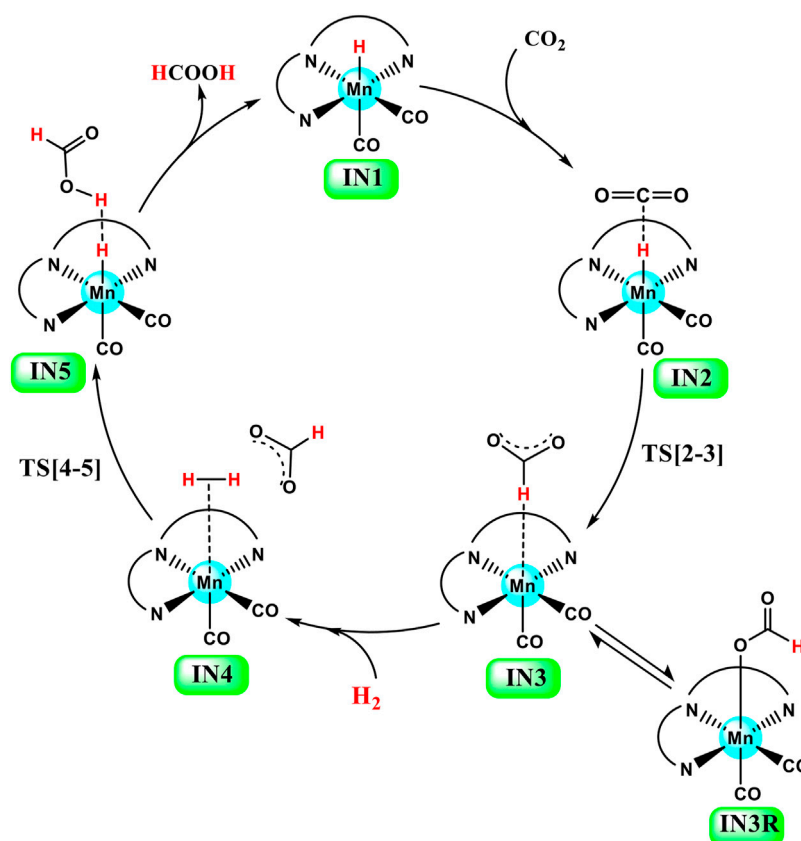
FIGURE 3 | General catalytic cycle of Mn(I)NNN-catalyzed hydrogenation of carbon dioxide to formic acid through the NC pathway for **Groups 1**, **2**, and **3** catalysts.

are commonly used during the designing of metal pincer complexes with limited combinations (**Figure 1**) (Choi and Lee., 2020; Jessica et al., 2015; Talukdar et al., 2019). The aromatic systems are known to provide better thermal stability to the catalyst complex by offering steric bulk and hydrophobic groups to minimize the leaching of the metals. However, it is very important to understand the impact of the position and the nature of the aromatic rings present in the pincer complexes on their catalytic performances. It would be impossible to study all these parameters using any experimental study, and hence, the DFT (density functional theory) would play an important role to throw light on the effect of aromatic rings on the efficacy of the catalysts. Herein, 15 catalysts were designed by changing the position and reactivity of the aromatic ring attached to pincer ligands. These 15 catalysts were further studied to understand the impact of the position and nature of the aromatic rings on carbon dioxide hydrogenation (**Figure 2**). The computationally designed catalysts are classified into three groups: 1) **Group 1**: No aromatic ring is placed on pincer ring carbons. 2) **Group 2**: The benzene ring is inserted at the C2—C3 carbons of the pincer ring. 3) **Group 3**: The N,N-dimethyl aniline ring is inserted at the C2—C3 carbons of the pincer ring in such a way that the N,N-dimethyl group is para to the C3 nitrogen. All three groups are further subdivided into **a**, **b**, **c**, **d**, and **e** classes based on the substituents attached to the terminal nitrogens of

the pincer ligands. The hydrogens attached to both the terminal nitrogens are replaced with differently activated aromatic rings in all the three groups like N,N-dimethyl aniline, pyridine, and pyrimidine (**Figure 2**). Catalysts **1a, 2a,** and **3a** contain all unsubstituted pincer nitrogen. The hydrogens of both the terminal nitrogen are replaced by an electron-donating group, N,N-dimethyl aniline, in **1b, 2b,** and **3b** catalysts, whereas catalysts **1c, 2c,** and **3c** contain pyridine and N,N-dimethyl aniline groups attached to both the terminal nitrogen of the Mn(I)NNN pincer complex. Catalysts **1d, 2d,** and **3d** are designed to have pyrimidine and N,N-dimethyl aniline groups attached to each terminal nitrogen of the pincer complexes. The two strong electrons withdrawing the pyrimidine groups are attached to the Mn(I)NNN pincer ring nitrogen in catalysts **1e, 2e,** and **3e** (**Figure 2**). All these 15 Mn(I)NNN pincer complexes are further used to explore their catalytic performance toward carbon dioxide hydrogenation (**Figure 3**).

RESULT AND DISCUSSION

Hydrogenation of Carbon Dioxide to Formic Acid Catalyzed by Group 1 Catalysts, 1a–1e

Catalysts **1a–1e** are designed to explore the impact of donating and withdrawing groups on the catalytic performance in the
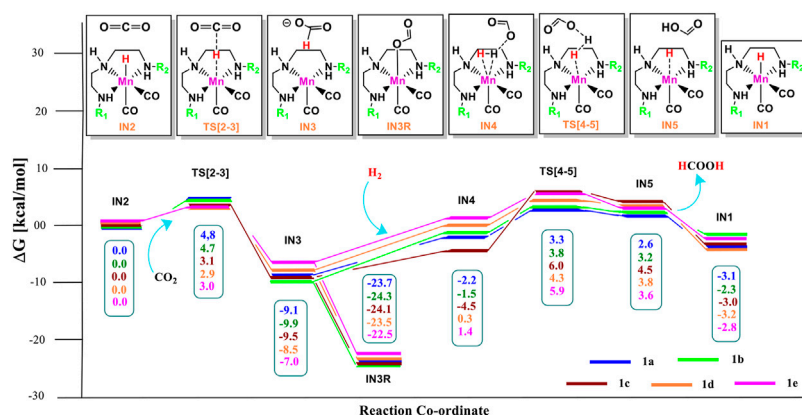
FIGURE 4 | Solvent-corrected relative Gibbs free energy profile for Mn(I)NNN-catalyzed formation of formic acid through the NC pathway for catalysts **1a–1e**. Calculations were carried out at the M06/6-31G(d,p)-SDD(Mn), SMD(H₂O) level of theory.
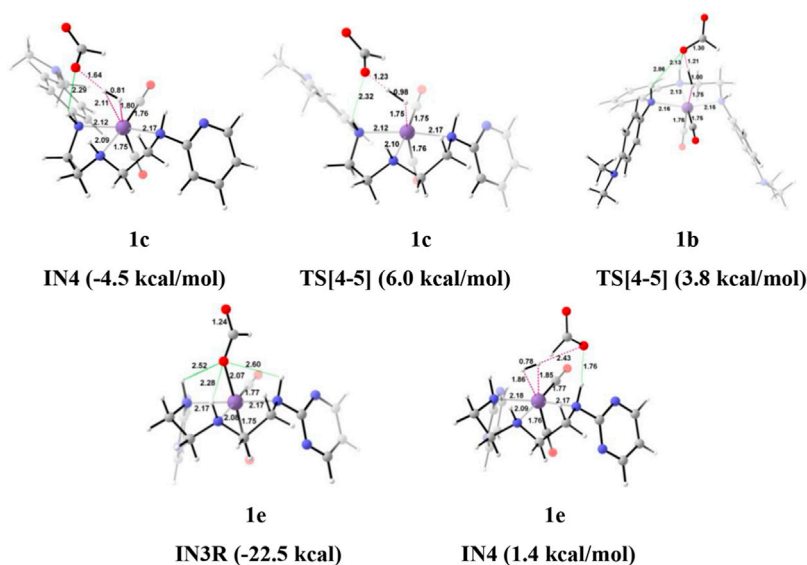
FIGURE 5 | The optimized geometries of the intermediates in the formation of formic acid from carbon dioxide. The bond lengths are in Å, and the relative Gibbs free energies are in parentheses (Figures are shown in **Supplementary Data Sheet S1** for all the optimized geometries of all the transition states and intermediates).

absence of any aromatic rings on the pincer ring carbons toward CO₂ hydrogenation (**Figure 2**). The intermediate **IN2** is obtained after the addition of CO₂ to the active catalyst complex **IN1** of the catalysts **1a–1e**. The relative Gibbs free energies of the transition state and the intermediate states are calculated by considering the relative Gibbs free energy of the **IN2** as 0.0 kcal/mol (**Figure 4**). The **IN2** is further converted into the **IN3** by transferring the hydride from the Mn center to the carbon dioxide carbon through the transition state **TS[2-3]**.

The relative Gibbs free energies for the **TS[2-3]** are ~3.0 kcal/mol for the catalyst complexes **1c**, **1d**, and **1e** and ~4.8 kcal/mol for the catalyst complexes **1a** and **1b**. The **IN3** of all three catalysts groups are stabilized with the relative Gibbs free energy of approximately ~−7.0 to −10.0 kcal/mol. The relative Gibbs free

energy of **IN3** is minimum for **1b** (−9.9 kcal/mol) and maximum for **1e** (−7.0 kcal/mol). The **IN3** further isomerizes to the **IN3R** (−22.5 to −24.3 kcal/mol) by forming an Mn—OCHO bond. This is the most stable state TDI (Turn-over Determining Intermediate), and hence, it is also a rate-determining state of the reaction. The **IN3R** again isomerizes to **IN3** with an energy barrier of ~15.0 kcal/mol, and then, the protonation takes place. The hydrogen molecule adds to **IN3** to provide the **IN4** comprising formic acid. The relative Gibbs free energy of the **IN4** is minimum for **1c** (−4.5 kcal/mol) and maximum for **1e** (1.4 kcal/mol) (**Figure 5**).

Interestingly, we found that in **Group 1**, the catalyst with a shorter Mn—N (**1a**, Mn—N = 2.13 Å) distance performs better than the catalyst with a longer Mn—N bond (**1e**,

1a

IN1 (-3.1 kcal/mol)

1b

IN1 (-2.3 kcal/mol)

1c

IN1 (-3.0 kcal/mol)

1d

IN1 (-3.2 kcal/mol)

1e

IN1 (-2.7 kcal/mol)

FIGURE 6 | The optimized geometries of the **Group 1 IN1** catalysts. The bond lengths are in Å, and relative Gibbs free energies are in parentheses (The optimized geometries of all the transition states and intermediates are disclosed in **Supplementary Data Sheet S1**).

Mn—N = 2.20 Å) distance (**Figure 6**). However, there is no significant change in the Mn—N bond distance during the catalytic reaction. The presence of a strong H-bond (HCOO—H$_2$ = 1.64 Å) in **1c** than in **1e** (HCOO—H$_2$ = 2.43 Å) lowers the relative Gibbs free energy in **1c** (−4.5 kcal/mol) than **1e** (1.36 kcal/mol) in **IN4**. However, **TS[4-5]** of **1c** is found to have higher Gibbs free energy than **1b**, due to strong H$_2$ polarization and strong bond-forming interactions in **1b** (1.00 Å) than in **1c** (0.98 Å).

A similar dihydrogen polarization is found to be efficient in the M—H$_2$ σ-complex of **1c** (0.81 Å) than in **1e** (0.78 Å). The **IN4** is further converted into **IN5**, the regenerated catalyst and formic acid complex through the **TS[4-5]** with the relative Gibbs free energy of 3.3–6.0 kcal/mol for all the catalysts. However, the activation energy barrier for this step is the lowest for **1a** (3.3 kcal/mol) and the highest for **1c** (6.0 kcal/mol). In this entire mechanism, the dihydrogen dissociation and catalyst regeneration steps are more energy demanding by 1–3 kcal/mol than the hydride transfer transition state for the catalyst complexes **1c**, **1d**, and **1e**. On the other hand, the catalysts complexes **1a** and **1b** show facile protonation via dihydrogen polarization than the

TABLE 1 | Catalytic performance of **Group 1** catalyst, **1a–1e**.

Catalyst group 1	Activation energy ($\Delta G^{\ddagger}$) (kcal/mol)
1a	23.9
1b	25.8
1c	27.1
1d	24.6
1e	25.7

hydride transfer from the Mn center to carbon dioxide. In overall CO$_2$ to formic acid formation, catalysts **1a** and **1d** have almost the same catalytic efficiency as the rest of the catalysts with $\Delta G^{\square}$ of 23.9 and 24.6 kcal/mol (**Table 1**), whereas catalyst complex **1c** is most sluggish toward carbon dioxide hydrogenation. This indicates that unsubstituted carbon centers of Mn(I)NNN with unsubstituted nitrogen pincer ligands of **Group 1** show better catalytic performance than the one with electron-withdrawing groups. The donating groups and moderate withdrawing groups at terminal nitrogen make **1b** and **1c** catalysts less reactive than the Mn(I)NNN complex **1a** and
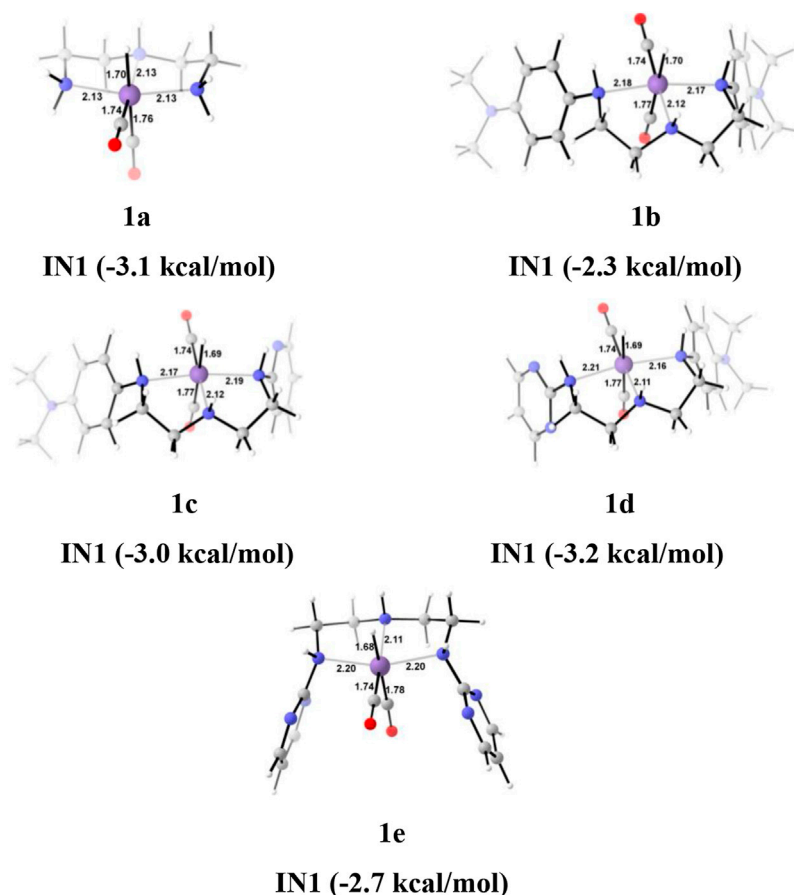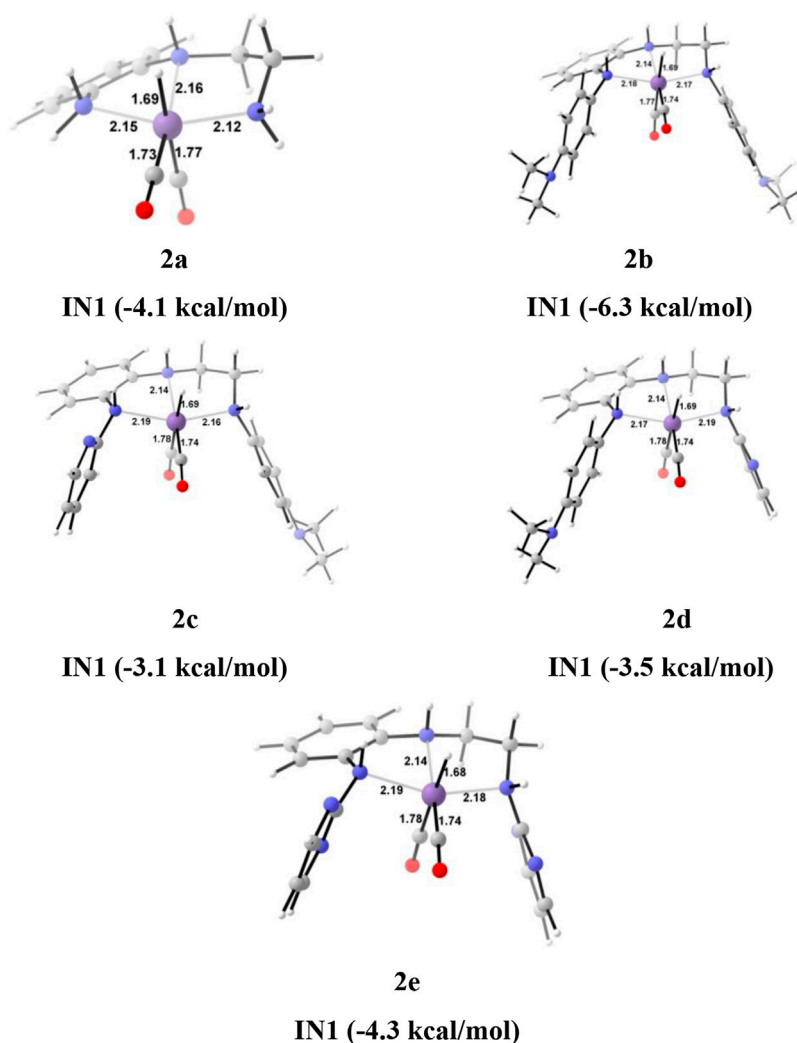
FIGURE 7 | The optimized geometries of the **Group 2 IN1** catalysts. The bond lengths are in Å, and relative Gibbs free energies are in parentheses (The optimized geometries of all the transition states and intermediates are disclosed in **Supplementary Data Sheet S1**).

1d. However, there is no drastic change in the reactivity when we change the N substituents in **Group 1** Mn(I)NNN pincer complexes.

Hydrogenation of carbon dioxide to formic acid catalyzed by Group 2 catalysts 2a–2e

The unsubstituted pincer ring carbons provided exciting results; therefore, we decided to investigate the effect of aromatic substituents of the pincer carbons (C2 and C3) on the catalytic performance (Curley et al., 2018; Kumar et al., 2019; Luca et al., 2020) (**Figure 2**). Herein, C2 and C3 carbons of catalysts **1a-1e** are used to attach the unsubstituted aromatic ring to form the new pincer complexes **2a-2e** (**Figure 7**). After the addition of carbon dioxide to these pincer complexes, **IN2** is formed. The relative Gibbs free energy of the **IN2** is considered as 0.0 kcal/mol to calculate the relative Gibbs free energies of the transition state and the intermediate states (**Figure 8**). The intermediate **IN2** converts

into the **IN3** through the transition state **TS[2-3]**. The activation energy barrier for the **TS[2-3]** is found to be maximum for catalyst **2b** (4.3 kcal/mol) and minimum for catalyst **2e** (1.9 kcal/mol). The **TS[2-3]** (1.9 kcal/mol) has the lowest relative Gibbs free energy among all the **Group 2** catalysts. This could be due to a strong H-bond [N(1) H...OCO = 2.7 Å, N(4) H...OCO = 2.3 Å, and N(7) H...OCO = 2.9 Å] among the **Group 2** catalysts (**Figure 9**). The **IN3** of **2a** (−11.2 kcal/mol) is the most stable, and **2b** (−8.1 kcal/mol) is less stable among all the catalysts. It has been reported in papers that **IN3** isomerizes to a more stable metal formate intermediate, **IN3R** (Boodsarin et al., 2018; Kumar et al., 2019). Herein, all the **IN3R** intermediates are stabilized by three strong H-bonds with a relative Gibbs free energy of ∼ −24.0 to −27.0 kcal/mol (All energies are added in the table in **Supplementary Data Sheet S1**). However, strong H-bonds [N(1) H...OCHO = 2.26 Å, N(4) H...OCHO = 2.28 Å, and N(7) H...OCHO = 1.93 Å] stabilize the **IN3R** of catalyst **2d** more effectively than the rest of the catalysts (**Figure 9**). The

FIGURE 8 | Solvent-corrected relative Gibbs free energy profile for Mn(I)NNN-catalyzed formation of formic acid through the NC pathway for catalysts **2a–2e**. Calculations were carried out at the M06/6-31G(d,p)-SDD(Mn), SMD(H₂O) level of theory.

FIGURE 9 | The optimized geometries of the transition state in the formation of formic acid from carbon dioxide for catalysts **2a–2e**. The bond lengths are in Å, and relative Gibbs free energies are in parentheses (Figures are shown in **Supplementary Data Sheet S1** for all the optimized geometries of all the transition states and intermediates).

isomerization energy barrier for **IN3R** to **IN3** is ~15 kcal/mol for all the catalysts except **2d** (18.0 kcal/mol). When **IN3R** changes to **IN3**, then the hydrogen molecule adds to the **IN3** to provide the intermediate **IN4**. In the **IN4**, there is an increase in the Gibbs free energy by 2–9 kcal/mol than **IN3**.

In the Mn—H₂ σ-complex, the **IN4** of catalyst **2a** is most stable (−8.3 kcal/mol), whereas **2c** is the least stable (0.1 kcal/mol) (**Figure 9**) among all the catalysts. The presence of stronger H-bonds [N(1) H...OCHO = 1.8 Å and N(4)

H...OCHO = 1.78 Å] offer better stability than all the catalysts (~0 to −4 kcal/mol). The **IN4** of **2a** shows an Mn-H₂ σ-complex with an Mn center, and the remaining catalysts show a distorted Mn-H₂ σ-complex, where one Mn—H$_a$ (1.88 Å) is longer than the other Mn—H$_b$ (1.82 Å) bond (Structure in **Supplementary Data Sheet S1**). These distortions in the Mn—H bond could be due to strong dihydrogen polarization. The **IN4** converts into **IN5** through the **TS [4-5]**, where the strong dissociation of a dihydrogen bond is observed in all the catalysts. The H-bond stabilizes the **TS[4-5]**

TABLE 2 | Catalytic performance of **Group 2** catalyst, **2a–2e**.

Catalyst group 2	Activation energy (ΔG‡) (kcal/mol)
2a	24.7
2b	22.1
2c	27.2
2d	27.7
2e	22.8

with the relative Gibbs free energy of 2.0 to 5.0 kcal/mol. The **IN5** contains the product, formic acid, and the regenerated catalyst complex. The **IN5** further expels formic acid and provides regenerated catalysts, **2a–2e**. The ΔG for the entire catalytic reaction is found to be minimum for catalysts **2b** (22.1 kcal/mol) and **2e** (22.8 kcal/mol) and maximum for catalysts **2c** (27.2 kcal/mol) and **2d** (27.7 kcal/mol) (**Table 2**). This indicates that in **Group 2**, catalysts show better catalytic performance when both the terminal nitrogen are attached to either electron-donating groups, N,N-dimethyl aniline, or strong electron-withdrawing groups, pyrimidine. On the other hand, the catalytic

performance slows down when these two terminal nitrogens carry mixed electron-withdrawing and donation groups **2a** and **2c**. However, catalyst **2a** with an unsubstituted terminal nitrogen shows average performance toward carbon dioxide hydrogenation.

Hydrogenation of carbon dioxide to formic acid catalyzed by Group 3 catalysts, 3a–3e

The unsubstituted **Group 1**, as well as benzene, substituted **Group 2** manganese pincer complexes provided a deeper insight into their catalytic performances toward carbon dioxide hydrogenation reaction. Therefore, we also investigated the effect of the activated aromatic ring by placing N,N-dimethyl aniline at the C2—C3 of the pincer ligands of the Mn(I)NNN complex in **Group 3** (**Figures 2** and **10**) (Smith et al., 2018). Complexes **3a–3e** are designed to understand the effect of Mn(I)NNN complexes on carbon dioxide hydrogenation. After the addition of carbon dioxide to these pincer complexes, the **IN2** is formed. The relative Gibbs free energy of the **IN4** is considered as 0.0 kcal/mol to calculate the relative Gibbs free energies of the transition and the intermediate states (**Figure 11**). The **IN2** converts into the **IN3** through the transition state **TS[2-3]**. The
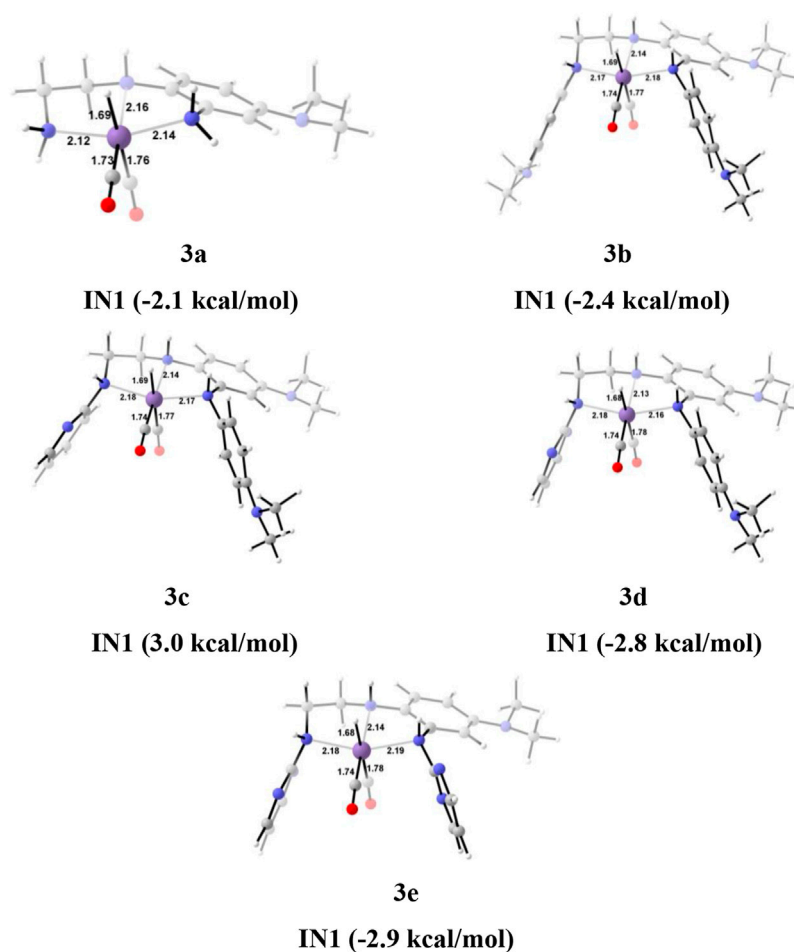
FIGURE 10 | The optimized geometries of the **Group 3 IN1** catalysts. The bond lengths are in Å, and relative Gibbs free energies are in parentheses (The optimized geometries of all the transition states and intermediates are disclosed in **Supplementary Data Sheet S1**).
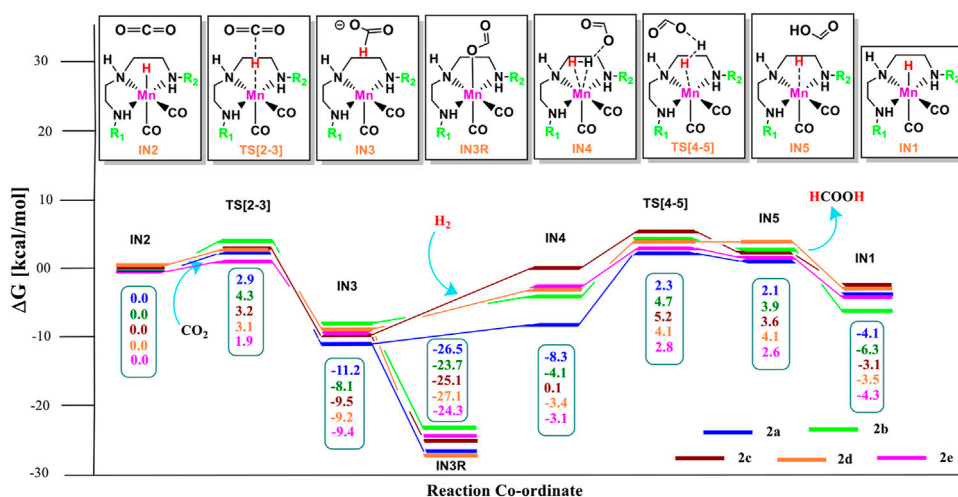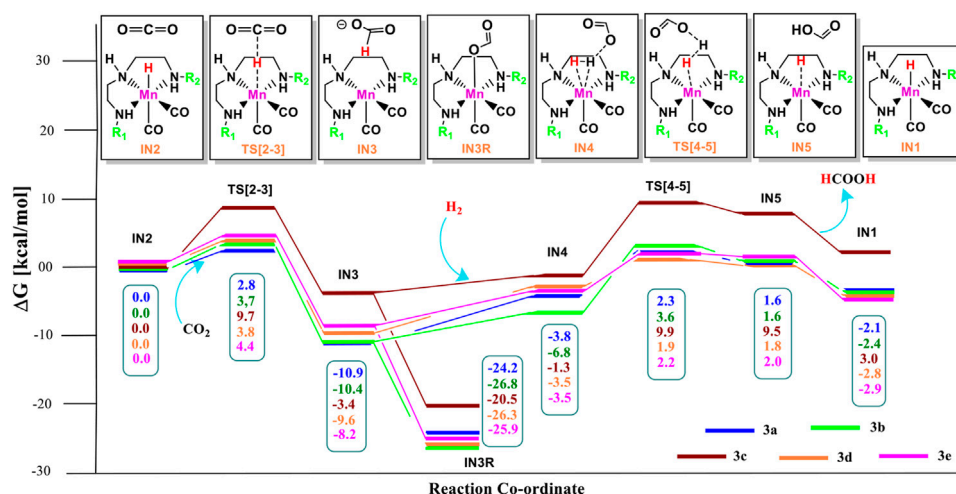
FIGURE 11 | Solvent-corrected relative Gibbs free energy profile for Mn(I)NNN-catalyzed formation of formic acid through the NC pathway for catalysts **3a–3e**. Calculations were carried out at the M06/6-31G(d,p)-SDD(Mn), SMD(H₂O) level of theory.
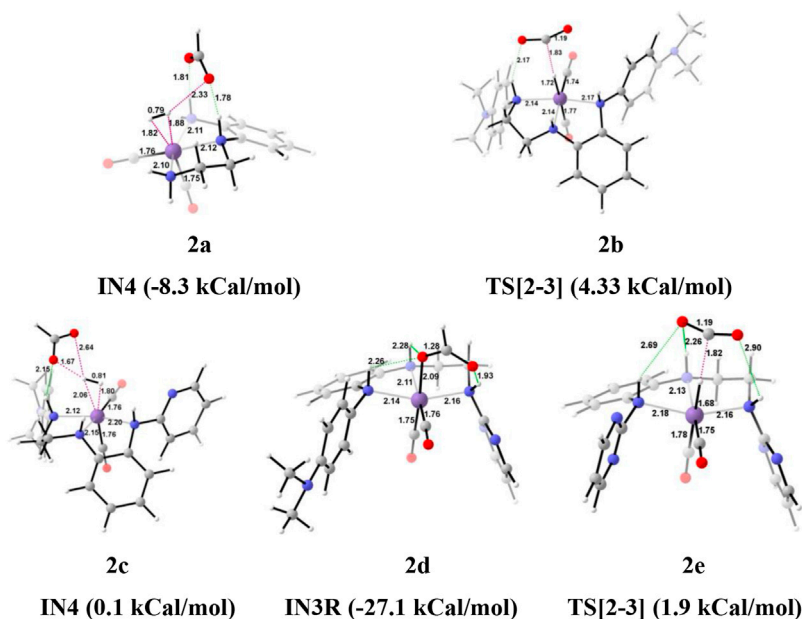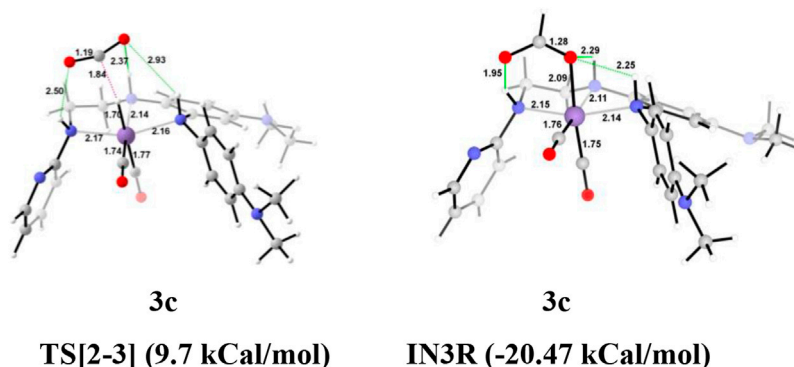

FIGURE 12 | The optimized geometries of the transition states **TS[2-3]** in the formation of formic acid from carbon dioxide for catalysts **3a–3e**. The bond lengths are in Å, and relative Gibbs free energies are in parentheses (The optimized geometries of all the transition states and intermediates are disclosed in **Supplementary Data Sheet S1**).

TABLE 3 | The catalytic performance of **Group 3** catalyst, **3a–3e**.

Catalyst group 3	Activation energy ($\Delta G^{\ddagger}$) (kcal/mol)
3a	24.4
3b	28.0
3c	33.4
3d	25.4
3e	25.3

relative Gibbs free energy of the **TS[2-3]** of all the catalysts is in the range of 3.0–4.0 kcal/mol except for catalyst **3c** (9.7 kcal/mol). The **TS [2-3]** [N(1) H...OCHO = 2.9 Å, N(4) H...OCHO = 2.4 Å, and N(7) H...OCHO = 2.5 Å] and **IN3R** [N(1) H...OCHO = 2.29 Å, N(4) H...OCHO = 2.25 Å, and N(7) H...OCHO = 1.95 Å] show moderate H-bonds in all the catalysts (**Figure 12**). After careful evaluation, it is observed that the **IN1** of **3c** has higher energy than the rest of the catalysts, and hence, the entire catalytic cycle, transitions states, and intermediates associated with this catalyst have

higher relative Gibbs free energy than the other catalysts of **Group 3**. The formation of **IN3** is found to be exergonic by 12.0–13.0 kcal/mol in all the catalysts of **Group 3**. The **IN3** isomerizes to the resting state, **IN3R**. The relative Gibbs free energy of the resting state **IN3R** is in the range of −24.0 to −27.0 kcal/mol except for catalyst **3c** (−20.5 kcal/mol). The **IN3R** is the rate-controlling state in the entire catalytic conversion. The **IN3R** again isomerizes to **IN3** to undergo further reaction to form product **IN5**. The dihydrogen molecule adds to the **IN3** to give the intermediate **IN4**. The **IN4** forms a classical σ-complex with an Mn center. Similar to **Group 2**, a strong Mn—H₂ σ-complex is formed in **IN4** of **3a**, while the remaining catalysts show a distorted Mn-H₂ σ-complex, where one Mn—Hₐ (1.88 Å) is longer than the other Mn—H_b (1.82 Å) bond (Structure in **Supplementary Data Sheet S1**). A strong polarization must have led to this distortion.

The **IN4** of the **3b** (−6.8 kcal/mol) is the most stable, and **3c** (−1.3 kcal/mol) is the least stable among all the catalysts of **Group 3**. The **IN4** further converts to the **IN5** through the transition state **TS**
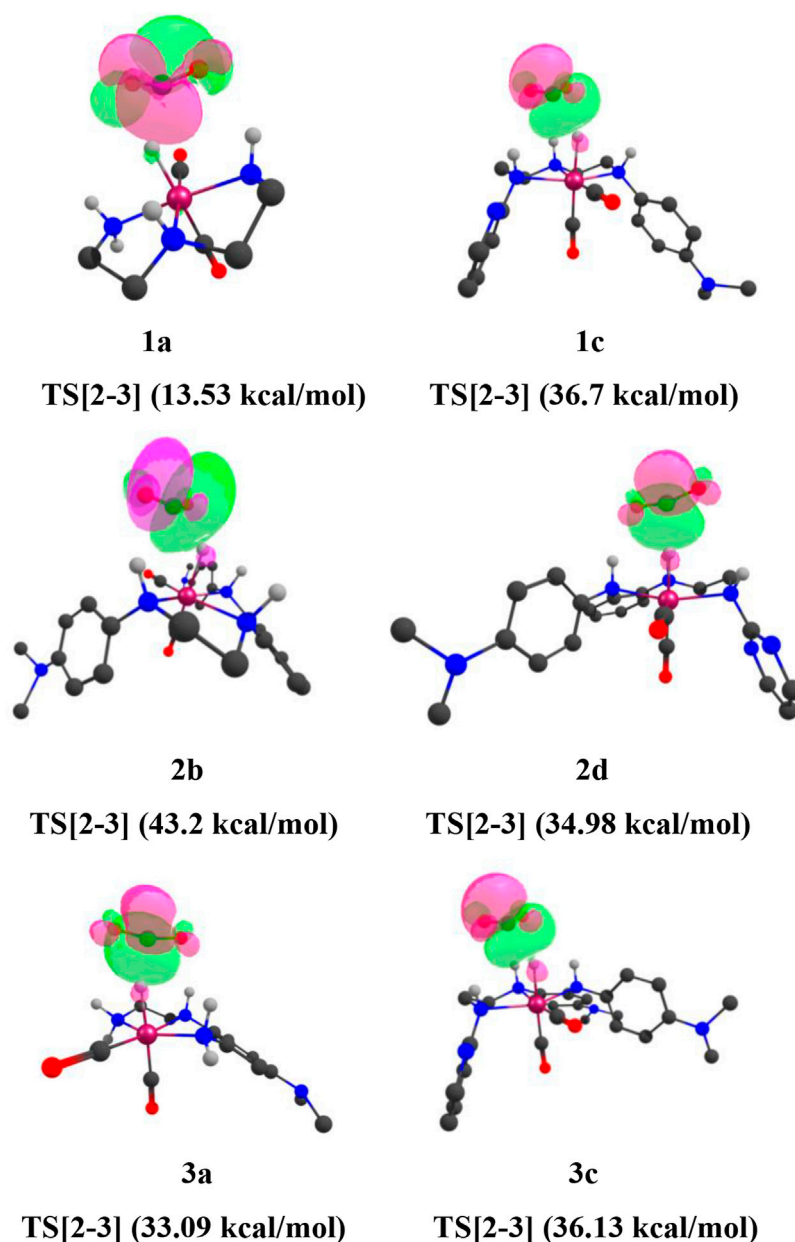
FIGURE 13 | (Mn)H—CO$_2$ interaction of natural bond orbitals (NBOs) of **TS[2-3]** of catalysts **1a**, **1d**, **1e**, **2a**, **2b**, **2e**, and **3a** (isovalue = 0.0174). Interaction energies are indicated in parentheses. The structures are visualized using the Chemcraft software (Chemcraft, 2021) (NBO for all catalysts are given in **Supplementary Data Sheet S1**).

[4-5] with a maximum relative Gibbs free energy for catalyst **3c** (9.9 kcal/mol) and minimum for catalyst **1a**, **1d**, and **1e** (~2.0 kcal/mol). The entire CO$_2$ hydrogenation is found to be thermodynamically favorable for all the catalysts except for catalyst **3c**. This indicates that electron-donating and weak-withdrawing groups at an Mn center make dihydrogen polarization and catalyst generation sluggish. On the other hand, unsubstituted terminal nitrogen and terminal nitrogen with strong withdrawing groups facilitate the dihydrogen polarization and carbon dioxide to the formic acid formation (**Table 3**).

NATURAL BOND ORBITAL

Natural bond orbital (NBO) analysis is performed to gain a mechanistic insight into the carbon dioxide hydrogenation reaction mechanism (Chemcraft, 2021). The Lewis acid–base pair present in the chemical species can be predicted from the second-order perturbative estimation of donor–acceptor stabilization energy (E_s). The NBO analysis of the transition states **TS[2-3]** provides the picture of relevant orbital interactions for the bond
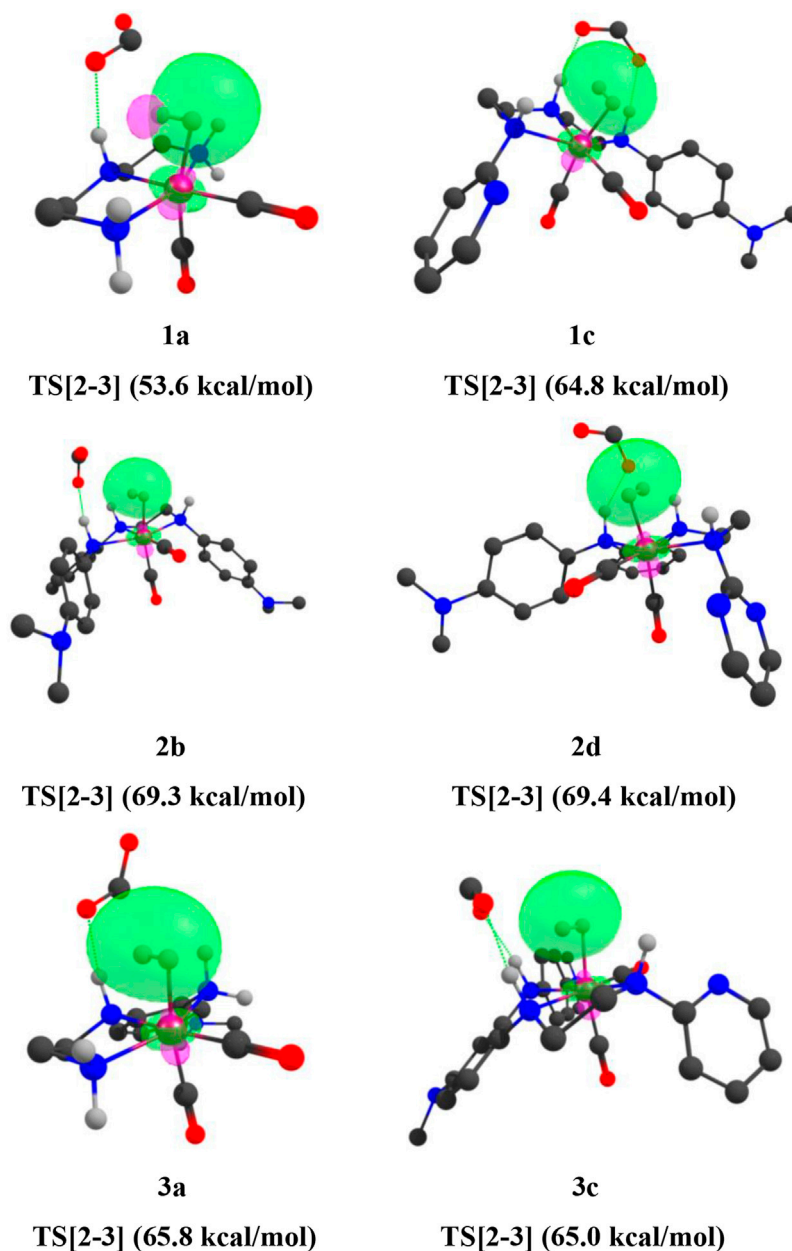
FIGURE 14 | Mn—H₂ interaction NBOs of **IN4** of catalysts **1a, 1d, 1e, 2a, 2b, 2e**, and **3a** (isovalue = 0.03). Interaction energies are indicated in parentheses. The structures are visualized using the Chemcraft software (Chemcraft, 2021) (NBO for all catalysts are given in **Supplementary Data Sheet S1**).

formation based on the second-order perturbative interaction energy. At the transition state **TS[2-3]**, prominent bond-forming interactions are observed for the C—H(a) bond. (**Figure 13**).

Here, the **TS[2-3]** of **1e** has stronger bond-forming interaction energy (45.01 kcal/mol) and lower relative Gibbs free energy(3.0 kcal/mol), whereas the **TS[2-3]** of **1a** shows weaker bond-forming interaction energy of (13.53 kcal/mol) and higher relative Gibbs free energy (4.8 kcal/mol). A similar trend is observed when NBO analysis is performed for the **IN4** of all the catalysts (**Figure 14**).

CONCLUSION

The structure–activity relationship study of computationally modeled Mn(I)NNN pincer complexes emphasize that the position and nature of the aromatic rings attached to the pincer ligands affect the catalytic performance to a considerable amount for carbon dioxide hydrogenation reaction. The **Group 2** Mn(I)NNN pincer complexes with benzene substituent at C2—C3 and identical substituents at both the terminal nitrogen are superior to all the catalysts from the three groups, whereas **Group 1** catalysts without any aromatic substituents at C2—C3 show moderate catalytic

performance, and **Group 3** catalysts with N,N-dimethyl aniline at C2—C3 are sluggish toward carbon dioxide hydrogenation.

DATA AVAILABILITY STATEMENT

The original contributions presented in the study are included in the article/**Supplementary Material**. Further inquiries can be directed to the corresponding authors.

AUTHOR CONTRIBUTIONS

SP and VA conceived the project. SVP carried out the computational calculations and analysis of data. All authors were involved in the manuscript writing and revision. All authors have made substantial, direct and intellectual contributions to the work, and approved it for publication.

FUNDING

ACKNOWLEDGMENTS

SUPPLEMENTARY MATERIAL

The Supplementary Material for this article can be found online at: https://www.frontiersin.org/articles/10.3389/fchem.2021.778718/full#supplementary-material

REFERENCES

Aleksandr, V. M., Christopher, J. C., and Truhlar, D. G. (2009). Universal Solvation Model Based on Solute Electron Density and on a Continuum Model of the Solvent Defined by the Bulk Dielectric Constant and Atomic Surface Tensions. *J. Phys. Chem. B.* 113, 6378–6396. doi:10.1021/jp810292n

Aleksandr, V. M., Christopher, J. C., and Truhlar, D. G. (2009). Universal Solvation Model Based on the Generalized Born Approximation with Asymmetric Descreening. *J. Chem. Theor. Comput.* 5, 2447–2464. doi:10.1021/ct900312z

Aresta, M. (2010). *Carbon Dioxide Recovery and Utilization*. Dordrecht: Kluwer Academic Publishers.

Balaraman, E., Gunanathan, C., Zhang, J., Shimon, L. J. W., and Milstein, D. (2011). Efficient Hydrogenation of Organic Carbonates, Carbamates and Formates Indicates Alternative Routes to Methanol Based on CO_2 and CO. *Nat. Chem.* 3, 609–614. doi:10.1038/nchem.1089

Bernskoetter, W. H., and Hazari, N. (2017). Reversible Hydrogenation of Carbon Dioxide to Formic Acid and Methanol: Lewis Acid Enhancement of Base Metal Catalysts. *Acc. Chem. Res.* 50, 1049–1058. doi:10.1021/acs.accounts.7b00039

Bertini, F., Glatz, M., Gorgas, N., Stöger, B., Peruzzini, M., Veiros, L. F., et al. (2017). Veiros, Karl Kirchner and Luca GonsalviCarbon Dioxide Hydrogenation Catalysed by Well-Defined Mn(I) PNP Pincer Hydride Complexes. *Chem. Sci.* 8, 5024–5029. doi:10.1039/c7sc00209b

Bertini, F., Gorgas, N., Stöger, B., Peruzzini, M., Veiros, L. F., Kirchner, K., et al. (2016). Efficient and Mild Carbon Dioxide Hydrogenation to Formate Catalyzed by Fe(II) Hydrido Carbonyl Complexes Bearing 2,6-(Diaminopyridyl)diphosphine Pincer Ligands. *ACS Catal.* 6 (5), 2889–2893. doi:10.1021/acscatal.6b00416

Boodsarin, S., Wodrich, M. D., and Corminboeuf, C. (2018). Unraveling Metal/Pincer Ligand Effects in the Catalytic Hydrogenation of Carbon Dioxide to Formate. *Organometallics* 37 (24), 4568–4575. doi:10.1021/acs.organomet.8b00490

BP Statistical Review of World Energy (2019).*BP Statistical Review of World Energy*. 68th ed. London, United Kingdom: BPp.l.c.

Campos, J., Hintermair, U., Brewster, T. P., Takase, M. K., and Crabtree, R. H. (2014). Catalyst Activation by Loss of Cyclopentadienyl Ligands in Hydrogen Transfer Catalysis with Cp*Ir III Complexes. *ACS Catal.* 4 (3), 973–985. doi:10.1021/cs401138f

Carpenter, J. E., and Weinhold, F. (1988). Analysis of the Geometry of the Hydroxymethyl Radical by the "different Hybrids for Different Spins" Natural Bond Orbital Procedure. *J. Mol. Struct. THEOCHEM.* 169, 41–62. doi:10.1016/0166-1280(88)80248-3

Centi, G., and Perathoner, S. (2009). Opportunities and Prospects in the Chemical Recycling of Carbon Dioxide to Fuels. *Catal. Today.* 148, 191–205. doi:10.1016/j.cattod.2009.07.075

Chemcraft (2021). *Chemcraft - Graphical Software for Visualization of Quantum Chemistry Computations.* Available at: https://www.chemcraftprog.com.

Choi, J., and Lee, Y. (2020). Catalytic Hydrogenation of CO2 at a Structurally Rigidified Cobalt center. *Inorg. Chem. Front.* 7, 1845–1850. doi:10.1039/c9qi01431d

Curley, J. B., Smith, N. E., Bernskoetter, W. H., Hazari, N., and Mercado, B. Q. (2018). Catalytic Formic Acid Dehydrogenation and CO2 Hydrogenation Using Iron PNRP Pincer Complexes with Isonitrile Ligands. *Organometallics.* 37 (21), 3846–3853. doi:10.1021/acs.organomet.8b00534

CYLview. (2020). *Université de Sherbrooke.* Available at: http://www.cylview.org.

Dörthe, M., Peter, S., Henrik, J., and Beller, M. (2016). Formic Acid as a Hydrogen Storage Material - Development of Homogeneous Catalysts for Selective Hydrogen Release. *Chem. Soc. Rev.* 45, 3954–3988. doi:10.1039/c5cs00618j

Foster, J. P., and Weinhold, F. (1980). Natural Hybrid Orbitals. *J. Am. Chem. Soc.* 102, 7211–7218. doi:10.1021/ja00544a007

Frisch, M. J., Trucks, G. W., Schlegel, H. B., Scuseria, G. E., Robb, M. A., Cheeseman, J. R., et al. (2016). *Gaussian 16, Revision C.01.* Wallingford C. T: Gaussian, Inc.

Fukui, K. (1970). Formulation of the Reaction Coordinate. *J. Phys. Chem.* 74, 4161–4163. doi:10.1021/j100717a029

Fukui, K. (1981). The Path of Chemical Reactions - the IRC Approach. *Acc. Chem. Res.* 14, 363–368. doi:10.1021/ar00072a001

Furstner, A. (2016). Iron Catalysis in Organic Synthesis: A Critical Assessment of what it Takes to Make This Base Metal a Multitasking Champion. *ACS Cent. Sci.* 2 (11), 778–789.

Ganesh, I. (2014). Conversion of Carbon Dioxide into Methanol - a Potential Liquid Fuel: Fundamental Challenges and Opportunities (A Review). *Renew. Sustain. Energ. Rev.* 31, 221–257. doi:10.1016/j.rser.2013.11.045

Garbe, M., Junge, K., and Beller, M. (2017). Homogeneous Catalysis by Manganese-Based Pincer Complexes. *Eur. J. Org. Chem.* 2017, 4344–4362. doi:10.1002/ejoc.201700376

Garbe, M., Wei, Z., Tannert, B., Spannenberg, A., Jiao, H., Bachmann, S., et al. (2019). Enantioselective Hydrogenation of Ketones Using Different Metal Complexes with a Chiral PNP Pincer Ligand. *Adv. Synth. Catal.* 361 (8), 1913–1920. doi:10.1002/adsc.201801511

Ge, H., Chen, X., and Yang, X. (2016). A Mechanistic Study and Computational Prediction of Iron, Cobalt and Manganese Cyclopentadienone Complexes for Hydrogenation of Carbon Dioxide. *Chem. Commun.* 52, 12422–12425. doi:10.1039/c6cc05069g

Glendening, E. D., Reed, A. E., Carpenter, J. E., and Weinhold, F. (1987). "Extension of Lewis Structure Concepts to Open-Shell and Excited-State Molecular Species," Ph.D. Thesis. (Madison, WI: University of Wisconsin).

Global Monitoring Division (2019). "Global Greenhouse Gas Reference Network-Trends in Atmospheric Carbon Dioxide. National Oceanic and Atmospheric Administration," in *Earth System Research Laboratory* (Mauna Loa, Hawaii, U.S.December: U.S. Department of Commerce), 5.

Hariharan, P. C., and Pople, J. A. (1973). The Influence of Polarization Functions on Molecular Orbital Hydrogenation Energies. *Theoret. Chim. Acta.* 28, 213–222. doi:10.1007/bf00533485

Hay, P. J., and Wadt, W. R. (1985). Ab Initio effective Core Potentials for Molecular Calculations. Potentials for K to Au Including the Outermost Core Orbitals. *J. Chem. Phys.* 82, 299–310. doi:10.1063/1.448975

Hehre, W. J., Ditchfield, R., and Pople, J. A. (1972). Self-Consistent Molecular Orbital Methods. XII. Further Extensions of Gaussian-type Basis Sets for Use in Molecular Orbital Studies of Organic Molecules. *J. Chem. Phys.* 56, 2257–2261. doi:10.1063/1.1677527

Huff, C. A., and Sanford, M. S. (2011). Cascade Catalysis for the Homogeneous Hydrogenation of CO2 to Methanol. *J. Am. Chem. Soc.* 133, 18122–18125. doi:10.1021/ja208760j

Irina, O., Tamm, T., Ahlquist, M. S. G., and Ahlquist, G. (2016). Reduced State of Iridium PCP Pincer Complexes in Electrochemical CO2 Hydrogenation. *ACS Catal.* 6 (6), 3834–3839. doi:10.1021/acscatal.6b01233

Jain, P., Pal, S., and Avasare, V. (2018). Ni(COD)2-Catalyzed Ipso-Silylation of 2-Methoxynaphthalene: A Density Functional Theory Study. *Organometallics.* 37, 1141–1149. doi:10.1021/acs.organomet.8b00046

Jan, P., Eder, W., Stöger, B., Realista, S., Martinho, P. N., Calhorda, M. J., et al. (2020). Synthesis, Characterization, and Catalytic Reactivity of {CoNO}8 PCP Pincer Complexes. *Organometallics* 39 (14), 2594–2601. doi:10.1021/acs.organomet.0c00167

Jessica, D. C., Dekarske, J. R., McCulloch, B. J., and Ozerov, O. V. (2015). Cyclometallation of the NNN Pincer Ligand in Complexes of Platinum. *Inorg. Chem. Front.* 2, 912–916. doi:10.1039/c5qi00102a

Jessica, S. F., Wan, K. Y., Sues, P. E., and Morris, R. H. (2017). Ketone Asymmetric Hydrogenation Catalyzed by P-NH-P′ Pincer Iron Catalysts: An Experimental and Computational Study. *ACS Catal.* 7 (1), 316–326. doi:10.1021/acscatal.6b02489

Jörg, E., and Huang, K.-W. (2017). Formic Acid as a Hydrogen Energy Carrier. *ACS Energ. Lett.* 2 (1), 188–195. doi:10.1021/acsenergylett.6b00574

Kar, S., Goeppert, A., Kothandaraman, J., and Prakash, G. K. S. (2017). Manganese-Catalyzed Sequential Hydrogenation of CO2 to Methanol via Formamide. *ACS Catal.* 7, 6347–6351. doi:10.1021/acscatal.7b02066

Kar, S., Rauch, M., Kumar, A., Leitus, G., Ben-David, Y., and Milstein, D. (2020). Selective Room-Temperature Hydrogenation of Amides to Amines and Alcohols Catalyzed by a Ruthenium Pincer Complex and Mechanistic Insight. *ACS Catal.* 10, 5511–5515. doi:10.1021/acscatal.0c01406

Kar, S., Sen, R., Kothandaraman, J., Goeppert, A., Chowdhury, R., Munoz, S. B., et al. (2019). Mechanistic Insights into Ruthenium-Pincer-Catalyzed Amine-Assisted Homogeneous Hydrogenation of CO2 to Methanol. *J. Am. Chem. Soc.* 141 (7), 3160–3170. doi:10.1021/jacs.8b12763

Kassem, B., Thenert, K., Wiesenthal, J., Hoppe, C., and Klankermayer, J. (2020). Utilization of Formic Acid as C1 Building Block for the Ruthenium-Catalyzed Synthesis of Formaldehyde Surrogates. *ChemCatChem* 12 (7), 1944–1947. doi:10.1002/cctc.201902332

Kothandaraman, J., Goeppert, A., Czaun, M., Olah, G. A., and Prakash, G. K. S. (2016). Conversion of CO2 from Air into Methanol Using a Polyamine and a Homogeneous Ruthenium Catalyst. *J. Am. Chem. Soc.* 138, 778–781. doi:10.1021/jacs.5b12354

Kumar, A., Daw, P., Espinosa-Jalapa, N. A., Leitus, G., Shimon, L. J. W., Ben-David, Y., et al. (2019). CO2 Activation by Manganese Pincer Complexes through Different Modes of Metal-Ligand Cooperation. *Dalton Trans.* 48, 14580–14584. doi:10.1039/c9dt03088c

Langer, R., Diskin-Posner, Y., Leitus, G., Shimon, L. J. W., Ben-David, Y., and Milstein, D. (2011). Low-Pressure Hydrogenation of Carbon Dioxide Catalyzed by an Iron Pincer Complex Exhibiting Noble Metal Activity. *Angew. Chem. Int. Ed.* 50, 9948–9952. doi:10.1002/anie.201104542

Liu, P., Xu, X., Dong, X., Keitz, B. K., Herbert, M. B., Grubbs, R. H., et al. (2012). Z-selectivity in Olefin Metathesis with Chelated Ru Catalysts: Computational Studies of Mechanism and Selectivity. *J. Am. Chem. Soc.* 134, 1464–1467. doi:10.1021/ja2108728

Luca, P., Danielle, L., Justo, P., and Nielsen, M. (2020). Recent Progress with Pincer Transition Metal Catalysts for Sustainability. *Catalysts* 10 (7), 773. doi:10.3390/catal10070773

Miriam, N., Mori, K., Salinas-Torres, D, Kuwahara, Y., and Yamashita, H. (2019). New Approaches toward the Hydrogen Production from Formic Acid Dehydrogenation over Pd-Based Heterogeneous Catalysts. *Front. Mater.* 6, 2296–8016. doi:10.3389/fmats.2019.00044

Peris, E., and Crabtree, R. H. (2018). Key Factors in Pincer Ligand Design. *Chem. Soc. Rev.* 47, 1959–1968. doi:10.1039/c7cs00693d

Reed, A. E., Curtiss, L. A., and Weinhold, F. (1988). Intermolecular Interactions from a Natural Bond Orbital, Donor-Acceptor Viewpoint. *Chem. Rev.* 88, 899–926. doi:10.1021/cr00088a005

Reed, A. E., and Weinhold, F. (1985). Natural Localized Molecular Orbitals. *J. Chem. Phys.* 83, 1736–1740. doi:10.1063/1.449360

Reed, A. E., Weinstock, R. B., and Weinhold, F. (1985). Natural Population Analysis. *J. Chem. Phys.* 83, 735–746. doi:10.1063/1.449486

Smith, J. D., Chih, E., Piers, W. E., and Spasyuk, D. M. (2018). Tuning Iridium (I) PCcarbeneP Frameworks for Facile Cooperative N2O Reduction. *Polyhedron* 155, 281–290. doi:10.1016/j.poly.2018.08.054

Talukdar, K., Issa, A., and Jurss, J. W. (2019). Synthesis of a Redox-Active NNP-type Pincer Ligand and its Application to Electrocatalytic CO2 Reduction with First-Row Transition Metal Complexes. *Front. Chem.* 7 (330), 330–2646. doi:10.3389/fchem.2019.00330

Tang, S., von Wolff, N., Diskin-Posner, Y., Leitus, G., Ben-David, Y., and Milstein, D. (2019). Pyridine-Based PCP-Ruthenium Complexes: Unusual Structures and Metal-Ligand Cooperation. *J. Am. Chem. Soc.* 141, 7554–7561. doi:10.1021/jacs.9b02669

Wang, W.-H., Muckerman, J. T., Fujita, E., and Himeda, Y. (2013). Mechanistic Insight through Factors Controlling Effective Hydrogenation of CO2 Catalyzed by Bioinspired Proton-Responsive Iridium(III) Complexes. *ACS Catal.* 3, 856–860. doi:10.1021/cs400172j

Wen, J., Wang, F., and Zhang, X. (2021). Asymmetric Hydrogenation Catalyzed by First-Row Transition Metal Complexes. *Chem. Soc. Rev.* 50, 3211–3237. doi:10.1039/d0cs00082e

Wesselbaum, S., Moha, V., Meuresch, M., Brosinski, S., Thenert, K. M., Kothe, J., et al. (2015). Hydrogenation of Carbon Dioxide to Methanol Using a Homogeneous Ruthenium-Triphos Catalyst: from Mechanistic Investigations to Multiphase Catalysis. *Chem. Sci.* 6, 693–704. doi:10.1039/c4sc02087a

Wesselbaum, S., vom Stein, T., Klankermayer, J., and Leitner, W. (2012). Hydrogenation of Carbon Dioxide to Methanol by Using a Homogeneous Ruthenium-Phosphine Catalyst. *Angew. Chem. Int. Ed.* 51, 7499–7502. doi:10.1002/anie.201202320

Zell, T., and Milstein, D. (2015). Hydrogenation and Dehydrogenation Iron Pincer Catalysts Capable of Metal-Ligand Cooperation by Aromatization/Dearomatization. *Acc. Chem. Res.* 48, 1979–1994. doi:10.1021/acs.accounts.5b00027

Zhang, Y., MacIntosh, A. D., Wong, J. L., Bielinski, E. A., Williard, P. G., Mercado, B. Q., et al. (2015). Iron Catalyzed CO2hydrogenation to Formate Enhanced by Lewis Acid Co-catalysts. *Chem. Sci.* 6, 4291–4299. doi:10.1039/c5sc01467k

Zhao, Y., and Truhlar, D. G. (2008a). Density Functionals with Broad Applicability in Chemistry. *Acc. Chem. Res.* 41, 157–167. doi:10.1021/ar700111a

Zhao, Y., and Truhlar, D. G. (2008b). The M06 Suite of Density Functionals for Main Group Thermochemistry, Thermochemical Kinetics, Noncovalent Interactions, Excited States, and Transition Elements: Two New Functionals and Systematic Testing of Four M06-Class Functionals and 12 Other Functionals. *Theor. Chem. Account.* 120, 215–241. doi:10.1007/s00214-007-0310-x

Quantum Dynamics of Rotational Transitions in CN (*X* $^2\Sigma^+$) by H$^+$ Collisions

Bhargava Anusuri[1], T. J. Dhilip Kumar[2] and Sanjay Kumar[1]*

[1]*Department of Chemistry, Indian Institute of Technology Madras, Chennai, India,* [2]*Department of Chemistry, Indian Institute of Technology Ropar, Rupnagar, India*

Collisional cross-sections of inelastic rotational excitations of CN in its ground electronic state (X$^2\Sigma^+$) by H$^+$ scattering are studied by the exact quantum mechanical close-coupling (CC) method at very low collision energies (0–600 cm^{-1}) relevant to interstellar atmospheres. *Ab initio* rigid rotor potential energy surface computed at MRCI/*cc-p*VTZ level of accuracy has been employed. Rate coefficients for the rotational excitations have also been calculated. The obtained results are compared with previous theoretical calculations and analyzed whether proton collisions could be significant sources for rotationally excited CN as a possible source for cosmic microwave background of about 3 K from the interstellar media.

Keywords: Proton-CN, collisions, quantum calculations, rotational excitations, cross sections, interstellar medium

INTRODUCTION

As early as 1965, cosmic microwave background radiation (CMBR) measurements were carried out, and an analysis of radio wave intensities revealed that there exists approximately isotropic CMBR corresponding to black body radiation of about 3 K (Penzias and Wilson, 1965; Dicke et al., 1965; Stokes et al., 1967)[1]. These radiations are considered as remnant radiation occurring due to falling out of the big-bang fireball. The near isotropic nature of CMBR also suggested that the Universe is full of 3 K CMBR (Dicke et al., 1965).

Subsequently, the rotational temperature of interstellar CN molecule was measured (Field and Hitchcock, 1966; Thaddeus and Clauser, 1966) in terms of the population ratio of the first rotationally excited state to the ground rotational state (n$_1$/n$_0$), which was found to be 0.55 ± 0.05. Using $\frac{n_1}{n_0} = \frac{(2j'+1)}{(2j+1)} e^{-\frac{\Delta E_{0 \to 1}}{k_b T}} = 0.5$, where j stands for the rotational quantum number, $\Delta E_{0 \to 1}$ is the energy difference of the two rotational energy levels (2 B = 2 × 1.8997 cm^{-1}, B: diatomic rotational constant of CN, Huber and Herzberg, 1979), k_b (= 0.695 cm^{-1} K^{-1}) is the Boltzmann constant, one estimates the rotational temperature of interstellar CN molecule to be approximately 3 K.

The fact that the rotationally-excited (j' = 1) CN molecule could be one of the primary sources for the CMBR (of about 3 K) has led to exploring various mechanisms and pathways that lead CN molecules to rotationally excited states. The CN radical has a permanent dipole moment, and therefore one expects it would have a higher probability for rotational excitations with electrons, protons, and ions. It can exist in two regions: 1) neutral hydrogen clouds (H-I region) and 2) ionized-hydrogen clouds (H-II region). In the H-I region, the cloud temperature can increase by several thousand degrees by cloud-cloud collisions, finally decreasing via infrared emissions. Here, the atomic hydrogen does not get ionized. However, minor

---

[1]Dedicated to Professor Saurav Pal, Director, IISER Kolkata, India.

constituents like Li, Mg, C, Si, Fe, etc., may get ionized liberating electrons through photoionization (Nishimura, 1968). Typically, the number density of these ions is approximated to be $N_{ion} = N_e = 1.6 \times 10^{-3}$ cm^{-3}. Therefore, the rate of collisions of the ions (with CN) is expected to be minimal compared to that of the electron because of the latter's lighter (thousand times smaller) mass. Another energy source for the H-I cloud can be from the low-energy (in MeV range) component of the cosmic-ray protons. If the flux is appropriate, they can ionize the atomic hydrogen present as the principal constituent in the cloud. In such conditions, the cloud temperature is estimated to be around 100 K (Hayakawa et al., 1961)[7] with $N_e = N_p = 0.03$ cm^{-3}.

In the H-II region, the gas exists in a completely ionized form. It gets heated up from lights emitted from stars up to a typical temperature of 10^4 K. The gas density varies, resulting in high and low-density regions. An estimate of the low density could be around $N_e = N_p < 0.1$ cm^{-3}.

Since the density of H$^+$ is estimated to be an order of magnitude higher in the H-II region, it is appropriate to study the collisional excitation rates with CN molecules. Considering the temperature range of 100–1000 K of the gas in the H-II region, the collision energy (in the center of mass frame, $E_{c.m}$) corresponds to 0.01 and 1.0 eV, respectively. Takayanagi and Itikawa (1968) carried out early theoretical calculations of rotational excitation of CN molecule by electron collisions using the close-coupling and the Born-approximation methods at $E_{c.m}$ = 0.01, 0.1, and 1.0 eV. The interaction potential has been modeled in terms of the dipole, polarization, and short-range electrostatic interactions. Excitations by protons were studied in the classical framework using the trajectory impact parameter method. Later, Jamieson et al. (1975) studied the rotational excitations of CN molecule by proton collisions by impact parameter method using a modified interaction potential used earlier for the e^- + CN system (Crawford et al., 1969; Allison and Dalgarno, 1971). This interaction potential was based on dipole and polarization interactions. They obtained approximate solutions for rotational excitations based on Born and the "exponential" approximations, and the obtained integral cross sections were compared with those obtained from the close-coupling method. The calculations were carried out for $E_{c.m}$ = 0.04—500 eV. Since long-range interactions are present in e^-/H$^+$ interactions with CN molecule leading to significant inelastic effects, it was desirable to test the validity of decoupling approximations of angular momenta to carry out efficient and reliable calculations. Subsequently, DePristo and Alexander (DePristo and Alexander, 1976) investigated decoupling approximations of angular momenta, namely decoupled l—dominant (DLD) method (DePristo and Alexander, 1975) using the model interaction potential. Various theoretical aspects were discussed, and cross-sections for rotational excitations were calculated at $E_{c.m}$ = 0.04, 0.1 and 1.0 eV with dipole moments of CN, μ = 1.1 D and 1.45 D.

POTENTIAL ENERGY SURFACE

The bound HCN$^+$ ion has a collinear geometry. There are two energetically low-lying electronic states in the collinear geometry:
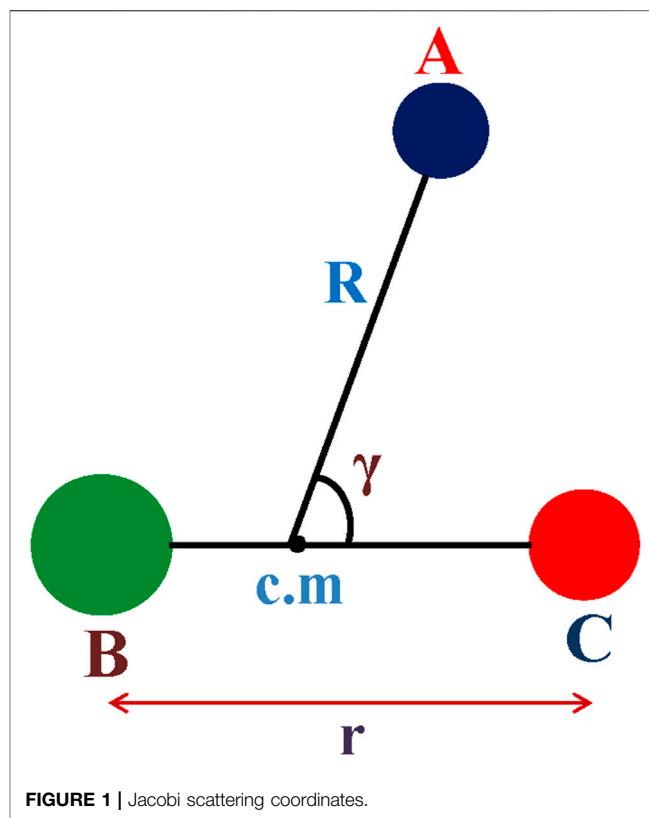
FIGURE 1 | Jacobi scattering coordinates.

$1^2\Sigma^+$ and $1^2\Pi$. Asymptotically, The former correlates to the inelastic channel, H$^+$ + CN(X$^2\Sigma^+$), and the latter to charge transfer channel, H (^{2}S) + CN$^+$ ($^2\Sigma^+$). The computed energy for the asymptotic charge transfer channel is 0.278 eV higher than that of the inelastic channel. Around the equilibrium geometry and the Franck-Condon region, the $1^2\Pi$ state is lower in energy, and the computed energy difference between the $1^2\Pi$ and the $1^2\Sigma$ states is 0.979 eV (Anusuri and Kumar, 2016). For the off-collinear geometry, the $1^2\Pi$ state splits into the $^2A'$ and $^2A''$ states. The $^2\Sigma^+$ state correlates to the $^2A'$ state. The nondegenerate states' potential energy surfaces (PES) interact in the vicinity of collinear geometry with off-collinear distortions. Thus, the bound HCN$^+$ constitutes a Renner-Teller system (see, KÖppel et al., 1979; Perić et al., 1983; and references therein), exhibiting strong vibronic interactions between the ground $^2\Pi$ and the first excited $^2\Sigma^+$ states. The existence of Renner-Teller coupling complicates the assignment of vibrational progressions. For a brief account of the vibrational progression studies, see reference (Anusuri and Kumar, 2016) and the references therein.

For the scattering studies involving the inelastic channel, H$^+$ + CN(X$^2\Sigma^+$), it is crucial to examine the (nonadiabatic) involvement of the $1^2\Pi$ state, which correlates to the endoergic charge transfer channel, H (^{2}S) + CN$^+$ ($^3\Pi$). Since only the inelastic rotational excitations of the CN molecules upon collisions of H$^+$ are studied, the potential energy surface is generated in the Jacobi scattering coordinates (**Figure 1**): r is the interatomic distance of the diatom BC (CN), **R** is the distance of H$^+$ from the center of mass of BC (CN), and γ = cos^{-1} (**R.r**) is

FIGURE 2 | Contour plot of rigid-rotor PES of HCN⁺ ($1^2\Sigma^+$/ $1^2A'$) as a function of R and γ with r fixed at $r_{eq} = 2.23\ a_0$. The spacing between the contours is 0.2 eV.
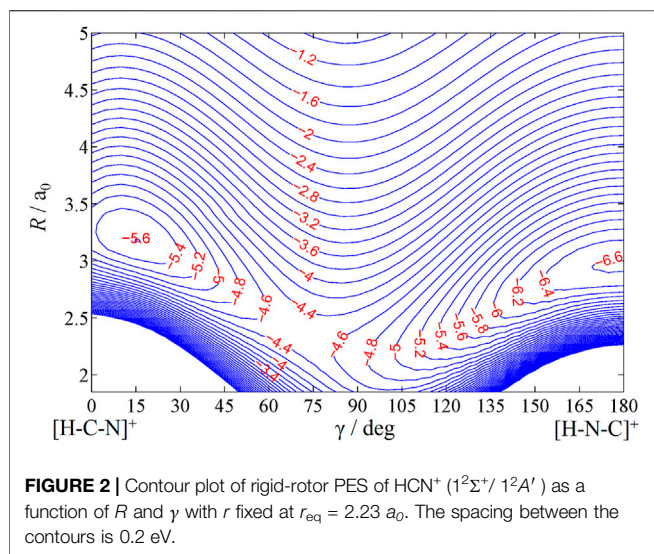
the angle between **R** and **r**. H⁺ approaching C-end is considered as $\gamma = 0°$ and N-end as $\gamma = 180°$. Our earlier study (Anusuri and Kumar, 2016) found that the potential energy curve of $1^2\Pi$ state crosses with that of the $1^2\Sigma^+$ state around R = $5a_o$ in the collinear geometry. For off-collinear geometry, the energy order is $1^2A' < 1^2A'' < 2^2A'$. The A' states correlate to the inelastic channel while the A'' correlates to the charge transfer channel. The two A' states are reasonably well separated energetically. There is no radial coupling between the $1A'$ and $1A''$ states. The radial coupling between the $1A'$ and $2A'$ states are significantly small for $r = r_{eq}$; It shows up little strength in the repulsive regions of the PESs and for stretched values of r. However, the nonadiabatic interactions arising through the spin-orbit coupling for the collinear geometries and the radial couplings for close-collinear geometries may not be ignored. Considering that the scattering processes of the present study do not involve any charge transfer outcome and that we are interested only in the low rotational excitations, we believe that the nonadiabatic interactions of the higher states would be significantly less, and scattering the rigid-rotor surface of the $1^2\Sigma^+$/ $1A'$ states would largely capture the collision dynamics. Therefore, we describe below the details of the rigid rotor PES computations.

Calculations were carried out in the C_{2v} symmetry for collinear geometries and the C_s symmetry for off-collinear geometries. The ground state RR surface was computed for the $1^2\Sigma^+$/$1^2A'$ symmetry for the collinear/off-collinear approaches. Computations were done at internally contracted multi-reference configuration interaction (Knowles and Werner, 1988; Werner and Knowles, 1988; Knowles and Werner, 1992) level of accuracy with Dunning's (Dunning, 1989) cc-pVTZ basis set using MOLPRO 2010.1 (Werner et al., 2010) suite of programs. A total of 780 geometries were computed with r fixed at $r_{eq} = 2.23\ a_o$: $\gamma = 0°–180°$ (15°); R = 0.8–1.8 (0.2), 1.9–4.0 (0.1), 4.2–7.0 (0.2), 7.5–10.0 (0.5), 11.0–15.0 (1.0). R is in atomic units, and the numbers in the parentheses indicate the step size in the interval.

The computed basis set superposition error (BSSE) was small and varied systematically in the range 0.04–0.01 eV for R 3.0 a_o to

5.0 a_o, and falls off rapidly and becomes negligible (less than 10^{-4} eV) for R > 5.0 a_o. R = 3.0 a_o approximately signifies the bottom of the interaction well. We believe that the BSSE correction will still have a very small correction on the computed cross sections and rates, and therefore, we did not include them. The effect of the augmented basis set was also very small as interaction potential values varied on the second decimal places in eV. We believe that the potential energy surface generated using the cc-pVTZ basis set is sufficiently accurate for the scattering calculations.

The contour plot of the rigid-rotor surface is shown in **Figure 2**. To study the dynamics, we need the long-range asymptotic interaction potential up to large R values where the interaction potential dies down. For large values of R, the interaction potential is generally expanded in multipolar terms. Here, the charge on H⁺ interacts with the dipole, quadrupole, and polarizability components of CN, and the asymptotic interaction potential $V_{as}(R)$ is given as:

$$V_{as}(R) \sim \frac{\mu}{R^2}P_1(\cos\gamma) + \frac{Q}{R^3}P_2(\cos\gamma) - \frac{\alpha_0}{2R^4} - \frac{\alpha_2}{2R^4}P_2(\cos\gamma)$$
$$+ O(P_3)$$

(1)

where μ (−1.362 D) is the dipole moment, Q (0.368 ea_0^2) is the quadrupole moment, α_0 (17.92 a_0^3) and α_2 (10.58 a_0^3) are the polarizability components of CN(X$^2\Sigma^+$) at $r = r_{eq}$. P's are the Legendre polynomials. The mentioned values were obtained by the ab initio calculations using the same basis set and the computational methodology.
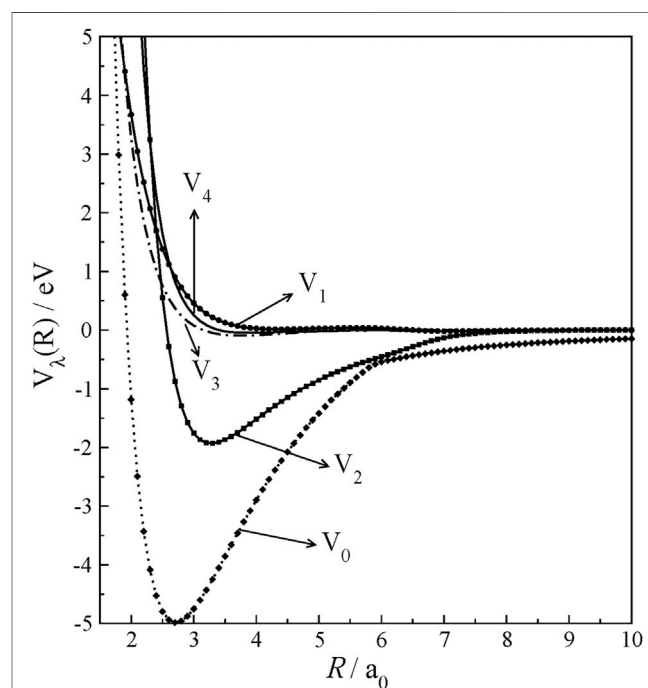

FIGURE 3 | Radial multipolar expansion coefficients of HCN⁺ rigid-rotor potential as a function of R at $r = r_{eq}$.
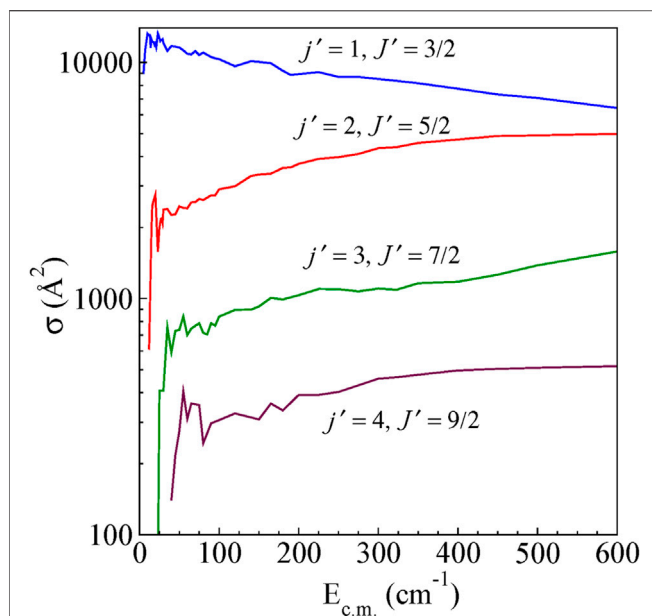
FIGURE 4 | State-to-state integral cross sections for rotational excitations for $\Delta J = \Delta j$ transitions from the initial level $j = 0$ and $J = \frac{1}{2}$ for H$^+$ + CN ($j = 0$, $J = \frac{1}{2}$) $\rightarrow$ H$^+$ + CN (j', J').
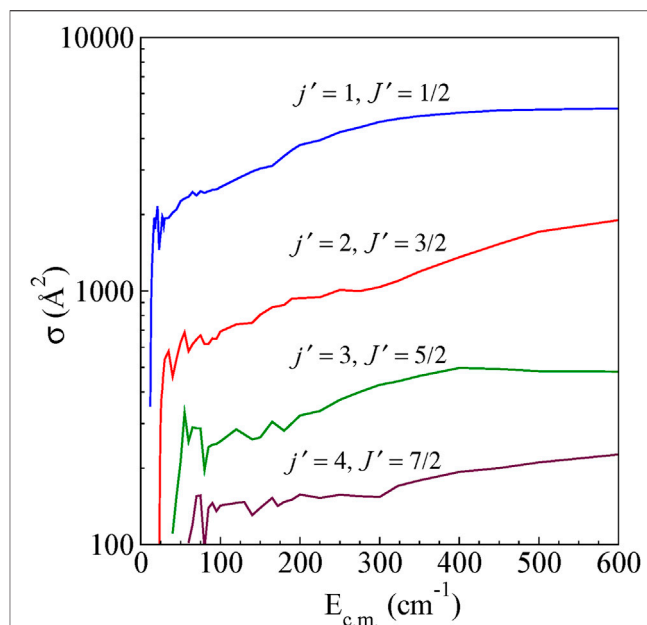
FIGURE 5 | State-to-state integral cross sections for rotational excitations for $\Delta J \neq \Delta j$ transitions from the initial level $j = 0$ and $J = \frac{1}{2}$ for H$^+$ + CN ($j = 0$, $J = \frac{1}{2}$) $\rightarrow$ H$^+$ + CN (j',J').

Multipolar Expansion

The rigid-rotor interaction potential has been fitted to the following analytic expression:

$$V\left(R, r = r_{eq}, \gamma\right) = \sum_{\lambda} V_{\lambda}\left(R\right)P_{\lambda}\left(\cos\gamma\right) \qquad (2)$$

where V_{λ}'s are expansion coefficients with λ varying from 0 to 12 (number of γ values) and P_{λ}'s are Legendre polynomials.

V_{λ} were numerically obtained at the computed grid points using the Legendre polynomials' orthogonality. Once their dependence on grid points of R is known, each V_{λ} was fitted with a cubic spline fit. The interaction anisotropy can be examined in terms of V_{λ}'s plotted as a function of R and shown in **Figure 3**. V_0, which gives spherically averaged interaction potential, exhibits a deep well and extends its strength beyond $R = 10.0$ a_0 in long-range interactions given in charge-multipole interactions. Interestingly, V_1, V_3, and V_4 components are very small throughout R, and they are repulsive and show their strength only at closer approaches. Next to V_0, V_2 only shows an interaction well. Therefore, it suggests that rotational excitations at low collision energies will be governed by only a few low V_{λ}'s.

SCATTERING CALCULATIONS

The molecular energy levels in CN (X $^2\Sigma^+$) are described by Hund's case 2) limit. The theoretical framework for the scattering of a molecule in $^2\Sigma^+$ electronic state was given by Alexander (Alexander, 1982). The rotational fine structure levels in the CN molecule here are labeled by the quantum numbers j and J. j is the

rotational angular momentum, whereas J is the total angular momentum. J is given by $J = j + s$ where s is the electronic spin angular momentum. For CN molecule in $^2\Sigma^+$ electronic state, the J levels will be $J = j + \frac{1}{2}$ (labeled as e) and $J = j - \frac{1}{2}$ (labeled as f).

Full close-coupling calculations have been carried in very low collision energy range of 0–600 cm^{-1} for rotational excitations from $j = 0$ to j' = one to four levels. Time-independent coupled scattering equations (Arthurs and Dalgarno, 1960) have been solved to compute cross-sections implemented in the HIBRIDON package (Alexander et al., 2011). The close-coupled radial equations were numerically integrated using the log derivative propagator (Manolopoulos, 1986). The following input parameters are taken in the calculation: rotational constant, $B_e = 1.89102$ cm^{-1}, D_0 (centrifugal distortion constant) = 6.4 $\times$ 10^{-6} cm^{-1}, spin-splitting constant $\gamma_0 = 7.2549 \times 10^{-3}$ cm^{-1} (Huber and Herzberg, 1979) and reduced mass of the system, $\mu = 0.970{,}404$ a.u. with values of R_{min} and R_{max} as 1.4 and 200 a_0, respectively with $\Delta R = 0.1$ a_0. The value of CN bond length is fixed at 2.23 a_0 (rigid-rotor approximation). The main focus of the present study is to have the first meaningful yet reliable estimates of the cross sections for rotational excitation for $j = 0$ - j' = 1, using the full quantum calculations in vibrational manifold v = 0. Therefore, rigid-rotor calculations would capture the collision dynamics since there would hardly be any centrifugal distortions in the CN bond the small rotational excitation(s). The cross sections are computed for energies up to 600 cm^{-1}. At least three energetically closed rotational channels were included in the calculations at a particular $E_{c.m}$ to ensure numerical convergence of cross section within the acceptable limit (up to third decimal place). Maximum value of rotational quantum number taken is $j_{max} = 18$ at $E_{c.m} = 600$ cm^{-1}. Also, the convergence of cross-

Collision energy $E_{c.m}$ (eV)	Present study		Jamieson et al., 1975 (CC)		DePristo and Alexander, (1976)	
	$\sigma_{0\to1}$ (10^{-12} cm^2)	$\sigma_{0\to2}$ (10^{-14} cm^2)	$\sigma_{0\to1}$ (10^{-12} cm^2)	$\sigma_{0\to2}$ (10^{-14} cm^2)	$\sigma_{0\to1}$ (10^{-12} cm^2)	$\sigma_{0\to2}$ (10^{-14} cm^2)
0.04	1.31	54.7	0.48	0.26	0.79	4.4
0.06	1.23	65.7	1.22	2.02	—	—
0.08	2.28	138.2	1.89	7.04	—	—

sections is achieved through a sufficient number of partial waves; for instance, at $E_{c.m}$ = 500 cm^{-1}, l (total angular momentum) is kept at 580. The CC calculations have been performed from an energy value corresponding to the opening of the lowest inelastic channel to a total energy of 600 cm^{-1}.

Integral Cross-Sections

The integral cross-sections for rotationally inelastic excitations obtained from the full close-coupling calculations in the energy range (5–600 cm^{-1}) are shown as a function of $E_{c.m}$ for excitations from the ground (j = 0, J = 1/2) rotational level to higher rotational levels for $\Delta J = \Delta j$ transitions and $\Delta J \neq \Delta j$ transitions in **Figure 4** and **Figure 5**, respectively. The rotational excitations are plotted for $j = 0 \to j'$ = one to four levels. In the case of $j = 0$ to j' = 1 transition, the cross sections oscillate at low energies for both $\Delta J = \Delta j$ as well as for $\Delta J \neq \Delta j$. The cross section for $\Delta J = \Delta j$ from the energetic threshold rises to a maximum and shows a large decreasing plateau with increasing collision energy. For $\Delta J \neq \Delta j$ the cross sections show a monotonic increasing behavior with an increase in $E_{c.m}$. Near the threshold, all the cross sections show oscillatory behavior presumably due to the formation of scattering resonances. We have also observed a propensity for $\Delta J = \Delta j$ transitions compared to that of $\Delta J \neq \Delta j$ transitions, which is a common feature in the scattering of molecules in $^{2S+1}\Sigma$ electronic state (Alexander et al., 1986). This propensity is reported in He-CN scattering also (Lique et al., 2010).

The total state-to-state (j') cross sections were obtained by summing the cross sections for the $\Delta J = \Delta j$ and $\Delta J \neq \Delta j$ transitions. The computed integral cross sections for $0 \to 1$ and $0 \to 2$ are compared in **Table 1** and earlier theoretical estimates. The earlier theoretical values were reported in units of cm^2. Therefore, we also report our values in the same units for better comparison and convenience.

The cross sections are compared at three collision energies, $E_{c.m}$ = 0.04, 0.06 and 0.08 eV. The $0 \to 1$ cross sections compare reasonably well with the previous calculations for these energies. The cross sections for $0 \to 2$ excitations are approximately two orders of magnitude less than that of $0 \to 1$ excitations. The present calculations yield consistently higher magnitudes for $0 \to 2$ excitations than those obtained in earlier calculations. The $0 \to 1$ cross sections are mostly governed by long-range effects (Harrison et al., 2012). Since the long-range interaction potential description is similar for the earlier and the present studies, there is an overall good agreement. But the direct $0 \to 2$ transitions are governed by the V_2 multipolar term, the next strongest term after the V_0 term in the interaction potential expansion.

FIGURE 6 | State-to-state rate as a function of temperature for 0–600 K computed for $\Delta J = \Delta j$ transitions from the initial level j = 0 and J = ½ for H$^+$ + CN (j = 0, J = ½) $\to$ H$^+$ + CN (j', J').

Rate Coefficients

The computed rotational cross-sections are used to calculate rate-coefficient as a function of temperature:

$$k_{N,j \to N'j'}(T) = \sqrt{\frac{8k_BT}{\pi\mu}}\left(\frac{1}{k_BT}\right)^2 \int_0^\infty \sigma(E)Ee^{(-E/k_BT)}dE \quad (3)$$

where k_B is the Boltzmann constant, μ is the reduced mass of the system, and E = $E_{c.m}$. The state-to-state rate coefficients for rotational transitions over a range of temperatures computed for both $\Delta J = \Delta j$ and $\Delta J \neq \Delta j$, up to T = 600 K, are shown in **Figure 6** and **Figure 7**, respectively.

The rates are higher for $j = 0 \to j'$ = 1 transition, similar to cross sections, and decreases for other higher excitations. The rate coefficients are calculated by averaging the obtained cross section over a Boltzmann distribution of kinetic energy.

The rate coefficient for $j = 0$ to j' = 1 excitation in CN by proton scattering was estimated to be about the order of 10^{-7} cm^3 s^{-1} by Jamieson et al., 1975 at 80 K, which is the temperature of interstellar clouds. It is lower by a factor of ten compared to that obtained from the electron scattering calculations with CN. In our present calculation, we obtained a rate coefficient of 1.74×10^{-7} cm^3 s^{-1}.
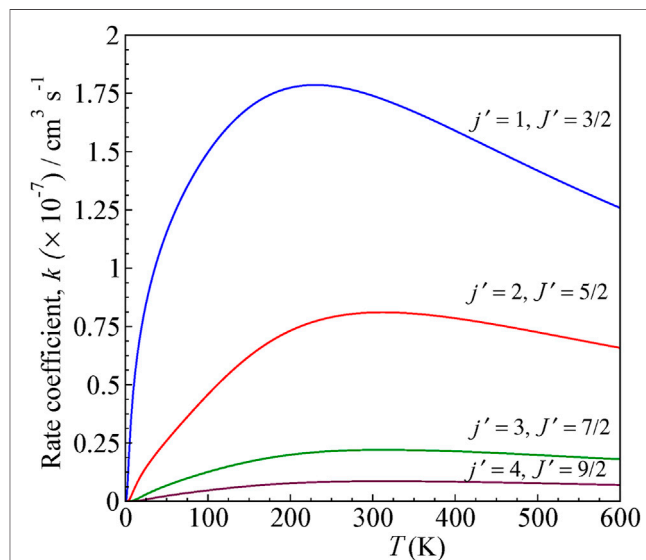
FIGURE 7 | State-to-state rate as a function of temperature for 0–600 K computed for $\Delta J \neq \Delta j$ transitions from the initial level $j = 0$ and $J = \frac{1}{2}$ for $H^+ + CN$ $(j = 0, J = \frac{1}{2}) \rightarrow H^+ + CN$ (j',J').

are studied on the PES for low collision energies between $0-600 \text{ cm}^{-1}$ by solving close-coupled equations. The cross-sections are calculated for inelastic rotational transitions for $J = 0 \rightarrow J' = $ 1-4 one to four using close-coupling method.

The rate coefficients in the temperature range 0–600 K have been calculated. The rate coefficients for $j = 0 \rightarrow j' = 1$ transition in H^+ scattering of CN is found to be of the order of $10^{-7} \text{ cm}^3 \text{ s}^{-1}$. It is an order of magnitude less than that of electron scattering at the average temperature of interstellar clouds (~80 K). In clouds of the H-II region where H^+ density could be relatively larger (>> 0.1 cm^{-3}) H^+ collision could lead to $0 \rightarrow 1$ rotational excitation of CN, which could become comparable to that obtained in collision with electrons.

DATA AVAILABILITY STATEMENT

The raw data supporting the conclusion of this article will be made available by the authors, without undue reservation.

AUTHOR CONTRIBUTIONS

BA carried out the major computational work and analysis. He also prepared the first draft of the manuscript. TD was also involved in part for both computations and analysis. SK contributed to the conception and draft revisions. All authors contributed to manuscript revision, read and approved the submitted version.

SUMMARY AND CONCLUSIONS

Ab initio rigid-rotor PES obtained at MRCI/*cc-p*VTZ level of theory has been employed to study the inelastic rotational excitations in CN by H^+ scattering. The ground electronic state PES asymptotically correlates to H^+ (^{1}S) + CN ($^2\Sigma^+$) for H^+ + CN system. The contour plot of [HCN]$^+$ shows deeper interaction wells corresponding to two collinear configurations. The long-range interaction potential is obtained in charge–dipole, -quadrupole, and polarizability interactions. The potential anisotropy of the system has been analyzed in terms of radial multipolar expansion. The rotational transitions

ACKNOWLEDGMENTS

REFERENCES

Alexander, M. H., Manolopoulos, D., Werner, H. J., Follmeg, B., Vohralik, P. F., Lemoine, D., et al. (2011). HIBRIDON (Version 4.3.7) Is a Package of Programs for the Time-independent Quantum Treatment of Inelastic Collisions and Photodissociation. Available at: http://www2.chem.umd.edu/groups/alexander/hibridon/hib43/hibhelp.html.

Alexander, M. H. (1982). Rotationally Inelastic Collisions between a Diatomic Molecule in a 2Σ+ Electronic State and a Structureless Target. *J. Chem. Phys.* 76, 3637–3645. doi:10.1063/1.443401

Alexander, M. H., Smedley, J. E., and Corey, G. C. (1986). On the Physical Origin of Propensity Rules in Collisions Involving Molecules In2Σ Electronic States. *J. Chem. Phys.* 84, 3049–3058. doi:10.1063/1.450286

Allison, A. C., and Dalgarno, A. (1971). Rotational Excitation of CN by Electron Impact. *Astron.&Astrophys.* 13, 331–332. Available at: https://ui.adsabs.harvard.edu/abs/1971A%26A.13.331A/abstract.

Anusuri, B., and Kumar, S. (2016). Ab Initio adiabatic and Quasidiabatic Potential Energy Surfaces of H++ CN System. *J. Chem. Sci.* 128, 287–296. doi:10.1007/s12039-015-1022-8

Arthurs, A. M., and Dalgarno, A. (1960). The Theory of Scattering by a Rigid Rotator. *Proc. R. Soc. Lond. A.* 256, 540–551. doi:10.1098/rspa.1960.0125

Crawford, O. H., Allison, A. C., and Dalgarno, A. (1969). Electron Impact Excitation of CN. *Astron. Astrophys.* 2, 451–452.

DePristo, A. E., and Alexander, M. H. (1975). Anl-dominant Simplification of the Close-coupled Equations for Collisions between Atoms and Diatomic Molecules. *J. Chem. Phys.* 63, 3552–3559. doi:10.1063/1.431794

DePristo, A. E., and Alexander, M. H. (1976). Decoupling Approximations for Rotationally Inelastic Collisions between Ions and Polar Molecules: H+-CN. *J. Phys. B: Mol. Phys.* 9, 2713–2721. doi:10.1088/0022-3700/9/15/020

Dicke, R. H., Peebles, P. J. E., Roll, P. G., and Wilkinson, D. T. (1965). Cosmic Black-Body Radiation. *ApJ* 142, 414–419. doi:10.1086/148306

Dunning, T. H. (1989). Gaussian Basis Sets for Use in Correlated Molecular Calculations. I. The Atoms boron through Neon and Hydrogen. *J. Chem. Phys.* 90, 1007–1023. doi:10.1063/1.456153

Field, G. B., and Hitchcock, J. L. (1966). The Radiation Temperature of Space at λ 2.6 MM and the Excitation of Interstellar CN. *ApJ* 146, 1–6. doi:10.1086/148853

Harrison, S., Tennyson, J., and Faure, A. (2012). Calculated Electron Impact Spin-Coupled Rotational Cross-Sections for2S+ 1Σ+linear Molecules: CN as an Example. *J. Phys. B: Mol. Opt. Phys.* 45, 175202–175209. doi:10.1088/0953-4075/45/17/175202

Hayakawa, S., Nishimura, S., and Takayanagi, T. (1961). Radiation from the Interstellar Hydrogen Atoms. *Pub. Astro. Soc. Jpn.* 13, 184–206. Available at: https://ui.adsabs.harvard.edu/abs/1961PASJ.13.184H/abstract.

Huber, K. P., and Herzberg, G. (1979). *Constants of Diatomic Molecules*. New York: Van Nostrand.

Jamieson, M. J., Kalaghan, P. M., and Dalgarno, A. (1975). Rotational Excitation of CN Molecules by Proton Impact. *J. Phys. B: Mol. Phys.* 8, 2140–2148. doi:10.1088/0022-3700/8/12/025

Knowles, P. J., and Werner, H.-J. (1988). An Efficient Method for the Evaluation of Coupling Coefficients in Configuration Interaction Calculations. *Chem. Phys. Lett.* 145, 514–522. doi:10.1016/0009-2614(88)87412-8

Knowles, P. J., and Werner, H.-J. (1992). Internally Contracted Multiconfiguration-Reference Configuration Interaction Calculations for Excited States. *Theoret. Chim. Acta* 84, 95–103. doi:10.1007/BF01117405

Köppel, H., Cederbaum, L. S., Domcke, W., and von Niessen, W. (1979). Vibronic Coupling in Linear Molecules and Linear-To-Bent Transitions: HCN. *Chem. Phys.* 37, 303–317. doi:10.1016/0301-0104(79)85031-4

Lique, F., Spielfiedel, A., Feautrier, N., Schneider, I. F., Kłos, J., and Alexander, M. H. (2010). Rotational Excitation of CN(X Σ2+) by He: Theory and Comparison with Experiments. *J. Chem. Phys.* 132, 024303–024308. doi:10.1063/1.3285811

Manolopoulos, D. E. (1986). An Improved Log Derivative Method for Inelastic Scattering. *J. Chem. Phys.* 85, 6425–6429. doi:10.1063/1.451472

Nishimura, S. (1968). Cooling of Interstellar Clouds of Neutral Hydrogen and the Abundance of Molecular Hydrogen. *Pub. Astro. Soc. Jpn.* 20, 239–253. Available at: https://ui.adsabs.harvard.edu/abs/1968PASJ.20.239N/abstract.

Penzias, A. A., and Wilson, R. W. (1965). A Measurement of Excess Antenna Temperature at 4080 Mc/s. *ApJ* 142, 419–421. doi:10.1086/148307

Perić, M., Mladenović, M., Peyerimhoff, S. D., and Buenker, R. J. (1983). Ab Initio study of the Isomerization HNC → HCN. I. Ab Initio Calculation of the HNC ⇌ HCN Potential Surface and the Corresponding Energy Levels. *Chem. Phys.* 82, 317–336. doi:10.1016/0301-0104(83)85237-9

Stokes, R. A., Partridge, R. B., and Wilkinson, D. T. (1967). New Measurements of the Cosmic Microwave Background at λ=3.2cm and λ=1.58cm-Evidence in Support of a Blackbody Spectrum. *Phys. Rev. Lett.* 19, 1199–1202. doi:10.1103/physrevlett.19.1199

Takayanagi, K., and Itikawa, Y. (1968). Rotational Excitation of the Interstellar CN Molecule. *Pub. Astro. Soc. Jpn.* 20, 376–384. Available at: https://ui.adsabs.harvard.edu/abs/1968PASJ.20.376T/abstract.

Thaddeus, P., and Clauser, J. F. (1966). Cosmic Microwave Radiation at 2.63 Mm from Observations of Interstellar CN. *Phys. Rev. Lett.* 16, 819–822. doi:10.1103/physrevlett.16.819

Werner, H. J., and Knowles, P. J. (1988). An Efficient Internally Contracted Multiconfiguration-Reference Configuration Interaction Method. *J. Chem. Phys.* 89, 5803–5814. doi:10.1063/1.455556

Werner, H. –J., Knowles, P. J., Knizia, G., Manby, F. R., and Schütz, M. (2010). "MOLPRO," version 2010.1, a package of ab initio programs.

Nitrogen Fixation at the Edges of Boron Nitride Nanomaterials: Synergy of Doping

Venkata Surya Kumar Choutipalli [1,2,3], Karthikraja Esackraj [2,3] and Venkatesan Subramanian [1,2,3]*

[1]Inorganic and Physical Chemistry Laboratory, CSIR-Central Leather Research Institute, Chennai, India, [2]Centre for High Computing, CSIR-Central Leather Research Institute, Chennai, India, [3]Academy of Scientific and Innovative Research (AcSIR), Ghaziabad, India

Synthesis of ammonia at ambient conditions is very demanding yet challenging to achieve due to the production of ammonia fuel, which is considered to be a future fuel for sustainable energy. In this context, computational studies on the catalytic activity of the edge sites of boron nitride nanomaterials for possible nitrogen reduction into ammonia have been investigated. Geometrical and electronic properties of zigzag and armchair B-open edges of BN sheet (B_{OE}) models have been unraveled to substantiate their catalytic nature. Results reveal that B_{OE} sites exhibit very high potential determining steps (PDS) of 2.0 eV. Doping of carbon (C) at the nitrogen center, which is vicinal to the B_{OE} site reduces the PDS of the N_2 reduction reaction (NRR) (to 1.18–1.33 eV) due to the regulation of charge distribution around the active B_{OE} site. Further, the NRR at the C doped at various edge sites of a boron nitride sheet (BNS) has also been studied in detail. Among the 12 new C-doped defective BNS models, 9 model catalysts are useful for nitrogen activation through either chemisorption or physisorption. Among these, **ZC_N**, **AC_N**, and **ZC_{BV}** models are efficient in catalyzing NRR with lower PDS of 0.86, 0.88, and 0.86 eV, respectively. The effect of carbon doping in tuning the potential requirements of NRR has been analyzed by comparing the relative stability of intermediates on the catalyst with and without carbon doping. Results reveal that C-doping destabilizes the intermediates compared to non-doped systems, thereby reducing the possibility of catalyst poisoning. However, their interactions with catalysts are good enough so that the NRR activity of the catalyst does not decrease due to C-doping.

Keywords: nitrogen reduction, catalysis, small molecules activation, DFT, doping, boron nitride, edge

INTRODUCTION

A century ago, ammonia was the savior of the world in the form of fertilizer which grew crops faster when food crises arrived due to the growing population (Aber et al., 1989; Bogaard et al., 2013; Galloway et al., 2017). For the extensive use of ammonia, Haber and Bosch developed an industrial method (the Haber-Bosch (HB) process) to synthesize ammonia artificially (Smith, 2002). The HB process addressed the world's ammonia problem, and about 40% of the global population now relies on this process for ammonia synthesis (Howard and Rees, 1996; Kitano et al., 2015). However, the HB process is responsible for 1–2% of global energy consumption and 3% of CO_2 emission due to the combustion of fossil fuels to generate H_2 as the source of ammonia (Alexandratos and Bruinsma,

Nitrogen Fixation at the Edges of Boron Nitride Nanomaterials:
Synergy of Doping

Graphical Abstract |
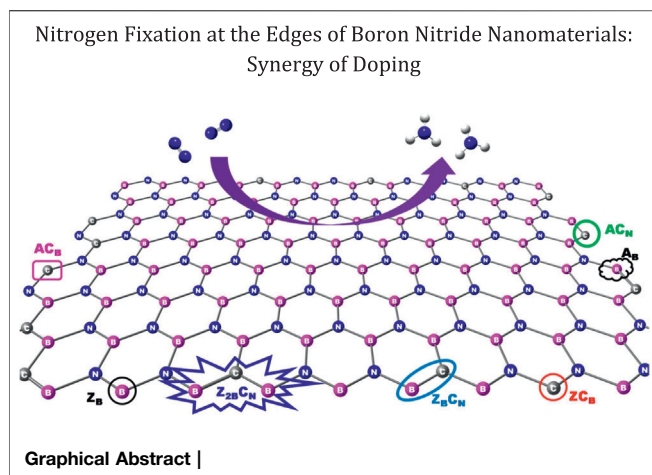
2012; Glibert et al., 2014; van der Ham et al., 2014; Zheng et al., 2020). Hence, the HB process should be relooked at for its environmental concerns. On the other hand, today's major concern is climate change due to emission of carbon or green house gases (GHG). Hence, carbon-free energy storage is one of the major targets for sustainable energy and environment (Spatzal et al., 2014; McEnaney et al., 2017; Guo et al., 2018). In this context, ammonia is believed to be a future fuel owing to its advantages (Chehade and Dincer, 2021). Ammonia contains 17.8% of H_2 by weight and its energy density by volume is nearly double that of liquid hydrogen (Lan and Tao, 2014; Kobayashi et al., 2019). Its physicochemical properties are similar to propane. Hence, the storage/transport methods developed for propane could also be used for ammonia. Therefore, by capturing, storing, and shipping hydrogen for use in emission-free fuel cells and turbines, ammonia is very handy (Guo and Chen, 2017; Kobayashi et al., 2019). Direct combustion of ammonia in power plants and ship engines leads to the carbon-free emission of fuel waste (Hinokuma et al., 2015; Chakraborty et al., 2017). Green production of ammonia, where oxidation of water is the source of H_2 production thereby reducing N_2 to synthesize ammonia, is the one of the important alternatives for carbon-free emission (Ye et al., 2017; Rouwenhorst et al., 2019; Yapicioglu and Dincer, 2019; Rouwenhorst et al., 2020; Salmon and Bañares-Alcántara, 2021). One more alternative is the electrochemical conversion of N_2 to ammonia. Hence, it is obvious to develop efficient and sustainable electrocatalysts for the nitrogen reduction reaction (NRR).

Two-dimensional (2D) materials are widely employed for various applications owing to their unique properties (Schwierz et al., 2015; Wang et al., 2016; Ashworth and Foster, 2018; Wang et al., 2018; Zhu et al., 2021). These materials exist as multi-layered materials with one-atom thick planes, which stack on top of each other (Mittal et al., 2015). Weak attractive van der Waals forces mainly govern the stabilization of these stacked layers. The surface parallel to the plane of 2D materials is called the basal plane, and the edge plane refers to the plane that is perpendicular to the surface. The basal plane surface shows atomic flatness and low defect density. On the other hand, the edge plane contains dangling bonds and defects (Velický et al., 2019). Some of the functional

groups are seen at the edges due to abrupt lattice termination and their reactivity. Hence, the edge sites display special properties, *viz*., unsaturated coordination, accumulated charge density, and spin density (magnetic properties) (Fujii and Enoki, 2013; Zhang et al., 2013; Fujii et al., 2014; Bellunato et al., 2016). Previously, comparative studies on the reactivity of the edge and the graphene's basal plane have been made (Randin and Yeager, 1972; Bowling et al., 1989; Rice and McCreery, 1989). Various experimental revelations on adsorption, electron transfer (ET), and capacitance demonstrated that the edge plane is electrochemically active whereas the basal plane either exhibits vanishingly low electrochemical activity or is completely inactive (Randin and Yeager, 1975; McDermott et al., 1992; Banks et al., 2005). Recent advances in electrochemical imaging and localized electrochemical measurements have clearly elucidated that the edges and defects are more reactive than the basal plane (Davies et al., 2005; Tan et al., 2012; Zhang et al., 2014; Zhong et al., 2014).

Atomic layer thin h-BN can also exhibit different properties due to the distinct structure of their edge states (Ooi et al., 2006; Golberg et al., 2010; Zeng et al., 2010). For example, doping of carbon at either the boron or nitrogen site of h-BN exhibits magnetism (Okada and Oshiyama, 2001; Li et al., 2009). It is well known from previous studies that boron-based catalysts have a high potential for the nitrogen reduction reaction (Zhao and Chen, 2017; Zhang et al., 2019). Therefore, it is natural to expect that these boron edges of h-BN may catalyze N_2 reduction. Boron-based activation involves an "acceptance-donation" mechanism between B and N_2, which is similar to that of transition metal-assisted N_2 activation (Lv et al., 2019; Shi et al., 2019). Here, the binding between boron and hydrogen has been inhibited by an sp^3-hybridized boron atom, suppressing the HER in acidic conditions (Hering-Junghans, 2018; Yu et al., 2018; Liu et al., 2019). Similar structural features can be found in B-centers of BN nanomaterials. Previous studies have shown that edge states of 2D materials are highly reactive which are regulated by the edge centers (Velický and Toth, 2017; Momeni et al., 2020). The adjustable edge structures fine-tune these reactivities. These intrinsic features are responsible for making these edges highly efficient catalytic sites. Therefore, the role of edge sites in catalyzing NRR has been investigated systematically using density functional theory (DFT)-based methods. Both zigzag and armchair edges have been considered for evaluation. In addition, the effect of carbon doping at various edge sites has also been investigated. All the possible mechanistic pathways have been traced to establish the minimum energy reaction pathway for the nitrogen reduction reaction. The present computational exploration of catalytic activities of B-centers would definitely add value to the knowledge portfolio of this research topic and accelerate the development of NRR catalysts.

Computational Details

A DFT-based Perdew-Burke-Ernzerhof (PBE) (Adamo and Barone, 1999) hybrid functional method was adopted with a 6-31G(d) (Hariharan and Pople, 1973; Hehre et al., 1986) basis set. The non-covalent interactions between the systems were modeled using Grimme's dispersion-corrected (PBE-D3) functional theory (Grimme et al., 2010). Vibrational frequency analysis was carried
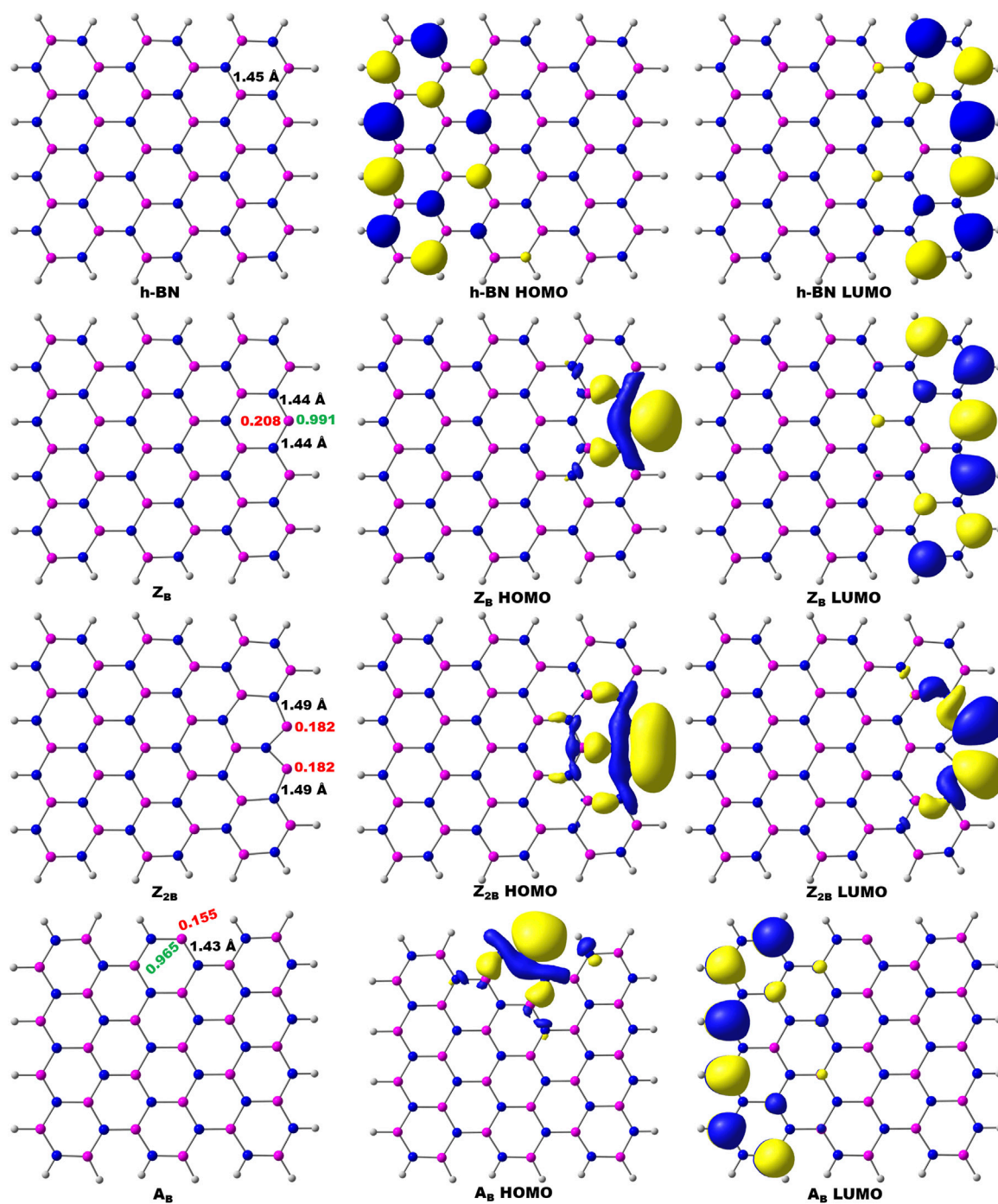
FIGURE 1 | Optimized geometries of pristine and B-open edge defective BNS calculated at the PBE/6-31G(d) level of theory. Frontier molecular orbitals of the corresponding systems are given. Charge and spin densities on the active site are shown in red and green color, respectively. Color indication: Pink-B, Blue-N, and White-H.

out to verify whether the optimized geometries were in minima or maxima on the potential energy surface. The absence of imaginary frequency criteria was used to characterize the minimum energy geometry. As the calculations involve intermediates with open-shell configuration, spin-polarized (unrestricted) calculations were performed. Population analysis was carried out at the same level

of theory to find the charge transfer at each elementary step of the reaction. All the quantum chemical calculations were performed with the G09 suite of the program (Frisch et al., 2009). Density of states (DOS) calculations were obtained at the GGA-PBE level as implemented in the DMol^3 program (Delley, 2000) using the optimized geometries calculated at the PBE/6-31G(d) level of theory.
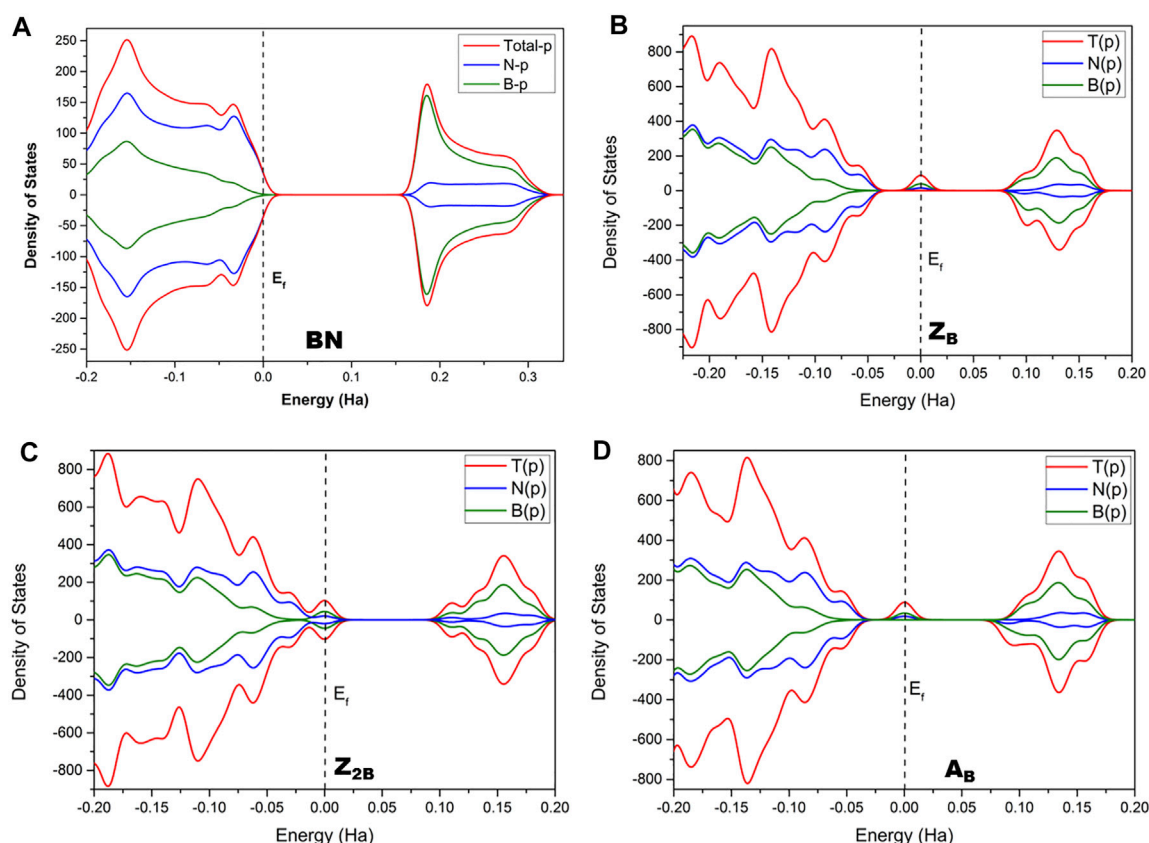
FIGURE 2 | Calculated density of states (DOS) of **(A)** pristine h-BNS, **(B) Z$_B$**, **(C) Z$_{2B}$**, and **(D) A$_B$** defective BNS.

The feasibility of nitrogen adsorption on the catalyst was predicted by computing the interaction energy (E$_{ads}$) using the following equation:

$$E_{ads} = E_{adsorbate+catalyst} - \left(E_{adsorbate} + E_{catalyst} \right) \qquad (1)$$

Where E$_{adsorbate/catalyst}$, E$_{adsorbate}$, and E$_{catalyst}$ are the total energies of the adsorbate–catalyst, the isolated adsorbate, and the defective BNS, respectively. According to this definition, a negative E$_{ads}$ indicates exothermic adsorption.

The Computational Hydrogen Electrode (CHE) (Nørskov et al., 2004; Rossmeisl et al., 2005) model was applied for simulating the effect of the concerted transfer of protons and electrons to all the elementary steps of the reaction. The model involves the calculation using the formula as given in **Eq. 2**.

$$\frac{1}{2}G_{H_2} = G\left(H^+ + E^-\right) \qquad (2)$$

RESULTS AND DISCUSSION

Geometries of Model Systems

Both zigzag and armchair boron nitride nanomaterials have been considered to assess the catalytic properties of their edge centers.

The model systems chosen for this investigation are depicted in **Figure 1**. For brevity, the following nomenclature was used throughout the text. Zigzag and armchair models are denoted as **Z** and **A**. BN systems with one and two B-open edges (B$_{OE}$) at the zigzag edge are called **Z$_B$** and **Z$_{2B}$**, respectively. Similarly, the same at the armchair edge is referred to as **A$_B$**. The symbols **C$_B$** and **C$_N$** represent carbon doping at boron and nitrogen sites, respectively. Similarly, **C$_{BV}$** and **C$_{NV}$** refer to carbon doping at boron-vacancy and nitrogen-vacancy, respectively. The notation, **N$_x$H$_y$H$_z$** (x = 1,2 and y, z = 0–6) represents different intermediates observed in the nitrogen reduction reaction.

The conventional nitrogen reduction process is initiated with the activation of N$_2$ by the surface of the models. This step is very important for the subsequent reduction steps to form ammonia. However, these steps are significantly affected by the electronic properties of the model catalysts. Hence, a prior understanding of the geometrical and electronic properties of designed models is important. In that context, it is necessary to compute the DOS of pristine BNS and BNS with defects such as zigzag open edge and armchair open edge. The calculated results are depicted in **Figure 2**. In addition, the possibility of formation in such defective systems is also a very important aspect to be considered for their experimental feasibility. Hence, defect formation energies of **Z$_B$**, **Z$_{2B}$**, and **A$_B$** have been calculated as 4.17, 8.29, and 4.10 eV, respectively which are in the range of

TABLE 1 | Calculated cohesive energy (E_{coh}) and defect formation energies (E_{def}) of BN systems at the PBE/6-31G(d) level of theory.

S. No	Model	E_{coh} (eV)	E_{def} (eV)	S. No	Model	E_{coh} (eV)	E_{def} (eV)
1	Z_B	−5.59	4.16	10	ZC_N	−5.59	4.02
2	Z_{2B}	−5.61	8.29	11	ZC_NH	−5.58	−0.47
3	A_B	−5.67	4.10	12	ZC_{NV}	−5.56	0.60
4	Z_BC_N	−5.62	−1.70	13	AC_B	−5.62	1.94
5	$Z_{2B}C_N$	−5.64	−2.11	14	AC_BH	−5.58	−0.42
6	A_BC_N	−5.62	−1.87	15	AC_{BV}	−5.57	0.42
7	ZC_B	−5.62	2.31	16	AC_N	−5.59	4.01
8	ZC_BH	−5.59	−0.78	17	AC_NH	−5.57	−0.11
9	ZC_{BV}	−5.57	0.79	18	AC_{NV}	−5.57	0.28

FIGURE 3 | Optimized geometries of various possibilities of N₂ adsorption on B-open sites of BN systems. **(A)** Side-on mode on Z_B, **(B)** end-on mode on Z_B, **(C)** side-on mode on Z_{2B}, and **(D)** side-on mode on A_B calculated at the PBE/6-31G(d) level of theory. Color indication: Pink-B, Blue-N, and White-H.
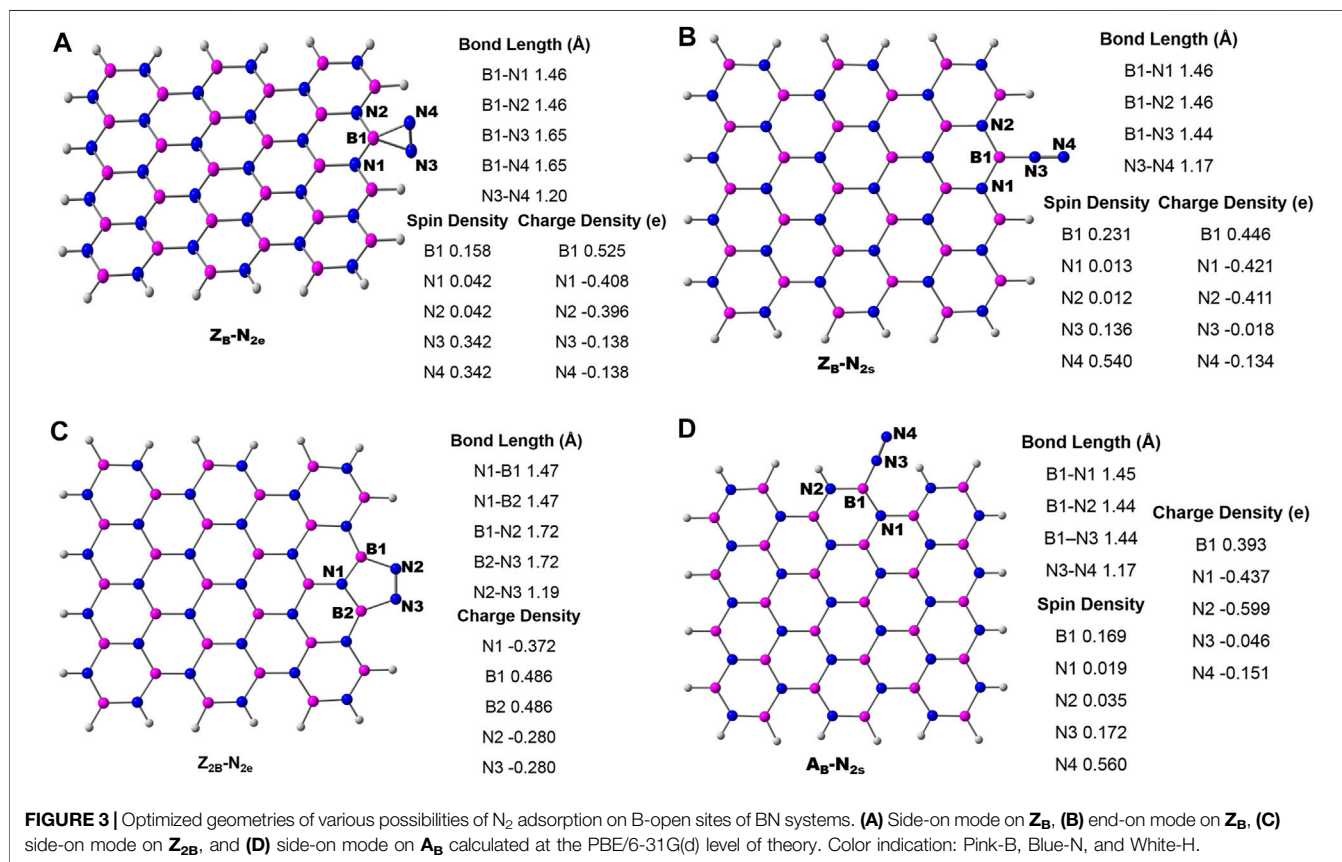
experimental limitations. Hence, these results indicate their experimental feasibility. The defect formation energies of all the defective systems that are considered in this study have been given in **Table 1**.

It is well known that h-BN is a wide bandgap insulator, and experimental band gap values are in the range of 4.0–5.6 eV (Panchakarla et al., 2009; Golberg et al., 2010; Wu et al., 2013; Xue et al., 2013). It does not exhibit magnetism. The calculated value from this investigation is found to be 4.25 eV. It is already reported that PBE functional underestimates band gap values (Janesko, 2011; Hollins et al., 2012; Pari et al., 2016). Moreover, this value may arise from the effect of edge passivation of chosen model systems by hydrogen. However, our group has demonstrated the usefulness of truncated models as replicas

for periodic 2D materials and catalysis of oxidation of alcohols into aldehydes (Vijaya Sundar and Subramanian, 2013; Jeyaraj et al., 2015). In the case of B_{OE}, the partial wave appears at the Fermi level, indicating the conducting nature of defective BN systems. Thus, these systems are suitable for catalytic applications due to defective sites and associated effective electron transfer.

Further, charge densities on the active sites have also been analyzed in detail to understand the activity of B_{OE} sites. In pristine h-BN (passivated by hydrogen), the charge density on the boron atom of the boron edge is 0.26 e. The charge density for the B-open edge site is 0.20 e. It is noted from the results that the pristine BNS does not exhibit any spin density and is non-magnetic. However, the spin density on Z_B is 0.99, which is localized on a B_{OE} indicating its magnetic behavior. In similar

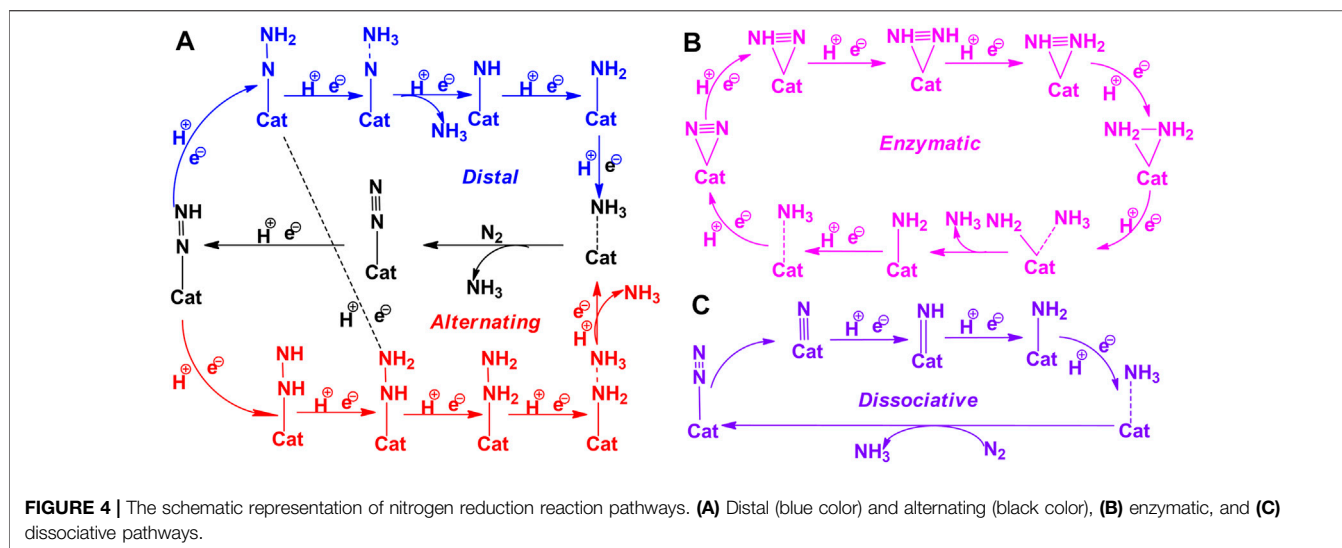**FIGURE 4 |** The schematic representation of nitrogen reduction reaction pathways. **(A)** Distal (blue color) and alternating (black color), **(B)** enzymatic, and **(C)** dissociative pathways.

lines, Z_{2B} exhibits a reduced positive charge (0.25 e) and increased spin density (0.97) on open B-sites. These inherent properties of defective systems render the open B-site of Z_B highly reactive when compared to the pristine BN.

N$_2$ Adsorption

The two possible modes of the adsorption pattern of N$_2$ on the surface are end-on (Schrock) and side-on (enzymatic) modes. In the end-on adsorption mode, N$_2$ binds to the active site through one of its nitrogen atoms (N$_{2s}$). While in the side-on mode, N$_2$ molecule binds parallel (*N$_{2e}$) to the surface of BNS. The optimized geometries of N$_2$ adsorption modes on B$_{OE}$ are given in **Figure 3**. Both the modes are energetically possible for Z_B with the adsorption energies of -0.57 (end-on) and −0.16 eV (side-on). The corresponding adsorption elongates the N-N bond from 1.11 to 1.16 Å (end-on) and 1.11 to 1.20 Å (side-on). In this process, N$_2$ gains 0.15 e from Z_B in the end-on mode. The same for the side-on mode is 0.28 e. The high charge transfer and concomitant elongation of the N-N bond imply the activation propensity of Z_B in enzymatic mode. Similarly, results from N$_2$ activation by Z_{2B} reveal that the side-on mode dominates the end-on mode. In this mode, Z_{2B} exhibits high interaction energy of −2.39 eV with N$_2$ leading to a charge transfer of 0.56 e from Z_{2B} to N$_2$. This interaction is responsible for the appreciable lengthening of N-N from 1.11 to 1.28 Å due to the availability of more B-active sites for interaction.

An armchair B-open edge (A$_B$) exhibits only the end-on mode of N$_2$ adsorption (**Figure 3D**), despite many trials in different orientations. The adsorption energy of this mode is −0.32 eV with a charge transfer of 0.19 e from A$_B$ to the N$_2$ molecule. The N-N bond length increases from 1.11 to 1.17 Å. It is clear that the zigzag edge of BN nanomaterials can activate nitrogen. Specifically, the energetics of adsorption through the side-on mode on Z_{2B} indicates a chemisorption process. Considerable transfer of electron density from the BNS surface to N$_2$ accompanies this activation along with appreciable lengthening of the N-N bond. It is pertinent to mention that the strong

interaction between BNS and the substrate leads to catalyst poisoning due to difficulties in the desorption of products. The calculations show that the N-open edge cannot activate N$_2$. Hence, the reduction of N$_2$ using the B-open edge model has been taken for detailed elucidation.

N$_2$ Reduction at B-Open Site Edge BN Systems

Reduction of activated N$_2$ at the B$_{OE}$ site involves six successive protonation steps to produce ammonia. In the case of an end-on mode adsorbed system, reduction begins at the distal nitrogen site (which is away from the BNS surface) to produce the first NH$_3$ molecule. Subsequently, a further attack occurs at the proximal N atom linked to the B atom, leading to the release of the second NH$_3$ molecule. This reaction pathway is referred to as the "distal mechanism." The reduction of the end-on mode of N$_2$ may occur in an alternating pathway. In this pathway, both the activated nitrogen atoms are protonated in an alternative fashion to yield ammonia. Typically, the adsorption of the side-on mode occurs with the aid of an alternating pathway. The complete nitrogen reduction reaction pathways have been given in **Figure 4**. Adopting these reaction pathways, Gibbs free energies of all the elementary steps have been systematically calculated to unravel the minimum reaction pathway or most feasible pathway for the nitrogen reduction reaction. The results are depicted in **Figure 5**. The free energy profile of NRR catalyzed by the B-open edge (Z_B) site is illustrated in **Figure 5A**. Since adsorption of N$_2$ with Z_B occurs in all possible modes, distal, alternating, and enzymatic pathways have been investigated. Except for the final ammonia desorption step, the elementary step with maximum endergonicity is called the potential determination step (PDS), and the corresponding Gibbs free energy is denoted as ΔG_{PDS}. In the literature, this potential is also called the limiting potential of the NRR, which describes the possibility of the nitrogen reduction reaction.

For the Z_B mode of absorption, the first step of hydrogenation of *N$_2$ to form *N-NH is endothermic. The energy requirements

FIGURE 5 | Calculated Gibbs free energy profiles of NRR catalyzed by **(A) Z_B**, **(B) Z_2B**, and **(C) A_B** defective systems at the PBE/6-31G(d) level of theory. PDS represents the potential determining step of the pathway.
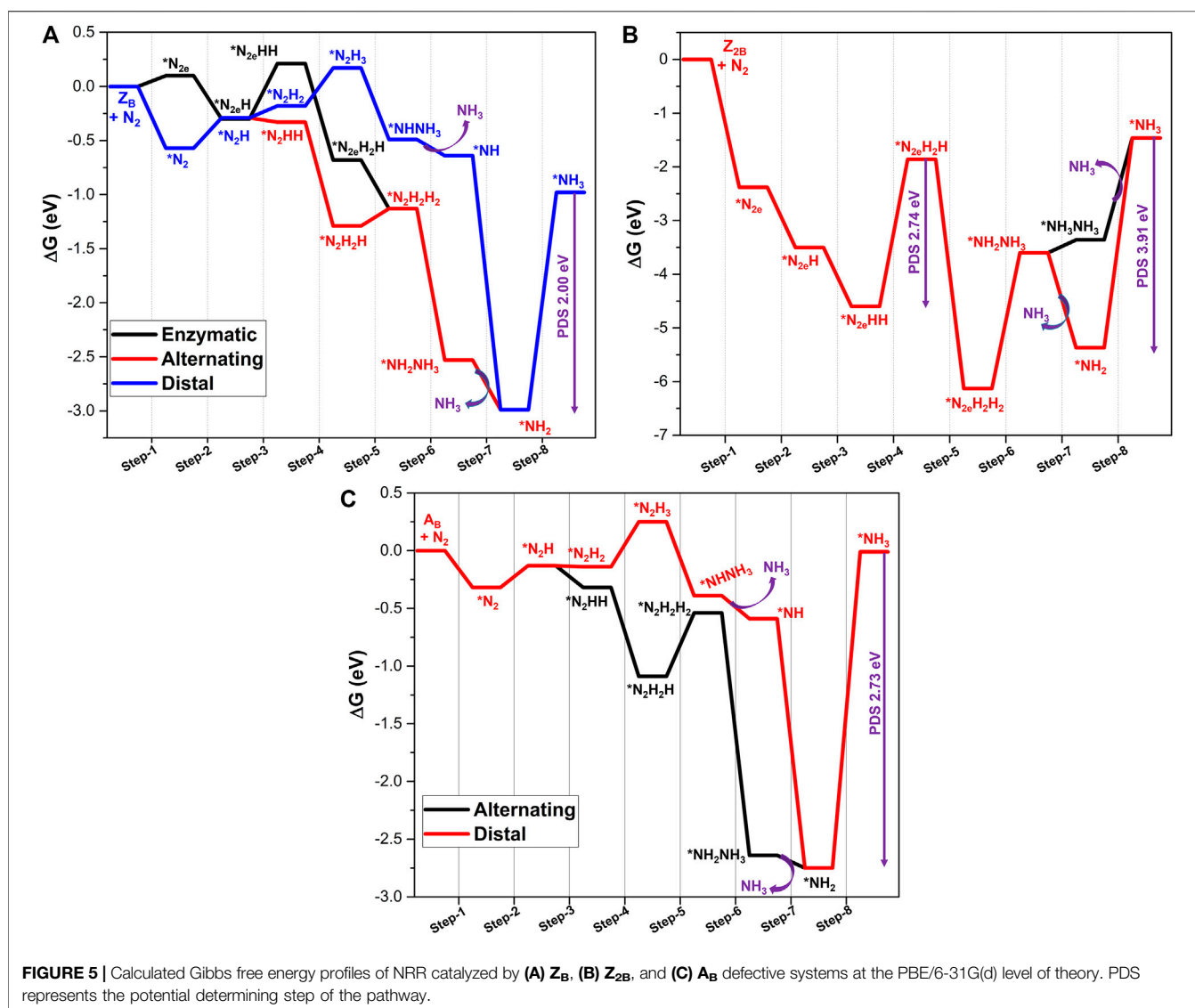
for end-on and side-on modes are 0.27 and 0.11 eV, respectively. The lower endergonicity in the case of the side-on mode indicates that the possibility of activation of N_2 is high in the side-on mode when compared to the end-on mode. Following the reduction of end-on mode-activated species, further hydrogenation provides the selectivity between distal and alternating pathways. Second protonation (step 3) leads to the formation of $*N_2H_2$ (distal) and $*N_2HH$ (alternating) intermediates with energetics of 0.12 and −0.03 eV, respectively. This step favors the alternating pathway over the distal pathway. Hence, an alternating pathway is further considered. In step 4, the third hydrogen is added to the distal nitrogen to form $*N_2H_2H$, and this step is downhill by −0.96 eV. Adopting the same pathway, the fourth hydrogen is added to the proximal nitrogen in step 5 to get $*N_2H_2H_2$. In this step, the complete scission of the N-N bond is observed to form two NH_2 adducts. This step is an endergonic one with the energetics of 0.16 eV. The subsequent fifth protonation (step 6) results in the

formation of the first NH_3 molecule at the active site and NH_2 adduct. This step is associated with the release of high energy of −1.39 eV. It can be seen from the free energy profile that step 7, corresponding to desorption of NH_3, is also an exergonic reaction (−0.46 eV). Final protonation (step 8) involves the formation of a second NH_3 molecule. However, this step is highly endergonic and turns out to be a potential determining step with energetics of 2.00 eV. In the case of the side-on mode of adsorption, the first hydrogen addition is exergonic by −0.39 eV. This exergonicity is attributed to the significant activation of N_2 by Z_B in the side-on mode of adsorption. In this mode, reduction follows an enzymatic pathway where protonation occurs in an alternating fashion. The second proton addition is an uphill step with 0.50 eV followed by formation of two downhill intermediates $*N_{2e}H_2H$ (−0.88 eV) and $*N_{2e}H_2H_2$ (−0.45 eV). Interestingly, the $*N_{2e}H_2H_2$ intermediate resembles the intermediate of step 5 in the alternating pathway. Hence, further reduction steps follow

the alternating mechanism. Nitrogen reduction at the zigzag B-open edge demands energy due to the appreciable interaction of active site with nitrogen and stabilization of the products.

Results from calculations on nitrogen reduction at two B-open edge sites ($\mathbf{Z_{2B}}$) (**Figure 5B**) reveal that the first protonation step is downhill by −1.11 eV, due to the considerable activation of N₂ by $\mathbf{Z_{2B}}$. In the subsequent reduction step (step 3), formation of *N₂HH takes place, and the corresponding energy is −1.10 eV. In step 4, the third proton is added to the distal nitrogen to form the *N₂H₂H intermediate. Formation of this intermediate costs high energy of 2.74 eV. The fourth protonation gives a hydrazine adduct at the active site along with complete scission of the N₂ bond. The completion of this step yields two NH₂ species to the active sites. It can be seen from the energy profile that this step is associated with the favorable free energy of −4.27 eV. The fifth protonation leads to the formation of the first ammonia molecule; however, this step requires free energy of 2.53 eV. Since the interaction between the catalysts and the intermediate is considerably high in the previous step, a subsequent reduction is associated with a very high potential requirement (2.53 eV). This step is followed by the desorption of first ammonia molecule and it is related to energy of 0.24 eV. Prior to the desorption of the first ammonia molecule, the final protonation at the NH₂ adduct gives the second ammonia molecule. In this intermediate, both the ammonia molecules are bound to the active site. It can be seen from the energy profile that it is a downhill step (−1.76 eV). The energetics indicate the favorable formation of ammonia molecules.

The complete energy profile for the various intermediates and products in the reaction as catalyzed by the armchair open B-edge site ($\mathbf{A_B}$) model is given in **Figure 5C**. It is clear from the figure that the first protonation is uphill by 0.19 eV, followed by the second protonation. The second protonation adopts more a feasible alternating pathway when compared to the distal pathway. The free energies associated with step 3 are −0.01 and −0.19 eV for distal and alternating pathways, respectively. Hence, further reduction occurs via an alternating pathway. The third protonation leads to the formation of *N₂H₂H, which is exergonic in energy by −0.77 eV. The formation of *N₂H₂H₂ (step 5) is an uphill process (0.55 eV). In this step, the N-N bond is completely cleaved. After the formation of ammonia in the fifth protonation step, the energy of −2.09 eV is released. Desorption of the first ammonia molecule is a downhill process (−0.11 eV), and subsequently, protonation of the intermediate leads to the formation of the second NH₃. It can be observed that this step is highly endergonic in nature and emerges as PDS with 2.74 eV.

Carbon Doping at the Edges of BN

It is clear from the energetics of NRR by B-open edge systems that the active B-sites strongly interact with molecular nitrogen and intermediates of NRR. Thus, the desorption of the product from the surface is energetically demanding, and connectedly poisoning catalysts is highly possible. Hence, the activity of these open B-edges should be tuned to facilitate the NRR in an efficient manner. In this context, the catalytic performance of BN can be improved by doping.

Specifically, we have considered doping of carbon (C), sulfur (S), and phosphorous (P) on the various chosen models. However, our computational results showed that doping of S and P are energetically unsuitable for N₂ reduction. Hence, these systems are not considered for further exploration. Analysis of literature information shows that there are abundant experimental details on the effect of carbon doping on the BN systems (Chen et al., 2018; Marbaniang et al., 2018; Almahmoud and Talla, 2019). It is found from previous studies that carbon doping can alter the catalytic properties of BN systems. Therefore, doping of carbon has been investigated in detail.

The schematic of different possibilities of carbon doping in BN materials is shown in **Figure 6**. It can be noticed from the optimized geometries of carbon-doped BN systems (**Figure 7**) that carbon doping is carried out at the nitrogen atom, which is vicinal to the B-open edge site of $\mathbf{Z_B}$, $\mathbf{Z_{2B}}$, and $\mathbf{A_B}$. These doped models are referred to as $\mathbf{Z_BC_N}$, $\mathbf{Z_{2B}C_N}$, and $\mathbf{A_BC_N}$. The charge population analysis of these systems revealed that this strategy may regulate the charge redistribution around the B open site so that the high limiting potentials of NRR obtained for open B-active sites may be tuned significantly. Similar arguments have also been advanced in previous reports (Jiang et al., 2007; Ni and Wang, 2015; Mao et al., 2019).

There is a compelling evidence that these doped C-sites may act as active sites for possible catalytic applications. Therefore doping of the C atom at various possible positions of both zigzag and armchair edges of pristine BN may lead to new defective systems. The optimized geometries at the PBE/6-31G(d) level of theory are presented in the Supplementary Material (SM) as **Supplementary Figures S1, S2**. It is clear from the geometries of C-doped systems (**Figure 7**, **Supplementary Figures S1, S2**) that the edge B atoms of C-doped BN on the B-edge move in an inward direction and the associated symmetry of the BN system is lost. The optimized geometries of N₂ adsorption modes on C-doped BN are presented in the SM (**Supplementary Figures S3–S5**). In this section, results from calculations on the catalytic activities of both B_{OE} and C-doped active sites at edges are presented.

NRR at B-Open Edge Site in the Presence of C-Doping

The calculated defect formation energies of all the model systems (**Figure 6**) are listed in **Table 1**. It is clear from the energy values that these defective systems are thermodynamically possible, and it may require minimal external energy input for their creation. It is evident from the previous report that the adjustment of carbon doping within h-BN systems can be made in a more controllable fashion when compared to the incorporation of B and N in graphene (Ci et al., 2010; Huang et al., 2015). These reports have encouraged us to explore further calculations on the nitrogen reduction reaction.

The free energy profiles of possible NRR catalyzed by $\mathbf{Z_BC_N}$, $\mathbf{Z_{2B}C_N}$, and $\mathbf{A_BC_N}$ are presented in **Figure 8**. The absorption of molecular nitrogen with $\mathbf{Z_BC_N}$ is studied by adopting an end-on mode of adsorption. The calculated absorption energy is (0.02 eV). Previous reports have shown that the nitrogen
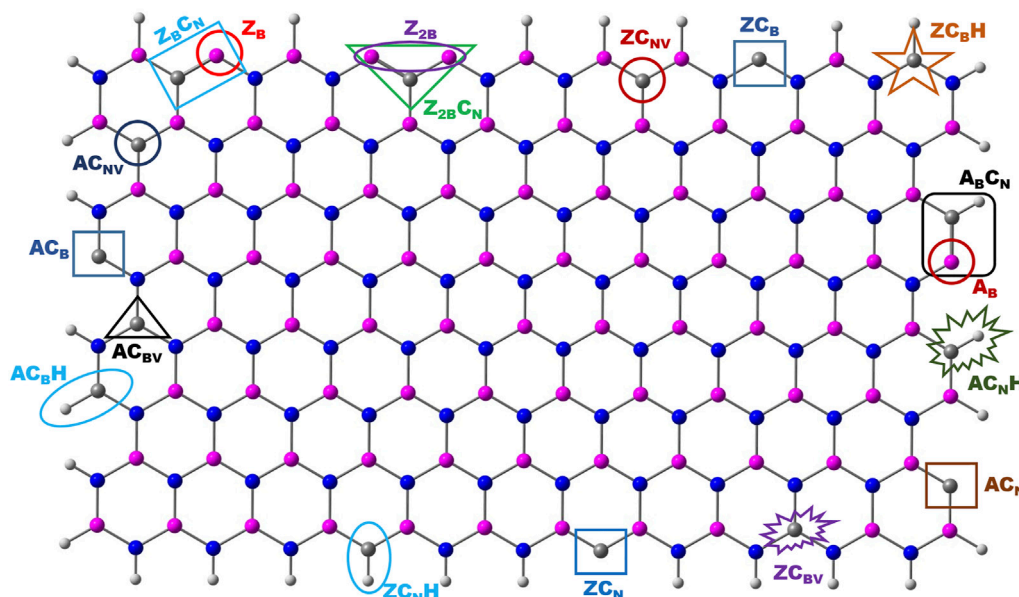
FIGURE 6 | Schematic representation of various possible edge sites for carbon doping in the BN system.
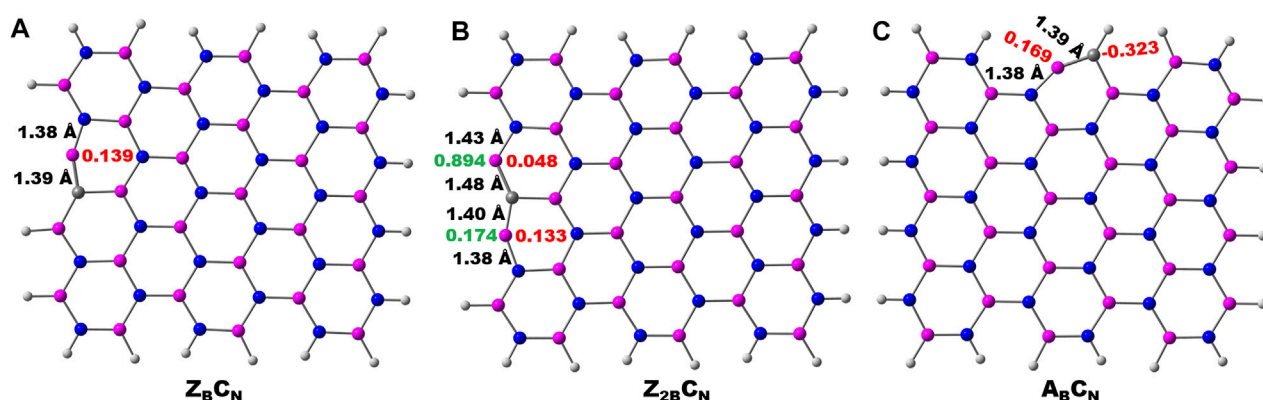
FIGURE 7 | Optimized geometries of carbon doping at the N atom vicinal to the B-open edge active site calculated at the PBE/6-31G(d) level of theory. Important bond lengths around active sites are given in black-colored font. The charge and spin densities on the active site are shown in red and green-colored font, respectively.

reduction from the marginally endergonic adsorption of N$_2$ on the catalyst system is still possible (Liu et al., 2018; Tian et al., 2018). It is evident from **Figure 8A** that the first protonation (step 2) is again an endergonic reaction with the energetics of 1.33 eV. As explained earlier, second protonation (step 3) has possibilities for either distal or alternating pathways. It is clear from the energetics of step 3 that the alternating pathway (−0.54 eV) is more feasible. Hence, an alternating pathway is further investigated from this point. The protonation of alternating intermediate *N$_2$HH yields *N$_2$H$_2$H in step 4. The value of free energy (−0.34 eV) shows the feasibility of this step. The formation of hydrazine can be noted in step 5. It involves the release of energy of −0.27 eV. At this particular step, possibility of a hybrid mechanism has also been studied to get *N$_2$H$_2$H from *NHNH$_3$. However, it is endergonic in nature by

0.21 eV. Hence, an alternating mechanism is continued in the remaining step.

The formation of ammonia is seen in step 6 with the release of energy (−0.93 eV). The subsequent desorption of ammonia is favorable (−0.28 eV). The final protonation step yields a second ammonia molecule (−0.25 eV). The comparison of **Z$_B$C$_N$** and **Z$_B$** results shows that in stark contrast to NRR by **Z$_B$**, the minimum energy pathway for **Z$_B$C$_N$** is favorable except for the first protonation step. This may be attributed to the presence of C-doping and associated changes in the charge distribution, which regulates the high-energy demanding steps into favorable reactions. Overall, the limiting potential decreases from 2.0 eV (in the case of **Z$_B$**) to 1.33 eV.

The calculated energetics associated with the side-on mode of adsorption of N$_2$ with C-doped defective **Z$_{2B}$** follows the same trend as observed in undoped **Z$_{2B}$**. The adsorption energy is

FIGURE 8 | Gibbs free energy profile diagrams of possible NRR pathways catalyzed by **(A) Z_BC_N, (B) $Z_{2B}C_N$,** and **(C) A_BC_N** calculated at the PBE/6-31G(d) level of theory. PDS is a potential determining step and * indicates the adsorption of intermediate on to the BNS.
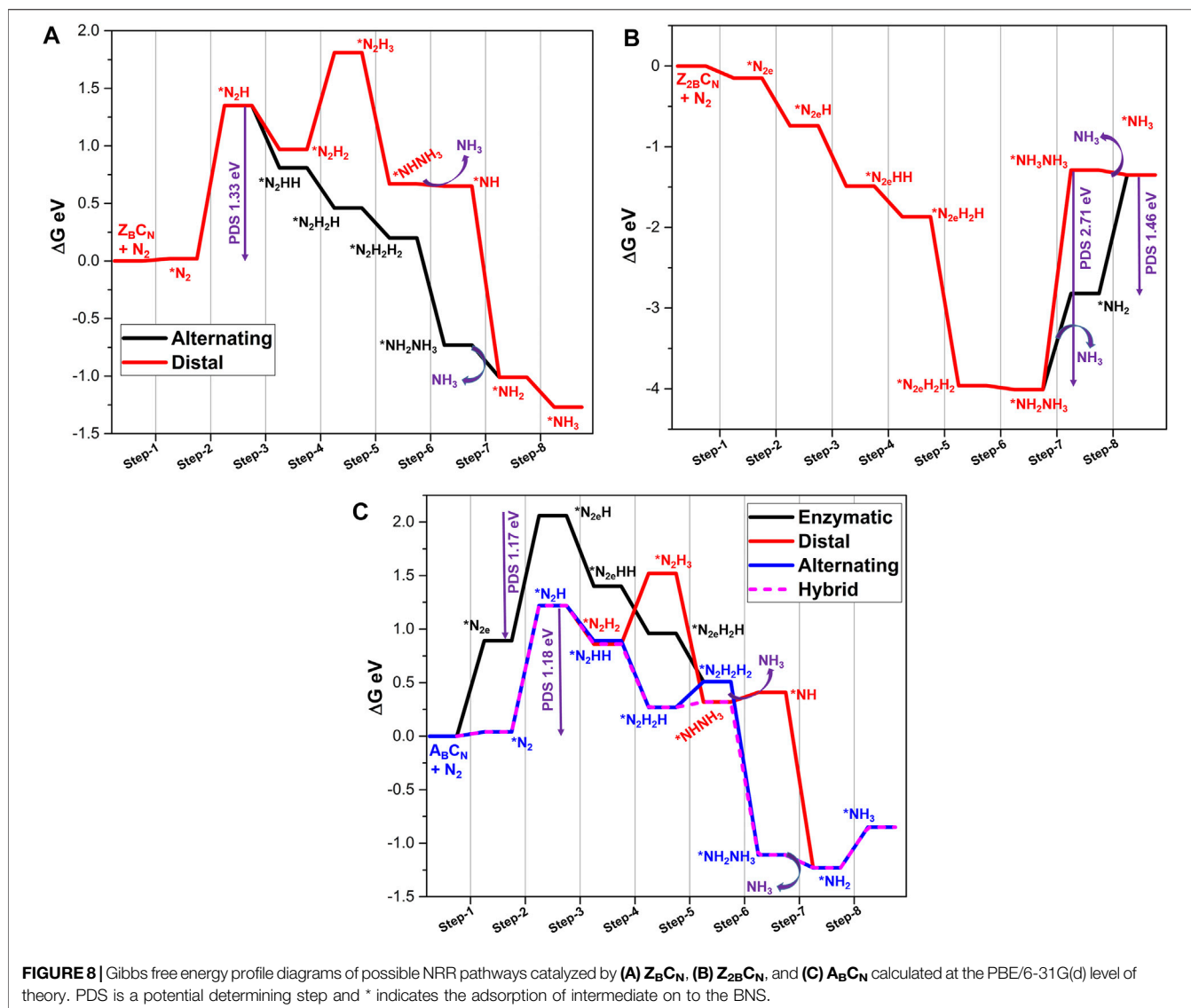
found to be -0.16 eV, which is less favorable when compared to N_2 adsorption on Z_{2B}. As a result of this adsorption, the N_2 bond is elongated to 1.19 Å with an electron transfer of 0.26 e to the N_2 molecule. These values are marginally less when compared to the undoped Z_{2B} system. The energy profile for this system is depicted in **Figure 8B** for an enzymatic pathway.

The first protonation step is associated with an energy of −0.59 eV to form the *$N_{2e}H$ intermediate. In accordance with the energetics of formation of *$N_{2e}HH$, the next step is also favorable. The free energies of further protonation steps to form *$N_{2e}H_2H$ (step 4), $N_{2e}H_2H_2$ (step 5), and *NH_3NH_2 (step 6) are −0.38, −2.08, and −0.05 eV, respectively. It is worth noting that both step 4 and step 6 are highly endergonic reactions in the case of Z_{2B}, which are modulated to be favorable reactions in the presence of a C-doped defective site. The final protonation step to form *NH_3NH_3 intermediate prior to desorption of the first ammonia molecule is akin to that in Z_{2B} with the free energy of 2.71 eV. It can be seen from the free energy profile (**Figure 8B**)

that desorption of the first ammonia molecule in step 7 is an uphill process (1.18 eV). The final reduction of *NH_2 to form the second ammonia molecule is also an endergonic process (0.46 eV). It is clear from the results that C-doping could modulate energetics of second ammonia molecule formation, and limiting potential is reduced from 2.74 (Z_{2B}) to 1.46 eV.

In the case of the C-doped armchair B-edge system (A_BC_N), both end-on and side-on modes of N_2 adsorption are possible, unlike the A_B system (where the only the end-on mode is observed). The adsorption energies are a non-spontaneous process, as evident from energy values. The lengthening of the N-N bond is observed in both modes along with charge transfer. Thus, in this model system, all the three reduction pathways are studied for NRR (**Figure 8C**). In the case of an end-on product, step 2 needs 1.18 eV for the first protonation due to the lower accumulation of charge density on N_2 species. The second protonation is a downhill process in both distal and alternating pathways. As evident from **Figure 8C**, the

marginal energy difference between free energies of these processes leads to problems in selectivity. Later, the alternating pathway emerged as a more feasible mechanism at the third protonation (step-4, $\Delta G = -0.62$ eV) compared to the distal pathway (0.65 eV). The fourth protonating step again changes its pathway from alternating to the distal pathway (0.05 eV) to form the *NHNH₃ intermediate. It can be seen from the energy profile that the alternating pathway results in the formation of hydrazine intermediate with an energy input of 0.24 eV. Desorption of the first ammonia molecule is endergonic in nature with the energetics of 0.09 eV. However, prior to the desorption step, the fifth protonation to *NHNH₃ is a downhill process with the energetics of -1.44 eV. This step facilitates the favorable desorption of the ammonia molecule from the catalyst surface with the energetics of -0.12 eV. The final reduction step needs an energy input of 0.38 eV to form a second ammonia molecule.
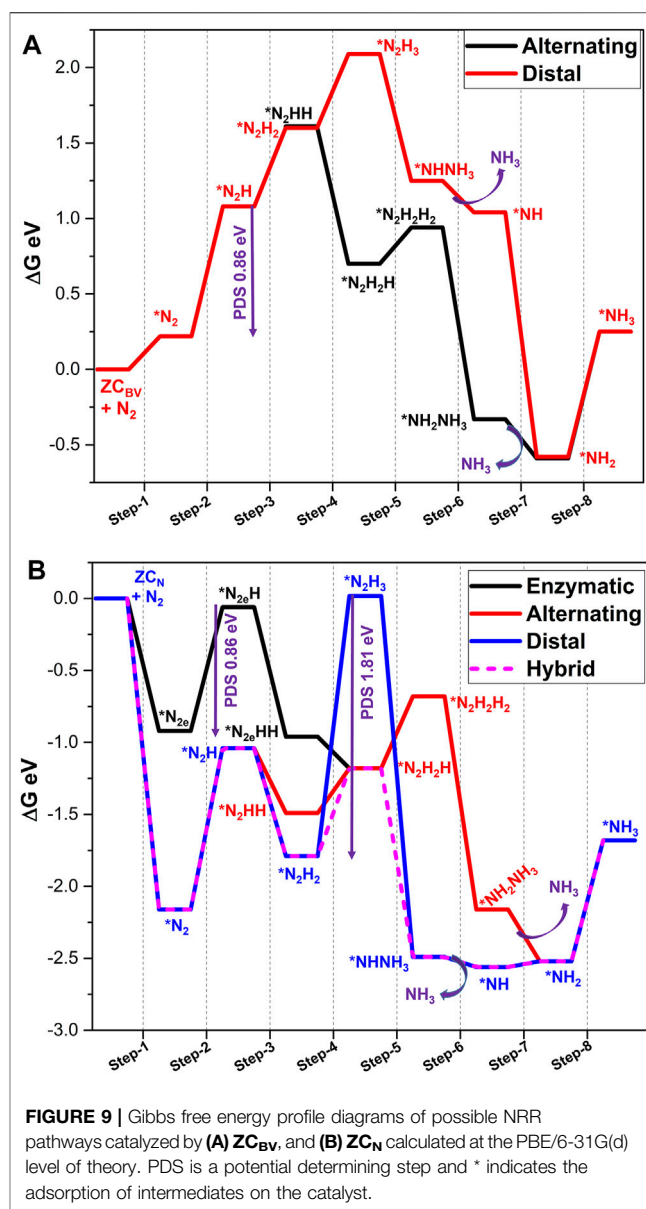
The reduction of the side-on mode N₂ in the enzymatic pathway proceeds through first protonation (1.17 eV), which is an endergonic step. Further reduction steps lead to the formation of the hydrazine adduct at step 5, which is similar to step 5 of an alternating pathway. Hence, further reductions from this intermediate exactly follow the metrics of an alternating pathway. Overall, the limiting potential of NRR is 1.17 eV, which is observed for the first protonation step in the enzymatic pathway. It is clear from the results that, without carbon doping, NRR catalyzed by A_B occurs with a limiting potential of 2.73 eV, whereas the same with carbon doping is reduced to 1.17 eV.

Nitrogen Reduction at C-Doped Active Sites

In this section, the role of C-doping in the model systems as an active site for catalyzing NRR has been elucidated. The calculated geometries of these models based on carbon at different zigzag and armchair edge sites are shown in **Supplementary Figures S1, S2**. Both zigzag and armchair ribbons have six possible sites each for C-doping. The spin polarized DOS calculations have been carried out in order to unravel the electronic properties of the newly designed defective BNS systems and the results are given in **Supplementary Figures S6, S7**. It is clear from the figures that in all the carbon-doped systems, new energy states have appeared at the Fermi level. These new energy levels indicate the spin asymmetry in the defective systems which may enhance the catalytic activity of these defective systems. The feasibility of the C-active site for catalyzing nitrogen reduction has been calculated using the approach as mentioned in the previous sections.

Carbon Doping at the Zigzag Edges

Six possible doping sites are referred to as **ZC_B** (carbon doping at the B-open zigzag edge), **ZC_BH** (carbon doping at the B-site which is H-passivated), **ZC_BV** (C-doping at the B-vacancy of the N-edge), **ZC_N** (carbon doping at the N-open zigzag edge), **ZC_NH** (carbon doping at the N-site which is H-passivated), and **ZC_NV** (C-doping at the N-vacancy of the B-edge). These sites have been taken for further investigation to reduce molecular nitrogen. In the case of **ZC_B**, the open C-active site is bonded to two adjacent N atoms. This carbon is coordinately unsaturated, and it can form a total of four bonds. Hence, the adsorption of the N₂ molecule at this

FIGURE 9 | Gibbs free energy profile diagrams of possible NRR pathways catalyzed by **(A) ZC_BV**, and **(B) ZC_N** calculated at the PBE/6-31G(d) level of theory. PDS is a potential determining step and * indicates the adsorption of intermediates on the catalyst.

particular site has been investigated. Both end-on and side-on modes of adsorption have been considered. As followed in the previous section, distal, alternating, and enzymatic pathways for reduction of molecular nitrogen have been adopted to evaluate the associated energetics. The energetics information associated with **ZC_B** is presented in **Supplementary Table S1**, and the free energy profile is given in **Supplementary Figure S8**. A strong bond formation can be observed between the C-active site and N₂ molecule. The distance between the two systems is 1.30 Å for end-on and 1.45 Å for side-on modes. The interaction between catalysts and the N₂ molecule is further substantiated by the favorable overlap of FMOs of model catalysts and the N₂ molecule. The charge transfer of 0.28/0.24 e (end-on/side-on) occurs from the model catalyst surface to the N₂ molecule. This leads to the elongation of N-N from 1.11 to 1.17 (end-on) and 1.26 Å (side-on). These geometrical and electronic features indicate

the activation of N$_2$ over **ZC$_B$**. From **Supplementary Figure S8**, it is clear that the hybrid pathway is most feasible pathway, where the first ammonia molecule is formed at step 5 with energetics of −1.55 eV. However, the following reduction steps are uphill leading to the formation of a second ammonia molecule with over reaction energy of 0.63 eV. For the formation of the second ammonia molecule (step 8), 1.33 eV is required which makes this step a PDS. The very strong interaction of *NH species with the ZC$_B$ system may be reason for the uphill potentials of step 7 and step 8 (**Supplementary Figure S8**).

The **ZC$_B$H** defective model system is formed by passivating the C-open site of **ZC$_B$** with hydrogen. A very weak end-on mode of adsorption of N$_2$ is observed with the energetics of 0.31 eV, and the interaction distance is 2.87 Å. However, favorable orbital overlapping and an electron transfer of 0.06 e into π* orbital of N$_2$ and marginal elongating the N-N bond (1.12 Å) confirms the activation of N$_2$ by **ZC$_B$H**. The calculated results for all the steps are summarized in **Supplementary Table S2**, and the corresponding energy profile is presented in **Supplementary Figure S9**. It is clear from the results that the formation of the first ammonia molecule occurs on the fourth protonation (step 5) and is an exergonic step by −0.78 eV. The formation of a second ammonia molecule is observed to be a PDS with the energetics of 1.02 eV. Overall, the NRR by **ZC$_B$H** follows a hybrid pathway with a PDS of 1.02 eV.

Another defective model system, **ZC$_{BV}$**, arises due to the replacement of the B atom at the N-edge with a carbon atom. It can be observed from the geometry that the carbon atom is protruded slightly outwards from the BN lattice. Due to the high electronegativity of the three vicinal nitrogen atoms, carbon has lost 0.44 e to the model catalyst during the creation of this defective system. Further, C carries a spin density of 0.65. These geometrical and electronic parameters may induce catalytic activity to this particular site. On interaction with the N$_2$ molecule, only the end-on type of adsorption is observed where the N$_2$ molecule is located at a distance of 2.60 Å with interaction energy of 0.22 eV. In this process, N$_2$ gains 0.17 e electrons from **ZC$_{BV}$**. The mechanistic aspects of ammonia formation catalyzed by **ZC$_{BV}$** are provided in **Supplementary Table S3** and **Figure 9A**. Like the earlier two cases, **ZC$_{BV}$** also follows a hybrid mechanism where the distal pathway dominates until step 3, and the alternating pathway becomes more feasible. Interestingly, **ZC$_{BV}$** catalyzes NRR with a lower PDS of 0.86 eV. Steps related to the formation of the first and second ammonia molecules occur with the energetics of 0.23 and 0.84 eV, respectively.

Nitrogen activation by **ZC$_N$** is observed in all the possible end-on and side-on modes. **ZC$_N$** arises by doping C atoms at the open N-edge site, which comprises two C-B bonds and is coordinately unsaturated. The C atom of this active site withdraws 0.12 e from BN and possesses a spin density of 0.23. Adsorption of N$_2$ on **ZC$_N$** results in very strong binding with interaction energies of −2.16 (end-on) and −0.92 eV (side-on). The electron transfer from the catalyst to N$_2$ molecule is observed as 0.13 (end-on) and 0.21 e (side-on). Therefore, the N-N bond is elongated to 1.15 and 1.22 Å, respectively.

Further, the details of subsequent reduction steps are given in **Supplementary Table S4** and **Figure 9B**. Results indicate that the end-on mode of adsorption of N$_2$ with **ZC$_N$** follows a hybrid pathway as observed in previous systems. The PDS observed for this pathway
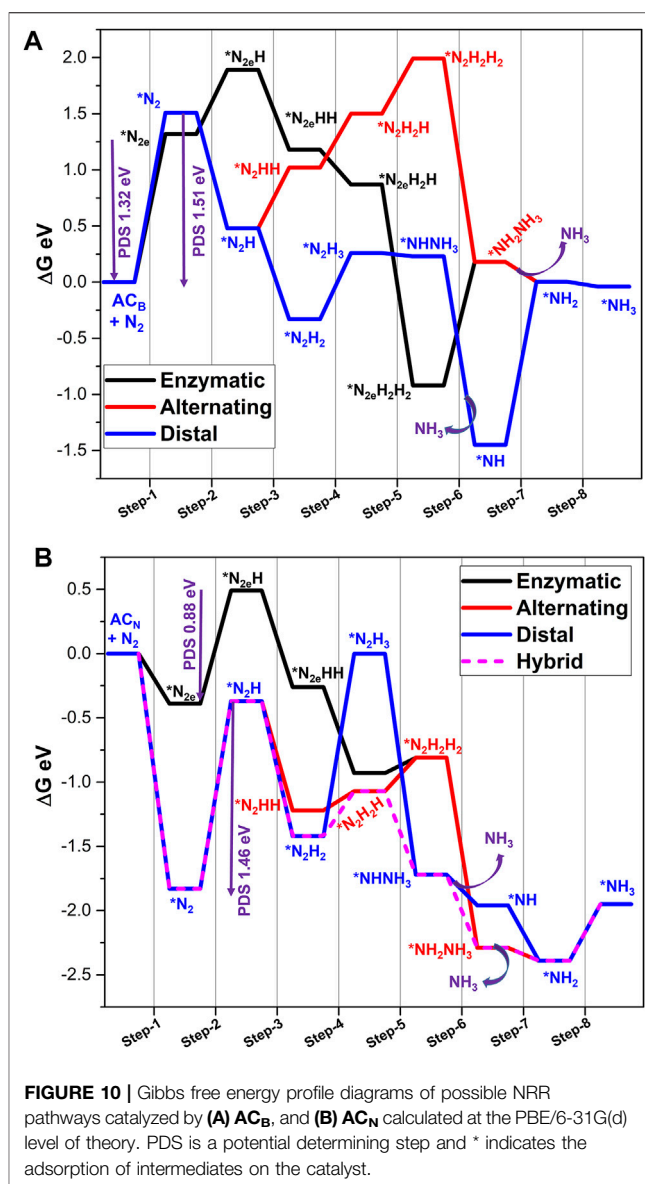
FIGURE 10 | Gibbs free energy profile diagrams of possible NRR pathways catalyzed by **(A) AC$_B$**, and **(B) AC$_N$** calculated at the PBE/6-31G(d) level of theory. PDS is a potential determining step and * indicates the adsorption of intermediates on the catalyst.

is the first protonation step with the energetics of 1.13 eV. However, reduction of the side-on mode model emerged as a more feasible pathway with PDS (step 2, 0.86 eV), which is lower than the hybrid pathway. Analysis of results reveals that the formation of the first ammonia molecule is observed as the PDS on the fifth protonation with the energetics of −2.38 eV, followed by the formation of the second ammonia molecule with energy requirements of 0.84 eV. Overall, carbon doping at the zigzag edge of BN systems **ZC$_{BV}$** and **ZC$_N$** can convert N$_2$ to ammonia. Overall, the enzymatic pathway dominates when compared to all other possibilities.

Carbon Doping at the Armchair Edges

Like zigzag BN, C-doping at armchair edges also resulted in six different defective BN model systems (**Supplementary Figure S2**). Among these, three models arise from doping of the C atom at different B-edge sites. In the other three models, doping of C at various N-edge sites has been completed. The nomenclature

TABLE 2 | Energetics of ammonia desorption step catalyzed by all the BNS systems.

S. No	System	ΔG_{des} (eV)	S. No	System	ΔG_{des} (eV)	S. No	System	ΔG_{des} (eV)
1	Z_B	0.35	6	A_BC_N	0.83	11	AC_B	0.27
2	Z_{2B}	1.44	7	ZC_B	0.14	12	AC_BH	0.09
3	A_B	0.89	8	ZC_BH	0.33	13	AC_{BV}	0.33
4	Z_BC_N	1.25	9	ZC_{BV}	0.27	14	AC_N	0.69
5	$Z_{2B}C_N$	1.34	10	ZC_N	0.65	15	AC_{NV}	0.37

adopted for these systems is analogous to the zigzag defective systems. AC_B indicates replacement of the B atom at the armchair edge with the carbon atom to obtain a C-open edge defective site, AC_BH: arising from the doping B-edge of an armchair with 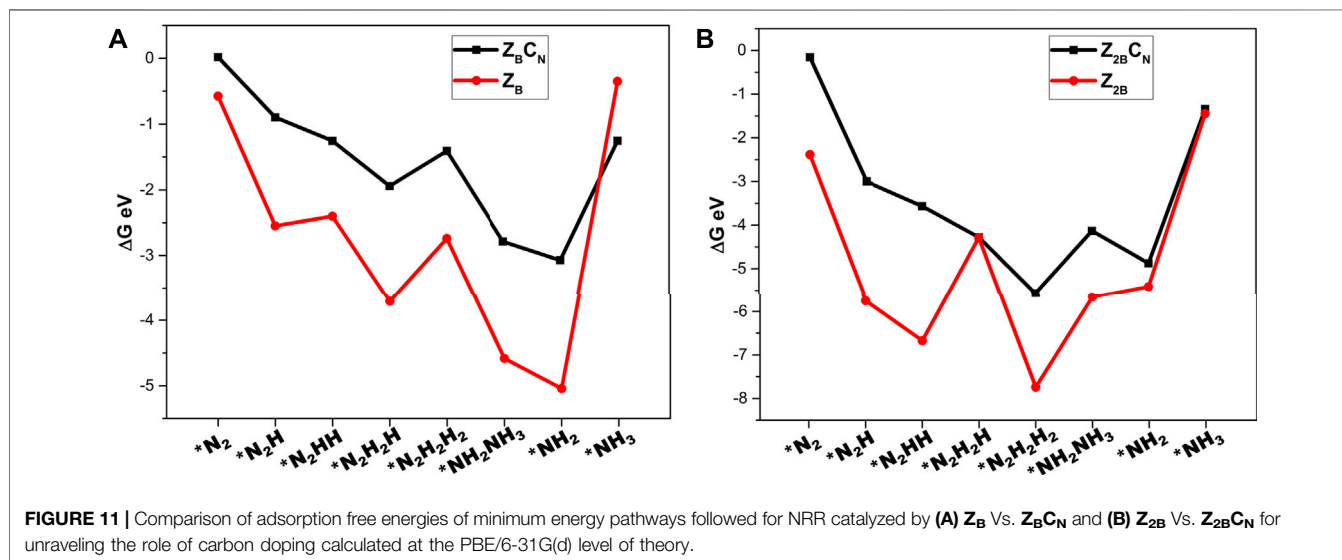C model, and is passivated with hydrogen, AC_{BV}: carbon-doped at the boron site which is connected to three nitrogen atoms, AC_N: the carbon atom is doped at the nitrogen site of the armchair edge, AC_NH: the carbon atom is doped at the nitrogen site of armchair edge, and it is passivated by H, and AC_{NV}: C-doping at the N-vacancy of the B-armchair edge.

It is clear from the results that AC_B and AC_N systems exhibit adsorption of nitrogen in both end-on and side-on modes. Hence, the subsequent reduction has been investigated by using distal, alternating, and enzymatic pathways. On the other hand, the remaining models show an only end-on mode of adsorption. In these models, only distal and alternating NRR pathways have been explored. The FMO analysis characterizes the nitrogen activation ability of these catalysts, and charge transfer into the π* orbitals of the N₂ molecule and N-N bond elongation.

Further, Gibbs free energies of reaction pathways of nitrogen reduction catalyzed by these systems are listed in **Supplementary Tables S5–S9**, and the energy profiles are depicted in **Figure 10** and **Supplementary Figures S10–S12** (SM). Scrutiny of the reaction of all the energy profiles reveals that the enzymatic pathway is a dominating mechanism for AC_N with a lower PDS of 0.88 eV, which makes this model highly suitable for NRR when compared to all the other models of armchair edge-doped systems. In the case of adsorption of N₂ in the

end-on mode on AC_N, the first protonation step is observed to be PDS (0.88 eV). The formation of the first ammonia molecule is an exergonic sixth protonation step (−2.29 eV), while the formation of the second ammonia molecule demands energy of 0.44 eV. Overall, NRR catalyzed by AC_N is spontaneous with energy of −1.95 eV. On the other hand, the remaining model catalysts adopt a hybrid pathway to attain a minimum energy pathway. However, they exhibit higher PDS than AC_N.

Overall, carbon doping at both zigzag and armchair edges resulted in 12 new defective model systems. Scrutiny of their ability to catalyze the NRR reveals that ZC_{BV}, ZC_N, and AC_N show appreciable activity among all the other catalysts. In ZC_N and AC_N, the enzymatic pathway emerges as the dominating one, whereas, for ZC_{BV}, NRR adopts a hybrid pathway with a lower PDS of 0.86 eV. It is also clear from the salient findings that carbon-doped model systems produced lower PDS than the B-open sites. On careful observation of all the energy profile diagrams of NRR, it is clear that NRR by some of the BNS systems is exothermic and is endothermic in the case of a few systems. For instance, the NRR catalyzed by ZC_B, ZC_BH, ZC_{BV}, AC_{BV}, AC_{NV}, and AC_BH is endothermic in nature. This may be due to the non-spontaneous nitrogen activation by all these catalysts, which is a potential demanding step (endothermic). In addition, poor nitrogen activation may lead to the high potential demanding first reduction step. These two steps are contributing to the endothermic nature of NRR in these systems. Overall, AC_N and ZC_N are the two prominent catalysts, where they catalyze the nitrogen reduction reaction with lower PDS of 0.88 and

FIGURE 11 | Comparison of adsorption free energies of minimum energy pathways followed for NRR catalyzed by **(A)** Z_B Vs. Z_BC_N and **(B)** Z_{2B} Vs. $Z_{2B}C_N$ for unraveling the role of carbon doping calculated at the PBE/6-31G(d) level of theory.
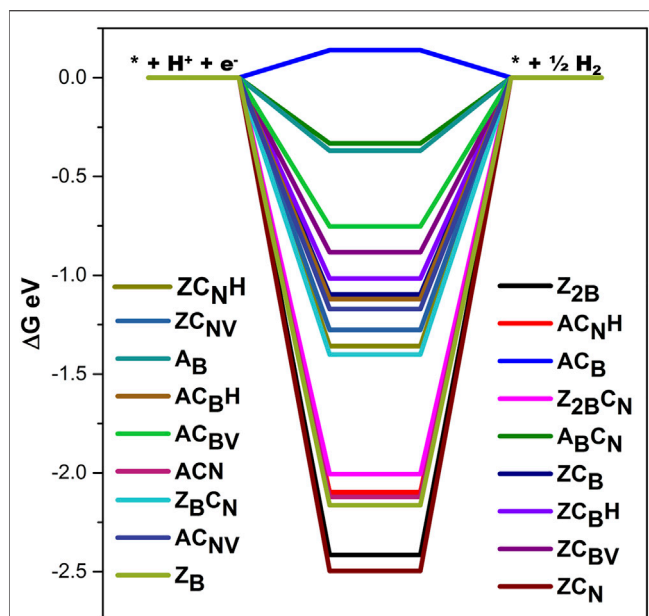
FIGURE 12 | Free energy profile for hydrogen evolution reaction energetics of defective BN systems considered in this study calculated at the PBE/6-31G(d) level of theory.

$\Delta G_{NH3}) - \Delta G_{BNS-NH3}]$ and the results are given in **Table 2**. It is clear from the table that most of the catalysts that are considered are good nitrogen reduction catalysts as they exhibit lower ammonia desorption energies (<0.86 eV, lowest PDS observed for NRR). The results indicate that the ammonia desorption step may not be the PDS for NRR catalyzed by BNS systems.

Role of C-Doping

In order to gain insight into the role of carbon doping in regulating the potentials of NRR, the comparison of the energetics of various intermediates in the models with and without carbon doping has been made in **Figure 11**.

It can be found from **Figure 11** that the adsorption energies of the intermediates decrease until the formation of the first ammonia molecule and subsequently increase after the formation of the second ammonia molecule. Furthermore, the intermediates of NRR interact more strongly with B-open edge sites when compared to interaction with B-open edges with C-doping. These findings indicate that C-doping weakens the binding strength of intermediates with the surface and decreases the chance of catalyst poisoning by the strong adsorption of intermediates on the surface of the model catalyst. It is interesting to note that carbon doping has a positive role in modulating the charge density distribution of the model catalyst surface and lowering the lower potential requirements.

As stated in the previous sections, each model system favors one reaction pathway. Among them, C_N open sites at the nitrogen edge of BN (both ZC_N and AC_N) and C_B active sites of ZC_{BV} exhibit highly appreciable activity towards nitrogen reduction with the lower limiting potentials of 0.86, 0.88, and 0.86 eV, respectively. The complete nitrogen reduction reactions of the earlier two models (ZC_N and AC_N) are energy-efficient. However, NRR by ZC_{BV} demands external energy for the reaction. These results are comparable with the recent reports on NRR by various catalysts such as boron-doped graphene systems (0.43–1.30 V) (Yu et al., 2018), H-BN nanomaterials (0.75 V) (Zhang et al., 2019), V_3C_2 MXenes (0.64 eV) (Azofra et al., 2016), and defect-free MoS_2 (0.68 eV) (Li et al., 2018).

0.86 eV in highly exothermic reaction pathways of total energies −1.95 and −1.68 eV, respectively.

Ammonia Desorption

Desorption of ammonia is one of the important parameters in nitrogen reduction. If the interaction of ammonia with the active site is very strong, then it is very difficult to desorb the ammonia molecule and it leads to either catalyst poisoning or disintegration of the ammonia molecule. To ensure such activity of the BNS systems, desorption of ammonia that is formed on the final elementary step has been investigated [$\Delta G_{des} = (\Delta G_{BNS} +$

TABLE 3 | The summary of the minimum energy pathways followed by all the model systems.

S. No	Model system	Minimum energy pathway	Remarks
1	Z_B	Alternating pathway	PDS is the final protonation step with energetics of 2.00 eV
2	Z_{2B}	Enzymatic pathway	PDS is the third protonation step to form *N₂H species with endergonicity of 2.74 eV
3	A_B	Alternating pathway	PDS is the final protonation step with energetics of 2.73 eV
4	Z_BC_N	Alternating pathway	First protonation step as PDS with energetics of 1.33 eV
5	$Z_{2B}C_N$	Enzymatic pathway	Sixth protonation as PDS with 1.45 eV
6	A_BC_N	Hybrid pathway	First protonation as PDS of 1.18 eV
7	ZC_B	Hybrid pathway	Second ammonia formation as PDS of 1.33 eV
8	ZC_BH	Hybrid pathway	Second ammonia formation as PDS of 1.02 eV
9	ZC_{BV}	Alternating pathway	PDS is the first protonation with 0.86 eV. Lowest among all the investigated catalysts
10	ZC_N	Enzymatic pathway	First protonation as PDS with 0.88 eV
11	ZC_NH	---	No feasible interaction with N₂
12	ZC_{NV}	---	No feasible interaction with N₂
13	AC_B	Hybrid pathway	Activation of nitrogen in enzymatic mode is PDS with 1.32 eV
14	AC_BH	Hybrid pathway	Second ammonia formation step as PDS with 0.91 eV
15	AC_{BV}	Hybrid pathway	First protonation step as PDS with 1.14 eV
16	AC_N	Enzymatic pathway	First protonation with 0.88 eV as PDS
17	AC_NH	---	No feasible interaction with N₂
18	AC_{NV}	Hybrid pathway	First protonation step as PDS with 1.32 eV

Selectivity Between HER and NRR

It is clear from the above discussions that carbon doping significantly enhances the catalytic ability of BN edge sites for nitrogen reduction. However, the competition for the hydrogen evolution reaction (HER) needs to be explored to assess the NRR ability of the model catalyst. As HER is competing with the reaction conditions of NRR, edge defective BN systems have also been investigated for HER ability. The calculated free energy profiles for different models are depicted in **Figure 12**. In general, the ideal Gibbs free energy of H adsorption for HER catalysts (ΔG_{*H}) is nearly 0.0 eV. It is clear from the present results that all the models exhibit favorable ΔG values for H adsorption except **AC$_B$**. Results demonstrate that carbon-doped zigzag BN systems are more efficient in inhibiting HER when compared to armchair counterparts. It is also evident that C-doping significantly weakens the absorption of H on edge B atoms of the zigzag BN system. Hence, most of the model systems considered in this study are good candidates for NRR by inhibiting HER.

CONCLUSION

In summary, a systematic investigation on the nitrogen reduction feasibility of B-open edge defective BN nanomaterials has been carried out. The effect of carbon doping on the catalytic properties of these B-sites has been assessed. The most favorable pathways adopted by the model systems studied are summarized in **Table 3**. The significant findings are summarized as follows:

1) Most of the models of edge sites with and without carbon doping activate nitrogen by either strong covalent interactions or weak non-covalent interactions.
2) Carbon doping significantly enhances the catalytic activity of B-open edge sites by modulating charge density distribution and reducing the limiting potential.
3) Carbon doping effectively decreases the interactions between catalysts and NRR intermediates and concomitant reduction in the poisoning of the model catalyst reducing the catalytic activity of edges towards nitrogen fixation.
4) Overall, carbon doping plays a positive role in modulating the catalytic ability of boron edge sites.

Since it is possible to create doped edge sites in h-BN experimentally, the present investigation clearly opens a new paradigm for the development of novel NRR catalysts. Thus, the edges of BN sheets may be successfully explored for the development of BN-based catalysts by suitable doping as explained in the above discussion.

DATA AVAILABILITY STATEMENT

The original contributions presented in the study are included in the article/**Supplementary Material**, further inquiries can be directed to the corresponding author.

AUTHOR CONTRIBUTIONS

VC: Conceptualization, computations and writing manuscript, KE: computations and analysis, VS: conceptualization and developing manuscript.

FUNDING

ACKNOWLEDGMENTS

SUPPLEMENTARY MATERIAL

The Supplementary Material for this article can be found online at: https://www.frontiersin.org/articles/10.3389/fchem.2021.799903/full#supplementary-material

REFERENCES

Aber, J. D., Nadelhoffer, K. J., Steudler, P., and Melillo, J. M. (1989). Nitrogen Saturation in Northern Forest Ecosystems. *BioScience* 39, 378–386. doi:10.2307/1311067

Adamo, C., and Barone, V. (1999). Toward Reliable Density Functional Methods without Adjustable Parameters: The PBE0 Model. *J. Chem. Phys.* 110, 6158–6170. doi:10.1063/1.478522

Alexandratos, N., and Bruinsma, J. (2012). World Agriculture towards 2030/2050: the 2012 Revision. Rome: FAO. ESA Working Papers 12-03

Almahmoud, E., and Talla, J. A. (2019). Band gap Tuning in Carbon Doped boron Nitride Mono Sheet with Stone-Wales Defect: a Simulation Study. *Mater. Res. Express* 6, 105038. doi:10.1088/2053-1591/ab39a3

Ashworth, D. J., and Foster, J. A. (2018). Metal-organic Framework Nanosheets (MONs): a New Dimension in Materials Chemistry. *J. Mater. Chem. A.* 6, 16292–16307. doi:10.1039/c8ta03159b

Azofra, L. M., Li, N., Macfarlane, D. R., and Sun, C. (2016). Promising Prospects for 2D D2-d4M3C2 transition Metal Carbides (MXenes) in N2 capture and Conversion into Ammonia. *Energy Environ. Sci.* 9, 2545–2549. doi:10.1039/c6ee01800a

Banks, C. E., Davies, T. J., Wildgoose, G. G., and Compton, R. G. (2005). Electrocatalysis at Graphite and Carbon Nanotube Modified Electrodes: Edge-Plane Sites and Tube Ends Are the Reactive Sites. *Chem. Commun.*, 829–841. doi:10.1039/b413177k

Bellunato, A., Arjmandi Tash, H., Cesa, Y., and Schneider, G. F. (2016). Chemistry at the Edge of Graphene. *Chem. Phys. Chem.* 17, 785–801. doi:10.1002/cphc.201500926

Bogaard, A., Fraser, R., Heaton, T. H. E., Wallace, M., Vaiglova, P., Charles, M., et al. (2013). Crop Manuring and Intensive Land Management by Europe's First Farmers. *Proc. Natl. Acad. Sci.* 110, 12589–12594. doi:10.1073/pnas.1305918110

Bowling, R., Packard, R. T., and Mccreery, R. L. (1989). Mechanism of Electrochemical Activation of Carbon Electrodes: Role of Graphite Lattice Defects. *Langmuir* 5, 683–688. doi:10.1021/la00087a022

Chakraborty, D., Damsgaard, C. D., Silva, H., Conradsen, C., Olsen, J. L., Carvalho, H. W. P., et al. (2017). Bottom-Up Design of a Copper-Ruthenium Nanoparticulate Catalyst for Low-Temperature Ammonia Oxidation. *Angew. Chem. Int. Ed.* 56, 8711–8715. doi:10.1002/anie.201703468

Chehade, G., and Dincer, I. (2021). Progress in green Ammonia Production as Potential Carbon-free Fuel. *Fuel* 299, 120845. doi:10.1016/j.fuel.2021.120845

Chen, S., Li, P., Xu, S., Pan, X., Fu, Q., and Bao, X. (2018). Carbon Doping of Hexagonal boron Nitride Porous Materials toward CO2 Capture. *J. Mater. Chem. A.* 6, 1832–1839. doi:10.1039/c7ta08515j

Ci, L., Song, L., Jin, C., Jariwala, D., Wu, D., Li, Y., et al. (2010). Atomic Layers of Hybridized boron Nitride and Graphene Domains. *Nat. Mater* 9, 430–435. doi:10.1038/nmat2711

Davies, T. J., Hyde, M. E., and Compton, R. G. (2005). Nanotrench Arrays Reveal Insight into Graphite Electrochemistry. *Angew. Chem. Int. Ed.* 44, 5121–5126. doi:10.1002/anie.200462750

Delley, B. (2000). From Molecules to Solids with the DMol3 Approach. *J. Chem. Phys.* 113, 7756–7764. doi:10.1063/1.1316015

Frisch, M. J., Trucks, G. W., Schlegel, H. B., Scuseria, G. E., Robb, M. A., Cheeseman, J. R., et al. (2009). *Gaussian 09*. Wallingford, CT, USA: Gaussian, Inc.

Fujii, S., and Enoki, T. (2013). Nanographene and Graphene Edges: Electronic Structure and Nanofabrication. *Acc. Chem. Res.* 46, 2202–2210. doi:10.1021/ar300120y

Fujii, S., Ziatdinov, M., Ohtsuka, M., Kusakabe, K., Kiguchi, M., and Enoki, T. (2014). Role of Edge Geometry and Chemistry in the Electronic Properties of Graphene Nanostructures. *Faraday Discuss.* 173, 173–199. doi:10.1039/c4fd00073k

Galloway, J. N., Leach, A. M., Erisman, J. W., and Bleeker, A. (2017). Nitrogen: the Historical Progression from Ignorance to Knowledge, with a View to Future Solutions. *Soil Res.* 55, 417–424. doi:10.1071/sr16334

Glibert, P. M., Maranger, R., Sobota, D. J., and Bouwman, L. (2014). The Haber Bosch-Harmful Algal Bloom (HB-HAB) Link. *Environ. Res. Lett.* 9, 105001. doi:10.1088/1748-9326/9/10/105001

Golberg, D., Bando, Y., Huang, Y., Terao, T., Mitome, M., Tang, C., et al. (2010). Boron Nitride Nanotubes and Nanosheets. *ACS Nano* 4, 2979–2993. doi:10.1021/nn1006495

Grimme, S., Antony, J., Ehrlich, S., and Krieg, H. (2010). A Consistent and Accurate Ab Initio Parametrization of Density Functional Dispersion Correction (DFT-D) for the 94 Elements H-Pu. *J. Chem. Phys.* 132, 154104. doi:10.1063/1.3382344

Guo, J., and Chen, P. (2017). Catalyst: NH3 as an Energy Carrier. *Chem* 3, 709–712. doi:10.1016/j.chempr.2017.10.004

Guo, C., Ran, J., Vasileff, A., and Qiao, S.-Z. (2018). Rational Design of Electrocatalysts and Photo(electro)catalysts for Nitrogen Reduction to Ammonia (NH3) under Ambient Conditions. *Energ. Environ. Sci.* 11, 45–56. doi:10.1039/c7ee02220d

Hariharan, P. C., and Pople, J. A. (1973). The Influence of Polarization Functions on Molecular Orbital Hydrogenation Energies. *Theoret. Chim. Acta* 28, 213–222. doi:10.1007/bf00533485

Hehre, W. J., Radom, L., Schleyer, P. V. R., and Pople, J. (1986). *Ab Initio Molecular Orbital Theory*. New York: Wiley.

Hering-Junghans, C. (2018). Metal-Free Nitrogen Fixation at Boron. *Angew. Chem. Int. Ed.* 57, 6738–6740. doi:10.1002/anie.201802675

Hinokuma, S., Shimanoe, H., Matsuki, S., Kawano, M., Kawabata, Y., and Machida, M. (2015). Catalytic Activity and Selectivities of Metal Oxides and Pt/Al2O3 for NH3 Combustion. *Chem. Lett.* 45, 179–181. doi:10.1246/cl.151031

Hollins, T. W., Clark, S. J., Refson, K., and Gidopoulos, N. I. (2012). Optimized Effective Potential Using the Hylleraas Variational Method. *Phys. Rev. B* 85, 235126. doi:10.1103/physrevb.85.235126

Howard, J. B., and Rees, D. C. (1996). Structural Basis of Biological Nitrogen Fixation. *Chem. Rev.* 96, 2965–2982. doi:10.1021/cr9500545

Huang, C., Chen, C., Zhang, M., Lin, L., Ye, X., Lin, S., et al. (2015). Carbon-Doped BN Nanosheets for Metal-free Photoredox Catalysis. *Nat. Commun.* 6, 7698. doi:10.1038/ncomms8698

Janesko, B. G. (2011). Comparing Modern Density Functionals for Conjugated Polymer Band Structures: Screened Hybrid, Minnesota, and Rung 3.5 Approximations. *J. Chem. Phys.* 134, 184105. doi:10.1063/1.3589145

Jeyaraj, V. S., Kamaraj, M., and Subramanian, V. (2015). Generalized Reaction Mechanism for the Selective Aerobic Oxidation of Aryl and Alkyl Alcohols over Nitrogen-Doped Graphene. *J. Phys. Chem. C* 119, 26438–26450. doi:10.1021/acs.jpcc.5b07070

Jiang, D.-E., Sumpter, B. G., and Dai, S. (2007). Unique Chemical Reactivity of a Graphene Nanoribbon's Zigzag Edge. *J. Chem. Phys.* 126, 134701. doi:10.1063/1.2715558

Kitano, M., Kanbara, S., Inoue, Y., Kuganathan, N., Sushko, P. V., Yokoyama, T., et al. (2015). Electride Support Boosts Nitrogen Dissociation over Ruthenium Catalyst and Shifts the Bottleneck in Ammonia Synthesis. *Nat. Commun.* 6, 6731. doi:10.1038/ncomms7731

Kobayashi, H., Hayakawa, A., SomarathneKunkuma, K. D. K. A. a., and Okafor, E. C. (2019). Science and Technology of Ammonia Combustion. *Proc. Combust. Inst.* 37, 109–133. doi:10.1016/j.proci.2018.09.029

Lan, R., and Tao, S. (2014). Ammonia as a Suitable Fuel for Fuel Cells. *Front. Energ. Res.* 2, 1–4. doi:10.3389/fenrg.2014.00035

Li, J., Zhou, G., Chen, Y., Gu, B.-L., and Duan, W. (2009). Magnetism of C Adatoms on BN Nanostructures: Implications for Functional Nanodevices. *J. Am. Chem. Soc.* 131, 1796–1801. doi:10.1021/ja805632p

Li, X., Li, T., Ma, Y., Wei, Q., Qiu, W., Guo, H., et al. (2018). Boosted Electrocatalytic N2 Reduction to NH3 by Defect-Rich MoS2 Nanoflower. *Adv. Energ. Mater.* 8, 1801357. doi:10.1002/aenm.201801357

Liu, C., Li, Q., Zhang, J., Jin, Y., Macfarlane, D. R., and Sun, C. (2018). Theoretical Evaluation of Possible 2D Boron Monolayer in N2 Electrochemical Conversion into Ammonia. *J. Phys. Chem. C* 122, 25268–25273. doi:10.1021/acs.jpcc.8b10021

Liu, C., Li, Q., Wu, C., Zhang, J., Jin, Y., Macfarlane, D. R., et al. (2019). Single-Boron Catalysts for Nitrogen Reduction Reaction. *J. Am. Chem. Soc.* 141, 2884–2888. doi:10.1021/jacs.8b13165

Lv, X., Wei, W., Li, F., Huang, B., and Dai, Y. (2019). Metal-Free B@g-CN: Visible/Infrared Light-Driven Single Atom Photocatalyst Enables Spontaneous Dinitrogen Reduction to Ammonia. *Nano Lett.* 19, 6391–6399. doi:10.1021/acs.nanolett.9b02572

Mao, X., Zhou, S., Yan, C., Zhu, Z., and Du, A. (2019). A Single boron Atom Doped boron Nitride Edge as a Metal-free Catalyst for N2 Fixation. *Phys. Chem. Chem. Phys.* 21, 1110–1116. doi:10.1039/c8cp07064d

Marbaniang, P., Patil, I., Lokanathan, M., Parse, H., Catherin Sesu, D., Ingavale, S., et al. (2018). Nanorice-like Structure of Carbon-Doped Hexagonal Boron Nitride as an Efficient Metal-free Catalyst for Oxygen Electroreduction. *ACS Sustain. Chem. Eng.* 6, 11115–11122. doi:10.1021/acssuschemeng.8b02609

McDermott, M. T., Kneten, K., and Mccreery, R. L. (1992). Anthraquinonedisulfonate Adsorption, Electron-Transfer Kinetics, and Capacitance on Ordered Graphite Electrodes: the Important Role of Surface Defects. *J. Phys. Chem.* 96, 3124–3130. doi:10.1021/j100186a063

McEnaney, J. M., Singh, A. R., Schwalbe, J. A., Kibsgaard, J., Lin, J. C., Cargnello, M., et al. (2017). Ammonia Synthesis from N2and H2O Using a Lithium Cycling Electrification Strategy at Atmospheric Pressure. *Energ. Environ. Sci.* 10, 1621–1630. doi:10.1039/c7ee01126a

Mittal, G., Dhand, V., Rhee, K. Y., Park, S. J., Kim, H.-J., and Jung, D. H. (2015). Investigation of Seawater Effects on the Mechanical Properties of Untreated and Treated MMT-Based Glass Fiber/vinylester Composites. *Ocean Eng.* 108, 393–401. doi:10.1016/j.oceaneng.2015.08.019

Momeni, K., Ji, Y., Wang, Y., Paul, S., Neshani, S., Yilmaz, D. E., et al. (2020). Multiscale Computational Understanding and Growth of 2D Materials: a Review. *Npj Comput. Mater.* 6, 22. doi:10.1038/s41524-020-0280-2

Ni, B., and Wang, X. (2015). Face the Edges: Catalytic Active Sites of Nanomaterials. *Adv. Sci.* 2, 1500085. doi:10.1002/advs.201500085

Nørskov, J. K., Rossmeisl, J., Logadottir, A., Lindqvist, L., Kitchin, J. R., Bligaard, T., et al. (2004). Origin of the Overpotential for Oxygen Reduction at a Fuel-Cell Cathode. *The J. Phys. Chem. B* 108, 17886–17892. doi:10.1021/jp047349j

Okada, S., and Oshiyama, A. (2001). Magnetic Ordering in Hexagonally Bonded Sheets with First-Row Elements. *Phys. Rev. Lett.* 87, 146803. doi:10.1103/physrevlett.87.146803

Ooi, N., Rajan, V., Gottlieb, J., Catherine, Y., and Adams, J. B. (2006). Structural Properties of Hexagonal boron Nitride. *Model. Simul. Mater. Sci. Eng.* 14, 515–535. doi:10.1088/0965-0393/14/3/012

Panchakarla, L. S., Subrahmanyam, K. S., Saha, S. K., Govindaraj, A., Krishnamurthy, H. R., Waghmare, U. V., et al. (2009). Synthesis, Structure, and Properties of Boron- and Nitrogen-Doped Graphene. *Adv. Mater.* 21, 4726–4730. doi:10.1002/adma.200901285

Pari, S., Cuéllar, A., and Wong, B. M. (2016). Structural and Electronic Properties of Graphdiyne Carbon Nanotubes from Large-Scale DFT Calculations. *J. Phys. Chem. C* 120, 18871–18877. doi:10.1021/acs.jpcc.6b05265

Randin, J.-P., and Yeager, E. (1972). Differential Capacitance Study on the Basal Plane of Stress-Annealed Pyrolytic Graphite. *J. Electroanal. Chem. Interfacial Electrochem.* 36, 257–276. doi:10.1016/s0022-0728(72)80249-3

Randin, J.-P., and Yeager, E. (1975). Differential Capacitance Study on the Edge Orientation of Pyrolytic Graphite and Glassy Carbon Electrodes. *J. Electroanal. Chem. Interfacial Electrochem.* 58, 313–322. doi:10.1016/s0022-0728(75)80089-1

Rice, R. J., and McCreery, R. L. (1989). Quantitative Relationship between Electron Transfer Rate and Surface Microstructure of Laser-Modified Graphite Electrodes. *Anal. Chem.* 61, 1637–1641. doi:10.1021/ac00190a010

Rossmeisl, J., Logadottir, A., and Nørskov, J. K. (2005). Electrolysis of Water on (Oxidized) Metal Surfaces. *Chem. Phys.* 319, 178–184. doi:10.1016/j.chemphys.2005.05.038

Rouwenhorst, K. H. R., Van Der Ham, A. G. J., Mul, G., and Kersten, S. R. A. (2019). Islanded Ammonia Power Systems: Technology Review & Conceptual Process Design. *Renew. Sustain. Energ. Rev.* 114, 109339. doi:10.1016/j.rser.2019.109339

Rouwenhorst, K. H. R., Engelmann, Y., van 't Veer, K., Postma, R. S., Bogaerts, A., and Lefferts, L. (2020). Plasma-driven Catalysis: green Ammonia Synthesis with Intermittent Electricity. *Green. Chem.* 22, 6258–6287. doi:10.1039/d0gc02058c

Salmon, N., and Bañares-Alcántara, R. (2021). Green Ammonia as a Spatial Energy Vector: a Review. *Sustain. Energ. Fuels* 5, 2814–2839. doi:10.1039/d1se00345c

Schwierz, F., Pezoldt, J., and Granzner, R. (2015). Two-Dimensional Materials and Their Prospects in Transistor Electronics. *Nanoscale* 7, 8261–8283. doi:10.1039/c5nr01052g

Shi, L., Li, Q., Ling, C., Zhang, Y., Ouyang, Y., Bai, X., et al. (2019). Metal-free Electrocatalyst for Reducing Nitrogen to Ammonia Using a Lewis Acid Pair. *J. Mater. Chem. A* 7, 4865–4871. doi:10.1039/c8ta11025e

Smith, B. E. (2002). Nitrogenase Reveals its Inner Secrets. *Science* 297, 1654–1655. doi:10.1126/science.1076659

Spatzal, T., Perez, K. A., Einsle, O., Howard, J. B., and Rees, D. C. (2014). Ligand Binding to the FeMo-Cofactor: Structures of CO-bound and Reactivated Nitrogenase. *Science* 345, 1620–1623. doi:10.1126/science.1256679

Tan, C., Rodríguez-López, J., Parks, J. J., Ritzert, N. L., Ralph, D. C., and Abruña, H. D. (2012). Reactivity of Monolayer Chemical Vapor Deposited Graphene Imperfections Studied Using Scanning Electrochemical Microscopy. *ACS Nano* 6, 3070–3079. doi:10.1021/nn204746n

Tian, Y.-H., Hu, S., Sheng, X., Duan, Y., Jakowski, J., Sumpter, B. G., et al. (2018). Non-Transition-Metal Catalytic System for N2 Reduction to NH3: A Density Functional Theory Study of Al-Doped Graphene. *J. Phys. Chem. Lett.* 9, 570–576. doi:10.1021/acs.jpclett.7b03094

van der Ham, C. J. M., Koper, M. T. M., and Hetterscheid, D. G. H. (2014). Challenges in Reduction of Dinitrogen by Proton and Electron Transfer. *Chem. Soc. Rev.* 43, 5183–5191. doi:10.1039/c4cs00085d

Velický, M., and Toth, P. S. (2017). From Two-Dimensional Materials to Their Heterostructures: An Electrochemist's Perspective. *Appl. Mater. Today* 8, 68–103. doi:10.1016/j.apmt.2017.05.003

Velický, M., Toth, P. S., Woods, C. R., Novoselov, K. S., and Dryfe, R. a. W. (2019). Electrochemistry of the Basal Plane versus Edge Plane of Graphite Revisited. *The J. Phys. Chem. C* 123, 11677–11685. doi:10.1021/acs.jpcc.9b01010

Vijaya Sundar, J., and Subramanian, V. (2013). Novel Chemistry for the Selective Oxidation of Benzyl Alcohol by Graphene Oxide and N-Doped Graphene. *Org. Lett.* 15, 5920–5923. doi:10.1021/ol402958h

Wang, Z., Zhu, W., Qiu, Y., Yi, X., Von Dem Bussche, A., Kane, A., et al. (2016). Biological and Environmental Interactions of Emerging Two-Dimensional Nanomaterials. *Chem. Soc. Rev.* 45, 1750–1780. doi:10.1039/c5cs00914f

Wang, F., Wang, Z., Yin, L., Cheng, R., Wang, J., Wen, Y., et al. (2018). 2D Library beyond Graphene and Transition Metal Dichalcogenides: a Focus on Photodetection. *Chem. Soc. Rev.* 47, 6296–6341. doi:10.1039/c8cs00255j

Wu, J., Yin, L., and Zhang, L. (2013). Tuning the Electronic Structure, Bandgap Energy and Photoluminescence Properties of Hexagonal boron Nitride Nanosheets via a Controllable Ce3+ Ions Doping. *RSC Adv.* 3, 7408–7418. doi:10.1039/c3ra23132a

Xue, Y., Liu, Q., He, G., Xu, K., Jiang, L., Hu, X., et al. (2013). Excellent Electrical Conductivity of the Exfoliated and Fluorinated Hexagonal boron Nitride Nanosheets. *Nanoscale Res. Lett.* 8, 49. doi:10.1186/1556-276x-8-49

Yapicioglu, A., and Dincer, I. (2019). A Review on Clean Ammonia as a Potential Fuel for Power Generators. *Renew. Sustain. Energ. Rev.* 103, 96–108. doi:10.1016/j.rser.2018.12.023

Ye, L., Nayak-Luke, R., Bañares-Alcántara, R., and Tsang, E. (2017). Reaction: "Green" Ammonia Production. *Chem* 3, 712–714. doi:10.1016/j.chempr.2017.10.016

Yu, X., Han, P., Wei, Z., Huang, L., Gu, Z., Peng, S., et al. (2018). Boron-Doped Graphene for Electrocatalytic N2 Reduction. *Joule* 2, 1610–1622. doi:10.1016/j.joule.2018.06.007

Zeng, H., Zhi, C., Zhang, Z., Wei, X., Wang, X., Guo, W., et al. (2010). "White Graphenes": Boron Nitride Nanoribbons via Boron Nitride Nanotube Unwrapping. *Nano Lett.* 10, 5049–5055. doi:10.1021/nl103251m

Zhang, X., Xin, J., and Ding, F. (2013). The Edges of Graphene. *Nanoscale* 5, 2556–2569. doi:10.1039/c3nr34009k

Zhang, G., Kirkman, P. M., Patel, A. N., Cuharuc, A. S., Mckelvey, K., and Unwin, P. R. (2014). Molecular Functionalization of Graphite Surfaces: Basal Plane versus Step Edge Electrochemical Activity. *J. Am. Chem. Soc.* 136, 11444–11451. doi:10.1021/ja505266d

Zhang, Y., Du, H., Ma, Y., Ji, L., Guo, H., Tian, Z., et al. (2019). Hexagonal boron Nitride Nanosheet for Effective Ambient N2 Fixation to NH3. *Nano Res.* 12, 919–924. doi:10.1007/s12274-019-2323-x

Zhao, J., and Chen, Z. (2017). Single Mo Atom Supported on Defective Boron Nitride Monolayer as an Efficient Electrocatalyst for Nitrogen Fixation: A Computational Study. *J. Am. Chem. Soc.* 139, 12480–12487. doi:10.1021/jacs.7b05213

Zheng, M., Li, Y., Ding, K., Zhang, Y., Chen, W., and Lin, W. (2020). Nitrogen Fixation on Metal-free SiC(111) Polar Surfaces. *J. Mater. Chem. A.* 8, 7412–7421. doi:10.1039/d0ta00981d

Zhong, J.-H., Zhang, J., Jin, X., Liu, J.-Y., Li, Q., Li, M.-H., et al. (2014). Quantitative Correlation between Defect Density and Heterogeneous Electron Transfer Rate of Single Layer Graphene. *J. Am. Chem. Soc.* 136, 16609–16617. doi:10.1021/ja508965w

Zhu, R., Duan, H., Zhao, Z., and Pang, H. (2021). Recent Progress of Dimensionally Designed Electrode Nanomaterials in Aqueous Electrochemical Energy Storage. *J. Mater. Chem. A.* 9, 9535–9572. doi:10.1039/d1ta00204j

Conflict of Interest: The authors declare that the research was conducted in the absence of any commercial or financial relationships that could be construed as a potential conflict of interest.

Publisher's Note: All claims expressed in this article are solely those of the authors and do not necessarily represent those of their affiliated organizations, or those of the publisher, the editors and the reviewers. Any product that may be evaluated in this article, or claim that may be made by its manufacturer, is not guaranteed or endorsed by the publisher.

On the Endocircular Li@C$_{16}$ System

Yi-Fan Yang and Lorenz S. Cederbaum*

Theoretical Chemistry, Institute of Physical Chemistry, University of Heidelberg, Heidelberg, Germany

The endocircular Li@C$_{16}$ is a promising system as it can form both a charge-separated donor-acceptor complex and a non-charge-separated van der waals complex. By employing the state-of-the-art equation-of-motion coupled-cluster method, our study shows that the carbon ring of this system possesses high flexibility and may undertake large distortions. Due to the intricate interaction between the guest Li$^+$ cation and the negatively charged ring, this system can form several isomers possessing different ground states. The interesting electronic structure properties indicate its applicability as a catalyst candidate in the future.

Keywords: charge-separated, van der vaals forces, noncovalent interactions, electronic structure, ab intio calculation

I INTRODUCTION

Carbon allotropes, e.g., graphene (Xiang et al., 2012), fullerene (Yan et al., 2016), carbon nanotubes (Serp et al., 2003) etc., are playing important roles in the field of catalysis. One of the reasons for those successful catalytic applications is the non-covalent functionalization between carbon allotropes and reactants (Umadevi et al., 2014; Georgakilas et al., 2016). Here, we briefly mention common examples of non-covalent interactions, e.g., interactions forming electron donor-acceptor complex (D'Souza and Ito, 2009; Lim et al., 2016), and van der Waals interactions (Sun et al., 2021).

Carbon allotropes doped with guest atoms can improve their catalystic properties and have been successfully applied in many fields, such as artificial photosynthesis (Rudolf et al., 2016), N$_2$ activation (Kumar et al., 2016), electrochemical water splitting (Singh et al., 2016), and electrochemical oxygen reduction (Guo et al., 2020) etc., The improvement of the catalytic properties is in many cases due to the roles played by guest atoms in charge-separated donor-acceptor complexes (Sherigara et al., 2003; Hu et al., 2017), or in stronger van der waals interactions which are enhanced by the guest atom (Biroju et al., 2017; Bawari et al., 2019). It is noteworthy that donor-acceptor charge-separated states may have substantial potential for applications in the field of catalysis (Meng et al., 2020) and as shown in a theoretical study, the change of charge distribution is a reason for enhancing the catalytic property of donor-acceptor charge-separated systems (He et al., 2017).

It is a well-accepted idea that alkali guest atoms can easily form charge-separated donor-acceptor systems with carbon allotropes (Ohkubo et al., 2012; Wang et al., 2012; Yang et al., 2019a). Recently, our group discovered that carbon allotropes with alkali guest atoms can form non-charge-separated states, like caged-electron states in endohedral fullerenes (Yang et al., 2019b), split-electron states in endohedral fullerenes (Yang and Cederbaum, 2021a), and encircled-electron states in carbon rings (Yang and Cederbaum, 2021b). By electronically exciting an endocircular Li carbon ring system, the interaction between the carbon rings and the Li guest atom can shift from donor-acceptor essentially electrostatic interaction to van der waals interaction and vise versa (Yang and Cederbaum, 2021b). This unique property of the Li atom points to potential applications as a catalyst.

With different interaction effects between Li and the carbon rings in different electronic states, the system would prefer different positions of the guest Li. Our calculations on the neutral Li@C$_{12}$

showed that it possesses D_{6h} symmetry in its electronic ground state, indicating that finding the correct geometry of this endocircular system is still a challenge for the popular density functional theory (DFT), which predicts an off-center geometry of the neutral Li@C_{12} (Yang and Cederbaum, 2021b). Hence it is necessary to optimize the Li carbon ring geometries by employing state-of-the-art high level *ab initio* methods, to obtain reliable geometries (Yang and Cederbaum, 2021b). Due to the considerable amount of computational resources required by high-level methods, one can only optimize relatively small endocircular Li carbon ring systems. In this paper, we focus on computing accurately the geometries and electronic structures of next smallest example, i.e., neutral Li@C_{16}, which is expected to exhibit an off-center endocircular structure (Yang and Cederbaum, 2021b).

II COMPUTATIONAL DETAILS

The C_{16} carbon ring is formed by short and long bonds, which we just call for simplicity triple and single bonds, repectively. Acoording to our calculations there are three structures of planar off-center neutral Li@C_{16} with different off-center Li positions. To lower the total energy of the system, Li can move from the center of the ring towards one of the single C-C bonds, one of the triple C-C bonds, or towards one of the C atoms. The first two structures are found to be in C_{2v} symmetry and the last one is in C_s symmetry.

By employing the state-of-the-art equation-of-motion coupled-cluster singles and doubles method for electron affinities (EA-EOM-CCSD) (Nooijen and Bartlett, 1995) with the CFOUR code (Matthews et al., 2020), we optimized the geometries of ground states of neutral Li@C_{16} isomers in C_{2v} symmetry. The basis sets used are Dunning correlation-consistent triple-zeta basis sets (cc-pVTZ). (Dunning, 1989; Prascher et al., 2011).

We employ the corresponding cationic wavefunction of Li$^+$@C_{16} as the reference wavefunction of the EA-EOM-CCSD calculations, since these cationic closed-shell systems are suitable reference states for describing the binding of an additional electron and thus for the calculations of the ground and excited states of the neutral Li@C_{16} system. In this paper, the electron binding energy (EBE) is referred to as the energy gain of the neutral Li@C_{16} systems obtained by adding an electron to its cation in the respective geometry of the neutral system. This electron is addressed as the excess electron. At the optimized geometries, we also calculated the single point energies of the low-lying states of neutral Li@C_{16} at EA-EOM-CCSD/cc-pVTZ level. The core orbitals of C and Li atoms were not frozen in all the EA-EOM-CCSD studies.

Due to the high computational cost involved, we did not carry out the geometry optimization of neutral Li@C_{16} in C_s symmetry with the EA-EOM-CCSD method. Instead, we employed the density functional theory. The performance of various DFT functionals for carbon rings has been discussed in several studies (Jin et al., 2015; Kaiser et al., 2019). Most DFT functionals have been found to be unreliable in treating
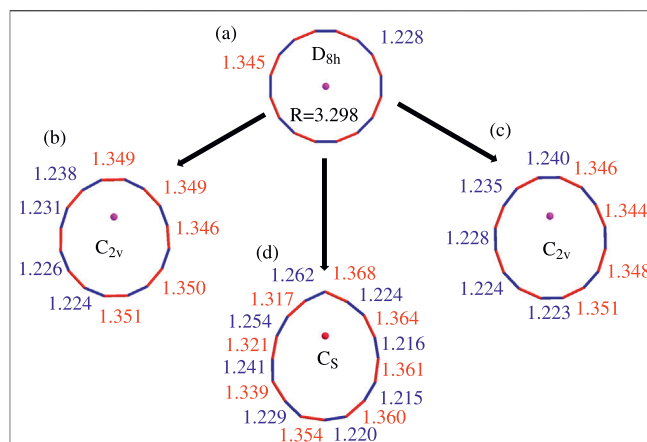

FIGURE 1 | Computed optimized geometries of the ground state of neutral Li@C_{16}. **(A)** In D_{8h} symmetry (at EA-EOM-CCSD/cc-pVTZ level). **(B)** In C_{2v} symmetry with off-center Li$^+$ towards the single C-C bond (at EA-EOM-CCSD/cc-pVTZ level). **(C)** In C_{2v} symmetry with off-center Li$^+$ towards the triple C-C bond (at EA-EOM-CCSD/cc-pVTZ level). **(D)** In C_s symmetry with off-center Li$^+$ towards one carbon atom (at ωB97XD/cc-pVTZ level). The bonds colored in red and blue are the single and triple C-C bonds, respectively.

carbon ring systems. The ωB97XD (Chai and Head-Gordon, 2008) functional has been found to perform well predicting the correct polyynic geometry of the ground state of cyclo [18] carbon ring system (Baryshnikov et al., 2019; Liu et al., 2020). It has been just now applied to another endocircular lithium carbon ring system by other researchers (Liu et al., 1872022). Accordingly, we employed here ωB97XD with the cc-pVTZ basis set, using the Gaussian 09 package (Frisch et al., 2009). For completeness we also optimized the C_{2v} structures by employing this DFT method and compare them with those obtained via the EA-EOM-CCSD method.

III RESULTS AND DISCUSSION

A The Equilibrium Geometries of Li@C_{16}

Planar even number carbon rings C_n have attracted considerable attentions (Prinzbach et al., 2006; Jin et al., 2015; Baryshnikov et al., 2019; Kaiser et al., 2019; Liu et al., 2020). These species can be divided into two classes, i.e., C_{4m+2} and C_{4m}, where m is a natural number. The former ones may possess aromaticity property, resulting in cumulenic geometry formed by double C-C bond only, since they satisfy Hückel's rule (Arulmozhiraja and Ohno, 2008; Heaton-Burgess and Yang, 2010). The latter ones are polyynic and do not satisfy this rule, forming alternating single and triple C-C bonds. As a well investigated example, theoretical studies on neutral C_{20} show that its geometry is polyynic (Jin et al., 2015; Yang and Cederbaum, 2020).

There are amazingly few papers focusing on endocircular carbon rings. In our previous study (Yang and Cederbaum, 2021b), we have optimized the electronic ground state equilibrium geometry of Li@C_{16} in D_{8h} symmetry. As shown in **Figure 1A**, the equilibrium structure is polyynic with

alternating single and triple bonds. As the electronic ground state possesses a charge-separated nature, where Li appears as a cation and the carbon ring is negatively charged, it is likely that the Li is off-center in this system in order to minimize the energy. Indeed, the EA-EOM-CCSD computations showed that at D_{8h}, where the Li is at the center of the ring, the system possesses imaginary frequencies, indicating that structures with in-plane off-center Li^+ cation are energy favored. However, a reliable ground state geometry of $Li@C_{16}$ with an off-center guest Li^+ cation, which certainly distorts the C_{16} ring is still unknown.

A.1 Results

According to our extended search, there are three possible structures of off-center neutral $Li@C_{16}$, two in C_{2v} symmetry and one in C_s symmetry. The two structures in C_{2v} symmetry differ in the off-center position of the Li^+ cation, see structures (B) and (C) in **Figure 1**. Their Li^+ cations moved from the center towards a single and a triple bond, respectively. Differently, the Li^+ cation of structure in C_s symmetry moved from the center towards a carbon atom as shown (D) in **Figure 1**.

In contrast to the highly symmetric structure (A) where all triple bonds (colored in blue in **Figure 1**) and all single bonds (colored in red in **Figure 1**) have the same length, this is clearly not the case for the other structures. In particular, in structure (B) the bond lengths of the four triple C-C bonds which are closer to the off-center Li^+ cation are longer, while the other four triple C-C bonds are shorter than their counterparts in structure (A). In contrast, nearly all the single C-C bonds in structure (B) are longer than their counterparts in structure (A).

For the second C_{2v} geometry seen in structure (C), one can see that the triple C-C bonds have undergone similar changes in comparison to structure (A). The bond lengths of the triple C-C bonds closer to the off-center Li^+ cation are elongated while the bond lengths of the single C-C bonds in particular those closer to the Li^+ (upper part of **Figure 1C**) became considerably longer than their counterparts in the highly symmetric structure (A).

The distortion of the carbon ring of structure (D) which possesses C_s symmetry is more significant than in the C_{2v} structures (B) and (C). In particular, the uppermost carbon atom in **Figure 1D** is pushed out such that the upper five carbon atoms nearly form a triangular shape. In spite of the strong changes the ring experienced in (D) compared to the highly symmetric structure (A), it is noteworthy that the various bonds are still alternating and can be classified in shorter and longer (or triple and single) bonds. In the next subsection we attempt to quantify the distortions of the C_{2v} and C_s structures.

The coordinates of all optimized geometries computed in this paper by EA-EOM-CCSD and DFT are shown in **Supplementary Tables S1, S2**, respectively. We have also computed the vibrational frequencies at EA-EOM-CCSD level for structures (a), (b) and (c) and at DFT level for all the four structures. The results are collected in **Supplementary Tables S3, S4**, respectively. Based on the frequency calculations, one finds that the structures (a) and (b) are saddle points, while structures (c) and (d) are minima on the potential energy surface.

A.2 Discussion and Comparison Between Equation-of-Motion Coupled-Cluster and Density Functional Theory

In the structures (b), (c), and (d) the Li^+ cation is off-center and the carbon ring is distorted. To better understand the differences of the distortion in the various structures, we would like to introduce simple quantities which quantify the situation and compare the results for the structures computed by the EA-EOM-CCSD and DFT methods.

We investigate two quantities. The first one is the distance between the Li^+ ion and the center of the carbon ring. As the center we take the center of mass of the ring (without Li) and as the masses are all the same and the ring is planar, we simply have

$$x_{center} = \frac{\sum x_i}{N},$$
$$y_{center} = \frac{\sum y_i}{N}, \tag{1}$$

where (x_i, y_i) are the coordinates of ith carbon atom in the plane and N is the number of carbon atoms. The coordinates of center of mass which we obtained are shown in **Supplementary Tables S1, S2**. With these coordinates of the center of the ring, one can calculate the distance $R_{Li-center}$ between the Li^+ cation and the center of the ring.

Apart from the Li^+ cation which is shifted off-center as described by $R_{Li-center}$, we investigate a second measure which describes the distortion of the carbon ring. For that, we calculate the standard deviation σ_r of the carbon-center distances:

$$\sigma_r = \sqrt{\frac{\sum_{i=1}^{N}(r_i - R)^2}{N}}, \tag{2}$$

where N is the number of carbon atoms in the system and r_i and R are the carbon-center distance of ith C atom and the average carbon-center distance, respectively. The results for all the four structures are shown in **Table 1**.

As one can see from **Table 1**, the overall distortion is growing along the structures (A), (B), (C), and (D) and this applies to both the shift of the Li^+ cation away from the center and the distortion of the carbon ring itself. As mentioned above, optimized geometries are available for all structures on the DFT level and, except for the structure (D) which is of C_s symmetry, also on the EA-EOM-CCSD level of theory. For the two structures (B) and (C) of C_{2v} symmetry the distortion is clearly larger if the geometry is optimized on the EA-EOM-CCSD level of theory.
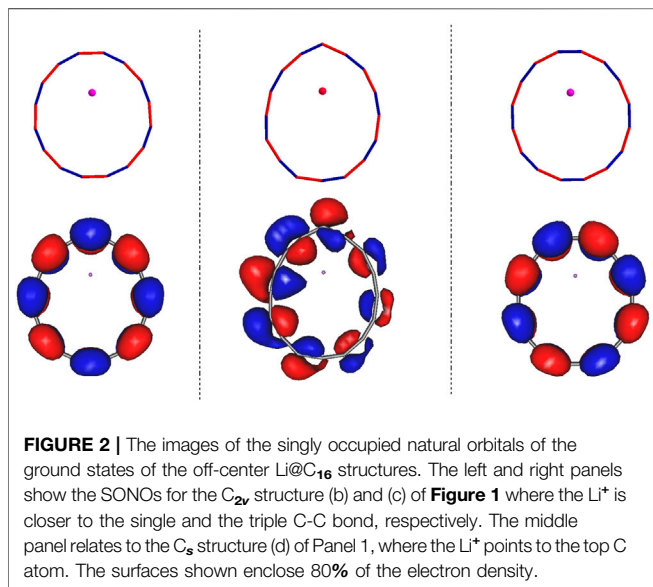
The structure (D) is particularly intersting. Compared to the two structures in C_{2v} symmetry at DFT level, the structure (D) in C_s symmetry possesses a slightlier larger $R_{Li-center}$ but a much larger σ_r than all the other systems. This larger σ_r is the result of narrowing the ring on one side and elongating it on the other (see **Figure 1**). We will further illuminate the uniqueness of the structures in the following section.

B The Singly Occupied Natural Orbitals of $Li@C_{16}$ in Different Geometries

In all the structures discussed above the Li has donated an electron to the carbon ring resulting in ionic bonding. The

TABLE 1 | The distance $R_{Li-center}$ between the Li^+ cation and the center of the carbon ring, and the standard deviation σ_r of the distances of the carbon atoms and the ring center of the $Li@C_{16}$ systems studied here. These quantities serve as a measure for the distortion of the structure considered. It is clearly seen that the distortion is growing along the structures (A), (B), (C), and (D) and that it is larger if the geometry is optimized on the EA-EOM-CCSD level of theory. The coordinates used are those of the optimized geometries at both EA-EOM-CCSD and DFT level of theory, see text. The data of struture (A) are taken from (Yang and Cederbaum, 2021b). B. The singly occupied natural orbitals of $Li@C_{16}$ in different geometries.

	Structure (A)	Structure (B)	Structure (C)	Structure (D)
$R_{Li-center}$ at EA-EOM-CCSD level (Å)	0.000	1.367	1.385	–
σ_r at EA-EOM-CCSD level (Å)	0.000	0.114	0.130	–
$R_{Li-center}$ at DFT level (Å)	0.000	1.237	1.244	1.263
σ_r at DFT level (Å)	0.000	0.112	0.117	0.236

FIGURE 2 | The images of the singly occupied natural orbitals of the ground states of the off-center $Li@C_{16}$ structures. The left and right panels show the SONOs for the C_{2v} structure (b) and (c) of **Figure 1** where the Li^+ is closer to the single and the triple C-C bond, respectively. The middle panel relates to the C_s structure (d) of Panel 1, where the Li^+ points to the top C atom. The surfaces shown enclose 80**%** of the electron density.

FIGURE 3 | The binding energies of the low-lying electronic states of $Li@C_{16}$ obtained at the EA-EOM-CCSD level of theory at the optimized geometries of the respective structures **(A–D)**. For the structures see **Figure 1** The data of $Li@C_{16}$ in D_{8h} are taken from (Yang et al., 2019b). For more details see text. Charge-separated states are shown in red and non-charge-separated (encircled-electron) states are colored in blue.

resulting singly occupied natural orbital (SONO) describes this excess electron residing on the ring in the presence of its interaction with all the other electrons. The SONOs of the stationary states of $Li@C_{16}$ on the ground electronic potential energy surface along with the corresponding geometries are shown in **Figure 2**. The left, right, and the middle panels correspond to the structures (b), (c) and (d), respectively. It is particularly relevant to notice that the SONOs of both the C_{2v} structures (b) and (c) as well as that of the highly symmetric structure (a) [see (Yang and Cederbaum, 2021b)] are vertical to the plane of the carbon ring, i.e., they form an antibonding pi-electron arrangement. The irreducible representations of these orbitals are B_2 and A_2, respectively. The reason for the different natural orbitals of structures of (b) and (c) is clear: These orbitals reflect the different relative positions between the electronic off-center Li^+ cation and the electron cloud. Due the charge-separated nature of the electronic ground energy surface of $Li@C_{16}$, electrostatic effects play an important role in the stability of this system and their impact on the ring is strongly affected by the position of Li^+ cation.

The SONO of structure (d) is of interest by itself. As shown in our previous study (Yang and Cederbaum, 2021b), the lowest two charge-separated states of $Li@C_n$ ($n = 4$ m) are quasi-degenerate
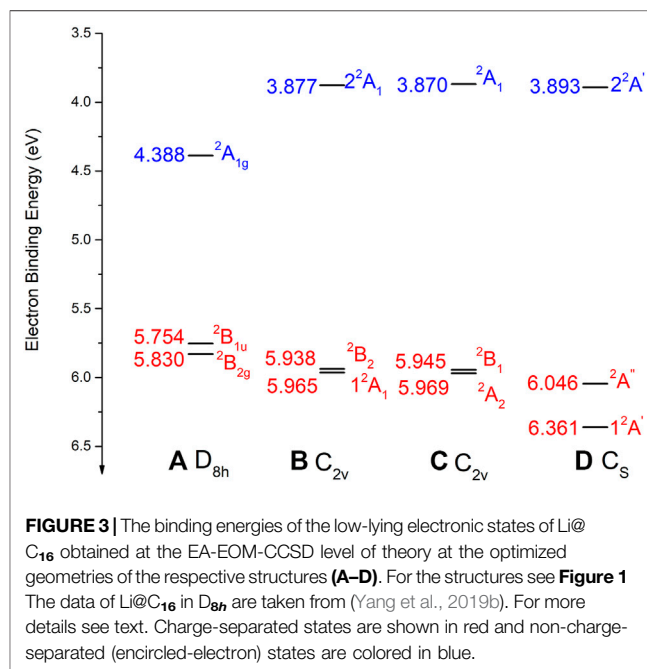
and different in symmetry. These two states are gerade and ungerade with respect to reflection through the carbon ring plane. The ungerade state possesses a SONO vertical to the carbon ring plane, while the natural orbital of gerade state is in plane. As we can see in **Figure 2**, the ungerade state is the ground state of structures in C_{2v} symmetry, which is similar to the counterpart in D_{8h} symmetry (Yang and Cederbaum, 2021b). In contrast to the C_{2v} structures, the ground state of $Li@C_{16}$ in C_s is gerade with respect to reflection through the carbon ring plane, i.e., the SONO forms an antibonding in-plane electron arrangement. It is noteworthy that due the C_s symmetry the SONO is distorted and the electron cloud on the left is larger than that on the right as shown in the middle panel of **Figure 2**. In addition, its carbon ring is narrower than the rings in the other two off-center structures. Such strong distortion of the ring in structure (d) may increase the energy of the system substantially as it increases the ring strain. Nevertheless, the structure may still be energy favored, because the total energy of the system is lowered by the resulting stronger electrostatic attraction between the

TABLE 2 | The total and relative energies of the low-lying states of the structures (a) to (d) of Li@C_{16} shown in **Figure 1**, computed at the EA-EOM-CCSD level of theory at the optimized geometries reported [i.e., optimized via EA-EOM-CCSD for structures (a), (b) and (c) and via DFT for structure (d)]. Also shown are the relative energies of the ground states of structures (a) to (d) calculated at the DFT level of theory at the geometries optimized on the DFT level. The data of structure (a) are taken from (Yang and Cederbaum, 2021b).

	Structure (a)			Structure (b)		
	$^2B_{2g}$	$^2B_{1u}$	$^2A_{1g}$	$^2B_2$	1^2A_1	2^2A_1
Total energy (a.u.)	−615.562 645	−615.559 854	−615.509 658	−615.580 837	−615.579 862	−615.504 114
Relative energy at EA-EOM-CCSD (eV)	0.499	0.575	1.941	0.004	0.030	2.091
Relative energy at DFT level (eV)	0.354	–	–	0.002	–	–
	Structure (c)			Structure (d)		
	$^2A_2$	$^2B_1$	$^2A_1$	$1^2A'$	$^2A'$	$2^2A'$
Total energy (a.u.)	−615.580 971	−615.580 104	−615.503 831	−615.576 574	−615.564 247	−615.483 727
Relative energy at EA-EOM-CCSD level (eV)	0.000	0.024	2.099	0.120	0.455	2.646
Relative energy at DFT level (eV)	0.000	–	–	−0.033	–	–

negatively charged ring and the Li$^+$ cation. The combination of both effects results in this low-symmetry structure (d).

The question arises: Which structure is the global minimum among the structures (c), and (d)? We will attempt to provide an answer in the next subsection.

C The Low-Lying Electronic States of Li@ C_{16} in Different Structures

The low-lying electronic states of Li@C_{16} have been computed for all the structures discussed above at the EA-EOM-CCSD level of theory. The resulting EBEs, i.e., the electron binding energies gained by adding an electron to the closed-shell Li$^+$@C16 cation at the respective geometry, are collected in **Figure 3**. As already investigated in our previous study (Yang and Cederbaum, 2019b), there are two kinds of electronic states in all Li@C_n endocircular systems. Charge-separated states as discussed above and non-charge-separated states called encircled-electron states where Li and the carbon ring are both neutral. In larger rings the latter states can be rather low-lying in energy. This is not the case for the still too small ring in Li@C_{16}.

As seen in **Figure 3**, all the low-lying charge-separated states of the off-center structures (b), (c) and (d) possess higher binding energies than the at-center structure of D_{8h} symmetry and these EBEs grow with the distortion of the ring. This trend is obviously due to the growing electrostatic interaction of Li$^+$ and the negatively charged ring. In contrast to this trend of the charge-separated states, the EBEs of the non-charge-separated encircled-electron states of these species decrease in value along the same structures. This finding is in accord with the fact that the EBEs of the latter states are largest for highly symmetric structures (Yang and Cederbaum, 2021b) and thus decrease the more the SONOs are distorted by the off-center cation.

It is noteworthy that the EBEs of the electronic ground states of structures (b) and (c) are similar in value. Moreover, the two lowest-lying states are quasi-degenerate as their relative energy roughly amounts to only 0.03 eV. The structure (c) is slightly energy favored. The electronic ground state of structure (d) possesses the highest EBE among the found structures. Its electronic ground state is lower in energy than its first excited state by 0.32 eV. Clearly, the highly distorted ring geometry has a stronger influence on state lying in the plane than on the one vertical to the plane.

The total energies of the electronic ground and excited states of all structures investigated are collected in **Table 2**. These energies have been computed on the EA-EOM-CCSD level at the optimized geometries reported above. As can be seen, the ground state energies of all the structures with off-center Li$^+$ are rather close to each other. According to the present calculations, the ground state of structure (c) is lowest in energy among all the species, but the electronic ground state potential energy surface connecting all the computed structures is rather flat. The ground state energy of (b) is nearly the same as that of (c) and that of (d) is 0.1 eV higher than that of (c). However, we have to remember that in contrast to the structures (a), (b), and (c) which have been optimized on the EA-EOM-CCSD level, the geometry of (d) has been optimized due to cost reasons on the DFT level. On the DFT level, (d) is the global minimum and it is seen from the EA-EOM-CCSD data in **Table 2** that either this is incorrect or the DFT geometry is rather imprecise so that the above mentioned 0.1 eV can be overcompensated by a geometry shift. Indeed, for the C_{2v} structures (b) and (c) it has been found that the DFT calculations underestimate the overall distortion (see **Section A.2**) and this can also be expected for structure (d). The question which of the structures (c) or (d) relates to the global minimum still remains open.

IV CONCLUSION

Non-covalent interactions, such as in charge-separated donor-acceptor complexes and in non-charge-separated van der waals systems, plays an important role in the field of catalysis. The carbon allotropes accommodating guest atoms have promising applications in this field, since these compounds may possess these two kinds of non-covalent interactions. In this paper we studied the off-center geometry of one of these promising species Li@C_{16}.

We have performed an extended search for stationary structures of neutral Li@C_{16} and found that there are three structures with Li$^+$ off-center and a negatively charged carbon ring rather close in energy. By employing a state-of-the-art equation-of-motion coupled-cluster method, we have optimized the geometries of two of the three possible off-center structures of the neutral

endocircular Li@C$_{16}$ system and due to cost reasons the third, low symmetry structure, has been optimized by a suitable DFT method. All the structures are showing alternating single and triple C-C bond pattern, regardless of the position of Li$^+$ cation. Moreover, all the structures are considerably distorted by the off-center Li$^+$ cation. The similar energies of the structures and their distortions show that the carbon rings are rather flexible which can be considered as an interesting property of the endocircular systems. Since the energy landscape is shallow and the geometries of energetically nearby structures are very different, one encounters at finite temperature severe large amplitude motion of both the nagetively charged carbon ring and of the Li cation.

In addition to the geometries of the structures we have also calculated the total energies and the binding energies of the low-lying electronic states of the three structures at their respective optimized geometries employing the state-of-the-art equation-of-motion coupled-cluster method. The calculations show that charge-separated as well as encircled-electron states are among the low-lying electronic states of each of the structures. The charge-separated states are favored energetically. The structures are the result of the balance between the ionic attraction of Li$^+$ and the negatively charged ring and the energy paid by distorting the ring.

The singly occupied natural orbitals describing the excess electron on the carbon ring in the presence of all other electrons have been computed and analyzed. The analysis sheds light on the different structures found. There is a one to one relationship between such a natural orbital and the structure. This makes clear why several structures close by in energy are to be expected on the electronic potential energy surface.

Until now there are no experimental studies on endocircular Li@C$_n$ and we hope that the interesting results found will stimulate such studies.

DATA AVAILABILITY STATEMENT

The original contributions presented in the study are included in the article/**Supplementary Material**, further inquiries can be directed to the corresponding author.

AUTHOR CONTRIBUTIONS

Y-FY carried out the numerical calculations. Both authors have contributed equally to the analysis of the results and the writing of manuscript.

FUNDING

ACKNOWLEDGMENTS

SUPPLEMENTARY MATERIAL

The Supplementary Material for this article can be found online at: https://www.frontiersin.org/articles/10.3389/fchem.2022.813563/full#supplementary-material

REFERENCES

Arulmozhiraja, S., and Ohno, T. (2008). CCSD Calculations on C14, C18, and C22 Carbon Clusters. *J. Chem. Phys.* 128, 114301. doi:10.1063/1.2838200

Baryshnikov, G. V., Valiev, R. R., Kuklin, A. V., Sundholm, D., and Ågren, H. (2019). Cyclo[18]carbon: Insight into Electronic Structure, Aromaticity, and Surface Coupling. *J. Phys. Chem. Lett.* 10, 6701–6705. doi:10.1021/acs.jpclett.9b02815

Bawari, S., Pal, S., Pal, S., Mondal, J., and Narayanan, T. N. (2019). Enhanced photo-electrocatalytic hydrogen generation in graphene/hbn van der waals structures. *J. Phys. Chem. C* 123 (28), 17249–17254. doi:10.1021/acs.jpcc.9b01996

Biroju, R. K., Das, D., Sharma, R., Pal, S., Mawlong, L. P. L., Bhorkar, K., et al. (2017). Hydrogen Evolution Reaction Activity of Graphene-MoS2 van der Waals Heterostructures. *ACS Energ. Lett.* 2, 1355–1361. doi:10.1021/acsenergylett.7b00349

Chai, J.-D., and Head-Gordon, M. (2008). Long-range Corrected Hybrid Density Functionals with Damped Atom-Atom Dispersion Corrections. *Phys. Chem. Chem. Phys.* 10, 6615–6620. doi:10.1039/B810189B

D'Souza, F., and Ito, O. (2009). Supramolecular Donor-Acceptor Hybrids of Porphyrins/phthalocyanines with Fullerenes/carbon Nanotubes: Electron Transfer, Sensing, Switching, and Catalytic Applications. *Chem. Commun.*, 4913–4928. doi:10.1039/B905753F

Dunning, T. H., Jr. (1989). Gaussian Basis Sets for Use in Correlated Molecular Calculations. I. The Atoms boron through Neon and Hydrogen. *J. Chem. Phys.* 90, 1007–1023. doi:10.1063/1.456153

Frisch, M. J., Trucks, G. W., Schlegel, H. B., Scuseria, G. E., Robb, M. A., Cheeseman, J. R., et al. (2009). *Gaussian, 09 Revision E.01*. Wallingford CT: Gaussian Inc.

Georgakilas, V., Tiwari, J. N., Kemp, K. C., Perman, J. A., Bourlinos, A. B., Kim, K. S., et al. (2016). Noncovalent Functionalization of Graphene and Graphene Oxide for Energy Materials, Biosensing, Catalytic, and Biomedical Applications. *Chem. Rev.* 116, 5464–5519. doi:10.1021/acs.chemrev.5b00620

Guo, Y., Liu, J., Yang, Q., Ma, L., Zhao, Y., Huang, Z., et al. (2020). Metal-tuned Acetylene Linkages in Hydrogen Substituted Graphdiyne Boosting the Electrochemical Oxygen Reduction. *Small* 16, e1907341. doi:10.1002/smll.201907341

He, T., Gao, G., Kou, L., Will, G., and Du, A. (2017). Endohedral Metallofullerenes (M@C60) as Efficient Catalysts for Highly Active Hydrogen Evolution Reaction. *J. Catal.* 354, 231–235. doi:10.1016/j.jcat.2017.08.025

Heaton-Burgess, T., and Yang, W. (2010). Structural Manifestation of the Delocalization Error of Density Functional Approximations: C4N+2 Rings and C20 Bowl, Cage, and Ring Isomers. *J. Chem. Phys.* 132, 234113. doi:10.1063/1.3445266

Hu, P., Su, H., Chen, Z., Yu, C., Li, Q., Zhou, B., et al. (2017). Selective Degradation of Organic Pollutants Using an Efficient Metal-free Catalyst Derived from Carbonized Polypyrrole via Peroxymonosulfate Activation. *Environ. Sci. Technol.* 51, 11288–11296. doi:10.1021/acs.est.7b03014

Jin, Y., Perera, A., Lotrich, V. F., and Bartlett, R. J. (2015). Coupled Cluster Geometries and Energies of C20 Carbon Cluster Isomers - A New Benchmark Study. *Chem. Phys. Lett.* 629, 76–80. doi:10.1016/j.cplett.2015.04.006

Kaiser, K., Scriven, L. M., Schulz, F., Gawel, P., Gross, L., and Anderson, H. L. (2019). An Sp-Hybridized Molecular Carbon Allotrope, Cyclo[18]carbon. *Science* 365, 1299–1301. doi:10.1126/science.aay1914

Kumar, D., Pal, S., and Krishnamurty, S. (2016). N2 Activation on Al Metal Clusters: Catalyzing Role of BN-Doped Graphene Support. *Phys. Chem. Chem. Phys.* 18, 27721–27727. doi:10.1039/C6CP03342C

Lim, G. N., Obondi, C. O., and D'Souza, F. (2016). A High-Energy Charge-Separated State of 1.70 eV from a High-Potential Donor-Acceptor Dyad: A Catalyst for Energy-Demanding Photochemical Reactions. *Angew. Chem.* 128, 11689–11693. doi:10.1002/ange.201606112

Liu, Z., Lu, T., and Chen, Q. (2020). An Sp-Hybridized All-Carboatomic Ring, Cyclo[18]carbon: Electronic Structure, Electronic Spectrum, and Optical Nonlinearity. *Carbon* 165, 461–467. doi:10.1016/j.carbon.2020.05.023

Liu, Z., Wang, X., Lu, T., Yuan, A., and Yan, X. (1872). Potential Optical Molecular Switch: Lithium@cyclo[18]carbon Complex Transforming between Two Stable Configurations. *Carbon* 187, 78–85. doi:10.1016/j.carbon.2021.11.005

Matthews, D. A., Cheng, L., Harding, M. E., Lipparini, F., Stopkowicz, S., Jagau, T.-C., et al. (2020). "CFOUR, Coupled-Cluster Techniques for Computational Chemistry, a Quantum-Chemical Program Package," *J. Chem. Phys.* 152, 214108. doi:10.1063/5.0004837 Watts and the integral packages MOLECULE (J. Almlöf and P.R. Taylor), PROPS (P.R. Taylor), ABACUS (T. Helgaker, H.J. Aa. Jensen, P. Jørgensen, and J. Olsen), and ECP routines by A. V. Mitin and C. van Wüllen. For the current version, see http://www.cfour.de.

Meng, X., Wang, L., Chen, L., Xu, M., Liu, N., Zhang, J., et al. (2020). Charge-separated Metal-Couple-Site in NiZn alloy Catalysts towards Furfural Hydrodeoxygenation Reaction. *J. Catal.* 392, 69–79. doi:10.1016/j.jcat.2020.10.003

Nooijen, M., and Bartlett, R. J. (1995). Equation of Motion Coupled Cluster Method for Electron Attachment. *J. Chem. Phys.* 102, 3629–3647. doi:10.1063/1.468592

Ohkubo, K., Kawashima, Y., and Fukuzumi, S. (2012). Strong Supramolecular Binding of Li+@C60 with Sulfonated Meso-Tetraphenylporphyrins and Long-Lived Photoinduced Charge Separation. *Chem. Commun.* 48, 4314–4316. doi:10.1039/C2CC31186K

Prascher, B. P., Woon, D. E., Peterson, K. A., Dunning, T. H., and Wilson, A. K. (2011). Gaussian Basis Sets for Use in Correlated Molecular Calculations. Vii. Valence, Core-Valence, and Scalar Relativistic Basis Sets for Li, Be, Na, and Mg. *Theor. Chem. Acc.* 128, 69–82. doi:10.1007/s00214-010-0764-0

Prinzbach, H., Wahl, F., Weiler, A., Landenberger, P., Wörth, J., Scott, L. T., et al. (2006). C20 Carbon Clusters: Fullerene-Boat-Sheet Generation, Mass Selection, Photoelectron Characterization. *Chem. Eur. J.* 12, 6268–6280. doi:10.1002/chem.200501611

Rudolf, M., Kirner, S. V., and Guldi, D. M. (2016). A Multicomponent Molecular Approach to Artificial Photosynthesis - the Role of Fullerenes and Endohedral Metallofullerenes. *Chem. Soc. Rev.* 45, 612–630. doi:10.1039/C5CS00774G

Serp, P., Corrias, M., and Kalck, P. (2003). Carbon Nanotubes and Nanofibers in Catalysis. *Appl. Catal. A: Gen.* 253, 337–358. doi:10.1016/S0926-860X(03)00549-0

Sherigara, B. S., Kutner, W., and D'Souza, F. (2003). Electrocatalytic Properties and Sensor Applications of Fullerenes and Carbon Nanotubes. *Electroanalysis* 15, 753–772. doi:10.1002/elan.200390094

Singh, S. K., Kumar, D., Dhavale, V. M., Pal, S., and Kurungot, S. (2016). Strategic Preparation of Efficient and Durable NiCo Alloy Supported N-Doped Porous Graphene as an Oxygen Evolution Electrocatalyst: A Theoretical and Experimental Investigation. *Adv. Mater. Inter.* 3, 1600532. doi:10.1002/admi.201600532

Sun, Y., Terrones, M., and Schaak, R. E. (2021). Colloidal Nanostructures of Transition-Metal Dichalcogenides. *Acc. Chem. Res.* 54, 1517–1527. doi:10.1021/acs.accounts.1c00006

Umadevi, D., Panigrahi, S., and Sastry, G. N. (2014). Noncovalent Interaction of Carbon Nanostructures. *Acc. Chem. Res.* 47, 2574–2581. doi:10.1021/ar500168b

Wang, J., Liao, K.-S., Früchtl, D., Tian, Y., Gilchrist, A., Alley, N. J., et al. (2012). Nonlinear Optical Properties of Carbon Nanotube Hybrids in Polymer Dispersions. *Mater. Chem. Phys.* 133, 992–997. doi:10.1016/j.matchemphys.2012.02.003

Xiang, Q., Yu, J., and Jaroniec, M. (2012). Graphene-based Semiconductor Photocatalysts. *Chem. Soc. Rev.* 41, 782–796. doi:10.1039/C1CS15172J

Yan, Q.-L., Gozin, M., Zhao, F.-Q., Cohen, A., and Pang, S.-P. (2016). Highly Energetic Compositions Based on Functionalized Carbon Nanomaterials. *Nanoscale* 8, 4799–4851. doi:10.1039/C5NR07855E

Yang, Y.-F., and Cederbaum, L. S. (2020). Bound States and Symmetry Breaking of the Ring C20− Anion. *J. Chem. Phys.* 152, 244307. doi:10.1063/5.0012926

Yang, Y.-F., and Cederbaum, L. S. (2021a). Caged-electron States and Split-Electron States in the Endohedral Alkali C60. *Phys. Chem. Chem. Phys.* 23, 11837–11843. doi:10.1039/D1CP01341F

Yang, Y. F., and Cederbaum, L. S. (2021b). Endocircular Li Carbon Rings. *Angew. Chem. Int. Ed.* 60, 16649–16654. International edition doi:10.1002/anie.202105222, German edition doi:10.1002/ange.202105222

Yang, Y.-F., Gromov, E. V., and Cederbaum, L. S. (2019a). Caged-electron States in Endohedral Li Fullerenes. *J. Phys. Chem. Lett.* 10, 7617–7622. doi:10.1021/acs.jpclett.9b02934

Yang, Y.-F., Gromov, E. V., and Cederbaum, L. S. (2019b). Charge Separated States of Endohedral Fullerene Li@C20. *J. Chem. Phys.* 151 (11), 114306. doi:10.1063/1.5120017

Advantages of publishing in Frontiers

OPEN ACCESS
Articles are free to read for greatest visibility and readership

FAST PUBLICATION
Around 90 days from submission to decision

HIGH QUALITY PEER-REVIEW
Rigorous, collaborative, and constructive peer-review

TRANSPARENT PEER-REVIEW
Editors and reviewers acknowledged by name on published articles

Frontiers
Avenue du Tribunal-Fédéral 34
1005 Lausanne | Switzerland

Visit us: www.frontiersin.org
Contact us: frontiersin.org/about/contact

REPRODUCIBILITY OF RESEARCH
Support open data and methods to enhance research reproducibility

DIGITAL PUBLISHING
Articles designed for optimal readership across devices

FOLLOW US
@frontiersin

IMPACT METRICS
Advanced article metrics track visibility across digital media

EXTENSIVE PROMOTION
Marketing and promotion of impactful research

LOOP RESEARCH NETWORK
Our network increases your article's readership